Cerebral vascular patterns associated with theta and gamma rhythms during unrestrained behavior and REM sleep

Antoine Bergel

To cite this version:

Antoine Bergel. Cerebral vascular patterns associated with theta and gamma rhythms during unrestrained behavior and REM sleep. Neurobiology. Université Sorbonne Paris Cité, 2016. English. NNT : 2016USPCC239 . tel-01799067

HAL Id: tel-01799067
https://theses.hal.science/tel-01799067
Submitted on 24 May 2018

Thèse de Doctorat de l'Université Sorbonne Paris Cité
Préparée à l'Université Paris Diderot

Ecole Doctorale 474
Interdiscplinaire Européenne Frontières du Vivant

Laboratoire Neuroscience Paris Seine
Equipe Réseaux Corticaux et Couplage Neurovasculaire

Cerebral Vascular Patterns associated with theta and gamma rhythms during unrestrained behavior and REM sleep

Study by functional Ultrasound and Electroencephalography

Par Antoine BERGEL

Thèse de Doctorat de Sciences du Vivant
dirigée par Bruno CAULI et Ivan COHEN

Présentée et soutenue publiquement à Paris le 13 décembre 2016

Président du Jury :	Michael ZUGARO	Directeur de Recherche	Collège de France
Rapporteurs :	Valérie EGO-STENGEL	Chargée de Recherche	UNIC CNRS
	Bruno POUCET	Chargé de Recherche	Univ. Aix-Marseille
Examinateurs :	Jérôme EPSZTEIN	Chargé de Recherche	INMED Marseille
	Desdemona FRICKER	Chargée de Recherche	CNPP Paris V
Co-directeurs de thèse :	Bruno CAULI	Directeur de Recherche	UPMC
	Ivan COHEN	Chargé de Recherche	UPMC

Titre de la thèse : Réponses hémodynamiques cérébrales associées aux rythmes thêta et gamma lors du mouvement libre et du sommeil paradoxal

Résumé : Le rythme thêta est un rythme cérébral associé à l'activité locomotrice et au sommeil paradoxal. Bien que son implication dans la communication entre régions du cerveau et processus mnésiques ait largement été démontrée, il persiste un manque de données extensives dû à la difficulté d'imager l'ensemble de l'activité cérébrale dans des conditions naturelles de locomotion et d'exploration. Dans cette thèse, j'ai développé une approche qui combine l'enregistrement des potentiels de champs locaux à l'imagerie ultrasonore fonctionnelle (fUS) sur l'animal en mouvement libre. Pour la première fois, j'ai pu révéler les réponses hémodynamiques associées au rythme thêta dans la plupart des structures du système nerveux central avec de bonnes résolutions spatiale (100 x 100 x 400 μm) et temporelle (200 ms). Pendant la locomotion et le sommeil, les variations hémodynamiques de l'hippocampe, du thalamus dorsal et du cortex (retrosplenial, somatosensoriel) corrèlent fortement avec la puissance instantanée du signal thêta hippocampique, avec un décalage temporel variant de 0.7 s à 2.0 s selon les structures. De manière intéressante, les rythmes gamma hippocampiques moyen (55-95 Hz) et rapide (100-150 Hz) expliquent la variance des signaux hémodynamiques mieux que le seul rythme thêta, alors que le rythme gamma lent (30-50 Hz) est non pertinent. L'hyperémie fonctionnelle de l'hippocampe suit séquentiellement la boucle tri-synaptique (gyrus denté - région CA3 - région CA1) et se renforce considérablement à mesure que la tâche progresse. Lors du sommeil paradoxal, j'ai observé une hyperémie tonique globale ainsi que des activations phasiques de grande amplitude initiées dans le thalamus et terminant dans les aires corticales, que nous avons appelées "poussées vasculaires". De fortes bouffées d'activité gamma rapide (100-150 Hz) précèdent de manière robuste ces poussées vasculaires, l'inverse n'étant pas vrai. Dans l'ensemble, ces résultats révèlent la dynamique spatio-temporelle des signaux hémodynamiques associés à la locomotion et au sommeil paradoxal et suggèrent un lien fort entre rythmes thêta, gamma rapide et activité vasculaire globale.

Mots-clés : Imagerie Ultrasonore Fonctionnelle - Electroencéphalographie - Rythme Thêta - Rythme Gamma - Hémodynamique - Locomotion - Sommeil Paradoxal - Hippocampe

Thesis Title: Cerebral Vascular Patterns associated with theta and gamma rhythms during unrestrained behavior and REM sleep

Abstract: Theta rhythm is a prominent oscillatory pattern of EEG strongly associated with active locomotion and REM sleep. While it has been shown to play a crucial role in communication between brain areas and memory processes, there is a lack of extensive data due to the difficulty to image global brain activity during locomotion behavior. In this thesis, I developed an approach that combines local field potential recordings (LFP) and functional ultrasound imaging (fUS) to unrestrained rats. For the first time, I could image the hemodynamic responses associated with theta rhythm in most central nervous system (CNS) structures, with high spatial (100 x 100 x 400 μm) and temporal (200 ms) resolutions. During running and REM sleep, hemodynamic variations in the hippocampus, dorsal thalamus and cortices (S1BF, retrosplenial) correlated strongly with instantaneous theta power, with a delay ranging from 0.7 to 2.0 s after theta peak. Interestingly, mid (55-95 Hz) and high gamma (100-150 Hz) instantaneous power better explained hemodynamic variations than mere theta activity, while low-gamma (30-50 Hz) did not. Hippocampal hyperaemia followed sequentially the trisynaptic circuit (dentate gyrus - CA3 region - CA1 region) and was considerably strengthened as the task progressed. REM sleep revealed brain-wide tonic hyperaemia, together with phasic high-amplitude vascular activation starting in the dorsal thalamus and fading in cortical areas, which we referred to as “vascular surges”. Strong bursts of hippocampal high gamma (100-150 Hz) robustly preceded these surges, while the opposite was not true. Taken together, these results reveals the spatio-temporal dynamics of hemodynamics associated with locomotion and REM sleep and suggest a strong link between theta, high-gamma rhythms and brain-wide vascular activity.

Keywords: Functional Ultrasound Imaging - Electroencephalography - Theta Rhythm - Gamma Rhythm - Hemodynamics - Locomotion - REM sleep - Hippocampus

“All of old. Nothing else ever.
Ever tried. Ever failed. No matter.
Try again. Fail again. Fail better.”

Samuel Beckett, *Worstward Ho* (1982)

Remerciements

Je tiens tout d'abord a remercier les membres du jury: Bruno Poucet et Valérie Ego-Stengel d'avoir accepté de rapporter mon travail de thèse et d'avoir pris le temps de lire et corriger mon (long) manuscrit, Jérôme Epsztein, Desdemona Fricker et Michaël Zugaro pour avoir accepté d'en faire partie en qualité d'examinateur et pour leurs remarques et conseils avisés. Je tiens ensuite à remercier Bruno Cauli d'avoir accepté d'être directeur de mon travail de thèse et de l'avoir suivi avec attention, me soumettant de nombreuses idées de lecture et me proposant un recul scientifique approfondi. Enfin, je tiens à remercier Ivan Cohen, pour avoir encadré mon travail durant ces quatre longues années, riches en rebondissements. Je te remercie de m'avoir fait confiance sur ce projet ambitieux, de m'avoir appris que la recherche est un travail de longue haleine dont les fondations sont le goût des choses bien faites et la recherche d'idées nouvelles. Merci enfin de m'avoir soutenu dans mon travail.

Ces quatre années de thèse ont été une bien belle aventure, tant par les pauses-café, rencontres, discussions scientifiques et extra-scientifiques que j'ai faites au laboratoire. Je remercie toutes les personnes qui ont rendu cette expérience inoubliable. Je pense notamment aux membres de l'équipe RCCN: Bertrand, pour m'avoir écouté et soutenu, Ludo pour avoir accepté sans broncher mes vols de café intempestifs, Lim-Anna pour avoir enduré avec moi ces longues heures de chirurgie, et tous les membres passés ou présents de l'équipe: Sophie, Najete, Régine, Sandrine, Agnès, Gabrielle, Xavier. Je remercie évidemment les membres des autres équipes (notamment la mafia du fond du couloir) pour leur aide, les coups de main et le temps qu'ils m'ont accordé. Je pense notamment à Samir, Steve, Tom, Katia, Malou, Jérémie, Philippe, Julien et tous les autres. Une mention spéciale à mes deux collègues / partenaires café Mickaël et Juliette pour leur écoute dans les moments difficiles et pour m'avoir montré que malgré les difficultés qu'on rencontre en thèse, le soutien des pairs est une source d'énergie formidable.

Faire une thèse interdisciplinaire est une expérience rare par la diversité et la richesse des différentes communautés que l'on découvre. Ce fut pour moi l'occasion de connaître le fourmillant univers du CRI, qui regroupe pêle-mêle créativité, interdisciplinarité et non-conformisme. En plus des belles rencontres, j'y ai trouvé une vision de la science et de l'enseignement profondément en accord avec les valeurs que je défends. Je remercie donc tous les membres de l'équipe Frontières du Vivant qui contribuent a faire de cette Ecole Doctorale un lieu d'échange et d'apprentissage unique. Je remercie aussi les profs et membres du staff de la licence, et surtout les trois promotions d'étudiants, qui par leur liberté de penser et leur créativité ont contribué à faire de moi un meilleur enseignant. Ce projet m'a aussi permis d'interagir avec les membres de l'Institut Langevin. Merci donc à Mickaël Tanter de m'avoir permis de travailler sur ce magnifique projet des ultrasons fonctionnels et à tous les membres de l'équipe dont le savoir et la technique m'ont beaucoup apporté. Merci donc à Jean-Luc, Thomas, Charlie, Elodie et tous les autres. Je remercie enfin les deux membres de mon comité de thèse Karim Benchenane et Didier Chatenay pour le temps qu'ils m'ont consacré, leurs précieuses remarques et nombreux conseils.

A bien y réfléchir, cette thèse est le produit d'ingrédients visibles et mesurables. Comme le café, les plats Picard ou les gouttes de sueur (le travail, en somme, ce qui risque d'en étonner plus d'un). Mais elle est aussi par beaucoup d'aspects le résultat de choses moins voyantes, moins rhythmiques et moins quantifiables. C'est sûrement l'incroyable cercle d'amis qui m'accompagne depuis maintenant de nombreuses années, leur présence, leurs conseils et leur écoute qui en composent l'un des ingrédients essentiels... Un clin d'oeil donc à tous mes potes de l'ASA Maisons-Alfort, ce petit club de volley qui a tout d'une grande famille, et ses jeunes avec qui je ne suis pas prêt d'oublier les trajets du dimanche matin à traverser de l'Ile-de-France. Ensuite, parce que cette thèse a débuté quelque part entre les canapés de la K-Fet et l'organisation du FSC, merci à Alizée, Marwa, Auré, Juliane et Mehdi pour ces années macadamia, les petits voyages en Titine et les plus grands, les soirées karaoke, les repas sushi, les frites une fois, et surtout pour votre amitié sincère. Il y a ceux que j'ai rencontrés avant la thèse, à l'époque où je pensais encore qu'on est vieux à 30 ans et que les thésards ne portent exclusivement que des vestons à carreaux: Enri, Sa, Alex, Stefan my Stockholm buddies who made my Swedish years the most unforgettable time in my student life (this is something), mais aussi la team Telecom, entre Bed & Nuts, gala et poker. Nico, bien sûr, Charlot, Fred, Lulu, Cricri, et les autres, avec qui le goût de la bière, des livres et des voyages n'est pas pareil qu'avec les autres. Enfin, il y a ceux qui ont toujours été là ou alors depuis tellement longtemps qu'on n'arrive plus à (ou ne veut plus) compter, les Saint-Mauriens de longue date. Marion, merci simplement pour ta présence et ton soutien sans faille, pendant toutes ces années passées et celles à venir. Thib, de la prépa à nos discussions politiques de fin de soirée, merci d'être toujours là et pour tout le reste. Hug et Boune, les sessions kebab/piscine sont moins drôles sans vous, mais je sais qu'elles le redeviendront à Genève, au Brésil ou n'importe où. Ju merci pour ton honnêteté et ta spontanéité lors de nos sessions bière. Lud, merci pour les soirées Poker à essayer de pas gueuler trop fort quand on gagne un gros coup ! Et puis tous les autres avec qui je ne compte plus les voyages au ski, les randos, les soirées belote et le reste : Gregou, Jé, Ad, Patoche, Claire, ET, Al, Tiphaine, Blandine et tous les autres.

Enfin, je tiens à remercier ma famille. Ma mère qui depuis longtemps m'a donné le goût de la recherche et des maths et qui s'est beaucoup impliqué dans mon orientation tout au long de mes études. Voilà ce que ca donne ! Merci à mon père pour son soutien constant, sa bienveillance de père et pour avoir contribué à considérablement améliorer notre protocole de chirurgie. Merci d'être là. Enfin, mon frère et ma soeur avec qui les relations peuvent être houleuses mais que j'ai toujours autant de plaisir à retrouver pour partager discussions et éclats de rire. J'espère qu'il nous en reste encore beaucoup. Merci à vous deux pour votre soutien. Et enfin, je tiens à remercier Eva qui m'a beaucoup écouté, conseillé et soutenu tout au long de la thèse et particulièrement pendant la phase de rédaction. On a survécu à deux rédactions de thèse, franchement maintenant le reste c'est des vacances. Merci pour tout ce que tu m'apportes chaque jour, moi aussi je te dois beaucoup...

Bonne lecture !

Contents

List of Figures

List of Abbreviations

ATP	Adenosine Triphosphate
BOLD	Blood-Oxygen Level Dependent
CA1	Cornus Ammonis 1
CA2	Cornus Ammonis 2
CA3	Cornus Ammonis 3
CBF	Cerebral Blood Flow
CBV	Cerebral Blood Volume
CFC	Cross-Frequency Coupling
CTC	Communication Through Coherence
COX	Cyclo-Oxygenase
ECoG	Electrocorticography
EEG	Electroencephalography
EMG	Electromyography
fUS	functional Ultrasound
GC	Granule Cell
HbO	Oxyhemoglobin
HbR	Deoxyhemoglobin
HbT	Total Hemoglobin
HF	Hippocampal Formation
HFO	High-Frequency Oscillations
ICA	Independent Component Analysis
IOSI	Intrinsic Optical Signal Imaging
LEC	Lateral Entorhinal Cortex
LIA	Large Irregular Activity
LFP	Local Field Potential
LS	Lateral Septum
LSCI	Laser Speckle Contrast Imaging
MEC	Medial Entorhinal Cortex
MEG	Magnetoencephalography
MRI	Magnetic Resonance Imaging
MS	Medial Septum
MUA	Multi-Unit Activity
NIRS	Near-Infrared Spectroscopy
PAM	Photo-Acoustic Microscopy
PCA	Principal Component Analysis
PET	Positron-Emission Tomography
PFC	Prefrontal Cortex
PRF	Pulse Repetition Frequency

RBC	Red Blood Cells
STDP	Spike-Timing Dependent Plasticity
SVD	Singular Value Decomposition
SWR	Sharp-Wave Ripples
SWS	Slow-Wave Sleep
TPLSM	Two-Photon Laser Scanning Microscopy
US	Ultrasound
VSDI	Voltage-Sensitive Dye Imaging

Part I

Introduction

General Introduction

> "The main way in which brains actually contribute to the success of survival machines is by controlling and coordinating the contraction of muscles."
> Richard Dawkins, *The Selfish Gene* (1976)

Why do we have a brain? And why does it give us such an advantage on other species? In his famous book, Richard Dawkins gives an elegant - and provocating - answer: our brains are just the result of a vast program designed and built by our genes, for one purpose, and one purpose only: survival. He depicts our body as a "survival machine". To better explain his point of view, he compares us to a civilization in Andromeda, 200 light-years away, wanting to spread their culture to distant worlds. Because of the physical constraints on traveling such long distances, Andromedans send all the information they want to transmit in a long unbroken radio message. This message actually contains instructions on how to build a giant computer and the program to run it, in order to establish their civilization on Earth. Just as the Andromedans, our genes have to build a brain. Because, they cannot decide or anticipate what environment we will have to live into, our genes *are* this long message to build an autonomous survival machine able to adapt and cope with a changing environment: our brain [Dawkins, 1989].

This view is directly inspired from Charles Darwin century-old groundbreaking discovery of natural selection. He first postulated that all living entities have evolved in a direction that would maximize the individual survival rate over other individuals within their species [Darwin, 1866]. Hence, primitive cellular organizations have had the decisive advantage of their own protective membrane. Hence, first animals to benefit muscles have been able to move in space and conquer new environments. Hence, mammalians with a centralized organ such as a brain have been able to adapt by taking the appropriate action in an ever-changing environment. On this evolutionary scale, brain is a rather recent invention. It is however important to note that "recent" species have often evolved towards reducing the relative size of low-level organs, such as liver or lungs, and increasing the relative size of the brain, at the cost of higher energy demands.

Our brain indeed gives us a decisive advantage on plants, for instance: an additionnal degree of adaptability. While plants or insects reproduce the same scheme to grow and expand, they struggle to interpret and analyse the constraints of their changing environment. Brain allows individuals to have a self-referenced strategy and to cope differentially with their individual needs. Thus, it is not surprising that it provides us with high-level cognitive functions, such as memory, decision-making and sensorimotor processing, while keeping the control on vital functions such as thermo-regulation, energy supply and waste removal.

Studying and understanding such a complex organ is thus very challenging. We can list at least 4 major directions: 1. One must integrate highly-specialized modules encompassing multiple levels of organization across, at varying spatial and temporal scales, in a global, interactive, dynamic network. 2. One should capture all the aspects of the brain activity not focusing only on one aspect of information - neuronal for instance - denying the importance of other events. 3. One should develop tools to monitor brain activity while minimizing intrinsic experimental biases. 4. One should aim at isolating functional units, linking structure to function, in order to decrease the global complexity of the system. Hence, the scientific approach should ideally be integrative, multi-modal, ecological and functional. As Science progresses, this can be achieved by combining imaging techniques or approaches like *in vivo/in-vitro* studies. It is also crucial to bridge the gap between disciplines allowing researchers with specialized background to better communicate and work in concert to develop more comprehensive methods of investigation.

A crucial challenge we meet here is to understand how specialized regions in the brain communicate when a subject is performing a complex task. Oscillatory electrical activity is thought to be an effective solution to exchange messages reliably and to synchronize modular information contained in neuronal firing. However, little is known about the metabolic and vascular aspects of neuronal oscillations, which require sustained energy supply for a time ranging from a few seconds to several minutes. We propose here an approach to better understand this coupling and to have an insight into global hemodynamic brain patterns, during periods of intense electrical activity.

In Chapter 1, we present the current state-of-the-art about brain oscillations and neural communication. We discuss the generating mechanisms of such oscillations and their putative functions for communication in a dynamic neural network. In Chapter 2, we discuss the importance of one specific brain oscillation: theta rhythm and its functional role in spatial navigation. We will insist on the interactions between distant brain areas through the phenomenon of cross-frequency coupling. Chapter 3 will give the reader an overview of the current *in vivo* brain imaging techniques. The functional coupling between electrical events and vascular events will be presented stressing on the multiple facets and regional dependence of electrical and vascular activity throughout the brain. In Chapter 4, we describe the technical aspects of our approach: we have developed a new protocol (mfUS-EEG) including surgery, electrode-making, conditioning and synchronized recordings analysis. In Chapter 5 and Chapter 6, we will present our main results through the different articles that have been published or currently under preparation. The first article details the mfUS-EEG protocol and gives two proofs of concept. The second article deals with the dynamic spread of the vascular pattterns associated with theta and gamma rhythms. Finally, we will discuss our findings in Chapter 7, point out the limitations of our approach and give clues for further extension and new scientific questions that this work has raised.

Chapter 1

Cellular Assemblies, brain rhythms and neural communication

From the earliest studies in psychology until the most recent advances in neuro-imaging, neuroscience has made considerable progress in recording brain activity, with low to absent invasiveness, increasing power and efficiency. While the scientific community is gathering huge amount of data on brain activity, the analysis and understanding of those signals is far from complete. This stems from the peculiar fact that the code used by neurons to communicate remains elusive.

In this chapter, I will provide evidence in favor of a central place for brain oscillations in neural communication. I will first present electroencephalography, from its origin to recent advances in high-density recordings, discussing the origin and relative contribution of cellular events to the recorded signal. Then, I will develop on the notions of cell assemblies and brain rhythms. Finally, I will discuss the phenomenon of phase synchronization between distant brain regions as a candidate for neural communication.

1.1 Electroencephalography

Electroencephalography is the parent of all imaging techniques, since the pioneering work of Richard Caton, first reported in 1875. Its ease of use, low cost, low-to-absent invasiveness (whether the electrode is inserted in the tissue or not) and high temporal resolution make it a popular tool to record the electrical activity of neuronal networks. Importantly, EEG measures at the macroscopic scale the summed fluctuations in the electric potential at the microscopic scale [Buzski et al., 2012].

1.1.1 Invention

The anteriority of the discovery of "brain rhythms" has been a subject of intense debate among scientists. The first to record electrical activity in the intact brain was Dr Richard Caton, which he described in a short 15-line abstract, dated 1875 [Caton, 1875]. He reported negative currents in the brain of rabbits and monkeys "that appear to have a relation to its [the gray matter] function". He used a string galvanometer (a primitive analogical amperemeter) and non-polarizable clay electrodes (see Figure 1.1).

Forty years later, Hans Berger reported extensively the observations he had made on the electrical activity of the human brain, through intact skull and patients with skull defects. He commonly used himself and his son Klaus, 16, as guinea pigs for his experiments (see Figure 1.1). Berger has been the first to record brain activity in the human intact brain, but importantly he was the first to describe the "alpha rhythm" as a rhythmic prominent 10Hz- pattern, over the occipital region of the skull, when a patient closes his eyes. Moreover, he proved that this oscillation was not an artifactual consequence of respiration or blood pressure changes. He later claimed that EEG was an outstanding technological breakthrough but also a major discovery for its diagnosis value [Berger, 1929].

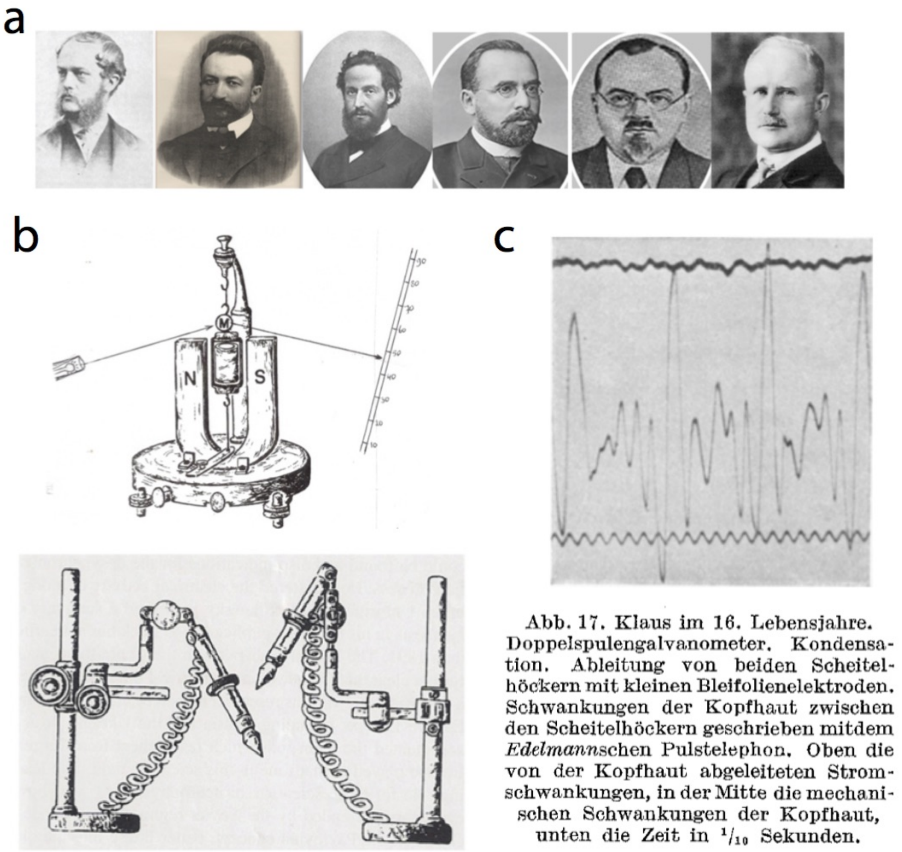

Abb. 17. Klaus im 16. Lebensjahre. Doppelspulengalvanometer. Kondensation. Ableitung von beiden Scheitelhöckern mit kleinen Bleifolienelektroden. Schwankungen der Kopfhaut zwischen den Scheitelhöckern geschrieben mitdem *Edelmann*schen Pulstelephon. Oben die von der Kopfhaut abgeleiteten Stromschwankungen, in der Mitte die mechanischen Schwankungen der Kopfhaut, unten die Zeit in $^1/_{10}$ Sekunden.

Figure 1.1 – The discovery of Electroencephalography and brain rhythms (a) Several scientists claimed anteriority in the discovery of EEG (from left to right: R. Caton, A. Beck, E. von Marxow, V. Danilevsky, V. Neminski and H. Berger). Richard Caton is recognized as the first scientist to record electroencephalographic signals while Berger is viewed as the father of "brain rhythms" **(b)** String galvanometer and clay-recording electrodes used by A. Beck in his experiments **(c)** Original recording by H. Berger on his 16 year old son. **(a-b)** adapted from [Coenen and Zayachkivska, 2013] **(c)** adapted from [Berger, 1929].

A much less remembered discovery is the one made by Adolf Beck when he was working with Cybulski in Krakow. As a master student, he first began to measure the excitability at different points of the frog spinal chord and reported that while spontaneous currents were already fluctuating, sciatic nerve stimulation added to these oscillations. His doctorate work extended this finding and he first described what is now referred to as "evoked potentials" and desynchronization after sensory stimulation [Beck, 1890]. Adolf Beck's work though posterior to Caton, embraced a large body of domains and settled the milestones for electroencephalography research.

1.1.2 From scalp electrodes to high density recordings

Electroencephalography can monitor the activity of neurons in a variety of manners, depending on the experimenter's needs. The main principle is based on the fact that brain activity implies the displacement of ionic charge carriers, called *primary currents*, through cellular membranes that result in *secondary currents* in the extracellular medium. In turn, these currents create fluctuations in the electrical field potential surrounding the tissue, which are sensed by a recording electrode.

The spatial reach - that is the amount of individual units that contribute to the resulting signal - can vary from one million to less than a hundred, depending on the protocol used. I will present the most widely used protocols in extracellular brain electrophysiology. They are all aimed at capturing variations of the electric potential in the extracellular space at a sub-millisecond scale. These signals exhibit temporal oscillations, at different frequencies, which are classified in distinct frequency bands (see Figure 1.2).

1.1.2.1 EEG

Electroencephalography (EEG) is the most widely used technique to monitor brain activity. Surface electrodes are fixed onto the scalp with contact gel to minimize the attenuation by soft tissue and maximize signal conduction to sense electrical activity. The signal recorded is a spatiotemporally smoothed summation of individual units recorded over the whole brain network. Because of the canceling out of uncorrelated activity in the resulting signal, EEG reflects highly synchronous activity of a large number of neurons, such as synchronous 1Hz delta waves in sleep. The spatial reach of EEG, which is the maximal distance within which volume conduction occurs, is estimated between 1 cm to 5 cm (and even longer for coordinated events), resulting in a spatial resolution ranging between 1 cm^3 and 400 cm^3 [Nunez and Srinivasan, 2006].

Common setups use 64 to 128 electrodes regularly spaced in an EEG-headset. As the electrical potential can only be measured between two points, the resulting signal is the difference between all electrodes and a global reference electrode (monopolar setup). One can also subtract the signal from adjacent electrodes (bipolar setup) thereby artificially using recording electrodes as reference channel.

1.1.2.2 ECoG

Electrocorticography (ECoG) improves some of the limitations of EEG at the cost of invasiveness. Electrodes - namely screws, grid or strips - are placed in direct contact with the *dura mater*, which removes the signal distortion by bone and skin. The spatial resolution of the recorded signal can be substantially improved below 5 mm^2. However, this tool cannot be used chronically in humans due to the need to expose the meninges. The spatial reach and quality of the signal depend on the size, shape and material of the recording electrode.

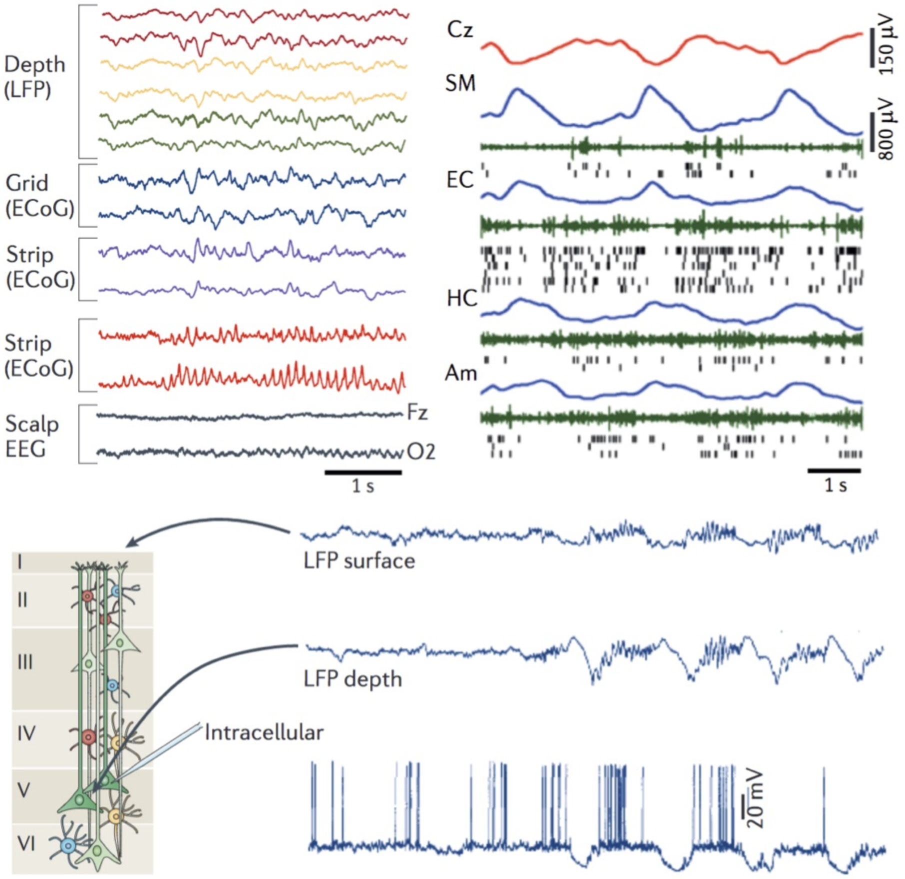

Figure 1.2 – EEG, ECoG and LFP recordings display the same temporal structure **(a)** Simultaneous recordings of three types of electroencephalographic measurements. LFP and ECoG recordings have higher-frequency content and larger amplitudes than scalp EEG, due to the reduced spatio-temporal averaging **(b)** Comparison between EEG (red) and LFP in different structures. The high frequency component of LFP (green) enables fast action potential extraction. **(c)** Comparison between surface LFP, depth LFP and intracellular recordings. The depth LFP and intracellular recording conveys the same frequency content, except for individual spikes, directly available in intracellular recordings. **(a-c)** adapted from [Buzski et al., 2012]

1.1.2.3 LFP

Local Field Potential (LFP) records the activity of any brain structure, at the cost of some damage to the tissue located on the track of the recording electrode. Electrodes need to be insulated to allow current flow only at the tip, before being inserted in the extracellular space in the aimed structure. Their diameter can vary from 100 μm to less than 10 μm. Several protocols allow impedance control to extend or reduce the spatial reach of the electrode [Pine, 1980; Brggemann et al., 2011; Chung et al., 2015].

Local Field Potential events are supposed to reflect local discharges but can sense correlated activity in distant brain regions through volume conduction. The high acquisition sampling rate (up to 40 kHz) captures fast events such as action potential of individual neurons. It has been shown [Nunez and Srinivasan, 2006] that filtering the recorded signal in the frequency domain can separate two aspects of the brain electrical activity:

- The low-frequency component (0-500 Hz) results from the summation across a local population of neurons of their individual synaptic currents. Synchronous synaptic activity is required for this signal to surpass electrode noise levels.
- The high-frequency component (500 Hz-5 kHz) results from action potentials from individual neurons. These currents are too transient to result in coherent summation, yet their individual amplitude is sufficient to pick up non-synchronous, single unit activity.

Thus, in most scientific work, LFP refers to the low-frequency, synaptic, component of such signal ($<$ 500Hz) and multi-unit activity (MUA) to the higher frequency component.

The widespread use of tetrodes and, more recently, the advent of multi-electrode arrays and silicon probes has allowed considerable advances in understanding the generation and propagation of neural events. Because the precise positioning of electrodes can be inferred *a posteriori* via lesionning protocols, the analysis of the differential signal between two neighboring electrodes can convey precise temporal information such as electric wave propagation or phase shift between structures [Bragin et al., 1995; Lubenov and Siapas, 2009; Patel et al., 2012].

The most precise recordings of neural activity are observed by intracellular recording procedure, using micro-electrodes or patch-clamp electrodes. These techniques give access to the precise subliminal fluctuations in membrane potential and the spiking activity simultaneously. However, it is difficult to obtain intracellular recording in a large number of cells concomitantly, making extracellular recordings the reference to study network activity.

1.1.3 The origin of extracellular currents

By placing a conductive electrode into or at the surface of the skull, one can sense the fluctuations in the electrical field surrounding the tissue. In theory, all ionic processes from every excitable membrane generate extracellular potentials which superimpose in the recorded signal. The temporal coordination, amplitude and frequency of these currents shape the resulting LFP waveform. Thus, it is critical to weigh the relative contribution of all those processes in EEG. This is the framework of *forward-modeling*: inferring macroscopic signals from microscopic events.

1.1.3.1 Synaptic activation

Synaptic currents are thought to be the main contributors of LFP, first because they constitute the major source of extracellular currents in physiological conditions and second, because their relatively slow timing enables summation to create measurable potential change [Nunez and Srinivasan, 2006]. When a transmembrane current flows inside the intracellular space during synaptic activation, an extracellular flow of ions has to leave the cell in the opposite direction to maintain electroneutrality in the intracellular space. The first current is called *primary current* whereas the balancing current is referred to as *return current*. By convention, the site where positive charges enter the cell membrane is called a *sink*, whereas a site where positive charges leave the cell is called a *source*. Because of the high velocity of electric waves in the medium, the delay between the onsets of primary and return currents can be neglected.

If the sink and source are significantly distant apart, this leads to the electrical configuration of a dipole, which in turn generate secondary currents throughout the extracellular space by volume conduction: positive charges flow towards the sink and negative charges flow towards the source, orthogonally to the field lines of the resulting dipole. These currents are responsible for the variation of the electric potential recorded by the electrode, but concomitant excitation by a relatively large number of cells has to occur to create detectable potential fluctuations [Gloor, 1985]. Because synaptic activation in physiological conditions is often rhythmic and occurs at different locations on the membrane, studies have investigated the dependence on stimulation frequency and current injection site. A phenomenon called *intrinsic low-pass filtering* was found to occur and to be stronger at the soma than at the basal dendrites of the neuron [Lindn et al., 2010]. See Figure 1.3.

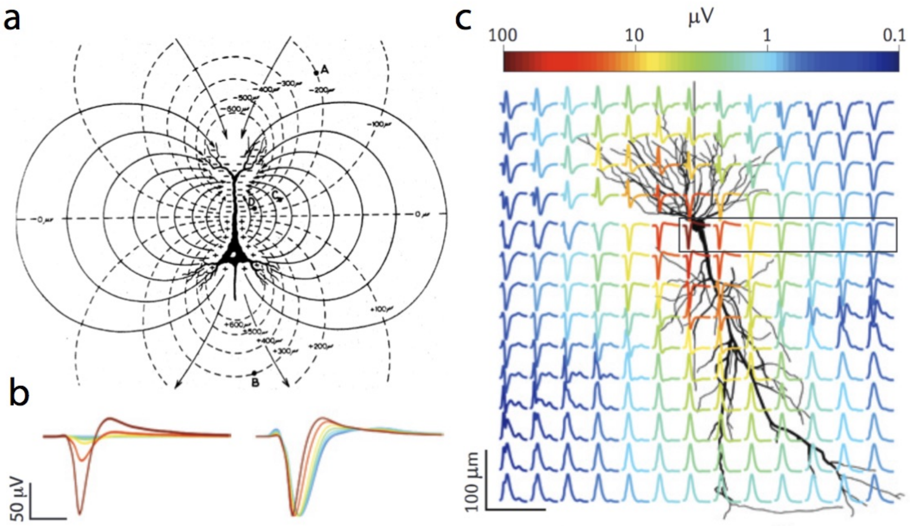

Figure 1.3 – Forward modeling scheme: from extracellular currents to the Local Field Potential (a) Electric field conforming to that of a dipole created by synaptic excitation of a single cortical pyramidal neuron. Secondary currents are shown in solid lines, crossing the iso-potential lines orthogonally (dashed lines). **(b) (c)** Forward modeling of a passive layer-5 pyramidal neuron injected with current into its basal dendrite. Extracellular potentials are color-coded according to their response latency. Note that the fastest responses occur in the vicinity of the soma. LFP exhibits EPSP close to the injection site, whereas it exhibits IPSP at the soma and apical dendrites. **(a)** adapted from [Gloor, 1985] **(b-c)** adapted from [Buzski et al., 2012].

1.1.3.2 Fast action Potentials

Until recently, fast sodium action potentials were thought not to contribute significantly to the LFP, because, though they generate large-amplitude deflections in the potential near the soma, their short duration (< 2 ms) makes co-occurrence of such events relatively rare [Andersen et al., 1971]. However, individual neurons firing together (for example, those receiving excitatory inputs from the same neurons) in a precise temporal window can actively contribute to the LFP [Glickfeld et al., 2009; Bazelot et al., 2010].

1.1.3.3 Calcium spikes

Sodium spikes are not the only axonal events that can take part in shaping the extracellular potential. Calcium spikes differ from the aforementioned by two major features: first, they are large (10-50 ms) and last substantially longer (10-100 ms) which make temporal summation occur more frequently and second they can be triggered by back-propagating action potentials to the synaptic site, and can therefore occur substantially after synaptic activity [Wong et al., 1979].

1.1.3.4 Other events

As mentioned above, all processes that contribute directly or indirectly to extracellular currents can play a role in the fluctuation of LFP, in particular processes that influence directly the passive or active properties of neurons. These include the resonance properties of neurons [Llins, 1988], but also spike after-hyperpolarization [Buzsaki et al., 1988], membrane excitability or the electrical activity of other neurons through gap junctions [Barth, 2003].

Though the first contributors to LFP appear to be straightforward, the latter are more complex because they depend both on the internal state of neurons, their type, but also on the activity of the remainder of the network. Depending on the network connectivity, the frequency of stimulation, such influence can vary greatly. Last, an indirect type of interaction known as *ephaptic effect* can occur: neurons are active entities that can “sense” the variation in the neighboring electrical potential and can, in turn, actively react and add a positive retro-action to these fluctuations. Hence, it is not straightforward whether large oscillations in the LFP subserve a function or whether they are a side effect of the normal functioning of the network.

1.1.4 Major Factors Shaping LFP

The two most important determinant of the strength of the LFP are the spatial alignment of neurons and the temporal synchrony of the dipole generated by primary currents [Lindn et al., 2011].

1.1.4.1 Cytoarchitecture of the generators

Pyramidal neurons have long and thick apical dendrites which can generate strong dipoles along the somato-dendritic axis because the primary sinks or sources are separated from return currents by significant distances. Inversely, spherically symmetric neurons, such as thalamo-cortical neurons or basket cells with dendrites spatially distribute in all directions, cannot. Thus, pyramidal neurons generate an *open field* structure, as opposed to the *close field* structure of other cells [Einevoll et al., 2013]. An open field structure is obtained when the sink and source are significantly distant apart, resulting in a sizeable current dipole thus inducing substantial ionic flow in the extracellular medium. Conversely, a close-field structure results in spatially restrained field lines, that do not generate substantial secondary currents.

Moreover, the typical laminar organization of pyramidal neurons in the cortex or hippocampus, where pyramidal neurons are spatially aligned, enhances the superposition of active dipoles and produces sizeable potential fluctuations. This explains why the amplitude of the

LFP is largest in the cortex than in subcortical structure and also why desynchronized EEG predominates in mammalian species (except for rodents), due the highly folded nature of their cortex [Niedermeyer and Silva, 2005]. Indeed a laminar organization is a prerequisite to produce brain oscillations. The dendritic arborization can also play a role in the way dendritic intracellular currents are transmitted to the extracellular medium.

1.1.4.2 Temporal correlations

Another major factor that directly influences the amplitude of the recorded LFP is the degree of temporal correlation - or synchrony - of LFP generators. Thus, if the primary transmembrane currents originate from asynchronous events, they will seldom produce a significant contribution to the LFP (unless they last for a substantial time). However, correlated spike trains might generate strong extracellular currents, though they are very transient, for instance when several pyramidal neurons receive input from the same location or during burst firing. The most striking example of this is the emergence of large-amplitude LFP signals observed in the cerebellar cortex when synchrony is imposed from an extracellular source [Kandel and Buzski, 1993].

1.1.4.3 Forward and Inverse Problem

So far, I tried to isolate and weigh the different contributors at the cellular level in their contribution to the recorded LFP. This is known as the forward problem or forward modeling. One faces the inverse problem when trying to infer microscopic events (such as current sinks or sources) from macroscopic recorded events. A considerable progress has been made in this field and it becoming possible to determine precisely the current source density - a quantity that represent the net current entering or leaving the extracellular space - using tetrodes, high density electrode arrays or silicon probes.

1.1.5 Precautions in the interpretation of LFP data

1.1.5.1 Volume Conduction

Volume conduction is the phenomenon responsible from the transmission of the electric field to movement of ions in the extracellular space, and production of the recorded signals. The characteristics of volume conduction depend on the features of the conductive medium and are mathematically described by Maxwell's quasi-static approximation. However, volume conduction poses a problem in the interpretation and localization of the primary signal as well as the functional meaning of the relationship between signals recorded from different brain locations. Namely, volume conduction can be responsible for contamination of large-amplitude signals generated in brain structure that superimpose in an electrode location where the signal is relatively weak.

1.1.5.2 Locality of the Local Field Potential

Modeling studies have estimated the spatial reach - which can be defined as the distance within which 95% of the recorded signal originates - of LFP between 200 μm to several millimeters. The discrepancies in these studies are partly explained by the fact that the temporal correlations in the underlying synaptic events are a major confounding factor. Biophysical forward modeling revealed that LFP has a spatial reach of about 200 μm in case of uncorrelated sources, whereas LFP signals increased without bounds with population size in highly synchronous sources [Lindn et al., 2011].

It remains unclear however to what extent distant neurons contribute to the local field potential, because synchronized synaptic inputs from distant individual neurons have been shown to generate strong potential fluctuations up to the mm range, because the distant location of generators from the recording electrode is counterbalanced by the increased number of contributors [Kajikawa and Schroeder, 2011]. Hence, it is difficult to have an accurate evaluation of the required number of neurons to elicit detectable LFP oscillations. In any case, the term local field potential appears to be misleading and some authors have proposed the more neutral term of *Electrical Field Potential*, to not assume that the spatial reach of depth electrodes indeed is local.

1.1.5.3 Frequency dependence

Local Field Potential recordings display a characteristic profile in that the magnitude of the LFP power signal is inversely proportional to the frequency of the signal, which is due to two main effects. First, the electrical properties of pyramidal cell dendrites exhibit intrinsic filtering in the sense that high-frequency transmembrane currents exhibit much less LFP fluctuations than for low-frequency ones. This effect is greater if transmembrane currents occur at the somatic or apical dendrites. Second, the conversion of synaptic input correlations into correlations between single-neuron LFP contribution is much more easily achieved at low frequencies than at high frequency, mainly due to the fact that high frequency events have shorter time windows. Some authors have also argued that the properties of the extracellular medium can enhance this low-pass filtering effect [Bdard and Destexhe, 2009; Leski et al., 2013] (See Figure 1.4).

1.1.5.4 Spike-LFP correlations

Due to the uncertainties in the interpretation of LFP, the varying contribution of individual neurons and its dependence on precise electrode position relative to neurons, network connectivity and regional population types is still a subject of active research. However, spiking activity contributes to the LFP in many different ways, and the phenomenon of spike contamination to LFP has been shown to occur especially in the high-frequency bands [Ray and Maunsell, 2010]. Still, there is a complex relationship between spiking activity and LFP and large-amplitude currents may be associated with strong, moderate or absent spiking.

1.2 Cell assemblies

The second part of the twentieth century has witnessed decisive technological developments and major discoveries in cellular communication such as the recording and modeling of action potentials [Hodgkin and Huxley, 1952] and the discovery of receptive fields in the visual cortex [Hubel and Wiesel, 1959]. These have undoubtedly changed our understanding of the brain and prompted the development of bio-inspired neural networks like the perceptron [Rosenblatt, 1958], genetic algorithms [Fraser, 1957] or self-organizing maps [von der Malsburg, 1973]. Since then, the way information is stored and processed in the brain is a subject of hot

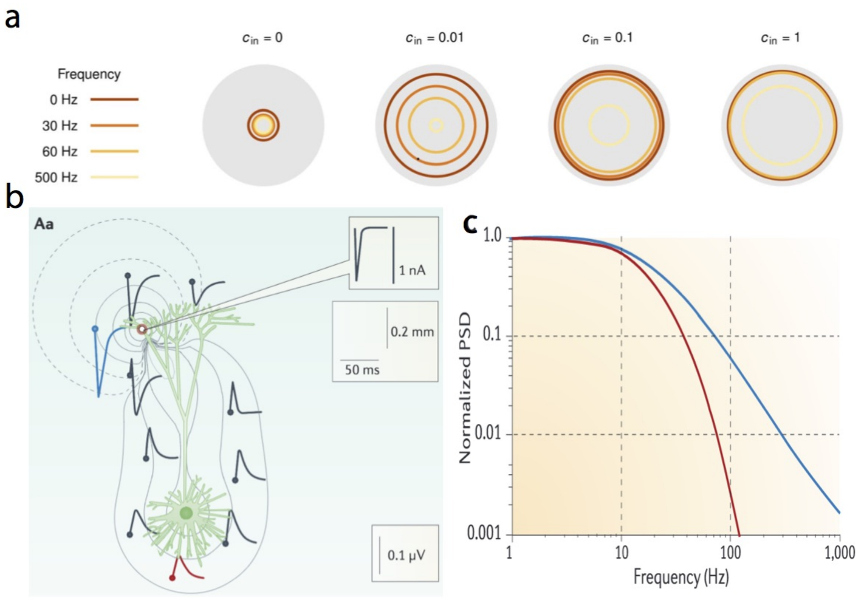

Figure 1.4 – Frequency dependence of Local Field Potential signal (a) Spatial reach of the LFP for different frequency and degrees of synaptic correlation. Note the strong attenuation at high frequency for moderate correlated input (C=0.1, 500Hz) **(b-c)** Forward-modeling of a passive layer-5 pyramidal neuron injected with current into its basal dendrite. The intrinsic dendrite filtering is shown at two recording sites: it is stronger at basal (red) than apical (blue) dendrites. **(a)** adapted from [Leski et al., 2013] **(b-c)** adapted from [Einevoll et al., 2013].

debate and the past decades have seen a paradigm shift from population *rate coding*, where information is contained in the firing rate of neurons, to *temporal coding*, where information is contained in the precise timing of action potentials. This can be seen as the confirmation of an old postulate formulated by Donald Hebb in 1949: the existence of cell assemblies [Hebb, 1949]. In this section, I present evidence for the existence of such cell assemblies and for brain rhythms as a means to exchange information efficiently between distant brain areas.

1.2.1 Convergence within the brain

Brain architecture exhibits typical convergence from primary sensory areas specialized in the processing of low-level information to association areas that combine this information into high-level conceptual representations. The utmost example of this organization is the processing of visual information in cerebral cortex, where primary layer neurons are grouped and organized in cortical columns that respond selectively to low-level aspects of stimuli such as orientation and direction [Hubel and Wiesel, 1959].

This has led to the hypothesis that convergence could be the ultimate way of representing information and concepts of “grandmother cell” [Lettvin et al., 1959], “gnostic unit” [Konorski, 1967] or “cardinal neurons” [Barlow, 1972] have emerged as a possible strategy to encode highly specific stimuli in individual neurons. Some experimentalists have indeed reported invariant highly specific individual neuronal representations in the firing of individual neurons of human epileptic patients, such as the well-known “Jenifer Aniston” or “Halle Berry” neurons [Quiroga et al., 2005]. This convergence has long been observed in the visual system, especially in the infero-temporal cortex of the monkey since the discovery of face-selective cells by Charles Gross in 1969 [Gross et al., 1969], but the question remains whether this way to code information is universal or not.

1.2.2 The binding problem

Though the total number of available neurons in the brain (about 10^{11} neurons) does not contradict this hypothesis, this type of encoding is questionable in terms of robustness and processing time efficacy. But more importantly, it raises the issue of *perceptual binding*: If information is coded by a small number of individual neurons, how can we have a conscious unified perception of a complex scene when information is segregated in discrete objects? The "binding problem" indirectly asks how brain region communicate and how information is selected and transmitted from primary regions to higher-level areas. The experiment led by Francis Crick and Christof Koch to investigate the neural correlates of consciousness showed that individual units who fired synchronously around 40 Hz were part of the same conscious perception, whereas those who showed no synchrony at 40 Hz were not [Crick and Koch, 1990]. Subsequent work, especially the binocular rivalry experiment from Engel and Singer in the visual cortex of macaque monkeys, supported this hypothesis - known as coding through phase synchronization - in which cellular percepts were resulting of large cellular assemblies firing synchronously at a given phase of the ongoing oscillation [Sheinberg and Logothetis, 1997; Engel and Singer, 2001].

1.2.3 Hebb's postulate

This view is no different from the postulate formulated by Donald Hebb in 1949. In his influential book, *The organization of behavior*, he stated that information was not centralized but distributed in the brain in large neuronal assemblies. These neuronal assemblies can be described in a very broad fashion as a set or subset of cells coding for different aspects of the same stimulus [Hebb, 1949]. The way these cell assemblies organize follows a general principle than can be summed up as "cells that fire together, wire together", meaning that cells that tend to be active at the same time will strengthen their connections, so that future reactivations of only a subset of the cell assembly would trigger the activation of the rest of the network.

1.2.4 Experimental Evidence

Hebb's view of brain coding has received considerable support in many disciplines. Auto- associative neural networks based on Hebbian learning such as Hopfield networks have shown to perform memory storing, pattern rivalry and completion extremely efficiently [Hopfield, 1982]. Learning by association can be explained easily in the Hebbian framework. The discoveries of long-term potentiation by Bliss and Lomo [Bliss and Lmo, 1973] and spike-timing dependent plasticity rule (STDP) by Bi and Poo [Bi and Poo, 1998] gave strong credit to the idea that the simultaneous activation of two neurons strengthens their connectivity. And finally, the discoveries of cell assemblies in the rat hippocampus, which showed vast synchronous neuronal firing at different phases of theta rhythm validated Hebbian theory [Harris et al., 2003]. (See Figure 1.5).

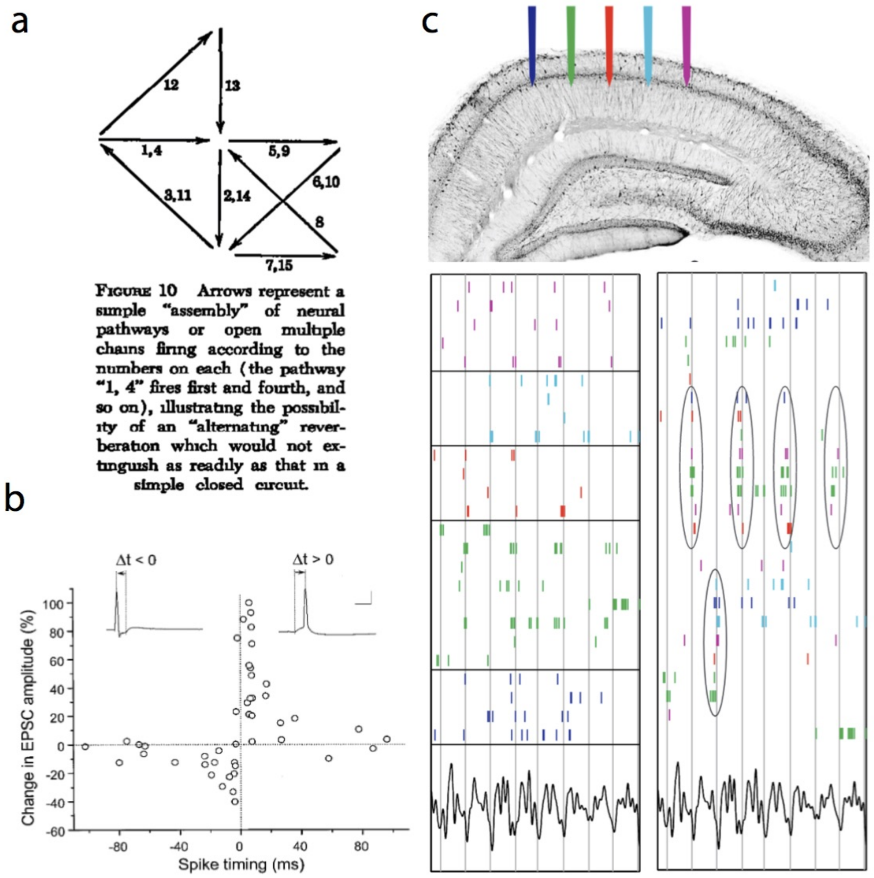

FIGURE 10 Arrows represent a simple "assembly" of neural pathways or open multiple chains firing according to the numbers on each (the pathway "1, 4" fires first and fourth, and so on), illustrating the possibility of an "alternating" reverberation which would not extinguish as readily as that in a simple closed circuit.

Figure 1.5 – The concept of cell assemblies to encode information - Postulate and supportive data (a) Schematic Representation of a reverberant cell assembly by Hebb - Arows represent neuronal connections and numbers represent connection strength **(b)** Experimental data showing evidence for spike-timing dependent plasticity (STDP) in rat hippocampal neurons - Note the short timing window [0-20 ms] for synaptic potentiation to occur, suggesting precise timing in pre-post synaptic events **(c)** Cell assemblies are widely distributed in the hippocampus of behaving rats. When individual neurons are grouped relative to their preferred spiking theta phase, widely distributed cell assemblies firing synchronously appear. **(a)** adapted from [Hebb, 1949] **(b)** adapted from [Bi and Poo, 1998] **(c)** adapted from [Harris et al., 2003].

1.3 Brain rhythms

While Hebbian theory is supported by experiments, it does not address the communication between cell assemblies. Hebb unveiled the major principle for their formation and maintenance, but he was missing how they communicate. An influential current hypothesis is that cell assemblies collectively process information through the central role of brain rhythms.

1.3.1 Functional Classification

Brain rhythms can be described as rhythmic oscillations of the electroencephalogram that are the proxy of physiological coordination and temporal synchrony in one or several structures. As said before, Hans Berger described the first brain rhythm in 1929, as a prominent rhythmic oscillation at 8 to 12 Hz, strongest over the occipital region of the skull, specifically occurring when the subject closes his eyes. He named it the “alpha rhythm”.

The classification of brain rhythms was formalized in 1974 based exclusively on clinical records and mainly centered on the study of human EEG, attributing Greek letters to frequency bands. However, many other relevant features of brain oscillations can be used such as regionalization, duration of occurrence, the intra or inter-individual pattern variability and whether or not they have a behavioral correlate. Based on these considerations, 10 to 20 different brain rhythms have been listed, ranging from infra-slow activity (<1Hz) to ultrafast rhythms such as hippocampal ripples (150-250Hz).

As shown in Figure 1.6, brain rhythms are remarkably preserved across mammalian species, despite great changes in brain size, weight and cyto-architectural organization. It is important to note that the most striking fact about brain rhythms is that they cover a wide range of behaviors (sleep, anesthesia, preparatory movement, eye-closing, focused attention, dreaming, etc.), a wide range of temporal and spatial scales and an even larger range of species, from mammals to insects. They play a major role in normal brain development and abnormal neural synchronization has been linked to a large body of cognitive deficits. My thesis focuses on theta rhythm, while a more complete and detailed review of cortical rhythms can be found in [Buzski, 2006].

1.3.2 Generation

1.3.2.1 Global Mechanisms

Several studies have described the generation of brain oscillations, including *in vivo*, *in vitro* and modeling studies. Different patterns of generations have been proposed and it is likely that each neural oscillation has a specific generation process, depending on the frequency, regionalization or physiological context [Nunez and Srinivasan, 2006; Buzski, 2006]. However, two main generation patterns seem to occur broadly in the brain: 1. Oscillations might result from entrainment of a population of neurons, each firing consistently at every cycle of the oscillation, driving excitation to other neurons in the network, in a pattern similar to rhythmic depolarization in a pacemaker. Entraining neurons are thus called pacemaker neurons. 2. Oscillations are maintained by feedback loops inducing rhythmic periods of excitation and inhibition that would result in rhythmic flow of ions in the extracellular space. The typical pattern is described in Figure 1.7: Pyramidal cells activate neighboring interneurons, which in turn inhibit excitatory input. The interneurons are in turn dis-facilitated, enabling another round of activation. Thus propagation delays and cell types would control the frequency of the resulting oscillation [Freeman, 1991].

1.3.2.2 Neurons as resonators

It is important to note that neurons exhibit resonance properties [Llins, 1988], some neurons might be entrained at a given frequency whereas they will remain passive at other frequencies. The phase-response property of neurons - that is the way neurons fire postsynaptic potential in response to the exact timing of occurrence of presynaptic activity - is a critical factor for the shape of resulting oscillations [Wang, 2010]. Oscillations in the membrane electrical potential could also be caused by neurons for which the firing probability is modulated by

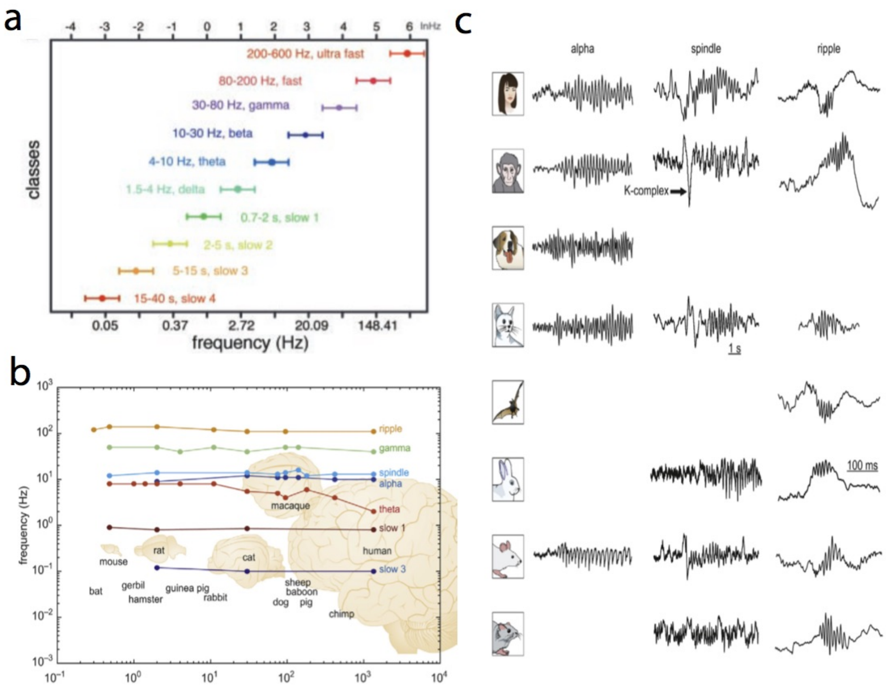

Figure 1.6 – Brain Rhythms are universally present across mammalian species (a) Functional classification of brain rhythms. The actual classification defines frequency bands of equal length on a logarithmic scale and follows Hans Berger first initiative (Greek letters). **(b)** Major rhythms are preserved in most mammalian species, irrespective of brain size and weight. **(c)** Example of brain rhythms recorded in different mammalian species. Note the similarity in ripple patterns. **(a-c)** adapted from [Buzski et al., 2013].

the frequency of the LFP oscillations. These neurons could fire at a different frequency from that of LFP oscillations, or at no particular frequency [Schnitzler and Gross, 2005].

1.3.2.3 Balance between excitation and inhibition

Balance between excitation and inhibition is a crucial factor for oscillations to occur. When inhibition is blocked pharmacologically in the cortex, activity becomes epileptic [Dichter and Ayala, 1987] and individual neuron properties such as stimulus selectivity are also affected. Thus the interplay between excitation and inhibition might affect cellular responses directly and indirectly by impairing physiological brain oscillations. Modelling studies have shown that both local and long-range inhibition is required for neurons to synchronize in the cortex [Buzsaki, 2004]. The typical example of this is given by the thalamo-cortical recurrent network: the rhythmic entrainment of cortical neurons by thalamic neurons involves rhythmic local inhibition by reticular thalamic neurons leading to UP and DOWN states observed in the cortex during slow-wave sleep [Steriade et al., 1993] (See Figure 1.7).

1.3.2.4 Laminar structure

As mentioned previously in subsection 1.1.4, the laminar structure and the spatial alignment of pyramidal neurons is a critical factor to record large amplitude signals. In such struc-

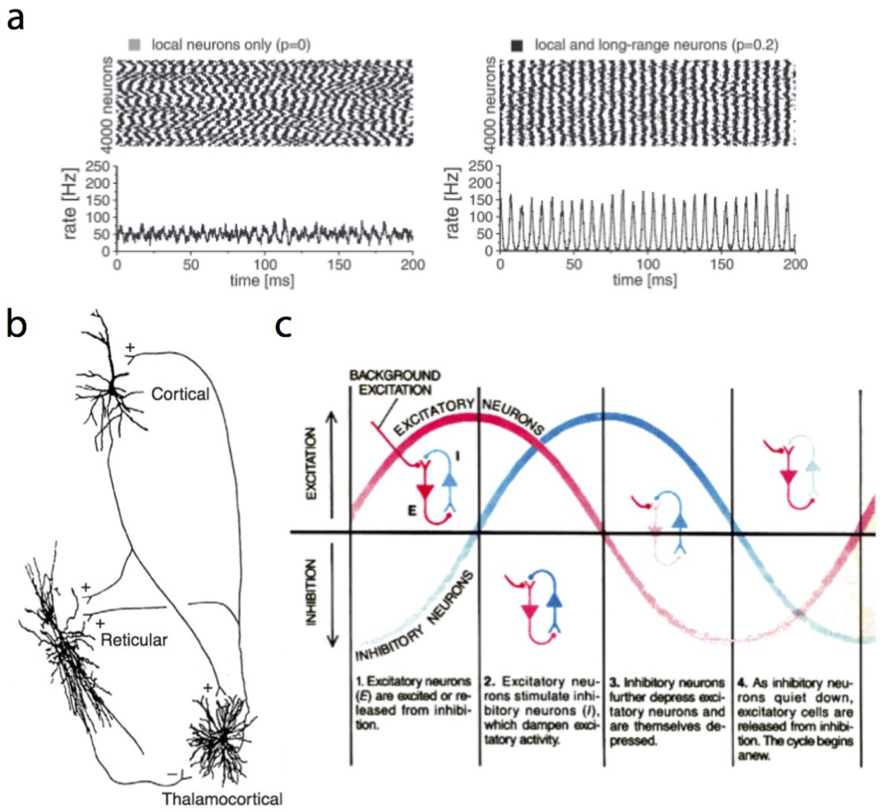

Figure 1.7 – **The generation of brain rhythms requires a balance between excitation and inhibition together with local and long-range connectivity. (a)** Modeling of brain rhythm generation in different network architecture. Local inhibition is not sufficient to generate brain-wide rhythmicity **(b)** Schematic representation of the thalamo-cortical recurrent network mixing long-range excitatory connections between cortex and thalamus and local inhibition by reticular neurons in the thalamus **(c)** Generic cyclic pattern of reverberation in local networks to keep sustained rhythmic activity over time.**(a)** adapted from [Wang, 2010] **(b)** adapted from [Steriade et al., 1993] **(c)** adapted from [Freeman, 1991].

tures, the substantial distance between sinks and sources creates larger dipoles, resulting in a broader rhythmic flow of ions in and out of the extracellular space. Hence, neurons are more likely to synchronize to the ongoing oscillation than in close-field configuration.

1.3.2.5 Downward versus Upward Causation

Recent studies show that oscillations in the Local Field Potential result from neuronal activity, which in turn influence excitability of surrounding neurons. Thus, there is a strong interplay between *top-down* effects (local oscillations influencing neuronal activity) and *bottom-up* effects (the firing of individual units triggering mesoscopic changes in extracellular potential). These two complementary phenomena are respectively called *downward* and *upward* causation. Evidence for downward causation - that is that the phase of LFP oscillations modulates individual spiking of neurons - has been presented in studies showing spike-field coupling [Steriade et al., 1993; Canolty et al., 2006]. For example, the modulation of membrane potential in slices of rat visual cortex has been shown to modulate the excitability of individual neurons [Volgushev et al., 1998]. However, evidence for upward causation is less common but a few studies have interestingly reported that rhythmic depolarizing current (including step depolarization and burst stimulation) injections in a single cell can trigger major pattern changes in the LFP recorded several millimeters away from the injection site and even transitions between brain states, strongly similar to transitions between REM and non-REM sleep episodes [Li et al., 2009a].

1.3.3 The function of brain rhythms

The overall preservation of brain rhythms in species, their widespread observation in almost all major areas of the brain - from limbic, hippocampal and cortical stuctures - and their implication on a wide range of behavioral states suggest that they are not just a by-product of the brain's normal functioning. Selective suppression studies have brought a definite proof of their involvement in cognition through memory processes and task performance.

1.3.3.1 Behavioral correlates

Though the first classification of brain rhythms aimed at making associations between oscillation types and cognitive states (such as eye closing, focused attention or sleep), such a relationship may not always be obvious. A given oscillation might be associated with several apparently contradictory behaviors (such as theta rhythm during running and paradoxical sleep) and conversely, a putative brain state can consist of a mixture of rhythms, either alternating in time or even nested into one another (See Figure 1.8). Abnormal rhythms have been observed in pathological cases such as epilepsies and their typical spike-wave pattern [Gibbs et al., 1959]. As a result, brain rhythms should be considered as a macroscopic proxy of underlying microscopic processes reflecting the network state, but not a state of their own. Their length, frequency of occurrence and pattern type can thus help to classify brain internal dynamics. For example, these features are at the basis of sleep stage classification [Loomis et al., 1937; Dement and Kleitman, 1957].

1.3.3.2 Brain rhythms and performance

Behavioral neuroscience has accumulated strong evidence that the efficiency of brain rhythms and more precisely the strength of the coherence between brain rhythms in distant regions in often related to performance in a wide range of cognitive tasks including contextual learning, T-maze spatial alternation and working memory tasks. Benchenane and colleagues have demonstrated that in a rule-shifting spatial memory task, electrophysiological responses exhibit variability, with some trials showing high coherence between prefrontal cortex and dorsal hippocampus and others showing low coherence. The degree of coherence correlated with success rate both during learning and test phases [Benchenane et al., 2010]. Other studies showed that efficient cross-frequency coupling within anatomical structures explains the performance in contextual learning and alternation tasks [Tort et al., 2008; Yamamoto et al., 2014]. This holds true in numerous studies including various brain states and species [Lakatos et al., 2008; Axmacher et al., 2010]. Hence, brain state affects performance and does so by the efficient "use" of specific brain rhythms. Indeed, some studies have shown that changes in performance cannot be explained by the lone power of brain oscillations, but rather by a more efficient coupling or communication among brain rhythms.

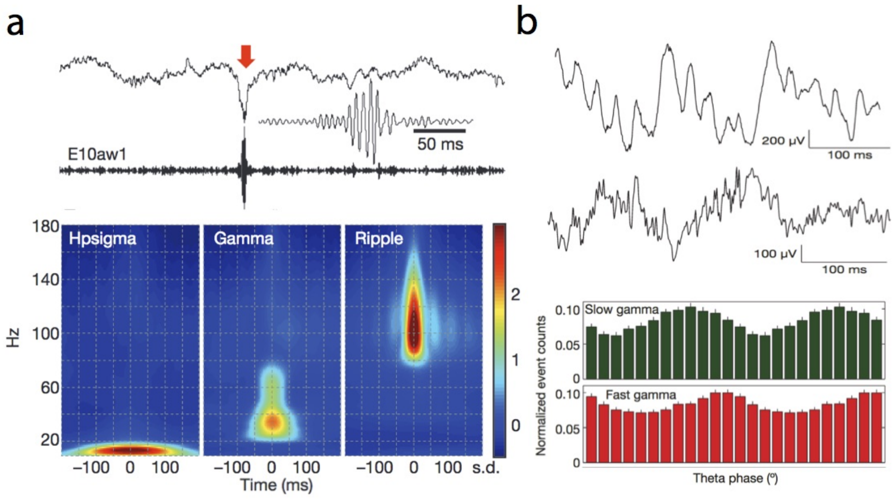

Figure 1.8 – Cross-frequency coupling: brain rhythms are often coupled and embedded into one other Two examples of cross-frequency coupling: **(a)** Sharp-wave Ripples (SWR) observed during non-REM sleep in monkeys. Those consist of large low-frequency deflections (K complexes), intermingled with high frequency oscillations in the gamma range (30-50 Hz) and ripple range (> 100 Hz). **(b)** Gamma rhythm co-occurs with theta oscillations during running in the rat CA1 regions. Slow gamma (30-50 Hz) occurs preferentially on the descending phase of theta oscillations, while high-gamma (100-150 Hz) predominates during the ascending phase of theta, suggesting two separate circuits and function for each frequency band. In both cases, the phase of the ongoing slow oscillation modulates the amplitude of the high oscillation. **(a)** adapted from [Logothetis et al., 2012] **(b)** adapted from [Colgin et al., 2009].

1.3.3.3 Selective Suppression

Decisive conclusions came from selective suppression studies: by means of subtle electric stimulation through electrodes implanted in the ventral hippocampal commissure, Girardeau and colleagues could selectively detect and abolish sharp-wave ripple (SWR) events during slow-wave sleep (SWS). These ultrafast oscillations have long been proposed [Buzski, 1989], and later proved, to facilitate replay of past events for memory consolidation [Lee and Wilson, 2002; Foster and Wilson, 2006]. Rats stimulated during SWR events showed clear deficits in memory consolidation in a conventional radial maze task, whereas rats stimulated during control periods did not [Girardeau et al., 2009; Ego-Stengel and Wilson, 2010]. More recently, Boyce and colleagues used the same principle to prove that REM sleep was selectively implicated in memory contextual memory and novelty learning. By silencing optogenetically GABA neurons in the medial septum during REM sleep episodes, they showed that theta activity was necessary to reinforce memory traces. Importantly, the abolition of theta activity during paradoxical sleep only affected contextual memory recall while cued memory-test was left unchanged, showing hippocampal dependence [Boyce et al., 2016].

1.3.3.4 Pathological conditions

The fact that the EEG has often been linked to a specific behavioral or cognitive state has prompted its use to detect the electrophysiological signature of high cognitive functions such as consciousness or meditation. Abnormal oscillatory profiles have often been observed in patients suffering from severe pathological condition (schizophrenia, epilepsy) and EEG is now commonly used to diagnose and treat these diseases (for instance, to reveal the precise location of epileptic foci before surgery).

Hence, disrupted distant-brain communication and abnormal synchronizations is associated with several pathological conditions and neuropsychiatric disorders including epilepsy, schizophrenia, dementia, and in particular, basal ganglia disorders such as Parkison's disease [Traub, 2003; Jeong, 2004; Hutchison et al., 2004]. Evidence from insect studies show that synchronization is associated with sparsening of odor representation [Perez-Orive et al., 2002] and that a balanced pattern in synchronization and desynchronization both in time and space is fundamental for the brain to function efficiently [Schnitzler and Gross, 2005].

1.4 Communication through Phase Synchronization

How is the information distributed in the brain? What is the nature of the neural code? How do single units communicate? The opposition between the seemingly random firing of individual neurons and the transient repetitive patterns in LFP recordings (like the alpha rhythm first discovered by Hans Berger) raised the question of the encoding of information within the brain and conversely, its decoding.

1.4.1 Cross-frequency coupling

Fast and slow oscillations are not associated with the same spatial scale and therefore modulate activity of different cell population sizes. Considering the low-pass filtering effect occurring in the extracellular medium, the fast timescales necessary for gamma frequency synchronization (between 5 to 30 milliseconds) cannot easily be transmitted to large-scale networks, whereas low-frequency oscillations can [Von Stein and Sarnthein, 2000]. Thus, combining high and low frequencies can be seen as an efficient means to transmit information throughout the brain at a fine temporal scale, in a process similar to frequency modulation.

Cross-frequency coupling (CFC) is a statistical dependence between the different frequency components of a brain oscillation: the classical example is *phase-amplitude cross-frequency coupling*, where the phase of the slow-frequency oscillation modulates the amplitude of the high frequency oscillation (see Figure 1.8). CFC can also display phase-phase coupling or phase-frequency coupling [Jensen and Colgin, 2007]. It has been observed in a variety of experimental conditions, across species and anatomical structures [Bragin et al., 1995; Osipova et al., 2008; Tort et al., 2009; Axmacher et al., 2010]. It has received considerable attention because in the case of phase-amplitude coupling, because there are functional correspondence between the low-frequency phase - the local excitability - and the high-frequency amplitude - the local cell assembly activity [Lakatos, 2005; Jensen and Colgin, 2007]. This view is compatible with the communication through coherence hypothesis that I will introduce later [Fries, 2005].

In Figure 1.8, I present two examples of CFC. The first example is the co-occurrence of high-amplitude low-frequency deflections and low-amplitude high-frequency oscillations both in the gamma (30-50 Hz) and ripple band (100-150 Hz) in the macaque monkey. When aligning all SWR events to the oscillation trough, which corresponds to the moment of highest excitability, we can see that the amplitude of higher oscillations is phase-locked to the trough of the K-complex [Logothetis et al., 2012]. The very same phenomenon occurs in the CA1 region of a behaving rat, where fast (55-95Hz) and slow (30-50Hz) gamma superimpose at different preferred phases of the theta oscillation. These two gamma-bands show spike-field correlations in different regions of the brain and are thus thought to synchronize neural events from different regions. Precisely, low-gamma is involved in CA3-CA1 coherence whereas high-gamma showed MEC-CA1 coherence [Colgin et al., 2009].

Tort and colleagues have demonstrated that phase-amplitude coupling can be dynamic and rapidly changing in a task-related manner [Tort et al., 2008], but more importantly they have shown that the strength of CFC is a robust predictive biomarker of learning, and not a mere byproduct of brain activity, independent of behavior. This finding can be seen as an increase in communication gain (and thus energy saving), because enhanced CFC does not entail enhanced energy demands [Tort et al., 2009].

1.4.2 The Communication Through Coherence Hypothesis

Phase synchronization is thus a dynamic, broad and wide phenomenon in the brain. If some of its mechanisms are currently being studied, revealing band-specific cell populations [Wulff et al., 2009], the functions of phase-amplitude coupling remain elusive. Several postulates have been proposed such as “coincidence detection” between two cell assemblies projecting into the same target region. Another framework proposes that phase synchronization provides “windows of opportunity” for cell assemblies to either potentiate or depress. Depending on the phase occurence of the synaptic inputs, those might arrive during high excitability periods and lead to LTP or the opposite effect might occur (see Figure 1.9). This phenomenon would be an efficient way to form or actualize the connection between large cell assemblies, during memory encoding or maintenance [Fell and Axmacher, 2011].

Fries first formulated a promising proposition in 2005 suggesting that phase synchronization enable enhanced neural communication between cell assemblies thus providing dynamic and efficient distant communication between sending and receiving areas. This is known as the Communication Through Coherence (CTC) hypothesis [Fries, 2005].

1.4.2.1 Principle

The main idea of CTC is that if high excitability is associated with the trough of the ongoing oscillations, then stimuli consistently time-locked to the trough of the oscillation would benefit more effective transmission than the ones time-locked to the peak of the oscillation. In short, strong effective communication requires coherence. In Figure 1.9, I present a schematic representation of three brain regions oscillating in phase (blue-red) and out-of-phase (blue-black). The communication between the first two regions is more effective because spike leaving one region consistently arrive during high excitability periods. If the two regions do not oscillate in phase or at the same frequency, then inputs arrive at random phase of the excitability cycle and will have a lower effective connectivity *in fine*.

This framework not only integrates the notions of cell assemblies and brain rhythms, as

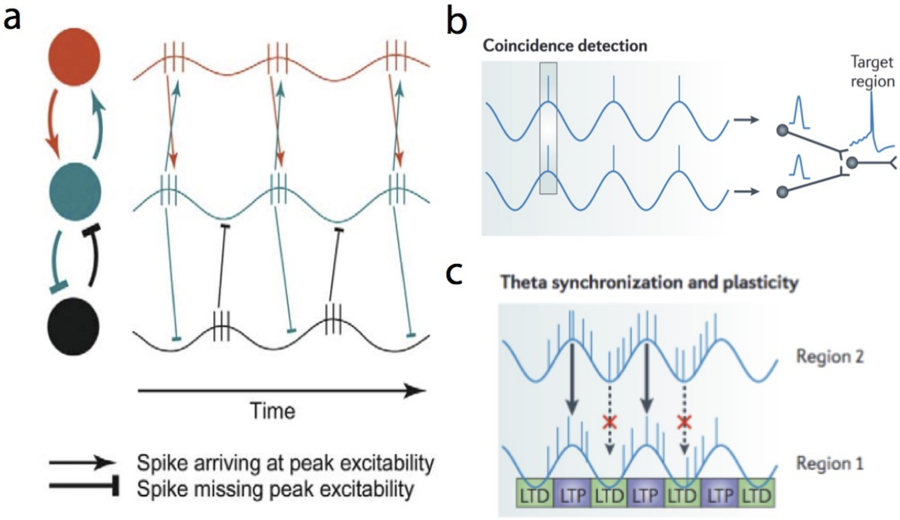

Figure 1.9 – Communication through Phase Synchronization across distant brain areas (a) Neural Synchronization results in enhanced neural communication: two brain areas oscillating in phase can share information efficiently because spike leaving the sending region arrive at peak excitability in the receiving region whereas regions oscillating out-of-phase receive spikes in low excitability periods. **(b)** Putative functions of phase-synchronization. Two brain areas oscillating in phase can send spike to a target region synchronously. Synchronization can thus serve as a coincidence detector to form cell assemblies. **(c)** Putative effect of theta-synchronization: alternating periods of high and low excitability might result in successive LTP and LTD windows to segregate neural ensembles and enhance synaptic weights at specific theta phases. **(a)** adapted from [Fries, 2005] **(b-c)** adapted from [Fell and Axmacher, 2011].

a mechanism for effective communication, but also explains how a postsynaptic region can "select" between competing inputs: those arriving at maximal excitability benefit from higher synaptic gain and are more efficiently processed than other competing presynaptic trains.

1.4.2.2 Challenges

The first formulation of the CTC hypothesis was challenged by several studies, because it did not account for the increasing conduction delays between distant regions. Hence, taking these delays into account would make zero-phase synchronization uneffective. To cope with this problem, Fries proposed that multi-directional synchronization occurs with conduction delays [Fries, 2015] and that they account for the inter-laminar phase inversion observed in physiological conditions [Bragin et al., 1995; Kerkoerle et al., 2014]. These typical inter-laminar delays compensate with the conduction delays both in the feedforward gamma flow transmission and re-entrant feedback in the sending areas [Bastos et al., 2015].

1.4.2.3 Experimental Evidence

The CTC hypothesis has received considerable experimental support. Several studies have reported that postsynaptic rhythm modulates input gain in synaptic transmission [Cardin et al., 2009], that strong effective connectivity requires coherence between pre and post-synaptic groups [Womelsdorf et al., 2007] and that communication is implemented through selective coherence [Schoffelen et al., 2011].

This assumption is in accordance with the observation that oscillations are traveling waves, such as theta waves traveling along the septo-temporal axis of the hippocampus [Lubenov and Siapas, 2009; Patel et al., 2012] or gamma flow in the macaque cortex [Markov et al., 2014]. The CTC hypothesis also entails a classical tradeoff between efficient communication and phase coding: indeed, effective communication requires using the widest available phase range, in order to best differentiate among distinct cell assemblies. But neural synchronization is maximal when most action potentials occur at the phase of peak excitability, which imposes a trade-off between robustness and efficacy of neural communication.

1.4.2.4 Open Questions

The CTC hypothesis gives a functional framework for cell assemblies, brain rhythms and neural synchronization. It emphasizes the role of coherence as a flexible dynamic tool for effective communication. However, it also sets unresolved questions:

- Can we effectively modulate neural synchronization without changing other aspects of neural activity, to enhance or reduce communication?
- What are the cell types and mechanisms of top-down control over, for instance, gamma-band synchronization?
- How does this transpose to distant communication when cortical gamma rhythms are very local?

1.5 Conclusion

In this chapter, I presented how electroencephalography pioneered brain activity monitoring as early as 1875. It takes advantage of volume conduction to record the synchronous activity of extracellular currents generated in cortical microcircuits. The Local Field Potential (LFP) recordings can monitor changes in the extracellular potential at high temporal resolution and reflects mostly the synaptic inputs of uncorrelated events. The spatial reach of LFP can be substantially higher for synchronous activity.

Since the pioneering work of Hans Berger in 1929, brain rhythms have been extensively studied and classified. They vary in frequency, amplitude, localization and behavioral correlates. These rhythms are generated by pacemaker neurons and entrained by reverberant excitation and inhibition loops. Fast rhythms have a lesser spatial extent than slow rhythms and reflect neuronal processing at different spatiotemporal scales. Brain rhythms are often embedded into one another in a phenomenon known as cross-frequency coupling.

Considerable evidence is accumulating for brain rhythms as an effective means to synchronize large distributed cell assemblies, to enhance neural communication and provide windows for synaptic modification. In this framework, variations in the extracellular potential can be seen as fluctuations in excitability resulting in an increased synaptic gain for regions oscillating in phase synchrony. This proposition seems appealing in light of the experimental evidence that has established a functional link between rhythms and performance, memory processes and inter-regional communication.

Chapter 2

Hippocampus, Memory and Theta Rhythm

How is the external world represented in our brain? And how do brain rhythms contribute to extract relevant information from this internal representation of time and space? Spatial navigation requires indeed multiple cognitive functions such as perception, memory, learning or motivation, and entails a tight coordination between the structures involved in these diverse functions. Experimental studies have unraveled neurons which firing rate is highly specific to a given aspect of spatial information such as location, head-direction, speed, or even time spent in a given location. This strongly suggests the existence of modular cerebral structures, for the encoding and processing of spatial information. In this chapter, I present the structures involved in the representation of space and memory and I develop on the crucial role of theta oscillations in encoding, processing and retrieval of spatial memory.

2.1 The hippocampus: Memory and Space

2.1.1 The HM case

Henri Molaison, better known as HM, was a patient, whose condition has been extensively studied from 1957 to his death in 2008 by (among others) Brenda Milner, William Scoville and Suzanne Corkin. This lone experimental case has brought a decisive contribution to our understanding of memory and how our brain proceeds and stores information. In short, HM suffered from pharmacoresistant epileptic seizures, which considerably impaired his everyday life. In September 1953, at age 27, he underwent bilateral medial temporal lobe resection, after neurosurgeon W. Scoville had localized these regions as epileptic foci (see Figure 2.1).

Though the surgery was successful in terms of controlling his epilepsy, HM later developed severe *anterograde amnesia* - the inability to form new explicit memories - and progressive *retrograde amnesia* - the loss of memories preceding his surgery [Scoville and Milner, 1957]. Strikingly, HM's intellectual abilities were left unaltered: he showed no deficit in short-term memory storing. His ability to learn procedures was completely unchanged and he showed normal performance and progression in motor skill learning such as mirror writing [Milner, 1962; Corkin, 1965]. Later, HM was shown to have decreased ability to report pain, hunger and thirst [Hebben et al., 1985].

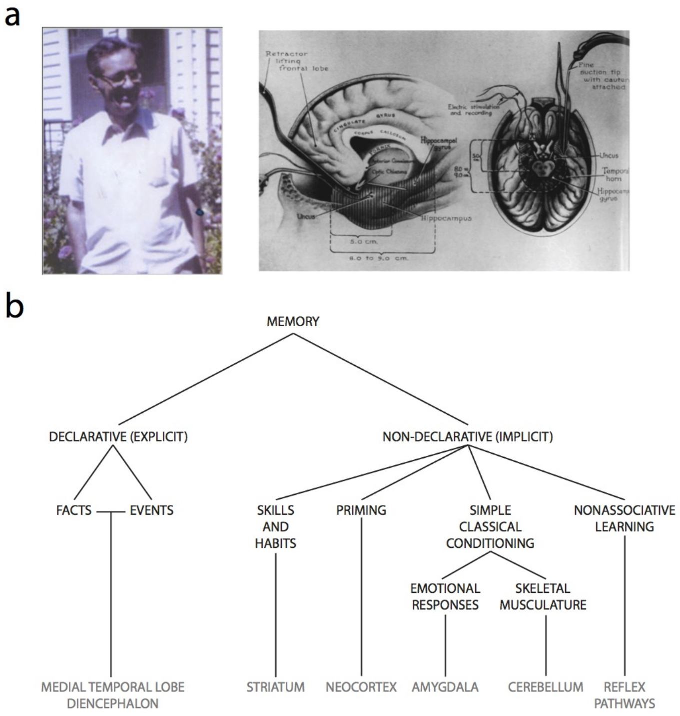

Figure 2.1 – Patient HM and the discovery of independent memory systems (a) HM (Henri Molaison - left) underwent bilateral medial temporal lobe removal. Schematic representation of the brain showing the dimensions of the hippocampal resection (right) **(b)** Taxonomy of memory systems and associated brain structures by Squire. Note the hierarchical structure of Squire's taxonomy and the fact that the double dissociation between declarative hippocampus-dependent and implicit memory is the first node of the tree. Medial Temporal Diencephalon stands for Hippocampus. **(a)** adapted from [Scoville and Milner, 1957] **(b)** adapted from [Squire, 1992].

The HM case was field-opening in neuroscience because it demonstrated the existence of a double dissociation (two independent systems) between *declarative memory* - the memories and knowledge than we can consciously access - and *non-declarative memory* - the learning of procedures and motor skills. While the first memory system required an intact hippocampus, the latter did not, because patient HM could still perform reliably. The question whether HM was an isolate case or if the hippocampus was critical for memory across species was set.

2.1.2 Memory Systems and classification

This was the first established demonstration of the existence of two distinct memory systems in the brain: one hippocampus-dependent, was involved in the formation and consolidation of self-referenced episodic memories and another one, hippocampus-independent, dedicated to the learning of specific procedures and motor tasks [Squire, 1986]. This classification was further enriched, notably by the dichotomy between *semantic memory*, as the memory of facts, usually referred as “knowledge”, and *episodic memory*, as the memory of events or the “autobiographic memory” [Squire, 1992]. The experimental findings on patient HM have triggered considerable interest in the hippocampus and adjacent structures, leading to a better understanding of its anatomy and its key role in memory processes, in both humans and animals (see Figure 2.1).

2.1.3 Space finds its place in the hippocampus

In parallel with the findings on patient HM, the discovery of place cells in 1971 by John O'Keefe gave the hippocampus a central role for the representation of space. John O'Keefe and his graduate student Jonathan Dostrovsky found that the firing pattern of hippocampus CA1 pyramidal neurons was strongly and robustly modulated by their location relative to spatial cues in a maze [O'Keefe and Dostrovsky, 1971]. In a similar manner to what Hubel and Wiesel described in 1962, these cells had receptive fields depending exclusively on the animal's location and head direction, which could hence be delimited in space. O'Keefe naturally called this preferred location a *place field* (see Figure 2.2).

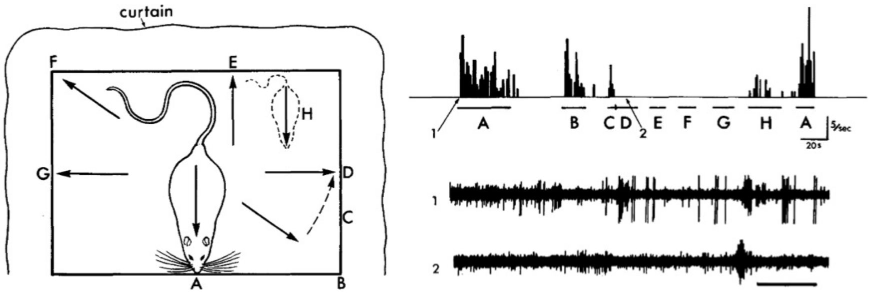

Figure 2.2 – First description of place cells by O'Keefe and Dostrovsky in 1971 O'Keefe and Dostrovsky reported "eight units that responded solely or maximally when the rat was situated at a particular part of the testing platform facing in a particular direction". The best example of one of these units is shown (right): the cell fires specifically when the rat is in a given location with its head pointing in A or B. Note that the first description of place cells gives a critical importance to head direction. Adapted from [O'Keefe and Dostrovsky, 1971].

Besides the novelty of this discovery, there are two striking facts about place cells. First, they do not depend on the sensory cues that the animal receives because the firing pattern of place cells is independent of the animal's trajectory to reach the place field. Thus, contrary to Hubel and Wiesel's orientation cells, they code for a high-order representation of space in the brain. Second, this representation of space is remarkably allocentric (not self-referenced), robust, stable in time and appears only a few minutes after novel environment exposure [O'Keefe and Nadel, 1978].

Place cells suggest the existence and integration of self-motion signals, such as speed, head-direction and proprioceptive signals. This low-level information is a necessary basis for the elaboration of a "cognitive map" and was demonstrated subsequently, as I will introduce later in details [Taube et al., 1990; Hafting et al., 2005]. The representation of space in the hippocampus seems to be shared across species and place cells have been found in monkeys [Ono et al., 1991], humans [Ekstrom et al., 2005], together with evidence for head-direction signals and self-motion representation [Chadwick et al., 2015]. Thus, it seems that the hippocampus possesses anatomical features that make it well suited for space representation in a broad range of species.

2.1.4 An integrative theory for time and space?

In regard of the diversity of the accumulating experimental evidence assigning a key role to the hippocampus, researchers have tried to integrate both the memory-related and space-related aspects (and more recently the emotional aspect) into a comprehensive model of hippocampal function. Computational modeling studies have tried to reproduce experimental results, based on the anatomical description of the hippocampus. David Marr developed a framework in which he proposed that the recurrent connections in CA3 are used to encode sensory inputs in a robust manner, for a subsequent transfer to cortical areas [Marr, 1971].

In the last decades, many theories about the hippocampal implication in memory and space have been proposed including the Declarative Theory of Hippocampal Function [Scoville and Milner, 1957; Squire, 1986], the Multiple-Trace Theory [Nadel and Moscovitch, 1997], The Dual-Process Theory [Aggleton and Brown, 1999] or the Cognitive Map Theory [O'Keefe and Nadel, 1978]. The Relational Theory [Cohen and Eichenbaum, 1995] is interesting in the sense that it does not assume anything on the type of stimulus processed by the hippocampus. It proposes that the hippocampus, because of its peculiar anatomical configuration is required to make associations between perceptually and conceptually distinct items. In this respect, spatial processing is just an example of relational processing. Experimental studies showing that information is stored in sequences through recurrent connections in CA3 support this theory [Redish and Touretzky, 1997]. The debate is still very open and recent findings suggest that rich and complex pattern coding schemes co-exist in the hippocampus.

2.2 The Hippocampal Formation

Its peculiar anatomy endows the hippocampus with specific functions. In this section, I describe the known anatomical features of the hippocampus and review experimental evidence for a functional differentiation of hippocampal sub-regions. I focus on the rat hippocampal formation (HF), giving insight from human and monkeys when relevant.

2.2.1 General Organization

The hippocampus is a medial temporal structure present in all mammalian species and strongly connected to all major regions in the brain. It is organized along an axis called septo-temporal (also called dorsal-ventral or “long” axis) in rodents. In humans or monkeys this axis is posterior-to-anterior (see Figure 2.3). The basic intrinsic circuitry is preserved across species but shows different extrinsic connectivity along the long axis, which raises the question whether the dorsal and ventral parts subserve the same function. Some authors even proposed that ventral and dorsal hippocampus can be considered as different organs [Fanselow and Dong, 2010]. The total volume of the human hippocampus is about 100 times that of the rat, and 10 times that of the monkey [Andersen, 2007].

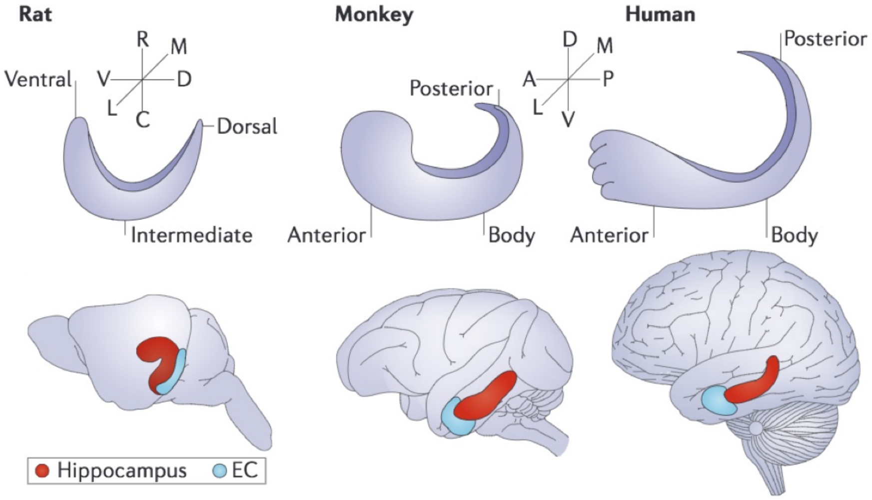

Figure 2.3 – Hippocampal formation in the brain of rats, monkeys and humans The general axial organization of the hippocampus and entorhinal cortex is preserved across species. In rats, the axis is septo-temporal and dorsa-ventral, whereas it is antero-posterior in monkeys and humans. Note the 90-degree orientation shift of the hippocampus long axis between primates and rodents. Adapted from [Strange et al., 2014].

2.2.2 Neuro-anatomy along the Transverse Axis

2.2.2.1 Anatomical Projections within the Hippocampus

Thanks to decades of research on the hippocampus, a relative consensus about its anatomical description has emerged, yet the inventory of its connections to other brain regions, and the area delineation based on molecular expression are still evolving. Ramon y Cajal did the pioneer work on hippocampal neuro-anatomy: his famous drawings remain the first precise anatomical description of the hippocampus and adjacent structures. He divided, the hippocampus into two major regions: a large-celled region, the *regio inferio* (the actual Dentate Gyrus) and smaller-celled region: *the regio superio* (the actual CA region) [Ramn y Cajal, 1911]. In a strict sense, the hippocampus is constituted of three major subfields CA1, CA2 and CA3, as was first described the Lorente de No [Lorente De N, 1934]. CA stands for *Cornu Ammonis*, first introduced by French neuro-anatomist De Garengeot in 1742, because of its horn-like shape. A broader definition encompasses the Hippocampal Formation (HF), including the Dentate Gyrus (DG), subiculum (Sub), presubiculum, parasubiculum and entorhinal cortex (EC). The main justification for the inclusion of these six regions is that they are linked one to the next by a major unidirectional pathway (see Figure 2.4). The first three links of this pathway has been early documented [Andersen et al., 1971] and will be described below. The hippocampus shows a consistent laminar structure, resulting from the alignment of pyramidal cells. The CA2 region is not described in details here mainly because of its relative small size compared to other regions, though it functional implication in spatial navigation has recently been demonstrated [Kay et al., 2016].

Dentate Gyrus

The DG is the first step of hippocampal processing. It receives direct synaptic input from EC through the perforant path. It is composed mainly of two cell types, the granule cell (GC) and the DG interneurons, arranged in three layers:

- The molecular layer, which contains the dendritic trees of GC
- The granule cell layer holding the cell bodies of GC
- The polymorphic layer or *hilus* that contains the mossy fiber collaterals and interneurons, mainly basket cells and hilar interneurons.

The GC cells axons form the mossy fiber pathway that connects to the CA3 region.

CA3 Region

The CA3 region is composed of four layers:

- The *stratum radiatum*, which contains direct entorhinal afferents and apical dendrites of pyramidal cells.
- The *stratum lucidum* which contains thorny excrescences with complex spine shapes. These excrescences connect the mossy fibers to CA3 pyramidal cells.
- The *stratum pyramidale* which contains the cell bodies of CA3 pyramidal cells.
- The *stratum oriens* which contains the basal dendrites of the CA3 pyramidal cells and most of recurrent collaterals.

The mossy fiber synapse is one of the largest and most powerful synapse in the brain. A single CA3 pyramidal cell can receive input from as much as 72 granule cells [Amaral et al., 2007]. There are about 3,500 perforant-path synapses from EC layer II and 12,000 recurrent collaterals from CA3 pyramidal cells [Andersen, 2007].

CA1 Region

The CA1 region receives input from the CA3 pyramidal cells by the Schaeffer's collaterals. This region is also composed of four layers:

- The *stratum lacunosum-moleculare* which contains direct entorhinal afferents and apical dendrites of pyramidal cells.
- The *stratum radiatum* which contains the Schaeffer collaterals and the commissural fibers.
- The *stratum pyramidale* which contains the cell bodies of CA1 pyramidal cells
- The *stratum oriens* which contains the basal dendrites of the CA1 pyramidal cells.

The CA1 and CA3 regions contain only 300,000 to 400,000 pyramidal cells (compared to the 1.2 million of GC). However this region contains various types of interneurons such as basket cells, bistratified cells, trilaminar cells, etc.

Subiculum

The subiculum lies at the very end of the hippocampal formation. Some authors group subiculum, presubiculum and parasubiculum in the *subicular complex*, while others mention the *parahippocampal region* including parasubiculum, presubiculum, EC, perirhinal and postrhinal cortex. These regions present distinct anatomical features. The subiculum starts when the dense pyramidal cell layer of CA1 begins to broaden. It mainly receives input from CA1 region and from EC. The subicululm is the main output pathway of the hippocampal formation to all main subcortical regions including Nuccleus Accumbens (NAcc), septal nuclei, hypothalamus and amygdala.

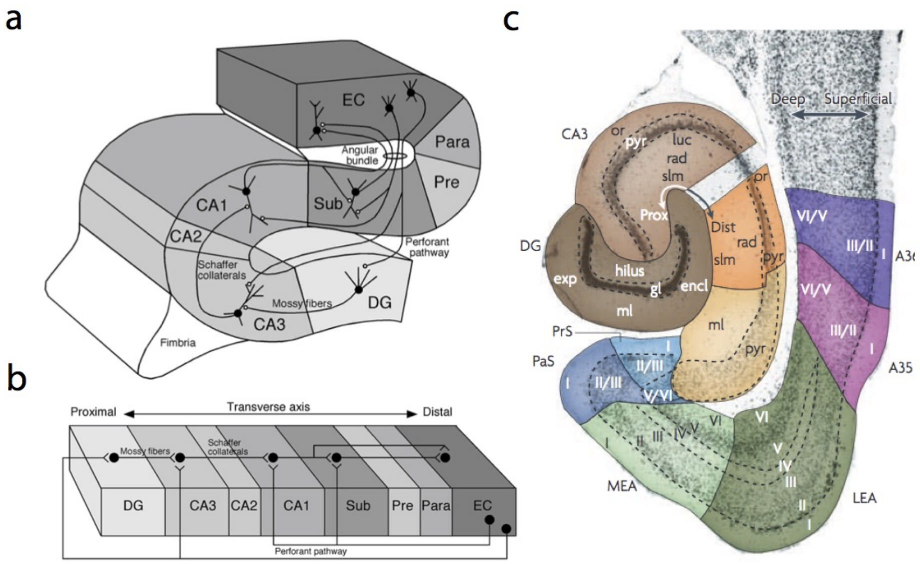

Figure 2.4 – **The intrinsic circuitry of the hippocampal formation in rats (a)** The hippocampal formation is composed of multiple unidirectional connections between distinct anatomical areas. The entorhinal cortex projects through the perforant pathways grouped into the angular bundle to DG, CA3 and CA1 regions and subiculum. Mossy fibers connect DG to CA3, which connects CA1 through Schaeffer's collaterals. CA1 projects back to EC while subiculum project to subcortical areas through the fimbria-fornix pathway. **(b)** Unfolded circuitry of the hippocampal formation. **(c)** Nissl stained segmentation of major structures in the HF and parahippocampal formation. **(a-b)** adapted from [Andersen, 2007] **(c)** adapted from [van Strien et al., 2009].

Entorhinal Cortex

The EC is both the entry point of the hippocampal circuit and its output. Like all cortical structures, it is organized in six layers (layer I to VI). Axons project directly to DG and CA3 through EC-layer II, while direct projections to CA1 and subiculum originate from layer III. The recurrent connections from the subicular complex terminate in layer IV. Once again, the number of synapses connecting EC to the DG is much larger (18,000) than to CA3 (3,500) or CA1 regions (2,500). The EC is the main source of projections to and from the neocortex, suggesting that it receives direct input from major sensory areas.

2.2.2.2 Major Fiber Bundles in the Hippocampal Formation

The major fiber-tract that consitutes the intrinsic connectivity of the HF is called the *angular bundle*. The first part of this circuitry is commonly referred to as the trisynaptic circuit including the perforant path (synapse 1), the mossy fibers (synapse 2) and Schaeffer's collaterals (synapse 3). This definition based on combined anatomical and electrophysiological considerations, states that the output of the hippocampus is directly transmitted to cortical and subcortical areas. Because it is now clear that these structures project mainly to EC and subiculum, the trisynaptic circuit should be only considered as a part of the intrinsic hippocampal formation circuitry.

The second and third major pathways in the hippocampal formation are *fimbria-fornix pathways* and dorsal and ventral *hippocampal commissures*. The first connects the HF to major subcortical structures including septal nuclei, striatum, thalamus, and hypothalamus and mammillary bodies. The latter groups the fibers crossing the brain midline to connect corresponding fields in the contralateral HF regions.

More recently, several direct pathways connecting directly the hippocampus to the prefrontal cortex have been discovered using retrograde tracers. The prefrontal cortex (PFC) and hippocampus have well-established roles in memory encoding and retrieval [Bontempi et al., 1999; Kennedy and Shapiro, 2004; Benchenane et al., 2010]. The mechanisms underlying these functions remain elusive, but recent studies using selective optogenetics silencing show that direct projections from Ventral Hippocampus to mPFC are critical for encoding - but not retrieval - of task-relevant spatial cues [Spellman et al., 2015]. Another recent study has established a direct projection from Prefrontal Cortex to Hippocampus (CA1 region) critically involved in top-down control of spatial memory, as measured in contextual fear response [Rajasethupathy et al., 2015]. Hence, new pathways are being discovered suggesting that our understanding of hippocampal neuro-anatomy is constantly evolving.

2.2.2.3 Hippocampal connectivity and information processing

Though common connections in the neocortex are largely reciprocal [Felleman and Van Essen, 1991], hippocampal connections are mostly unidirectional, which results in specific functions. First, the entorhinal cortex receives both the input (in its superficial layers) from and sends the output (from its deep layers) to the rest of the brain (mainly neocortex), suggesting a recurrent network and setting an important role to hippocampal-cortical interactions. Second, the hippocampus is highly connected to all major brain regions (which is preserved across species) both to cortical (via EC) and subcortical structures (via fimbria-fornix). Third, the hippocampus contains many types of interneurons suggesting multiple excitatory-inhibitory loops and granting it various resonant properties. Fourth, the hippocampal formation exhibits both serial (unidirectional synapses) and parallel (recurrent connections) processing: The advantage of these alternating pattern organization is that in successive layers the neuronal representations can be iteratively segregated (at parallel stages) and integrated (at recursive stages) [Buzsaki, 2011]. Finally, there is a striking degree of convergence and divergence in the HF, in the sense that neurons in the polymorphic layer of DG can spread information to 75% of the remainder of the network along the septo-temporal axis. This means that a small regional change in the hippocampus can largely affect distant brain regions [Andersen, 2007].

2.2.3 Neuro-anatomy along the Septo-temporal axis

Early experimental evidence has suggested that the hippocampal formation shows regional differences in its electrophysiological properties, in terms of spike discharges patterns between its dorsal and ventral parts [Elul, 1964] and lesion studies have shown that animal behavior is differentially affected depending on the location of the lesion along the dorso-ventral axis [Hughes, 1964; Nadel, 1968]. Based on the denser anatomical connections from the ventral hippocampus to the amygdala [Swanson et al., 1978], it was proposed that ventral and dorsal parts of the hippocampal formation had functionally different roles: the dorsal part would be associated with spatial processing, while the more ventral part would be associated with emotional memory [Gray and McNaughton, 1982]. Despite 50 years of active research, this question is still controversial.

2.2.3.1 Anatomical Gradients

The transverse hippocampal neuro-anatomy described above is not homogenous along the septo-temporal axis, both in terms of cortical and subcortical connectivity. The connections from the EC to the hippocampus preserve a topological organization: the dorsal parts of the EC connect preferentially to the dorsal parts of the hippocampus (see Figure 2.5) [Dolorfo and Amaral, 1998]. This topography is smooth without abrupt transitions from one structure to the other. The cortical projections to the EC are also topographically arranged in the same way: the cingulate areas involved in emotional regulation (infralimbic and prelimbic structures) connect preferentially with the ventral part of the EC, while the retrosplenial cortex, a structure known to be involved in spatial processing, targets the dorsal part of the EC. As a result, the cortical-hippocampal connectivity shows a topology that maps different cortical areas to HF regions preferentially, via preserved topographical re-routing by EC [Jones and Witter, 2007].

The subcortical-hippocampal connectivity displays the same gradient pattern: for instance, the dorsal half of the hippocampus projects to a small part of the lateral septum (LS), whereas more ventral part projects to increasing portions of the lateral septum. Because the LS preserves this topology in its projection to the hypothalamus, it comes out that dorsal and ventral parts of the HF are connected differentially to the hypothalamus, implying a different endocrine and autonomic response, which in turn modifies behavior differentially [Risold and Swanson, 1996].

2.2.3.2 Genetic Gradients

As opposed to anatomical projections, which show a gradual linear transition along the septo-temporal axis, gene expression domains show abrupt transitions and discontinuities. The recent development of genome-scale *in situ* hybridization has allowed 3D gene expression atlases of the whole brain [Lein et al., 2007]. This enables to delimit precisely and objectively anatomical regions that share overlapping gene expression domains. Such an analysis has demonstrated that the CA3 region can be separated into 9 anatomical domains (see Figure 2.5). Importantly, these CA3 domains have sharp borders and do not follow known anatomical delimitations for CA3, whereas CA1 and DG seem to respect a tripartite architecture between ventral, intermediate and dorsal hippocampus [Thompson et al., 2008].

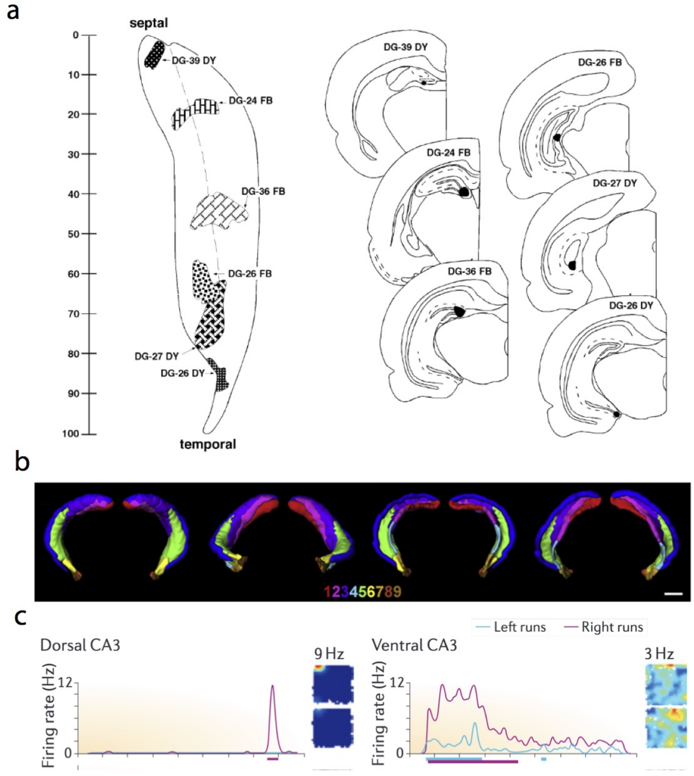

Figure 2.5 – Anatomy, Gene-expression and Functional Organization suggest different patterns of organization along the hippocampal dorso-ventral axis (a) Anatomical projections between Dentate Gyrus (DG) and Entorhinal Cortex (EC) suggest smooth gradual transition of connectivity between the ventral and dorsal parts of the hippocampus **(b)** Genome-scale in situ hybridization reveal 9 sharply delimited domains in area CA3 **(c)** Place fields show a gradual monotonic increase in size along the dorso-ventral axis in CA3 region of rats. **(a)** adapted from [Dolorfo and Amaral, 1998] **(b)** adapted from [Thompson et al., 2008] **(c)** adapted from [Kjelstrup et al., 2008].

Such changes could explain the different electrophysiological properties observed along the septo-temporal axis, such as neuronal excitability or synaptic plasticity. It is however important to mention that individual genes show a much higher variability in their expression pattern, including step-like changes, gradual changes and sharp demarcations. The opposite is also true for anatomical connections, with, for example, an abrupt division between the ventral two-third and dorsal one-third of the HF: mossy fibers and Schaeffer's collateral do not cross this subdivision [Amaral and Witter, 1989]. Thus, the organization of the hippocampus along this axis might be a superposition of sharp domains and continuous smoothly graded transitions [Strange et al., 2014].

2.2.3.3 Functional differentiation

The functional differentiation of the hippocampus is still debated and studies have led to conflicting results and extensive discussions [Moser and Moser, 1998; Fanselow and Dong, 2010; Strange et al., 2014]. I will however mention some important results about dorso-ventral functional segregation of the hippocampal function.

Though place cells do not exhibit a particular topography, in the sense that neighboring place fields in actual space do not transpose easily to neighboring cells in the CA1/CA3 regions [O'Keefe and Nadel, 1978], the size of place fields and the oscillation frequency exhibit long-axis progressive gradients so that ventral place fields cover a wider range and are less selective than dorsal ones (see Figure 2.5) [Kjelstrup et al., 2008]. This change is mirrored by an increase in grid spacing along the dorso-ventral axis of the EC, but in contrast to the aforementioned this gradient shows discrete step-like increases [Stensola et al., 2012].

Abrupt changes are also found in the functional role of the hippocampus to mediate fear learning: anatomical projections to the amygdala are present only in the ventral two-thirds of the hippocampus. This explains why the ventral hippocampus but not the dorsal part plays a key role in mediating unconditioned fear behavior [Bannerman et al., 2002]. Finally, some studies have revealed a specific role for the intermediate part of the hippocampus. Selective lesions along the septo-temporal axis have shown that the intermediate hippocampus is specifically critical for rapid place learning [Bast et al., 2009]. The functional organization of the hippocampus seems to reveal both continuous and discontinuous patterns along the HF long axis, which might result from the fact that anatomical and genetic organization superimpose in both.

2.3 Neural Patterns in Rodent Hippocampus

The hippocampus is thus a complex network with a peculiar architecture displaying both unidirectional and recurrent connectivity along its transverse axis and functional gradients along its septo-temporal axis. The high degree of variability in interneurons together with its strong connectivity to almost all major cortical and subcortical structures suggests a strong implication in a broad range of functions and behaviors. In this section, I review its most salient electrical patterns, which include both large-scale (theta rhythm) and more local (sharp-wave ripples and gamma rhythms) oscillations. I also present briefly the main individual cell types discharge profiles with behaviorally-relevant correlates, such as place cells or grid cells. The putative functions of theta rhythm are presented in a separate section below.

2.3.1 Brain Rhythms

2.3.1.1 Two mutually exclusive hippocampus states

The oscillatory activity of the hippocampus in awake rodents is dominated by two major oscillatory profiles, a high-amplitude irregular pattern called *Large Irregular Activity* (LIA) associated with stationary and consummatory behaviors such as grooming and eating, and a small-amplitude highly regular slow activity, associated with locomotion, head movement, arousal, anxiety - and surprisingly REM sleep - first named *Rhythmic Slow Activity*, and now commonly referred as *theta rhythm* [Green and Arduini, 1954; Vanderwolf, 1969; O'Keefe and Nadel, 1978].

These two states are mutually exclusive. LIA is accompanied by sharp-wave ripples (SWR) complexes, which are a superposition of a large amplitude slow deflection and a fast oscillation in the 140-220 Hz frequency range. Gamma oscillations (30-100Hz) can be associated with both LIA and theta. Other transient oscillations have been reported such as beta rhythm [Berke et al., 2008] or flutter [Nerad and Bilkey, 2005], but they seem of minor relative importance. During sleep, the hippocampus is also dominated by LIA (NREM sleep), theta (REM sleep), an intermediate profile known as Slow-Irregular Activity (SIA) [Jarosiewicz et al., 2002] and, as more recently described, slow-oscillations similar to cortical slow-waves during SWS [Wolansky et al., 2006].

The classical understanding of this dichotomy between LIA and theta in the hippocampus is that they reflect complementary functional states. Theta has long been related to spatial memory [Landfield et al., 1972; Winson, 1978] and influential models of gradual memory transfer from hippocampus to neocortex have been proposed [Marr, 1971]. In view of this evidence, theta rhythm is commonly described as the *online* state of the hippocampal network, associated with memory formation, whereas LIA and associated SWR represent its *offline* mode, associated with memory consolidation and transfer to cortical areas [McNaughton, 1983; Buzski, 1989] (see Figure 2.6).

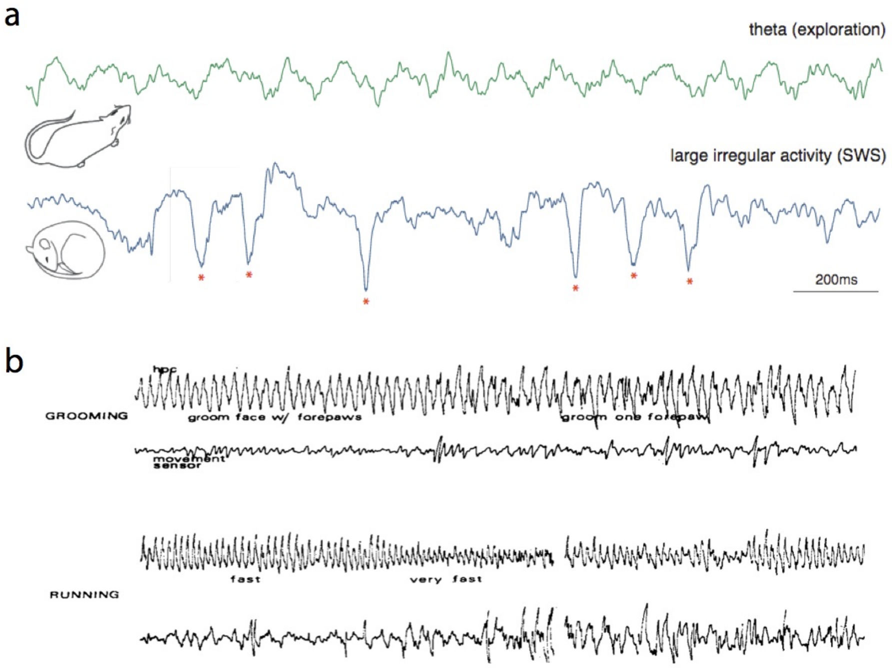

Figure 2.6 – Brain Rhythms in the Hippocampus (a) The hippocampus displays two mutually exclusive oscillatory profiles: theta associated with exploration, locomotion and REM sleep and large irregular activaty (LIA) prominent during quiet waking and SWS. **(b)** Theta rhythm is divided into two major oscillatory profiles: type I theta (8-12 Hz) strongly associated with locomotion and suppressed by urethane anesthesia (not shown) and type II theta (4-8 Hz) associated with immobility, arousal and anxiety, suppressed by atropine. **(a)** adapted from [Girardeau and Zugaro, 2011] **(b)** adapted from [Kramis et al., 1975].

2.3.1.2 Theta

In this section, I present an up-to-date picture of theta rhythmicity, and experimental evidence about its functional relevance.

Profile

Theta rhythm was early reported in rabbits [Jung and Kornmller, 1938] but later discovered in most mammals including cats, rats, mice, bats, monkeys and humans [Ekstrom et al., 2005; Ulanovsky and Moss, 2007; Jutras et al., 2013]. Most prominent in the hippocampus where amplitudes can reach 1 to 2 mV, the oscillations are present in many cortical and subcortical regions. In the hippocampus, it displays a characteristic laminar profile with a gradual phase shift along the dorso-ventral axis, so that superficial and deep layers oscillate with phase inversion [Bragin et al., 1995]. The strongest signal can be recorded from stratum radiatum in the CA1 region. Current source analysis reveals multiple theta dipoles in CA1: inhibition from local interneurons that receive direct projections from the medial septum (MS) creates a source in the stratum pyramidale, CA3 input creates a sink in the stratum radiatum and EC afferents create another sink in the stratum lacunosum moleculare, which disappears after EC lesion [Ylinen et al., 1995; Kamondi et al., 1998; Buzski, 2002] (see Figure 2.7).

Behavioral Correlates

Theta rhythm is robustly observed during movement and exploratory behaviors, such as running, walking, sniffing, head-turning and jumping [Vanderwolf, 1969]. It exhibits higher amplitude during movement versus passive behavior, especially when sensory sampling occurs at theta frequency [Terrazas et al., 2005], and theta power is strongly correlated to running speed (theta frequency also correlates with running speed) [Rivas et al., 1996; Lever et al., 2009] rhythmic sniffing [Macrides et al., 1982], head movement [Ledberg and Robbe, 2011] and whisking. However, mere exploratory whisking does not exhibit theta phase locking, which suggests that theta rhythm is involved in behaviorally relevant stimulus sampling [Berg et al., 2006].

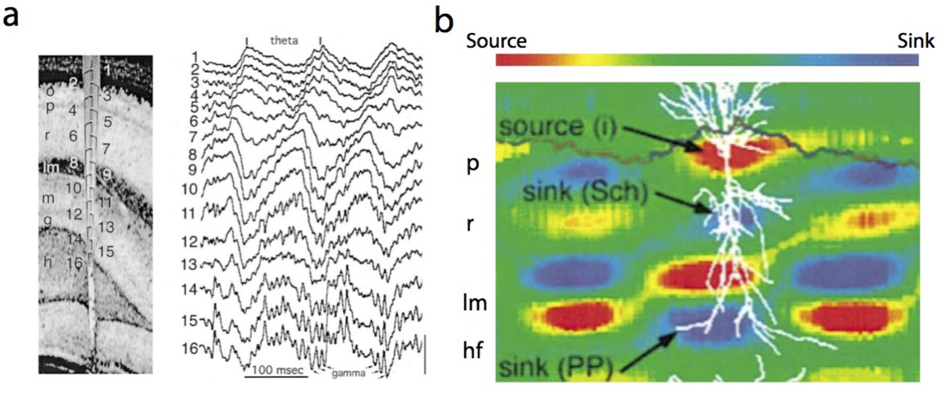

Figure 2.7 – Laminar Profile of Theta Rhythms and Generators in the Hippocampus **(a)** Intra-hippocampal recording of 16 sites along the dorso-ventral axis in a freely moving rat shows phase inversion on both sides of the rhinal sulcus (between r and lm, site 7 and 8). The strongest amplitudes are recorded in the stratum radiatum (r) and stratum lacunosum moleculare (lm). Note that gamma oscillations superimpose on theta strongly in the deep layer especially the hilus **(h)** **(b)** Current Source Density analysis reveals multiple theta dipoles in the hippocampus including a local source in the pyramidal layer and two sinks: one in the stratum radiatum (Schaeffer's collaterals) and one in the stratum lacunosum moleculare (Perforant Paths from EC). **(a)** adapted from [Bragin et al., 1995] **(b)** adapted from [Kamondi et al., 1998].

Classical Type I and Type II distinction

Early studies have distinguished two types of hippocampal theta which can be separated based both on pharmacologic and behavioral grounds. Kramis and colleagues reported that immobility-related theta (type II) oscillates in the 4-8 Hz-frequency band, is mediated by cholinergic agonists and is suppressed by systemic injections of atropine (this minimally affects locomotion theta in rabbits and rats) [Kramis et al., 1975]. Conversely, locomotion-related theta (type I) oscillates in the 8-12 Hz-frequency band and is abolished by most-anesthetics such as ethyl ether or urethane. It has a non-cholinergic profile and is likely mediated by serotonin agonists [Vanderwolf and Baker, 1986; Crooks et al., 2012] (see Figure 2.6).

The function of type II theta is less clear than type I and can be viewed as a sensory theta, linked to anxiety, as it is observed in the presence of predators [Sainsbury, 1998] or in terms of preparatory movement [Bland and Oddie, 2001]. Some authors have proposed an integrative view of hippocampal theta based on the linear relationship between theta frequency and running speed. Burgess proposed that the two types of theta are two components of the same relationship: the type II atropine-sensitive component of theta corresponds to the *intercept* of this relationship and is independent of running speed and entorhinal afferents, whereas type I theta corresponds to the *slope* of this relationship and is mainly driven by EC. They also described velocity-controlled oscillators: neurons whose firing show theta-band modulation increasing with running speed [Geisler et al., 2007]. A potential role for this flexible theta modulation would be to maintain robust phase locking of sensory events to theta irrespective of running speed. This is commonly referred to as the *dual-oscillator model* [Burgess, 2008].

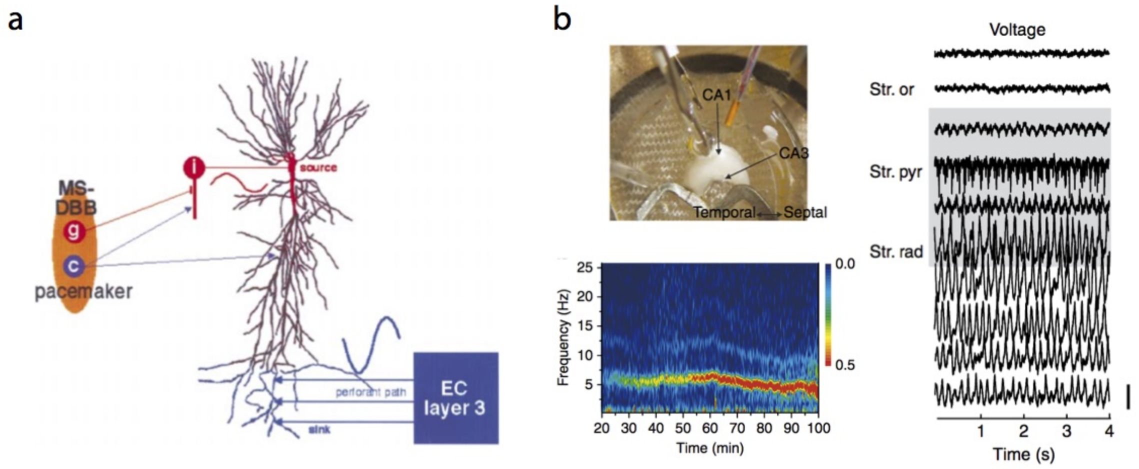

Figure 2.8 – **Multiple Oscillators Can Elicit Theta Rhythmicity (a)** The classic model of theta generation proposes that GABAergic neurons from MS-DBB provide pacemaker inhibition to hippocampal interneurons whereas cholinergic afferents modulate cell excitability via EC projections. **(b)** Evidence that theta rhythms can emerge spontaneously in-vitro without MS afferents. Note the high similarity between *in vitro* and *in vivo* theta recording, especially phase reversal between superficial and deep layers. **(a)** adapted from [Buzski, 2002] **(b)** adapted from [Goutagny et al., 2009].

Medial Septum Classic Model

An early finding by Green and Arduini showed that bilateral lesion to the medial septum (MS) disrupts both types of theta activity [Green and Arduini, 1954]. This led to the classic view of theta generation (see Figure 2.8): Medial Septum-Diagonal Band of Broca (MS-DBB) area entrains hippocampal neurons at theta frequency in two manners: GABAergic MS interneurons act as "pacemaker cells" and drive DG, CA3 and CA1 hippocampal principal cells by rhythmically entraining inhibitory interneurons, which are phase-locked to theta [Toth et al., 1997]. The cholinergic interneurons of the septum do not fire rhythmically at theta frequency but are believed to modulate the excitability of other hippocampal neurons. Cholinergic inhibition has been shown to create theta activity in deafferented hippocampal slices [Konopacki et al., 1987]. This finding has considerably prompted the interest in *in vitro* protocols to study rhythmic network activity. The role of MS is likely more complex, as shown by the evidence that septal interneurons project to different types of interneurons in the hippocampus, which fire at different phases of the theta cycle [Somogyi et al., 2013].

Multiple Theta Oscillators in the Hippocampus

Surgical removal of the EC disrupts the current source in the *stratum lacunosum moleculare* and the remaining theta rhythm is blocked by atropine. Hence, EC cortex provides sufficient excitatory drive to entrain CA1 neurons but is not sufficient for type II theta to occur [Ylinen et al., 1995]. It has been demonstrated that medial septum afferents are not necessary to produce theta rhythm: Goutagny and colleagues have shown that theta rhythms can spontaneously occur in an isolated intact hippocampal preparation, with a similar profile as *in vivo* theta. This theta activity pertained after CA3 removal and local inactivation of intermediate hippocampus did not eliminate theta but resulted in a lack of coherence between septal and temporal poles [Goutagny et al., 2009]. Together, these results suggest that theta rhythm can be produced by local interactions between hippocampal interneurons and pyramidal cells (see Figure 2.8).

Theta are traveling waves

A question remains about the origin of the needed excitatory drive provided in the isolated hippocampus preparation. Some authors have suggested that it might arise from intrinsic properties of some pyramidal neurons that promote resonance at theta frequency. It has been found that many hippocampal neurons which exhibit theta rhythmic firing express Hyperpolarization-activated cyclic nucleotide-gated (HCN) channels, which are also expressed in the MS. These channels mediate slow depolarizing currents that can drive the membrane back to threshold to trigger action potentials, and thus pertain rhythmic activity [Maccaferri and McBain, 1996; Varga et al., 2008]. Recent evidence shows that theta rhythms are not stationary but traveling along the septo-temporal axis during normal locomotion [Lubenov and Siapas, 2009; Patel et al., 2012] (see Figure 2.9) and that theta can propagate backwards and display reverse flow in the hippocampus following subiculum rhythmic excitation in *in vitro* intact hippocampus preparation [Jackson et al., 2014]. These results suggest that theta waves result from a network of weakly coupled oscillators and that the septal hippocampal pole entrains the temporal pole into theta rhythmicity.

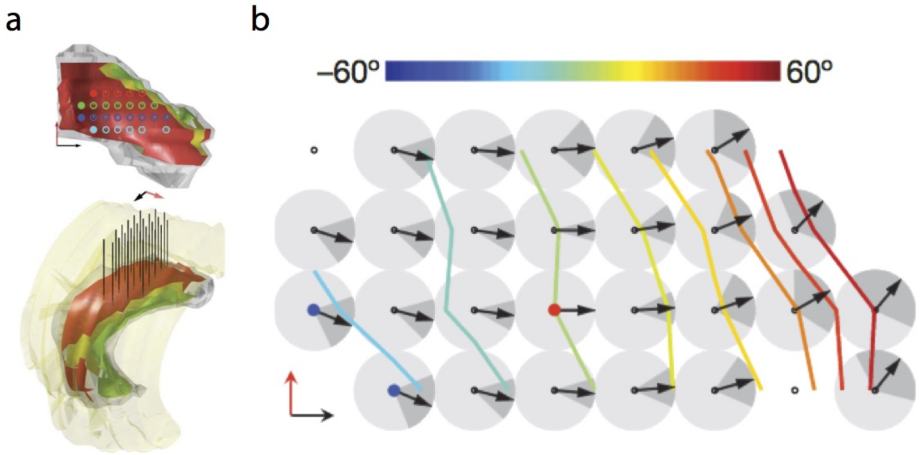

Figure 2.9 – Theta waves are traveling along the septo-temporal axis of the hippocampus (a) High density silicon probes implanted along both the transverse and dorso-ventral axes of the hippocampus **(b)** The bidimensional profile of instantaneous phase reveals wavefronts of theta waves traveling along the dorso-ventral axis. Adapted from [Lubenov and Siapas, 2009].

2.3.1.3 Sharp-Wave Ripples

Profile

Sharp Wave Ripples complexes (SWR) are the dual of theta activity in the hippocampus. They are observed in the CA1 region during waking immobility, slow-wave sleep (SWS) and consummatory behaviors [Buzski, 1986; Lee and Wilson, 2002; Jadhav et al., 2012]. They are constituted of large deflections in the 10-15 Hz-frequency band (sharp waves) accompanied with fast oscillations: ripples (> 100 Hz) (see Figure 2.6). SWR are mainly restricted to the hippocampus but can be observed in the EC [Chrobak and Buzski, 1996] and they are thought to be generated locally as they robustly occur in hippocampal slices [Kubota, 2002]. Sharp wave ripples have been demonstrated to carry the replay of previous experience [Wilson and McNaughton, 1994; Lee and Wilson, 2002]. The fact that this replay displayed a strong temporal compression was believed to convey encoding of spatial experience at a temporal scale consistent with the time constants of STDP [Bi and Poo, 1998]. Later studies showed that selective disruption of SWR during SWS impaired memory, definitely establishing the role of replay in memory consolidation [Girardeau et al., 2009; Ego-Stengel and Wilson, 2010].

Generation

The actual evidence about SWR generation shows that sharp waves are excitatory events that arise from CA3 afferents, whereas ripples are generated locally in the CA1 region by basket cells interneurons. CA1 place cells have been demonstrated to be phase-locked to ripples whereas CA3 place cells are not [Csicsvari et al., 1999]. CA1 ripple frequency has been found to positively correlate with sharp-wave magnitude in sleeping rats, which could be a mechanism of modulation for CA1 to send stronger output to downstream target, such as neocortical sites implicated in memory storing [Sullivan et al., 2011]. Finally, it has been shown that CA1 place cells receive shunting inhibition from ripples and that LTP between

CA3 and CA1 decreased in hippocampal slices, supporting the idea that ripples support memory consolidation by inhibiting encoding mechanisms and sending only the most strongly encoded patterns to downstream targets [English et al., 2014].

Function

The classical putative function of SWR is to perform offline memory consolidation, which is consistent with the unconscious state of SWS but the discovery of awake SWR and reverse replay has shed a new light on our understanding of SWR [Foster and Wilson, 2007]. Recent evidence has shown functional implication in memory tasks during active "online" processing. It is critical for normal processing that place cells fire at times when the animal is outside of their place field (during sleep for instance): in this case, they need another type of excitatory input which can be provided by sharp waves [English et al., 2014]. Two influential studies have supported the idea that SWR are involved in spatial planning: Jadhav and colleagues have first demonstrated that disruption of awake sharp-wave ripples impaired memory-guided trajectory planning and Pfeifer and colleagues have observed that place cells sequences observed during SWR (occurring during rest periods of the task) encode paths subsequently taken by the animal to reach goal locations [Jadhav et al., 2012; Pfeiffer and Foster, 2013]. SWR have also been involved in intrinsic processes like memory retrieval, future event envisioning or imagining experience that has never happened [Carr et al., 2012].

2.3.1.4 Gamma

Profile

Gamma rhythms have long been observed in visual cortical areas [Gray et al., 1989]. Hippocampal gamma rhythms have received late attention, mainly owing to the fact that they are of lower amplitude than theta, SWR or cortical gamma [Hughes, 1964]. Additionally, gamma rhythms encompass multiple frequency bands, ranging from 25 Hz to 150 Hz. In rodents, accumulating evidence shows that gamma can be divided into, at least, two distinct components: low-gamma (slow-gamma) oscillations in the 25-50 Hz and high-gamma (or fast gamma) oscillations in the 60-100 Hz frequency range [Bragin et al., 1995; Csicsvari et al., 2003; Colgin et al., 2009]. Some authors have reported an additional high gamma band in the range of 100-150 Hz, or high frequency oscillations (HFO), but this latter subdivision is less widely spread [Belluscio et al., 2012; Tort et al., 2013].

Generation

The dominant model of gamma generation proposes that slow and fast gamma rhythms are generated by different mechanisms in CA1: slow gamma activity dominates in stratum radiatum and is modulated by CA3 interneurons, whereas fast gamma is most prominent in the stratum lacunosum moleculare and results from MEC inhibitory entrainment (see Figure 2.10). Inhibitory interneurons seem to be crucial for gamma generation because inhibitory events recorded in both CA1, CA3 and DG pyramidal cells are synchronous with gamma rhythm and fast-spiking interneurons consistently fire at gamma frequency [Csicsvari et al., 2003]. Theta phase modulates both gamma amplitude and gamma phase, thus it is likely that specific inhibition or excitation at particular theta phase may trigger gamma rhythmicity. Consistent with this idea, parvalbumin-positive interneurons blockade reduces theta-gamma coupling in transgenic mice [Wulff et al., 2009]. Finally, some interneurons have been found to exhibit phase locking at both slow and fast gamma, suggesting that a portion of CA1 could produce both types of gamma depending on the strength of excitatory and inhibitory inputs [Schomburg et al., 2014].

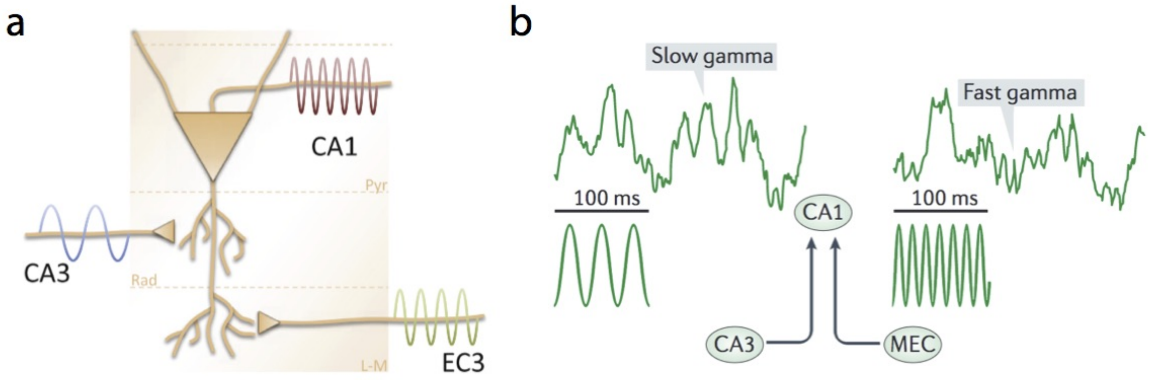

Figure 2.10 – Mechanisms of generation and putative function of gamma rhyhtms **(a)** CA1 region receive multiple input that are involved in gamma oscillation: local inhibition by fast spiking interneurons (red), CA3 collaterals (blue) and EC perforant pathway (green) **(b)** Two types of gamma commonly observed superimposed on theta oscillation: Slow gamma (25-50 Hz) supports coordination between CA3 and CA1 while fast gamma (55-100 Hz) supports MEC-CA1 communication. **(a)** adapted from [Schomburg et al., 2014] **(b)** adapted from [Colgin, 2016].

Function

Gamma rhythms can be thought of as complementary mechanisms subserving different aspects of memory processing. A growing body of evidence supports the idea that high gamma is required to synchronize the hippocampal-entorhinal complex for successful memory encoding, while slow-gamma is involved in memory retrieval by allowing efficient communication with the CA3 recurrent network, a region known to store previously experienced memory traces [Redish and Touretzky, 1997] (see Figure 2.10). In support of the first hypothesis, a recent study showed that fast but not slow-gamma power in the MEC was reduced by scopolamine injections resulting in impaired memory encoding without affecting retrieval [Newman et al., 2013]. Fast gamma modulation has been reported to correlate with ongoing behavior such as running speed on a linear track [Ahmed and Mehta, 2012], performance of a spatial alternation task [Yamamoto et al., 2014] and to encode recent locations and ongoing trajectories [Zheng et al., 2016]. In support of the second hypothesis, theta phase slow-gamma amplitude coupling has been shown to reflect performance in odor-association task and to occur at the time where memory retrieval is necessary [Tort et al., 2008]. Coordination between LEC and CA1 was found to develop during odor-task learning, possibly to facilitate sensory cues from LEC to trigger odor representation in CA3 [Igarashi et al., 2014]. Finally, Bieri and colleagues provided evidence that slow gamma was selectively associated with prospective coding, a process thought to reflect memory retrieval, while high gamma was stronger during retrospective coding [Bieri et al., 2014].

2.3.2 Individual neurons coding for space

John O'Keefe along with Edvard and May-Britt Moser have been awarded the 2014 Nobel Prize in Medicine and Physiology for their discoveries of "cells that constitute a positioning system in the brain", namely *place cells*, found in the CA1 and CA3 regions of the hippocampus, which encode a rat location in a given environment [O'Keefe and Dostrovsky, 1971], and grid cells in the medial entorhinal cortex (MEC) that fire rhythmically along a geometrically-regular grid pattern when a rat forages through its environment [Hafting et al., 2005]. These neurons' activity relate closely to theta oscillations through a phenomenon called phase precession (see next section), suggesting that the animal's location in a place field is robustly encoded in the phase relative to the ongoing theta oscillation both for place and grid cells [O'Keefe and Recce, 1993; Hafting et al., 2008]. Phase precession shows unequivocally that a tight relationship exists between the firing of individual cells and the phase of local oscillations reflecting network activity of large cell ensembles.

Subsequent studies have found a large number of neuron types that exhibit discharge profiles modulated by the animal's behavior. Head direction cells in the presubiculum fire when the animal's head is pointing into one direction, exactly like a compass [Ranck, 1984; Taube et al., 1990]. Boundary cells in the subiculum, fire preferentially in the proximity of a task-relevant landmark such as a wall or gap [Lever et al., 2009]. Recent findings have unveiled a whole new range of neurons that encode complex information such as elapsed time in a given location (*time cells* [Pastalkova et al., 2008; Kraus et al., 2013]), place cells modulated by the location of reward in a spatial alternation tasks (*splitter cells* [Wood et al., 2000; Frank et al., 2000]) and cells showing discharge rate increase proportional to running speed (*speed cells* [Kropff et al., 2015]).

All these neurons participate in the neural representation of space and contribute to "path integration", that is the calculation of optimized trajectories in an environment. Some of these units convey high-level information (place cells, head-direction cells) derived from, but independent of primary sensory cues in a visual scene. Others are believed to integrate sensorimotor information such as limb movement, visual and somatotopic cues to derive "objective" representation of space or locomotion (grid cells, speed cells), while others correspond to internal representations of space or time that can change dynamically according to task demands (time cells, splitter cells). How this information is integrated and transmitted to carry on complex tasks remains to be elucidated.

2.4 Function of Theta Rhythms

Despite decades of research about theta rhythmicity, its functional relevance remains a source of great debate. This is partly due to the omnipresence of this activity in a wide range of tasks and species. The similarity of theta patterns across species is still controversial and I review here the state-of-the-art, mainly based on rodent studies.

2.4.1 Information Packaging

Due to its high connectivity to subcortical structures, the hippocampus receives a rich multimodal flow of information. Theta rhythm is supposed to coordinate the inflow from sensorimotor areas to sample them into discrete 'chunks'. In this view, one theta cycle can be seen as a discrete processing unit that contains information about the current state of the environment at a given moment [Bland and Oddie, 2001; Colgin, 2013]. This view of incremental processing is especially well-suited in processes like pattern completion or comparison between network predictions and environmental inputs, which are believed to occur in the hippocampal network [Gardner-Medwin, 1976; Vinogradova, 2001].

Supporting this idea, theta rhythmicity has been shown to correlate with the movements used to acquire sensory stimuli like running and whisking in rats, working memory in monkeys. Theta is not phase-locked to whisking in rats when they are merely sampling in the air rather than actively sampling task-relevant stimuli [Berg et al., 2006]. Furthermore, sensory stimulation at theta frequency was shown to increase theta power, which suggests that theta-frequency intake of stimuli might be optimal for downstream processing [Kepecs et al., 2007; Ledberg and Robbe, 2011; Abe et al., 2014].

Electrophysiological evidence also supports the idea that theta cycle is critical for internal representation of the environment. In an elegant experiment, Jezek and colleagues made rats familiar with two different environments, each one containing recognizable spatial cues. After the animals had acquired a stable representation of both environments, they were placed in a third environment, which could be switched to resemble either one of the two environments. They observed that a transition from one environment to the other could trigger "network flickering": a period of time during which both internal representations were activated in the CA1 region before stabilizing to the actual environment. Importantly, each environment representation was nested into one theta cycle and 99% of theta cycles contained only one representation, suggesting that theta segregates spatial representations [Jezek et al., 2011]. Another study has provided similar results with head direction cells in the medial entorhinal cortex (see Figure 2.11): cells that fired when the animal was pointing its head in the preferred direction did so every second theta cycle ("cycle skipping"), while cells that fired out of their preferred phase did so on every cycle, resulting in a segregation of two population of neurons at each theta cycle [Brandon et al., 2013].

2.4.2 Metric Coding and Temporal Organization

The most important discovery about brain rhythms is perhaps the phenomenon of *phase precession*, because it has provided a strong link between place cells that encode location in their firing rate, and theta rhythm, which coordinates large neuronal ensembles [O'Keefe and Recce, 1993]. Phase precession relies on the fact that place cells fire at a slightly higher frequency than ongoing theta oscillation when a rat crosses a place field, resulting in a gradual shift of the place cell discharge from the peak (when the animal enters the place field) to the trough (when the animal leaves the place field) of the ongoing theta oscillation (see Figure 2.12ab). The relationship between the firing rate of a place cell and theta phase is so robust, that it can be used to predict the position of the animal within its field accurately. More importantly, the fact that successive place fields are overlapping results in formation of theta sequences that encode the animal trajectory [Skaggs et al., 1996] (see Figure 2.12c).

These theta sequences display temporal compression, allowing for LTP strengthening synaptic weight between successive place cells. Hence, these sequences are preferentially reactivated

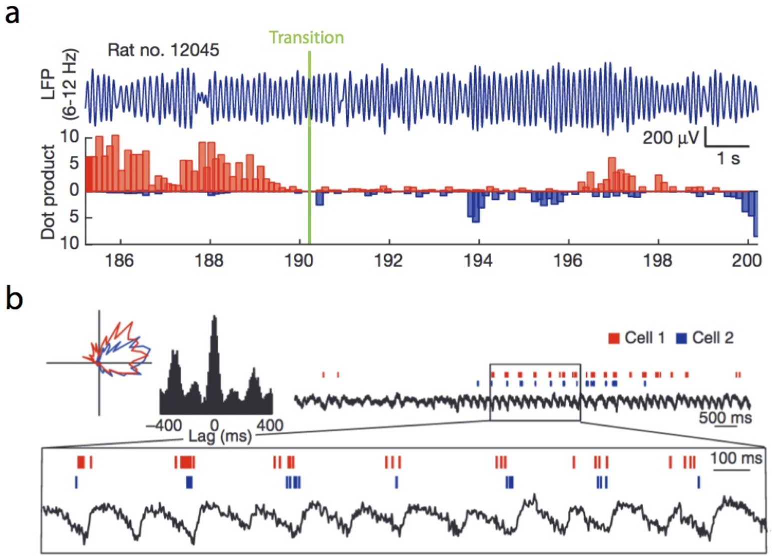

Figure 2.11 – Segregation of spatial representations across theta cycles (a) Example of network flickering between two environment representations. Before transition (green line), the red environment representation is stable. After transition, the network flickers by alternating blue and red representations before stabilizing to the blue representation. Note that each theta cycle contains only one of a given environment. **(b)** Cycle skipping in head-direction cells: example of two cells with overlapping preference map. These cells fire consistently every second cycle of theta oscillation. **(a)** adapted from [Jezek et al., 2011] **(b)** adapted from [Brandon et al., 2013].

during SWS both after forward and backward travel [Lee and Wilson, 2002; Cei et al., 2014]. A recent study showed that the inactivation of medial septum in rats disrupted the organization of these sequences and impaired performance in a delayed non-matching to sample task, which suggests that theta rhythm is a necessary condition for the formation of such sequences [Wang et al., 2014]. However, theta rhythm is not required for the formation of place fields in rats [Brandon et al., 2014]. Theta sequences do not merely reflect stronger connections between place cells: they represent task-relevant concepts such as a path to a reward or the planning of future events [Gupta et al., 2012; Pfeiffer and Foster, 2013]. Lisman and Idiart presented an influential model in which they proposed that several objects are individually coded at different phases of the ongoing theta oscillation. According to this model, each cell assembly coding for a given object fires within the same gamma cycle (each of these cycles occurring at a particular theta phase) and that the series of objects is represented into the same theta cycle [Lisman and Idiart, 1995]. Hence, their model predicts that the maximal memory load for associative tasks is 7 +/− 2 independent items, corresponding to the ratio between gamma and theta periods. Importantly, it gives a functional role for phase-amplitude coupling and theta sequences. The ability of the hippocampus to encode sequences can thus explain why it is critically important for both spatial tasks and episodic memories [Cohen and Eichenbaum, 1995; Buzski and Moser, 2013].

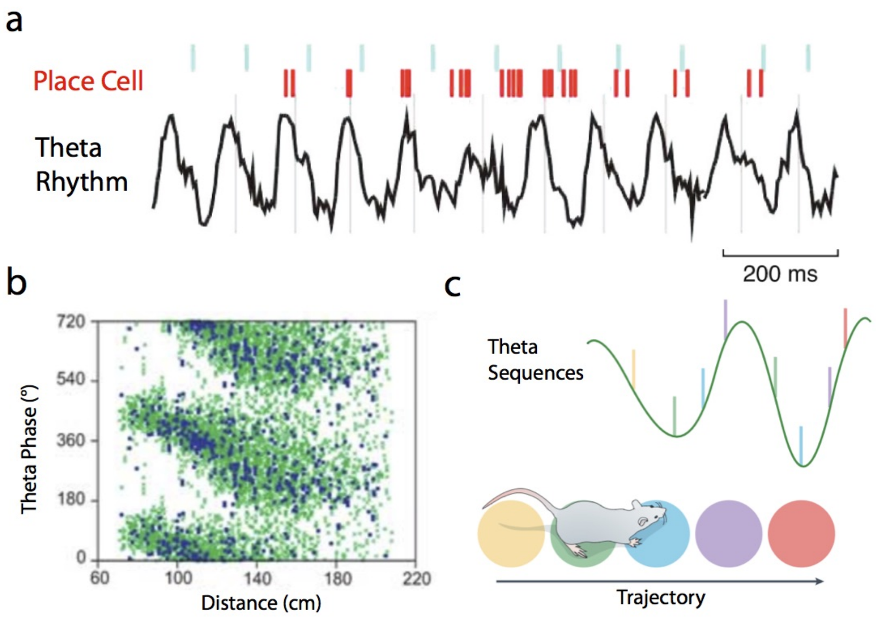

Figure 2.12 – Phase precession in hippocampal place cells and the formation of theta sequences (a) Place cell action potentials (red ticks) and theta rhythm (black) as a rat crosses a place field. Note the gradual shift of place cell firing at earlier theta phases, from the peak to the trough of theta oscillation (blue ticks) **(b)** Raster plot of the relationship between distance on a linear track and theta phase for two place cells. Each dot corresponds to an action potential. Note the linear dependence between theta phase and distance within the place field. **(c)** As a rat crosses several place fields, phase precession results in theta sequences that correspond to temporal compression of the animal trajectory. **(a)** adapted from [Huxter et al., 2003] **(b)** adapted from [Senior et al., 2008] **(c)** adapted from [Colgin, 2016].

2.4.3 Theta and memory

The early studies on theta activity have highlighted the fact that the extent of theta activity in electroencephalogram predicted how quickly and how well animals learned and remembered [Landfield et al., 1972; Winson, 1978]. They established theta rhythm as a necessary substrate for a variety of memory tasks in a wide range of species [Huerta and Lisman, 1995; Cavanagh and Frank, 2014]. However, the exact mechanisms of the functional role of theta in memory function remain difficult to integrate in a comprehensive model. In this section, I present a model based on phase coding relative to theta oscillations for memory encoding and retrieval, together with recent evidence supporting this view (see Figure 2.13).

One challenge of all memory systems is to encode novel information in the face of interference from previously encoded associations (proactive interference). This problem can be linked to the wide framework of exploration versus exploitation: exploration (learning) is rewarding because of new acquired experience at the cost of increased energy demands, while exploitation (retrieving) is rewarding in terms of instantaneous outcome, at the cost of decreasing system performance. A common solution is to temporally separate exploration and exploitation into different modes: that is having an encoding and a retrieval mode in the case of memory. Hasselmo first proposed such a model, suggesting that theta phase does exactly that: it segregates

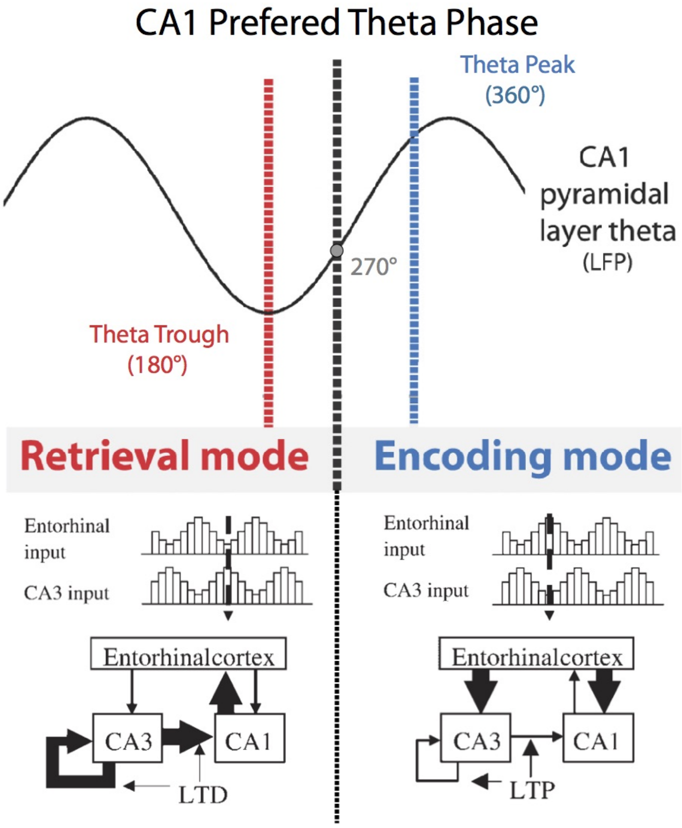

Figure 2.13 – Phase Coding Model supporting Encoding and Retrieval modes at different phases of Theta The encoding mode corresponds to high EC-CA3 and EC-CA1 synchrony. Because of conduction delays CA3-CA1 connections undergo LTP to encode associations (right). The retrieval mode occurs at the trough of theta when entorhinal inputs are absent CA3-CA1 communication is strong, while LTD occurs in the CA3-CA1 network (left). Adapted from [Hasselmo et al., 2002].

the hippocampus between a *retrieval mode* and an *encoding mode*. In the encoding mode, EC input (driven by sensory areas) primarily reaches CA3 region, then CA1 region and LTP occurs to update the network provided relevant sensory cues according to task relevance. In the retrieval mode, CA3-CA1 recurrent communication is enhanced while LTP is blocked not to interfere with previously acquired experience [Hasselmo et al., 2002; Kunec et al., 2005].

This model received strong experimental support and gamma oscillations are likely candidates to mediate encoding and retrieval modes. The seminal study by Colgin and colleagues has established that CA1 coordinates with MEC during fast gamma while CA3-CA1 communication is strong during slow gamma. Importantly these slow and fast gamma episodes occur in a mutually exclusive fashion at different theta phases and robust spike-field coupling was demonstrated in both MEC and CA3, relative to CA1 theta phase [Colgin et al., 2009]. Schomburg and colleagues provided recent evidence that fast and slow gamma rhythms were strongly associated with different phases of theta oscillation and related to frequency-specific and region-specific dipoles in the CA1 region. They also demonstrated that CA1 was weakly entrained by slow gamma and produced a specific output gamma oscillation of its own [Schomburg et al., 2014].

In another study, optogenetic techniques were used to inhibit CA1 at particular phases of theta during a maze encoding/retrieval memory task. As predicted by Hasselmo, stimulation in the encoding segment enhanced performance when it occurred at the peak of theta, while stimulation at the trough of theta enhanced performance in the retrieval segment [Siegle and Wilson, 2014]. Recent evidence however challenges this view of encoding/retrieval relative to theta phase: Yamamoto and colleagues observed a transient fast gamma burst during the retention period of a delayed non-match to sample T-maze task. This burst robustly preceded the animal correct choices but not the incorrect ones. The disruption of this burst resulted in lower performance [Yamamoto et al., 2014]. According to the current model, slow but not fast gamma oscillations should mediate memory performance during the retention period, thus the exact role for gamma synchrony still needs further research.

2.4.4 Interregional communication

As mentioned in subsection 1.4.1, theta rhythm is a relatively slow oscillation that can easily spread across distant brain areas and can modulate efficiently faster local oscillations like gamma rhythms. Thus, theta coherence can result in increased synaptic gain transfer during sensory information processing, in accordance with the CTC hypothesis [Fries, 2005]. Accordingly, theta modulation has been observed between hippocampus and many cortical and subcortical regions including septum, medial prefrontal cortex, striatum, ventral tegmental area and amygdala, on a variety of spatial memory tasks.

Jones and Wilson first reported that the firing of neurons in the prefrontal cortex was modulated by theta phase and that theta coherence was stronger during correct-choice trials relative to error ones. This theta coherence was however absent during forced turn trials, which require no decision from the animal [Jones and Wilson, 2005]. Similar findings were found in a delayed non-matching to sample task [Hyman et al., 2011] and theta coherence was shown to predict performance and rule acquisition accurately in a T-maze task with periodically switching contingency rule [Benchenane et al., 2010]. Interregional theta coherence was also observed between the striatum and the hippocampus in the period between tone and turn selection in a tone-cued reward task [DeCoteau et al., 2007] (see Figure 2.14). These modulations in interregional coherence are thus band-specific, task-relevant and dynamically changing on a sub-second timescale.

This large-scale theta coordination was also observed in a wide variety of tasks involving the emotional/anxiety component of theta activity. Hence, theta coupling between lateral amygdala and CA1 increased significantly in animals displaying behavioral signs of fear or when conditioned fear stimuli were presented [Seidenbecher et al., 2003]. Similar results were found between the ventral hippocampus and prefrontal cortex in mice exposed to anxiogenic areas [Adhikari et al., 2010]. Finally, animal models of schizophrenia showed disrupted interregional communication [Sigurdsson et al., 2010] and interventions that restored normal performance on a cognitive control task also reestablished theta synchrony [Lee et al., 2012]. In a nutshell, acute and chronic lesion studies impairing theta rhythmicity often lead to impaired information transfer, reduced long-range synchronization and decreased performance in spatial memory tasks [Schnitzler and Gross, 2005]. Together, these results suggest that theta synchrony is critical for both spatial and emotional memory and coordinates a wide

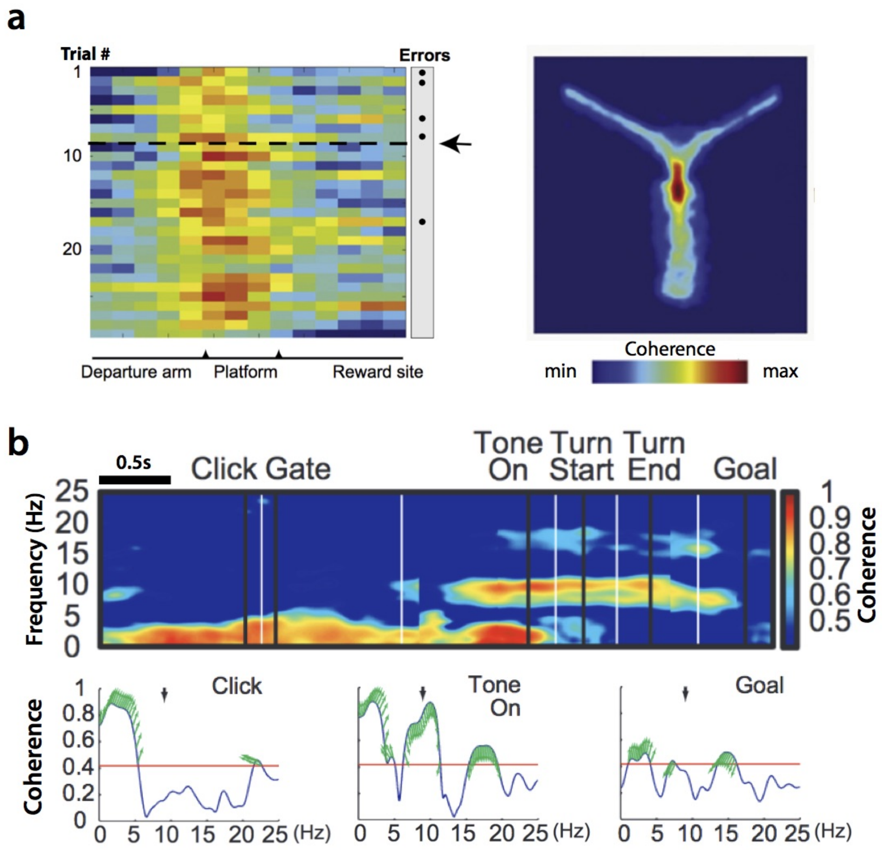

Figure 2.14 – Theta Rhythm coordinates interregional communication (a) Hippocampal-prefrontal coherence predicts rule acquisition in a periodically switching Y-maze task. Coherence is maximal at choice point. **(b)** Coherence between striatum and hippocampus increases significantly during tone onset until choice point in a tone-cued memory task. **(a)** adapted from [Benchenane et al., 2010] **(b)** adapted from [DeCoteau et al., 2007].

set of tasks involving various brain regions.

2.4.5 REM sleep Theta

REM sleep was first categorized "paradoxical sleep", because despite its apparent similarity with SWS, it is a state characterized by high hormonal activity, rapid-eye movement, increase in blood pressure and ventilation, and dreaming [Maquet et al., 1996]. In terms of physiological profile, it is extremely hard to differentiate REM sleep from an awake state, especially from active state like theta rhythmicity, the only difference being low electromyogram indicating complete muscle atonia. In rodents, REM sleep is characterized by low-amplitude theta activity, similar to what is observed during running. Some authors have reported surges of arterial pressure [Sei and Morita, 1996] and the presence of high-frequency oscillations [Buzski and Silva, 2012], which suggests that REM sleep is a highly active state in terms of neural processing. Why it is so similar to awake states and why it contains high theta rhythmicity in rodents is still elusive.

REM sleep was first postulated to be important for emotional memory [Hutchison and Rathore, 2015]. The transient nature of REM sleep and the fact that it is mainly prominent in the last part of the night have made REM sleep experimentation somewhat underrated. However, REM sleep has recently been shown to be critical for the reorganization of hippocampal excitability [Grosmark et al., 2012] and memory consolidation [Boyce et al., 2016]. Comparatively to awake theta, REM sleep theta is characterized by lower amplitude [Montgomery et al., 2008], a different profile in the coupling with gamma [Belluscio et al., 2012] and reversal theta activity, starting from downstream regions like subiculum is thought to arise preferentially during REM sleep [Jackson et al., 2014]. Thus, REM sleep is a highly active electrophysiological state, which shows strong similarities to aroused awake activity and likely involved in homeostasis and memory consolidation.

2.5 Conclusion

In this section, I reviewed the critical role of the hippocampus in episodic memory both for the formation of newly acquired experience and for the strengthening of memories. Conversely, lesion studies have shown that some memory systems are hippocampus-independent. It is also a key structure for spatial processing containing cells that encode high-level information such as location, irrespective of the primary sensory stimulation. A comprehensive model of memory in the hippocampus should thus integrate both its episodic memory and spatial components.

The anatomy of the hippocampal formation (hippocampus proper and entorhinal cortex) is unique because it alternates parallel, recurrent and serial processing. It is highly connected to the rest of the brain, which suggests a strong implication in a broad range of tasks. The main connectivity along the transverse axis is unidirectional with powerful synapses between EC and DG, while other brain regions display bidirectional connections. The hippocampus displays both anatomic, genetic and functional gradients along the septo-temporal axis, containing graduate and abrupt transitions, suggesting that the ventral and dorsal parts of the hippocampus subserve distinct functions. A sharp functional dissociation between spatial processing in the dorsal hippocampus and emotional/anxiety related behaviors in the ventral hippocampus is however questionable.

The electric patterns of the hippocampus alternate between two mutually exclusive states: a low-amplitude highly regular theta activity associated with movement and arousal, and a diffuse irregular high amplitude pattern known as large-irregular activity, associated with immobility and sleep. Theta rhythmicity can be divided into type I (8-12 Hz) theta which is locomotion-related anesthetics-sensitive, and type II theta (4-8 Hz) which is atropine-dependent and associated to arousal/anxiety. Theta rhythm is critical for memory especially for the formation of theta sequences, which are time compressed neural representations of sequentially-ordered sensory events. These sequences are critical for memory consolidation through a phenomenon called replay during sharp-wave ripple events. Moreover, theta activity is thought to enhance communication between distant brain regions in a task-relevant manner and a likely mechanism for memory processing is that theta phase triggers slow gamma to enhance EC-CA1 coordination during memory encoding, whereas fast gamma supports memory retrieval through sustained CA1-CA3 communication.

Chapter 3

In Vivo Functional imaging and neurovascular interactions

Electroencephalography has triggered considerable advances in our understanding of brain functions but it suffers limitations that are difficult to overcome, despite the development of high-density recording and new signal processing methodologies. First, volume conduction is intrinsically present in electrographic recordings and renders source localization challenging. Second, its invasiveness precludes a generalized use for human studies but also damages surrounding tissues, especially with an increased number of recording sites. Third, deep and small-sized structures are hard to reach. Fourth, it does not reveal all the facets of neural activity such as metabolism, which are known to play a critical role in a large body of diseases and dysregulations. Fifth, high quality recordings are hard to maintain on the long term. Finally, simultaneous dense cell sampling (> 100 cells) is hard to achieve.

In particular, the coupling between metabolic, hemodynamic and neural events is a critical question in neuroscience that is gathering growing attention. In order to understand the underlying mechanisms of this coupling, one solution is to develop multimodal approaches to monitor simultaneously metabolic and electrographic events. This new framework requires methodologies to bridge the gap between past and present research. As an example, current brain atlases need to be updated to integrate cellular-resolution mapping of brain tissue. Common notions such as “neural activation” or “functional unit” might need revision in order to give a complete picture of brain function.

In this section, I present the current state-of-the-art about *in vivo* brain imaging methods. I review recent advances in brain atlases and neurovascular coupling in the first two sections. Then I present the current methods available to monitor brain activity *in vivo* in large-scale networks, emphasizing the context of awake behavior. I organized these different modalities in subgroups according to the type of information they provide and the degree of constraint that they impose on the subject. Finally, I position ultrasound imaging - that I focused on in this thesis - in this framework. Recent insights about the hemodynamics of the rodent and human brain during spatial navigation are discussed separately in Chapter 7.

3.1 Brain Atlas and vascular Network

3.1.1 Brain Atlases

Relating structure to function requires a complete knowledge of brain neuro-anatomy. The development of accurate brain atlases is thus a necessary condition for functional brain imaging. Golgi silver staining, first introduced by Golgi in 1873 and further improved by Ramon y Cajal, is one of the most elegant and efficient methods for distinguishing the morphology of neurons [Sotelo, 2003]. Since then, early brain atlases were made available, based on myelin-stained sections [Knig and Klippel, 1974], Nissl-staining [Pellegrino, 1995] or India ink staining [Greene, 1955]. Paxinos and Watson implemented histochemical staining to produce the first atlas including precise labelling of most brain structures [Paxinos and Watson, 1982] (see Figure 3.1). This atlas could be used for stereotaxic implantation and electrode localization. It still remains a reference in electrophysiological studies in rodents, because it includes incremental enrichment such as immunohistochemical markers and genetic expression patterns [Paxinos et al., 2009a,b]. However, these techniques require brain extraction, manual reconstruction of 3D datasets and preclude labelling of deep tissue in the intact brain. Additionally, such labelling is often based on lone anatomical grounds.

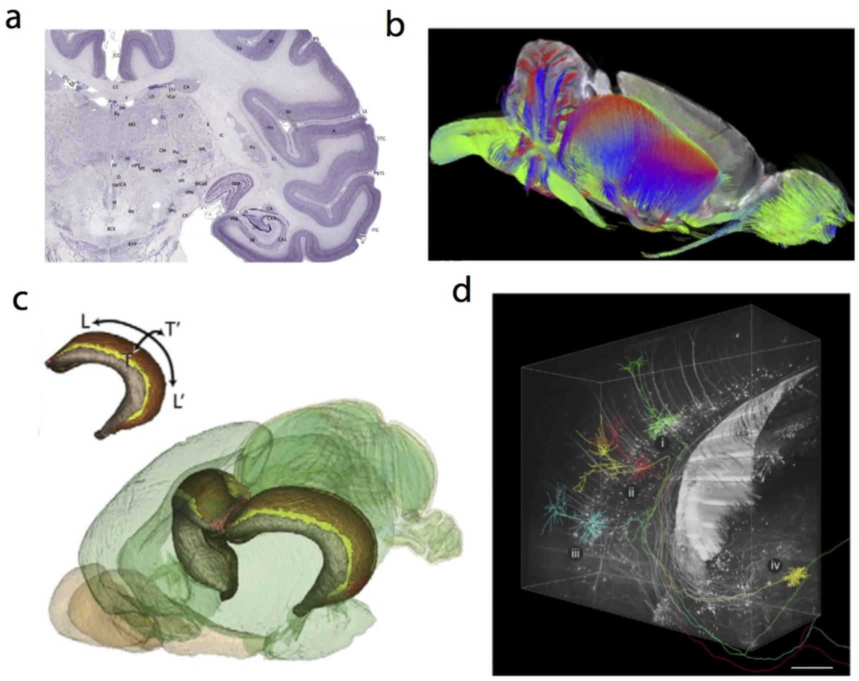

Figure 3.1 – **Mutliple brain atlases of the rat brain (a)** Coronal sections of Nissl-stained rat brain slice and superimposed manual region labelling **(b)** Diffusion Tensor Imaging can be used to extract fiber connectivity between regions **(c)** MRI based segmentation of the hippocampal subregions in 3D **(d)** High resolution (1 x 1 x 2 μm) 3D volume of somatosensory cortex, auditory cortex and distal hippocampus. Note the precise reconstruction of individual neurons across the cortical layers **(a)** adapted from [Paxinos, 2004] **(b)** adapted from [Johnson et al., 2012] **(c)** adapted from [Kjonigsen et al., 2015] **(d)** adapted from [Gong et al., 2013].

To overcome this limitation, magnetic resonance imaging (MRI) is a powerful tool, because it provides structural images of the intact brain. MRI generates whole-brain volumetric data with micrometric spatial resolution, both in humans and sedated animals but also in fixed tissues injected with a contrast agent [Johnson et al., 1993]. MR atlases have evolved to 3D mapping of the whole rat brain, at ever-increasing resolution from 0.115 x 0.115 mm [Suddarth and Johnson, 1991] to an actual 0.025 x 0.025 mm in-plane resolutions [Johnson et al., 2012]. Contrast analysis can reveal the precise composition of the tissue including cortical structures, fibers bundles and vascular network [Dorr et al., 2007; Xue et al., 2014]. More recently, a new class of atlases has emerged making use of population average analysis to estimate inter-individual variability and construct species-specific brain templates [Valds-Hernndez, 2011; Chuang et al., 2011]. MRI-based atlases now emerge as a new reference, because the precise 3D representation of brain structures such as hippocampus, and labelling of their subregions, is now available [Papp et al., 2014; Kjonigsen et al., 2015] (see Figure 3.1).

Finally, staining techniques have been improved to provide uniform whole-brain staining of immunohistochemistry in rodents [Chung et al., 2013; Wu et al., 2014]. Optical tomography can now provide brain-wide network labelling at cellular resolution either by removing brain tissue through laser ablation and imaging brain tissue sequentially [Tsai et al., 2003], by performing ultrathin physical sectioning to perform array tomography [McCormick et al., 2004] or by fast-imaging transparent rodent brain [Dodt et al., 2007; Chung et al., 2013; Yang et al., 2014] (see Figure 3.1). *In situ* hybridization can additionally provide genome-wide atlas of brain expression [Lein et al., 2007], while high-throughput histology can reconstruct with great spatial resolution the composition of cortical tissues [Blinder et al., 2013]. Hence, this profusion of anatomical data requires analytical methods to perform multiple atlas registration. This is a challenging and tedious task and raises the question of the relevance of anatomical delineations.

3.1.2 The Rat Brain vascular Network

The cerebral vascular network is complex, species-dependent and quite variable from one individual to another. To the best of our knowledge, no vascular atlas of the rat brain has been proposed and the reference technique used for a global reconstruction of the vascular architecture still is the injection of staining agents like neoprene/black ink, which requires manual reconstruction to produce volumetric data.

Cross-species vascular Organization

Rats share a similar global brain vascular organization with many mammals, including humans. The same hierarchy between arterial and venous systems applies including dissociation between anterior cerebral circulation and posterior cerebral circulation. Cerebral arteries and veins almost never run in pairs though they connect through a complex network of capillaries. Additionally, in both species, numerous anastomoses (direct connections between neighbouring vessels) create considerable redundancy while A-V shunts (direct communication between arterial and venous blood) are absent. Rats display however specific differences compared to humans in the architecture of the polygon of Willis and strong inter-individual variability [Scremin, 1995].

Global architecture

The vascular system of the rat brain is more heterogeneous and complex than in most other organs. It exhibits a large variability in capillary structure and density across regions. While capillaries in most areas possess endothelial cells that considerably hinder the passage of water-soluble molecules, some regions have higher permeability rendering most blood constituents available to nerve cells [Gross et al., 1986]. The numerous arterial and venous anastomoses observed in rodents result in robustness to ischemia [Scremin, 1995].

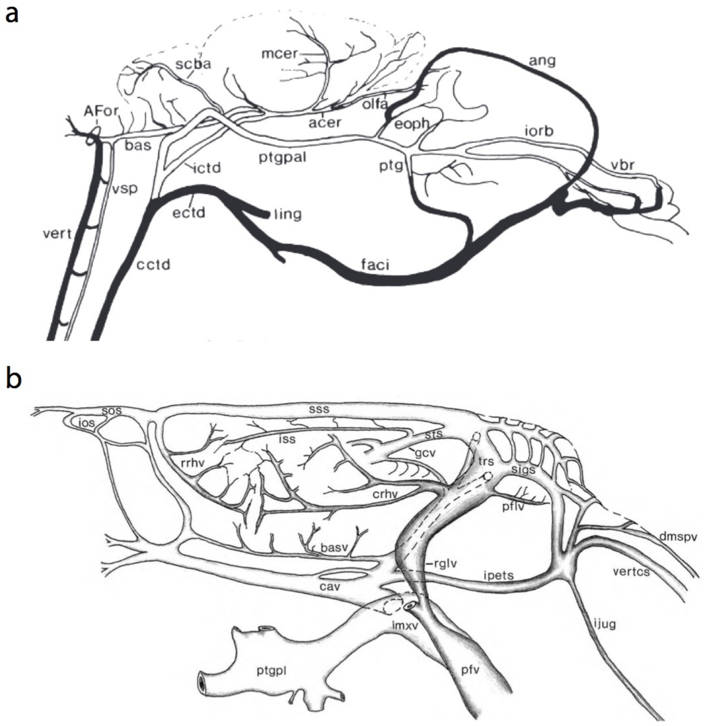

Figure 3.2 – Lateral View of the Arterial and Venous Systems in the rat brain (a) ang - Angular artery (facial) ; acer - Anterior cerebral artery (internal carotid) ; bas - Basilar artery (vertebral) ; eoph - External ophthalmic artery (pterygopalatine) ; faci - Facial artery (external carotid) ; iorb - Infraorbital artery (pterygopalatine) ; ictd - Internal carotid artery (common carotid) ; ling - Lingual artery (external carotid) ; ectd - External carotid artery (common carotid) ; olfa - Olfactory artery (anterior cerebral) ; ptgpal - Pterygopalatine artery (internal carotid) ; scba - Superior cerebellar artery (basilar) ; vert - Vertebral artery (subclavian) ; vbr - Vibrissal arteries (infraorbital) **(b)** AFor - Alar foramen ; cav - Cavernous sinus (inferior petrosal sinus, interpterygoid emissary vein) ; ios - Inferior olfactory sinus (rostral confluence of sinuses) ; ipets - Inferior petrosal sinus (internal jugular vein) ; sigs - Sigmoid sinus (internal jugular vein) ; sts - Straight sinus (caudal confluence of sinuses) ; sos - Superior olfactory sinus (rostral confluence of sinuses) ; sss - Superior sagittal sinus (caudal confluence of sinuses) ; trs - Transverse sinus (retroglenoid vein) ; vertcs - Vertebral canal sinus (vertebral vein, vertebral - epidural plexus) ; bast - Basal vein (cavernous sinus) ; crhv - Caudal rhinal vein (transverse sinus) ; dmspv - Dorsomedian spinal vein (vertebral canal sinus) ; gcv - Great cerebral vein of Galen (straight sinus) ; ijug - Internal jugular vein (superior vena cava) ; imxv - Internal maxillary vein (posterior facial) ; its - Inferior sagittal sinus ; mcerv - Middle cerebral vein (basal) ; pflv - Parafloccular vein (transverse sinus) ; pfv - Posterior facial vein (external jugular) ; ptgpl - Pterygoid venous plexus (internal maxillary) ; rglv - Retroglenoid vein (internal maxillary, superficial temporal) ; rrhv - Rostral rhinal vein (rostral confluence of sinuses) ; vspv - Ventral spinal vein (radicular, vertebral). Adapted from [Scremin, 1995].

The global architecture of the rat is composed of two separate systems: an arterial system and a venous system (see Figure 3.2). Four major arteries assure the arterial blood supply to the brain: two common carotids and two vertebral arteries, which divide into a complex network. A remarkable anatomical feature of the arterial network, first noticed by Gabriel Fallopius in 1561 and extensively described by Thomas Willis in 1664, is the network of anastomoses at the basis of the brain that constitute a circle (*circle of Willis* or *Willis polygon*) [Willis, 1664]. The pial arteries form a complex network with considerable redundancy paving the surface of the brain. This network displays a strong plasticity across development and is thought to play a major role in resistance to infarction [Coyle, 1984]. Finally, three main venous outflow systems are responsible for blood drainage and waste elimination: the dorsal system containing the retroglenoid vein (which connects to the transverse sinus), the lateral and the ventral venous system. Like arteries, these three networks are connected by numerous anastomoses.

Vascular Patterns in the Hippocampus

The blood supply to the hippocampus is provided by the posterior cerebral artery which gives rise to the *longitudinal hippocampal artery.* It runs initially in the same initial direction as its parent vessel and follows the longitudinal axis of the hippocampus. A second artery, the *anterior choroidal artery* emanates from the internal carotid to course hippocampus along the anterior face of its dorso-ventral axis. The *postlateral choroidal artery* stems from the hippocampal artery to course in anterior, dorsal and medial direction to provide a transverse arterial blood supply to the hippocampus. The longitudinal artery divides at regular intervals into perpendicular short *transverse hippocampal arteries* that course in the hippocampal fissure (see Figure 3.3) [Coyle, 1978].

Arterial and venous networks are strikingly segregated along the dorso-ventral axis of the hippocampus, alternating almost regularly between transverse arteries and veins. Interestingly, the vascular network of the rat hippocampus is inhomogeneous along the septo-temporal axis: ventral hippocampus exhibits higher levels of capillary vascularization while dorsal hippocampus exhibits significantly higher capillary density [Grivas et al., 2003]. These anatomical differences between larger blood vessels in the dorsal part of the hippocampus and denser capillary networks in its ventral part might explain the selective vulnerability of hippocampus to ischemia, as infarct recovery is known to be critically dependent on blood flow rates [Smith et al., 1984; Moser and Moser, 1998].

Vascular Patterns in the Cortex

One peculiar property of the pial artery network that maps the surface of the cortical mantel is its relatively insensitiveness to blockades in one branch of the network [Schaffer et al., 2006]. It can easily reroute blood distribution towards sustained energy demands in a dynamic fashion [Devor et al., 2007], thus it is important to know if the penetrating arterioles and venules exhibit the same cortical modular organization as orientations columns observed throughout the cortex. Though this idea of a “neurovascular module” has received experimental support [Nishimura et al., 2007], recent evidence has challenged this view.

In the cortex, penetrating arterioles flow downwards into the parenchyma while venule flow upwards to the cortical surface, which allows for arteriole and venule segregation based on

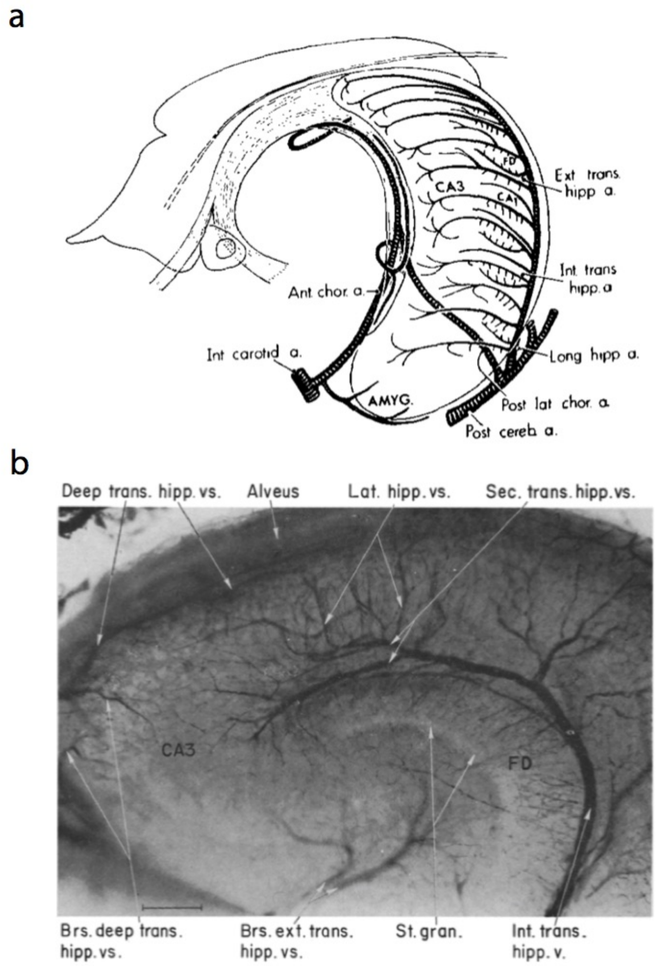

Figure 3.3 – Vascular Patterns of the Rat Hippocampus The hippocampus is supplied in arterious blood by two major arteries: the long hippocampal artery (arising from the posterior cerebral artery) and the anterior choroid artery (arising from internal carotid) running along the dorso-ventral axis of the hippocampus. External and internal transverse arteries assure transverse blood supply **(b)** Transverse vascularization of the dorsal hippocampus runs through the hippocampal fissure to supply blood to hippocampal subregions. Dorsal hippocampus display larger blood vessels and less dense capillary network than ventral hippocampus (not shown). **(a)** adapted from [Coyle, 1976] **(b)** adapted from [Coyle, 1978].

the direction of blood flow [van Raaij et al., 2012]. Kleinfeld and colleagues have used high-throughput histology to reconstruct the complete angio-architecture over multiple cubic millimeters of the mouse barrel cortex. Interestingly, their results showed that cortical microvasculature is independent of the typical columnar structure of the primary somatosensory areas. Calculated patterns of blood flow in the network were in addition unrelated to the location of columns [Blinder et al., 2013]. These results highlight the different structural organization between vascular and neuronal networks, suggesting specific functional organization for each system.

3.2 Neurovascular coupling: a bridge across spatial scales

Though it represents only 2% of the body mass, the brain uses approximately 20% of the body's total energy budget [Dudley and Sokoloff, 1999] and contrary to other organs, it is highly dependent on a continuous well-regulated blood supply. Small reductions in Cerebral Blood Flow (CBF) preclude cerebral protein synthesis and efficient electric signaling, whereas large reductions entail the cerebral area to stop working within seconds and irreversible damage to occur within minutes [Leker and Shohami, 2002]. As a result, the brain is endowed with several mechanisms that prevent dysregulation in blood supply. The first one is the ability to shut down systemic circulation and to reroute blood when needed. The second is *autoregulation*, a feedback system that balances CBF fluctuations to maintain it within a desired range. The last one is the cascade of signaling that ensures CBF increase meets energy demands in the regions where activity increases. This phenomenon, known as *functional hyperemia*, was first observed more than 100 years ago and plays a crucial role in energy supply and waste elimination.

3.2.1 Functional hyperemia

Normal neuronal functioning requires energy, even when the brain is supposedly at rest. This energy, provided by adenosine triphosphate (ATP, the main source of energy in the body) through oxygen and glucose consumption, is mostly used to reverse ion influxes that underlie synaptic and action potential transmission. Before the discovery of functional hyperemia, changes in brain vessels diameter were thought to be impossible. In a series of experiments dated 1880, Angelo Mosso observed that a strong emotional stimulus could trigger vasodilation in the brain of patients with skull defects [Mosso, 1880]. These findings were subsequently confirmed by a seminal study by Roy and Sherrington ten years later, in which they stated "the brain possesses an intrinsic mechanism by which its vascular supply can be varied locally in correspondence with local variation in functional activity" [Roy and Sherrington, 1890]. They postulated that regional activity would trigger the release of vasoactive agents in the extracellular space that reach blood vessels by diffusion to produce relaxation of the vascular tone.

Since then, a considerable effort has been made to understand the mechanisms of CBF regulation at various levels along the vascular tree. Subsequent studies have established the vasomotor function of nerves [Talbott et al., 1929] and the involvement of various neurotransmitters and molecules, though their mode of action is more complex than a mere diffusion process [Cauli, 2010]. More recently, new results have challenged the classic understanding of neurovascular coupling suggesting an interplay between different actors including neurons, astrocytes and smooth muscle cells, both in arterioles and capillaries [Attwell et al., 2010]. Because all brain imaging techniques rely on proxy measures of neuronal activity that are related to blood flow, oxygenation, or metabolism [Raichle, 1998], it is crucial to unravel the mechanisms of neurovascular coupling both to interpret neuro-imaging data but also for a fundamental understanding of vascular dysfunctions [Hillman, 2014].

3.2.2 The neurovascular unit

The classical view of neurovascular coupling is that of a feedback system, in which energy consumption through neural activity triggers the emission of a metabolic signal to increase CBF locally in order to meet higher energy demands. This metabolic signal was thought to be endogenous, linked to oxygen or glucose depletion, or carbon dioxide excess. Several studies have maintained animals in hyperoxic or hyperglycemic state, without noticing any change in functional hyperemia, surprisingly revealing that neither oxygen nor glucose regulate blood flow in this way. This suggests instead a direct control of neurovascular tone instead of retro-feedback signaling (see Figure 3.4) [Wolf et al., 1997; Lindauer et al., 2010]. Reciprocally, subsequent studies have shown that neurotransmitter-mediated signaling plays a direct role in neurovascular regulation, and that much of this direct control is mediated by astrocytes [Attwell et al., 2010; Petzold and Murthy, 2011]. Hence, the idea of an anatomical unit - including neurons, astrocytes, smooth muscle cells and endothelial cells - performing local regulation of CBF has emerged and is now commonly accepted and referred to as the *neurovascular unit* [Harder et al., 2002; Lo et al., 2003; Iadecola, 2004].

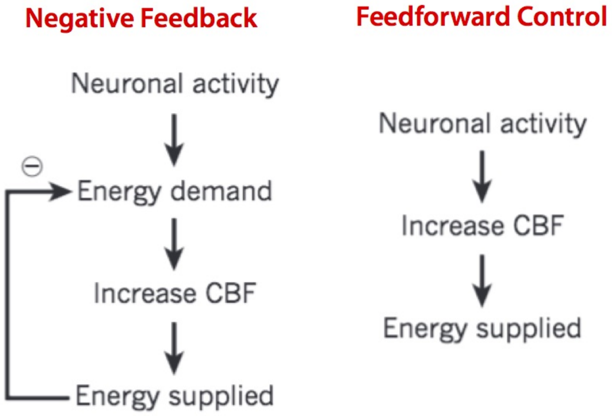

Figure 3.4 – Two opposing schemes for the regulation of blood supply in the brain Adapted from [Attwell et al., 2010].

Large cerebral arteries divide into pial arteries, which map the surface of the parenchyma. Pial arteries are composed of three layers: (1) endothelial cells in direct contact with blood in the lumen (2) smooth muscle cells with contractile properties, (3) leptomeningeal cells innervated by perivascular nerves. Endothelial cells forms a continuous nonfenestrated layer lining the walls of pial arteries and are the main components of the blood-brain barrier. Gap junctions tightly connect adjacent endothelial cells and enable intracellular transmission and selective permeability of the blood-brain barrier. Smooth muscle cells are very dense in pial arteries giving them strong contractile properties and a large diameter range. Leptomeningeal cells are the main constituents of *arachnoid* and *pia mater*. They surround tightly both arteries, veins and nerves that penetrate or leave the central nervous system (see Figure 3.5a).

Pial arteries then divide into penetrating arterioles through the Virchow-Robin space, which curves into the *pia mater*. These arterioles are constituted of a layer of endothelial cells and a thin layer of smooth muscle cells in direct contact with astrocytic endfeet and neuronal projections (see Figure 3.5ab). At the level of capillaries, smooth muscle cells are traded for pericytes - small cells involved in vasculogenesis and the blood-brain barrier [Winkler et al., 2011] - and the whole vascular circumference of a vessel can be composed of a single endothelial cell. The atrocytic endfeet have an extended contact surface at the level of capillaries, suggesting strong astrocytic control over the capillary network (see Figure 3.5c). Endothelial cells play a key role in signaling by releasing vasoactive agents that can either constrict or dilate the surrounding smooth muscles. [Iadecola, 2004; Drake and Iadecola, 2007]. Contrary to arterioles, veins and venules have few contractile properties: they have more of a drainage role and undergo blood flow variation rather than diameter change. Venule dilation can however be observed consequently to sustained arteriole dilation over long stimulation periods [Bouchard et al., 2009; Drew et al., 2011].

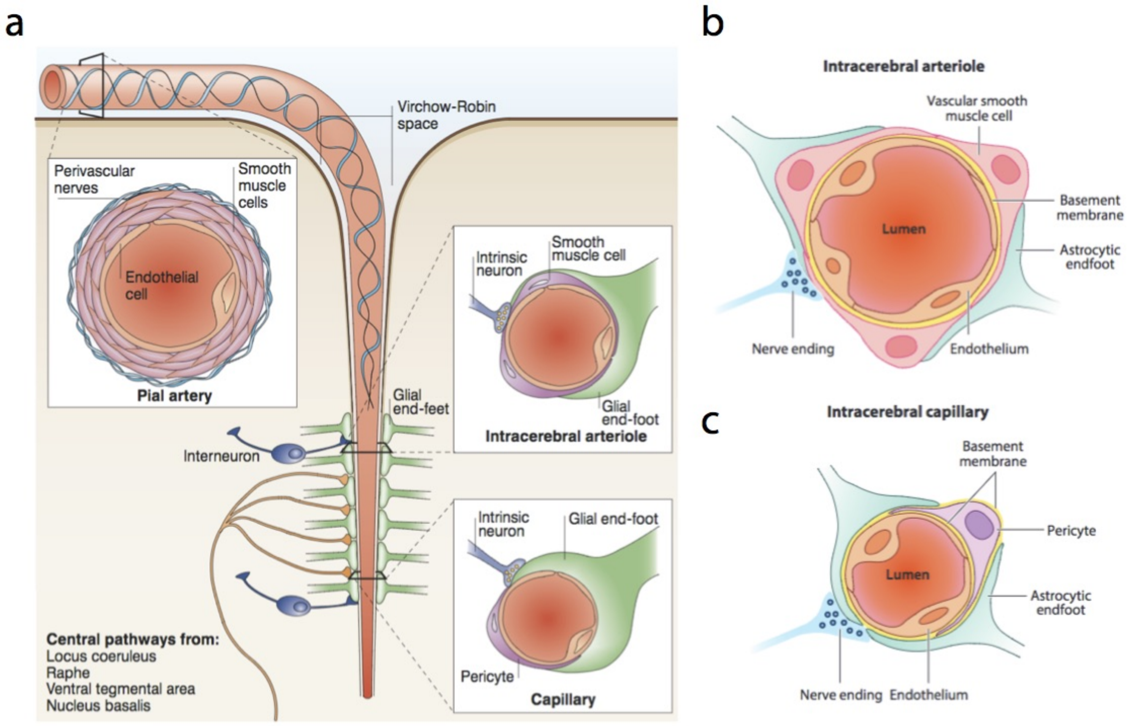

Figure 3.5 – The Neurovascular Unit Local Blood Flow regulation relies on an anatomical and functional ensemble called the neurovascular unit including neurons, astrocytes, endothelial cells and smooth muscle cells. **(a)** Pial arteries are strongly innervated and possess multilayered endothelial cells. Penetrating arterioles are fully covered with a layer smooth muscle cells in direct contact with astrocytic endfeet and neuron terminations. Capillaries however possess pericytes instead of smooth muscle cells and the astrocytic contact is relatively more extended **(b)** Magnification of intra-cerebral arteriole and capillary composition shown in **(a)**. **(a)** adapted from [Iadecola, 2004] **(b)** adapted from [Andreone et al., 2015].

3.2.3 Cerebral blood flow regulation

3.2.3.1 Autoregulation

Automatic dilation and constriction of pial vessels counterbalance the variations in CBF to maintain it to a controlled value. Smooth muscle cells and pericytes convert the chemical signal that originates from endothelial cells into a change in vascular diameter. This phenomenon occurs mainly in basal arteries of Willis polygon and pial arteries, occasionally in arterioles and capillaries [Prewitt et al., 2002]. Autoregulation is only effective in a certain range of blood pressure, namely between 60 and 150 mm-Hg for arterial pressure [Duchemin et al., 2012]. Autoregulation is also the mechanism that protects the brain blood flow in physiological situations, such as exercise and in pathological situations such as cardiogenic shock. Therefore, it is responsible for the macroscopic vascular tone [Iadecola, 1993].

3.2.3.2 Active regulation

In the control of vessel diameter, the main difference between pial arteries, intra-cerebral arterioles and capillaries is the nature, position and abundance of contractile cells. Until recently, only arterioles were thought to control vascular tone but experimental evidence has shown that active regulation is the result of both pericytes, astrocytes and neuronal activity.

Neurons and interneurons

The involvement of neurons in neurovascular coupling is established. A global central pathway originating from Locus Coerelus, Raphe and Ventral Tegmental area is known to modulate regional blood flow, through the vasodilator acetylcholine (ACh) and the constrictor serotonin (5HT) [Arneric et al., 1988; Vaucher and Hamel, 1995]. A second pathway involves cortical interneurons that act directly on smooth muscle cells. Different subpopulations have been identified releasing different vasoactive agents, including nitric oxide (NO) and vasoactive intestinal peptide (VIP) to dilate or neuropeptide Y (NPY) and somatostatin (SOM) to constrict vessels. Depending on their type, interneurons can thus either increase of decrease the vascular tone [Cauli, 2004].

Astrocytes

The overwhelming majority of astrocytes have direct contact with arterioles, capillaries or ascending venules [McCaslin et al., 2011] and their role in neurovascular regulation is now established since the seminal discovery that calcium uncaging in astrocytic endfeet resulted in vessel dilation both *in vitro* in rat cortical slices [Zonta et al., 2003] and *in vivo* in the mouse somatosensory cortex [Takano et al., 2006]. Glutamatergic activation triggers the production of powerful vasoactive agents through an increase in intracellular calcium in astrocytes, which in turn initiates the production of prostaglandin E (PGE), through the synthesis of arachnoid acid (AA). Cyclo-oxygenase 1 (COX 1) inhibitors block this vasodilation, while COX 2 do not, suggesting that it is mediated by prostanoids.

Recent findings have begun to question the role of astrocytic regulation in neurovascular coupling: Nizar and colleagues showed that mice lacking astrocytic inositol triphosphate receptors (necessary for arachnoid acid generation) still exhibited normal stimulus-evoked hemodynamic responses [Nizar et al., 2013]. Another study found that astrocytes do not express mGluR5s in the adult brain, which is presumably on the pathway for glutamate astrocytic regulation [Sun et al., 2013]. Hence, the role of astrocytes as a primary mediator in neurovascular response in the cortex is less certain.

Pericytes and propagated vasodilation

Pericytes have been demonstrated to control vascular tone *in vitro* in both isolated retinas and cerebellar slices [Peppiatt et al., 2006; Hamilton et al., 2010]. *In vivo* studies also suggested that pericyte constriction plays a role after stroke [Yemisci et al., 2009]. Whether pericyte regulation is an active or passive process requires further investigation but the fact that pericytes express contractile proteins suggests an active role in neurovascular regulation.

Finally, retrograde propagation of vasodilation has been recently observed during functional hyperemia [Tian et al., 2010; Chen et al., 2011]. Early studies suggested that vasodilation restricted to downstream branches influences weakly CBF, unless larger upstream pial arteries also relax [Duling et al., 1987]. Subsequent studies found fast retrograde propagation, implying backward signaling by endothelial hyperpolarization through gap junctions. The propagation speed of arterial dilation onset was estimated around 2 $mm.s^{-1}$ [Chen et al., 2011]. This signal can travel distances exceeding 1 mm with limited attenuation [Bagher and Segal, 2011; Wlfle et al., 2011].

To summarize, three signal pathways - two local and one global - have been identified and work in a complementary push-pull manner to either dilate or constrict vessels. These pathways, shown in Figure 3.6, employ various types of neuromodulators and cellular types [Cauli, 2010; Kleinfeld et al., 2011]. A comprehensive model has to integrate the multiple actors (including astrocytes and pericytes) of neurovascular regulation to conciliate both the long-range and local signaling pathways in the generation of hemodynamic signals [Attwell et al., 2010].

3.2.4 Hemodynamic response

Many physical parameters change significantly after neuronal stimulation including blood oxygenation, carbon dioxide concentration, vessel diameter and cerebral blood flow, which in turn depend on multiple biophysical variables such as vascular resistance, vascular geometry and blood pressure. The change in these parameters consequent to neuronal stimulation is commonly referred to as *hemodynamic response*, encompassing a broad set of physiological changes in the vascular network. Several *in vivo* studies have attempted to disentangle the different aspects of the hemodynamic response and to characterize separately their spatiotemporal dynamics in several brain regions [Dunn et al., 2005; Devor et al., 2007; Berwick et al., 2008; Hillman et al., 2007; Stefanovic et al., 2008; Shen et al., 2015]. However, while many different mechanisms have been proposed, none of them have been incontrovertibly validated to explain the behavior of the vascular network during functional hyperemia. Such a characterization is complex, because of the regional dependence, multiple stimulation paradigms and the specificity of each recording technique.

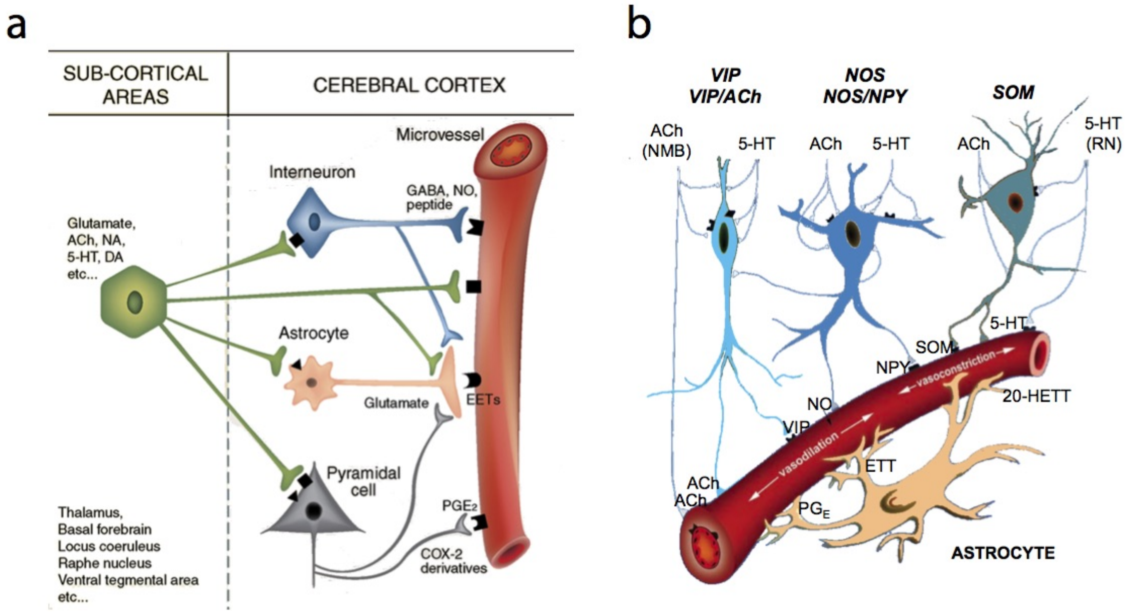

Figure 3.6 – The three main pathways for active blood flow regulation (a) The vascular tone can be regulated locally by interneurons and pyramidal cells, or via astrocytes. Projections from subcortical areas can exert a long-range control over vascular tone **(b)** The three main pathways of active regulation work in a push-pull manner involving a large number of vasoactive agents. Adapted from [Cauli, 2004].

3.2.4.1 Ambiguous link between cerebral blood flow, local field potential and spikes

Synchronous recordings of hemodynamics and neuronal activity have provided contrasted results, because they show a complicated relationship between CBF, LFP and spiking activity. Early studies have shown that the amplitude of the hemodynamic response shows a positive correlation with spiking activity in the visual cortex area V5 [Smith et al., 2002] while V1 neurons showed adaptation to sustained visual stimulation resulting in a decreased spiking rate, while LFP and BOLD remained elevated [Logothetis et al., 2001]. Conversely, Mathiesen and colleagues have demonstrated that the stimulation of parallel fibers in the cerebellum leads to a reduction of spiking activity of Purkinje cells tohether with an increase in LFP and synaptic activity [Mathiesen et al., 1998]. However, the same cerebellar region treated with GABA receptor agonists led to increased LFP signals coupled to a reduction in blood flow [Caesar et al., 2003]. Hence, the link between electrophysiology and CBF remains elusive and it is likely that synaptic processes underlying CBF increase are dependent on local circuitry and balanced exhibition/inhibition ratio.

In a very recent study, O'Herron and colleagues recorded simultaneously the sensory- evoked responses of individual blood vessels in the parenchyma of cats and rats, while recording neuronal activity using glutamate and calcium sensors. This study importantly compared two species that are known to show visual orientation maps (cats) or not (rats), in order to relate individual vessel responses to neural activity in a large portion of the cortex (see Figure 3.7).

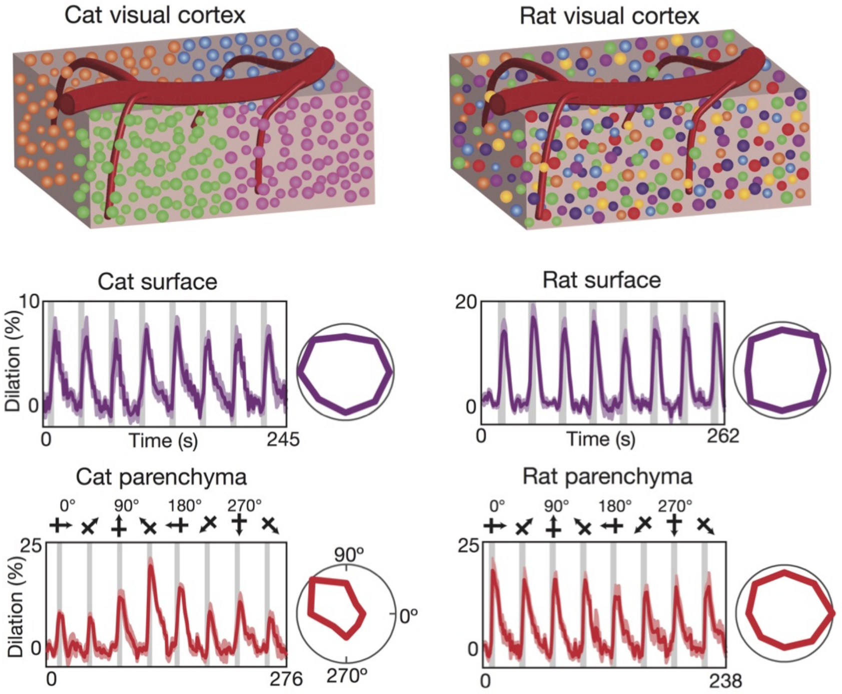

Figure 3.7 – Individual vessels selective to orientation in the cat parenchyma Cat visual cortex (left) is topologically organized respective to stimulus orientation (orientation maps, color dots) while rat visual cortex is not. Layer II/III arterioles (red) in cats showed a robust dependence on stimulus orientation while pial arteries (purple) did not. These orientation maps matched closely the neural orientation maps (colored dots). The rat visual cortex contains only vessels that responded to stimulus without orientation selectivity. Adapted from [OHerron et al., 2016].

They found that individual responses displayed orientation preference in parenchymal vessels of layer II/III but only in penetrating arterioles of cats. This response was absent in rats. Importantly, they found that these individual vessels had the same orientation preference than neighboring neurons, but responded less selectively: vessels responded robustly to stimuli that evoked little to no activity. This challenges the idea that neural activity triggers vessels responses and suggest that neural and vascular events are decoupled for low-amplitude stimuli [OHerron et al., 2016].

3.2.4.2 The spatiotemporal dynamics of the hemodynamic response are complex

The hemodynamic response is usually assumed to occur with a small delay relative to spiking stimulation and to be restrained locally. Intrinsic Optical Signal Imaging (see subsubsection 3.3.2.1) is adapted to investigate the fine details of hemodynamic signals both in time and space because it possesses good spatiotemporal resolution and carries information about the level of oxygenation of blood. Several studies have been using paw [Chen et al., 2011] or whisker stimulation in the anesthetized rodent [Berwick et al., 2008], or visual stimulation in the awake monkey [Sirotin et al., 2009].

These studies reveal early capillary diameter increase in the parenchyma (<1 s) after stimulus onset. This increase results in CBF augmentation, which could explain the total hemoglobin rate (HbT) rise and the “initial dip” observed in BOLD responses [Buxton et al., 2004]. Penetrating arterioles and pial arteries dilate retrogradely from the stimulation region, suggesting retrograde propagation of vasodilation, between 1 s to 2 s after stimulation. Venous oxygenation increases between 2 s to 6 s after stimulation, without notable increase in diameter. The hemodynamic response exhibits different profiles relative to stimulus length: for short stimuli, the temporal shape remains the same, with non-linear scaling of amplitude. For prolonged stimulation however, it displays a plateau-like response [Dunn et al., 2005]. After stimulus cessation, some studies have reported arterial vasoconstriction, which could correspond to the post-stimulus “undershoot” observed in BOLD responses [Devor et al., 2008] (see Figure 3.8).

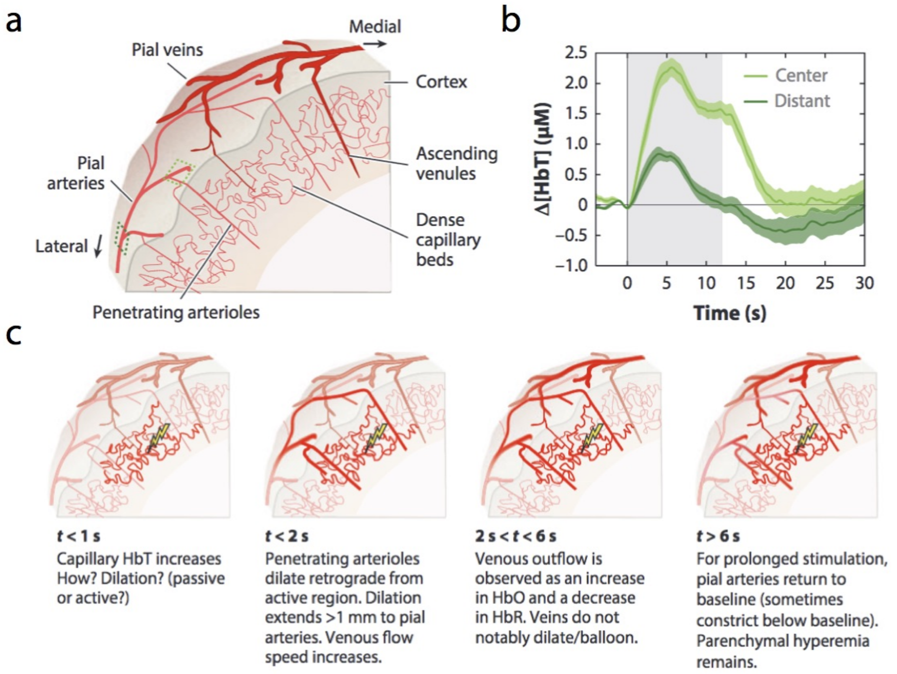

Figure 3.8 – Spatiotemporal dynamics of the Hemodynamic Response in the Rat Cortex (a) Cortical vascular organization in the rat during paw stimulation under anesthesia **(b)** Distant (dark green) and local (light green) hemodynamic response averaged over all trials **(c)** Sequential responses relative to paw stimulation. Capillaries show fast HbT increase (< 1 s), penetrating arterioles and pial arteries dilate retrogradely (< 2 s), before venous outflow (< 6 s). Parenchymal hyperemia remains only for long stimulations while pial arteries return to baseline. Adapted from [Chen et al., 2011].

3.2.4.3 Blood Flow Exceeds Energy Demands

Recent findings suggested that oxygen plays an important role in neurovascular regulation. Gordon and colleagues have shown that extra-physiological rises in oxygen concentration led to vasoconstriction, while vasodilation normally occurs [Gordon et al., 2008]. Lin and colleagues have shown that neurovascular coupling is highly non-linear and that the increase in CBF and oxygenation is at least 4-fold larger than the increase in ATP consumption [Lin et al., 2010]. Hence, blood flow increases raise oxygen level far exceeding energy demands, leading to local hyper-oxygenation. The relative delay between neural stimulation and peak blood flow confirms that neurons do not rely upon functional hyperemia to meet their initial energy needs [Hillman, 2014]. The exact mechanism by which oxygen modulates neurovascular coupling still remains elusive.

3.3 *In Vivo* Functional Imaging of Brain Networks

The past decades of research in neuroscience have seen the emergence of *in vivo* functional brain imaging, from the breakthrough of Positron Emission Tomography (PET) and functional Magnetic Resonance Imaging (fMRI), to the progressive use of light for high-speed hemodynamic and neuronal activity monitoring, and finally to the introduction of optogenetics and more recently functional ultrasound imaging. All these techniques have considerably brought forward our understanding of brain functions at ever-increasing spatiotemporal resolution and decreasing processing time and cost.

In practice there is a trade-off between the size of imaging field, tissue penetration, spatial and temporal resolution, sensitivity, processing speed and cost. Additionally, one would like to capture brain activity in the most natural conditions, that is when a subject is awake and freely moving. Though the past decades have been dominated by fMRI studies, not a single technology has overcome all these constraints. This challenge becomes increasingly complex when activity is monitored during behavioral tasks, because it often implies movement and thus miniaturization.

Most probing results have emerged through the combination of several modalities, because the weaknesses of a given modality can be compensated by the strength of another. Electrophysiology and more recently optical techniques can record neuronal activity in the mobile animal, yet electrode insertion damages tissues and light diffraction limits sampling. Conversely, fMRI and PET record brain-wide metabolism, with tradeoffs in sensitivity and resolution at the cost of subject immobilization or animal sedation. In this section, I provide an overview of state-of-the art techniques available in the framework of functional network dynamics.

3.3.1 The advent of Functional Imaging

3.3.1.1 The early days of functional Imaging

Despite the early discovery of functional hyperemia and the link between the “internal state of the brain” and measurable physiological modifications, the first half of the twentieth century has been relatively quiet. One possible reason is an influential study by Leonard Hill, falsely denying a relationship between brain function and brain circulation [Hill, 1896]. It was only in the early 1950’s that functional imaging was brought forward by the development of techniques like autoradiography [Landau et al., 1955], X-ray computed tomography scan [Hounsfield, 1973] or scintillation [Lassen et al., 1978]. Positrons chemical properties and their biological relevance were long known, but the idea that positron distribution within a brain section could be accurately reconstructed from its emission triggered the design and construction of the first tomographs [Ter-Pogossian et al., 1975; Phelps et al., 1975].

In 1988, a study challenged the conventional view that local blood blow increases should match oxygen consumption: Fox and colleagues showed that an increase in local blood flow triggered an increase in glucose consumption, but a relatively small increase in oxygen consumption [Fox et al., 1988]. Hence, the ratio between oxyhemoglobin (HbO) and deoxyhemoglobin (HbR) should vary during functional hyperemia, resulting in a fall in HbR. As HbR was long known to be paramagnetic [Pauling and Coryell, 1936], it became clear that one could study functional hyperemia, if able to sense the fluctuations in the magnetic field caused by deoxygenated blood. Ogawa and colleagues brought the proof of concept of BOLD imaging by manipulating the oxygen concentration breathed by sedated rats, while performing MRI acquisition. They observed that detailed anatomy of the rat brain, especially veins and venules were only visible when the animal breathed room air compared to pure oxygen, and labeled this phenomenom *blood- oxygen level dependent* contrast (see Figure 3.9) [Ogawa et al., 1990].

Positron Emission Tomography (PET)

The principle of PET relies on the detection of gamma rays emitted from the annihilation of positrons by electrons. Radioactive tracers, such as ^{15}O or ^{18}F are injected into the body and, due to their short half-lives (between 2 to 110 minutes) they spontaneously emit positrons, which are in turn annihilated by electrons. Sokoloff and colleagues brought the proof of principle that radioactive nuclides could be used to study brain glucose metabolism in 1977, in a wide-ranging group of animal experiments [Sokoloff et al., 1977]. Fludeoxyglucose (^{18}F) is an analog of glucose, which is most commonly used to infer glucose uptake by the tissues, because phosphorylation prevents the radionuclides to leave the cell, once absorbed. Hence, the only “way-out” is the radioactive decay, which is proportional to the amount of radionuclide absorbed by the tissue (glucose uptake) [Reivich et al., 1979].

Another strategy is to use oxygen bound to a water molecule ($H_2^{15}O$) to image local changes in CBF, making use of its short half-life (123 seconds). When injected into the brain, it circulates within 10 to 20 seconds in the body and functional hyperemia can be detected by contrast images with resting-state CBF images [Fox and Raichle, 1986]. PET is now well established for a wide range of brain receptors, proteins and enzymes. It has allowed considerable achievements in clinical research on cerebrovascular diseases, oncology, depression and anxiety but, despite improving methodology, appears to have diminished in use [Jones and Rabiner, 2012]. The high cost of functioning, the need for an invasive tracer and its low temporal resolution have reduced its impact and precluded massive utilization.

Functional Magnetic Resonance Imaging (fMRI)

Nuclear Magnetic Resonance is a phenomenon based on the properties of water molecules in a magnetic field, which resonate at different frequencies depending on tissue composition. More precisely, fMRI relies on the measurement of the relaxation time of blood constituents, which is sensitive primarily to local concentrations of paramagnetic deoxyhemoglobin (HbR) [Ogawa et al., 1990]. When plunged into a strong magnetic field, HbR molecules behave like magnets and align with field lines. Thus, variations in the magnetic field trigger relaxation in HbR molecules, which in turn convey information about blood composition. The BOLD signal (previously introduced) increases with decreasing HbR concentration and can be used

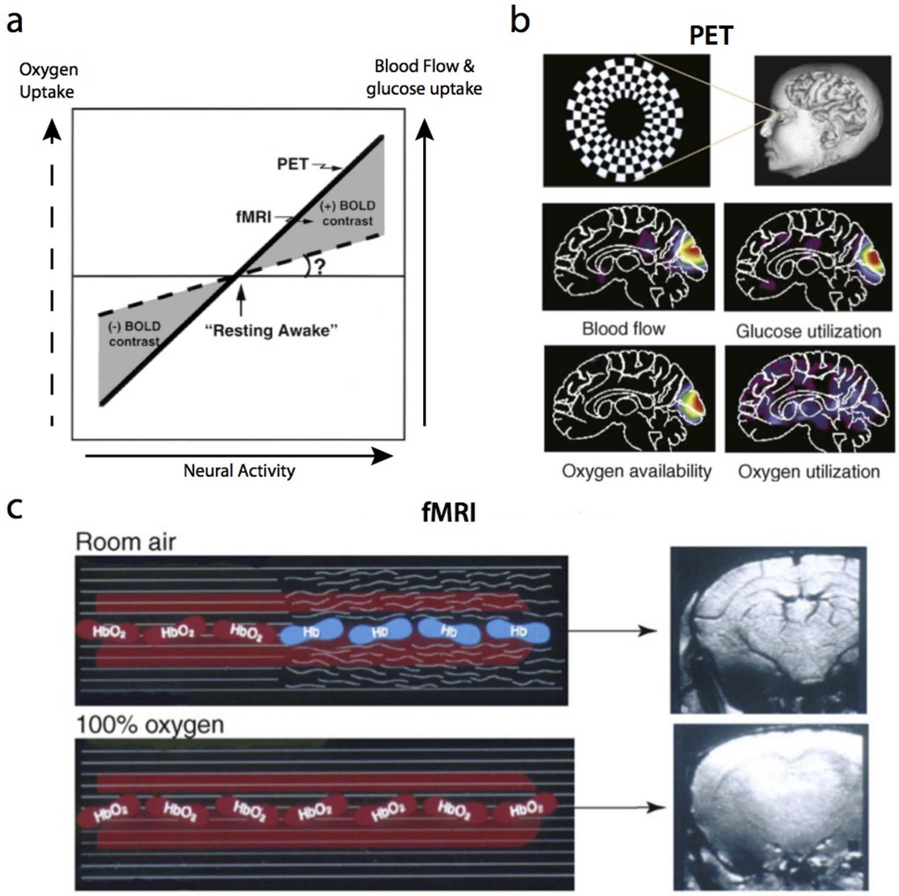

Figure 3.9 – Positron Emission Tomography and functional Magnetic Resonance Imaging (a) PET and fMRI do not measure the same signal: Neural activity leads to increased blood flow and glucose uptake by the cell resulting in positive PET contrast. Conversely, neural activity leads to a relative slower increase in oxygen consumption (dashed line), resulting in decreasing deoxyhemoglobin and positive BOLD contrast. **(b)** Seminal study by Fox and colleagues in alert monkeys challenged the classic view that oxygen consumption matched oxygen availability in the brain. Note the relative difference in oxygen and glucose utilization. **(c)** Proof of concept of blood-oxygen-level-dependent contrast in rats as a proxy to measure brain activity concurrent to increase oxygen concentration in the brain. BOLD contrasts are only visible when sedated rats breath room air due to HbR increase. **(a)** adapted from [Raichle, 1998] **(b)** adapted from [Fox et al., 1988] **(c)** adapted from [Ogawa et al., 1990].

to produce three-dimensional mapping of functional brain activity (see Figure 3.10) [Hillman, 2014].

This technique has several key features that make it a reference to assess network dynamics: good spatiotemporal resolution, whole-brain assessment of activity, absent invasiveness and constant interaction with the subject during the experiment. However, it requires immobilization in a massive device and adapting experimental paradigms. fMRI and BOLD imaging in particular have clearly dominated the field of cognitive neuroscience in the past two decades. This is perhaps due to a combination of high-quality images, new methodologies in data analysis (image averaging, statistical models such as Generalized Linear Models) and involvement of cognitive psychologists in task designing. The introduction of event-related fMRI is triggered an important paradigm shift because individual events can now be resolved with accuracy, revealing the statistical variability of the physiological response to stimulation [Rosen et al., 1998; Logothetis, 2015].

3.3.1.2 What does BOLD measure?

Depsite widespread use, BOLD signal is still poorly understood, because it is a relatively indirect assessment of brain activity and relies on a cascade of competing vascular and metabolic events, such as CBF, CBV and cerebral metabolic rate of oxygen ($CMRO_2$). A common misconception is that BOLD provides a direct measurement of oxygen consumption. On the contrary, classical positive BOLD signals arising from functional hyperemia correspond to a decrease in HbR and a local over-oxygenation [Attwell et al., 2010]. This response typically begins within 500 ms and peaks 3 to 5 s after stimulus onset, even for short stimuli (< 1 s, dynamics are more complex for long stimulation). Negative BOLD signals are intrinsically hard to interpret, because they can arise from different mechanisms, such as pure oxygen consumption, which could explain the initial dip observed at the onset of BOLD responses [Malonek and Grinvald, 1996], or arteriole constriction, leading to a decreased blood flow and blood deoxygenation (see Figure 3.10).

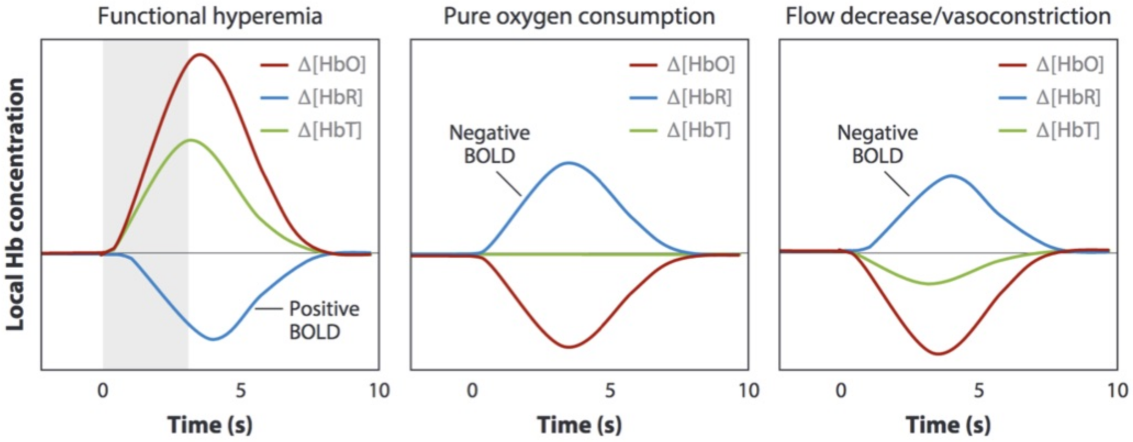

Figure 3.10 – Interpretation of Negative Blood-Oxygen Level Dependent (BOLD) signal (a) Classic positive BOLD signal during functional hyperemia: CBF increases leads to local blood hyperoxygenation. Oxyhemoglobin (HbO-red) and total hemoglobin (HbT-green) concentrations increase, while deoxyhemoglobin (HbR-blue) concentration decreases, leading to positive BOLD signals. The hemodynamic response peaks 3-5 s after stimulation (gray shaded) and returns to baseline 7-10s after stimulus onset **(b)** Pure oxygen consumption is the conversion of HbO to HbR at constant blood volume. It results in an increase in HbR concentration, mirrored by a decrease of HbO concentration resulting in negative BOLD signal. **(c)** Vasoconstriction mainly occurs at arteriole level leading to a combined decrease in HbT and HbO concentration. Thus, relative HbR concentration increases also, leading to negative BOLD. Adapted from [Hillman, 2014].

The link between BOLD signal and neuronal activity is also difficult to establish. Studies have been inconclusive or contradictory when monitoring simultaneously BOLD, neuronal and vascular events suggesting a possible regional dependency of BOLD response [Handwerker et al., 2004; Hirano et al., 2011] and differences between normal and pathological conditions [Shmuel et al., 2002; Schridde et al., 2008]. The linear dependence of BOLD response on neuronal activation is also brought into question [Friston et al., 2000]. Some studies have attempted to investigate which components of neuronal activity were reflected best in BOLD signal. Goense and Logothetis have found that, though local field potential (LFP) and multi-unit activity (MUA) make significant contributions to the BOLD response, LFP is a better and more reliable predictor especially in the 20-60 Hz range, suggesting that BOLD is primarily determined by synaptic input [Goense and Logothetis, 2008]. Conversely, Sirotin and Das have investigated the coupling between neural events and hemodynamic signals in alert monkeys performing a visual task: they found that hemodynamic responses could be divided into two components, one of which was reliably predicted by neural responses while the other was independent of visual input. Strikingly, the latter showed increases in cerebral blood volume in anticipation of trial onsets, even in darkness [Sirotin and Das, 2009] (see Figure 3.11). These results suggest a complex relationship between neural activity and hemodynamics and highlight the need for further investigation of BOLD signal generation and modeling.

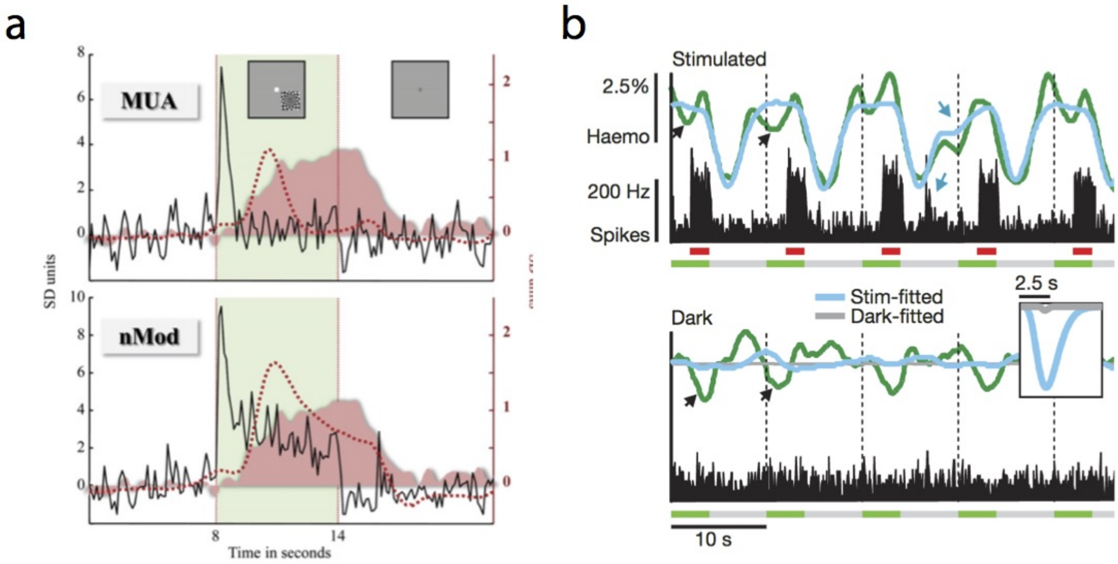

Figure 3.11 – Two conflicting examples of relationship between BOLD signal and neural activity (a) In alert monkeys, Local Field Potentials are a better predictor of BOLD signal, than multi-unit activity (MUA). Computed projection of BOLD activity (dashed line) based on the convolution between neural activity (black) and a classic BOLD HRF (not shown). The predicted response reflects the actual BOLD signal (light red) more reliably based on the 20-60 Hz band of the LFP (nMod) than based on the multi-unit activity **(b)** Hemodynamic and neural responses to visual stimulation in monkeys alternating light and dark conditions. In the normal condition, stimulation- induced spiking activity in V1 is robustly monitored, while it is absent in darkness. The hemodynamic response can be divided in two components of similar strength: a neural-evoked component (light blue) showing robust prediction of spiking activity and another stimulation-related anticipatory component that is present in both conditions (green), probably due to adaptation to the task. **(a)** adapted from [Goense and Logothetis, 2008] **(b)** adapted from [Sirotin and Das, 2009].

3.3.1.3 Recent advances and future directions

Motion tracking of rodents that are allowed to move freely inside a PET scanner is under development, but the technical challenges are substantial and no quantitative brain imaging has been carried out under these conditions. Schulz and colleagues have developed a fully equipped setup with a miniaturized PET imaging device. They can simultaneously assess the metabolic changes and control the concentration of the radiotracer via catheter injection. This constitutes an important breakthrough in functional imaging of metabolism on awake animals and confirms the necessity to develop tools to account simultaneously for behavior and metabolism [Schulz et al., 2011]. Additionally, fMRI can now be performed at unprecedented resolution (100 to 150 μm), due to increased signal-to-noise ratio, so that high-resolution fMRI starts to reveal the vascular and metabolic heterogeneity of the cortex. Penetrating arterioles and venules have been visualized in rats [Yu et al., 2014] and inter-regional (between layer in the cortical structure) and inter-individual differences can now be assessed precisely [Vigneau-Roy et al., 2014]. Thus the future challenges for next-generation fMRI will be to integrate this variability and to refine the existing mesoscopic models of BOLD signal generation and CBF fluctuations [Goense et al., 2016].

3.3.2 Optical Imaging of hemodynamics

Optical imaging techniques make use of the various interactions between light and matter to reveal biochemical processes tightly linked to neural activity. A variety of imaging technologies have been developed in the past twenty years to understand the functional link between neurons, glial cells and blood vessels. Optical methods offer excellent spatiotemporal resolution and can be nicely coupled with electroencephalography or among each other. Importantly, optical techniques can now record the variations of electric potential in the brain and can allow for simultaneous recording of large cell ensembles (up to 1,000 cells) including sparsely active cells. To date, the limited access to deep tissue is the major drawback. I review here some of the major techniques used in clinics and research.

3.3.2.1 Intrinsic Optical Signal Imaging (IOSI)

IOSI has been developed early after the discovery that neural activity, which could be observed with external probes (see subsubsection 3.3.3.1), was often distorted by slower intrinsic signals [Grinvald et al., 1986]. These intrinsic signals reflect the changes in the optical properties of the tissue during functional hyperemia including fluctuations in CBF, oxygenation or cell size. The classical optical intrinsic signal is derived from the change in absorbance spectra between HbO and HbR (see Figure 3.12). By using the appropriate wavelength to illuminate the tissue, one can independently assess the concentration in HbO and HbR. The total blood volume can be reconstructed from total hemoglobin concentration (HbT).

The main advantage of IOSI is the monitoring of blood volume and oxygenation over a large portion of cortical tissue, without the need of extrinsic probes. The good spatial resolution (50 μm), temporal resolution (5-10 ms) and acquisition frame rate (up to 110 frames per second) makes it especially adapted to study the time course of the hemodynamic response [Dunn et al., 2005; Chen et al., 2011]. The recorded signal is an aggregate of parenchymal vessels, penetrating arterioles, venules and pial vessels activities. IOSI can be nicely coupled to laser speckle imaging or calcium imaging [Bouchard et al., 2009]. Though IOSI requires bone-thinning or cranial window approaches, it has recently been extended to head-fixed rats,

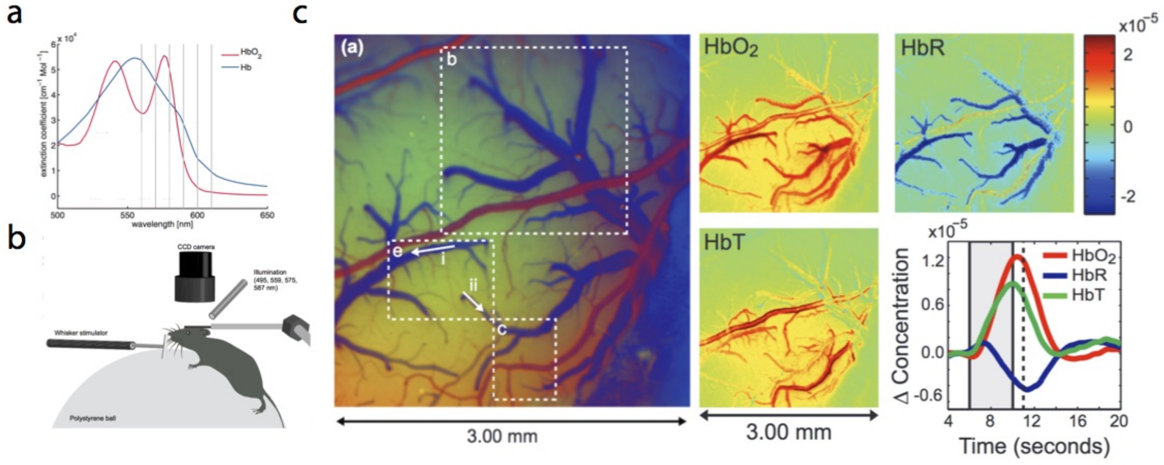

Figure 3.12 – Intrinsic Optical Imaging of neural activity in the anesthetized and behaving rat (a) Different absorption spectra of oxyhemoglobin (red) and deoxyhemoglobin (blue) **(b)** Schematic view of intrinsic optical imaging setup for awake head-fixed rodents undergoing whisker stimulation for hemodynamic response characterization **(c)** IOSI can monitor independently fluctuations in oxygenation and blood volume over a large portion of cortical tissues. Average maps across trials of HbO, HbR and HbT during whisker stimulation. High temporal resolution allows for precise characterization of hemodynamic responses **(a)** adapted from [Weber, 2015] **(b)** adapted from [Sharp et al., 2015] **(c)** adapted from [Bouchard et al., 2009].

thus overcoming the bias induced by animal sedation (see Figure 3.12). Sharp and colleagues trained mice to run on a spherical treadmill to alleviate for stress, while they maintained head-fixation with a head-plate fixed onto the skull with dental cement [Sharp et al., 2015]. However, removing a large portion of bone and *dura mater* poses problems in terms of tissue stabilization and mechanical artifacts due to respiration. Transposition of IOSI to freely moving animals via fiber optics might be possible in the future, at the cost of reduced system performance related to miniaturization.

3.3.2.2 Laser Speckle Contrast Imaging (LSCI)

First introduced in the 1980s, LSCI is a powerful tool for full-field imaging of blood flow. Recently, LSCI has gained increased attention, in part due to its rapid adoption for blood flow studies in the brain and its ability to get images through the intact skull [Li et al., 2009b]. LSCI interprets the difference in speckle patterns, which is an intensity pattern caused by matter diffraction from a set of monochromatic light such as a laser. Red blood cells induce differences in speckle contrast, leading to a direct measure of CBF. LSCI displays many advantages such as low cost, ease of use, wide field of view and excellent resolution. Observation is limited to the cortical surface, due to poor depth resolution and limited tissue penetration.

Miao and colleagues have recently applied LSCI to mobile imaging (see Figure 3.13): their imager weights 20 g and includes an image sensor, an optical lens and associated hardware to generate real-time images with high spatiotemporal resolution. Complementarily, Murari and colleagues have proven that LSCI can be coupled to other optical techniques in freely moving

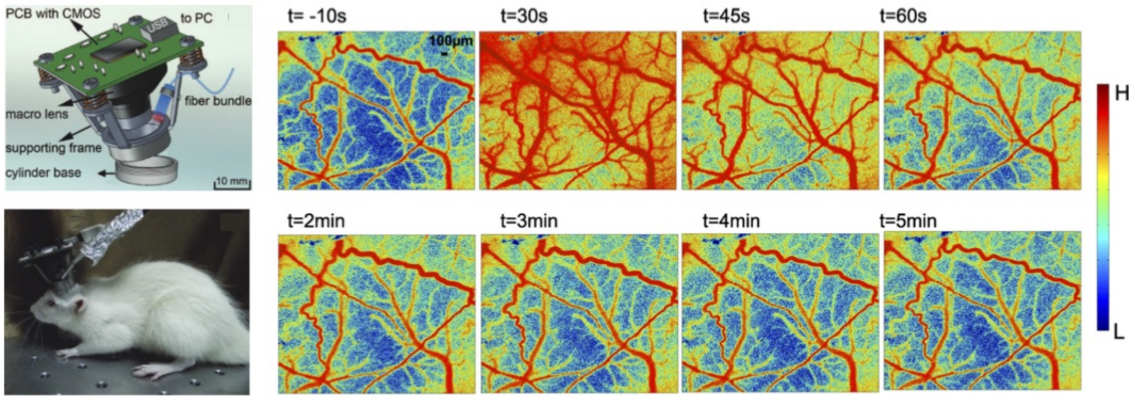

Figure 3.13 – Portable Laser Speckle Imaging System in the behaving animal (a) Design of the miniature head-mounted laser-speckle imager including fiber bundle for illumination, macro-lens and CMOS sensor **(b)** View of a rat wearing the imager during experiment **(c)** Pseudo-color images displaying the vascular responses during and after a 10s electrical stimulation of peripheral trigeminal nerve fibers. Color map display instantaneous blood velocity. Note that peak velocities are reached 30 s after electric stimulation and falls back to baseline 120s after stimulation **(a-b)** adapted from [Miao et al., 2011] **(c)** adapted from [Li et al., 2009b].

animals, which should in the future allow parallel acquisitions of structural and functional information [Murari et al., 2007; Miao et al., 2011].

3.3.2.3 Functional Near infrared spectroscopy

fNIRS takes advantage of the relative transparency of brain tissue to near-infrared light, for a typical wavelength range between 650 and 2,500 nm. It was first applied in rats and humans in 1977 [Jobsis, 1977]. Because HbO and HbR have different absorption spectra in this range, fNIRS can estimate the relative oxygenation of blood when several proper wavelengths are simultaneously used. fNIRS is totally non-invasive, portable and can be used for continuous measurement over prolonged periods of time. It has been successfully used to map motor, visual, and resting-state connectivity in small animal models [Zhang et al., 2005; Mesquita et al., 2010; Khan et al., 2010]. fNIRS is currently used in humans coupled to encephalography to reveal event-related optical signals, similar to evoked potentials commonly seen in EEG/MEG. Medvedev and colleagues have thus reported an "optical N200" wave in humans performing a Go/NoGo task, robustly correlated to EEG activity [Medvedev et al., 2010].

fNIRS is limited by scattering due to the inhomogeneity of the tissue and by absorption, restricting brain activity monitoring to cortical areas. The actual critical challenge is to increase its low signal-to-noise ratio and to develop tools for source-localization. However, fNIRS has many potential clinical applications such as diagnosis, brain reorganization after surgery and motor recovery. Due to its many advantages and relative low-cost, fNIRS is extensively used in clinical and fundamental applications. As for mobile imaging, no physical principle impedes the transposition of this technology to freely moving animals as lightweight stable illumination devices have already been developed.

3.3.2.4 Photo-Acoustic Microscopy (PAM)

The photo-acoustic effect is the generation of sound waves consecutive to light absorption in a tissue. High optical contrast, ultrasonic spatial resolution and high penetration depth are combined in PAM, to generate optical images of deep structures in the brain. The key features of this technology include high sensitivity, mainly because blood has higher optical absorption than other components in the tissue, and independent assessment of oxygenated and deoxygenated blood. Experimenters can tradeoff optical resolution for deeper penetration by selecting the parameters of illumination. High penetration at the cost spatial resolution is obtained in OR-PAM (micrometric resolution, mm-range penetration depth) whereas AR-PAM offers 45 μm spatial resolution up to 3 mm in depth.

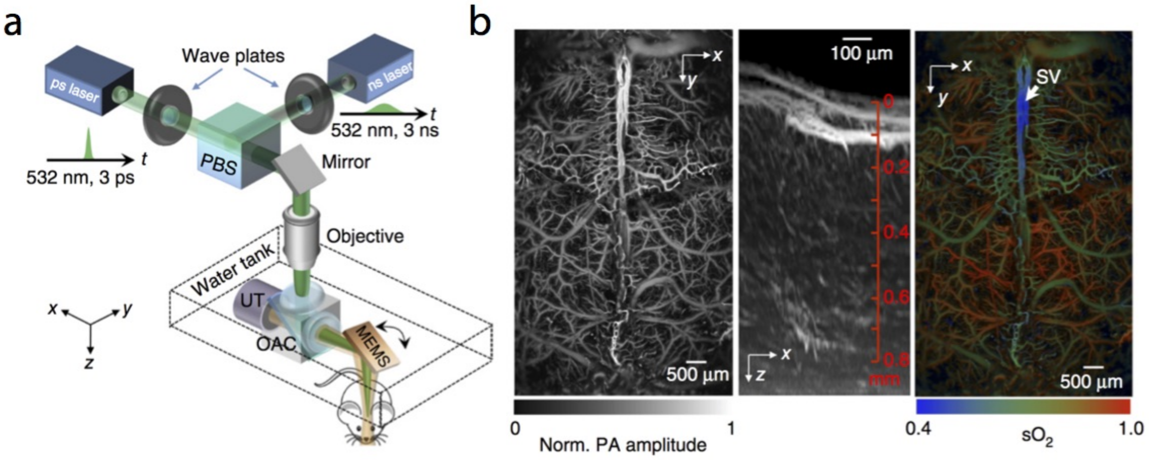

Figure 3.14 – Fast functional Photoacoustic Microscopy of the Mouse Brain (a) Schematic of the photo-acoustic microscopy system through intact skull of anesthetized mice **(b)** Projected brain vasculature of a 0.6 x 0.6 mm^2 region over the anterio-posterior (left) and dorso-ventral axes (middle) obtained through PAM. Maps of oxygen saturation of hemoglobin can be generated to assess functional responses to stimulation (right). Adapted from [Yao et al., 2015].

PAM is complementary to other optical techniques (IOSI, LSCI) to understand neurovascular coupling because it combines hemodynamic monitoring of blood oxygenation in depth at the capillary level. As most of the metabolic exchange occurs in the capillaries, it is critical to assess hemodynamics at this scale with sufficient temporal resolution. Wang and colleagues have recently proposed fast-functioning PAM of the mouse brain through intact skull reaching spatial resolution of 3 μm at optical focus and 15 μm outside of focus, over a 3 x 2 mm^2 field of view [Yao et al., 2015] (see Figure 3.14). Zemp and colleagues have also achieved *in vivo* PAM, by designing a 4 by 6 cm probe weighing about 500 g to obtain images of the microvasculature of a Swiss Webster Mouse with a spatial resolution of 7.5 μm. These devices are compatible with clinical applications such as dermatology, but some efforts on miniaturization still have to be achieved to allow chronic recording in small animal models [Hajireza et al., 2011].

3.3.2.5 Two-Photon Laser Scanning Microscopy (TPLSM)

Fluorescence microscopy is based on the use of fluorescent probes, called fluorophores, which can absorb light at a specific wavelength (excitation wavelength) and re-emit at a longer wavelength (emission wavelength). Conventional microscopy requires intense near-monochromatic light and suffers from light scattering by the brain tissue, which has precluded *in vivo* imaging at the cellular and sub-cellular resolution until the advent of TPLSM [Denk et al., 1990]. TPLSM relies on two-photon absorption, a phenomenon described by Goeppert-Mayer in 1931, stating that fluorescent proteins can be excited by the absorption of two photons containing half of the energy required to reach the excitation threshold. However, these two photons need to be absorbed in a short time window, because the intermediate state between first and second absorption is particularly unstable. Thus two-photon absorption is statistically probable only at the focal point of the laser, which increases resolution and gives access to deep structures.

Fluorophores can either be injected into the body via systemic circulation or synthetized endogenously in genetically modified strains. TPLSM typically uses near-infrared excitation light, which offers several advantages including suppressed background signals, higher penetration depth and reduced phototoxicity [Denk et al., 1994; Theer et al., 2003]. The potential for TPLSM to resolve fine details in the microvasculature (including changes in diameter of individual vessels and blood cells flow at millisecond resolution), neurons or astrocytes concurrently with neural activity is extremely high [Shih et al., 2012]. Calcium indicators (see subsubsection 3.3.3.2) are especially suited for physiological signaling in the brain as it is involved in a wide range of functions.

However, this technique suffers from limited field of view and considerable processing time to form an image, which imposes a trade-off between resolution, sampling speed and explored volume. Recent work has extended the exploration capabilities of TPLSM to achieve whole-brain functional imaging at unprecedented resolution and speed in the zebra-fish larvae, by illuminating tissue volume from the sides. This technology called functional light-sheet imaging microscopy has proved that the overall fraction of brain volume covered with single-cell resolution is thus estimated to be around 80 % of total brain volume [Ahrens et al., 2013; Wolf et al., 2015]. Portable TPLSM has also been developed early in head-stabilized rats using optical fiber for light excitation [Dombeck et al., 2007] and in freely-moving animals [Helmchen et al., 2001; Ghosh et al., 2011].

3.3.3 Extrinsic Optical Imaging of electrical activity

3.3.3.1 Voltage-Sensitive Dye Imaging (VSDI)

The use of fluorescent extrinsic dyes for optical imaging was first established in the squid giant axon [Tasaki et al., 1969], then demonstrated in single neurons without averaging [Salzberg et al., 1973] and finally validated *in vivo* in 1984 [Grinvald et al., 1984]. Voltage-sensitive dyes were highlighted due to their fast response time and the linear measurement of membrane potential. The physical principle relies on the properties of voltage-sensitive or potentiometric dye molecules, which change their level of light absorbance or fluorescence proportionnally to membrane potential fluctuations, by actively interacting with cell membrane during neuronal signaling. The spatial resolution (50 μm or less) is significantly smaller than the typical size of a pyramidal neuron. It is limited by optics and light scattering, and the temporal resolution (10 μs) is close to the duration of an action potential. Unfortunately, light scattering constrains imaging to a depth of around 0.5 - 1 mm into the tissue, limiting the potential for exploration to surface activity, and the chemical toxicity of dyes makes it unsuitable for clinical applications [Grinvald and Hildesheim, 2004].

As dendrites cover most of the cortical surface, VSDI mostly reflects postsynaptic activity rather than action potentials. Two main types of dyes can be used: dyes undergoing changes in absorbance or in fluorescence. Due to their chemical properties, the latter are slightly slower than the first ones. *In vivo* imaging requires a minimal overlap between hemoglobin and dye absorption spectra to distinguish potentiometric changes from vascular events. Dyes can either be applied directly onto large surfaces of the brain that are exposed after craniotomy (extrinsic dyes) or can be genetically encoded based on the insertion of voltage-sensitive fluorescent probes into voltage-gated potassium or sodium channels [Siegel and Isacoff, 1997; Akemann et al., 2010; Gong et al., 2013].

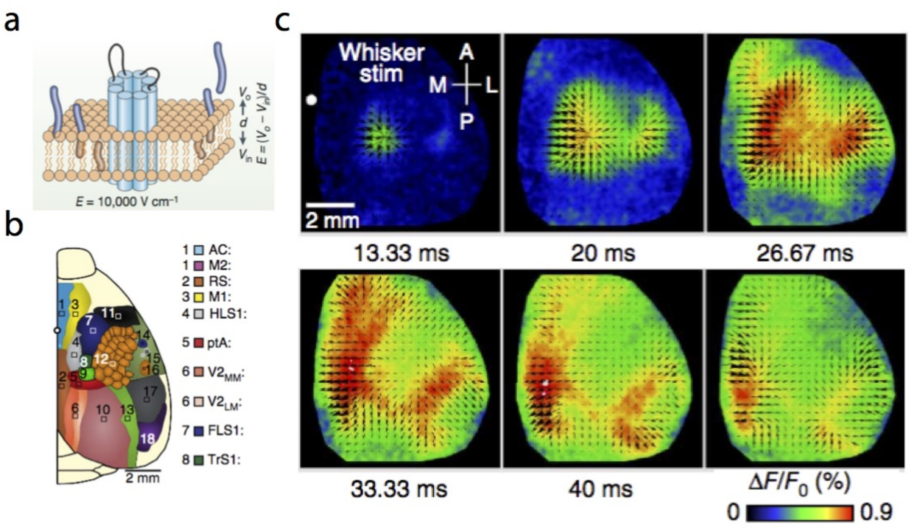

Figure 3.15 – Voltage Sensitive-Dye Imaging can monitor membrane potential in the awake mouse (a) Schematic representation of voltage sensitive dyes (dark blue) penetration in the membrane depending on synaptic potential. **(b)** Whole-hemisphere labelling of cortical region the mouse cortex **(c)** Color-coded spatiotemporal dynamics of propagation in response to whisker stimulation. Black arrows represent the direction of propagation. Note the bidirectional propagation arising from a single source located in the barrel cortex. Adapted from [Mohajerani et al., 2013].

VSDI is particularly suited to studying the spatiotemporal patterns of activity, like sensory binding during motion perception and visual illusions in cortical areas [Jancke et al., 2004], functional domains in the retina [Grinvald et al., 1994] or spreading depression in cortical areas [Farkas et al., 2008; Obrenovitch et al., 2009]. Importantly, VSDI can easily be coupled to electroencephalography, which gives complementary information about deep neural activity. VSDI has provided new insights about spontaneous activity, revealing that ongoing activity can contain spatiotemporal patterns that resemble those evoked by external stimuli [Kenet et al., 2003]. More recently, Murphy and colleagues have demonstrated that spontaneous activity consists in a superposition of sensory processing "modes" including vision, audition and touch. By comparing stimulus-evoked spreading patterns and direct activation using channel-rhodopsin, they found that these spatiotemporal patterns reflect long-range monosynaptic connections between cortical areas [Mohajerani et al., 2013] (see Figure 3.15). VSDI can thus provide precise information about the integration of sensory stimulation, functional connectivity and spatiotemporal activation patterns in awake animals.

3.3.3.2 Calcium Imaging

The intracellular calcium concentration is involved in a variety of processes including presynaptic exocytose, synaptic plasticity and gene transcription. Importantly, intracellular calcium concentration rises 10 to 100 times during action potentials [Berridge et al., 2000]. This has prompted the development of optical probes expressing the intracellular calcium signals as fluorescent changes. Early studies have made use of several endogenous calcium-activated proteins such as aequorin [Shimomura et al., 1962], requiring techniques like electroporation or sharpened multi-electrode to deliver dyes into individual neurons. But a major breakthrough was the development of genetically encoded calcium indicators [Nakai et al., 2001; Tian et al., 2009], which could target genetically identified neurons. The most widely used calcium-indicator, GCaMP, allows for *in vivo* mammalian recordings of large cell ensembles [Tallini et al., 2006].

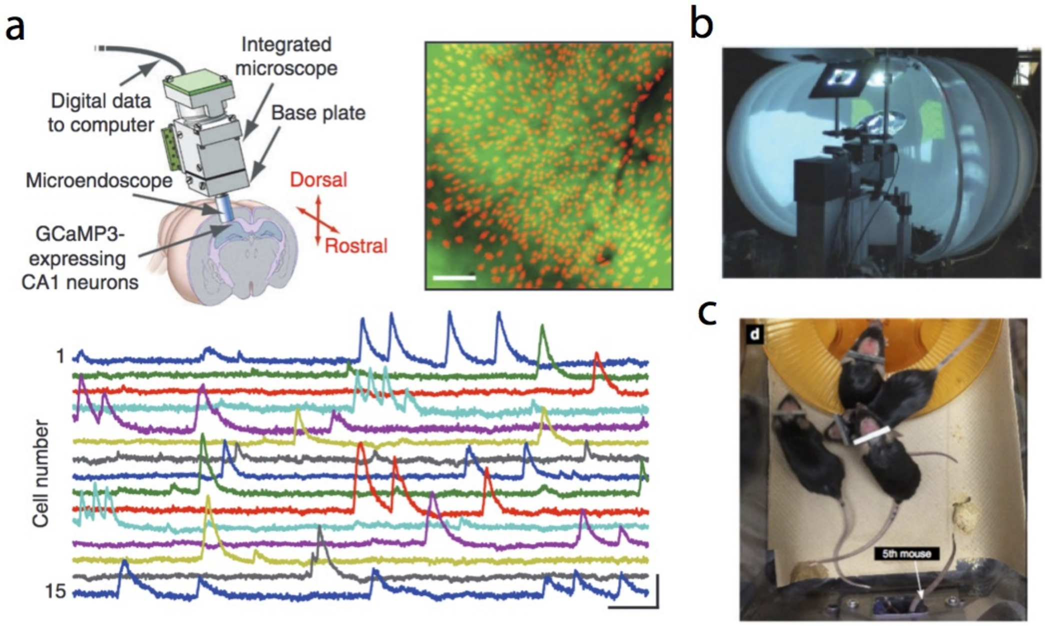

Figure 3.16 – Calcium Imaging Monitoring of large cell ensembles (a) Portable one-photon epifluorescence microscope in freely-moving mice can monitor activity of large cell ensembles over several weeks to explore long-term dynamics of CA1 place cells **(b)** Virtual reality setup used in spatial navigation tasks in head-restrained mice **(c)** Semi-automated learning procedures for mice to undergo imaging sessions with minimal experimenter intervention. Mice wear head-bar specifically designed to fit the reward chamber (bottom) and receive light illumination during reward in head-restrained conditions. **(a)** adapted from [Ziv et al., 2013] **(b)** adapted from [Dombeck et al., 2010] **(c)** adapted from [Murphy et al., 2016].

Two complementary paradigms have emerged for calcium imaging in behaving mammals: those involving head-restrained protocols and those permitting unrestrained behavior (for a review, see [Hamel et al., 2015]). The main advantages of head-fixed protocols are the use of conventionally sized optical apparatus, the control of mechanical vibrations, the ease of auxiliary manipulations such as mid-session drug delivery or visually guided electrical recording [Lovett-Barron et al., 2014]. Virtual reality approaches (see Figure 3.16) allow control of sensory input such as artificial mismatch between motor behavior and visual feedback, and comparison of spatial navigation related activation between natural behavior and virtual reality [Dombeck et al., 2010].

Calcium imaging in freely-moving conditions require miniaturization and flexible tethers like optical fibers [Ghosh et al., 2011] to study behaviors that require active exploration, natural movement or behaviors incompatible with head-fixation such as mating or fighting. The challenge of miniaturization imposes design trade-offs, though proof of principle in behaving mice and rats has been brought [Helmchen et al., 2001; Flusberg et al., 2005]. Portable two-photon microscopes require an optical fiber to deliver ultrashort-pulsed laser illumination to the microscope, albeit at low sampling rates. Unfortunately, they have never progressed in practice beyond the anesthetized state. However, camera-based one-photon epifluorescence microscopes have achieved broad field of views at fast frame rate in behaving mice [Ghosh et al., 2011; Ziv et al., 2013]. The integrated microscope has 0.5 mm^2 field of view, which permits dense sampling of up to 1,000 neurons simultaneously. High-throughput imaging can be achieved through hybrid methods, like coupling two-photon optogenetic activation stimulation and calcium imaging in head-restrained mice [Packer et al., 2015] or similarly in transgenic freely moving mice, that are trained for automated head-fixation tasks (see Figure 3.16) [Murphy et al., 2016].

3.3.4 Functional Ultrasound imaging

Conventional ultrasonography for medical diagnosis emerged in the 1970s long after the invention of sonar on which it takes ground [Chilowsky and Langevin, 1920]. Ultrasonography bears the paradox to be at the same time the most widely used technique in medical imaging (including cardiology, obstetrics, elastography) and rather absent in neuroimaging studies [Tanter and Fink, 2014]. However, recent advances in computing power, reconstruction algorithms and surgical techniques have prompted the emergence of high-resolution ultrasonography with unprecedented resolution and signal-to-noise ratio in fetuses, infants [Demene et al., 2015], humans in peroperative conditions and in rodent studies [van Raaij et al., 2011; Mac et al., 2011]. Several key features of ultrasound (US) waves make them a good candidate to study brain activity, including excellent tissue penetration, high spatial coherence, good sensitivity and moderate cost. However, due to the screening nature of the skull, bones still constitute a major obstacle to US waves, which requires circumventing approaches such as cranial window, thinning approaches or imaging through fontanelle in infants.

Ultrasonography uses a wide range of frequencies from 1 to 20 MHz, with the classical tradeoff between resolution (defined by wavelength) and penetration in the tissue, because attenuation of sound waves increases at higher frequencies / shorter wavelengths. Sound waves are produced by acoustic transducers that convert electrical currents into mechanical pulses of sound. When an ultrasound wave encounters a change in acoustic impedance (bone, tumor),

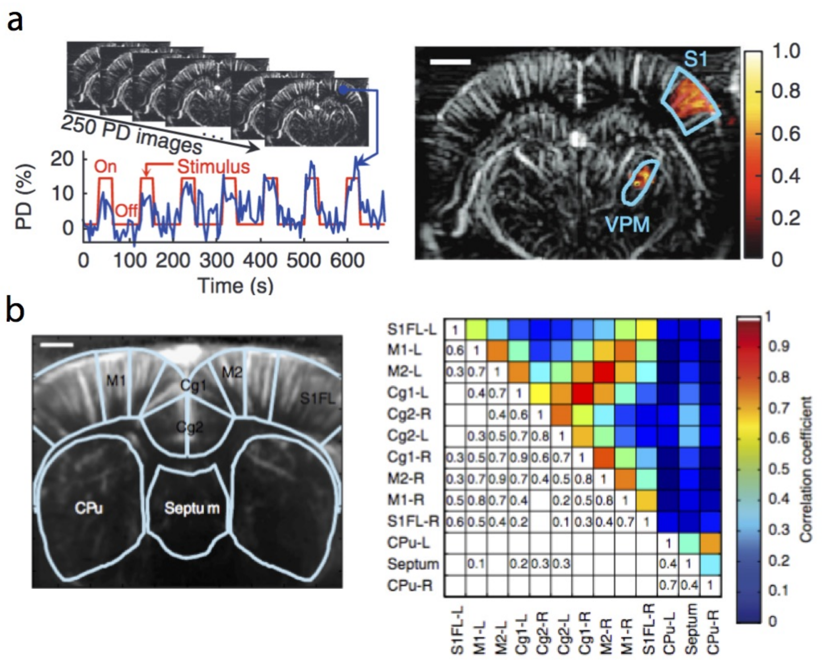

	S1FL-L	M1-L	M2-L	Cg1-L	Cg2-R	Cg2-L	Cg1-R	M2-R	M1-R	S1FL-R	CPu-L	Septum	CPu-R
S1FL-L	1												
M1-L	0.6	1											
M2-L	0.3	0.7	1										
Cg1-L		0.4	0.7	1									
Cg2-R			0.4	0.6	1								
Cg2-L		0.3	0.5	0.7	0.8	1							
Cg1-R	0.3	0.5	0.7	0.9	0.6	0.7	1						
M2-R	0.3	0.7	0.9	0.7	0.4	0.5	0.8	1					
M1-R	0.5	0.8	0.7	0.4		0.2	0.5	0.8	1				
S1FL-R	0.6	0.5	0.4	0.2		0.1	0.3	0.4	0.7	1			
CPu-L											1		
Septum		0.1		0.2	0.3	0.3					0.4	1	
CPu-R											0.7	0.4	1

Figure 3.17 – In vivo functional Ultrasound Imaging on anesthetized rats (a) Proof of concept for functional Ultrasound (fUS) in anesthetized rats. (Left) Power Doppler images are acquired at 0.33 Hz during 30 s whisker-stimulation followed by 60-s rest periods (red curve) repeated 10 times. Example of the temporal dynamics of Power Doppler signal from one pixel in primary somatosensory cortex (blue) (Right) Correlation maps using Pearson coefficient for each pixel in the image. Significant correlations ($r > 0.2$) are found in the somatosensory cortex (S1) and thalamus (VPM) **(b)** Functional connectivity during forepaw stimulation under anesthesia. Cross-correlation matrix shows symmetrical cortico-cortical coupling and subcortical-cortical decoupling during stimulation **(a)** adapted from [Mac et al., 2011] **(b)** adapted from [Osmanski et al., 2014b].

part of the sound wave is back-propagated to the transducers. The detection of these echoes is used to form images of the tissue over the whole imaging plane. The classical imaging mode of ultrasound uses a linear array of transducers (Bmode) to localize echoes. It emits focused waves and forms images line-by-line. Another widely used method takes advantages of the Doppler effect: moving objects generate echoes arriving at the transducer with a frequency that is shifted from the emission frequency. Reception frequency is higher for objects moving toward the transducers, and smaller for objects moving away. Doppler ultrasonography can generate precise images of blood flow deep into the body (5 cm at 5 MHz, see Table E.2) but only recently has it been able to resolve small venules and arterioles.

Functional Ultrasound Imaging (fUS) is derived from ultrafast imaging based on emission and reception of plane waves at very high repetition rates (up to 20,000 repetitions per second). This process results in the generation of compound images over a 200 ms period, from which Doppler images are generated [Mace et al., 2013]. The resulting signal contains a low-frequency rhythmic component, which reflects large amplitude changes due to heartbeat-induced pulsatility in the tissue and a high-frequency residual from echogenic particles (red blood cells) moving in the imaging field. Thus ultrafast imaging can provide images of both cerebral blood volume (CBV - Power Doppler) and cerebral blood flow (CBF - Color Doppler) with a spatial resolution of 100 μm (lower for surface imaging) and a temporal resolution of 200 ms. For a detailed description of conventional and functional Ultrasound see section 4.1.

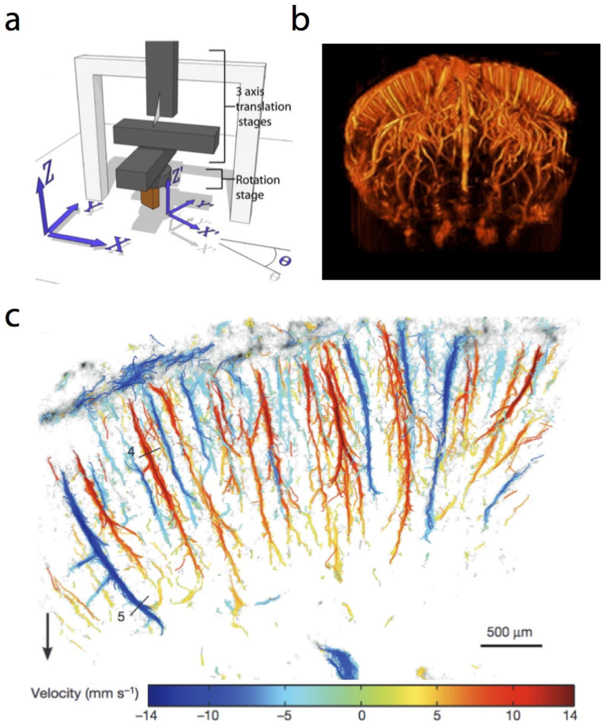

Figure 3.18 – Recent advances in functional Ultrasound Imaging of brain vasculature in vivo (a) Setup for fast optical tomography in anesthetized animals **(b)** Whole-brain reconstruction of 4-dimensional mapping of blood flow. Basal arteries of the Willis polygon are visible **(c)** Microvasculature in the somatosensory cortex of thinned-skull rats using ultrafast Ultrasound Localization Micoscropy (uULM). Penetrating arterioles and venules are clearly resolved. Smaller vessels can be distinguished. Velocity and direction of blood flow are color-coded **(a-b)** adapted from [Demen et al., 2016] **(c)** adapted from [Errico et al., 2015].

fUS has first been developed on the anesthetized animal. After undergoing craniotomy, the probe is placed onto the *dura mater*, with saline filling the space between the probe and the meninges in order to best facilitate the conduction of ultrasound waves. The proof of principle that fUS could monitor hemodynamics changes was given in anesthetized rats undergoing mechanical stimulation of the vibrissae and after focal injection of 4-aminopyridine (4AP), a substance that is known to trigger tissue hyper-excitability resulting in generalized epileptiform seizures. In the first case, CBV fluctuations in the barrel cortex and the thalamus strongly correlated with the mechanical stimulation of the vibrissae, with the strongest correlations in the corresponding barrel field. In the second case, fUS monitoring for over 2 hours revealed waves of hyper-perfusion followed by hypo-perfusion traveling from the site of injection throughout the brain, highlighting the fact that fUS displays high sensitivity and capabilities for recording functional dynamics over prolonged periods of time. Subsequent studies showed that fUS could reliably reveal functional domains upon electric forepaw stimulation [van Raaij et al., 2012], odor-evoked patterns of vascular activity in the olfactory bulb and pyriform cortex [Osmanski et al., 2014a] and functional connectivity with high spatiotemporal resolution [Osmanski et al., 2014b] (see Figure 3.17). However, all of these studies were performed in the anesthetised animal, highlighting the need for protocol adaptation.

More recently, several studies showed that ultrasound imaging could convey high-resolution reconstruction of the brain microvasculature. The first approach was aiming at generating 4-dimensional mapping of the whole vascular system of a rat brain (3 dimensions in space, 1 dimension in time), through ultrafast Doppler tomography [Demen et al., 2016]. This method provides full reconstruction at high spatial resolution (100 μm x 100 μm x 400 μm) and high sensitivity to flow in small vessels (< 10 mm.s^{-1}) without the need for any contrast agent. The second approach makes use of the injection of microbubbles into the circulation to provide reconstruction of the microvasculature at unprecedented resolution, beyond the sound diffraction limit (10 μm, similar to optical resolution) deep into the tissue (ten millimeters below the surface) [Errico et al., 2015]. This process relies on the individual tracking of non-linear echoes generated by the micro-bubbles and can be performed through the intact skull (see Figure 3.18). Thus, functional ultrasound is a promising technique to study functional dynamics both in clinical and fundamental research.

3.3.5 An overview of *in vivo* functional imaging

I have presented multiple optical techniques for *in vivo* recording of brain activity. These techniques can be classified in three main groups based on resolution, field of view and transposition to mobile animals (see Table 3.1): (1) fMRI and PET can resolve BOLD signal and glucose metabolism in the whole brain at good spatial resolution (MRI) but low temporal resolution. These techniques are currently used in human studies but require immobilization, though PET has recently been applied to mobile animals [Schulz et al., 2011]. (2) VSDI, IOSI and one-photon microscopy can resolve cortical dynamics at very high temporal resolution revealing the spatiotemporal dynamics of electrical activity (VSD) or hemodynamics (IOSI) to provide regional responses to functional activation. They have been successfully applied to mobile imaging but lack penetration (3) TPLSM, PAM and fNIRS can penetrate deeper in brain tissue (from 0.5 mm to 3 mm) at the cost of decreasing spatial resolution. Only TPLSM can provide full information of neuronal activity (calcium imaging) and hemodynamics simultaneously. These techniques have been applied to mobile imaging but need further improvement to resolve more than cortical circuits.

US imaging can play an important role in the years to come, because technical improvements have been achieved to monitor hemodynamics in depth in mobile animals. It can be coupled with electroencephalography and most optical techniques (to assess blood oxygenation for instance), provided a sufficient improvement on lightweight apparatus. Microvasculature is already resolved at very high spatiotemporal resolution in cortical structure and at moderate resolution in whole brain networks. To date, there is no physical obstacle for a generalized use of this technique in functional probing of neural circuits in both normal and pathological states.

	Whole-brain			Voltage-based	Optical					Ultrasound
	EEG Electroencephalography	fMRI Functional Magnetic Resonance Imaging	PET Positron Emission Tomography	VSDI Voltage-sensitive Dye Imaging	IOS Intrinsic Optical Imaging	LSCI Laser Speckle Contrast Imaging	PAM Photo-Acoustic Microscopy	fNIRS Functional Near Infrared Spectroscopy	TPLSM Two-photon Laser Scanning Microscopy	fUS Functional Ultrasound
Param. Measured	Field Potential	BOLD	CBF, Glucose uptake	Membrane Potential	HbO, HbR, CBV	CBV	HbO, HbR, CBV	HbO, HbR, CBV	HbO, HbR, CBV	CBV, CBF
Field of View	Whole	Whole	Whole	Surface	Surface	Surface	Plane	Whole	1 cm^2	Plane
Penetration	cm	-	-	≈ 1 mm	1-2 mm	0.5-1 mm	1-3 cm	1-3 cm	0.5-1 mm	cm
Spatial Res.	cm	25-100 μm	0.1-1 mm	50 μm	10 μm	10 μm	100 μm	1 cm	1 μm	100 μm
Time Res.	20 μs	1 s	1 min	< 1 ms	1 ms	100 μs	1 ms	1 ms	1 s	200 ms
Invasivity	none	none	contrast agent	**toxic**	cranial window	trans-cranial	cranial window	trans-cranial	cranial window	cranial window
Mobility	yes	no	wearable	yes	head-fixed	yes	head-fixed	yes	yes	yes
Year	1929	1990	1975	1984	1986	1991	2006	1992	1990	2011

Table 3.1 – **An overview of *in vivo* functional imaging** In vivo imaging techniques can be divided in two major groups: those monitoring global brain activity usually at the cost of subject immobilization or animal sedation and those monitoring local activity at high spatio-temporal resolution at the cost of limited field of view or surface imaging. Ultrasound Imaging proposes an interesting alternative to image large brain networks with good spatio-temporal resolution and high sensitivity.

3.4 Conclusion

Relating structure to function is one of the recurrent goals of neuroscience. This requires precise anatomical characterization, which is still mostly performed by staining techniques based on morphological grounds. However, recent advances in optics and genetics allows for finer segregation of functional domains, connectivity and microvasculature. Future investigation needs to integrate this rich information onto existing brain atlases, to bridge the gap between past and present research, especially when studying vascular patterns for which no reference atlas yet exists.

Apart from electroencephalography, most brain imaging techniques rely on proxy measures of neural activation through hemodynamic activity. The coupling between neural and vascular events has been established in 1890, and called *functional hyperemia*. Surprisingly, this cascade of signaling does not rely on feedback metabolic signals consequently to increased energy demands, but rather on direct signaling intrinsically associated with neural events. The dynamics of vascular responses are slower than neural events and region-specific. They rely on a functional and anatomical entity called *neurovascular unit*, involving neurons, astrocytes, pericytes and smooth muscle interacting in a variety of means through multiple signaling pathways.

Early whole-brain functional imaging such as PET and fMRI, which can record brain activity non-invasively in humans, has revolutionized our understanding of brain function. MRI through BOLD signaling has clearly dominated neuroimaging in the past two decades, despite high cost and low temporal-resolution. More recently, optical techniques underwent a spectacular development reaching extremely high spatiotemporal resolution unveiling fine details of hemodynamic signals, albeit limited in tissue penetration. Genetically encoded calcium indicators now clearly propose an alternative to the use of electrodes, allowing recording of large cell ensembles in genetically-targeted neurons. Ultrasound imaging has a strong features such as tissue penetration and high sensitivity, which might give it a more central place in neuroimaging studies in the near future.

Part II

Personal Contribution

Chapter 4

Methods

4.1 Functional Ultrasound Imaging of the Brain

4.1.1 Physical Properties of Ultrasound Waves

Ultrasound (US) waves bear the paradox of being at the same time routinely used in medical diagnosis and rather absent in brain imaging studies [Tanter and Fink, 2014]. This is mainly due to the fact that US waves are well suited for estimating the properties of homogeneous media, whereas bones have a strong attenuating and distorting effect that preclude a general use to assess cerebral blood flow. Additionally, computing power becomes increasingly demanding to estimate subtle variations in blood vessel signals and to form high-resolution images in reasonable time. On the other hand, US waves possess properties that make them one-of-a-kind: they have excellent tissue penetration (compared to light, their wavelength is several orders of magnitude lower, which allows them to penetrate deeper in a tissue), they weakly interact with matter, renderiing their normal use completely safe for the body, they have good spatial coherence and their implementation is relatively easy to use at low financial cost. Their overall absence as a brain imaging modality is thus surprising.

It is only recently, that US has been demonstrated to be suited for cerebral blood volume (CBV) and cerebral blow flow (CBF) imaging. This major breakthrough relies on two recent technological and scientific advances: (1) the ability to send short ultrasonic pulses and receive echoes at ultrafast frame rate (up to 20,000 pulses per second) (2) the ability to synthetically sample all pixels in a given plane at once, rather than focusing ultrasound pulses sequentially to form a full image. This latter phenomenon, known as *coherent compounding*, has long been described by Mathias Fink and Mickael Tanter at Institut Langevin [Montaldo et al., 2009]. When applied to brain imaging, it results in a significant increase in signal-to-noise ratio, resulting in detailed images of the brain vasculature *in vivo*, for blood velocities as low as 5 mm.s^{-1}.

Ultrasound Waves Speed Range

US waves travel in water at a constant speed of 1540 m.s^{-1}. Under the assumption that brain can be considered as an homogeneous aqueous medium, US velocity in the brain is assumed constant and equal to the one in water. The choice of ultrasound emission wavelength relies on a trade-off between the size of imaging field (limited by tissue penetration) and the resolution

Vessel Type	Vessel Diameter	RBC Speed	Reference
Large Cerebral Arteries	$>100\ \mu$m	15 cm.s^{-1} (up to 50 cm.s^{-1})	[Li et al., 2010]
Pial Arteries	10 - 50 μm	around 25 mm.s^{-1}	[Shih et al., 2009]
Penetrating Arterioles	10 - 30 μm	10 - 25 mm.s^{-1}	[Nishimura et al., 2007]
		(depending on blood vessel size)	[Shih et al., 2012]
Capillaries / Venules	$<10\ \mu$m	0.5 - 1 mm.s^{-1}	[Nguyen et al., 2011]

Table 4.1 – Red blood cells speed distribution in the arterial system RBC speed is mostly dependent on vessel type and size. The dilating properties of the arterial system are responsible for the great variations observed between regions during functional activation. In this table, we summed the estimates of RBC speed. Note that 25 mm.s^{-1} seems to be an upper bound for RBC speed in all vessels except for large cerebral arteries.

of the image (limited by ultrasound emission wavelength). As an example, the adult brain of a rat does not exceed 10 mm in depth: 15 MHz or 18 MHz US waves can penetrate 1 cm in depth with limited attenuation, thus providing a spatial resolution of 100 μm. On the contrary, US waves used in medical imaging lie in a frequency range between 3 to 5 MHz, providing a decent millimetric resolution up to 5cm in depth. For a detailed review on ultrasound wave propagation, see [Rousseau, 2003] and Appendix E.

Red Blood Cells Speed Range

US waves have many applications like elastography (probing tissue elasticity from distance) or shock wave delivery. In this thesis, we focused on the property of ultrasound to echo on particles that present a change in acoustic impedance with their surrounding medium. This is the case for red blood cells, which speed can thus be estimated using the Doppler Effect. Red blood cells speeds have been measured at different locations in the vascular system, summarised in Table 4.1. To the best of our knowledge, we did not find any measure of blood velocity exceeding 25 mm.s^{-1} outside the large cerebral arteries, which are less likely to be involved in functional hyperaemia, resulting from selective tissue activation. As a result, the sampling frequency of ultrasound f_s has been set to optimise speed detection in the range [0 - 25 mm.s^{-1}].

4.1.2 Conventional Echography

Echography can be used in different modes depending on the type of signal the experimenter wants to acquire. We will present briefly “Amode” and “Bmode” and we will extend on Doppler Imaging Mode.

Amode

Amode (Amplitude Mode) allows for precise measures of acoustic impedance changes along a single line. The amplitude of the echo gives an estimate of medium reflexivity (propension to generate echo) and tissue attenuation, while the delay provides information about the location of the echogenic particle. It is seldom used except for eye or skin treatment to perform precise measures of distance. The use of linear transducer arrays can improve source localisation by analysing the delay difference in the received signals between neighbouring transducers.

Bmode

Bmode (Brilliance Mode) is the most widely used acquisition mode. It generalizes Amode to form two-dimensional images over a whole plane. The probe "sweeps" along the imaging plane, by performing one-dimensional measures for each line of an image. The resulting image is thus a juxtaposition of each acquisition of the ultrasound beam. One of the major advantages of Bmode sequence is that it can be performed continuously in real-time by refreshing the lines in the image when the ultrasound sweep is performed. Though, there is a trade-off between spatial resolution and processing time, spatial smoothing is a solution to interpolate missing information between beam directions. Bmode gives mainly structural information on the composition of a static medium.

Doppler mode

The Doppler Mode is used to get information about moving echogenic particles. It is based on the well-known *Doppler effect*, which is a change in wave frequency between an emitter and a receiver, resulting from the relative movement between the two. When an emitting source is moving towards or away from a receiver, two consecutive pulses do not have to travel exactly the same distance to reach the sensor (the second one has to travel a somewhat shorter distance in the first case, longer in the latter), which results in a receiving frequency that is slightly different from the emission frequency. This frequency shift is called *Doppler frequency* and is proportional to the relative speed of displacement between the source and the receiver (the proportionality coefficient is the ratio between particle speed and the speed of ultrasound in the medium). In our case, the source (transducer array) is static but the echogenic particles are in movement at a certain speed v. This is the physical parameter we aim at estimating. Virtually this configuration is equivalent to a moving ultrasound-emitting source (red blood cells) towards a static receiving sensor (linear transducer array).

Pulsed Doppler

Because the transducer array cannot be used in emission and reception at the same time, the experimenter first has to send ultrasound pulses (emission) and then wait for echoes (reception). In theory, sending a single pulse and computing the frequency shift between the start and end of the pulse could give an estimate of the Doppler frequency generated by moving red blood cells. This is almost impossible in practice because the change in frequency generated by RBC moving at 25 mm.s^{-1} in comparison with the ultrasound propagation speed of 1540 m.s^{-1} results in a shift of a few kHz in a 15MHz pulse, which is extremely hard to evaluate. An alternative strategy is to repeat the emission and reception of short pulses (3-4 cycles) at high frequency to get "stroboscopic measures" of the Doppler signal. By doing so, one can consider that the particle is static during the duration of a single pulse (3 cycles at 15 MHz result in a 200-ns pulse) but not between two successive emission-reception cycles. Hence, the Doppler signal can be reconstructed by repeating emission/reception cycles at the frequency f_s. Figure 4.1 illustrates the Doppler signal reconstruction from a single echogenic particle moving towards the transducer.

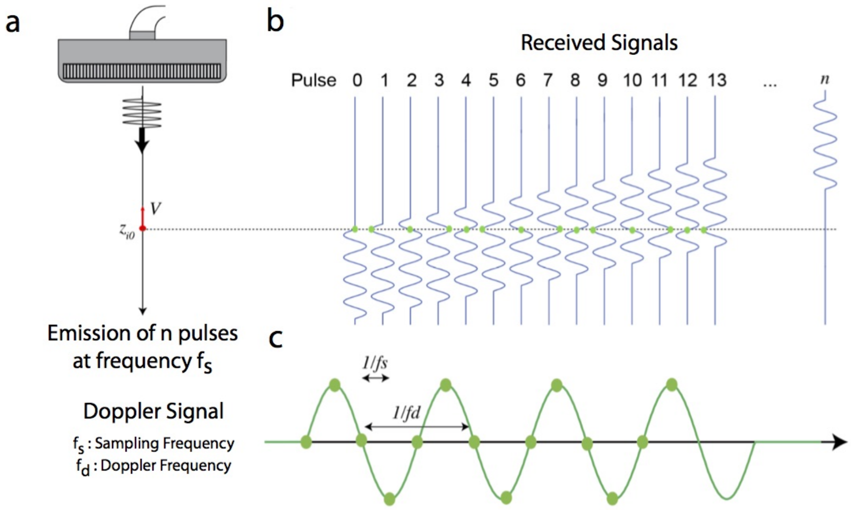

Figure 4.1 – Conventional Pulsed Doppler Principle for a single echogenic particle at constant speed Conventional Ultrasound uses pulsed sequences to infer echogenic particle speed. **(a)** The echogenic particle, initially in position z_{io}, moves with constant speed towards the transducer. **(b)** Short pulse sequences are emitted at frequency f_s to get "stroboscopic" measures of echogenic particle displacement. Due to the particle movement, delays between two consecutive emission-reception are not constant and a "Doppler Signal" can be reconstructed by the phase difference induced by particle movement. **(c)** By sampling received pulse at a given depth, we obtain a synthetic temporal dilation of Doppler signal, which frequency is proportional to the echogenic particle speed v. Adapted from [Mac, 2012].

The Pulse-Repetition Frequency (PRF) is the determining factor at which Doppler Signal is sampled. To avoid consecutive pulse train overlap, the time between to pulse emissions must be greater than the time required by US waves to travel in the medium back and forth to the transducer. For a 2 cm-deep imaging plane, this corresponds to an upper bound of 38 kHz. Also, to avoid multiple reflections and to limit the amount of energy absorbed by the medium, an additional delay is imposed resulting in a PRF of 20 kHz. However, to correctly sample the Doppler signal in a given line, one has to get enough samples to be able to estimate a wide range of speeds. A large number of repetitions results in a richer Doppler signal at the cost of increased processing time and higher signal distortion between the first and last line of the image. This limitation of Pulsed Doppler is hard to overcome because it stems from physical constraints. For this reason, echographic images are often acquired in blocks rather than line-by-line. This is commonly done by synthetic focalisation of ultrasound waves, where each linear transducer sends pulses with a small delay. Introducing a constant delay between distal and proximal transducers in a linear array can thus provide focalisation at a given depth in the imaging plane (focal depth). In this case maximal energy is transmitted in this focal zone, which in turn provides better echoes and better resolution.

4.1.3 Ultrafast Doppler Imaging

Ultrafast Sequence

Ultrafast Doppler imaging makes uses of plane waves rather than focalised waves. At first glance, plane waves seem less informative because energy is spread over the whole imaging plane, leading to noisy echoes and low-resolution images. Plane waves however show higher spatial coherence for high-frequency pulse trains and, unlike spherical waves, power does not decrease with distance. Repeating plane wave emissions with different tilt angles and summing the received echoes over a sequence of multiple angles - a process know as *coherent compounding* - can counterbalance the drop in resolution and re-instate focalisation in all points of the imaging plane [Montaldo et al., 2009]. Because PRF is very high (namely 20 kHz), a sequence of 20 tilted angles can be acquired in 1 millisecond, a time interval during which echogenic particles can be considered static. The coherent summation of these low-resolution images leads to *compound images*. Importantly, these compound images can be acquired at high rate (1 kHz) for every pixel in the image simultaneously. As a result, Doppler Frequency estimation can be performed for a large number of samples without prohibitively increasing processing time. In Figure 4.2 and Table 4.2 we give a time-equivalent comparison of conventional Pulsed Doppler and Ultrafast Doppler sequences. The duration and total transmitted power are the same in both cases but the sampling of Doppler signal for each pixel increases 8-fold in the Ultrafast Sequence.

Parameter	Focused	Compound
Ultrasound frequency	15 MHz	15 MHz
Pulse width	3 cycles	3 cycles
Aperture	4 mm	12 mm
Focal depth	10 mm	-
Maximal depth	20 mm	20 mm
Pulse repetition frequency, PRF	16 kHz	16 kHz
Sampling Frequency	1 kHz	1 kHz
Number of angles	-	16
Lines in a block	16	-
Number of blocks	8	-
Number of firings	5120	5120
Acquisition time	0.32 s	0.32 s
Number of frames	40	320

Table 4.2 – Experimental Parameters Used for a Time-Equivalent comparison of the Focused Method and the Ultrafast compound Method. The main difference is the number of images (8 times greater in the ultrafast compound method) for the same number of firings and the same acquisition time. Adapted from [Mace et al., 2013].

Color Doppler and Power Doppler

As a result, ultrafast sequence leads to 320 compound images acquired in 320 ms. Each pixel in this compound image contains the Doppler signal generated by multiple echogenic particles. Though, we only presented the Doppler signal generated by a single particle in the Pulsed Doppler Sequence, the same principle applies in the Ultrafast Doppler imaging. Moreover, the Doppler Signal generated by multiple echogenic particles is an aggregate of many particles flowing at different speeds. We can extract different physiological parameters by looking at the Fourier Transform of the Doppler Signal. First, all pixels in compound images do not map static brain locations, because of tissue pulsatility mainly due to heartbeat and major vessel pulsation. This component is low-frequency and peaks around 5 Hz in adult rats [Azar et al., 2011] and can easily be removed by high-frequency filtering. This step is known as *clutter filtering* and can be optimized by singular value decomposition (SVD). Second, the Doppler spectrum carries multiple types of information. After high-pass filtering, it has the following properties (1) centered on the Doppler Frequency corresponding to the RBC mean axial speed

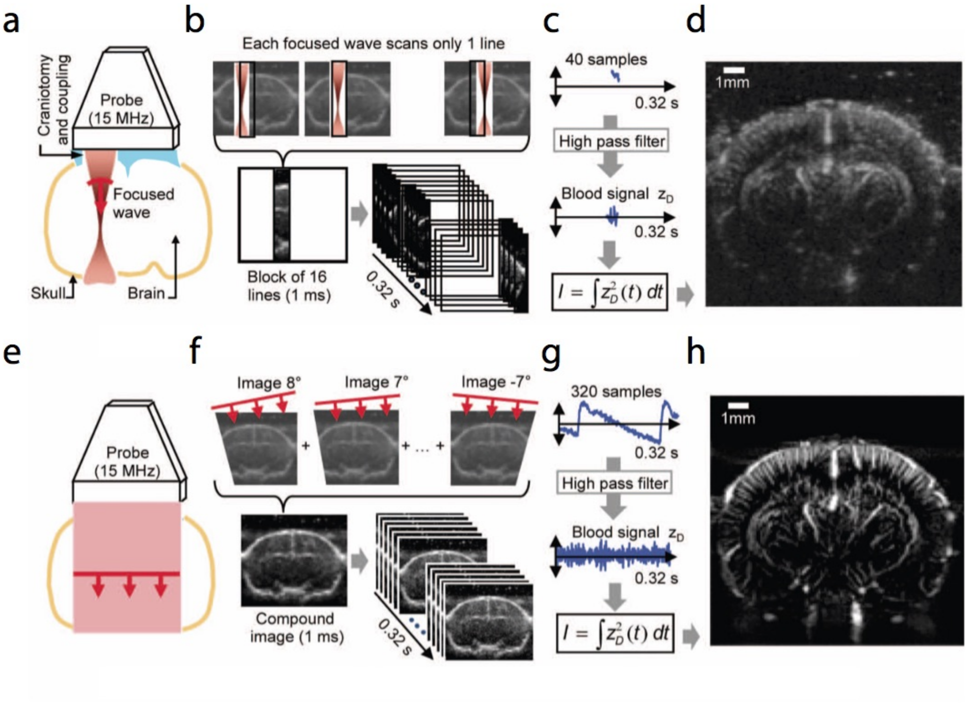

Figure 4.2 – Time-equivalent comparison between Conventional Doppler (top row) and Ultrafast Doppler (bottom row) modes. (a) Schematic description of the experimental setup: The 15-MHz probe is set in the coronal plane above the rat brain exposed by a cranial window. For conventional doppler, focused ultrasonic waves are used. **(b)** Acquisition sequence: The image is subdivided into blocks of 16 lines. One block is small enough to be scanned line by line with focused waves in less than 1 ms. Each block is imaged 40 times at 1 kHz for a total acquisition time of 0.32 s. **(c)** Signal processing: a 40-sample-long signal is obtained for each pixel. High-pass filtering is applied to reject tissue echoes. The mean intensity of the blood signal is calculated from the blood signal. **(d)** Power doppler image obtained with conventional Doppler mode. **(e)** Schematic description for the Ultrafast Doppler mode. The experimental setup is the same. For Ultrafast Doppler, plane ultrasonic waves are emitted. **(f)** Acquisition sequence: 16 plane waves are transmitted with different tilt angles in less than 1 ms for the building of one compound image. One ultrafast Doppler image results of 320 such compound images acquired in only 0.32 s. **(g)** Signal processing with 320 time points. **(h)** Ultrafast Doppler image. Adapted from [Mace et al., 2013].

(2) proportional to the total number of RBC that have crossed the sample volume during one acquisition. (3) its extent or width depends on the RBC speed and pulse wavelength [Mace et al., 2013].

Physiological parameters measured

Two main parameters with physiological significance can be extracted from Doppler images (Figure 4.3). We form Power Doppler Images by computing the total spectrum power for each pixel. In conditions of constant hematocrit density and shear rates, Power Doppler is, in first approximation, proportional to the partial volume of blood in a voxel [Shung et al., 1992]. Hence, Power doppler gives no information on the blood velocity but is associated with another relevant hemodynamic parameter: the volume of blood within a voxel (CBV). Second, the mean frequency of the spectrum conveys information about the direction and

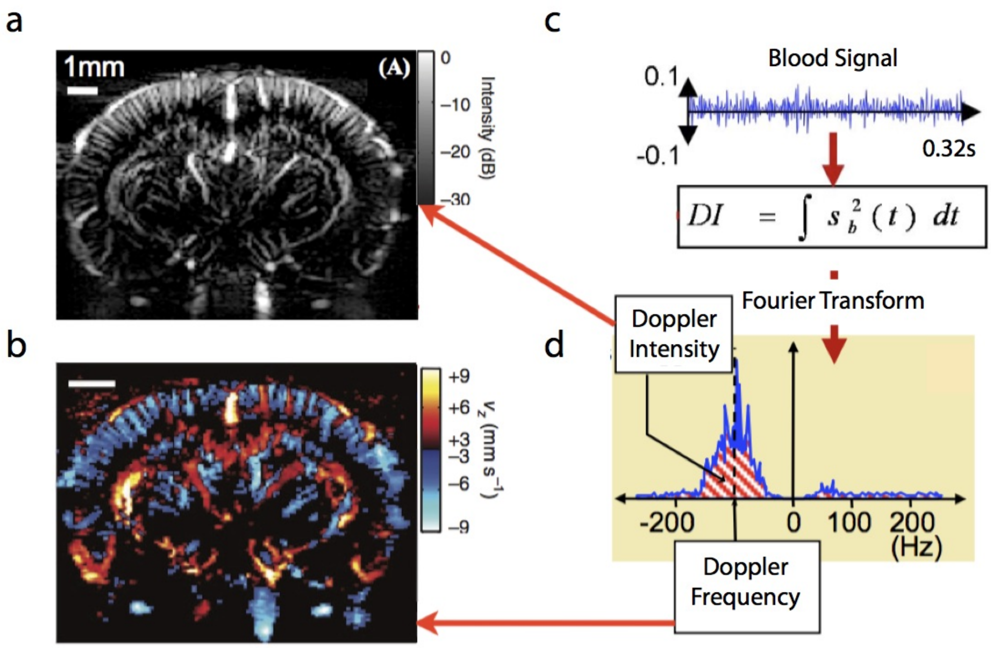

Figure 4.3 – Ultrafast Doppler Signal Contains two types of signal : Color Doppler and Power Doppler (a) Example of Power Doppler Image. Pixel Intensity is proportional to the power of the blood signal spectrum in **(d)**. **(b)** Example of Color Doppler Image. Pixel color is proportional to the mean Doppler frequency of the blood signal spectrum in **(d)**. **(c)** Blood Signal is obtained for each pixels after high-pass filtering of compound images. Power Spectrum is obtained after Fast Fourier Transform. **(d)** The Power Spectrum is an aggregate of all echogenic that have crossed a single voxel during the timing of one acquisition (320 ms). Hence, the mean Doppler Frequency is an estimation of the dominant speed in a given time (CBF) while the average Power Frequency is associated with the power of the received echoes, which relates to the amount of echogenic particles in a given time (CBV). Hence, the Power Doppler is more robust to aliasing than Color Doppler.

intensity of RBC speed in a given time window. It thus relates directly to Cerebral Blood Flow (CBF). In this thesis, we exclusively used Power Doppler images because this measure is more robust to aliasing and because in first approximation functional hyperemia leads to vessel dilation that results both in local CBV and CBF increases. It could be interesting to investigate how these two physiological parameters take part in the hemodynamic response and if regional variations are observed, which is likely [Devonshire et al., 2012].

4.1.4 Limitations

Absorption

During normal propagation, the medium absorbs part of the ultrasound waves energy, resulting in decreased beam intensity deep in the tissue. This absorption follows an exponential decay. It is thus very common to adjust the gain depending on the image depth to counterbalance this effect, which has the drawback of amplifying noise signal simultaneously in the deep portions of the images. In this thesis, we currently corrected depth absorption by computing mean and standard deviation for each horizontal line in the images and by adjusting offset and scale accordingly. A second effect amplifies the latter because wavefronts have higher spatial coherence in upper regions of the image compared to deep regions simply because ultrasound beams that reach deep tissues have undergone considerable interaction with the medium compared to the early back-propagated ones.

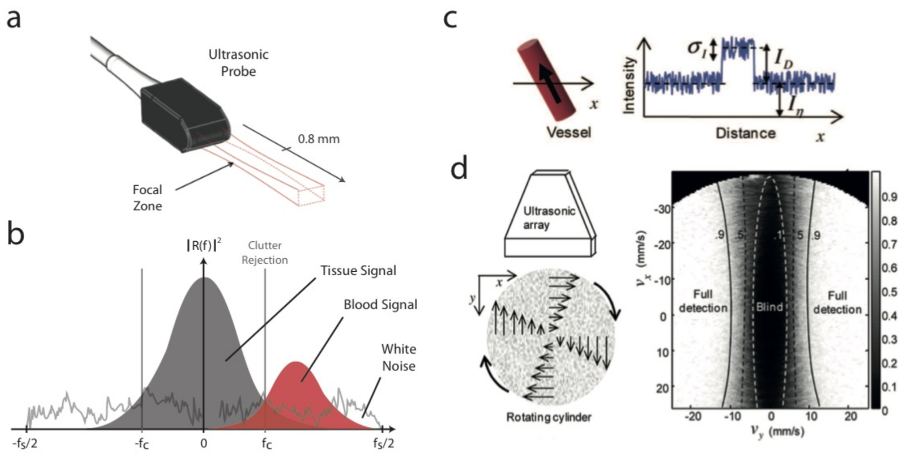

Figure 4.4 – Limits of Ultrafast Doppler Imaging (a) Ultrasonic Probes are equipped with focal lenses to ensure that ultrasound waves in-plane propagation. This induces a focal zone with maximal transmitted power, 8-mm distant from linear transducer array. **(b)** The Doppler Spectrum is an aggregate of echoes generated by tissue movement resulting from vessel pulsatility and red blood cell movement in the vessels. Clutter filtering is an important step which is performed easier when axial blood velocity is high, resulting in a greater separation in tissue and blood signal spectra. **(c)** Sensitivity of Doppler ultrasound directly depends on blood axial velocity. Red blood cells are detected when standard-deviation of the generated echo is greater than baseline I_n. **(d)** A textured rotating cylinder is used to estimate minimal detection velocities. For axial velocities ¡ 4mm.s^{-1}, no Doppler signal is generated resulting in a blind zone in the center of the image. Full detection is obtained for velocities above 10 mm.s^{-1} (8mm.s^{-1}) at the focal zone.

Heat

It is probable that such high rates of imaging result in tissue heating. For human studies, the total power transmitted to the tissue should not exceed certain bonds that are set by the American Food & Drug Association and European Union. In our experiment, time-lapses imposed by processing present the advantage of preserving both the ultrasonic probe (which can be damaged after sustained high-rate use) and limiting the amount of energy that is transmitted to the tissue. For subsequent experiment, head temperature should be monitored to ensure that it remains in physiological range.

Focalisation

To ensure that the ultrasonic probes do not emit out-of-plane pulses, these are equipped with a lens that focalises ultrasound in a narrow beam. This leads to a focal zone where signal-to noise is better than in other regions of the image and to a typical transverse resolution around 400 μm.

Clutter Filtering

Clutter Filtering is an important step in Ultrafast sequence processing. The most direct approach is to threshold the frequency distribution by high-pass filtering. However, this has the drawback of removing the remainder of blood signal spectrum at low frequencies (see Figure 4.4). Recently, methods bases on singular value decomposition aim at evaluating the spatial properties of the images, to remove components affecting a majority of pixels, which is the case for tissue pulsation. Indeed, the first singular value components are strongly affected by heart rate. We can selectively remove these components, leaving blood signal unchanged. SVD can also be used to remove movement artifacts (see Appendix A).

Blind Field

The whole Doppler sequence relies on the estimation of axial velocity. It is important to note that ultrafast imaging is rather blind to lateral velocities. To estimate minimal speed detection in ultrafast sequences, one can use a textured rotating disk, which creates a two-dimensional mapping of various velocities and directions on a single imaging plane. As expected, the resulting images presented blind spots in locations where axial velocity is close to zero. The threshold for axial velocity detected was estimated around 5 mm.s^{-1} with a full detection for speeds higher than 8 mm.s^{-1} at the focal zone and around 10 mm.s^{-1} elsewhere (see Figure 4.4).

4.2 Animal Preparation

4.2.1 Animal Strain and Housing

Male Sprague Dawley rats were used in all experiments. They were hosted in 12h light-dark cycle controlled environment in pairs from 8 weeks to 12 weeks of age and individually afterwards. After surgery, rats underwent daily recording sessions for 2 to 3 weeks, for a maximal consecutive period of 7 days in a row. When possible, rats were recorded at the same time of day to minimize variability in recording conditions. Aged rats did not perform well when physical training started after 15 weeks of age, because they tend to reach obesity when fed *ad libitum*. Best results with physical training and habituation were obtained when conditioning was intitiated between 10 to 15 weeks of age.

4.2.2 Surgical Procedure

All animals received humane care in compliance with the European Communities Council Directive of 2010 (2010/63/EU), and the institutional and regional committees for animal care approved the study. Male Sprague Dawley rats aged 12-14 weeks underwent surgical craniotomy and implant of ultrasound-clear prosthesis. Anesthesia was induced with 2% isoflurane and maintained by ketamine/xylazine (80/10 mg/kg), while body temperature was maintained at 36.5°C with a heating blanket (Bioseb). A sagittal skin incision was performed across the posterior part of the head to expose the skull. Drilling and gently moving the bone away from the *dura mater* excised parietal and frontal flaps (15 mm AP x 14 mm ML). The opening exposed the brain between the olfactory bulb and the cerebellum, from Bregma +6 to Bregma -8 mm, with a maximal width of 15mm. Electrodes were implanted stereotaxically and anchored on the edge of the flap, with their connector fixed to the back of the head. A plastic sheet of polymethylpentene was sealed in place of the skull with acrylic resin (GC Unifast TRAD) and residual space was filled with saline. Polymethylpentene is a standard biopolymer used for implants, which has tissue-like acoustic impedance and allows undistorted propagation of US waves at the acoustic gel-prosthesis and prosthesis-saline interfaces (see Figure 4.5).

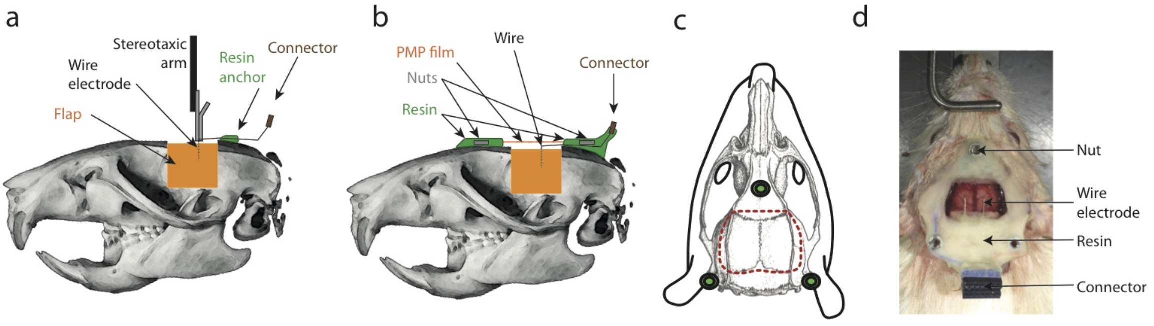

Figure 4.5 – Surgical Procedure for mfUS-EEG recordings (a) The surgical procedure to prepare the rat for simultaneous EEG and fUS recording proceeds in successive steps. First, a large bone flap is removed. Then electrodes are moved to the target position by stereotaxic micro-motion, and they are anchored to the edge of the flap with a droplet of resin. For clarity, only one electrode is shown. **(b)** Following sequential insertion of all the electrodes, the skull is replaced by an ultrasound clear prosthesis made of PMP. Finally, the prosthesis is sealed to the skull with resin and nuts are embedded in the resin for later attachment of the probe holder. **(c)** Schematic representation of the bone flap (red dotted line) and corresponding nut attachment points (green). **(d)** Picture after preparation.

We chose a prosthesis approach, which offers larger field of view and prolonged imaging condition over 4-6 weeks, compared to the thinned bone approach. Thinned-bone cranial windows present the drawback of not offering constant imaging quality over time, while impermeability is hard to maintain over time in full-cranial prosthesis approach. Polymethylpentene film of 250-μm thickness offers the best image quality, and provides good mechanical resistance and low permeability. Particular care was taken not to tear the *dura mater* in order to prevent cerebral damage. Three nuts used as attachment points for the probe holder are sealed above the nasal and lateral to the intraparietal bones. The surgical procedure, including electrode implantation, typically took 4-6 h. Animals recovered quickly and showed normal exploratory behavior 2 to 3 days after the surgery. After a conservative one week resting period, they were used for data acquisition.

4.2.3 Electrode Implantation

Intra-hippocampal handmade theta electrode bundles are composed of 25 μm insulated tungsten wire, soldered to miniature connectors. The difference with standard designs is the 90° angle elbow that is formed prior to insertion in the brain. This shape allows anchoring of the electrodes on the skull posterior to the flap. Four to six conductive ends are spaced by 1mm and glued to form 3mm-long, 50 μm thick bundles. The bundles are lowered in the dorsal hippocampus at stereotaxic coordinates AP = -4.0, ML = +/- 2.5, DV = -1.5 to

-4.5, in mm relative to Bregma. Hippocampal theta rhythm is confirmed by phase inversion across recording sites in successive hippocampal layers, time-frequency decomposition, and coincidence with periods of exploration and navigation. Early rats were implanted bilaterally, but we switched to unilateral implantation to decrease electrode fabrication time per animal. Two epidural screws placed above the cerebellum are used as reference and ground (see Figure 4.6).

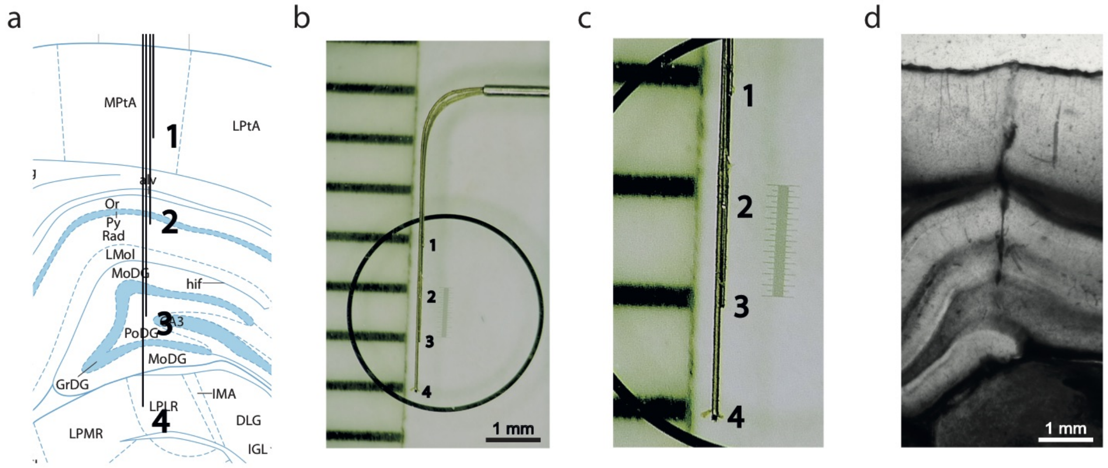

Figure 4.6 – Details of intra-hippocampal electrodes, implantation and localization **(a)** Hippocampal electrodes are made from a bundle of insulated tungsten wires soldered to a miniature connector at one end. Under binocular control the 50 μm guiding electrode (4) is juxtaposed with three 25 μm recording electrodes. The wires tips are positioned at fixed spacing in order to reach anatomical structures encompassing the dorsal hippocampus. Atlas from [Paxinos and Watson, 1982]. **(b-c)** They are glued with cyanoacrylate in the upper part of the bundle to avoid accidentally covering the recording tips. A millimeter scale and microscope scale slide (total length 1 mm) are used to precisely set the spacing. Note the 90° angle on the superior part of the bundle to enable electrode fixation onto the bone in (b). **(d)**Electrical lesionning is performed and 100 micron slices are collected for precise electrode tip post-localization.

4.2.4 Electrode Localization

Electrode localization was performed in two ways. Before each recording session *Bmode* images were acquired to select ultrasound plane and track electrode position, which were easily localised. When a plane was selected, a Doppler image was saved to allow for registration of electrodes onto vascular acquisition. The distance between two consecutive electrode tips was used to position precisely LFP recording sites on ultrasound images. This required that electrode directions is parallel to the imaging plane. An example of *Bmode* image and corresponding Doppler image is shown in Figure 4.7.

After euthanasia, brain were perfused with 4% para-formaldehyde solution and current injections (100 μA for 10 s) were performed to mark precisely recording sites. 50-μm slices were then prepared to record precise electrode location. Electrodes were kept to further test potential changes in electrode impedance before implantation and after euthanasia. Electrode detection on *Bmode* images could also be used as a landmark for better *a priori* estimation of plane selection, especially for diagonal planes. An example of recording-site lesion image is shown in Figure 4.6.

4.3 Experimental Protocol

The full experimental protocol for mfUS-EEG recordings is presented in Figure 4.7. We detail specific parts of this protocol below.

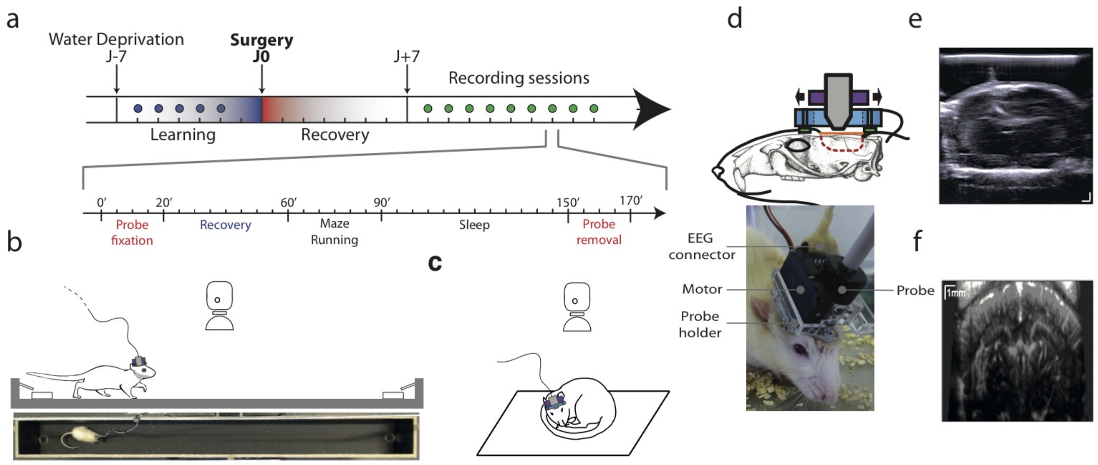

Figure 4.7 – Experimental Protocol and Setup Details (a) Protocol and typical recording session. Healthy Sprague Dawley rats undergo water deprivation protocol while they are conditioned to run back and forth on a 2.5 m-long 0.2 m-wide linear track for water reward. After surgery, rats are left to recover for another 7 days, before recording sessions are performed. A typical recording session lasts 3 hours. Probe is fixed under short isoflurane anesthesia (20 mn). **(b-c)** After a 40 mn recovery period, rats are recorded while they perform maze running (30 mn) and free exploration/sleep in another box (60 mn). Probe is then removed and rats return to their cage. **(d)** Details of probe fixation: Animal equipped with motorized translation stage, probe and EEG cable. **(e)** Bmode images are acquired to localize electrodes bundles and select the appropriate plane. **(f)** A corresponding fUS image is acquired to position static electrodes on Doppler images.

4.3.1 Animal Conditioning

Animals were trained before surgery. They were placed under a controlled water restriction protocol (weight maintained between 85 and 90% of the normal weight) and conditioned to run back and forth in a long rectangular maze for water reinforcement. The maze (225 x 20 cm) had 5 cm high lateral walls, and was placed 50 cm above ground. Drops of water were delivered through two small tubes coming out from the two end walls of the maze. Each time the animal crossed the maze; a single drop of water was delivered in alternate water tubes by opening an electronically controlled pair of solenoid valves. Daily training lasted 30 mn. Rats took about 2 sessions to reach a 60 maze travels criterion and perform reliably, crossing the mid-maze at fast speed, but were reinforced for at least two more days. Daily recording sessions lasted typically 30 mn (see Figure 4.7).

4.3.2 Probe fixation and Probe Holder Design

In order to attach the ultrasound probe and connect the EEG before a recording session, rats undergo short anesthesia for 20-25 min with 2% isoflurane. Acoustic gel is applied on the skull prosthesis, before the holder is screwed to the attaching nuts and the probe inserted into the holder. The gel does not dry out even for extended recordings up to 6-8 h. Animals are allowed a recovery period of 40 min from anesthesia before starting the recording session. Isoflurane is known to have a strong vasodilating effect of cerebral vascular system. It is thus critical to ensure that recorded signals are not biased by anesthetics. Additionaly, the animal behavior was abnormal right after wake from isoflurane (stress, head bumping, loss of balance) which returned to normal when recording session was initiated.

We used a miniature ultrasound probe (18 mm radius, 25 mm height) mounted on a lightweight head-anchored adjustable holder (18 g). The holder is motorized to explore consecutive planes, without direct interaction between the experimenter and the animal, and can be locked for maximum stability, which was done routinely for maze running (see Figure 4.7 d-f). Our probe holder design allows for flexibility in the selection of imaging plane, including a translation along the anteroposterior axis (which direction is defined by the nuts' position supporting the holder) and a rotation along the dorso-ventral axis along for coronal or diagonal plane selection. Distal regions were nevertheless hard to reach especially when they were in the posterior part of the brain (entorhinal cortex, subiculum, cerbellum) because they could not easily be encompassed in a diagonal plane due to the limited width of the probe.

4.3.3 Ultrasound recording procedure

Vascular images are obtained by the Ultrafast Doppler imaging sequence (see subsection 4.1.3). Each frame is a compound plane wave frame, that is, a coherent summation of beamformed complex in phase/quadrature images obtained from the insonification of the medium with a set of successive plane waves with specific tilting angles. This compound plane wave imaging technique enables to recreate *a posteriori* a good quality of focalization in the whole field of view with few ultrasound emissions. Given the tradeoff between frame rate, resolution and imaging speed, a Plane Wave Compounding using five 5°-apart angles of insonification (from -10° to +10°) has been chosen. In order to discriminate blood signals from tissue clutter, the Ultrafast Compound Doppler frame stack is high pass filtered using a 4th order Butterworth filter (cut-off frequency 50 Hz) along the temporal dimension, giving a high frequency in phase/quadrature frame stack whose energy in each pixel is then computed to build the ultrafast Power Doppler image. The signal measured by fUS and its sensitivity are presented in earlier theoretical and experimental work [Mac et al., 2011]. Briefly, fUS measures the amount of moving echogenic particles (red blood cells) and thus corresponds to cerebral blood volume (CBV). Importantly, this proportionality holds only if backscattering properties do no vary versus time. This assumption is valid while red blood cells backscattering properties such as hematocrit and shear rate remain time-invariant, which is most likely.

4.3.4 Ultrasound sequences

One current limitation of fUS is due to the transfer and processing time of the large amount of data required to form ("beamform") fUS images, as the raw images used to generate one compound frame are 200-fold larger than the frame itself. Hence, it is critical to beamform images during acquisition to avoid memory overload or prohibiting transfer time. We used two strategies to monitor hemodynamic signals, depending on the requirement of each experiment (see Figure 4.8).

Continuous Mode

The first strategy relies on a scheme acquisition processing transfer for each compound image. A compound frame is acquired in 200 ms followed by 2.8 s of beamforming and saving (recently, this step has been reduced to 1.0 s). This mode does not require large amount of memory and allows "continuous" recording with a frequency of acquisition of 1 image every 3 s (1.2 s in the new setup), close to the time constant of neurovascular coupling (1-2 s), for long periods of time (up to several hours). This strategy is well designed to capture long-lasting slow hemodynamic variations such as sleep however it is blind to fast variations occurring within a 3 s time window (1.2 s in the new setup).

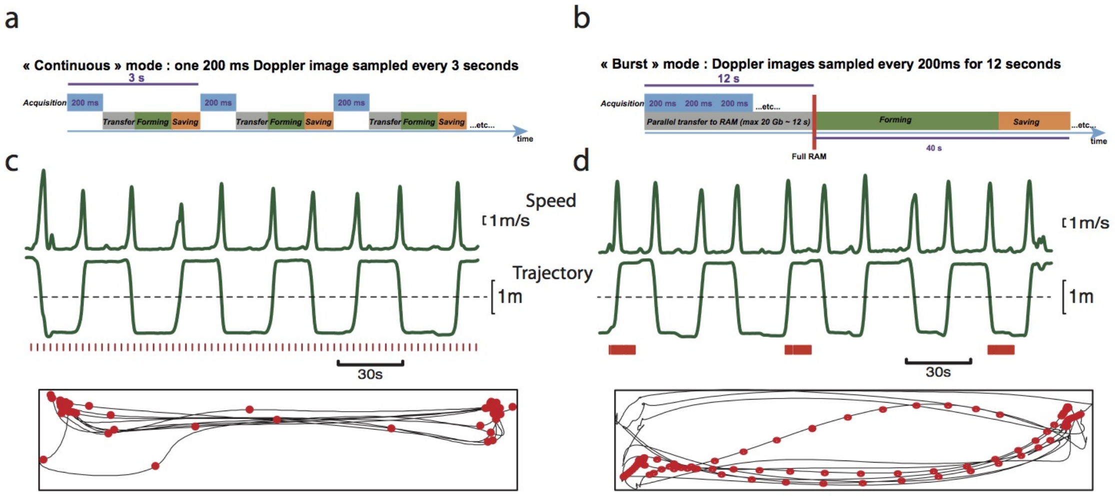

Figure 4.8 – **"Burst" and "Continuous" Imaging Modalities** The continuous and burst modes make distinct usage of the ultrasound scanner acquisition and processing power. **(a)** The "continuous" mode has the advantage to permit acquisition of virtually unlimited duration. For this mode, the Ultrafast acquisition is set to form a single fUS image (200 ms). The transfer and processing time (here 2.8 seconds) limits the final rate of CBV maps. **(b)** The "burst" mode has the advantage to sustain the Ultrafast frame rate up to the filling of the RAM memories (here 12 seconds), allowing to capture fast behavioral events such as maze crossing. Data is transferred in parallel with acquisition, and when buffer memory is full, data is processed (40 s) to form a series of fUltrasound images. We display two 3-mn long episodes recorded using continuous mode **(c)** and burst mode **(d)**. In "burst mode", we are able to capture the dynamics throughout a full maze crossing at the cost of extended processing time. Animal speed and trajectory (green). Red dots and red ticks correspond to one 200-ms fUS frame.

Burst Mode

The second strategy is based on continuous acquisition of raw images until full-RAM saturation. This "burst mode" uses an acquisition sequence of 6000 frames at a rate of 500 Hz for a total acquisition time of 12 s, which is followed by a 32 s-period to process and save the data. This generates high temporal resolution 12 s-long movie of fUltrasound images and allows capturing quick behavioral events such as a full crossing in our maze. Manual triggering is usually required to start the acquisition sequence, which started when the animal turned around in position for the next run. More recently, we have developed a "circular-burst" mode during which the probe fires continuously. When the experimenter triggers the acquisition, the frames recorded just before the trigger can be saved. Namely, we programmed this mode so that manual triggering would retain the last 3 seconds of acquisition and perform normal acquisition for the next 9 seconds. This overcomes the problem of "anticipating" when the animal starts running and allows for retrograde saving of fUS frames from manual trigger. This mode can be generalised according to the experiment requirement.

Since the acquisition in "burst mode" required 40 s for image reconstruction from ultrasound echoes, we could not capture every run. Thus, the number of runs acquired ranged from one fourth to one half of all the runs, depending on animal performance. It is important to note that these limitations do not stem from physical principles, but rather from contingent hardware. Increasing computing power and optimised software (notably in data transfer) provide perspective for continuous monitoring at high speed, thus generating continuous movies of fUltrasound images with a frequency of acquisition of 5 to 10 images per second, for prolonged periods of time.

IQ matrices

Importantly, IQ matrices that contain phase-quadrature signals of compound images are saved. This allows for flexible offline processing to carefully select time-integration steps (to virtually decrease temporal resolution at the cost of sensitivity), Doppler spectrum parameters (to either select large vessel or small ones depending on blood speed) or to form continuous high-sampling movies by implementing timing windows to form Doppler time series (in which case, the temporal sampling of the hemodynamic response can reach 500 frames per second).

4.4 Analysis

4.4.1 Atlas Registration

To date, we did not find any vascular atlas of the rat brain. fUS might prompt the emergence of reference vascular datasets in the near future. Today, however, we are currently lacking automatic methods to perform atlas registration and labelling, which is a critical step to identifying regions of interest in our datasets. Moreover, this poses a problem in statistical comparison and experiment reproducibility. The first approach was to map Paxinos atlas onto coronal acquisition of vascular data by using salient landmarks such as cortex edge and hippocampal transverse vascularisation. This presented two major drawbacks : first, region labelling could not be performed automatically and second, this could only be done for perfect coronal or sagittal planes. However this was impossible for diagonal planes parallel to the hippocampus septo-temporal axis.

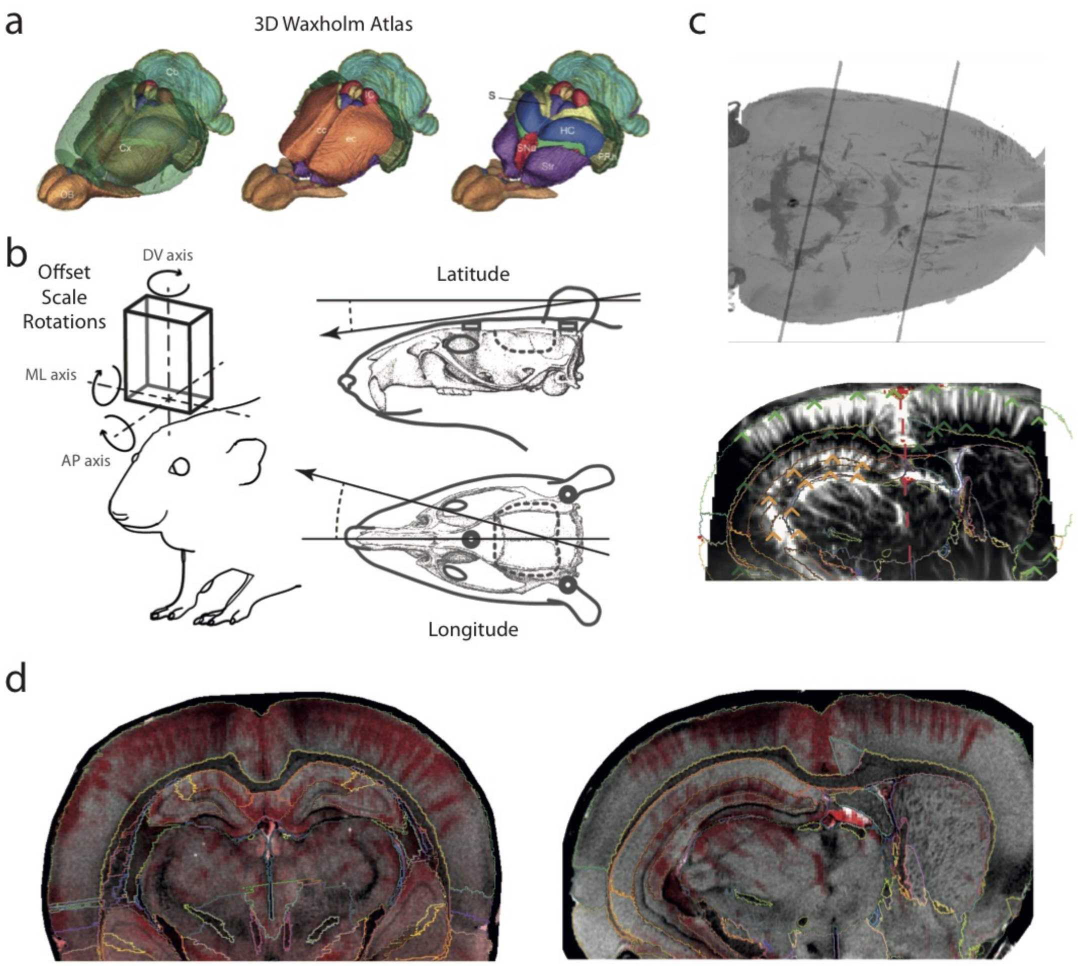

Figure 4.9 – Waxholm-based Atlas Registration of Vascular Images (a) Volumetric MR-based Waxholm atlas gives precise labelling of 79 brain regions, including hippocampal subregions. **(b)** Atlas registration of vascular events is performed by finding the physical parameters of probe and probe holder orientation to acquire vascular planes. In single-plane recordings, we listed 3 parameters for each axis (1 rotation, 1 offset value and 1 scaling value). In multi-plane recordings, we added 2 angles (latitude and longitude) corresponding to the probe holder axis and 2 values (offset and scale) corresponding to consecutive-plane spacing. **(c)** Top - Example of two diagonal planes superimposed on volumetric data. Bottom - We labeled vascular images with anatomically-salient landmarks including outer cortex edge (dark green), inner cortex edge (light green), dentate gyrus edge (orange) and brain mid-plane axis (red). These landmarks are used to minimise a global mean-square error between landmarks and corresponding region edge. **(d)** Our algorithm allows for registration of any vascular plane onto Waxholm atlas. We give two resulting registrations for a coronal plane (left) and a diagonal plane including whole hippocampus (right). **(a)** Adapted from [Papp et al., 2014].

We solved this by mapping our vascular images onto MR-based Waxholm volumetric datasets, which gives precise labelling of 79 brain regions. Importantly, this allowed for mapping of any vascular plane in this three-dimensional dataset. In Figure 4.9, we show that any plane can be obtained by a combination of three rotations, three translations and three compressions/dilations from a reference plane in the Waxholm space. Each plane is then uniquely defined by 9 parameters. Registration then consists in a classic optimization problem where the parameters are the coordinates of the plane in the three-dimensional Waxholm space. For single-plane recording, this corresponds to 9 parameters (3 rotation angles, 3 offset values and 3 scaling coefficients). For multi-plane recordings, one must also determine two additional angles that give the direction of displacement of the probe from one plane to the next (referred to as latitude and longitude). Finally, we listed and offset value and scale factor for the spacing between each plane. In total we listed 13 parameters for multi-plane recordings.

Finally, we introduced a global fitting error between the vascular plane (defined by the 9 or 13 coordinates in the Waxholm space) and the three-dimensional Waxholm space itself. To do so, we manually positioned landmarks on the vascular images. These landmarks, chosen for their salience, included outer cortex edge, inner cortex edge, dentate gyrus edge and brain mid-plane axis. The global fitting error is defined as the mean-squared distance between corresponding edges and landmarks. We used the Simplex algorithm to perform optimisation. This gave satisfactory results in reasonable processing time (around 15 minutes per recording) provided that the initial parameters are not too distant from the final values. We present the resulting registration for a coronal plane and a diagonal plane in Figure 4.9.

4.4.2 Image Processing

Mechanical stability

Stability within and across sessions is estimated from our recordings. Some frames are discarded when they show artifact echoes, which are caused by the animal bumping the probe against a hard surface such as cage or maze wall. Variation during a recording exhibits narrow standard deviation around average traces. This indicates good stability during a recording session. Reproducibility across recordings is quantified when measures across all animals are summarised. We have also computed a deformation map that tracks local displacement of individual pixels across a recording, by local estimation of successive images cross-correlation. The most common artefacts were observed both when the animal was grooming or eating, which is probably due to the movement of the jaws and the mechanical vibrations resulting from these behaviors. On average, we excluded 1% to 5% of the acquired frames per recording

Tissue deformation

Though mechanical stability of the probe onto the holder, and of the holder onto the animal's head was ensured by screw fixation, some regions of the images showed deformation from one frame to another. These deformation were mainly localised in the central parts of the cortex (located beneath the prosthesis center) and correlated strongly with the second derivative of accelerometer signal which indicated that it was linked to abrupt variations in head directions. We assume that this effect is due to inertia of the ultrasound gel onto to the mechanically flexible prosthesis. This effect was considerably lowered when we used 250-μm-thick prostheses instead of 125-μm-thick ones.

Regional Signal Extraction and Mean averaging

Vascular signals are extracted as pixel signals. Mean regional signals are computed after atlas overlay. The number of pixels contained in each region varied from 50 (CA2 region) to more than 2,000 (Thalamus). A typical image was 169 by 88, for a total number of 14,872 pixels. Before each running session, we recorded three activity bursts when the animal was quietly waiting for the task start in another box. This "pre-task" activity provide a reference signal but could hardly be used as a baseline for hemodynamic response because of the large separation between the two distributions. As a result, we computed temporally-averaged regional signal over the whole recording and to extract a $\frac{\Delta F}{F}$ signal for all regions. As a result, units for mean regional vascular events are expressed in percentage of change relative to the temporal average.

4.4.3 Signal Analysis

Speed Detection

Animal position is detected by applying a threshold on the image pixel intensity that distinguishes the bright animal on dark background. Cumulative distance and maximum crossing speed are computed using the trajectory smoothed with a time constant of 0.5 s. Ultrasound images are normalized according to the average value over all the non-running time, thus giving the relative change in vascular echo in percent of baseline.

LFP Analysis

EEG is filtered pass-band 6-10 Hz for hippocampal theta and respectively 30-50 Hz, 50-100 Hz and 100-150 Hz for the three gamma sub-bands. LFP power is computed as the square of the EEG signal integrated over a sliding window of characteristic width 0.5 s. We computed Pearson's correlation coefficient between EEG defined theta episodes and pixel intensity. This is how we determine the vascular correlate of theta episodes, which sometimes appears asymmetric, contrary to the EEG. Computation of Pearson's correlation coefficient between EEG and fUS pixel intensity is based on theta power curve for the maze experiment. Interestingly, the smoothing constant of gamma (but not theta, probably owing to the transient nature of gamma bursts) LFP amplitude signals has a strong impact on correlation strength. Highest correlations were obtained for a smoothing constant of 500 ms. Time-frequency Spectrograms are commonly performed by Wavelet Analysis with 1 Hz center frequency and 2 Hz frequency range. Theta phase is extracted by detecting zero-crossing in the theta-filtered signal.

Surge Detection

Vascular surges of activity were detected in two ways. The first method relies on thresholding the whole brain vascular response. Typically, when this response exceeded 1.5 standard-deviation for a sustained period of 5 seconds or more, we considered it as a surge in vascular activation. End of surge was detected when whole-brain vascular response fell back below the same threshold. The global intensity of the surge was defined as the temporal integration of whole-brain vascular response above threshold. The second method for vascular detection is based on counting the number of pixels which activity exceeds 2 standard-deviations of their own distribution for 5 seconds or more. When the number of pixels exceeded 20% of all pixels in an image, a surge was detected. The end of surge was set as the time when the proportion of activated pixels fell below threshold. The intensity of the surge was defined by the temporal integration of the proportion of active pixels over the surge episode, which led to a measure between 0 and 1.

4.4.4 Statistics

The data analyzed here were recorded in 42 sessions performed on 8 animals (22 coronal plane recording and 20 diagonal plane) and 60 REM episodes recorded on 6 animals. We chose sample sizes that gave consistent estimates of distance travelled over time, maximum speed. The number of animals (8) and maze crossings (above 100) are sufficiently large to test these distributions with small s.d./mean. The effect of the recording procedure is very significant; although our point is that it is of small amplitude. For control experiments, all our available data was pooled, as our analysis software routinely generates the numbers. We stopped counting when we realized that the measures converged quickly, so that including more recordings did not change the results. This is a general pre-established criterion. Experiments did not require randomisation. All statistics are given as mean +/- standard deviation.

Correlation significance

Statistical test is performed on Pearson's R coefficient using Student's t-distribution. Statistical significance on images used Bonferroni correction to account for the multiple testing over the large number of pixels. However, due to the high temporal sampling of vascular events during run acquisition, it is possible that oversampling artificially enhanced the strength of the observed correlation by increasing the number of recording points without increasing the variability of the dataset. This oversampling of hemodynamic responses can be avoided by computing autocorrelation lengths and subsampling datasets so that temporal measures fall out of the autocorrelation time. A second solution is to simply compare Pearson correlation values with the distribution of shuffled data. This is easily achieved for Spearman correlation because the distribution of shuffled Spearman correlations follows a normal distribution. However, this is somewhat trickier for Pearson correlations and can be achieved by direct shuffling or by inter-trial shuffling to preserve the temporal structure of aligned trials to run onset. For details see [Narayanan and Laubach, 2009].

Activation significance

To assess the question of significance of activation of either vascular or electrographic events, we looked at statistical distributions. When these distributions could be assimilated as normal distributions, we simply used a 2 standard-deviation threshold criterion to detect significant deviations from the mean signal. The major problem of this approach is that it depends on the relative statistics of each recording, meaning that rare low-amplitude events will be detected more easily than recurrent high-amplitude events. We are aware of this problem and are currently working to find unbiased methods to assess activation significance

Chapter 5

Article 1: EEG and functional Ultrasound imaging in mobile rats.

Sieu, L.-A., **A. Bergel**, E. Tiran, T. Deffieux, M. Pernot, J.-L. Gennisson, M. Tanter, and I. Cohen 2015. EEG and functional ultrasound imaging in mobile rats. *Nature Methods*, 12(9):831-834.

Summary

The development of functional Ultrasound (fUS) has triggered the introduction of a new modality to monitor cerebral hemodynamics and functional connectivity in anesthetized trepanned rats. Vascular patterns can be sampled with good spatiotemporal resolution (200 ms - 100 μm x 100 μm) and excellent sensitivity. Despite its potential, fUS is hindered by two obstacles (1) the immobilization of the animal entailing the use of anesthetics (2) the limited field of view restricted to a single plane. Ideally, *in vivo* studies on cerebral activations should be performed in natural conditions when the subject is awake and freely moving. The study of dynamic networks during normal and pathological states requires overcoming the constraints intrinsically associated with immobilization and the biases induced by anesthesia. Additionally, the access to the majority of brain structures is a prime necessity to understand complex dynamics.

In this article, we introduce in details the development of fUS on mobile animals coupled to electro-encephalography (mobilefUS, mfUS-EEG). This relies on several technological advances, including (1) a surgical procedure that we have developed at the laboratory including a large craniotomy, the implantation of intracranial electrodes and a permanent prosthetic skull transparent to ultrasound waves, giving access to a large portion of the brain (2) a lightweight miniature probe enabling unimpaired movement in tethered animals (3) a motorized probe-holder offering solid probe fixation onto the skull and sequential multi-plane imaging over the antero posterior axis (4) a software for the synchronization, display and analysis of electrographic events, vascular images and video files.

The proof of concept for mfUS-EEG is given in two separate applications (1) the monitoring of hemodynamic changes during spontaneous absence seizures in GAERS rats and (2) the study of hemodynamic responses associated with theta rhythm in unrestrained running rats.

The spatial navigation experiment (that I conducted) revealed bilateral hyper-perfusion in somatosensory cortex, dorsal hippocampus and dorsal thalamus, together with hypo-perfusion in ventral thalamus during running. The hippocampal pattern of activation was robust across sessions in the same animal and across animals, while cortical regions displayed stronger variability . The analysis of correlation delays between theta power envelope and vascular responses revealed an onset in the dorsal thalamus and a sustained activation in the hippocampus respectively 0.8 seconds and 2 seconds after maximal theta activity. The study on epileptic animals, revealed region-dependent correlation patterns including hyper-perfusion in somatosensory cortex and thalamus, concurrent with hypo-perfusion in the striatum. Cortical and thalamic regions displayed synchronous vascular oscillations during epileptic seizures.

EEG and functional ultrasound imaging in mobile rats

Lim-Anna Sieu[1,2], Antoine Bergel[1,3], Elodie Tiran[4], Thomas Deffieux[4], Mathieu Pernot[4], Jean-Luc Gennisson[4], Mickaël Tanter[4] & Ivan Cohen[1]

We developed an integrated experimental framework that extends the brain exploration capabilities of functional ultrasound imaging to awake and mobile rats. In addition to acquiring hemodynamic data, this method further allows parallel access to electroencephalography (EEG) recordings of neuronal activity. We illustrate this approach with two proofs of concept: a behavioral study on theta rhythm activation in a maze running task and a disease-related study on spontaneous epileptic seizures.

In vivo brain activity recordings can help unravel the mechanisms underlying complex behaviors and pathologies. Ideally, both neuronal activity and metabolic events are captured in the most natural conditions, when the subject is awake and freely moving. An increasing awareness exists that major issues of neurophysiology need to be addressed with such global approaches. For example, the basic mechanisms involved in functional network dynamics and pathologies including epilepsy can be deciphered only if the electrographic and metabolic components are sensed concomitantly[1,2]. However, the multiple feedback loops between electrographic and metabolic signals have mainly been tackled separately because of a lack of appropriate methods for accessing them together, thereby prompting the development of multimodal strategies.

In practice there is a compromise between the size of imaging field, time resolution, sensitivity, separability of processing and metabolism, and physical constraint on the animal. Electrophysiology and, as was more recently shown, optical techniques[3,4] can record neuronal activity in the mobile animal, yet sampling is limited by electrode size and light diffraction. In contrast, functional magnetic resonance imaging (fMRI) records brain-wide metabolism, with trade-offs in sensitivity and resolution and at the cost of subject immobilization or animal sedation[1]. Functional ultrasound imaging based on ultrafast Doppler processing (fUS) offers a way to monitor brain hemodynamics[5,6] and functional connectivity[7] in rodents with high spatiotemporal resolution and unique sensitivity. However, the limited transparency of the skull to ultrasound waves necessitates the removal of the bone and application of the ultrasound probe directly above the tissue, bathed in ultrasound-conductive saline, in an immobile, anesthetized animal.

To unfold the potential of fUS, we extend the technique to awake and mobile rats (mobile fUS, mfUS). Furthermore, we combine recording of cerebral hemodynamics at high spatiotemporal resolution and sensitivity with simultaneous monitoring of neuronal activity through EEG. Our integrated experimental setup relies on a set of technological advances: an ultrasound-permeable skull prosthesis; a lightweight ultrasound probe; a motorized head-mounted probe holder; an electrode implantation procedure; and a software environment for synchronized acquisition, playback and analysis of these multimodal signals.

We present the details of this experimental framework below (**Fig. 1**) and then demonstrate two applications (**Fig. 2**). We first searched for the functional correlate of theta rhythm, involved in brain area communication during spatial navigation tasks[8]. Second, we explored the neuronal and metabolic manifestations of spontaneous generalized, nonconvulsive, absence epilepsy seizures, as their initiation and generalization across brain areas remain debated questions[9–11].

To prepare rats for mfUS, we developed a new surgical procedure (**Supplementary Figs. 1** and **2**) that allows for chronic recording sessions (**Fig. 1a**). Craniotomy of the parietal and frontal skull bones (15 mm anteroposterior (AP) × 14 mm mediolateral (ML)) exposed the dura mater. For EEG purposes, we implanted intracranial stereotaxic electrodes, either hippocampal (**Supplementary Fig. 3**) or cortical, and anchored them at the edges of the window, with their connector fixed to the back of the head. Finally, a polymer prosthesis was sealed in place of the removed skull. Polymethylpentene film of 125-µm thickness offered the best image quality compared to polyvinyl chloride, polyoxymethylene, Udel polysulfone and polycarbonate, for available thickness in the range of 75–250 µm, and provided good mechanical resistance and low permeability. Thus, we could access the cortex and deep structures with a larger and deeper field of view and improved sensitivity over those provided by earlier cranial thinning procedures[7]. Three nuts used as attachment points for the probe holder were sealed above the nasal bone and lateral to the interparietal bone, and the animal was allowed to recover. For ultrasound recordings, we used a miniature ultrasound probe (18-mm radius, 25-mm height) mounted on a lightweight head-anchored adjustable holder (18 g; **Supplementary Figs. 4** and **5**).

---

[1]Institut de Biologie Paris-Seine, INSERM U1130, CNRS UMR 8246, University Pierre et Marie Curie UMCR18, Paris, France. [2]Institut des Neurosciences Translationnelles de Paris, Paris, France. [3]Ecole Doctorale Frontières du Vivant (FdV), Programme Bettencourt, Université Paris Diderot, Sorbonne Paris Cité, Paris, France. [4]Institut Langevin, Ecole Supérieure de Physique et de Chimie Industrielles de la ville de Paris ParisTech, Paris Sciences et Lettres Research University, CNRS UMR 7587, INSERM U979, Paris, France. Correspondence should be addressed to I.C. (ivan.cohen@upmc.fr).

RECEIVED 1 APRIL; ACCEPTED 26 JUNE; PUBLISHED ONLINE 3 AUGUST 2015; DOI:10.1038/NMETH.3506

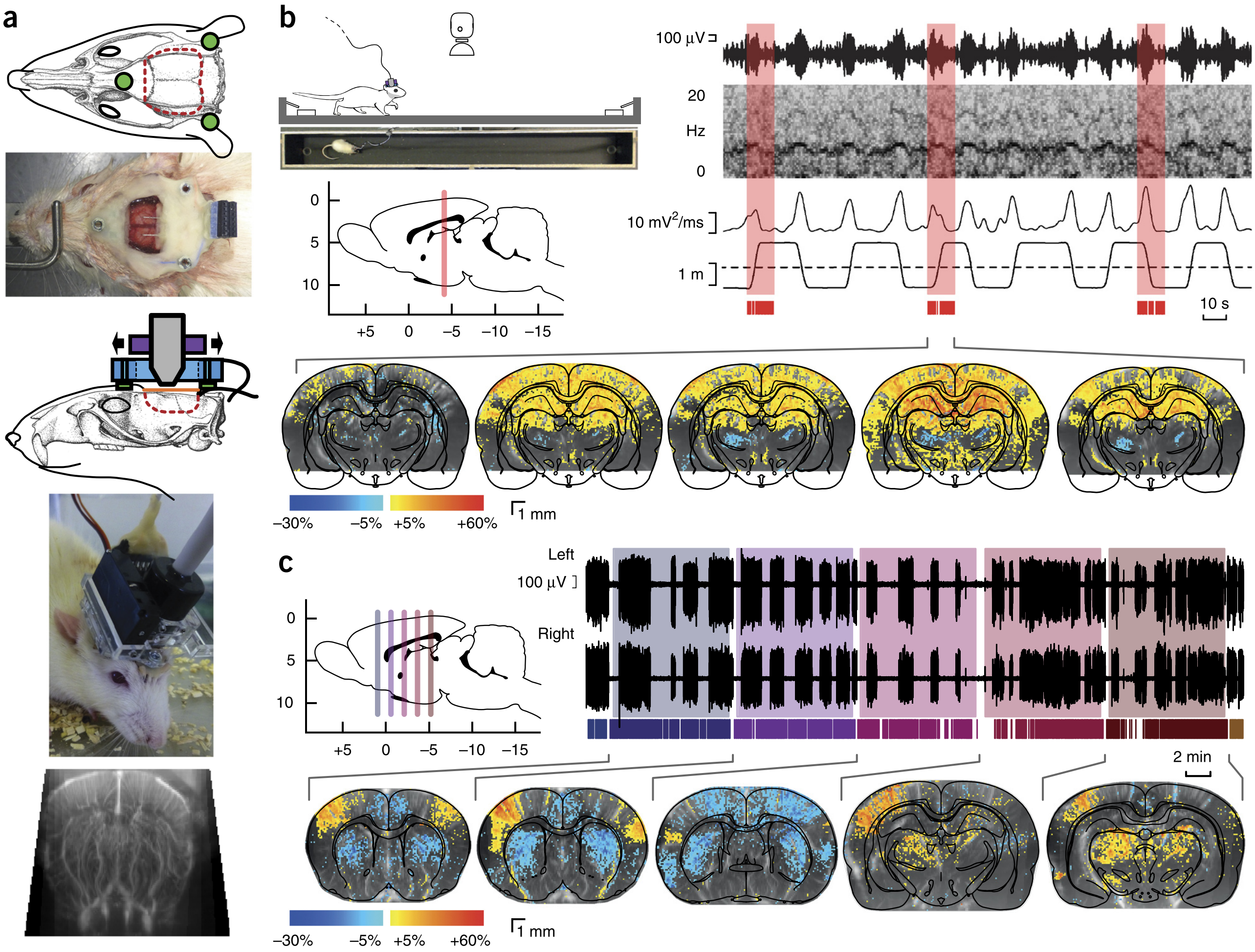

Figure 1 | Awake mobile EEG-fUS procedure and acquisition protocols. (**a**) Surgical procedure and probe setup. Schematic representation of window boundary (red dotted line), prosthetic skull (orange), attachment nuts (green), probe holder (blue), motor (purple) and probe (gray); surgery outcome with added hippocampal stereotaxic electrode and EEG connector; animal equipped with motorized translation stage; and raw mfUS view through the prosthesis. (**b**) Burst-mode acquisition for maze experiments. Left, schematic of the maze, water reward sites and overhead camera. An atlas side view, with the coronal imaging plane (red) is shown below. Right, EEG-behavior recording chart, with, from top to bottom, hippocampal local field potential, short-term Fourier transform spectrum and power in the theta band. The lower trace shows position along the maze; bottom red bars indicate timing of fUS images. Mid-maze crossing is indicated by the dotted line. The red shading represents the 12-s frames of fUS acquisition. Bottom, coronal ultrasound images acquired at high speed are averaged ($n = 25$ runs) for an example of five consecutive times around the reference. Color-coded overlay on vascular background shows pixel intensity change relative to baseline rest. Ventral areas were not acquired to increase burst duration. (**c**) Continuous-mode acquisition for seizure recording. Spontaneous generalized absence seizures are recorded from bilateral EEG. The fUS image trigger mark is shown below the EEG signal. Coronal planes (bottom) were acquired successively for 10 min each. Each color corresponds to a coronal plane. Color-coded overlay on vascular background shows pixel intensity change relative to baseline outside seizure. In **b**,**c** the changes in pixel intensity relative to baseline are shown where $P < 10^{-2}$ (Student's *t*-test with Bonferroni correction). Brain outlines are from the Paxinos-Watson atlas[19], Academic Press.

The device was fixed to the head while the animal was under short isoflurane anesthesia, with contact gel applied between the probe and prosthetic skull. The holder was motorized (**Supplementary Fig. 6**) to explore consecutive planes, without direct interaction between the experimenter and the animal, and could be locked for maximum stability.

We first recorded from rats walking along a linear maze to address how brain-wide networks activate during periods of hippocampal theta rhythm, which is a major mechanism proposed for intracerebral cross-area processing in episodic memory and spatial navigation tasks[8]. Healthy Sprague Dawley rats ($n = 8$) ran on a 2.25-m-long, 0.2-m-wide linear track to obtain a water reward. A single ultrasound imaging plane included the dorsal hippocampus, cortex with somatosensory areas, and thalamus. In order to temporally resolve hemodynamics as the animal crossed the maze, we used a 'burst-mode' ultrasound sequence (**Fig. 1b** and **Supplementary Fig. 7**), acquiring fUS compound frames at 500 Hz for 12 s. Acquisition was triggered when the animal turned around, and it was followed by a 40-s lapse to collect the data. For EEG recordings, we used hippocampal electrodes during this set of experiments. As expected, hippocampal theta was consistently associated with locomotion. Distance traveled over time was shorter (56–64%) than in control untethered, surgery-free rats ($P < 10^{-6}$; **Supplementary Fig. 8a**,**b** and **Supplementary Tables 1** and **2**). Yet, maximum speed was only slightly slower for the initial 15 min, with a nonsignificant ($P = 0.6$) difference of 1% thereafter.

In this experiment, single-pixel variations in the fUS images, relative to average baseline when the animal was at rest, ranged

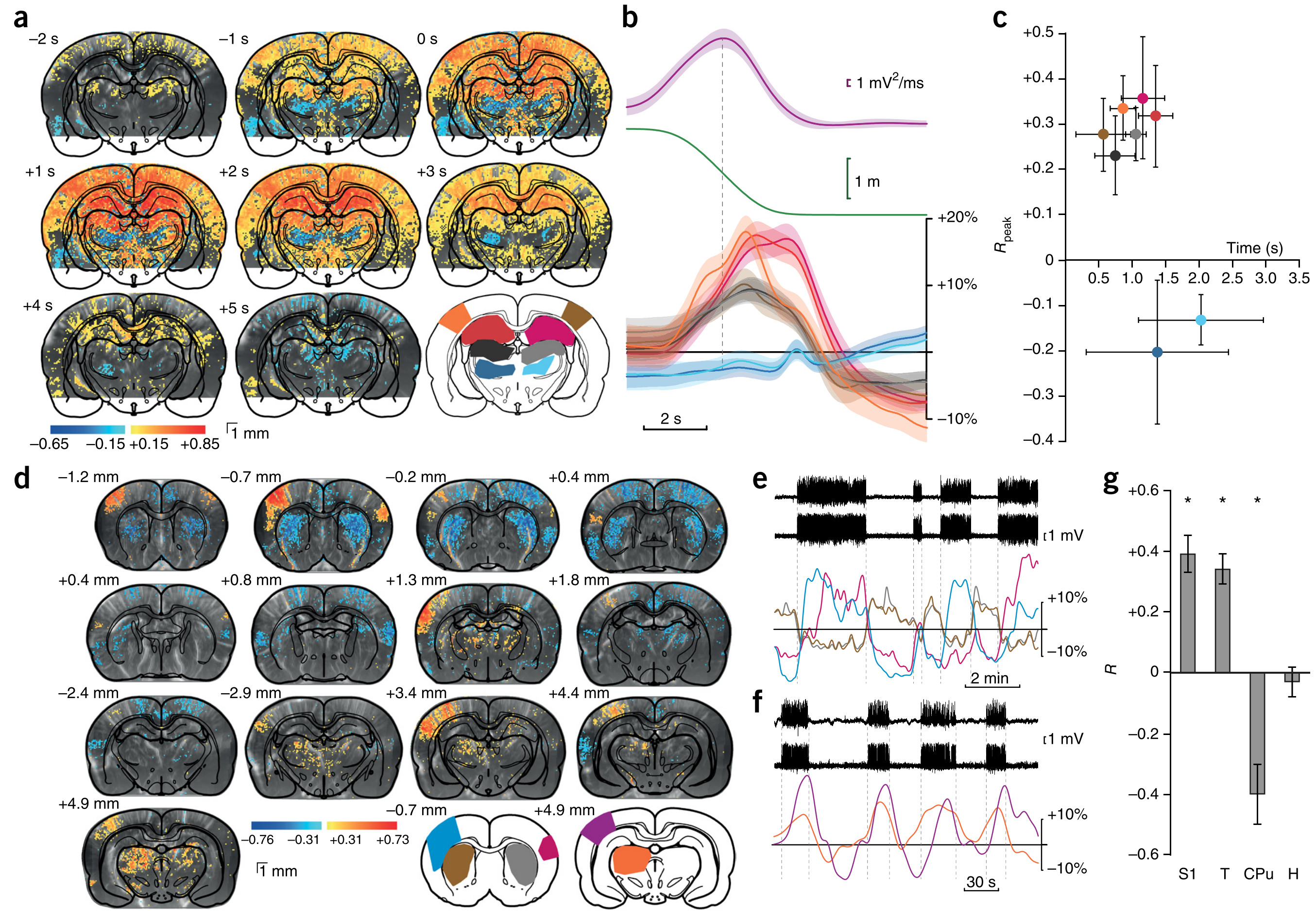

Figure 2 | Comparison of EEG and hemodynamic signatures of natural events. (**a**–**c**) Maze experiment cross-correlation between local field potential theta-band power and ultrasound signal for each pixel at varying time lag (−2 to +5 s) over $n = 20$ midline crossings acquired in 1 h. (**b**) Region variation of hemodynamic signal, relative to rest, is obtained by spatial averaging of pixels indicated on atlas layout (solid lines and envelopes, mean ± s.d.). Purple, theta power; green, trajectory; other colors correspond to colored regions in **a**. The vertical dotted line shows the reference midline-crossing time. (**c**) Value and delay of peak Pearson's correlation coefficient ($n = 6$ animals, mean ± s.d.). (**d**–**g**) Epilepsy experiment cross-correlogram between mfUS image and seizure, at zero time lag, for successive coronal planes. (**e**,**f**) mfUS signals in the areas color-marked on atlas layouts (**a**) were averaged and displayed together with the EEG recordings. (**g**) Perfusion averaged over significant areas ($n = 6$ animals, mean ± s.d., Student's *t*-test, * $P < 0.001$). In **a**,**d** the cross-correlation Pearson's *R* coefficient is color coded according to the scales below. Significant pixels are shown for $P < 10^{-2}$ (Student's *t*-test with Bonferroni correction). S1, somatosensory cortex; T, thalamus; CPu, caudate putamen; H, hippocampus.

from −30% to +60% (**Fig. 1b**), whereas brain area averages reached −10% to +20% (**Fig. 2b**). As expected, theta-band intrahippocampal EEG power peaked at top animal speed, which was coincident with crossing the middle of the maze, with a mid-height theta peak width of 3.2 ± 0.3 s (±s.d., $n = 8$). In order to quantify functional activation during the task, we computed the maps of Pearson's correlation coefficient between power in the theta band and pixel intensity, for varying time lags (**Fig. 2a**). Averaging pixels across anatomical areas revealed hyperperfusion in the somatosensory cortex, dorsal thalamus and hippocampus, and hypoperfusion in the ventral thalamus. These correlations were consistent with fUS signal time course (**Fig. 2b**). Hyperemia peaked at 0.7–1.5 s following the peak of hippocampal theta, which is consistent with signaling cascades that adapt blood flow to cognitive demand during the task[12]. The occasional asymmetry that we observed between the left and right cortical hemispheres may correlate with functional dominance[13]. Overall (**Fig. 2c**), our data reveal a pattern of combined hippocampal and widespread cortical activation in a short time window together with coordinated thalamic suppression during the navigation task. This pattern is consistent with observations in alert and still animals, in the context of a conditioning protocol[14]. In these instances, thalamic activity is suppressed during hippocampal-cortical interaction involved in episodic memory operations. In the present locomotion task, the dorsal thalamus was activated while the ventral thalamus was suppressed simultaneously.

In a second experiment, we scanned through the brain of an epileptic rat to address the heterogeneous alterations in neurometabolic coupling during hypersynchronous seizure activity[2]. We recorded spontaneous generalized absence seizures from bilateral cortical bipolar electrodes in genetic absence epilepsy rats from Strasbourg (GAERS, $n = 12$). We quantified both the relative time spent seizing and seizure duration, and we found no significant ($P = 0.3$ and $P = 0.98$, respectively) difference between EEG only and EEG-mfUS conditions (**Supplementary Fig. 8c**,**d** and **Supplementary Table 3**). For this experiment, we used 'continuous-mode' ultrasound acquisition (**Fig. 1c** and **Supplementary Fig. 7**), alternating between 200 ms to acquire one compound mfUS image and 2.8 s of processing. Multiple imaging planes were scanned for 10–15 min each.

In this experiment, we also found individual pixel changes ranging from −30% to +60%, relative to seizure-free baseline (**Fig. 1c**), whereas averaging over seizure-associated areas revealed changes from −10% to +20% (**Fig. 2e**,**f**). We found distinct patterns of correlation across structures along the AP axis. Hyperperfusion in the somatosensory cortex and thalamus was concomitant with hypoperfusion in the caudate putamen and no variation in the hippocampus. Although absence seizures are generalized throughout neocortex, vascular alterations showed spatial compartments, and lateralization in the frontal primary sensory cortex perfusion was observed in half of the animals (6/12 rats). Furthermore, the sensitivity of mfUS enabled the observation that consecutive seizures with a similar bilateral cortical EEG profile could display a distinct bilateral or unilateral perfusion course (**Fig. 2e**). Comparing the dynamics of cortical and thalamic areas coupled to seizure (**Fig. 2f**) revealed synchronous oscillations in the perfusion pattern. Thus, the responses we observed across anatomical structures (**Fig. 2g**) are compatible with EEG-fMRI experiments that found inversed electrographic-hemodynamic coupling between the cortex and caudate putamen[15] and with time-resolved EEG–near-infrared spectroscopy experiments indicating blood flow fluctuations around seizures initiation[16]. Having superior temporal and spatial resolution among these techniques, mfUS further points to cortical decoupling between electrographic activity and perfusion, with both static and transient components, in naturally occurring seizures.

We have developed a methodology that captures the hemodynamic state of the brain over its whole depth along with its electrographic activity in awake, mobile rats over repeated and prolonged periods of time. Despite the small size and weight of the probe, holder and cable, the system limits the distance and environment that the animal can explore, similarly to multichannel microdrive tetrode systems. Another limitation is a potential contribution of a locomotion effect to brain perfusion, for instance due to higher heart rate during running. Absence seizures correspond to animal freezing and still showed strong variations in hemodynamics. Furthermore, such a locomotion effect is expected to be uniform across brain areas, but we found both increases and decreases in perfusion, even in the running task. Thus, we exclude a locomotion effect in the tasks presented here, although it may become apparent during intensive locomotion activity.

We demonstrated how this methodology applies to both cognitive and pathological questions. Thus, substantial progress was achieved in observing the interplay between metabolism and neuronal electrical activity that governs global brain equilibrium. Whereas current plane-by-plane imaging could be adapted to address questions such as hippocampal–prefrontal cortex interaction[17,18] by rotating the probe from the current coronal orientation, synchronous volumic acquisition will become possible with future matrix-type probes. As it develops, mfUS imaging will become applicable to a wide range of protocols including complex behavioral tasks in healthy animals and neurovascular pathologies.

METHODS

Methods and any associated references are available in the online version of the paper.

Note: Any Supplementary Information and Source Data files are available in the online version of the paper.

ACKNOWLEDGMENTS

We gratefully acknowledge E. Yeramian and A. Bonnot for critical discussions and help with the manuscript. The research leading to these results has received funding from the European Research Council (ERC) under the European Union's Seventh Framework Programme (FP7/2007-2013)/ERC grant agreement no. 339244-FUSIMAGINE. This work was also partly supported by the Agence Nationale de la Recherche under the program "Future Investments" with the reference Laboratory of Excellence ANR-10-LABX-24 LABEX WIFI within the French Program "Investments for the Future" under reference ANR-10-IDEX-0001-02 PSL, the program "Investissements d'avenir" ANR-10-IAIHU-06 and a PhD fellowship from the University Paris Diderot FdV Bettencourt PhD program.

AUTHOR CONTRIBUTIONS

L.-A.S. designed the surgical procedure and prosthetic skull and performed and analyzed epilepsy experiments; A.B. designed the intrahippocampal recording procedure and performed and analyzed navigation experiments; E.T. and T.D. developed the burst-mode ultrasound recording sequence; M.P. and J.-L.G. developed the continuous-mode ultrasound recording sequence; J.-L.G. and M.T. designed and supervised the ultrasound scanner and probe; I.C. designed and supervised the experiments, designed the probe holder, and programmed acquisition and analysis software; I.C., L.-A.S. and A.B. wrote the paper.

COMPETING FINANCIAL INTERESTS

The authors declare no competing financial interests.

1. Logothetis, N.K. *Nature* **453**, 869–878 (2008).
2. Sada, N., Lee, S., Katsu, T., Otsuki, T. & Inoue, T. *Science* **347**, 1362–1367 (2015).
3. Kerr, J.N. & Nimmerjahn, A. *Curr. Opin. Neurobiol.* **22**, 45–53 (2012).
4. Packer, A.M., Russell, L.E., Dalgleish, H.W. & Häusser, M. *Nat. Methods* **12**, 140–146 (2015).
5. Macé, E. *et al. Nat. Methods* **8**, 662–664 (2011).
6. Macé, E. *et al. IEEE Trans. Ultrason. Ferroelectr. Freq. Control* **60**, 492–506 (2013).
7. Osmanski, B.F., Pezet, S., Ricobaraza, A., Lenkei, Z. & Tanter, M. *Nat. Commun.* **5**, 5023 (2014).
8. Buzsáki, G. & Moser, E.I. *Nat. Neurosci.* **16**, 130–138 (2013).
9. David, O. *et al. PLoS Biol.* **6**, 2683–2697 (2008).
10. Zheng, T.W. *et al. Epilepsia* **53**, 1948–1958 (2012).
11. Jacobs, J. *et al. Neuroimage* **45**, 1220–1231 (2009).
12. Koehler, R.C., Roman, R.J. & Harder, D.R. *Trends Neurosci.* **32**, 160–169 (2009).
13. LaMendola, N.P. & Bever, T.G. *Science* **278**, 483–486 (1997).
14. Logothetis, N.K. *et al. Nature* **491**, 547–553 (2012).
15. Mishra, A.M. *et al. J. Neurosci.* **31**, 15053–15064 (2011).
16. Roche-Labarbe, N. *et al. Epilepsia* **51**, 1374–1384 (2010).
17. O'Neill, P.K., Gordon, J.A. & Sigurdsson, T. *J. Neurosci.* **33**, 14211–14224 (2013).
18. Brincat, S.L. & Miller, E.K. *Nat. Neurosci.* **18**, 576–581 (2015).
19. Paxinos, G. & Watson, C. *The Rat Brain in Stereotaxic Coordinates* 6th edn. (Academic Press, 2007).

ONLINE METHODS

Animal preparation. All animals received humane care in compliance with the European Communities Council Directive of 2010 (2010/63/EU), and the study was approved by the institutional and regional committees for animal care. Male Sprague Dawley rats 10–12 weeks old and male GAERS rats (genetic absence epilepsy rats from Strasbourg) 8–16 weeks old underwent surgical craniotomy and implant of ultrasound-clear prosthesis. Anesthesia was induced with 2% isoflurane and maintained by ketamine/xylazine (80/10 mg per kg body weight), while body temperature was maintained at 36.5 °C with a heating blanket (Bioseb). A sagittal skin incision was performed across the posterior part of the head to expose the skull. Parietal and frontal flaps were excised by drilling and gently moving the bone away from the dura mater. The opening exposed the brain between the olfactory bulb and the cerebellum, from bregma +6 to bregma −8 mm, with a maximal width of 14 mm. Electrodes were implanted stereotaxically and anchored on the edge of the flap. A plastic sheet of polymethylpentene (PMP) was sealed in place with acrylic resin (GC Unifast TRAD), and residual space was filled with saline. We chose a prosthesis approach that offers a larger field of view and prolonged imaging conditions over 1–2 months compared to the thinned-bone approach[7]. Particular care was taken not to tear the dura in order to prevent cerebral damage. The surgical procedure, including electrode implantation, typically took 4–6 h. Animals recovered quickly, and after a conservative 1-week resting period, they were used for data acquisition.

In order to attach the ultrasound probe and connect the EEG electrodes before a recording session, rats underwent short anesthesia for 20–25 min with 2% isoflurane. Acoustic gel was applied on the skull prosthesis, and then the probe was inserted into the holder. The gel did not dry out even for extended recordings of up to 6–8 h. Animals were allowed to recover for 30 min before the recording session started.

Electrodes. The electrodes we used are based on regular polytrodes made of bundles of insulated tungsten wires, either multisite (for hippocampal theta) or bipolar (for epilepsy). The difference from standard design is the right-angle elbow that is formed before insertion in the brain (**Supplementary Fig. 2**). This shape allows us to anchor the electrodes on the skull anterior or posterior to the flap. Electrodes were implanted with stereotaxic-positioning micromotion and anchored one after the other; then the plastic film was applied to seal the skull. Two epidural screws placed above the cerebellum were used as reference and ground.

The intrahippocampal handmade theta electrode bundles are composed of 25-µm insulated tungsten wire, soldered to miniature connectors (**Supplementary Fig. 3**). Four to six conductive ends were spaced by 1 mm and glued to form 3-mm-long, 50-µm-thick bundles. The bundles were lowered in dorsal hippocampi at stereotaxic coordinates AP = −4, ML = ±2.5, DV = −1.5 to −4.5, in mm relative to bregma. Hippocampal theta rhythm was confirmed by phase inversion across recording sites in successive hippocampal layers, time-frequency decomposition, and coincidence with periods of exploration and navigation.

Cortical electrodes for absence epilepsy recordings comprised four bipolar electrodes implanted in the primary somatosensory cortex: S1BF = AP −3, L ± 5, DV −1.75 and S1Lp = AP +1, L ±6, DV −2, in mm relative to bregma.

Skull prosthesis. The prosthetic skull was composed of PMP (Goodfellow), a standard biopolymer used for implants. This material has tissue-like acoustic impedance, which allows undistorted propagation of ultrasound waves at the acoustic gel–prosthesis and prosthesis-saline interfaces. The prosthesis was cut out of a film of 125-µm thickness and sealed to the skull with resin.

Animal behavior. Animals for the maze experiment were trained before surgery. They were placed under a controlled water-restriction protocol (weight between 85% and 90% of the normal weight) and trained to run back and forth in a long rectangular maze for water reinforcement. The maze (225 cm × 20 cm) had 5-cm-high lateral walls and was placed 50 cm above ground. Drops of water were delivered through two small tubes coming out from the two end walls of the maze (**Fig. 1b**). Each time the animal crossed the maze, a single drop of water was delivered in alternate water tubes by opening an electronically controlled pair of solenoid valves. Daily training lasted 30 min. Rats took about two sessions to reach a score of 60 maze travels and perform reliably, crossing the mid-maze at fast speed, but training was reinforced for at least two more days. Daily recording sessions lasted 20–30 min, depending on animal motivation. Because the acquisition in burst mode required 40 s for image reconstruction from ultrasound echoes, we could not capture every run. The number of runs acquired ranged from one-fourth to one-half of all the runs, depending on animal performance and the timing of its spontaneous runs within the session. The data analyzed here were recorded in 12 sessions performed across 8 d. Epileptic animals were recorded in a regular housing cage with the cover removed.

Miniature ultrasound probe. The Ultrasonic probe (Vermon) is a linear array made of 128 transducers working at a 15-MHz central frequency (spatial pitch, 0.11 mm; transducer element, 2.000 × 0.110 mm^2; bandwidth, 46% at −6 dB, corresponding to 11–18 MHz). Image resolution is 0.110 × 0.110 mm^2. This probe has an acoustic lens with an elevation focal distance of 8 mm and an elevation focal width of 400 µm, corresponding to the thickness of the imaging plane. The active part is embedded in 18.5-mm-diameter and 25-mm-length molded resin. A 150-cm cable length and 12-g probe weight ensure a good freedom and comfort to move for the animal. Compared to in previous work[5,7], the probe was miniaturized (**Supplementary Fig. 1**). Dimensions (in cm) were reduced from 15 (height), 6 (width), 2.5 (thickness) to 2.5 × 1.85 × 1.85. The weight (in g) was reduced from 250 to 12. The cable was made more flexible by reducing its diameter from 11.5 mm to 6.9 mm. All these improvements did not affect sensitivity of the transducer array and were required to perform such experiments on moving animals.

Penetration of the ultrasound waves across 15 mm of rat brain allowed us to image the rat brain at all depths (as shown in **Fig. 1a**, bottom image). More generally, depth of penetration decreases with higher frequencies (smaller wavelength), while resolution simultaneously increases. Thus, there is a trade-off between resolution and depth of penetration, and 15 MHz is optimal for rat brain.

Although we designed the probe, it was manufactured by specialist company Vermon. Interested labs are welcome to contact us to share our customized probe design considerations.

doi:10.1038/nmeth.3506

Probe holder. The holder was made of two parts machined in Plexiglas for light weight and stiffness. First, a base plate with U-shaped side grooves, allowing translation of the mobile part, was attached to the head of the animal with three screws. Second, the mobile part presenting two sliding side edges was fitted into the base part. The probe was attached through a central opening in the mobile part. A linear servo motor (VS-19, Robotshop) was fixed to the mobile part and anchored on the base plate. It was controlled by custom-made electronics connected to the ultrasound scanner through USB port. Holder weight was 18 g, and overall size was 41-mm width, 34-mm length, 16-mm height. Digital information to reproduce the parts is provided as **Supplementary Data**.

The motor of the probe holder was controlled in steps of 125 μm. Motor accuracy was better than one step. The time to travel the range of 15 mm was about 2 s. There is no need for faster motion of the motor. Rather, when hemodynamics of distinct anatomical structures have to be compared, a better strategy is to rotate the probe to image a plane encompassing those structures. The current experimental limit for imaging lies not in drifts or instability of the electromechanical system but rather in the eventual leak in the prosthetic skull, generating gas bubbles that degrade imaging. This happens several weeks and up to 2 months after surgery.

Ultrasound imaging. Vascular images were obtained via the ultrafast compound Doppler imaging technique[5,20]. The probe was driven by a fully programmable GPU-based ultrafast ultrasound scanner (Aixplorer, Supersonic Imagine) relying on 24-GB RAM memory. In burst mode we used an acquisition sequence of 6,000 frames at a rate of 500 Hz for a total acquisition time of 12 s. A manual trigger was given when the animal finished drinking water and turned around in position for the next run. In the continuous mode, we acquired 200 ultrasound images at 1-kHz frame rate for 200 ms, repeating every 3 s. In both burst mode and continuous modes, each frame is a compound plane-wave frame, that is, a coherent summation of beamformed complex in phase/quadrature images obtained from the insonification of the medium with a set of successive plane waves with specific tilting angles[21]. This compound plane-wave imaging technique enabled us to recreate a posteriori a good quality of focalization in the whole field of view with very few ultrasound emissions. Given the trade-off between frame rate, resolution and imaging speed, a plane-wave compounding using five 5°-apart angles of insonification (from −10° to +10°) was chosen. As a result, the pulse repetition frequency (PRF) of plane wave transmissions was equal to 8 kHz. In order to discriminate blood signals from tissue clutter, we high-pass-filtered the ultrafast compound Doppler frame stack using a fourth-order Butterworth filter (cutoff frequency, 50 Hz) along the temporal dimension, giving a high frequency in phase/quadrature frame stack whose energy in each pixel we then computed to build the ultrafast power Doppler fUS image. Some frames were discarded before being incorporated in a recording when they showed artifact echoes, which are caused by the animal bumping the probe against a hard surface such as cage or maze wall.

The signal measured by fUS and its sensitivity are presented in earlier theoretical and experimental work[6]. Briefly, fUS measures moving echogenic particles, that is, red blood cells, and thus corresponds to cerebral blood volume (CBV). Importantly, this proportionality is valid only if backscattering properties do not vary versus time. This assumption is valid while red blood cells backscattering properties such as hematocrit and shear rate remain time invariant, which is most likely.

Ultrasound sequences. Technical specifications of the scanner used here include 16×, 6 GB/s PCI express bus, 12 core 3-GHz Xeon processor, NVidia Quadro K5000 GPU with a bus at 173 GB/s, providing 2.1 teraflops. One current limitation of fUS is due to the transfer and processing time of the large amount of data required to form ('beamform') fUS images. Yet, this limitation does not stem from physical principles but rather from contingent hardware. Although increasing computing power and optimized software provide perspective for continuous monitoring at high speed (200 ms per image), the current technology allows continuous recording with a temporal resolution close to the time constant of neurovascular coupling (1–2 s) and further allows 'burst' capture for quick behavioral events such as running a maze (**Supplementary Fig. 7**). The limitation for the continuous mode is the processing speed to transform a series of plane-wave acquisitions into compound images and then generate a fUS image. The limitation for the burst mode is the memory available to buffer plane wave images to later generate a movie of fUS images. Detailed codes and software for fUS acquisition are described in ref. 5. Additional Matlab code for the Doppler processing is included in **Supplementary Software 1**.

Ultrasound stability and reproducibility. Stability during a recording session and across sessions is estimated from our recordings. Variation during a recording is exemplified in **Figure 2b**, with narrow s.d. around average traces. This indicates good stability during a recording session. Reproducibility across recordings is quantified in **Figure 2c,g**, which summarize measures across all animals. It shows a good reproducibility.

We cannot completely exclude a contribution of a locomotion effect—for instance, due to higher heart rate during running. However, the maze task is not limited to running, as it involves navigation processing. Animals showed a learning curve when they were trained for the task. Furthermore, a locomotion effect would likely be uniform across the brain, whereas we found both increases and decreases in blood perfusion. Thus, such a potential effect is not strong enough to mask differential changes and dynamics across areas. Our animals did not engage in intensive motor activity, at least not above the requisite for most cognitive and pathology experiments. GAERS rats' seizures correspond to freezing behavior, and yet again they exhibited increases and decreases of similar amplitude compared to moving animals. This further supports that the technique can sense changes in perfusion unrelated to a locomotion effect.

EEG acquisition. Intracranial electrode signals were fed through a high input impedance, DC-cut at 1 Hz, gain of 1,000, 16-channel amplifier and digitized at 20 kHz (Xcell, Dipsi), together with a synchronization signal from the ultrasound scanner. Custom-made software based on Labview (National Instruments) simultaneously acquired video from a camera pointed at the recording stage.

Contrary to fMRI, which generates a strong magnetic field, there is no such cause for artifact with ultrasound. A regular amplifier

doi:10.1038/nmeth.3506

was used, and no additional electronic circuit for artifact suppression was necessary. A large-bandwidth amplifier was used, which can record both local field potentials (LFPs, 0.1–200 Hz) and multi-unit activity (MUA, 200–2,000 Hz), although we did not need this later feature in the work presented here. The spatial resolution of LFPs remains controversial depending on recording location and parameters, with estimates ranging from 250 µm to several millimeters in radius. MUA radius of detection is around 70–200 µm.

Analysis algorithms. In order to analyze series of track-crossing trials, we aligned them by setting each trial reference time when the rat crossed the middle of the maze. Animal position was detected by applying a threshold on the image pixel intensity that distinguished the bright animal on dark background. Cumulative distance and maximum crossing speed were computed using the trajectory smoothed with a time constant of 0.5 s.

Ultrasound images were normalized according to the average value over all the nonrunning or nonseizing time, thus giving the relative change in vascular echo in percent of baseline. Paxinos-Watson atlas[19] images were superimposed using the cortex as the main landmark. Statistical significance on images used Bonferroni correction to account for the multiple testing over the large number of pixels.

EEG signal was filtered with a 6- to 9-Hz pass-band for hippocampal theta. The power of theta was computed as the square of the EEG signal integrated over a sliding window with characteristic width of 0.5 s.

Epileptic seizures were detected when EEG electrodes presented at least 3 s of spike wave at a rate above 5 Hz, whereas a spike-wave interval of 3 s discriminated consecutive seizures. Seizures were defined using the EEG signal alone and were always bilateral. Because we used bipolar recording that ensured locality of the EEG signal close to each recording bipolar electrode, and as it is well accepted, the electrographic signs of these seizures are bilateral. In **Figure 2d** we show in color code the Pearson's correlation coefficient between EEG-defined seizures and pixel intensity. This is how we determined the vascular correlate of seizures, which often appears to be asymmetric, contrary to the EEG.

Computation of Pearson's R correlation coefficient between EEG signal and mfUS pixel intensity was based on the theta power curve for the maze experiment. For the epilepsy experiment, pixel intensity was correlated to the seizure status function (1 inside seizure, 0 outside). Statistical testing was performed on Pearson's R coefficient using Student's t-distribution.

Statistics. We chose sample sizes that gave consistent estimates of distance traveled over time, maximum speed and seizure pattern. The number of animals (above 15), maze crossings (above 100), seizure recording sessions (18 and 65) and seizures (above 800) are sufficiently large to test these distributions with small s.d./mean. The effect of the recording procedure is very significant, although our point is that it is of small amplitude. In **Figure 2** we stopped counting recordings when we realized that the distributions also had small coefficients of variation. The other figures did not require statistical testing.

For control experiments in **Supplementary Figure 8**, all our available data were pooled, as the numbers are routinely generated by our analysis software. For **Figure 2c,g** we stopped counting when we realized that the measures converged quickly, so that including more recordings did not change the results. This is a general preestablished criteria.

Experiments did not require randomization. Because quantification was performed by automated computer analysis, there was no need for blinding to group allocation. All statistics are given as mean ± s.d.

Code availability. Data were collected from ultrasound and video-EEG devices for off-line processing. We implemented the analysis software with Labview, and we provide sample data and code archive as a **Supplementary Software 2**. Moreover, example Matlab code for all post-processing steps presented in the paper are included as well in **Supplementary Software 1**. Probe motor controller microcode is provided in the **Supplementary Note**. We suggest that interested labs contact us for further information about the algorithms.

20. Montaldo, G., Tanter, M., Bercoff, J., Benech, N. & Fink, M. *IEEE Trans. Ultrason. Ferroelectr. Freq. Control* **56**, 489–506 (2009).
21. Bercoff, J. *et al. IEEE Trans. Ultrason. Ferroelectr. Freq. Control* **58**, 134–147 (2011).

doi:10.1038/nmeth.3506

Chapter 6

Article 2: Fast Gamma oscillations precede vascular activation during unrestrained running and REM sleep in rats. (In Preparation)

A. Bergel[1,3], L.-A Sieu [1,4], C. Demené[2], E. Tiran[2], T. Deffieux[2], M. Pernot[2], J.-L. Gennisson[2], M. Tanter[2] and I. Cohen[1]

1. INSERM U1130, CNRS UMR 8246, Université Pierre & Marie Curie UMCR 18, Paris, France
2. Institut Langevin, ESPCI ParisTech, PSL Research university, CNRS UMR 7587, INSERM U979, Paris, France
3. Université Paris Diderot, Sorbonne Paris Cité, Ecole Doctorale Frontières du Vivant (FdV), Programme Bettencourt, Paris, France
4. Institut de recherche translationnelle en Neurosciences ICM-A-IHU, Paris, France
Corresponding author: IC, ivan.cohen@upmc.fr

Fast gamma oscillations precede vascular activation during unrestrained running and REM sleep

Antoine Bergel, Lim-Anna Sieu, Charlie Demené, Elodie Tiran, Thomas Deffieux, Jean-luc Gennisson, Mathieu Pernot, Mickaël Tanter & Ivan Cohen.

Abstract

Neural oscillations play a major role in network communication, memory processes and task performance. Yet, their precise spatiotemporal dynamics and their role in coordinating brain areas during behavior still remain an experimental challenge to explore. Simultaneous brain-wide functional imaging and monitoring of electrical activity can help unravel the dynamics of neural synchronization. In this study, we used recently introduced mobile functional Ultrasound (mfUS-EEG) protocol to record simultaneously hippocampal local field potentials (LFP) and cerebral blood volume (CBV) fluctuations in rats performing a track-running task and during subsequent REM sleep. We observed theta rhythm simultaneous with vascular waves of activity starting in the dorsal thalamus and spreading along downstream regions of the hippocampal formation. These vascular activations were selectively associated with enhanced mid-gamma (50-100 Hz) and high-gamma (100-150 Hz) and showed strong adaptation as the task progressed. REM sleep revealed brain-wide tonic hyperaemia, together with phasic high-amplitude vascular activation starting in the dorsal thalamus and fading in cortical areas. The intensity of these phasic surges correlated with oscillation in the high gamma band and vascular cortical recruitment. These observations suggest fine delineations of brain oscillatory states and functional circuits based on concomitant vascular pattern and behavior, in accordance with information encoding during natural motion and consolidation of acquired experience during subsequent REM sleep.

Introduction

Brain oscillations have long been hypothesized to play a critical role in cognition, since the advent of electroencephalography, more than 140 years ago. Since then, the hippocampus has concentrated much interest and in particular one of its most salient activity pattern: theta rhythm [Buzsaki, 2002]. Theta oscillations are known to play a crucial part in memory encoding, consolidation and retrieval [Osipova et al., 2008; Rajasethupathy et al., 2015 ; Spellman et al., 2015 ; Boyce et al., 2016]. They have been observed across a wide range of species (bats, cats, rabbits, dogs, rodents, monkey & humans) and brain regions (hippocampus, entorhinal cortex, subiculum, striatum and thalamus) [Colgin, 2016]. Multiple roles for theta oscillations have been proposed including sensorimotor integration [Bland & Oddie, 2001], information packaging [Jezek et al., 2011], metric coding [O'Keefe & Recce, 1993] and inter-regional communication [Fell & Axmacher, 2011]. A prominent feature of theta oscillations is the presence of nested faster oscillations - typically in the 30-150 Hz range - which exhibit phase-amplitude coupling [Jensen & Cogin, 2007; Tort et al., 2008; Axmacher et al., 2016]. The exact nature of this coupling remains unknown but it is thought to promote the formation of theta sequences to encode series of independent items [Lisman & Idiart, 1995; Lisman & Jensen, 2013]. Gamma oscillations have been recorded in multiple brain regions [Buzsaki & Wang, 2012]. In the rodent hippocampus, they exhibit typical theta phase modulation profiles depending on the hippocampal layer, distal/proximal position and putative generation mechanism [Bragin et al., 1995; Csicsvari et al., 2003; Schomburg et al., 2014]. Low-gamma oscillations (30-50 Hz) are thought to arise from CA3 and reach CA1 on the ascending phase of theta, mid-gamma (50-100 Hz) oscillations are thought to mediate EC inputs onto CA1 and are most prominent at theta peak. Finally, fast-spiking local inhibitory interneurons drive CA1 with fast-gamma oscillations (100-150 Hz). An influential model about gamma oscillations is that they are the neuronal substrates of different complementary aspects of memory, supporting the idea that low-gamma are involved in memory retrieval while high-gamma is critical for memory encoding [Hasselmo, 2002; Colgin et al., 2009; Douchamps et al., 2013]. Evidence is still lacking to confirm or infer this model.

Functional brain imaging can provide valuable insight into the dynamics of brain oscillations, mainly owing to the increased field of view, the ability to record non-invasively and the denser sampling of silent units [Ogawa et al., 1990; Liao et al., 2013; Hamel et al., 2015]. Imaging studies have tried to adapt behavioral protocols used in rodent studies to reproduce task-dependent functional brain [Maguire et al., 1997; Astur et al., 2003; Chadwick et al., 2015]. Because deep neural activity is not accessible in humans, except in rare cases [Ekstrom et al., 2003], brain imaging can only probe neural activity indirectly. In most cases, imaging studies rely on proxy measures of neuronal activity through a phenomenon called neurovascular coupling, in which local neural activation triggers an increase in blood flow to meet higher energy demands and to assure waste product removal [Attwell et al., 2010; Kleinfeld et al., 2011; Uhlirova et al., 2016]. The exact mechanisms of this coupling remain however complex, showing regional dependence [Devonshire et al., 2012] and non-linearity [Lin et al., 2010], though they are at a fundamental requirement to interpret BOLD signal

[Logothetis et al., 2008; Hillman et al., 2014]. The recently developed mfUS-EEG modality can monitor the hemodynamic state of the brain over its whole depth along with its electrographic activity in awake, mobile rats over repeated and prolonged periods of time. The current setup has an in-plane resolution of 100 μm x 100 μm, out-of-plane resolution of 400 μm and temporal resolution of 200 ms. This makes it a well-suited tool for functional imaging of rodent behavior [Sieu et al., 2015].

In this study, we recorded simultaneously single plane hemodynamics and hippocampal LFP activity from animals trained to run on a linear track for water reward, both during task and subsequent REM sleep. Vascular data was obtained along a typical coronal plane (AP = -4.0 mm) that intersected dorsal hippocampus, thalamus, hypothalamus and cortex, including auditory cortex (AC), primary somatosensory cortex barrel field (S1BF) lateral parietal association cortex (LPtA) and retrosplenial cortex (RS). We also monitored vascular responses over a plane tilted 60° relative to coronal view that intersected hippocampus (dorsal, intermediate and ventral), thalamus (dorsal and ventral), cortex (anterior, midline and posterior) and caudate Putamen (CPu). We found that vascular activity specifically correlated with theta and high-gamma rhythmicity (> 50 Hz) in most regions. During running, a pattern of sequential activation starts in the dorsal thalamus and spreads along the trisynaptic hippocampal circuit, that strengthened as the task progressed. During REM sleep, we observed a background tonic hyperaemia and phasic brain-wide surges in vascular activity, revealing strong coupling between hippocampal and neocortical sites. Our data provides a new insight into the spatiotemporal dynamics of locomotion in response to stereotyped runs subsequent vascular activity during REM sleep. To our knowledge these observations have not been reported before. Our mfUS-EEG did not impede movement nor task performance and animals showed normal sleep patterns. We are convinced that this kind of multimodal approaches will shed a new light on the fundamental understanding of brain rhythms.

Material & Methods

Animal preparation

All animals received humane care in compliance with the European Communities Council Directive of 2010 (2010/63/EU), and the study was approved by the institutional and regional committees for animal care. Adult Sprague Dawley rats aged 10-15 weeks underwent surgical craniotomy and implant of ultrasound-clear prosthesis. Anesthesia was induced with 2% isoflurane and maintained by ketamine/xylazine (80/10 mg/kg), while body temperature was maintained at 36.5 °C with a heating blanket (Bioseb, France). A sagittal skin incision was performed across the posterior part of the head to expose the skull. Parietal and frontal flaps were excised by drilling and gently moving the bone away from the dura mater. The opening exposed the brain between the olfactory bulb and the cerebellum, from +6.0 to -8.0 mm relative to Bregma, with a maximal width of 14 mm. Electrodes were implanted stereotaxically and anchored on the edge of the flap. A plastic sheet of polymethylpentene (TPX) was sealed in place with acrylic resin (GC Unifast TRAD) and residual space was filled with saline. We chose a prosthesis approach which offers larger field of view and prolonged imaging condition over 4-6 weeks, compared to the thinned bone approach [Osmanski et al., 2014]. Particular care was taken not to tear the dura in order to prevent cerebral damage. The surgical procedure, including electrode implantation, typically took 4-6 h. Animals recovered quickly, and after a conservative one week resting period they were used for data acquisition. In order to attach the ultrasound probe and connect the EEG before a recording session, rats undergo short anesthesia for 20-25 min with 2% isoflurane. Acoustic gel is applied on the skull prosthesis, and then the probe is inserted into the holder. The gel does not dry out even for extended recordings of up to 6-8 h. Animals are allowed to recover for 40 min before starting the recording session.

Electrodes and Prosthesis

Electrodes are based on regular multisite polytrodes made of bundles of insulated tungsten wires. The difference with standard design is the right angle elbow that is formed prior to insertion in the brain. This shape allows anchoring the electrodes on the skull anterior or posterior to the flap. Electrodes are implanted with stereotaxic positioning micromotion and anchored one after the other, and then the plastic film is applied to seal the skull. Two epidural screws placed above the cerebellum are used as reference and ground. Intra-hippocampal handmade theta electrode bundles are composed of 25 μm insulated tungsten wire, soldered to miniature connectors. Four to six conductive ends are spaced by 1 mm and glued to form 3-mm long, 50-μm thick bundles. The bundles are lowered in dorsal hippocampi at stereotaxic coordinates AP = -4.0, ML = ± 2.5, DV = -1.5 to -4.5, in mm relative to Bregma. Hippocampal theta rhythm is confirmed by phase inversion across recording sites in successive hippocampal layers, time-frequency decomposition, and coincidence with periods of exploration and navigation.

The prosthetic skull is composed of polymethylpentene (PMP, Goodfellow, Huntington UK, goodfellow.com), a standard biopolymer used for implants. This material has tissue-like acoustic impedance, which allows undistorted propagation of ultrasound waves at the acoustic gel-prosthesis and prosthesis-saline interfaces. The prosthesis is cut out of a film of 250 μm thickness and sealed to the skull with resin.

An accelerometer was fixed onto the head of the animal together with the ultrasound probe holder. Three-axis analog signal was acquired using spare channels on the EEG digital acquisition circuit. The signal was pass filtered (1-10 Hz) and instantaneous power was estimated by applying a Gaussian smoothing window (width 500 ms) over the signal squared.

Animal behavior

Animals were trained before surgery. They were placed under a controlled water restriction protocol (weight between 85 and 90% of the normal weight) and trained to run back and forth in a long rectangular maze for water reinforcement. The maze (225 x 20 cm) had 5 cm high lateral walls, and was placed 50 cm above ground. Drops of water were delivered through two small tubes coming out from the two end walls of the maze (Fig. 1a). Each time the animal crossed the track a single drop of water was delivered in alternate water tubes by opening an electronically controlled pair of solenoid valves. Daily training lasted 30 min. Rats took about 2 sessions to reach a 60 crossing criterion and perform reliably, crossing the maze at fast speed, but were reinforced for at least two more days. Daily recording sessions lasted 20 to 30 min, depending on animal motivation. Since the acquisition in "burst mode" required 40 s for image reconstruction from ultrasound echoes, we could not capture every run. The number of runs acquired ranged from one fourth to one half of all the runs, depending on animal performance and the timing of its spontaneous runs within the session. The data analyzed here were recorded in 42 sessions performed across 6 animals.

Miniature ultrasound probe and Probe Holder

The Ultrasonic probe (Vermon, Tours, France) is a linear array made of 128 transducers working at a 15 MHz central frequency (spatial pitch 0.11 mm, transducer element 2.000 x 0.110 mm^2, bandwidth 46% at -6 dB, corresponding to 11-18 MHz). Image resolution is 0.110 x 0.110 mm^2. This probe has an acoustic lens with an elevation focal distance of 8 mm and an elevation focal width of 400 μm, corresponding to the thickness of the imaging plane. The active part is embedded in 18.5 mm diameter and 25 mm length molded resin. A 150 cm cable length and 12 g probe weight ensure a good freedom and comfort to move for the animal. Compared to previous work [Macé et al., 2011; Osmanski et al., 2014], the probe was miniaturized. Dimensions (in cm) were reduced from 15 (height), 6 (width), 2.5 (thick) to 2.5 x 1.85 x 1.85. The weight (in g) was reduced from 250 to 12. The cable was made more flexible by reducing its diameter from 11.5 to 6.9 mm. All these improvements did not affect sensitivity of the transducer array and were required to perform such experiments on moving animals. Penetration of the ultrasound waves across 15 mm of rat brain allows imaging rat brain at all depth. More generally depth of penetration decreased with higher frequencies (smaller wavelength), while resolution simultaneously increased. Thus there is a tradeoff between resolution and depth of penetration, and 15 MHz is optimal for rat brain. Although we designed the probe, specialist company Vermon manufactured it. Interested labs are welcome to contact us to share our customized probe design considerations.

The holder is made of two parts machined in Plexiglas for light weight and stiffness. First, a base plate with U-shaped side grooves, allowing translation of the mobile part, is attached to the head of the animal with three screws. Second, the mobile part presenting two sliding side edges is fitted into the base part. The probe is attached through a central opening in the mobile part. A linear servo-motor (Robotshop.com, VS-19) is fixed to the mobile part and anchored on the base plate. It is controlled by custom made electronics connected to the ultrasound scanner through USB port. Holder weight is 18 g, and overall size 41-mm width, 34-mm length, 16-mm height.

Ultrasound imaging

Vascular images are obtained via the Ultrafast Compound Doppler Imaging technique [Bercoff et al., 2011; Macé et al., 2011]. The probe is driven by a fully programmable GPU-based ultrafast ultrasound scanner (Aixplorer, Supersonic Imagine, Aix-en-Provence, France) relying on 24 Gb RAM. In "burst mode" we used an acquisition sequence of 6000 frames at a rate of 500 Hz for a total acquisition time of 12 s. Manual trigger was given when the animal finished drinking water, and turned around in position for the next run. In the "continuous mode", we acquired 200 ultrasound images at 1 kHz frame rate for 200 ms, repeating every 1.2 to 3 s. In both "burst mode" and "continuous mode" each frame is a Compound Plane Wave frame, that is, a coherent summation of beamformed complex in phase/quadrature images obtained from the insonification of the medium with a set of successive plane waves with specific tilting angles [Bercoff et al., 2011]. This compound plane wave imaging technique enables to recreate a posteriori a good quality of focalization in the whole field of view with very few ultrasound emissions. Given the tradeoff between frame rate, resolution and imaging speed, a Plane Wave Compounding using five 5°-apart angles of insonification (from -10° to +10°) has been chosen. As a result, the pulse repetition frequency (PRF) of plane wave transmissions was equal to 8 kHz. In order to discriminate blood signals from tissue clutter, the Ultrafast Compound Doppler frame stack is high pass filtered using a 4th order Butterworth filter (cut-off frequency 50 Hz) along the temporal dimension, giving a high frequency in phase/quadrature frame stack whose energy in each pixel is then computed to build the ultrafast Power Doppler fUltrasound image. Some frames are discarded before being incorporated in a recording when they show artifact echoes, which are caused by the animal bumping the probe against a hard surface such as cage or maze wall. The signal measured by fUltrasound and its sensitivity are presented in earlier theoretical and experimental work [Macé et al 2013]. Briefly, fUS measures moving echogenic particles, that is red blood cells, and thus corresponds to cerebral blood volume (CBV). Importantly, this proportionality is valid only if backscattering properties do no vary versus time. This assumption is valid while red blood cells backscattering properties such as hematocrit and shear rate remain time-invariant, which is most likely.

Ultrasound sequences

Technical specifications of the scanner used here include 16x, 6 Gb/s PCI express bus, 12 core 3 GHz Xeon processor, NVidia Quadro K5000 GPU with a bus at 173 Gb/s, providing 2.1 Teraflops. One current limitation of fUltrasound is due to the transfer and processing time of the large amount of data required to form ("beamform") fUS images. Yet, this limitation does not stem from physical principles, but rather from contingent hardware. Although increasing computing power and optimized software provide perspective for continuous monitoring at high speed (200ms per image), we show here that the current technology allows "continuous" recording with a temporal resolution close to the time constant of neurovascular coupling (1-2 s), and further allows "burst" capture for quick behavioral events such as running a maze. The limitation for the "continuous" mode is the processing speed to transform a series of plane wave acquisitions into compound images and then generate a fUltrasound image. The limitation for the "burst" mode is the memory available to buffer plane wave images to later generate a movie of fUltrasound images.

EEG acquisition

Intracranial electrode signals are fed through a high input impedance, DC-cut at 1 Hz, gain of 1000, 16 channel amplifier and digitized at 20 kHz (Xcell, Dipsi, Cancale, France), together with a synchronization signal from the ultrasound scanner. Custom made software based on Labview (National Instruments, Austin, TX, USA) simultaneously acquires video from a camera pointed at the recording stage. Contrary to fMRI, which generates strong magnetic field, there is no such cause for artifact with ultrasound. A regular amplifier is used, and no additional electronic circuit for artifact suppression is necessary. A large bandwidth amplifier was used, which can record both local field potentials (LFP, 0.1-200 Hz) and multiunit activity (MUA, 200-2 kHz), although we did not need this later feature in the work presented here. The spatial resolution of LFPs remains controversial depending on recording location and parameters, with estimates ranging from 250 μm to several mm radius. MUA radius of detection is around 70-200 μm.

Rhythmic oscillations in the LFP are extracted in the raw recording by applying band-pass filtering. In order to avoid phase shift a second order Bessel filter is applied two times to the signal, first onward and then backward. Distinct frequency sets were used for each band (Theta 6-10 Hz, high-gamma 100-150 Hz, mid-gamma 50-100 Hz, low-gamma 30-50 Hz). Instantaneous power for each band was estimated by applying a Gaussian smoothing window (width 500 ms) over the signal squared.

Analysis software and analysis

Data is collected from ultrasound and video-EEG devices for offline processing. We implemented the analysis software with Labview and MATLAB. We suggest interested labs to contact us for further enquiry in the algorithm. Animal position is detected by applying a threshold on the image pixel intensity that distinguishes the bright animal on dark background. Cumulative distance and maximum crossing speed are computed using the trajectory smoothed with a time constant of 0.5 s. Ultrasound images are normalized according to the average value over all the non-running time, thus giving the relative change in vascular echo in percent of baseline. Waxholm atlas is superimposed using the cortex as the main landmark. Statistical significance on images used Bonferroni correction to account for the multiple testing over the large number of pixels. EEG is filtered pass-band 6-9Hz for hippocampal theta. Power of theta is computed as the square of the EEG signal integrated over a sliding window of characteristic width 0.5s. Computation of Pearson's R correlation coefficient between EEG and mfUS pixel intensity is based on theta power curve for the maze experiment. Statistical test is performed on Pearson's R coefficient using Student's t-distribution. All statistics are given +/- standard deviation, unless otherwise noticed.

Results

We used a sensitive functional ultrasound imaging protocol combined to EEG recording in mobile rats [Sieu et al., 2015]. Electrodes were implanted in the dorsal hippocampus (AP = -4.0 mm, ML = 2.5 mm, DV = -2.5 mm). A pair of recording sites along the dorso-ventral axis was selected by the characteristic theta phase inversion in the local field potential. Theta and gamma power were computed from the differential signal between the two sites. Theta strongly correlated with speed and accelerometer power (r_1 = 0.783 ± 0.054, r_2 = 0.723 ± 0.086, n = 4 animals) (**Fig S1**). We computed power in three gamma sub-bands: low-gamma (30-50 Hz), mid-gamma (50-100 Hz) and high-gamma (100-150 Hz). This division into gamma sub-bands efficiently separates distinct types of gamma, thought to arise from independent mechanisms and to synchronize neural activity in CA1 with input from different regions [Schomburg et al., 2014]. We recorded brain activities associated with running on 7 animals across 32 sessions. Sleep was recorded in 4 animals, during 30 sessions for a total of 60 REM episodes, each lasting at least 30s. CBV fluctuations during typical RUN recordings were recorded at 500 Hz for 12 s periods, which provided Power Doppler images at 5 frames per second. During sleep CBV was sampled continuously at a frame rate of 0.33 Hz for one half of the recordings, of 0.8 Hz for the second half (latest scanners) (**Fig 1a**). Theta and High-Gamma power peaks were very prominent in CA1 in both RUN and REM conditions (**Fig 1b**). Low and high-gamma episodes were salient, but low gamma episodes occurred less frequently, especially during RUN, which might be due to our task design (**Fig 1c**). Both theta and gamma were stronger during RUN compared to REM. Theta and gamma showed phase-amplitude cross-frequency coupling, with low-gamma peaking on the ascending phase of theta, while mid-gamma power was maximal at theta peak, both during REM and RUN (**Fig 1d**). This 90°-shift is specific from recordings in CA1 region. RUN exhibited distinct gamma oscillations across the Theta cycle (Mid-gamma mean peak phase = 164°; High-gamma mean peak phase = 321°; 8 recordings), while REM contained only mid-gamma oscillations (**Fig 1d – 2b**). This LFP signature of CA1 recordings is in accordance with what was previously published in the literature [Belluscio et al. 2012, Schomburg et al, 2014]. Though overall distance traveled was lower in mfUS-EEG animals than in controls, our protocol did not impede instantaneous animal movement (no significant difference in peak speed). This can be explained by the higher load onto the animal's head, resulting in longer inter-trial interval, probably due to longer rest periods (**Fig S2**).

Hemodynamic signals robustly correlate with theta and high-gamma rhythms

To assess how functional hemodynamics correlated with LFP recordings, we extracted differential signals from neighboring recording sites, leading to 4 signals for animals implanted unilaterally (3 animals, 11 recordings) and 8 signals for animals implanted bilaterally (4 animals, 21 recordings), filtered in theta and three gamma frequency bands and computed power envelope signals by temporally smoothing instantaneous power (Gaussian kernel, constant 500 ms). First, we normalized individual pixel activity by temporal scaling (dividing each pixel signal by subtracting and dividing the mean value over the whole recording), leading to ΔS/S signals, with unit expressed in percent of variation relative to the mean (see Methods). Cross-correlations functions were computed for each pixel signal over a temporal range of lags typically from -1.0 s to +5.0 s, leading to three-dimensional correlation maps (two dimensions of space plus one temporal dimension corresponding to the lag). One such map is presented in **Figure S3**, where theta power is used as a reference. These maps display two types of information: the color-coded strength of correlation and the timing of maximal correlation, which varied significantly among pixels. To determine what frequency band best explained variability, we generated maps of the maximal correlation over all values of lag (Rmax) for each pixel. Resulting maps are presented for one animal in **Figure 4c**. Theta, mid-gamma and high-gamma displayed similar correlation maps while low-gamma did not yield any significant correlation, both during REM and RUN. REM activation maps were less variable across pixels. Strongest correlations were found in the dentate gyrus and dorsal thalamus for theta (Rmax = 0.736 ± 0.074, 32 sessions, 7 animals), while high-gamma yielded stronger correlations in CA1 and CA3 region (Rmax = 0.565 ± 0.083, 32 sessions, 7 animals). In order to pool recording across animals, where images could not be superimposed pixel-to-pixel, we computed mean variations across sets of neighboring pixels given by a volumetric atlas (see Methods, **Fig 4d**). Overall, high-gamma correlated stronger than theta in almost all brain regions during REM, while it did so mostly in cortical and CA1-3 regions during RUN. Overall, our results indicate that high-gamma better explained functional hemodynamics in most regions except for dorsal thalamus and dentate gyrus where theta power was most informative. Only linear dependences were taken into account here.

Wave of activation during running

To understand the spatiotemporal dynamics of the brain activation pattern during mobility, we first assessed individual pixel responses to locomotion. We divided each trial into bins of equal duration (500 ms) and averaged pixel activity within each bin, for a whole recoding. This approach leads to an average time sequence of individual responses to locomotion, but does not allow for statistical comparison across recordings, due to aberrant pixel superpositions (**Fig S4 c-g**). To overcome this limitation, we analyzed the time-lagged correlations of vascular responses during running in 10 animals (larger group including animals for which electrode implantation was not performed) in both coronal and diagonal planes (**Figs 2-3**). We used both animal speed, accelerometer power and theta power signals as a reference signal to extract time-lagged correlations in 12 regions (coronal) and 15 regions (diagonal). Because vascular activations were monitored for periods of 12 seconds interspersed with acquisition-free periods of varying duration, fUS-fUS cross-correlations could only be computed for a limited range of correlation lags. As an example, a 6-s correlation lag resulted in using only 50% of the total number of recorded frames to estimate a correlation. This limitation does not apply to LFP-fUS cross-correlation, because LFP signals are continuously monitored. The average run onset was 0.5 s ± 0.4 s after acquisition onset. Average theta peak was observed 1.7 s ± 0.2 s after run onset, concurrently with peak speed, and average vascular response peaked at 1.8 s ± 0.5 s (2561 trials, 37 sessions, 8 animals) after theta peak. Due to this average delay of 1.8 s, we computed cross-correlations functions for lags varying between -1.0 s and +6.0 s, to obtain the best time window to observe fUS activations. We observed a strong modulation in cross-correlation function in all regions. Highest correlations were obtained in dorsal thalamus, dorsal hippocampus and retrosplenial cortex (**Fig 2d**). Pixel cross-correlation maps revealed sequential activation along the trisynaptic circuit that we referr to as "trisynaptic vascular waves" (**Fig 2e**). When assessing regional cross-correlation among dorsal hippocampus areas, we observed that dentate gyrus (1.45 s ± .31 s, 15 sessions, n = 4 animals) peaked earlier than CA3 (1.71 s ± .47 s) and CA1 (1.76 s ± .48 s) region. This pattern was bilateral and robust across recording sessions (**Fig 2bc**). Average dentate response typically started earlier and lasted longer than CA1/CA3 responses, which were shorter, but of higher amplitude (**Fig 2f**). Activations were less intense and more variable in cortical regions, including an early response in the retrosplenial cortex and subsequent activation of the lateral association, somatosensory and auditory cortices (retrosplenial: r = 0.41 ± .23, S1BF: r = 0.27 ± .19, auditory: r = 0.27 ± .19). Consistent with previous observations, ventral thalamus displayed anti-correlation relative to animal speed.

Imaging in diagonal planes revealed similar patterns of activations in the dorsal thalamus, dentate gyrus and CA1 region. Cortical activations were strongly modulated by their relative position along the antero-posterior axis. Anterior cortex showed weak correlation to running, or – if any – long after theta rhythmicity, during reward uptake (anterior, presumably sensory lip and jaw, cortices) (Rmax = 0.37 ± .15, Tmax = 3.19 s ± .88, 17 sessions, n = 3 animals). On the contrary, midline (Rmax = 0.39 ± .07, Tmax = 1.10 ± .59) and posterior (Rmax = 0.34 ± .12, Tmax = 1.59 ± 1.30) cortices showed strong activation, preceding the dorsal hippocampus (**Fig 3f**). Caudate Putamen showed also segregation between its ventral and dorsal parts, in the same pattern as thalamus, but weaker (Rmax = 0.43 ± .14, Tmax = 3.28 ± .96). The trisynaptic sequential activation in the dorsal hippocampus was also visible on these planes, though harder to isolate between dentate and CA3 (due to the hippocampus being tangent to diagonal planes). To assess whether hippocampal activation was only restricted to the dorsal hippocampus, we analyzed both stimulus peak time and correlation strength between dorsal, intermediate and ventral activation. We used pixel relative depth onto the dorso-ventral axis for hippocampal delineations (Dorsal Hippocampus [-2.0; -4.0 mm] - Intermediate Hippocampus [-4.0; -6.0 mm] - Ventral Hippocampus [-6.0; -8.0 mm]). Dorsal and Intermediate hippocampi showed strong amplitude response, while ventral activation was overall weak. The short delay (0.20 ± .07 s) between intermediate hippocampus and dorsal hippocampus was not significant (p = 0.08). Our results suggest a pattern of activation in the dorsal two-thirds of the hippocampus associated with posterior cortical activation (V2 cortex). The septal region was visible on 5 recordings, and did not display strong vascular activation associated with navigation. On some recordings, subicular activation could be observed, revealing a continuation in CA1 activation (Rmax = 0.39 ± .15, Tmax = 2.46 ± .95, 8 sessions, n = 2 animals). The entorhinal cortex was observed only 4 times impeding statistical assessment

Adaptation of the functional response across repetitions in the task

In order to assess the variability of the vascular patterns observed during successive runs, we extracted start and end time of each run for each recording sessions (9 animals, 36 sessions). Thus, we computed animal position and speed over the whole recording and detected start and end time when the animal traveled across the track. This led to an average running time of

3.24 s (average 71.4 runs per session, of which 22.8 with scanner acquisition) at a mean running speed of 0.58 m/s (average peak speed: 0.82 m/s). We aligned all running trials on the start and end time of each run, leading to a normalized timescale between 0 (run start) and 1 (run end), on which we further aligned hemodynamics and LFP signal. Functional activation showed variability among trials (**Fig 5a**), which was not consistently paralleled in behavioral parameters including animal speed and accelerometer power signal (**Fig S5**). This inter-trial variability was strongly modulated by trial number in most regions, revealing an increase in vascular response amplitude and duration, which we referred to as "vascular adaptation". In **Fig 5**, we display three typical profiles of such adaptation patterns in CA1 region, dentate gyrus and retrosplenial cortex.

The pattern of vascular adaptation occurred while running speed and head acceleration remained constant across trials (see **Fig S5**). To quantify the profile of adaptation, we computed mean activation per trial and displayed this value over task progress (see **Fig 5b**), which revealed a global increase in most brain regions. This increase was stronger in subcortical than cortical regions. In parallel, theta power, speed and acceleration showed a slight decrease. Gamma power signal was constant in low-gamma band, while both mid and high-gamma power increased. Such patterns were observed in most animals. To compare among animals, we computed Spearman correlation coefficients between vascular mean trial activations and mean LFP power signals per trial, which revealed that high-gamma explained inter-trial variability in hippocampal and thalamic regions (dHpc: Rmax = .72 ± .08, dThal 0.58 ± .11, 17 sessions, n = 3 animals). In cortical regions however, mid-gamma was better correlated to hemodynamics (retrosplenial: Rmax = 0.57 ± .11, parietal: 0.42 ± .15). Finally, we grouped trials by bins of 10-mn duration, to display mean response according to session progression. We observed a strong progression in CA1 and CA3 region between task onset and task end that was robustly associated with high-gamma progression, while speed, theta and low-gamma remained constant. Dentate gyrus, and retrosplenial cortex vascular responses were relatively invariant along the task, suggesting that hippocampal high-gamma is selectively associated with vascular adaptation in the downstream regions in the hippocampal circuit.

High-gamma oscillations precede vascular surge in REM sleep

To assess if such relation between high-gamma rhythms and vascular activity was specific to running, we recorded vascular activity during REM sleep following the task (**Fig 6**). The average duration of a REM episode was 120.3 s with a ratio of REM over NREM sleep of 15.6 %. A typical example of vascular activity during REM is shown in **Figure 6a**. The hemodynamics signal was consistently higher than during NREM and quiet waking (QW: -0.32 ± .12, NREM: -0.26 ± .14, REM: +0.38 ± 0.30, s.d. units, **Fig 6c**). During REM we observed large phasic increases functional activity, characterized by high levels in most hippocampal and cortical regions, that we called "vascular surge". A typical surge is shown in **Fig 6b**, where dorsal thalamic and hippocampal activations clearly precede cortical ones. These surges were detected by thresholding the whole-brain vascular response with a statistical threshold of 1.5 standard-deviation units for a minimal time of 5s. This led to a total number of 160 surges overs 60 REM episodes (mean duration = 13.85s, 2.7 surges per REM episode on average). The occurrence of surges was positively correlated with REM duration (r_1 = 0.53). The vast majority of surges lasted between 5 and 15 seconds (113 surges, 70,6%). We computed two parameters to assess the intensity of a given surge, the integral of the mean whole brain signal during surge and the proportion of active pixels with sustained activity above threshold. The first parameter measures mean CBV intensity over surge duration, while the second measures the extent of the surge, in terms of a proportion of significantly active pixels, regardless of their relative activation. These two measures were strongly similar in most, but not all animals. They both positively correlated with surge duration (r_2 = 0.43, r_3 = 0.44), but we observed stronger variability for short surges than long ones in both measures (**Fig 6d**). This led us to assess the profile of short REM surges over long ones. We showed typical surge profile for short and long surges (**Fig 6e**). Short and mid surges display similar profiles, including strong thalamic and hippocampal hyperemia, with moderate cortical spread. Somatosensory cortex activity strongly increases between short and mid surges. For long surges, dorsal thalamus gradually decreases as the surge progressed with S1BF activation increased to reach hippocampal activation level in the late part of the surge.

To further explain the potential link between vascular surge activations and EEG, we analyzed the LFP frequency band signature before and after each vascular surge (**Fig 7**). REM sleep episodes were rich in gamma and theta activity. Typical surges are often preceded by an increase in theta power together with a frequency shift to the upper theta band, that we identified as phasic REM sleep bursts [Montgomery et al., 2008]. These phasic bursts of activity contained mid-gamma and high-gamma sustained activity, while low gamma was rather absent (**Fig 7a**). We looked for sustained theta and gamma activity in a 5 s time window preceding surge onset (**Fig 7b**). Typically we detected for LFP ‘burst’ episodes, when power signal rose above 2s.d and count the occurrence bursts preceding surges. This analysis was carried overs 2 animals for 10 REM episodes. We found that pre-surge LFP activity was strongly dominated by high-gamma (87.2 %) theta activity (76,9 %) and mid-gamma (74,1 %). Low gamma activity was only detected in a few cases (41,0 %). Conversely, we detected periods of increased gamma and theta activity (LFP “bursts”) and assessed the proportion of which were followed by a vascular surge. Once again, high-gamma activity elicited surges with stronger probability than any other band (High Gamma 77,2% - Mid Gamma 63,8 % - Low Gamma 34,8 % - Theta 50,8 %). Theta and mid-gamma were also significantly followed by vascular increases, whereas low gamma was not. To further classify we detected each burst in LFP activity over the 4 different sub-bands and computed the mean vascular response following each burst. This classification is shown in **Fig 7c**. High-gamma bursts elicit strongest responses in the hippocampus and neocortex while theta and mid-gamma vascular profile were weaker. We noticed that joint theta/high-gamma activity almost always elicited a vascular surge (not shown). Together, our data supports the idea that high gamma activity is a necessary, but not sufficient, condition for surge occurrence. Phasic theta activity is required to elicit strong cortical vascular response, which is perhaps a sign of strong hippocampo-cortical transfer for memory consolidation [Montgomery et al. 2008, Boyce et al; 2016].

Discussion

In this study, we demonstrated that brain-wide vascular activity closely mirror hippocampal neural activity in the mid-gamma (50-100 Hz) and high-gamma range (100-150 Hz). We described the vascular activations associated with natural locomotion and REM sleep. They involved brain-wide waves of activation starting in the dorsal thalamus and flowing along the trisynaptic circuit to fade in neocortical sites. To our knowledge, these patterns have not been observed previously. The major limitation of this study is that these complex patterns may be associated with many components during running and REM sleep, including motor activations, reward uptake and rule acquisition and consolidation. Further investigation is necessary to disentangle the functional correlates of these multiple components, such as a comparison between a reference state and an activated state. A second limitation of this work is that it does not make a direct link between gamma oscillations *per se* and corresponding vascular activations. We still need to investigate the effects of gamma modulation on the functional activity of the vascular network.

Gamma oscillations and vascular activity

Our results suggest that theta rhythm strongly correlates with CBV fluctuations in the dorsal thalamus, dentate gyrus and CA region, though to a lesser extent. However, we obtained similar correlation maps using theta power envelope, accelerometer and body speed. During REM, phasic episodes of theta activity correlated strongly with vascular patterns while tonic theta did not. Instead of theta activity, our results show that LFP fluctuations in the mid gamma [50-100 Hz] and high-gamma [100-150 Hz] ranges are robustly associated with CBV fluctuations both during running and REM sleep. Concurrently, low-gamma activity elicited weak to no vascular response in most brain regions. Mid-gamma and high-gamma robustly preceded CBF increases both during running and sleep. Mid-gamma was associated with vascular fluctuations in cortical regions whereas high-gamma best explained CBV fluctuations in the dorsal hippocampus and thalamus. Theta-phase modulation analysis of our LFP recordings revealed that vascular adaptation was parallel to the apparition of high-gamma oscillations at the trough of theta oscillations. These results still need to be confirmed over a larger sample of animals, but it is likely that several gamma mechanisms are involved in the vascular responses we observe. Determining what regions are associated with which sub-band remains to be done.

What are the physiological properties of gamma oscillations that specifically link them with CBV fluctuations? Though generated locally, gamma oscillations are observed in multiple regions in the brain including neocortex, entorhinal cortex, hippocampus, thalamus, striatum, olfactory bulb and thalamus [Buzsaki and Wang, 2012] with the ability synchronize over long-range connections [Traub et al., 1996]. Fast-spiking parvalbumin interneurons are known to drive gamma in the rodent cortex [Cardin et al., 2009; Sohal et al., 2009]. Removing this fast inhibition disrupts theta-gamma coupling [Wulff et al., 2009]. Thus, it is likely than the increase in blood volume concurrent with gamma oscillations reflect the cost of inhibition [Buzsaki et al., 2007].

Complex pattern of activity during running

Recent findings reported different CBV patterns in mice adjacent cortices (somatosensory and frontal) in response to voluntary locomotion, both in terms of electrical coupling [Huo et al., 2014] and separation between arteriole and venous blood [Huo et al., 2015]. Studies using autoradiography radiotracers in rats performing treadmill found changes in cerebral blood flow in dorso-lateral striatum, motor cortices and cerebellum [Holschneider and Maarek, 2004]. However, most of these studies rely on the use of treadmills or similar setups which generate different patterns of electrical activity than the ones observed in natural movement, possibly because of the discrepancies between vestibular and visual sensory inputs [Li et al., 2014].

During running, we found strong activations in multiple brain regions, some of which might be associated with sensory stimulation (dorsal thalamus), others with spatial processing (dorsal hippocampus, retrosplenial cortex) and others with reward (striatum). Diagonal planes revealed clear dichotomies between functional groups including (1) differential activations between ventral and dorsal thalamic regions, both in activation onset and strength. In some animals ventral thalamic activation occurred concurrently with frontal cortical activation during reward uptake (S1 lip region - S1 jaw) suggesting a possible thalamic relay in sensory stimulation of the face and limbs during reward (2) differential activations between anterior and posterior cortices. Anterior activation was strongly associated with dorsal striatum activation while posterior cortex was associated with dorsal hippocampus. (3) differential hippocampal subfields responses in their onset time and activation profile. Dentate activity started earlier and was more sustained during running while CA1 was more powerful, transient and “phasic”, suggesting that vascular activity is first restricted to dentate regions before spreading to activate downstream regions. Disentangling the relative implication of these activations in sensorimotor processing, cognition and reward will help make this pattern less complex.

Nature of vascular waves

We have been able to monitor vascular fluctuations of all structures contained in coronal and diagonal views, during unimpaired movement. Our recordings reveal a strong sequential pattern of activation originating in the dorsal thalamus and propagating to the dorsal hippocampus and neocortex, both during running and REM sleep episodes. The hemodynamic responses of these different regions presented specific activation profiles, which could map feed-forward inhibition in the trisynaptic circuit [Lawrence and McBain, 2003]. We estimated the propagation speed of the vascular waves we observed in a range between 1 and 10 mm/s. Electrical waves have already been shown to be non-stationary and to propagate from one region to the next [Lubenov and Siapas, 2009]. In vitro 5-Hz stimulation in deafferented mice hippocampal slices have revealed sequential “trisynaptic waves” which pattern is largely similar to the one we observed but on a 20-fold faster timescale [Stepan et al., 2015]. Some authors have also proposed that mechanical waves accompany the propagation of action potentials in the brain [Rvachev, 2010]. Our findings support the idea of a possible permissive mechanism for vascular wave propagation.

Relevance of Vascular Adaptation

Unexpectedly, we found vascular fluctuations that showed strong intrinsic variability, while behavioral parameters such as speed and acceleration remained constant. This variability was strongly associated with the timing during the task: start trials elicited weaker activation in downstream regions than end trials. This pattern was observed robustly in successive recordings in the same animal and strengthened across recording sessions, suggesting a reinforcement of vascular responses both during the task and across recording sessions. This progression was region-dependent and occurred markedly in the CA1 and CA3 region, dorsal thalamus and sensorimotor cortices. Vascular activations were more constant in the dentate gyrus and showed a slight decrease in retrosplenial cortex. We excluded a potential influence of recording electrode because control electrode-free animals displayed the same pattern.

This suggests that inter-trial averaging must be performed over small trial number. Because different regions did not present the same profile of adaptation, we suspect a specific functional role for this phenomenon. We propose vascular adaptation to be related to learning or synaptic plasticity. In our protocol, animals are over-trained, thus expecting and receiving reward at each run. It appears extremely profitable to efficiently encode and strengthen the spatial cues used in such context. This kind of adaptation could make functional hyperemia more efficient after repeated trials. What is the signaling pathway leading to vascular adaptation? It is probable that strong high-frequency stimulation generates important calcium influx in pyramidal neurons [Wong et al., 1979] and that this might trigger a cascade of signaling and metabolic changes [Lauritzen, 2005]. An important question is to address if such a pathway is mediated by neuronal (possibly involving cyclo-oxygenase 2) or by astrocytes (possibly involving epoxygenase) [Cauli et al., 2010]. It is also possible that different pathways are implicated in different aspects of the hemodynamic responses we observe, given that mid-gamma and high-gamma supposedly do not arise from the same mechanisms [Schomburg et al., 2014].

Vascular surges and interregional communication

In parallel with gamma activations during running, REM sleep vascular profile was strongly separable from quiet waking and NREM sleep. REM sleep episodes consist in elevated baseline (tonic hyperemia) in most brain regions and recurrent phasic increases in CBV levels that we called “surges” (phasic hyperemia). These surges originate in the thalamus and spread in the dorsal hippocampus and neocortex. The magnitude of the surge was strongly associated with cortical contamination, meaning that small surges had a limited cortical extent while large spread widely to cortical areas. One possible explanation of these surges is that is supports memory-consolidation and strengthens hippocampal output to cortical areas [Datta et al., 2005]. Given that REM sleep was recently proved to play a role in hippocampus-dependent memory task [Boyce et al., 2016], it is possible that such surges are implicated in this process. The strong similarity of vascular patterns observed during RUN and REM sleep suggests that surge episodes might be associated with replay of past events. However, these patterns presented subtle differences, notably the absence of dissociation between ventral and dorsal thalamus and higher variability in cortical recruitment in REM sleep compared to running, which could be associated with the different activation contexts including reward and actual movement or not.

Acknowledgements:

The research leading to these results has received funding from the European Research Council under the European Union's Seventh Framework Programme (FP7/2007-2013) / ERC grant agreement n° 339244-FUSIMAGINE. This work was also partly supported by the Agence Nationale de la Recherche under the program ‘‘Future Investments’’ with the reference Laboratory of Excellence ANR-10-LABX-24 LABEX WIFI within the French Program “Investments for the Future” under reference ANR-10-IDEX-0001-02 PSL and the program “Investissements d'avenir” ANR-10-IAIHU-06.

Bibliography

1. Astur, R. S. *et al*. fMRI Hippocampal Activity During a VirtualRadial Arm Maze. *Applied Psychophysiology and Biofeedback* **30,** 307–317 (2005).
2. Attwell, D. *et al*. Glial and neuronal control of brain blood flow. *Nature* **468,** 232–243 (2010).
3. Axmacher, N. *et al*. Cross-frequency coupling supports multi-item working memory in the human hippocampus. *Proceedings of the National Academy of Sciences* **107,** 3228–3233 (2010).
4. Belluscio, M. A., Mizuseki, K., Schmidt, R., Kempter, R. & Buzsaki, G. Cross-Frequency Phase-Phase Coupling between Theta and Gamma Oscillations in the Hippocampus. *Journal of Neuroscience* **32,** 423–435 (2012).
5. Bercoff, J. *et al*. Ultrafast compound doppler imaging: providing full blood flow characterization. *IEEE Transactions on Ultrasonics, Ferroelectrics and Frequency Control* **58,** 134–147 (2011).
6. Bland, B. H. & Oddie, S. D. Theta band oscillation and synchrony in the hippocampal formation and associated structures: the case for its role in sensorimotor integration. *Behavioural brain research* **127,** 119–136 (2001).
7. Boyce, R., Glasgow, S. D., Williams, S. & Adamantidis, A. Causal evidence for the role of REM sleep theta rhythm in contextual memory consolidation. *Science* **352,** 812–816 (2016).
8. Bragin, A. *et al*. Gamma (40-100 Hz) oscillation in the hippocampus of the behaving rat. *J. Neurosci.* **15,** 47–60 (1995).
9. Buzsáki, G., Kaila, K. & Raichle, M. Inhibition and Brain Work. *Neuron* **56,** 771–783 (2007).
10. Buzsáki, G. & Wang, X.-J. Mechanisms of Gamma Oscillations. *Annual Review of Neuroscience* **35,** 203–225 (2012).
11. Buzsáki, G. Theta oscillations in the hippocampus. *Neuron* **33,** 325–340 (2002).
12. Cardin, J. A. *et al*. Driving fast-spiking cells induces gamma rhythm and controls sensory

responses. *Nature* **459,** 663–667 (2009).

13. Cauli, B. Revisiting the role of neurons in neurovascular coupling. *Frontiers in Neuroenergetics* **2,** (2010).
14. Chadwick, M. J., Jolly, A. E. J., Amos, D. P., Hassabis, D. & Spiers, H. J. A Goal Direction Signal in the Human Entorhinal/Subicular Region. *Current Biology* **25,** 87–92 (2015).
15. Colgin, L. L. *et al*. Frequency of gamma oscillations routes flow of information in the hippocampus. *Nature* **462,** 353–357 (2009).
16. Colgin, L. L. Rhythms of the hippocampal network. *Nature Reviews Neuroscience* **17,** 239–249 (2016).
17. Csicsvari, J., Jamieson, B., Wise, K. D. & Buzsáki, G. Mechanisms of Gamma Oscillations in the Hippocampus of the Behaving Rat. *Neuron* **37,** 311–322 (2003).
18. Datta, S., Saha, S., Prutzman, S. L., Mullins, O. J. & Mavanji, V. Pontine-wave generator activation-dependent memory processing of avoidance learning involves the dorsal hippocampus in the rat. *J. Neurosci. Res.* **80,** 727–737 (2005).
19. Devonshire, I. M. *et al*. Neurovascular coupling is brain region-dependent. *NeuroImage* **59,** 1997–2006 (2012).
20. Douchamps, V., Jeewajee, A., Blundell, P., Burgess, N. & Lever, C. Evidence for Encoding versus Retrieval Scheduling in the Hippocampus by Theta Phase and Acetylcholine. *J. Neurosci.* **33,** 8689–8704 (2013).
21. Ekstrom, A. D. *et al*. Cellular networks underlying human spatial navigation. *Nature* **425,** 184–188 (2003).
22. Fell, J. & Axmacher, N. The role of phase synchronization in memory processes. *Nature Reviews Neuroscience* **12,** 105–118 (2011).
23. Goense, J., Bohraus, Y. & Logothetis, N. K. fMRI at High Spatial Resolution: Implications for BOLD-Models. *Frontiers in Computational Neuroscience* **10,** (2016).
24. Hamel, E. J. O., Grewe, B. F., Parker, J. G. & Schnitzer, M. J. Cellular Level Brain Imaging in Behaving Mammals: An Engineering Approach. *Neuron* **86,** 140–159 (2015).
25. Hasselmo, M. E., Bodelón, C. & Wyble, B. P. A Proposed Function for Hippocampal Theta Rhythm: Separate Phases of Encoding and Retrieval Enhance Reversal of Prior Learning. *Neural Computation* **14,** 793–817 (2002).
26. Hillman, E. M. C. Coupling Mechanism and Significance of the BOLD Signal: A Status Report. *Annual Review of Neuroscience* **37,** 161–181 (2014).
27. Holschneider, D. P. & Maarek, J.-M. I. Mapping brain function in freely moving subjects. *Neuroscience & Biobehavioral Reviews* **28,** 449–461 (2004).
28. Huo, B.-X., Gao, Y.-R. & Drew, P. J. Quantitative separation of arterial and venous cerebral blood volume increases during voluntary locomotion. *NeuroImage* **105,** 369–379 (2015).
29. Huo, B.-X., Smith, J. B. & Drew, P. J. Neurovascular Coupling and Decoupling in the Cortex during Voluntary Locomotion. *Journal of Neuroscience* **34,** 10975–10981 (2014).
30. Jensen, O. & Colgin, L. L. Cross-frequency coupling between neuronal oscillations. *Trends in Cognitive Sciences* **11,** 267–269 (2007).
31. Jezek, K., Henriksen, E. J., Treves, A., Moser, E. I. & Moser, M.-B. Theta-paced flickering between place-cell maps in the hippocampus. *Nature* **478,** 246–249 (2011).

32. Kleinfeld, D. *et al*. A Guide to Delineate the Logic of Neurovascular Signaling in the Brain. *Frontiers in Neuroenergetics* **3,** (2011).
33. Lauritzen, M. Opinion: Reading vascular changes in brain imaging: is dendritic calcium the key? *Nature Reviews Neuroscience* **6,** 77–85 (2005).
34. Lawrence, J. J. & McBain, C. J. Interneuron Diversity series: Containing the detonation – feedforward inhibition in the CA3 hippocampus. *Trends in Neurosciences* **26,** 631–640 (2003).
35. Li, J.-Y., Kuo, T. B. J., Yen, J.-C., Tsai, S.-C. & Yang, C. C. H. Voluntary and involuntary running in the rat show different patterns of theta rhythm, physical activity, and heart rate. *Journal of Neurophysiology* **111,** 2061–2070 (2014).
36. Liao, L.-D. *et al*. Neurovascular coupling: in vivo optical techniques for functional brain imaging. *BioMedical Engineering OnLine* **12,** 38 (2013).
37. Lin, A.-L., Fox, P. T., Hardies, J., Duong, T. Q. & Gao, J.-H. Nonlinear coupling between cerebral blood flow, oxygen consumption, and ATP production in human visual cortex. *PNAS* **107,** 8446–8451 (2010).
38. Lisman, J. E. & Idiart, M. A. Storage of 7 +/- 2 short-term memories in oscillatory subcycles. *Science* **267,** 1512–1515 (1995).
39. Lisman, J. E. & Jensen, O. The Theta-Gamma Neural Code. *Neuron* **77,** 1002–1016 (2013).
40. Logothetis, N. K. What we can do and what we cannot do with fMRI. *Nature* **453,** 869–878 (2008).
41. Lubenov, E. V. & Siapas, A. G. Hippocampal theta oscillations are travelling waves. *Nature* **459,** 534–539 (2009).
42. Macé, E. *et al*. Functional ultrasound imaging of the brain. *Nature Methods* **8,** 662–664 (2011).
43. Mace, E. *et al*. Functional ultrasound imaging of the brain: theory and basic principles. *IEEE Transactions on Ultrasonics, Ferroelectrics and Frequency Control* **60,** 492–506 (2013).
44. Maguire, E. A., Frackowiak, R. S. & Frith, C. D. Recalling routes around London: activation of the right hippocampus in taxi drivers. *The Journal of Neuroscience* **17,** 7103–7110 (1997).
45. Montgomery, S. M., Sirota, A. & Buzsaki, G. Theta and Gamma Coordination of Hippocampal Networks during Waking and Rapid Eye Movement Sleep. *Journal of Neuroscience* **28,** 6731–6741 (2008).
46. Ogawa, S., Lee, T.-M., Kay, A. R. & Tank, D. W. Brain magnetic resonance imaging with contrast dependent on blood oxygenation. *Proceedings of the National Academy of Sciences* **87,** 9868–9872 (1990).
47. O'Keefe, J. & Recce, M. L. Phase relationship between hippocampal place units and the EEG theta rhythm. *Hippocampus* **3,** 317–330 (1993).
48. Osipova, D., Hermes, D. & Jensen, O. Gamma Power Is Phase-Locked to Posterior Alpha Activity. *PLOS ONE* **3,** e3990 (2008).
49. Osmanski, B.-F., Pezet, S., Ricobaraza, A., Lenkei, Z. & Tanter, M. Functional ultrasound imaging of intrinsic connectivity in the living rat brain with high spatiotemporal resolution. *Nature Communications* **5,** 5023 (2014).

50. Rajasethupathy, P. *et al*. Projections from neocortex mediate top-down control of memory retrieval. *Nature* **526,** 653–659 (2015).
51. Rvachev, M. M. On axoplasmic pressure waves and their possible role in nerve impulse propagation. *Biophysical Reviews and Letters* **5,** 73–88 (2010).
52. Schnitzler, A. & Gross, J. Normal and pathological oscillatory communication in the brain. *Nature Reviews Neuroscience* **6,** 285–296 (2005).
53. Schomburg, E. W. *et al*. Theta Phase Segregation of Input-Specific Gamma Patterns in Entorhinal-Hippocampal Networks. *Neuron* **84,** 470–485 (2014).
54. Sieu, L.-A. *et al*. EEG and functional ultrasound imaging in mobile rats. *Nature Methods* **12,** 831–834 (2015).
55. Sohal, V. S., Zhang, F., Yizhar, O. & Deisseroth, K. Parvalbumin neurons and gamma rhythms enhance cortical circuit performance. *Nature* **459,** 698–702 (2009).
56. Spellman, T. *et al*. Hippocampal–prefrontal input supports spatial encoding in working memory. *Nature* **522,** 309–314 (2015).
57. Stepan, J., Dine, J. & Eder, M. Functional optical probing of the hippocampal trisynaptic circuit in vitro: network dynamics, filter properties, and polysynaptic induction of CA1 LTP. *Frontiers in Neuroscience* **9,** (2015).
58. Tort, A. B. L., Komorowski, R. W., Manns, J. R., Kopell, N. J. & Eichenbaum, H. Theta–gamma coupling increases during the learning of item–context associations. *PNAS* **106,** 20942–20947 (2009).
59. Traub, R. D., Whittington, M. A., Stanford, I. M. & Jefferys, J. G. A mechanism for generation of long-range synchronous fast oscillations in the cortex. *Nature* **383,** 621–624 (1996).
60. Uhlirova, H. *et al*. Cell type specificity of neurovascular coupling in cerebral cortex. *eLife* **5,** e14315 (2016).
61. Wong, R. K., Prince, D. A. & Basbaum, A. I. Intradendritic recordings from hippocampal neurons. *Proceedings of the National Academy of Sciences* **76,** 986–990 (1979).
62. Wulff, P. *et al*. Hippocampal theta rhythm and its coupling with gamma oscillations require fast inhibition onto parvalbumin-positive interneurons. *PNAS* **106,** 3561–3566 (2009).

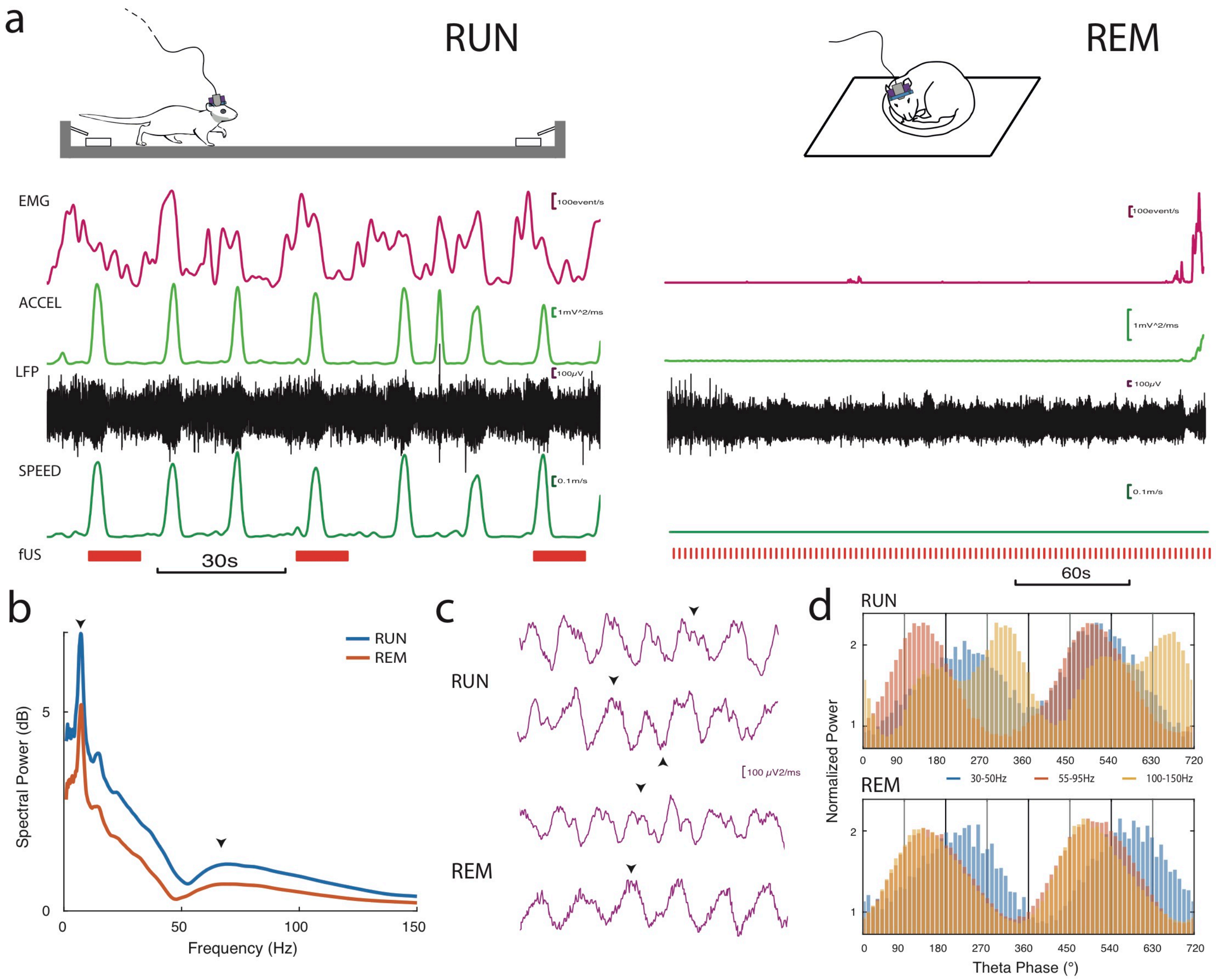

Figure 1: Simultaneous recording of hippocampal theta activity and hemodynamics during running and REM sleep (a) Recording Protocol during maze running (RUN) and typical REM sleep episode (REM). During running, electromyogram, accelerometer and LFP power are modulated by running speed. Hemodynamics are monitored at 500 Hz for 12-s epochs (red ticks). This protocol imposes 40s-lapse dead time for data processing during which the animal keeps running but no hemodynamics are recorded. **(b)** Time frequency spectrogramm displays high power in the theta-band (6-10 Hz) and mid-gamma (50-100 Hz) both during maze running and REM sleep. Gamma and theta power are higher during RUN than REM. **(c)** Mid-Gamma Power shows amplitude modulation by theta phase. Highest Power is found near the peak of theta oscillation (180°) **(d)** Slow-Gamma (30-50 Hz) Mid-Gamma (50-100 Hz) and High-Gamma (100-150) Hz power show theta phase modulation between RUN and REM. Note the 90°-shift between slow gamma and mid-gamma power peaks. High-gamma during RUN shows two distinct peaks around theta peak (180°) and theta trough (0°).

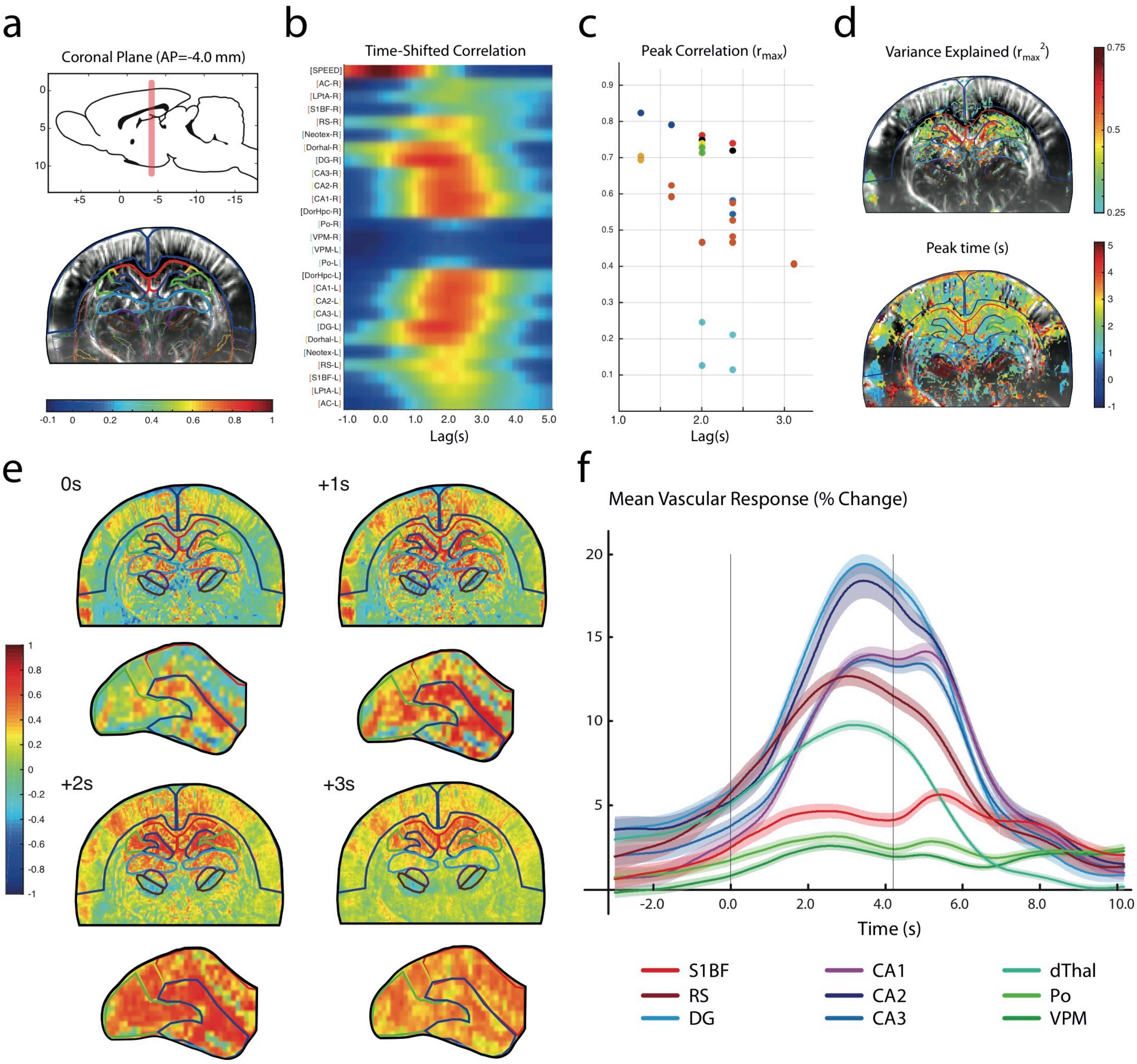

Figure 2: Hemodynamics during maze running show vascular propagation along the trisynaptic circuit **(a)** Typical Coronal Plane (AP = -4.0 mm from bregma) acquired by fUS. We use volumetric Waxholm atlas to perform semi-automatic registration (see Methods) and region labeling. We computed mean signal in 12 regions bilaterally : Neocortex (NeoCx - blue) including auditory cortex (AC) primary somatosensory cortex barrel field (S1BF) lateral parietal association cortex (LPtA) and retrosplenial cortex (RS) - Hippocampus including dentate gyrus (DG - blue), CA3 (green) CA2 (yellow) and CA1 region (red) - Thalamus, including dorsal thalamus (dThal - cyan), posterior thalamic nuclear group (Po) and ventral posteromedial thalamus (VPM). **(b-c)** Cross-Correlations between speed signal and 24 fUS regional signals. Highest correlations between speed and fUS signals were obtained for lags varying between 1.2 s (dorsal thalamus and dentate gyrus) to 2.2 s (CA regions - Neocortex), meaning that the hemodynamic reponse during running was region-dependent. Interestingly, we observed feedforward spread along the trisynaptic circuit in the hippocampus following DG - CA3 - CA1 scheme. Cortical areas peaked between 1.6 s to 3.0 s while thalamus showed strong difference between dorsal (dThal) and ventral subregions (Po and VPM). **(d)** Variance and peak time distributions. Speed explains variance in the hippocampus (maximally in the dentate gyrus) and dorsal thalamus. **(e)** Vascular propagation of activity starting in the dentate gyrus and dorsal thalamus and spreading to CA3 and CA1 regions. **(f)** Mean vascular responses to locomotion in 9 regions. Gray lines indicate run onset and stop. Each trial was rescaled to the average trial duration. Strongest responses are observed in the dentate gyris and CA2 region. Dorsal Thalamus (dThal) and retrosplenial cortex (RS) were active during running, whereas CA1 and CA3 started later and peaked after run end. (Mean response +/- s.e.d, n=15 recording sessions, 6 animals).

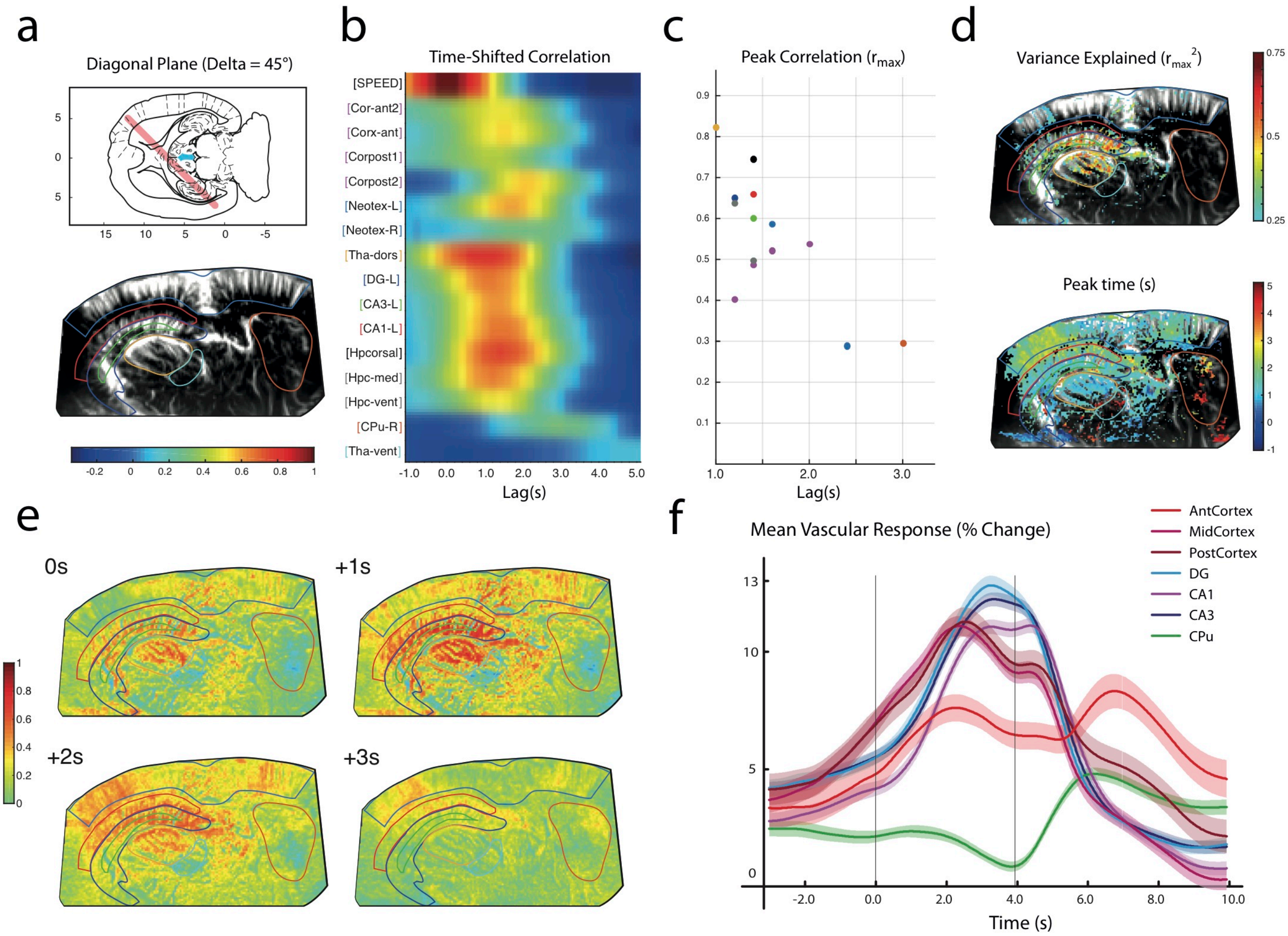

Figure 3: Whole brain hemodynamics during maze running dorsal hippocampal activation (a) Typical Diagonal Plane (Delta = 45° mm from antero-posterior axis) acquired by fUS. We use volumetric Waxholm atlas to perform semi-automatic registration (see Methods) and region labeling. We computed mean signal in 15 regions : Neocortex (NeoCx - blue) including anterior cortex (AC) midline cortex 1 (M1) midline cortex 2 (M2) and posterior cortex (RS) - Hippocampus including dentate gyrus (DG - blue), CA3 (green), CA1 region (red), Dorsal Hippocampus (dHpC - black), intermediate Hippocampus (iHpC - gray) and ventral hippocampus (vHpC - gray) - Thalamus, including dorsal thalamus (dThal - brown) and ventral thalamus (vThal - cyan) - Caudate Putamen (CPu - orange) . **(b-c)** Cross-Correlations between speed signal and 24 fUS regional signals. Consistent with coronal-plane recordings, highest correlations between speed and fUS signals were obtained for lags between 1.0 s (dorsal thalamus and dentate gyrus) to 2.2 s (CA regions - Neocortex), meaning that the hemodynamic reponse during running was region-dependent. We found higher activations in the dorsal and intermediate parts of the hippocampus than in the ventral part. No significant delay in activation onset was found. Cortical regions peaked between 1.6 s to 3.0 s while thalamus showed strong differece between dorsal (dThal) and ventral subregions (Po and VPM). Striatum was strongly activated 3.0 s after speed peak coincident with water uptake (reward). **(d)** Variance and Peak time distributions. Speed explains variance in the hippocampus (maximally in the dentate gyrus) and dorsal thalamus. **(e)** Vascular Propagation of activity along the septo-temporal axis of the hippocampus. Note that major activations are restricted to the dorsal half of the hippocampus. **(f)** Mean Regional Vascular Responses after trial alignement described in Fig. 2. Differential activations between dentate gyrus and CA1/CA3 regions are still visible. Note the different patterns in the cortical regions. Posterior and Midline cortices activity start prior to run onset and are maximal close to run peak. Anterior cortex strongly activates during reward uptake, concurrently with thalamus. Gray lines indicate run onset and stop. (Mean response +/- s.e.d, n=13 recording sessions, 5 animals).

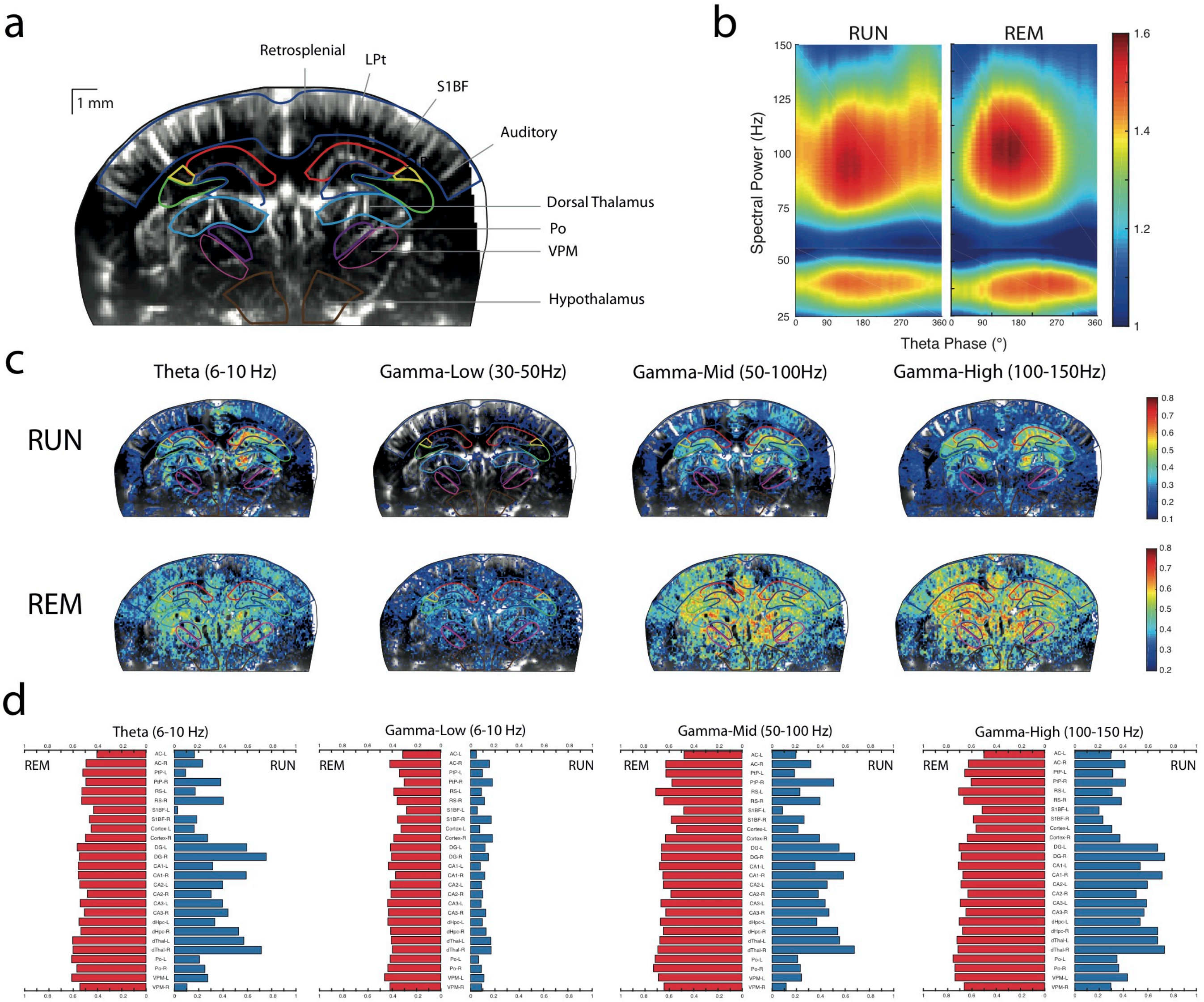

Figure 4: Theta and High-Gamma rhythms correlate with hemodynamic activity both during RUN and REM sleep. (a) Coronal fUS plane with 12 corresponding regions labeled after Waxholm registration **(b)** Wavelet based theta-phase spectrogram showing 3 different gamma sub-bands during RUN and two different gamma sub-bands during REM **(c)** Maximal correlation maps. For each voxel, the Pearson coefficient was calculated for lags varying between -1s and +2.5s for RUN episodes and between -1.5 s to +5.0 s for REM sleep. The maximal Pearson r_{max} and corresponding delay tmax was extracted similarly to Fig 2. We excluded voxels which maximal correlation was < 0.1 for RUN and < 0.2 for REM. Theta rhythm robustly explained variance in the dorsal thalamus and dentate while high gamma explained variance best in the CA3 and CA1 region. Low gamma did not correlate significantly with vascular activity and only weakly during REM. REM vascular activity was less variable across regions leading to a spatial smoothing of correlation maps **(d)** Maximal correlations between mean regional vascular signals and LFP power amplitude. Theta and gamma LFP signals were smoothed using 0.5 s gaussian kernel leading to a continuous envelope signal. Except for DG and dorsal thalamus, high-gamma envelope explained fUS signals better than theta activity, speed or accelerometer signal (see Supplementary).

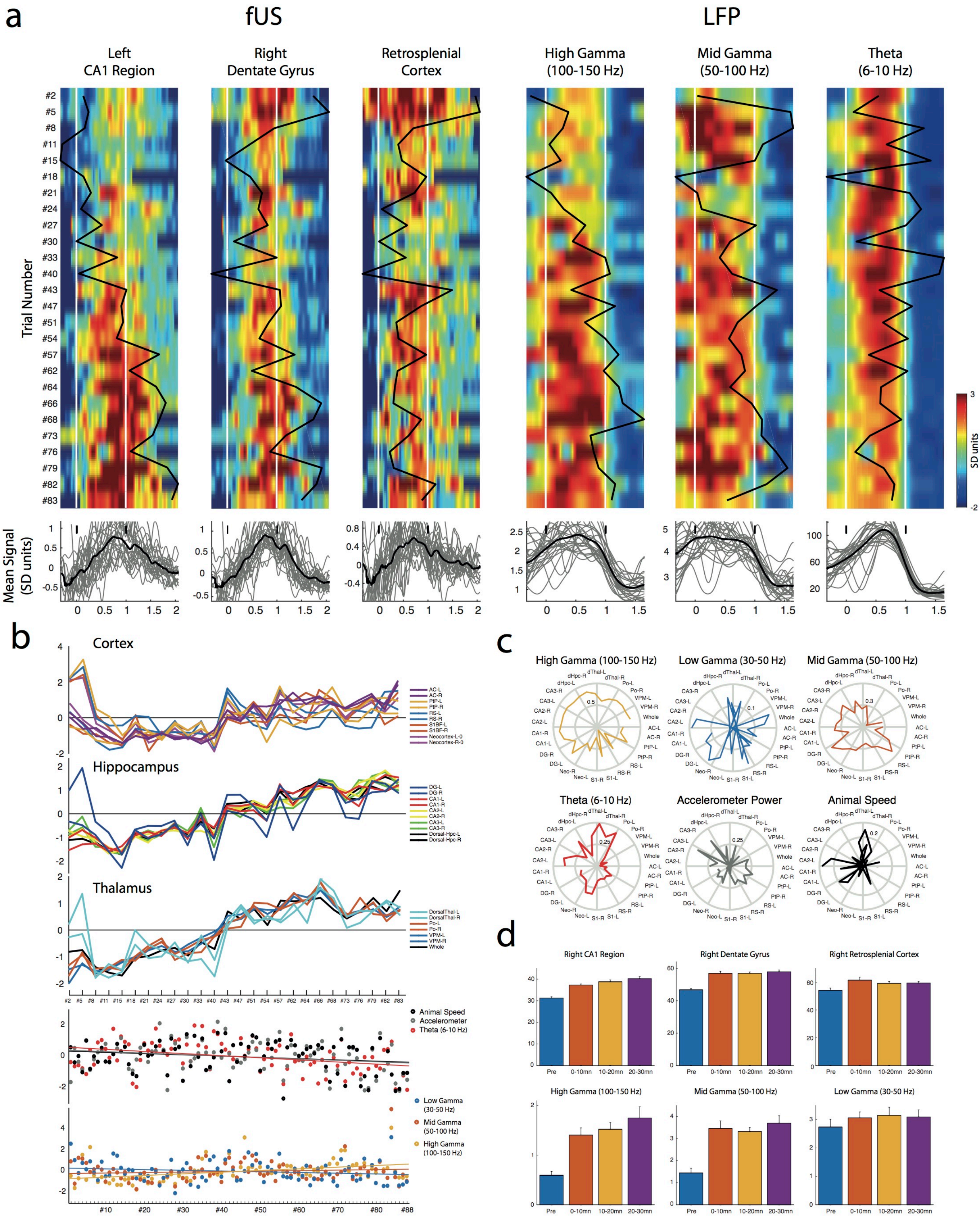

Figure 5: Vascular adaptation during the task parallels High Gamma Power increase

Figure 5: Vascular adaptation during the task parallels High Gamma Power increase (a) Top: Inter-trial display of vascular and electrographic events. All trials were aligned to the start and end (white lines) of each run leading to a normalized timing scale. Three regional vascular signals (left: CA1 region - Dentate Gyrus - Retrosplenial Cortex) and three LFP power signals (right: High Gamma - Mid Gamma and Theta) are displayed for comparison. Vascular signals showed strong inter-trial fluctuations including gradual increase in mean response (CA1), stable mean response (DG) and decreasing response over the course of the whole recording sessions. Vascular events are displayed in SD units (-2 to +3). These changes were not attributed to behavioral signals including speed, accelerometer an time spent running (see Supplementary Figure 5) Bottom: All trials (gray) and resulting mean signals (black) after timing normalization. **(b)** Top: Mean regional response versus trial number for all 8 cortical regions (top) 8 hippocampal regions (bottom) and 6 thalamic regions. Note the strong increase in the hippocampal (mainly CA) and thalamic regions. Bottom: Behavioral markers (speed, accelerometer and theta) showed a gradual decrease along the task while Low Gamma Power remained stable and high and mid Gamma showed increase. **(c)** Inter-trial Spearman Correlations between mean vascular progression and LFP power estimates, speed and acceleration. High-Gamma explained inter-trial progression in thalamus and hippocampal regions, while Mid-Gamma explained variance best in cortical regions. **(d)** Trial-averaged comparison between pre-task, start (0-10 mn), mid (10-20 mn) and end (20-30 mn) segments of the task. We extracted mean value for each trial and averaged for all trial in segment.

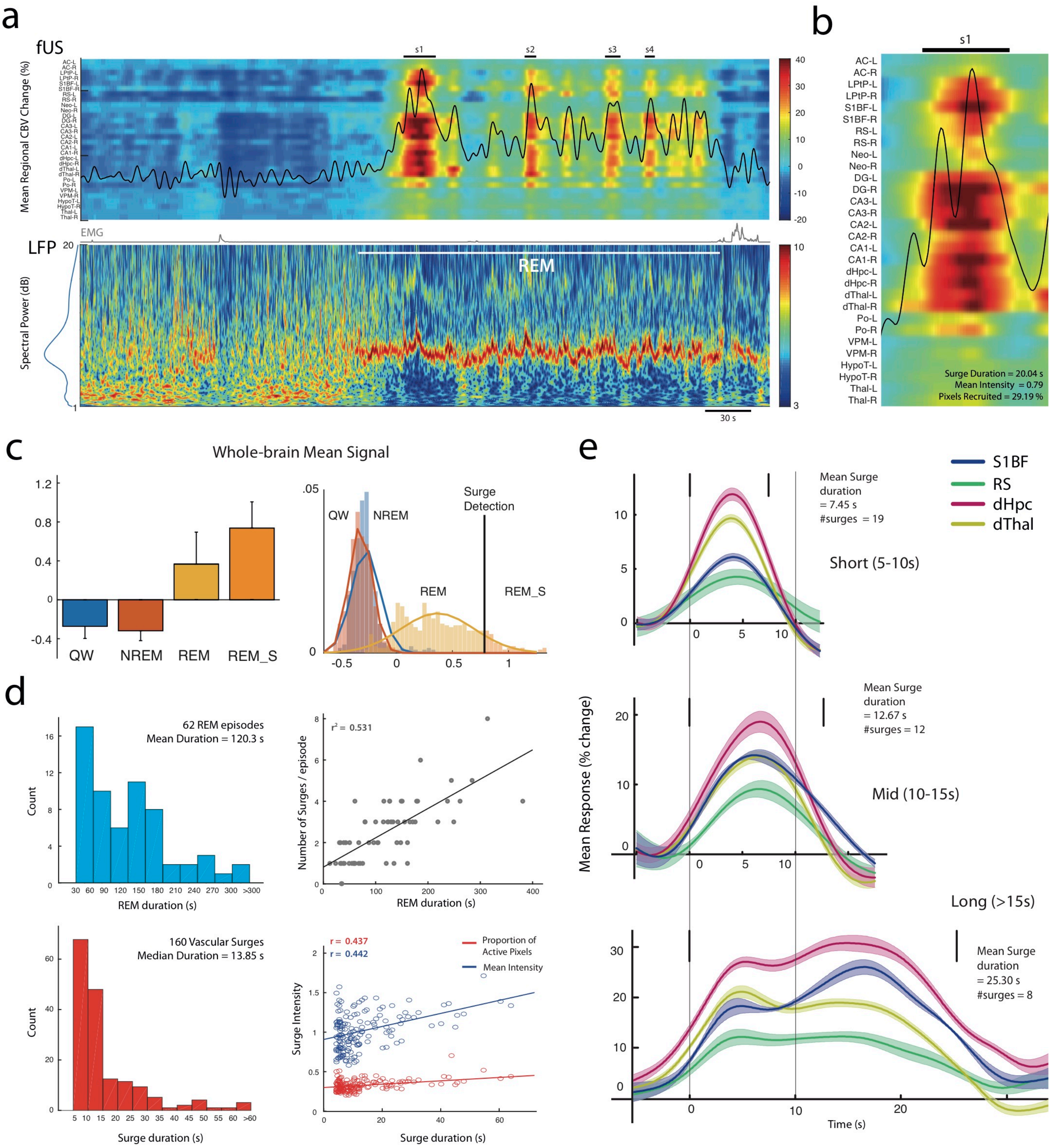

Figure 6: Hemodynamics of REM sleep show whole-brain synchronized fluctuations .

Figure 6: Hemodynamics of REM sleep show whole-brain synchronized fluctuations (a) Typical transition between NREM and REM sleep events **(Top)** Mean Regional CBV fluctuations in 26 recorded regions on a coronal plane and mean whole-brain vascular response overlay (black curve) **(Middle)** Electromyogram event frequency recorded from neck muscle activity **(Bottom)** Time-frequency spectrogram of hippocampal LFP electrode in the CA1 region. NREM sleep is characterized by desynchronised LFP between 0 Hz and 20 Hz and low-amplitude vascular fluctuations whereas REM sleep is characterised by sustained theta activity, higher vascular baseline and large-amplitude global "surges" of activation in most brain regions, ranging from 10 % to 50 % of signal increase (Delta F/F - Whole episode). These surges can be detected by thresholding the mean whole brain vascular response (black curve) or by thresholding individual pixel activity (see Methods). Example of four detected surges (s1 to s4 - black lines) **(b)** Details of a typical vascular surge during REM sleep episode. Dorsal Thalamus, Hippocampus and Neocortex (LPtP - S1BF) show large amplitude vascular activations, whereas ventral thalamic and hypothalamic regions show lower-amplitude hyperaemia. Note the earlier onset of dorsal thalamus and dentate gyrus in comparison with CA region and neocortex. **(c)** Whole-brain vascular distribution between quiet waking (QW), NREM sleep (NREM), REM sleep (REM) and REM surges (REM_S) : Temporal average within episode for one recording (+/- standard-deviation) (left) and histogram event distribution (right). (d) REM episodes and Surges statistics for all recording (6 animals). **(Left)** REM duration and Surge duration distributions **(Right Top)** Relationship between REM episode duration and surge occurrence. **(Right Bottom)** Relation between surge intensity and Surge duration (see Methods) show little correlation. Short surges (<15 s) show variable surge strength. **(e)** Variability of REM surge pattern. Surges are divided into short (5-10 s), mid (10-15 s) and long (>15 s). Mean Regional Response amplitude linearly increased with surge duration. Note the relative increase in hippocampal and somatosensory cortex responses. For long surges, thalamus response decreased over time while somatosensory cortex showed sustained hyperemia to match hippocampal level. Black ticks indicate surge onset and end in each group. Note that vertical scale is different across groups.

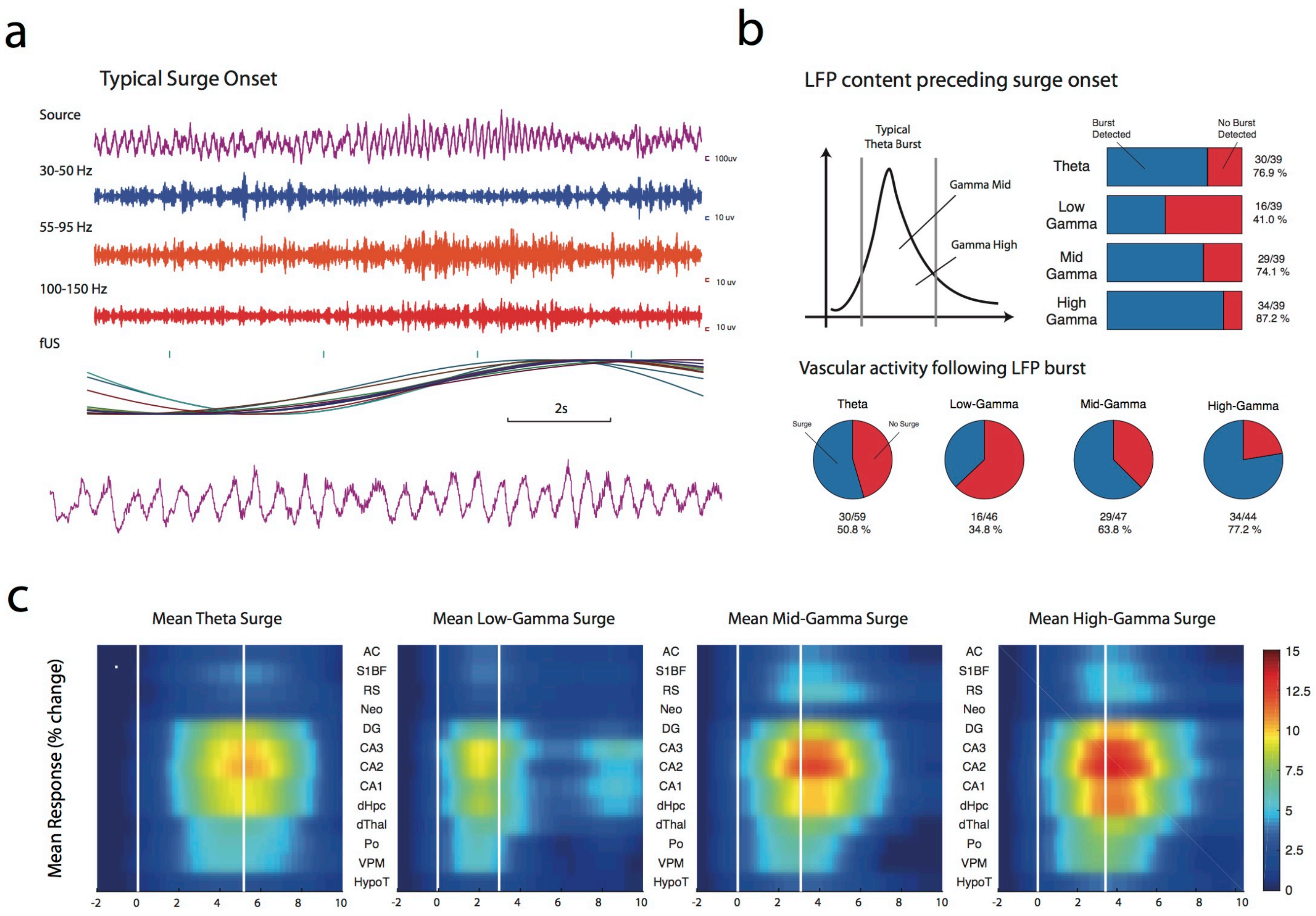

Figure 7: High-Gamma activity robustly precedes hippocampal vascular surges. (a) Phasic bursts of theta activity often precede vascular surges. Typical example of raw LFP signal from hippocampal electrode during REM sleep phasic theta episode. These phasic theta burst contain mid gamma and high gamma oscillations that are most prominent at the peak of theta and occur on the ascending phase of vascular surges. **(b) Top**: Statistical distribution of LFP events preceding vascular surges. For each vascular surge, we counted if the preceding 5 s contained significant burst activity in theta and three gamma subbands. **Middle**: For each LFP burst in theta and gamma band, we counted the propbability of occurence of a vascular surge. **Bottom** : Peak Timing Probability and Amplitude distribution of LFP events preceding surges. High gamma and Mid Gamma burst robustly preceded vascular activity, while a significant proportion of gamma events triggered weak to absent vascular events, leading to the conclusion that gamma is necessary but not sufficient for vascular surges to occur. **(c)** Band-specific Surge decomposition. For each LFP frequency band, we detected burst activity (threshold: 2 standard-deviation of whole-recording distribution). We averaged vascular responses for all detected theta and gamma burst and realigned them on burst start and end time. We display the mean vascular responsed associated with each LFP band. Note that theta burst typically last longer than gamma burst and that highest vascular responses are obtained in the hippocampus for mid and high gamma burst activity. Cortical areas are mainly recruited for mid and fast-gamma oscillations.

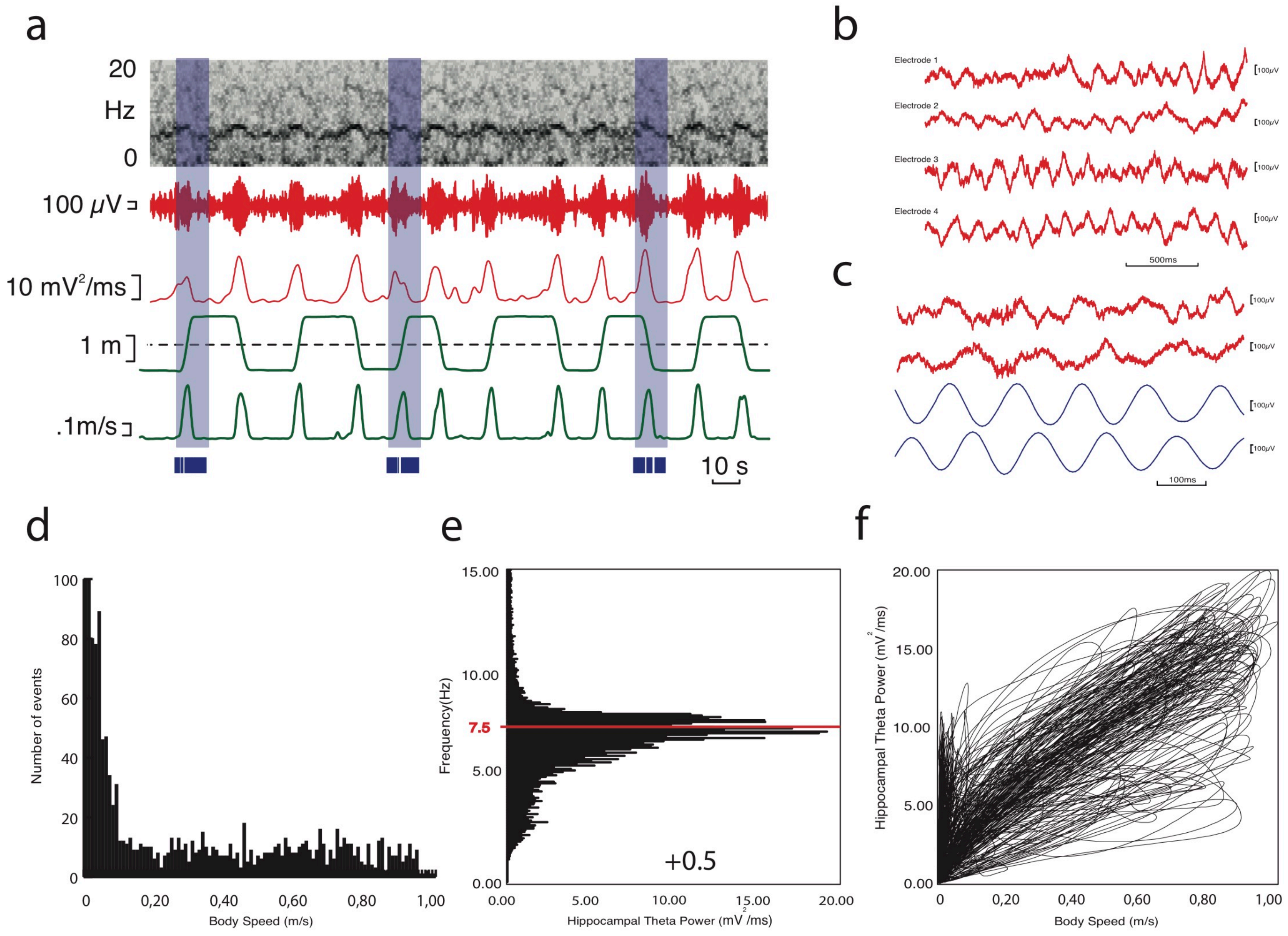

Figure S1: LFP recordings of theta activity in the rat hippocampus (a) Time frequency spectrogramm displays high energy in the theta-band (6-10 Hz) during maze running. Raw signal is filtered in this band and hippocampal theta power is extracted (red). This signal correlates strongly with the speed of the animal (green). Note the increase in frequency when peak running speed is obtained **(b-c)** Details of raw LFP signals from laminar electrodes presented early. Note the phase inversion between site 2 and site 3. We use the differential signal (2-3) to extract hippocampal theta power. **(d)** Histogramm of speed distribution during a typical recording session (30mn). Speed are evenly distributed between 0.1 and 1.0 m/s when the animal is running. Low speeds corrrespond to inter-trial episodes when the animal is drinking water from the tubes **(e)** Corresponding Frequency histogramm centered around 7.5 Hz. **(f)** Hippocampal theta power strongly correlated with spe ed of the animal (C=0.85). Note the linear relationship between the two variables.

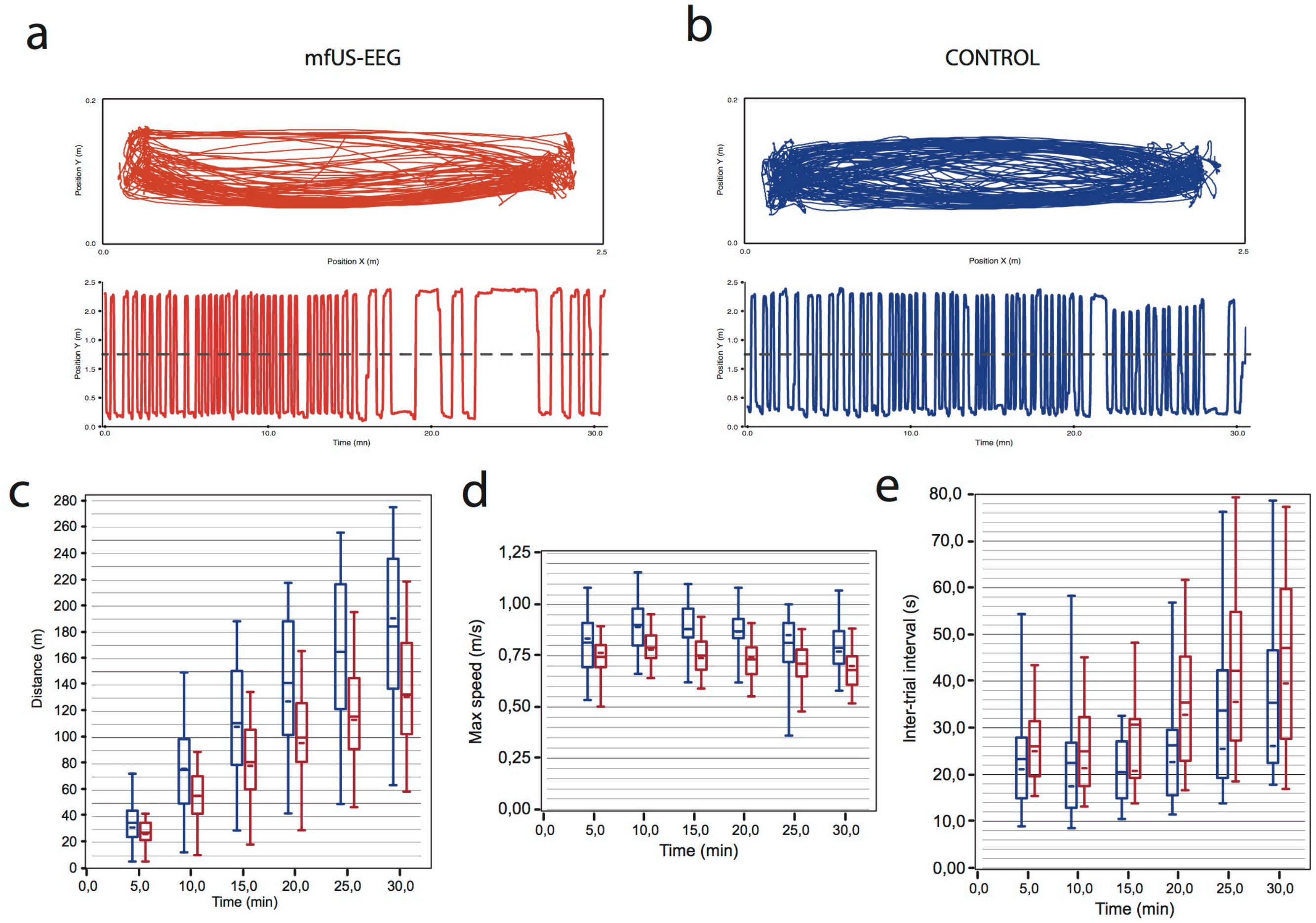

Figure S2: Effect of recording procedure on running (a-b) Typical trajectories observed in the mfUS-EEG condition (left, red) and untethered rats (right, blue), on the rectangular track as seen from above (up) and the distribution along the longitudinal axis versus time (down). Comparison of total distance traveled **(c)** maximum trial speed **(d)** and intertrial time interval between 30 mfUS-EEG recording and 26 controls after 5, 10, 15, 20, 25 and 30 mn. Tethered animals travel on average 70-79% less than control and mean travel is achieved 2 mn earlier. Maximum speeds is obtained between 5 mn and 15 mn for both groups. In this time interval, tethered animals speed peaks at 0.80 m/s while untethered animals peak at 0.88 m/s. Note the decay in peak speed between 5 mn and 30 mn affects control rats more than mfUS-EEG rats. Intertrial time interval is slowest between 5 to 15 mns for both groups. After this period it displays great variability among groups. All together, the effect of our recording procedure is significant but limited and it is more imputable to increased resting periods than to reduced movement. Graphs show mean, median, first and third quartile,1 and 99 percentiles.

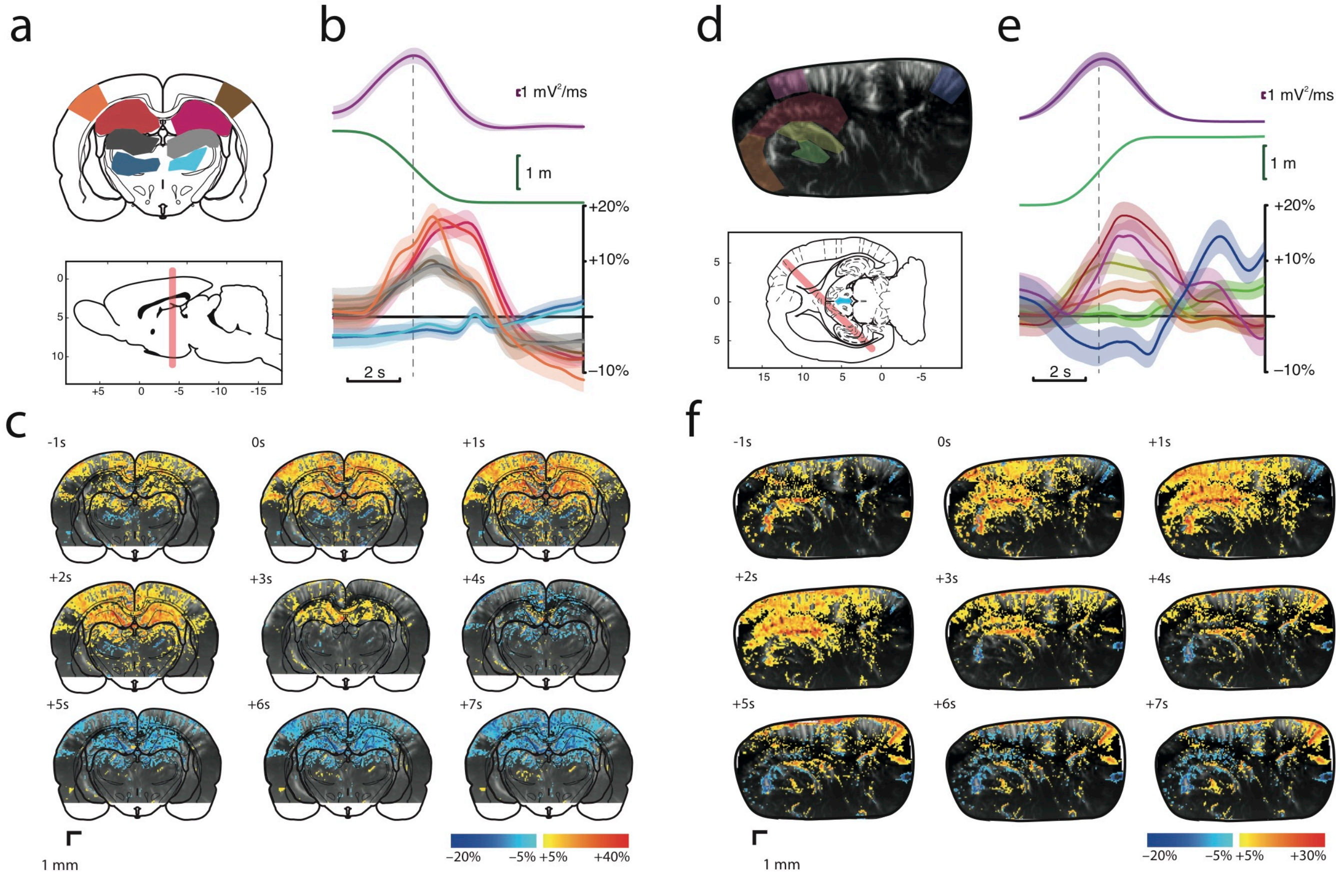

Figure S3: Hemodynamics of maze running Cerebral hemodynamics are monitored for 12 s episodes at 5 images/s for 30mn. Due to processing time, a 40 s-45 s «refractory» period follws each episode during which no fUS images is obtained. Rats are left to run freely during the whole recording session. Hence, we capture on average 1 trial over 4 runs. Data shown here is obtained from 20 runs. **(a-c)** Coronal plane hemodynamics. **(a)** Typical Coronal plane (-4.0 mm - AP axis) including dorsal hippocampus (dHpc) cortex, dorsal and ventral thalamus. This plane corresponds to the intra-hippocampal implantation allowing precise synchronous recording of LFP and hemodynamics at electrode tips location. 8 regions are segmented from the images using Paxinos atlas overlay. **(b)** Typical hemodynamic responses averaged across anatomical regions. After segmentation we extract mean signal from corresponding pixels for 8 regions somatosensory cortex (S1L brown, S1R orange), dorsal hippocampus (dHpcL red, dHpcR pink), dorsal thalamus (dThalL dark grey, dThalR light grey) and ventral thalamus (vThalL blue, vThalR cyan). Each trial is then realigned using mid-maze crossing as 0-reference (vertical dotted line). Mid maze crossing corresponds to mid travel along the longitudinal axis (green) and peak hippocampal theta power (purple). Responses are symmetrical except for S1. Hippocampal perfusion peak 1.5s after peak teak. All regions show hyperperfusion consecutive to a running except ventral thalamus which activity inscreases after running. **(c)** Individual pixel variations are realigned and binned into 1s-wide time windows to reconstuct a fUS movie. Maximal hyperpefusion (+40% relative to baseline) is found in the dorsal hippocampus and S1 cortex, while maximal hypoperfusion (-20% relative to baseline) is found in the ventral thalamus. Baseline is taken as mean signal over full recording, making relative perfusion 0-mean on average. **(d-f)** Diagonal plan hemodynamics. Plane includes left dorsal hippocampus (dHpc), ventral hippocampus (vHpc), dorsal thalamus (dThal), ventral thalamus (vThal), posterior cortex (S1) and anterior cortex (jaw region). Note the hyperperfusion in the anterior cortex peaking 6s after peak speed.

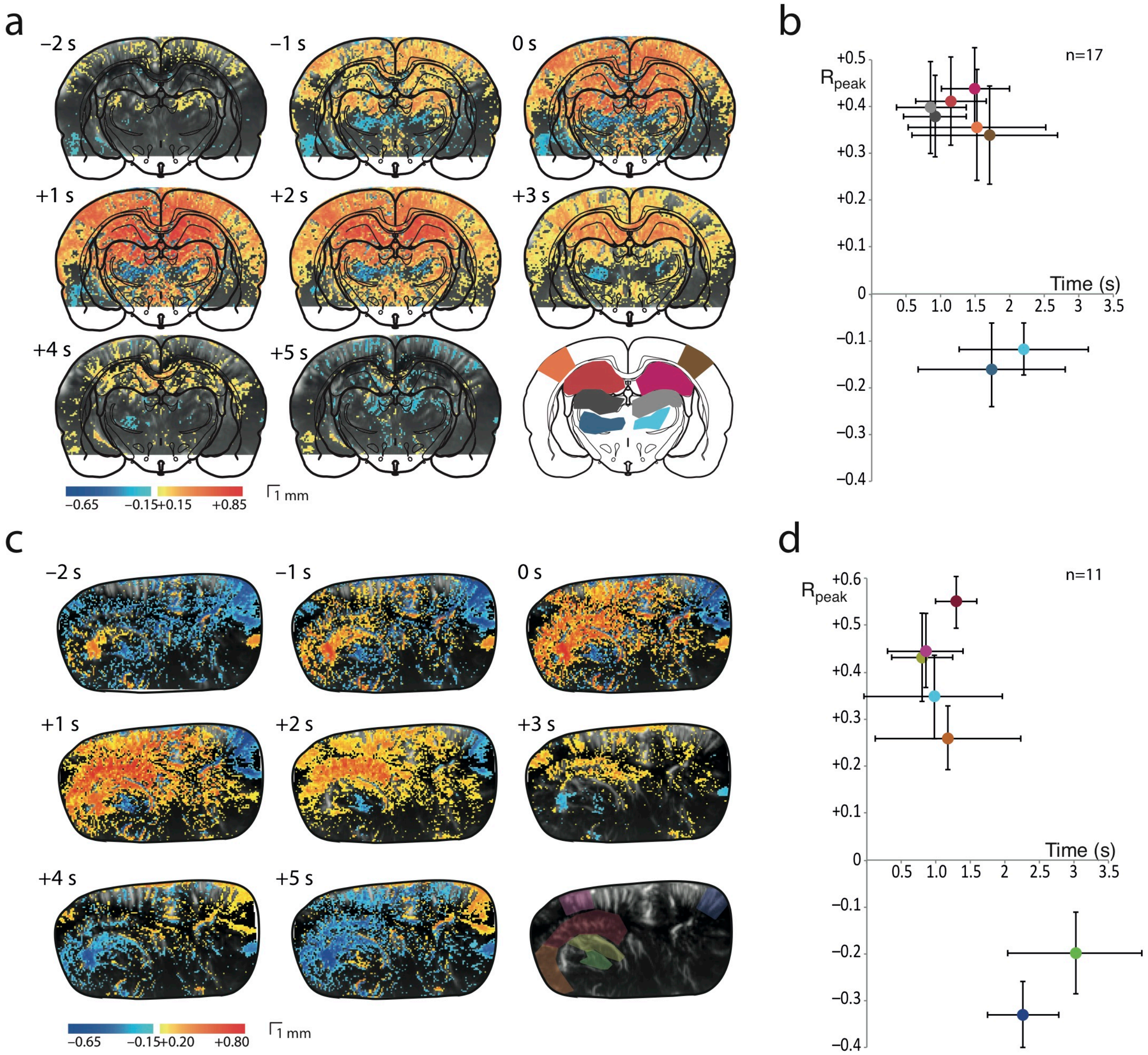

Figure S4: Cross-correlations between hemodynamic signal and electrical activity Maze experiment cross-correlation between local field potential theta-band power and ultrasound signal for each pixel at varying time lag (–2.0 to +5.0 s) over n = 20 midline crossings acquired in 30 mn, for coronal and diagonal planes. (a) Correlation maps computed from individual pixel responses and LFP theta-band power. There were no difference between LFP signals taken from left or right hippocampus (not shown). Maximal correlations is obtained for pixel in the dorsal hippocampus (r = 0.85) at +1.5 s time lag. Maximal anticorrelation is obtained for pixels in the ventral thalamus (r = -0.4) at +2.5 s time lags. (b) Distribution of maximal correlation Pearson coefficient and corresponding time-lags for 17 coronal plane recordings. Dorsal thalamus maximal correlation is obtained with 1.0 s time-lag, while dorsal hippocampus correlates strongly at 1.5-1.7s. Ventral thalamus and cortex display high variability suggesting complex inter-individual distributions. (c) Correlation maps computed from individual pixel responses and LFP theta band power over a diagonal field of view, including dorsal (dHpc) and ventral hippocampus (vHpc). Hyperfusion is significantly highly correlated to LFP in dorsal hippocampus than in ventral hippocampus, suggesting a lesser hemodynamic implication of ventral hippocampus in maze running. Note the strong incativation of jaw region anterior cortex (S1J) resulting in strong anti correlation at 0.0 s. (d) Distribution of maximal correlation Pearson coefficient and corresponding time-lags for 11 diagonal plane recordings. Ventral Hippocampus, Ventral thalamus and S1 cortex display high variability requiring finer analysis.

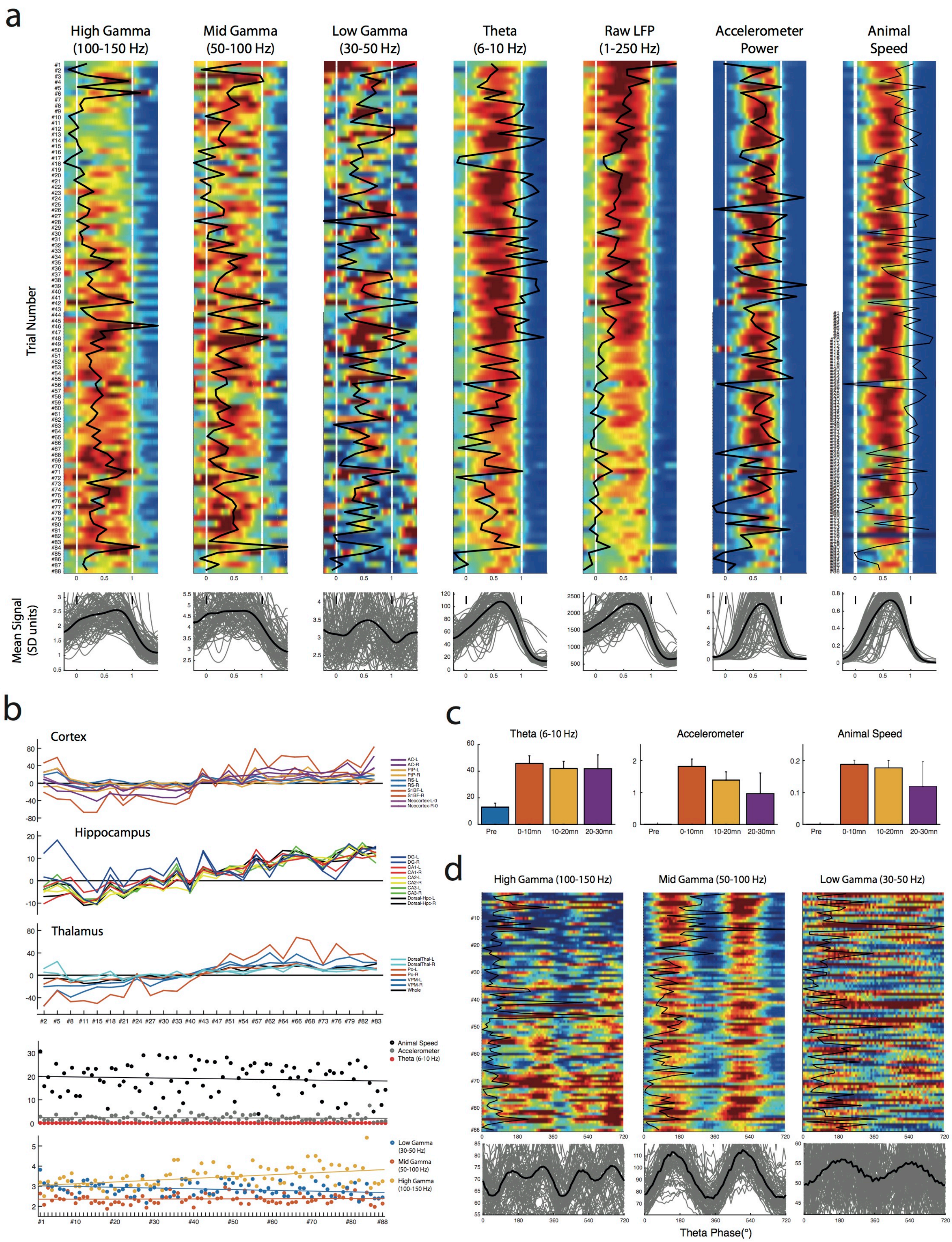

Figure S5: LFP Power signals and behavioral parameters during vascular adaptation

Figure S5: LFP Power signals and behavioral parameters during vascular adaptation (a) Trial Aligned Display of LFP Power Signal for the different gamma sub-bands (three left), theta and raw signals (center two) and body speed and accelerometer signals (two right). Because these signals are monitored continuously, adaptation is more visible. Note high-gamma monotonic increase starting around trial 30. **(b)** Top: Median regional response versus trial number for all 8 cortical regions (top) 8 hippocampal regions (bottom) and 6 thalamic regions. Median signals show increase restricted to hippocampus compared to Mean Bottom: Median Behavioral markers (speed, accelerometer) and Median LFP Gamma and theta evolution. **(c)** Trial-averaged comparison between pre-task, start (0-10mn), mid (10-20mn) and end (20-30mn) segments of the task. **(d)** Phase-Amplitude Cross Frequency Coupling evolution during task. CFC was computed between start and end of each run. Low Gamma displayed low modulation, Mid-Gamma display constant high-modulation while High-Gamma modulation progressed along the task. Note the 180°-shift between mid and high-gamma modulation patterns.

Chapter 7

Discussion

The main goal of this thesis was to investigate the vascular patterns associated with hippocampal theta and gamma rhythms. To achieve this goal, I have met several major technological challenges (1) designing and performing a novel surgical procedure including full craniotomy, intra-hippocampal electrode implantation and permanent prosthesis skull sealing (2) designing and performing animal conditioning to obtain stable periods of theta activity both during running episodes and REM sleep (3) developing new tools to record and analyse this rich and complex data. At the start of my PhD, functional Ultrasound was only available on anesthetized animals in acute experiment setup. With the help of the team, we have extended fUS to a framework where chronic simultaneous assessment of vascular and electrographic events is possible. This can be achieved for multiple regions of interest in a wide variety of behavioral paradigms. I hope that this work demonstrates the suitability of ultrasound imaging to study cognitive questions and that it will prompt a more extensive use of US waves in neuroscience behavioral studies.

Apart from the technological aspect of my work, I have gathered novel data on cerebral vascular responses in conditions close to natural movement. To the best of our knowledge, these patterns of vascular activations have never been observed in such conditions. The fact that we simultaneously monitored intracranial EEG signals can help us position these hemodynamic patterns in the framework of neuronal networks and brain rhythms, for which a large body of literature is available. Importantly, my work establishes that vascular activations observed both during spatial navigation and REM sleep are tightly and robustly associated with a certain type of gamma oscillations. The exact nature of this link still needs to be investigated in details. This matter is of crucial importance because, apart from animal studies, most of the data acquired in brain imaging - especially fMRI data - relies on indirect measures based on the complex relationship between neuronal and vascular activity.

7.1 The mfUS-EEG Method

7.1.1 Relevance for behavioral studies

fUS gives access to CBV and CBF monitoring in multiple cortical and sub-cortical structures with good spatial (100 μm x 100 μm x 400 μm) and temporal (200 ms) resolutions. Compared to the actual state-of-the-art available techniques, fUS presents several key advantages: (1) a high sensitivity that reveals individual trial variability circumventing the need for trial-averaging (2) a compatibility with electrographic recordings to compare hemodynamic patterns with their electrophysiological signatures (3) the possibility to study the animal in freely-moving conditions, which opens to a large body of behaviors and cognitive states. Our protocol offers such flexibility that animal movement is almost unimpaired. Fully-equipped rats for mfUS-EEG showed only differences with control rats at task onset in the total number of runs but not in peak speed indicating that the physical constraint imposed by the imaging system on the animal impairs long-term but not instantaneous performance.

The potential of fUS has been established in many applications ranging from peroperative use, early diagnosis of developmental disorder, transcranial stimulation and micro-vasculature assessment [Mac et al., 2011; Osmanski et al., 2014a; Errico et al., 2015]. However, the relevance of fUS for behavioral studies in neuroscience is not fully established. My work demonstrates that, despite important technological obstacles (full craniotomy, prosthetic implantation, lack of thorough reference vascular data), the type of information acquired is rich and informative. Importantly, we did not know if vascular activity during normal conditions would correspond to fluctuations in a detectable range.

Because many studies used electrical stimulation that can elicit unphysiological responses [van Raaij et al., 2011; Urban et al., 2014], it was unclear if natural movement and short periods of theta rhythm would elicit strong fluctuations in the vascular network. It appears that the level of these fluctuations is strongly separable from baseline activity (+/- 20% of variation relative to the mean), and so in many brain regions. Moreover, my data suggest that the different parts of a behavioral task as simple as stereotyped back-and-forth runs on a linear track encloses strong inter-trial variability, while classic behavioral and electrophysiological markers remain constant. This strongly questions the upfront averaging between start and end trials in *a priori* invariant conditions. Additionaly, sleep recording show that vascular activations are massive, brain-wide and complex during REM sleep. Given the importance of sleep in memory and normal behavior, the contribution of fUS to this field could be very large.

7.1.2 Type of information provided by fUS

Theoretically, the range of RBC speeds that fUS can correctly detect is axial speeds exceeding 10 mm.s^{-1}. This corresponds to vascular responses in pial arteries, penetrating arterioles and venules (see Table 4.1). To date, we cannot detect RBC speeds in the capillary bed because they are too slow (around 1 mm.s^{-1}), which is unfortunate because micro-circulation is thought to be the theater where most of the exchanges occur, in opposition to macro-circulation [Drake and Iadecola, 2007]. However, fUS provides an important source of information in the spatiotemporal dynamics of the hemodynamic response. The Doppler spectrum derived from compound images resulting from ultrafast acquisition contains different types of information. By filtering in the appropriate frequency range, one can exhibit responses corresponding to main vessels or smaller vessels in the parenchyma. This type of analysis would be fruitful to assess retrograde vasodilation and precise onset of hemodynamic responses [Chen et al., 2011; Hillman, 2014; Uhlirova et al., 2016].

In the current setup, we maximized the field of view in order to find regions associated with theta activity. To increase spatial resolution and sensitivity, one solution is to target a specific region. The decrease in image size can be converted into higher temporal sampling, resulting in higher sensitivity at low speeds. In the same fashion, spatial resolution can be lowered by increasing ultrasonic emission frequency at the cost of penetration depth. This would allow for finer resolution in the rat cortex or for whole-brain images in mice. Ultralight probes are currently under development to adapt mfUS in mice. Last, the use of contrast agents such as micro-bubbles can be a solution to image beyond the diffraction limit of US waves, even transcranially, but some development is necessary to make it available for behavioral studies.

7.1.3 The actual limits

mfUS-EEG is thus a promising technique but its technical and analytic development is far from mature. Though certain limits are imposed by physics and experimental feasibility, some others directly rely on computing power and miniaturization, which are constantly evolving. We list here the major limitations of mfUS-EEG as of 2016.

7.1.3.1 Technical Limits

Single Plane Imaging

The fact that fUS is limited to plane acquisition precludes the systematic monitoring of all brain structures during individual events. To overcome this problem, multi-plane imaging is one solution which entails averaging to compare vascular activations across planes. It also introduces time-distortion between planes taken at the start and planes taken at the end of acquisition, which can be worrisome if activations are not invariant. Another solution is to select target structures *a priori*, provided they can be intercepted by a single plane in the Waxholm space (for instance to include septal region, ventral, dorsal hippocampus and entorhinal cortex). This approach depends on the reliability and precision of plane selection based on visual anatomical landmarks before the experiment. Currently, we can only map Waxholm atlas *a posteriori*. Real-time atlas mapping is thus a clear direction of research for the years to come.

Pauses in the acquisition of fUS frames

In the current setup, the volume of acquired data is very large. Because a single Doppler image requires ultrafast acquisition of 200 compound frames and because the process of IQ demodulation to form compound images (beamforming) is not instantaneous, there is a trade-off between frame acquisition rate and computing time. The current strategy relies on the beamforming *in situ* which imposes "dead-time" periods of 32 s in "burst" mode and 1.0 s in "continuous" mode, to avoid memory overload. Another strategy, would be to save raw data without beamforming, in parallel with full continuous acquisition. To date, this strategy is ineffective because of limited data transfer capacity, but this will likely be feasible in the near future. However, such a sustained repetition of emission-reception cycles (the pulse repetition frequency is set at 20 kHz) will pose new problems in terms of total energy transmission and probe heating.

7.1.3.2 Protocol Limits

Need for a reference condition

We have extracted vascular patterns (as an absolute measure of brain hemodynamics) without a reference condition to compare with. Importantly, the definition of this reference state is not straight-forward because background activities show a strong diversity, even between supposedly "un-stimulated" states, such as quiet waking, light sleep and slow-wave sleep. It is known that most behavioral states are associated with distinct activation and deactivation patterns [Nir et al., 2013; Raichle, 2009]. Pre-task baseline activity levels gave a clear separate statistical distribution, precluding appropriate comparison. To overcome this, we have normalized activations by mean activity over a whole recording, which is questionable if vascular activations are an aggregate of multiple "regimes" (like UP and DOWN states, for instance). Depending on the object of study, one solution is to compare control trials and stimulus trial, in the same manner as classical T-maze task comparison (see subsection 7.3.2).

Cranial window necessity

The strongest obstacle for a broad utilization of mfUS-EEG protocol is the necessity for craniotomy. The prosthetic skull approach that we developed entails the removal of a large portion of the skull and the sealing of the prosthesis onto the bone (which requires complete impermeability and the absence of bubbles). Exposing such a large portion of brain tissue raises new questions about homeostasis after surgery, mechanical stability of the brain in the skull and tissue elasticity. This kind of surgery also requires to take great care of meninges (that stick to the inner wall of the skull in aged rats). This procedure is long (4-6 h on average) and requires practice to be performed routinely. Another solution is the thinned-bone approach, which we rejected for the impermanence of the field of view and the limited time window for data acquisition (which arises to a lesser extent in our approach).

7.1.3.3 Analysis Limits

Limits of correlation analysis

Pearson correlation analysis is commonly used as a standard measure of the statistic dependence between two variables (how much they tend to covariate). In this thesis, we used it to compare multi-modal signals such as theta power and mean vascular response in the dentate gyrus. However, Pearson correlation suffers some limitations such as blindness to non-linear associations and over-sensitivity to outliers [Pernet et al., 2013]. Recent evidence demonstrates that neurovascular coupling is non-linear [Lin et al., 2010], therefore, we should develop methods that take these non-linearities into account. Such type of analysis is routinely performed to explain variance in fMRI studies. Deconvolution techniques aim at estimating the best convolution kernel to generate a given time-series from another one. The differences observed between the averaged responses in the dentate gyrus (sustained response, low amplitude) and CA1 region (peaked response, high amplitude) suggest that such a method would give different results than mere correlation analysis.

Potential Locomotion effect

We cannot completely exclude a contribution of a locomotion effect, for instance due to higher heart rate during running. However, the maze task is not limited to running, as it involves navigation processing. Animals show a learning curve when they train for the task. Furthermore, a locomotion effect would likely be uniform across the brain, whereas we find both increases and decreases in blood perfusion. Thus, such a potential effect is not strong enough to mask differential changes and dynamics across areas. Our animals did not engage in intensive motor activity, at least not above the requisite for most cognitive and pathology experiments. A possible solution to account for this quantitatively is to record the animal's electrocardiogram and to use heart rate as an indirect estimation of a potential locomotion effect.

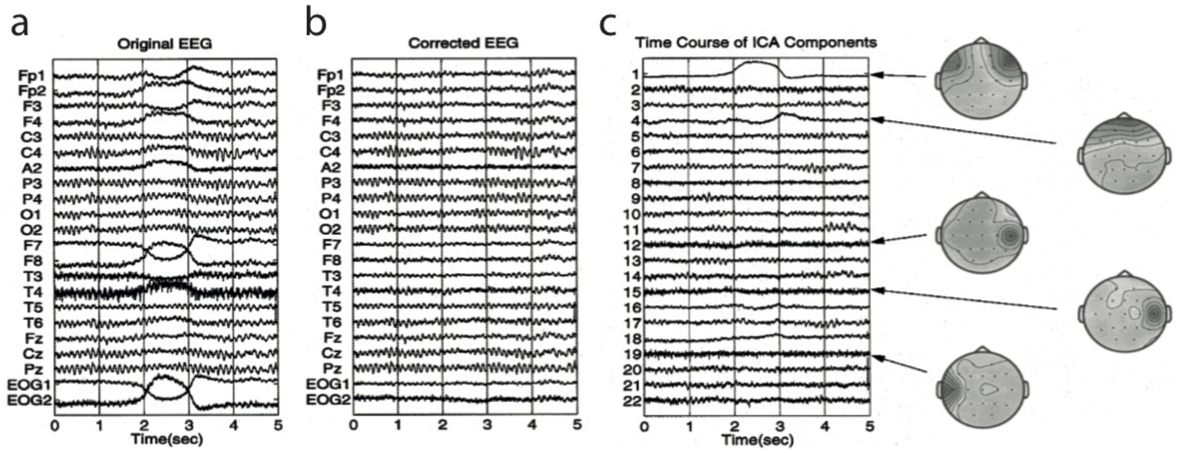

Figure 7.1 – Demonstration of electroencephalogram artifact removal by Independent Component Analysis (ICA) (a) A 5-s portion of an EEG time series containing a prominent slow eye movement. **(b)** Corresponding ICA component activations and scalp maps of five components accounting for horizontal and vertical eye movements (top two) and temporal muscle activity (lower three). **(c)** EEG signals corrected for artifacts by removing the five selected ICA components in **(b)**. Adapted from [Jung et al., 2000].

Large amount of data

One of the intrinsic problems of gain in both spatial, temporal resolutions and computing power is the exponential increase in data size. In the mfUS-EEG protocol, we are in a situation were the dimensionality of the data is too large (a single recording contains between 2000 and 5000 time samples of 15,000 pixels per image) to avoid reducing it by making projections. Additionally, LFP recordings are derived from multiple electrodes and can be filtered in multiple frequency bands. The mere display of this complex data is thus challenging. The main axis of projection that we have chosen in this thesis was to extract spatial averages in vascular images based on atlas overlay. Doing so decreases the data dimensionality from about 15,000 to 20-30. Additionally, we selected two LFP signals per animal that gave the highest correlations (only the best electrode is showed here). It is reasonable to think that making such projections might discard potential statistical dependences.

The structure of our data is however highly sparse (90% of the pixels in a given region show strong similarity). Thus we need methods to decrease the redundancy in vascular images. In first approximation, this can be implemented by Independent Component Analysis (ICA) and Principal Component Analysis (PCA). These two algorithms extract relevant axes or directions, onto which the dataset is represented in a more ordered way. Briefly, PCA finds the orthogonal axes that maximize variance prediction and ICA finds the axes that maximize mutual independence. Such an approach is commonly used in EEG for artifact removal and source detection [Jung et al., 2000; Hyvarinen and Morioka, 2016] (see Figure 7.1). Preliminary results show that ICA can extract functional activation components and remove movement artifacts. A second solution would be to use the intrinsic similarity of neighbouring pixels to build incrementally regions that minimize inter-region variability, such as the SLIC method. This approach is somewhat similar to K-means algorithm with a correlation criterion [Ren and Malik, 2003; Achanta et al., 2010].

Biases induced by regional averaging

The vascular fluctuations that we have recorded are an absolute measure of brain hemodynamics (proportional to the amount of red blood cells in the image). We extracted mean regional responses by averaging signals based on anatomical delineations. However, these regions contain both high-amplitude signals (large vessels) and low-amplitude ones (small vessels) in proportions that can be variable from one region to the other. This poses several problems. First, regional averaging gives a stronger weight to large vessels in most regions, though it might not be the most informative signal and might respond differently to stimulation. Second, this absolute signal depends on the depth of the recorded image (even after adjusting mean and standard-deviation). Comparing abruptly these regional signals without correction might be inappropriate. For example, the vascularization in the hippocampus is known to be different along the septo-temporal axis and between subfields. How this affects mean regional signals needs further investigation. Last, anatomical delineations, because they are not perfect, introduce false positive and might bias regional segmentation. Regions of interest could also be extracted from individual pixels signals based on their functional response to stimulation, so that averaging could be performed reliably.

7.1.4 Further Improvements

As mentioned above, fUS is constantly evolving. Technological improvement in computing power will soon allow **continuous acquisition** for periods exceeding 12 seconds, to acquire with high sampling a full REM episode or epileptic seizure. Miniaturized probes have already been delivered and tested to adapt mfUS-EEG on **awake mice** with encouraging results to perform **transcranially**, without the need of a contrast agent. Adapting mfUS-EEG to mice will open the door to the study of multiple pathologies, due to the availability of genetically-modified models. Another direction of active research is the design of **two-dimensional probe arrays** to perform real-time three-dimensional acquisitions. This will unlikely be achieved before 2 to 5 years. One of the current lacks of mfUS is that it discards information about blood oxygenation. **Coupling mfUS-EEG with optical techniques**, such as fNIRS offers a way to monitor simultaneously CBV, CBF and blood oxygenation levels to give a full picture of the hemodynamic and metabolic response, which is a very actual field of research. Finally, the generalization of optogenetics and more recently sonogenetics [Ibsen et al., 2015] offers the potentials to dynamically interact with neuronal networks and to monitor vascular responses with US waves.

7.2 Significant Advances

7.2.1 Brain imaging in movement

Free movement vs Virtual Reality

Spatial navigation is an extensive subject of research. But the current state-of-the art is divided in two types of studies. On the one hand, animal models make use of electrodes to monitor the neural correlates of specific aspects of brain navigation, which have been extremely successful in revealing place cells, head-direction cells, grid cells (described extensively in Chapter 2). On the other hand, human studies - mainly based on fMRI and virtual reality systems - have unraveled specific structures involved in path integration and spatial navigation in analogous task-designs as the ones used in animal studies. Experiments with virtual radial maze revealed evidence for hippocampal activity, frontal cortex activity [Astur et al., 2005] but also parhippocampus, precuneus and fusiform area[Shipman and Astur, 2008]. Similarily, fMRI recordings while participants made goal direction judgments based on a previously learned virtual environment showed activation in the human entorinhal/subicular region revealing a strong “goal-direction signal” [Chadwick et al., 2015]. Finally, the rare studies on epileptic patients have provided valuable results to expose the human neural correlates of location [Ekstrom et al., 2003] and frequency-specific correlates of memory [Watrous et al., 2013]. Though virtual-reality environments have unique attraits like reproducible conditions and modular control over sensorimotor cues, they cannot reproduce exactly the complex multi-sensory conditions observed in natural movement [Bohil et al., 2011].

Complex Pattern of activity

Our work brings a new light on the fundamental dynamics of functional hyperemia and on the spatio-temporal dynamics of the vascular network during active locomotion. Recent findings reported various CBV patterns in mice adjacent cortices (somatosensory and frontal) in response to voluntary locomotion, including different coupling to electrical activaty [Huo et al., 2014] and different quantitative separation between arteriole and venous blood [Huo et al., 2015]. The vascular activity during locomotion in deep structures is relatively underreported, due to the lack of appropriate methods. Studies using autoradiography radio-tracers in rats performing treadmill running found changes in CBF in dorso-lateral striatum, motor cortices and cerebellum [Holschneider and Maarek, 2004]. However, most of these studies rely on the use of treadmills or similar setups which generate different patterns of electrical activity than the ones observed in natural movement, possibly because of the discrepancies between vestibular and visual sensory inputs [Li et al., 2014].

During running, we found strong activations in multiple brain regions, some of which might be associated with sensory stimulation (dorsal thalamus), others with spatial processing (dorsal hippocampus, retrosplenial cortex) and others with reward (striatum). Diagonal planes revealed clear dichotomies between functional groups including (1) differential activations between ventral and dorsal thalamic regions both in activation onset and strength. In some animals ventral thalamic activation occurred concurrently with frontal cortical activation during reward uptake (S1lip region - S1 jaw) suggesting a possible thalamic relay in sensory stimulation of the face and limbs (2) differential activations between anterior and posterior cortices. Anterior activation was strongly associated with dorsal striatum activation while posterior cortex was associated with dorsal hippocampus. Motor cortical activations were observed in some rats. Disentangling the relative implication of these activations in sensorimotor processing, cognition and reward will help make this pattern less complex. This corresponds to one of the proposed experiments described in subsection 7.3.2.

Finally, we observed robust vascular patterns in the hippocampus across animals and sessions. The fundamental responses of hippocampal subfields presented subtle differences in their activation pattern. Dentate gyrus activity was sustained while the one in CA1 region was more transient and "phasic". What are the differences governing these changes ? More fundamentally, we can study the nature of the link between physical stimulation and response amplitude. Notably, we can investigate if this response is linear or if we find activation thresholds or regional dependences.

7.2.2 Propagation of "vascular brain waves"

Trisynaptic contamination

For the first time, we have been able to monitor vascular fluctuations of all structures contained in typical coronal and diagonal planes, during unimpaired movement. The vast majority of our recordings shows a strong sequential pattern of activation originating in the dorsal thalamus and propagating to the dorsal hippocampus and neocortex, both during running and REM sleep episodes. On some recordings, we could clearly observe subicular activation following the CA1 activation. Entorhinal cortex and septal regions were not systemically sampled due to the errors in plane selection protocol. The hemodynamic responses of these different regions present specific activation profiles, which could very well map feedforward inhibition in the trisynaptic circuit [Lawrence and McBain, 2003; Stepan et al., 2015].

Vascular surges of activity

The very same pattern can be observed during REM sleep episodes, which vascular profile displays striking differences with quiet waking and non-REM sleep. REM sleep episodes consist in elevated baseline in most brain regions and recurrent phasic increases in CBV levels that we called "surges". These surges originate in the thalamus and spread in the dorsal hippocampus and neocortex. The magnitude of the surge was strongly associated with cortical contamination, meaning that small surges had limited cortical extent while large ones spread widely to cortical areas. One of the possible explanation of these surges is that is supports memory-consolidation and strengthens hippocampal output to cortical areas [Datta et al., 2005]. Given that REM sleep was recently proved to play a role in hippocampus-dependent memory task [Boyce et al., 2016], it is possible that such surges are implicated in this process. The striking similarity of vascular patterns observed during RUN and REM sleep suggests that surges might be associated with replay of past events. However, these patterns presented subtle differences, notably the absence of dissociation between ventral

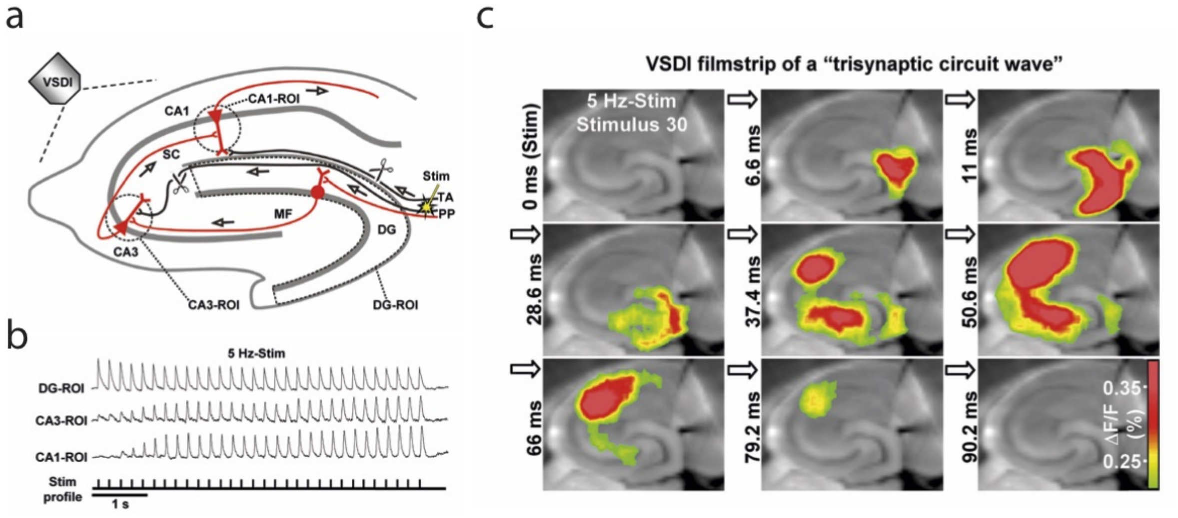

Figure 7.2 – The hippocampal trisynaptic circuit and monitoring of "trisynaptic circuit waves" by voltage-sensitive-dye imaging (VSDI). (a) Schematic drawing of the hippocampal trisynaptic circuit (marked in red). Scissors illustrate specific deafferentations. (b,c) VSDI filmstrip and recording traces depicting trisynaptic circuit waves evoked by theta-frequency (5Hz) stimulation of perforant path fibers. Warmer colors in **(c)** indicate higher neuronal activity (i.e., excitatory postsynaptic potentials and action potentials. Adapted from [Stepan et al., 2015].

and dorsal thalamus and higher variability in cortical recruitment in REM sleep compared to running.

What is the support of vascular waves?

Though it was difficult to give an estimate of the propagation speed of the vascular waves we observed, because the different structures were not linearly aligned, we are confident that such speed lies in a range between 1 and 10 mm.s^{-1}. Electrical waves have already been shown to be non-stationary and to propagate from one region to the next [Lubenov and Siapas, 2009; Patel et al., 2012]. *In vitro* 5-Hz stimulation in deafferented mice hippocampal slices have revealed sequential "trisynaptic waves" which pattern is strikingly similar to the one we observed, but on a 20-fold faster timescale (see Figure 7.2). Some authors have also proposed that mechanical waves accompany the propagation of action potentials in the brain [Rvachev, 2010]. The speed of propagation of our vascular waves does not contradict such a theory. Investigating if a "carrier" facilitates wave propagation or if they are just a by-product of sequential neural activation is an interesting transverse axis of research.

7.2.3 Vascular "Adaptation"

Another unexpected result in our study was that trial vascular fluctuations showed intrinsic variability, though behavioral parameters such as speed, acceleration remained constant. This variability was strongly associated with the timing during the task: start trials elicited weaker activation in downstream regions than end trials. This pattern was observed robustly in successive recordings in the same animal and strengthened across recording sessions, suggesting a reinforcement of the vascular response both during the task and across recording sessions. This progression was region-dependent and occurred markedly in the CA1 and CA3 regions, dorsal thalamus and sensorimotor cortices. Vascular activations were more constant in the dentate gyrus and showed a decrease in retrosplenial cortex. This “vascular adaptation” was present in most animals, though to a different extent and not always abruptly. We excluded a potential influence of electrode implantation because control electrode-free animals displayed the same pattern.

This phenomenon raises important questions. In terms of analysis, it suggests that inter-trial averaging must be performed over a small number of trials. Because different regions did not present the same profile of adaptation, it is important to question the functional relevance of this phenomenon. Importantly, this is relatively independent from performance or inversely associated with speed and theta rhythm. We propose vascular adaptation to be related to learning or synaptic plasticity. Due to the simplicity of the task, animals are in conditions of overtraining. Because reward is expected and given in 100 % of trials, it appears extremely profitable to properly encode and strengthen the spatial cues used in such context. This kind of adaptation could be similar to synaptic plasticity so that functional hyperemia occurs most effectively after repeated trials. We propose further experiments to test this hypothesis in subsection 7.3.1.

7.2.4 Gamma rhythms and neurovascular coupling

Several multi-modal studies have investigated the neural correlates of functional activation in a variety of protocols and species. This mainly stems from the intrinsic difficulty to interpret BOLD signal [Logothetis, 2008]. Such studies have already established a strong link between LFP signals in the gamma range, and multi-unit activity though to a lesser extent, and BOLD signals [Logothetis et al., 2001; Schlvinck et al., 2010] and more precisely between CBV fluctuations and high-frequency range ($>$ 50 Hz) activity [Niessing, 2005; Huo et al., 2014] (see Figure 7.3). However, this has never been done in conditions of free movement in animals performing a behavioral task, which is what we present here.

Theta implication

Though ubiquitously present in the brain, theta activities are not strongly associated with the fluctuations of CBV recorded in our task. Theta power correlates strongly with CBV fluctuations in the dorsal thalamus, dentate gyrus and CA region, though to a lesser extent. However, there is no evidence that these activations are linked to theta specifically and not to a given aspect of running. We obtained similar correlation maps using theta power envelope, accelerometer and body speed. During REM, phasic episodes of theta activity correlate strongly with vascular patterns while tonic theta did not. Once again, we cannot conclude whether this link arises from spurious correlations or not. However, the pattern of vascular adaptation observed in running rats was independent or inversely linked to theta activity. Thus, we propose that CBV fluctuations associated with theta activity result from common causes but do not cause vascular activations. To us, theta activity reflects global synaptic events which presence might be required to precisely time neuronal sequences and send them to distant brain regions. Conversely, vascular responses correspond to higher oscillations nested in theta activity. Theta, as a physiological process, does not seem to be linked

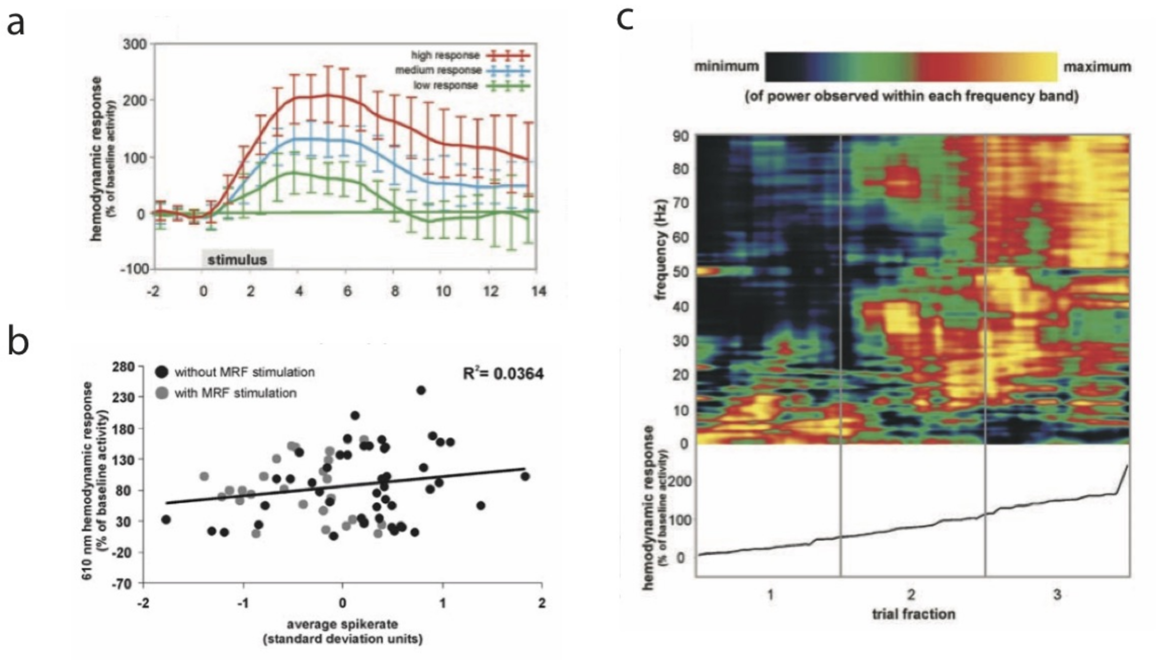

Figure 7.3 – Hemodynamic Signals Correlate Tightly with Synchronized Gamma Oscillations Hemodynamic and electrophysiological responses to different stimulus contrasts in the anesthetized monkey visual cortex. **(a)** Time course of the hemodynamic responses at 610 nm averaged over 26 recording blocks for each contrast level. **(b)** Regression plot of hemodynamic responses at 610 nm with the spike rates averaged over all normalized MUA channels. **(c)** Power spectra of all trials (n = 78 recording blocks) sorted in an ascending order according to hemodynamic response strength at 610 nm. The observed minimum and maximum activity is coded by black and yellow, respectively. Adapted from [Niessing, 2005].

to vascular events.

Two types of gamma activity

Instead of theta activity, our results show that LFP fluctuations in the mid gamma [50-100 Hz] and high-gamma [100-150 Hz] ranges are robustly associated with CBV fluctuations both during running and REM sleep. Strong evidence is accumulating of the co-modulation between theta and different gamma sub-bands and their differential implications in memory porcesses [Colgin et al., 2009; Montgomery et al., 2008, 2009]. Schomburg and colleagues demonstrated that these distinct frequency bands emanate from separate inputs that reach CA1 at different phases of theta oscillations, with low-gamma arising from CA3 region, mid-gamma from EC and high-gamma from local interneuron modulation [Schomburg et al., 2014]. We found similar patterns of gamma amplitude modulation by theta frequency.

Our results demonstrate that low-gamma activity elicits weak to no vascular response in most brain regions. If low gamma episodes were rather absent during running (which is probably linked to our protocol design), we could isolate significant low-gamma activity in REM episode which did not relate to significant vascular increases. On the contrary, mid-gamma and high-gamma were robustly correlated with CBF fluctuations, though not exactly in the same manner. During running, cross-correlations between gamma power and vascular responses contained a large proportion of pixels which response was better predicted by mid-gamma than theta oscillation, especially in the CA1 and CA3 region and some cortical regions. On the other hand, vascular adaptation patterns were not associated with an increase in mid-gamma, but rather in the high-gamma range. Phase modulation analysis revealed that vascular adaptation was parallel to the apparition of high-gamma oscillations at the trough of theta oscillations. These results still need to be confirmed, but it is likely that several gamma mechanisms are involved in the vascular responses we observe. Determining what regions are associated with which sub-band remains to be done.

Correlation is not Causation

Here we gave evidence for coupling or association between brain rhythms and cerebral activations. Vascular signals are not univocally linked to these rhythms. They typically co-occur with directionality: all of our results point towards electrical activation preceding vascular response. This suggests that, if any causal link should be made, it would support electrical events to be responsible for vascular activations. Gamma rhythmicity and vascular events have been assessed concomitantly in two different conditions and robust cross-correlations between these multimodal signals have been observed. However, the actual recording protocol does not precise the interplay between the two phenomena. To what extent modulation of gamma rhythms (through pharmacology for instance) would impact vascular events and potential cognitive dysfunction is a question of utmost importance. Our recordings in REM episodes suggest however that gamma activity is a necessary condition for strong vascular response to occur, but that the opposite is not true and that an additional factor might be needed to obtain a significant CBV increase. The nature of this factor still needs to be determined.

7.2.5 Physiological implications

What are the physiological properties of gamma oscillations that specifically link them with CBV fluctuations ? First, it is crucial to mention that though generated locally, gamma oscillations are observed in multiple brain regions including neocortex, entorhinal cortex, hippocampus, thalamus, striatum, olfactory bulb and thalamus [Buzski and Wang, 2012]. Patches of gamma oscillations can also synchronize over long-range connections [Traub et al., 1996]. The common denominator to all these structures is the presence of inhibitory neurons and their action through GABA-A synapses. Thus, it is likely than the increase in blood volume concurrent with gamma oscillations reflects the cost of inhibition [Buzski et al., 2007]. Several other arguments support the idea that inhibitory interneurons are strongly involved in gamma oscillations, notably the strong spike-field coherence that they display and the fact that inhibition tightly follows excitation, by about the duration of a gamma cycle (10-30 ms) [Buzski et al., 1983] and the evidence that fast-spiking parvalbumine interneurons drive gamma oscillations in the rat barrel cortex [Cardin et al., 2009; Sohal et al., 2009] . In this manner, perisomatic inhibition tightly synchronizes pyramidal spiking to fire in small temporal windows, possibly for the better encoding of sequences [Lisman and Jensen, 2013]. Removing this fast inhibition disrupts theta-gamma coupling [Wulff et al., 2009].

The second major question that our work raises is the one concerning the nature of the signaling pathway leading to vascular dilation. It is probable that sustained high-frequency stimulation generates large calcium influx in pyramidal neurons [Wong et al., 1979] and that this might trigger a cascade of signaling and metabolic changes [Lauritzen, 2005]. An important question to address would be if this pathway involves cyclo-oxygenase 2 and prostanoids in which case, it would be blocked by aspirin. It is also possible that different pathways are implicated in different aspects of the hemodynamic response we observe, given that mid-gamma and high-gamma supposedly do not arise from the same mechanisms. Once more, the debate whether CBF fluctuations are modulated in a feed-forward fashion by the direct signaling of neurons or if they arise from metabolic feedback signal, generated by increased energy demand, is re-opened. The fact that we found at least two separable implications of gamma oscillations in vascular regulation suggests a complex answer to these questions.

7.3 Perspectives

In this section, I propose several experiments that could help answer the open questions above. Some of these implementations would require adapting mfUS-EEG to existing protocols, while some others can be tested in the current setup.

7.3.1 Proposed Experiment # 1: Decomposing vascular patterns of mobility

Pharmacological modifications of Theta or Gamma Activity

The first option to investigate the relationship between theta, gamma rhythms and CBV would be to block pharmacologically brain rhythms and to investigate the effect on vascular responses. For instance, one can selectively interact on the different types of theta activity : type-I theta is mediated by serotonin agonists while type-II theta is blocked by cholinergic antagonists, such as atropine, with possibly different impacts on gamma rhythmicity. Similarly, one could think of selectively blocking gamma activity to see if the hemodynamic response is affected. The injection can be performed while the animal is performing the task during recording (through permanent cannule implantation, for instance) to assess the dynamics of theta/gamma blockade.

Modification of hemodynamic signaling pathways

The mechanisms of functional hyperemia and the pathways involved in vascular adaptation can be tested in the same manner by drug bolus injections. If they are mediated by COX 2, it should be blocked by aspirin. To investigate if this is mediated by astrocytes, one can inhibit the epoxyeicosatrienoic (EET) pathway by epoxygenase inhibitors (e.g. miconazole) injections. These two substances can be mixed with water for reward to avoid local bolus injection. In both cases (rhythms and vascular blockades), it is important that modifications do not affect performance and mobility, to ensure that the potential effect on hemodynamics is selective to the blockade.

Modulation of sensory input

In order to reveal the different components of the hemodynamic responses observed during running, there are several parameters that we can test. A simple protocol would be to switch light on and off (every second trial, for instance). This would allow for direct comparison in the same task between two consecutive trials. Somatosensory input from the whiskers could be temporally blocked by unilateral/bilateral anesthetics injection or by shaving whiskers unilaterally. Another possibility is to implement treadmill running on prepared mfUS-EEG rats. Ideally, the same rats could be tested from treadmill running and natural movement. One of major advantages of treadmill protocol is that one can control time and speed of run, together with virtual distance that must be traveled to get a reward. Our data suggests a strong variability in hemodynamic response on seemingly similar trials (speed, acceleration). This could be investigated by trying to reproduce such adaptation in treadmill running protocol, and - if present - see what parameters influence and to what extent.

7.3.2 Proposed Experiment # 2: Disentangling motor and cognitive responses

7.3.2.1 Selective implication of the hippocampus

One of the most straight-forward comparisons that could help disentangle pure motor processing from cognitively-relevant processing is the T-maze task (see Figure 7.4a). In such a setup, the rat alternates forced turns (sample trials) where one arm of the maze is blocked and the remaining arm is rewarded, and free turns (choice trials) during which the animal has to choose the arm that was not previously rewarded (in the classical version). The activations that are only present in choice turns are a signature of the cognitive processing responsible for the rat decision to take the right choice. It also provide error trials that can be related to electrophysiological recordings. This task can made more complex in a 4-arm version, that requires higher-level rule acquisition.

Similarly as the T-maze task, several behavioral tests have long been developed to test the different aspects of memory. We detail two examples that could be applied using fUS. In Figure 7.4b, animals learn to associate either a context (the texture of a box for instance) or a cue (a sound, in most cases) to an aversive stimulus (a mild electric shock). Such protocols are called *fear-conditioning*. In the first type of conditioning the animal has to recognize the different elements in a given context to associate with the stimulus, a process that is known to be hippocampus-dependent, whereas the second type of conditioning only implies the association of a single sensory cue to the aversive stimulus, which is known to be hippocampus-independent. Such a tool as mfUS-EEG could provide a full cartography of the vascular activations involved in both types of memory systems.

In Figure 7.4c, we show a recent experiment that has established the functional relevance of brain oscillations for better task performance. In this setup, rats first get to learn to discriminate two different contexts by being daily exposed to them. During the test phase, rats have to find buried rewards that are cued by two different odors. In context A, the buried reward is cued by odor A, whereas in the second context, the buried reward is cued by odor B. The acquisition of this task shows that performance is directly linked to the strength of phase-amplitude cross-frequency coupling between theta and low-gamma oscillation in the CA3 region. It would be interesting to investigate if vascular mirror display this kind of cognitive adaptation. This increase in CFC can also be observed for high-frequency oscillations such as high-gamma.

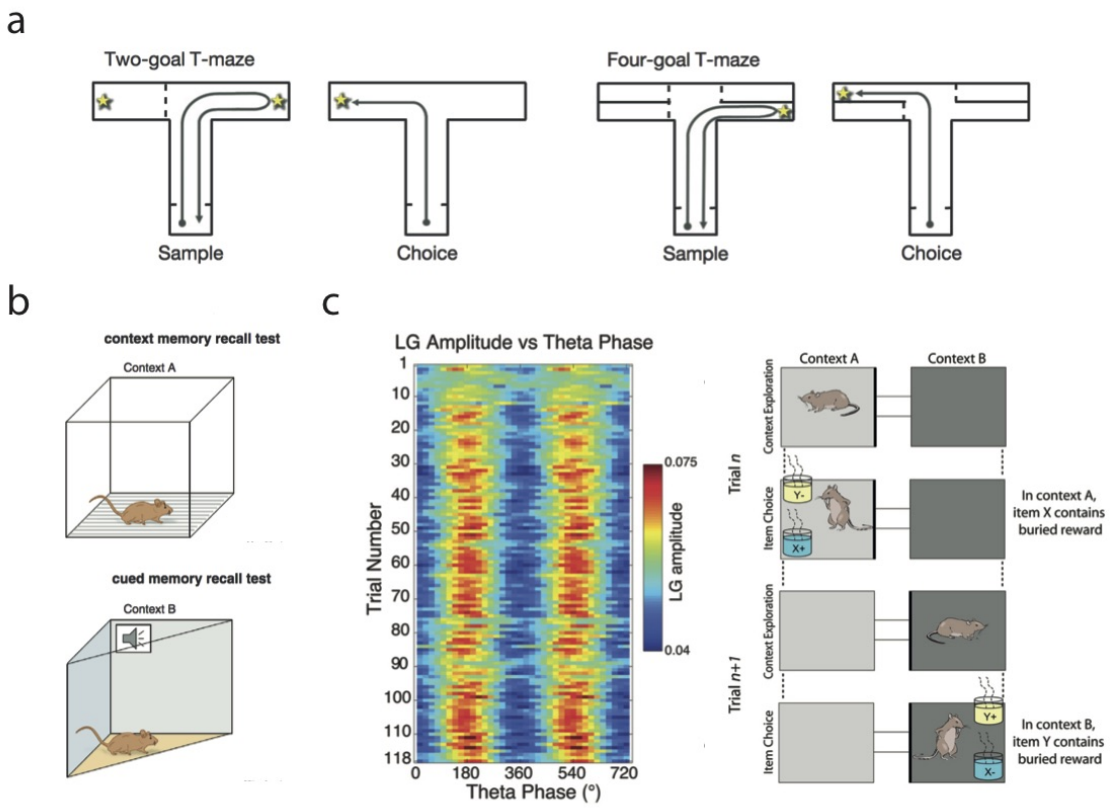

Figure 7.4 – Disentangling motor and cognitive hemodynamic responses List of proposed experiments to dissociate the motor and cognitive components of the vascular hemodynamic response. **(a)** Classical T-maze task (Left: two-arm version ; Right: four-arm version). In this task the animal perform two trials. In the "sample trial", the animal can only access the other rewarded arm. In the subsequent "choice" trial, all arms are available but only one is rewarded. The comparison between sample trials and choice trials reveal the selective activations linked with cognition **(b)** Two memory-recall test relying on distinct brain structures. (Top) In contextual memory recall the animal has associated context with response. This task is known to be hippocampus-dependent. (Bottom) In cued memory recall the animal has associated cue with response. This task is known to be hippocampus-independent. **(c)** Context-association task. The animal has to learn the relative positions of buried rewards in two different contexts. This task success rate is known to be dependent on theta-gamma cross-frequency coupling in the CA3 region (left). **(a)** Adapted from [Spellman et al., 2015] **(b)** Adapted from [Boyce et al., 2016] **(c)** Adapted from [Tort et al., 2009].

Reward prediction and error signals (predicitive coding)

Predictive coding is a framework that is gathering growing attention in neuroscience [Friston et al., 2015]. It states that most of our brain computing power and architecture is devoted to making predictions and inferences about the external world (top-down processing), to compare them with sensory input (bottom-up processing). This generates error signals containing information to modify the state of the network. One of the major questions about the phenomenon of vascular adaptation is how it is related to reward uptake and it is tempting to assume that this pattern corresponds to a form of "vascular plasticity" that strengthens, as the animal performs the task.

Because, we are in situation of certain reward, we cannot, in the current setup, see the potential activations associated with reward, even though we have detected significant activity in regions that are known to be involved in reward processing, such as striatum. It could be extremely informative to investigate the vascular correlates of unexpected reward (obtained but not predicted) or reward misses (not obtained while expected), events that are known to generate strong error signals at the cellular level [Schultz et al., 1997]. Whether or not these error signals have a vascular counterpart is a field-opening question.

Changing task rule : striatal vs cortical response (two complementary systems)

The T-maze task is one of the most classical tasks used in neuroscience. It can be used to teach rats different strategies, such as spatial alternation (opposite arm rewarded) or spatial persistance (same arm-rewarded), and to alternate between these strategies when expected reward is not obtained. Rats perform very well in such contexts because their learning capabilities are very flexible (they "learn how to learn"). What exactly happens when the task rule switches is a subject of active research. The current understanding is that two different systems operate in concert : one system is involved in routine processing aiming at automatizing and reducing the load of decision-making and cognitive control mechanisms (rendering its processing unconscious) and a system that is involved in novelty and non-predictability, constantly operating to detect changes and predictions errors, in order to adapt strategies. These two systems work in concert to open or close the perception-action loop [Sperry, 1952]. These two systems are at play in our experiment, but implementing task switching and comparing the evolution of vascular patterns before and after switch would provide a new insight on task-adaptation circuitry.

7.3.3 Proposed Experiment # 3: Neural Event-Triggered fUS acquisition

A final experiment that we propose relies on the recent development of neural-event triggered setup, that are currently being used to start imaging acquisition after neural detection. This kind of approach allows to acquire "snapshots" of brain activity at the precise onset of physiological events and is especially suited when processing time is prohibitive. This has been successfully implemented in EEG-fMRI protocols revealing strong hippocampal-cortical interactions during sharp-wave ripple events, for example [Logothetis et al., 2012]. In the same manner, it would be extremely valuable to trigger burst acquisitions at the onset of **sharp-wave ripples** or **spindles**. This should also be applied to fast-image **vascular surges** during REM sleep, though their online detection might not be straight-forward. A solution could be to detect phasic periods of REM sleep which are coupled to vascular surges. Finally, one could think of applying the same principle to image **epileptic seizures** onset or **theta sequences**.

General Conclusion

We have succeeded in adapting functional Ultrasound (fUS) Imaging to mobile animals. This methodology captures the hemodynamic state of the brain over its whole depth along with its electrographic activity in awake, mobile rats over repeated and prolonged periods of time. The current setup has an in-plane resolution of 100 μm x 100 μm, out-of-plane resolution of 400 μm and temporal resolution of 200 ms. The behavioral paradigm is established and stable recordings of theta episodes both during maze running and active locomotion have been acquired. Despite the small size and weight of the probe, holder and cable, the system limits the distance and environment that the animal can explore, in a way similar to multichannel microdrive tetrode recordings. This work opens the way to a more general use of functional ultrasound to study cognitive questions.

In this work, we have produced novel data that shed a new light on the vascular activations associated with mobility including (1) robust sequential activations in the dorsal hippocampal network during running, that follow the trisynaptic circuit 1.2 s to 2.0 s after theta peak. (2) highly variable patterns in most brain regions between task start and end, suggesting what we called “vascular adaptation” that still needs to be investigated. This phenomenon occurs robustly across animals and affects downstream regions more strongly that upstream regions, in the pattern described above (3) high-amplitude whole-brain sustained activity during REM sleep, including large surges of activation initiated in the thalamus and fading in the cortex. In all cases, vascular activations strongly and robustly correlated with the power of local fields potentials (LFP) in the hippocampus, in the theta (6-10 Hz), mid (50-100 Hz) and high gamma (100-150 Hz) frequency range, while low-gamma (30-50 Hz) did not. Our results suggests strong implications of fast gamma oscillations in the neurovascular processes underlying both running and REM sleep.

This methodology applies to both cognitive and pathological questions. However, substantial progress still needs to be achieved to observe the interplay between metabolism and neuronal electrical activity that govern global brain equilibrium. This novel kind of data also requires the development of new analytical methods to bridge the gap between vascular activations and reference studies based on electrode or fMRI recordings. Synchronous volumic acquisition will become possible with future matrix-type probes. As it develops, functional Ultrasound Imaging becomes applicable to a wide range of protocols including complex behavioral tasks in healthy animals and fundamental investigations of neurovascular pathologies.

Bibliography

Abe, R., T. Sakaguchi, K. Kitajo, D. Ishikawa, N. Matsumoto, N. Matsuki, and Y. Ikegaya
2014. Sound-induced modulation of hippocampal theta oscillations:. *NeuroReport*, 25(17):1368–1374. 2.4.1

Achanta, R., A. Shaji, K. Smith, A. Lucchi, P. Fua, and S. Ssstrunk
2010. Slic superpixels. Technical report, Ecole Polytechnique Fdrale de Lausanne (E. 7.1.3.3

Adhikari, A., M. A. Topiwala, and J. A. Gordon
2010. Synchronized Activity between the Ventral Hippocampus and the Medial Prefrontal Cortex during Anxiety. *Neuron*, 65(2):257–269. 2.4.4

Aggleton, J. P. and M. W. Brown
1999. Episodic memory, amnesia, and the hippocampal-anterior thalamic axis. *The Behavioral and Brain Sciences*, 22(3):425–444; discussion 444–489. 2.1.4

Ahmed, O. J. and M. R. Mehta
2012. Running Speed Alters the Frequency of Hippocampal Gamma Oscillations. *The Journal of Neuroscience*, 32(21):7373–7383. 2.3.1.4

Ahrens, M. B., M. B. Orger, D. N. Robson, J. M. Li, and P. J. Keller
2013. Whole-brain functional imaging at cellular resolution using light-sheet microscopy. *Nature Methods*, 10(5):413–420. 3.3.2.5

Akemann, W., H. Mutoh, A. Perron, J. Rossier, and T. Knpfel
2010. Imaging brain electric signals with genetically targeted voltage-sensitive fluorescent proteins. *Nature Methods*, 7(8):643–649. 3.3.3.1

Amaral, D. G., H. E. Scharfman, and P. Lavenex
2007. The dentate gyrus: fundamental neuroanatomical organization (dentate gyrus for dummies). *Progress in brain research*, 163:3–790. 2.2.2.1

Amaral, D. G. and M. P. Witter
1989. The three-dimensional organization of the hippocampal formation: A review of anatomical data. *Neuroscience*, 31(3):571–591. 2.2.3.2

Andersen, P.
2007. *The Hippocampus Book*. Oxford University Press, USA. Google-Books-ID: IQkTDAAAQBAJ. 2.2.1, 2.2.2.1, 2.4, 2.2.2.3

Andersen, P., T. V. Bliss, and K. K. Skrede
1971. Unit analysis of hippocampal population spikes. *Experimental Brain Research*, 13(2):208–221. 1.1.3.2, 2.2.2.1

Andreone, B. J., B. Lacoste, and C. Gu
2015. Neuronal and Vascular Interactions. *Annual Review of Neuroscience*, 38(1):25–46. 3.5

Arneric, S. P., M. A. Honig, T. A. Milner, S. Greco, C. Iadecola, and D. J. Reis
1988. Neuronal and endothelial sites of acetylcholine synthesis and release associated with microvessels in rat cerebral cortex: ultrastructural and neurochemical studies. *Brain research*, 454(1-2):11–30. 3.2.3.2

Astur, R. S., S. A. St. Germain, E. K. Baker, V. Calhoun, G. D. Pearlson, and R. T. Constable
2005. fMRI Hippocampal Activity During a VirtualRadial Arm Maze. *Applied Psychophysiology and Biofeedback*, 30(3):307–317. 7.2.1

Attwell, D., A. M. Buchan, S. Charpak, M. Lauritzen, B. A. MacVicar, and E. A. Newman
2010. Glial and neuronal control of brain blood flow. *Nature*, 468(7321):232–243. 3.2.1, 3.2.2, 3.4, 3.2.3.2, 3.3.1.2

Axmacher, N., M. M. Henseler, O. Jensen, I. Weinreich, C. E. Elger, and J. Fell
2010. Cross-frequency coupling supports multi-item working memory in the human hippocampus. *Proceedings of the National Academy of Sciences*, 107(7):3228–3233. 1.3.3.2, 1.4.1

Azar, T., J. Sharp, and D. Lawson
2011. Heart rates of male and female SpragueDawley and spontaneously hypertensive rats housed singly or in groups. *Journal of the American Association for Laboratory Animal Science*, 50(2):175–184. 4.1.3

Bagher, P. and S. S. Segal
2011. Regulation of blood flow in the microcirculation: role of conducted vasodilation. *Acta Physiologica*, 202(3):271–284. 3.2.3.2

Bannerman, D. M., R. M. J. Deacon, S. Offen, J. Friswell, M. Grubb, and J. N. P. Rawlins
2002. Double dissociation of function within the hippocampus: spatial memory and hyponeophagia. *Behavioral Neuroscience*, 116(5):884–901. 2.2.3.3

Barlow, H. B.
1972. Single units and sensation: a neuron doctrine for perceptual psychology? *Perception*, 1(4):371–394. 1.2.1

Barth, D. S.
2003. Submillisecond Synchronization of Fast Electrical Oscillations in Neocortex. *The Journal of Neuroscience*, 23(6):2502–2510. 1.1.3.4

Bast, T., I. A. Wilson, M. P. Witter, and R. G. M. Morris
2009. From Rapid Place Learning to Behavioral Performance: A Key Role for the Intermediate Hippocampus. *PLoS Biology*, 7(4):e1000089. 2.2.3.3

Bastos, A., J. Vezoli, C. Bosman, J.-M. Schoffelen, R. Oostenveld, J. Dowdall, P. DeWeerd, H. Kennedy, and P. Fries
2015. Visual Areas Exert Feedforward and Feedback Influences through Distinct Frequency Channels. *Neuron*, 85(2):390–401. 1.4.2.2

Bazelot, M., C. Dinocourt, I. Cohen, and R. Miles
2010. Unitary inhibitory field potentials in the CA3 region of rat hippocampus: Hippocampal inhibitory field potentials. *The Journal of Physiology*, 588(12):2077–2090. 1.1.3.2

Beck, A.
1890. Die Bestimmung der Localisation der Gehirn und Rckenmarksfunctionen vermittelst der elektrischen Erscheinungen. *Centralblatt fr Physiologie*, 4(4):473–476. 1.1.1

Belluscio, M. A., K. Mizuseki, R. Schmidt, R. Kempter, and G. Buzsaki
2012. Cross-Frequency Phase-Phase Coupling between Theta and Gamma Oscillations in the Hippocampus. *Journal of Neuroscience*, 32(2):423–435. 2.3.1.4, 2.4.5

Benchenane, K., A. Peyrache, M. Khamassi, P. L. Tierney, Y. Gioanni, F. P. Battaglia, and S. I. Wiener
2010. Coherent Theta Oscillations and Reorganization of Spike Timing in the Hippocampal- Prefrontal Network upon Learning. *Neuron*, 66(6):921–936. 1.3.3.2, 2.2.2.2, 2.4.4, 2.14

Berg, R. W., D. Whitmer, and D. Kleinfeld
2006. Exploratory Whisking by Rat Is Not Phase Locked to the Hippocampal Theta Rhythm. *Journal of Neuroscience*, 26(24):6518–6522. 2.3.1.2, 2.4.1

Berger, H.
1929. ber das elektrenkephalogramm des menschen. *European Archives of Psychiatry and Clinical Neuroscience*, 87(1):527–570. 1.1.1, 1.1

Berke, J. D., V. Hetrick, J. Breck, and R. W. Greene
2008. Transient 23-30 Hz oscillations in mouse hippocampus during exploration of novel environments. *Hippocampus*, 18(5):519–529. 2.3.1.1

Berridge, M. J., P. Lipp, and M. D. Bootman
2000. The versatility and universality of calcium signalling. *Nature Reviews Molecular Cell Biology*, 1(1):11–21. 3.3.3.2

Berwick, J., D. Johnston, M. Jones, J. Martindale, C. Martin, A. J. Kennerley, P. Redgrave, and J. Mayhew
2008. Fine Detail of Neurovascular Coupling Revealed by Spatiotemporal Analysis of the Hemodynamic Response to Single Whisker Stimulation in Rat Barrel Cortex. *Journal of Neurophysiology*, 99(2):787–798. 3.2.4, 3.2.4.2

Bi, G.-q. and M.-m. Poo
1998. Synaptic Modifications in Cultured Hippocampal Neurons: Dependence on Spike Timing, Synaptic Strength, and Postsynaptic Cell Type. *The Journal of Neuroscience*, 18(24):10464–10472. 1.2.4, 1.5, 2.3.1.3

Bieri, K., K. Bobbitt, and L. Colgin
2014. Slow and Fast Gamma Rhythms Coordinate Different Spatial Coding Modes in Hippocampal Place Cells. *Neuron*, 82(3):670–681. 2.3.1.4

Bland, B. H. and S. D. Oddie
2001. Theta band oscillation and synchrony in the hippocampal formation and associated structures: the case for its role in sensorimotor integration. *Behavioural brain research*, 127(1):119–136. 2.3.1.2, 2.4.1

Blinder, P., P. S. Tsai, J. P. Kaufhold, P. M. Knutsen, H. Suhl, and D. Kleinfeld
2013. The cortical angiome: an interconnected vascular network with noncolumnar patterns of blood flow. *Nature Neuroscience*, 16(7):889–897. 3.1.1, 3.1.2

Bliss, T. V. and T. Lmo
1973. Long-lasting potentiation of synaptic transmission in the dentate area of the anaesthetized rabbit following stimulation of the perforant path. *The Journal of physiology*, 232(2):331–356. 1.2.4

Bohil, C. J., B. Alicea, and F. A. Biocca
2011. Virtual reality in neuroscience research and therapy. *Nature Reviews Neuroscience*. 7.2.1

Bontempi, B., C. Laurent-Demir, C. Destrade, and R. Jaffard
1999. Time-dependent reorganization of brain circuitry underlying long-term memory storage. *Nature*, 400(6745):671–675. 2.2.2.2

Bouchard, M. B., B. R. Chen, S. A. Burgess, and E. M. C. Hillman
2009. Ultra-fast multispectral optical imaging of cortical oxygenation, blood flow, and intracellular calcium dynamics. *Optics Express*, 17(18):15670–15678. 3.2.2, 3.3.2.1, 3.12

Boyce, R., S. D. Glasgow, S. Williams, and A. Adamantidis
2016. Causal evidence for the role of REM sleep theta rhythm in contextual memory consolidation. *Science*, 352(6287):812–816. 1.3.3.3, 2.4.5, 7.2.2, 7.4

Bragin, A., G. Jando, Z. Nadasdy, J. Hetke, K. Wise, and G. Buzsaki
1995. Gamma (40-100 Hz) oscillation in the hippocampus of the behaving rat. *The Journal of Neuroscience*, 15(1):47–60. 1.1.2.3, 1.4.1, 1.4.2.2, 2.3.1.2, 2.7, 2.3.1.4

Brandon, M., J. Koenig, J. Leutgeb, and S. Leutgeb
2014. New and Distinct Hippocampal Place Codes Are Generated in a New Environment during Septal Inactivation. *Neuron*, 82(4):789–796. 2.4.2

Brandon, M. P., A. R. Bogaard, N. W. Schultheiss, and M. E. Hasselmo
2013. Segregation of cortical head direction cell assemblies on alternating theta cycles. *Nature Neuroscience*, 16(6):739–748. 2.4.1, 2.11

Brggemann, D., B. Wolfrum, V. Maybeck, Y. Mourzina, M. Jansen, and A. Offenhusser
2011. Nanostructured gold microelectrodes for extracellular recording from electrogenic cells. *Nanotechnology*, 22(26):265104. 1.1.2.3

Burgess, N.
2008. Grid cells and theta as oscillatory interference: Theory and predictions. *Hippocampus*, 18(12):1157–1174. 2.3.1.2

Buxton, R. B., K. Uluda, D. J. Dubowitz, and T. T. Liu
2004. Modeling the hemodynamic response to brain activation. *NeuroImage*, 23:S220–S233. 3.2.4.2

Buzsaki, G.
2004. Neuronal Oscillations in Cortical Networks. *Science*, 304(5679):1926–1929. 1.3.2.3

Buzsaki, G.
2011. Hippocampus. *Scholarpedia*, 6(1):1468. 2.2.2.3

Buzsaki, G., R. G. Bickford, G. Ponomareff, L. J. Thal, R. Mandel, and F. H. Gage
1988. Nucleus basalis and thalamic control of neocortical activity in the freely moving rat. *The Journal of Neuroscience: The Official Journal of the Society for Neuroscience*, 8(11):4007–4026. 1.1.3.4

Buzski, G.
1986. Hippocampal sharp waves: Their origin and significance. *Brain Research*, 398(2):242–252. 2.3.1.3

Buzski, G.
1989. Two-stage model of memory trace formation: A role for noisy brain states. *Neuroscience*, 31(3):551–570. 1.3.3.3, 2.3.1.1

Buzski, G.
2002. Theta oscillations in the hippocampus. *Neuron*, 33(3):325–340. 2.3.1.2, 2.8

Buzski, G.
2006. *Rhythms of the brain*. Oxford: Oxford Univ. Press. 1.3.1, 1.3.2.1

Buzski, G., C. A. Anastassiou, and C. Koch
2012. The origin of extracellular fields and currents EEG, ECoG, LFP and spikes. *Nature Reviews Neuroscience*, 13(6):407–420. 1.1, 1.2, 1.3

Buzski, G., K. Kaila, and M. Raichle
2007. Inhibition and Brain Work. *Neuron*, 56(5):771–783. 7.2.5

Buzski, G., L. W. Leung, and C. H. Vanderwolf
1983. Cellular bases of hippocampal EEG in the behaving rat. *Brain Research*, 287(2):139–171. 7.2.5

Buzski, G., N. Logothetis, and W. Singer
2013. Scaling Brain Size, Keeping Timing: Evolutionary Preservation of Brain Rhythms. *Neuron*, 80(3):751–764. 1.6

Buzski, G. and E. I. Moser
2013. Memory, navigation and theta rhythm in the hippocampal-entorhinal system. *Nature Neuroscience*, 16(2):130–138. 2.4.2

Buzski, G. and F. L. d. Silva
2012. High frequency oscillations in the intact brain. *Progress in Neurobiology*, 98(3):241–249. 2.4.5

Buzski, G. and X.-J. Wang
2012. Mechanisms of Gamma Oscillations. *Annual Review of Neuroscience*, 35(1):203–225. 7.2.5

Bdard, C. and A. Destexhe
2009. Macroscopic Models of Local Field Potentials and the Apparent 1/f Noise in Brain Activity. *Biophysical Journal*, 96(7):2589–2603. 1.1.5.3

Caesar, K., K. Thomsen, and M. Lauritzen
2003. Dissociation of spikes, synaptic activity, and activity-dependent increments in rat cerebellar blood flow by tonic synaptic inhibition. *Proceedings of the National Academy of Sciences*, 100(26):16000–16005. 3.2.4.1

Canolty, R. T., E. Edwards, S. S. Dalal, M. Soltani, S. S. Nagarajan, H. E. Kirsch, M. S. Berger, N. M. Barbaro, and R. T. Knight
2006. High Gamma Power Is Phase-Locked to Theta Oscillations in Human Neocortex. *Science*, 313(5793):1626–1628. 1.3.2.5

Cardin, J. A., M. Carln, K. Meletis, U. Knoblich, F. Zhang, K. Deisseroth, L.-H. Tsai, and C. I. Moore
2009. Driving fast-spiking cells induces gamma rhythm and controls sensory responses. *Nature*, 459(7247):663–667. 1.4.2.3, 7.2.5

Carr, M., M. Karlsson, and L. Frank
2012. Transient Slow Gamma Synchrony Underlies Hippocampal Memory Replay. *Neuron*, 75(4):700–713. 2.3.1.3

Caton, R.
1875. Electrical Currents of the Brain. *The Journal of Nervous and Mental Disease*, 2(4):610. 1.1.1

Cauli, B.
2004. Cortical GABA Interneurons in Neurovascular Coupling: Relays for Subcortical Vasoactive Pathways. *Journal of Neuroscience*, 24(41):8940–8949. 3.2.3.2, 3.6

Cauli, B.
2010. Revisiting the role of neurons in neurovascular coupling. *Frontiers in Neuroenergetics*, 2. 3.2.1, 3.2.3.2

Cavanagh, J. F. and M. J. Frank
2014. Frontal theta as a mechanism for cognitive control. *Trends in Cognitive Sciences*, 18(8):414–421. 2.4.3

Cei, A., G. Girardeau, C. Drieu, K. E. Kanbi, and M. Zugaro
2014. Reversed theta sequences of hippocampal cell assemblies during backward travel. *Nature Neuroscience*, 17(5):719–724. 2.4.2

Chadwick, M., A. Jolly, D. Amos, D. Hassabis, and H. Spiers
2015. A Goal Direction Signal in the Human Entorhinal/Subicular Region. *Current Biology*, 25(1):87–92. 2.1.3, 7.2.1

Chen, B. R., M. B. Bouchard, A. F. McCaslin, S. A. Burgess, and E. M. Hillman
2011. High-speed vascular dynamics of the hemodynamic response. *NeuroImage*, 54(2):1021–1030. 3.2.3.2, 3.2.4.2, 3.8, 3.3.2.1, 7.1.2

Chilowsky, C. and P. Langevin
1920. Procds et appareils pour la production de signaux sous-marins dirigs et pour la localisation distance d'obstacles sous-marins. 3.3.4

Chrobak, J. J. and G. Buzski
1996. High-frequency oscillations in the output networks of the hippocampalentorhinal axis of the freely behaving rat. *The Journal of Neuroscience*, 16(9):3056–3066. 2.3.1.3

Chuang, N., S. Mori, A. Yamamoto, H. Jiang, X. Ye, X. Xu, L. J. Richards, J. Nathans, M. I. Miller, A. W. Toga, R. L. Sidman, and J. Zhang
2011. An MRI-based atlas and database of the developing mouse brain. *NeuroImage*, 54(1):80–89. 3.1.1

Chung, K., J. Wallace, S.-Y. Kim, S. Kalyanasundaram, A. S. Andalman, T. J. Davidson, J. J. Mirzabekov, K. A. Zalocusky, J. Mattis, A. K. Denisin, S. Pak, H. Bernstein, C. Ramakrishnan, L. Grosenick, V. Gradinaru, and K. Deisseroth
2013. Structural and molecular interrogation of intact biological systems. *Nature*, 497(7449):332–337. 3.1.1

Chung, T., J. Q. Wang, J. Wang, B. Cao, Y. Li, and S. W. Pang
2015. Electrode modifications to lower electrode impedance and improve neural signal recording sensitivity. *Journal of Neural Engineering*, 12(5):056018. 1.1.2.3

Coenen, A. M. L. and O. Zayachkivska
2013. Adolf Beck: A pioneer in electroencephalography in between Richard Caton and Hans Berger. *Advances in Cognitive Psychology*. 1.1

Cohen, N. J. and H. Eichenbaum
1995. *Memory, Amnesia, and the Hippocampal System*. MIT Press. Google-Books-ID: B8zCCBedvDsC. 2.1.4, 2.4.2

Colgin, L. L.
2013. Mechanisms and Functions of Theta Rhythms. *Annual Review of Neuroscience*, 36(1):295–312. 2.4.1

Colgin, L. L.
2016. Rhythms of the hippocampal network. *Nature Reviews Neuroscience*, 17(4):239–249. 2.10, 2.12

Colgin, L. L., T. Denninger, M. Fyhn, T. Hafting, T. Bonnevie, O. Jensen, M.-B. Moser, and E. I. Moser
2009. Frequency of gamma oscillations routes flow of information in the hippocampus. *Nature*, 462(7271):353–357. 1.8, 1.4.1, 2.3.1.4, 2.4.3, 7.2.4

Corkin, S.
1965. Tactually-guided maze learning in man: Effects of unilateral cortical excisions and bilateral hippocampal lesions. *Neuropsychologia*, 3(4):339–351. 2.1.1

Coyle, P.
1976. Vascular patterns of the rat hippocampal formation. *Experimental neurology*, 52(3):447–458. 3.3

Coyle, P.
1978. Spatial features of the rat hippocampal vascular system. *Experimental neurology*, 58(3):549–561. 3.1.2, 3.3

Coyle, P.
1984. Diameter and length changes in cerebral collaterals after middle cerebral artery occlusion in the young rat. *The Anatomical Record*, 210(2):357–364. 3.1.2

Crick, F. and C. Koch
1990. Some reflections on visual awareness. *Cold Spring Harbor Symposia on Quantitative Biology*, 55:953–962. 1.2.2

Crooks, R., J. Jackson, and B. H. Bland
2012. Dissociable pathways facilitate theta and non-theta states in the median raphe-Septohippocampal circuit. *Hippocampus*, 22(7):1567–1576. 2.3.1.2

Csicsvari, J., H. Hirase, A. Czurk, A. Mamiya, and G. Buzski
1999. Oscillatory Coupling of Hippocampal Pyramidal Cells and Interneurons in the Behaving Rat. *The Journal of Neuroscience*, 19(1):274–287. 2.3.1.3

Csicsvari, J., B. Jamieson, K. D. Wise, and G. Buzski
2003. Mechanisms of Gamma Oscillations in the Hippocampus of the Behaving Rat. *Neuron*, 37(2):311–322. 2.3.1.4

Darwin, C.
1866. *On the Origin of Species by Means of Natural Selection: Or The Preservation of Favoured Races in the Struggle for Life*. John Murray. Google-Books-ID: mScMlgEACAAJ. I

Datta, S., S. Saha, S. L. Prutzman, O. J. Mullins, and V. Mavanji
2005. Pontine-wave generator activation-dependent memory processing of avoidance learning involves the dorsal hippocampus in the rat. *Journal of Neuroscience Research*, 80(5):727–737. 7.2.2

Dawkins, R.
1989. *The Selfish Gene*. Oxford University Press. Google-Books-ID: WkHO9HI7koEC. I

DeCoteau, W. E., C. Thorn, D. J. Gibson, R. Courtemanche, P. Mitra, Y. Kubota, and A. M. Graybiel
2007. Learning-related coordination of striatal and hippocampal theta rhythms during acquisition of a procedural maze task. *Proceedings of the National Academy of Sciences*, 104(13):5644–5649. 2.4.4, 2.14

Demene, C., T. Deffieux, M. Pernot, B.-F. Osmanski, V. Biran, J.-L. Gennisson, L.-A. Sieu, A. Bergel, S. Franqui, J.-M. Correas, I. Cohen, O. Baud, and M. Tanter
2015. Spatiotemporal Clutter Filtering of Ultrafast Ultrasound Data Highly Increases Doppler and fUltrasound Sensitivity. *IEEE Transactions on Medical Imaging*, 34(11):2271–2285. 3.3.4

Dement, W. and N. Kleitman
1957. The relation of eye movements during sleep to dream activity: an objective method for the study of dreaming. *Journal of Experimental Psychology*, 53(5):339–346. 1.3.3.1

Demen, C., E. Tiran, L.-A. Sieu, A. Bergel, J. L. Gennisson, M. Pernot, T. Deffieux, I. Cohen, and M. Tanter
2016. 4d microvascular imaging based on ultrafast Doppler tomography. *NeuroImage*, 127:472–483. 3.18, 3.3.4

Denk, W., K. R. Delaney, A. Gelperin, D. Kleinfeld, D. W. Strowbridge, D. W. Tank, and R. Yuste
1994. Anatomical and functional imaging of neurons using 2-photon laser scanning microscopy. *SPIE MILESTONE SERIES MS*, 175:585–596. 3.3.2.5

Denk, W., J. H. Strickler, and W. W. Webb
1990. Two-photon laser scanning fluorescence microscopy. *Science*, 248(4951):73–76. 3.3.2.5

Devonshire, I. M., N. G. Papadakis, M. Port, J. Berwick, A. J. Kennerley, J. E. Mayhew, and P. G. Overton
2012. Neurovascular coupling is brain region-dependent. *NeuroImage*, 59(3):1997–2006. 4.1.3

Devor, A., E. M. C. Hillman, P. Tian, C. Waeber, I. C. Teng, L. Ruvinskaya, M. H. Shalinsky, H. Zhu, R. H. Haslinger, S. N. Narayanan, I. Ulbert, A. K. Dunn, E. H. Lo, B. R. Rosen, A. M. Dale, D. Kleinfeld, and D. A. Boas
2008. Stimulus-Induced Changes in Blood Flow and 2-Deoxyglucose Uptake Dissociate in Ipsilateral Somatosensory Cortex. *The Journal of Neuroscience*, 28(53):14347–14357. 3.2.4.2

Devor, A., P. Tian, N. Nishimura, I. C. Teng, E. M. C. Hillman, S. N. Narayanan, I. Ulbert, D. A. Boas, D. Kleinfeld, and A. M. Dale
2007. Suppressed Neuronal Activity and Concurrent Arteriolar Vasoconstriction May Explain Negative Blood Oxygenation Level-Dependent Signal. *The Journal of Neuroscience*, 27(16):4452–4459. 3.1.2, 3.2.4

Dichter, M. A. and G. F. Ayala
1987. Cellular mechanisms of epilepsy: a status report. *Science*, 237(4811):157–164. 1.3.2.3

Dodt, H.-U., U. Leischner, A. Schierloh, N. Jhrling, C. P. Mauch, K. Deininger, J. M. Deussing, M. Eder, W. Zieglgnsberger, and K. Becker
2007. Ultramicroscopy: three-dimensional visualization of neuronal networks in the whole mouse brain. *Nature Methods*, 4(4):331–336. 3.1.1

Dolorfo, C. L. and D. G. Amaral
1998. Entorhinal cortex of the rat: Topographic organization of the cells of origin of the perforant path projection to the dentate gyrus. *The Journal of Comparative Neurology*, 398(1):25–48. 2.2.3.1, 2.5

Dombeck, D. A., C. D. Harvey, L. Tian, L. L. Looger, and D. W. Tank
2010. Functional imaging of hippocampal place cells at cellular resolution during virtual navigation. *Nature Neuroscience*, 13(11):1433–1440. 3.16, 3.3.3.2

Dombeck, D. A., A. N. Khabbaz, F. Collman, T. L. Adelman, and D. W. Tank
2007. Imaging Large-Scale Neural Activity with Cellular Resolution in Awake, Mobile Mice. *Neuron*, 56(1):43–57. 3.3.2.5

Dorr, A., J. G. Sled, and N. Kabani
2007. Three-dimensional cerebral vasculature of the CBA mouse brain: A magnetic resonance imaging and micro computed tomography study. *NeuroImage*, 35(4):1409–1423. 3.1.1

Drake, C. and C. Iadecola
2007. The role of neuronal signaling in controlling cerebral blood flow. *Brain and Language*, 102(2):141–152. 3.2.2, 7.1.2

Drew, P. J., A. Y. Shih, and D. Kleinfeld
2011. Fluctuating and sensory-induced vasodynamics in rodent cortex extend arteriole capacity. *Proceedings of the National Academy of Sciences*, 108(20):8473–8478. 3.2.2

Duchemin, S., M. Boily, N. Sadekova, and H. Girouard
2012. The complex contribution of NOS interneurons in the physiology of cerebrovascular regulation. *Frontiers in Neural Circuits*, 6. 3.2.3.1

Dudley, D. and L. Sokoloff
1999. Circulation and energy metabolism in the brain/Donald D. Clarke and Louis Sokoloff. In *Basic Neurochemistry: Molecular, Cellular and Medical Aspects. 6th edition.* Philadelphia: Lippincott-Raven. 3.2

Duling, B. R., R. D. Hogan, B. L. Langille, P. Lelkes, S. S. Segal, S. F. Vatner, H. Weigelt, and M. A. Young
1987. Vasomotor control: functional hyperemia and beyond. *Federation Proceedings*, 46(2):251–263. 3.2.3.2

Dunn, A. K., A. Devor, A. M. Dale, and D. A. Boas
2005. Spatial extent of oxygen metabolism and hemodynamic changes during functional activation of the rat somatosensory cortex. *NeuroImage*, 27(2):279–290. 3.2.4, 3.2.4.2, 3.3.2.1

Ego-Stengel, V. and M. A. Wilson
2010. Disruption of ripple-associated hippocampal activity during rest impairs spatial learning in the rat. *Hippocampus*, 20(1):1–10. 1.3.3.3, 2.3.1.3

Einevoll, G. T., C. Kayser, N. K. Logothetis, and S. Panzeri
2013. Modelling and analysis of local field potentials for studying the function of cortical circuits. *Nature Reviews Neuroscience*, 14(11):770–785. 1.1.4.1, 1.4

Ekstrom, A. D., J. B. Caplan, E. Ho, K. Shattuck, I. Fried, and M. J. Kahana
2005. Human hippocampal theta activity during virtual navigation. *Hippocampus*, 15(7):881–889. 2.1.3, 2.3.1.2

Ekstrom, A. D., M. J. Kahana, J. B. Caplan, T. A. Fields, E. A. Isham, E. L. Newman, and I. Fried
2003. Cellular networks underlying human spatial navigation. *Nature*, 425(6954):184–188. 7.2.1

Elul, R.
1964. Regional differences in the hippocampus of the cat. I. Specific discharge patterns of the dorsal and ventral hippocampus and their role in generalized seizures. *Electroencephalography and Clinical Neurophysiology*, 16:470–488. 2.2.3

Engel, A. K. and W. Singer
2001. Temporal binding and the neural correlates of sensory awareness. *Trends in Cognitive Sciences*, 5(1):16–25. 1.2.2

English, D. F., A. Peyrache, E. Stark, L. Roux, D. Vallentin, M. A. Long, and G. Buzski
2014. Excitation and Inhibition Compete to Control Spiking during Hippocampal Ripples: Intracellular Study in Behaving Mice. *The Journal of Neuroscience*, 34(49):16509–16517. 2.3.1.3

Errico, C., J. Pierre, S. Pezet, Y. Desailly, Z. Lenkei, O. Couture, and M. Tanter
2015. Ultrafast ultrasound localization microscopy for deep super-resolution vascular imaging. *Nature*, 527(7579):499–502. 3.18, 3.3.4, 7.1.1

Fanselow, M. S. and H.-W. Dong
2010. Are the Dorsal and Ventral Hippocampus Functionally Distinct Structures? *Neuron*, 65(1):7–19. 2.2.1, 2.2.3.3

Farkas, E., R. Pratt, F. Sengpiel, and T. P. Obrenovitch
2008. Direct, Live Imaging of Cortical Spreading Depression and Anoxic Depolarisation Using a Fluorescent, Voltage-Sensitive Dye. *Journal of Cerebral Blood Flow & Metabolism*, 28(2):251–262. 3.3.3.1

Fell, J. and N. Axmacher
2011. The role of phase synchronization in memory processes. *Nature Reviews Neuroscience*, 12(2):105–118. 1.4.2, 1.9

Felleman, D. J. and D. C. Van Essen
1991. Distributed hierarchical processing in the primate cerebral cortex. *Cerebral cortex*, 1(1):1–47. 2.2.2.3

Flusberg, B. A., E. D. Cocker, W. Piyawattanametha, J. C. Jung, E. L. M. Cheung, and M. J. Schnitzer
2005. Fiber-optic fluorescence imaging. *Nature Methods*, 2(12):941–950. 3.3.3.2

Foster, D. J. and M. A. Wilson
2006. Reverse replay of behavioural sequences in hippocampal place cells during the awake state. *Nature*, 440(7084):680–683. 1.3.3.3

Foster, D. J. and M. A. Wilson
2007. Hippocampal theta sequences. *Hippocampus*, 17(11):1093–1099. 2.3.1.3

Fox, P. T. and M. E. Raichle
1986. Focal physiological uncoupling of cerebral blood flow and oxidative metabolism during somatosensory stimulation in human subjects. *Proceedings of the National Academy of Sciences*, 83(4):1140–1144. 3.3.1.1

Fox, P. T., M. E. Raichle, M. A. Mintun, and C. Dence
1988. Nonoxidative glucose consumption during focal physiologic neural activity. *Science (New York, N.Y.)*, 241(4864):462–464. 3.3.1.1, 3.9

Frank, L. M., E. N. Brown, and M. Wilson
2000. Trajectory encoding in the hippocampus and entorhinal cortex. *Neuron*, 27(1):169–178. 2.3.2

Fraser, A.
1957. Simulation of Genetic Systems by Automatic Digital Computers I. Introduction. *Australian Journal of Biological Sciences*, 10(4):484. 1.2

Freeman, W. J.
1991. The physiology of perception. *Scientific American*, 264(2):78–85. 1.3.2.1, 1.7

Fries, P.
2005. A mechanism for cognitive dynamics: neuronal communication through neuronal coherence. *Trends in Cognitive Sciences*, 9(10):474–480. 1.4.1, 1.4.2, 1.9, 2.4.4

Fries, P.
2015. Rhythms for Cognition: Communication through Coherence. *Neuron*, 88(1):220–235. 1.4.2.2

Friston, K., A. Mechelli, R. Turner, and C. Price
2000. Nonlinear Responses in fMRI: The Balloon Model, Volterra Kernels, and Other Hemodynamics. *NeuroImage*, 12(4):466–477. 3.3.1.2

Friston, K. J., A. M. Bastos, D. Pinotsis, and V. Litvak
2015. LFP and oscillationswhat do they tell us? *Current Opinion in Neurobiology*, 31:1–6. 7.3.2.1

Gardner-Medwin, A. R.
1976. The recall of events through the learning of associations between their parts. *Proceedings of the Royal Society of London. Series B, Biological Sciences*, 194(1116):375–402. 2.4.1

Geisler, C., D. Robbe, M. Zugaro, A. Sirota, and G. Buzski
2007. Hippocampal place cell assemblies are speed-controlled oscillators. *Proceedings of the National Academy of Sciences*, 104(19):8149–8154. 2.3.1.2

Ghosh, K. K., L. D. Burns, E. D. Cocker, A. Nimmerjahn, Y. Ziv, A. E. Gamal, and M. J. Schnitzer
2011. Miniaturized integration of a fluorescence microscope. *Nature Methods*, 8(10):871–878. 3.3.2.5, 3.3.3.2

Gibbs, F. A., E. L. Gibbs, P. R. Carpenter, and H. W. Spies
1959. Electroencephalographic abnormality in ”uncomplicated” childhood diseases. *Journal of the American Medical Association*, 171:1050–1055. 1.3.3.1

Girardeau, G., K. Benchenane, S. I. Wiener, G. Buzski, and M. B. Zugaro
2009. Selective suppression of hippocampal ripples impairs spatial memory. *Nature Neuroscience*, 12(10):1222–1223. 1.3.3.3, 2.3.1.3

Girardeau, G. and M. Zugaro
2011. Hippocampal ripples and memory consolidation. *Current Opinion in Neurobiology*, 21(3):452–459. 2.6

Glickfeld, L. L., J. D. Roberts, P. Somogyi, and M. Scanziani
2009. Interneurons hyperpolarize pyramidal cells along their entire somatodendritic axis. *Nature Neuroscience*, 12(1):21–23. 1.1.3.2

Gloor, P.
1985. Neuronal generators and the problem of localization in electroencephalography: application of volume conductor theory to electroencephalography. *Journal of Clinical Neurophysiology: Official Publication of the American Electroencephalographic Society*, 2(4):327–354. 1.1.3.1, 1.3

Goense, J., Y. Bohraus, and N. K. Logothetis
2016. fMRI at High Spatial Resolution: Implications for BOLD-Models. *Frontiers in Computational Neuroscience*, 10. 3.3.1.3

Goense, J. B. and N. K. Logothetis
2008. Neurophysiology of the BOLD fMRI Signal in Awake Monkeys. *Current Biology*, 18(9):631–640. 3.3.1.2, 3.11

Gong, H., S. Zeng, C. Yan, X. Lv, Z. Yang, T. Xu, Z. Feng, W. Ding, X. Qi, A. Li, J. Wu, and Q. Luo
2013. Continuously tracing brain-wide long-distance axonal projections in mice at a one-micron voxel resolution. *NeuroImage*, 74:87–98. 3.1, 3.3.3.1

Gordon, G. R. J., H. B. Choi, R. L. Rungta, G. C. R. Ellis-Davies, and B. A. MacVicar
2008. Brain metabolism dictates the polarity of astrocyte control over arterioles. *Nature*, 456(7223):745–749. 3.2.4.3

Goutagny, R., J. Jackson, and S. Williams
2009. Self-generated theta oscillations in the hippocampus. *Nature Neuroscience*, 12(12):1491–1493. 2.8, 2.3.1.2

Gray, C. M., P. Knig, A. K. Engel, and W. Singer
1989. Oscillatory responses in cat visual cortex exhibit inter-columnar synchronization which reflects global stimulus properties. *Nature*, 338(6213):334–337. 2.3.1.4

Gray, J. A. and N. McNaughton
1982. *The Neuropsychology of Anxiety: An Enquiry Into the Function of the Septo-hippocampal System.* OUP Oxford. 2.2.3

Green, J. D. and A. A. Arduini
1954. Hippocampal electrical activity in arousal. *Journal of Neurophysiology*, 17(6):533–557. 2.3.1.1, 2.3.1.2

Greene, E. C.
1955. *Anatomy of the rat.* Hafner Pub. Co. Google-Books-ID: d6fwAAAAMAAJ. 3.1.1

Grinvald, A., L. Anglister, J. A. Freeman, R. Hildesheim, and A. Manker
1984. Real-time optical imaging of naturally evoked electrical activity in intact frog brain. *Nature*, 308(5962):848–850. 3.3.3.1

Grinvald, A. and R. Hildesheim
2004. VSDI: a new era in functional imaging of cortical dynamics. *Nature Reviews Neuroscience*, 5(11):874–885. 3.3.3.1

Grinvald, A., E. Lieke, R. D. Frostig, C. D. Gilbert, and T. N. Wiesel
1986. Functional architecture of cortex revealed by optical imaging of intrinsic signals. *Nature*, 324(6095):361–364. 3.3.2.1

Grinvald, A., E. E. Lieke, R. D. Frostig, and R. Hildesheim
1994. Cortical point-spread function and long-range lateral interactions revealed by real-time optical imaging of macaque monkey primary visual cortex. *The Journal of neuroscience*, 14(5):2545–2568. 3.3.3.1

Grivas, I., H. Michaloudi, C. Batzios, M. Chiotelli, C. Papatheodoropoulos, G. Kostopoulos, and G. C. Papadopoulos
2003. Vascular network of the rat hippocampus is not homogeneous along the septotemporal axis. *Brain Research*, 971(2):245–249. 3.1.2

Grosmark, A., K. Mizuseki, E. Pastalkova, K. Diba, and G. Buzski
2012. REM Sleep Reorganizes Hippocampal Excitability. *Neuron*, 75(6):1001–1007. 2.4.5

Gross, C. G., D. B. Bender, and C. E. Rocha-Miranda
1969. Visual receptive fields of neurons in inferotemporal cortex of the monkey. *Science (New York, N.Y.)*, 166(3910):1303–1306. 1.2.1

Gross, D., L. M. Loew, and W. W. Webb
1986. Optical imaging of cell membrane potential changes induced by applied electric fields. *Biophysical journal*, 50(2):339. 3.1.2

Gupta, A. S., M. A. A. van der Meer, D. S. Touretzky, and A. D. Redish
2012. Segmentation of spatial experience by hippocampal theta sequences. *Nature Neuroscience*, 15(7):1032–1039. 2.4.2

Hafting, T., M. Fyhn, T. Bonnevie, M.-B. Moser, and E. I. Moser
2008. Hippocampus-independent phase precession in entorhinal grid cells. *Nature*, 453(7199):1248–1252. 2.3.2

Hafting, T., M. Fyhn, S. Molden, M.-B. Moser, and E. I. Moser
2005. Microstructure of a spatial map in the entorhinal cortex. *Nature*, 436(7052):801–806. 2.1.3, 2.3.2

Hajireza, P., W. Shi, and R. J. Zemp
2011. Real-time handheld optical-resolution photoacoustic microscopy. *Optics express*, 19(21):20097–20102. 3.3.2.4

Hamel, E., B. Grewe, J. Parker, and M. Schnitzer
2015. Cellular Level Brain Imaging in Behaving Mammals: An Engineering Approach. *Neuron*, 86(1):140–159. 3.3.3.2

Hamilton, N. B., D. Attwell, and C. N. Hall
2010. Pericyte-mediated regulation of capillary diameter: a component of neurovascular coupling in health and disease. *Frontiers in Neuroenergetics*, 2:5. 3.2.3.2

Handwerker, D. A., J. M. Ollinger, and M. D'Esposito
2004. Variation of BOLD hemodynamic responses across subjects and brain regions and their effects on statistical analyses. *NeuroImage*, 21(4):1639–1651. 3.3.1.2

Harder, D. R., C. Zhang, and D. Gebremedhin
2002. Astrocytes Function in Matching Blood Flow to Metabolic Activity. *Physiology*, 17(1):27–31. 3.2.2

Harris, K. D., J. Csicsvari, H. Hirase, G. Dragoi, and G. Buzski
2003. Organization of cell assemblies in the hippocampus. *Nature*, 424(6948):552–556. 1.2.4, 1.5

Hasselmo, M. E., C. Bodeln, and B. P. Wyble
2002. A Proposed Function for Hippocampal Theta Rhythm: Separate Phases of Encoding and Retrieval Enhance Reversal of Prior Learning. *Neural Computation*, 14(4):793–817. 2.13, 2.4.3

Hebb, D. O.
1949. *The Organization of Behavior: A Neuropsychological Theory*. Psychology Press. 1.2, 1.2.3, 1.5

Hebben, N., S. Corkin, H. Eichenbaum, and K. Shedlack
1985. Diminished ability to interpret and report internal states after bilateral medial temporal resection: case H.M. *Behavioral Neuroscience*, 99(6):1031–1039. 2.1.1

Helmchen, F., M. S. Fee, D. W. Tank, and W. Denk
2001. A Miniature Head-Mounted Two-Photon Microscope: High-Resolution Brain Imaging in Freely Moving Animals. *Neuron*, 31(6):903–912. 3.3.2.5, 3.3.3.2

Hill, L.
1896. *The physiology and pathology of the cerebral circulation; an experimental research.* London, J. & A. Churchill. 3.3.1.1

Hillman, E. M. C.
2014. Coupling Mechanism and Significance of the BOLD Signal: A Status Report. *Annual Review of Neuroscience*, 37(1):161–181. 3.2.1, 3.2.4.3, 3.3.1.1, 3.10, 7.1.2

Hillman, E. M. C., O. Bernus, E. Pease, M. B. Bouchard, and A. Pertsov
2007. Depth-resolved optical imaging of transmural electrical propagation in perfused heart. *Optics Express*, 15(26):17827–17841. 3.2.4

Hirano, Y., B. Stefanovic, and A. C. Silva
2011. Spatiotemporal Evolution of the Functional Magnetic Resonance Imaging Response to Ultrashort Stimuli. *The Journal of Neuroscience*, 31(4):1440–1447. 3.3.1.2

Hodgkin, A. L. and A. F. Huxley
1952. Propagation of electrical signals along giant nerve fibers. *Proceedings of the Royal Society of London. Series B, Biological Sciences*, 140(899):177–183. 1.2

Holschneider, D. P. and J.-M. I. Maarek
2004. Mapping brain function in freely moving subjects. *Neuroscience & Biobehavioral Reviews*, 28(5):449–461. 7.2.1

Hopfield, J. J.
1982. Neural networks and physical systems with emergent collective computational abilities. *Proceedings of the National Academy of Sciences*, 79(8):2554–2558. 1.2.4

Hounsfield, G. N.
1973. Computerized transverse axial scanning (tomography): Part 1. Description of system. *The British journal of radiology*, 46(552):1016–1022. 3.3.1.1

Hubel, D. H. and T. N. Wiesel
1959. Receptive fields of single neurones in the cat's striate cortex. *The Journal of physiology*, 148(3):574–591. 1.2, 1.2.1

Huerta, P. T. and J. E. Lisman
1995. Bidirectional synaptic plasticity induced by a single burst during cholinergic theta oscillation in CA1 in vitro. *Neuron*, 15(5):1053–1063. 2.4.3

Hughes, J. R.
1964. Responses From the Visual Cortex of Unanesthetized Monkeys1. *International Review of Neurobiology*, 7:99–152. 2.2.3, 2.3.1.4

Huo, B.-X., Y.-R. Gao, and P. J. Drew
2015. Quantitative separation of arterial and venous cerebral blood volume increases during voluntary locomotion. *NeuroImage*, 105:369–379. 7.2.1

Huo, B.-X., J. B. Smith, and P. J. Drew
2014. Neurovascular Coupling and Decoupling in the Cortex during Voluntary Locomotion. *Journal of Neuroscience*, 34(33):10975–10981. 7.2.1, 7.2.4

Hutchison, I. C. and S. Rathore
2015. The role of REM sleep theta activity in emotional memory. *Frontiers in Psychology*, 6. 2.4.5

Hutchison, W. D., J. O. Dostrovsky, J. R. Walters, R. Courtemanche, T. Boraud, J. Goldberg, and P. Brown
2004. Neuronal Oscillations in the Basal Ganglia and Movement Disorders: Evidence from

Whole Animal and Human Recordings. *The Journal of Neuroscience*, 24(42):9240–9243. 1.3.3.4

Huxter, J., N. Burgess, and J. O'Keefe
2003. Independent rate and temporal coding in hippocampal pyramidal cells. *Nature*, 425(6960):828–832. 2.12

Hyman, J. M., M. E. Hasselmo, and J. K. Seamans
2011. What is the Functional Relevance of Prefrontal Cortex Entrainment to Hippocampal Theta Rhythms? *Frontiers in Neuroscience*, 5. 2.4.4

Hyvarinen, A. and H. Morioka
2016. Unsupervised Feature Extraction by Time-Contrastive Learning and Nonlinear ICA. *arXiv preprint arXiv:1605.06336*. 7.1.3.3

Iadecola, C.
1993. Regulation of the cerebral microcirculation during neural activity: is nitric oxide the missing link? *Trends in Neurosciences*, 16(6):206–214. 3.2.3.1

Iadecola, C.
2004. Neurovascular regulation in the normal brain and in Alzheimer's disease. *Nature Reviews Neuroscience*, 5(5):347–360. 3.2.2, 3.2.2, 3.5

Ibsen, S., A. Tong, C. Schutt, S. Esener, and S. H. Chalasani
2015. Sonogenetics is a non-invasive approach to activating neurons in Caenorhabditis elegans. *Nature Communications*, 6:8264. 7.1.4

Igarashi, K. M., H. T. Ito, E. I. Moser, and M.-B. Moser
2014. Functional diversity along the transverse axis of hippocampal area CA1. *FEBS Letters*, 588(15):2470–2476. 2.3.1.4

Jackson, J., B. Amilhon, R. Goutagny, J.-B. Bott, F. Manseau, C. Kortleven, S. L. Bressler, and S. Williams
2014. Reversal of theta rhythm flow through intact hippocampal circuits. *Nature Neuroscience*, 17(10):1362–1370. 2.3.1.2, 2.4.5

Jadhav, S. P., C. Kemere, P. W. German, and L. M. Frank
2012. Awake Hippocampal Sharp-Wave Ripples Support Spatial Memory. *Science*, 336(6087):1454–1458. 2.3.1.3

Jancke, D., F. Chavane, S. Naaman, and A. Grinvald
2004. Imaging cortical correlates of illusion in early visual cortex. *Nature*, 428(6981):423–426. 3.3.3.1

Jarosiewicz, B., B. L. McNaughton, and W. E. Skaggs
2002. Hippocampal Population Activity during the Small-Amplitude Irregular Activity State in the Rat. *The Journal of Neuroscience*, 22(4):1373–1384. 2.3.1.1

Jensen, O. and L. L. Colgin
2007. Cross-frequency coupling between neuronal oscillations. *Trends in Cognitive Sciences*, 11(7):267–269. 1.4.1

Jeong, J.
2004. EEG dynamics in patients with Alzheimer's disease. *Clinical Neurophysiology*, 115(7):1490–1505. 1.3.3.4

Jezek, K., E. J. Henriksen, A. Treves, E. I. Moser, and M.-B. Moser
2011. Theta-paced flickering between place-cell maps in the hippocampus. *Nature*, 478(7368):246–249. 2.4.1, 2.11

Jobsis, F. F.
1977. Noninvasive, infrared monitoring of cerebral and myocardial oxygen sufficiency and circulatory parameters. *Science*, 198(4323):1264–1267. 3.3.2.3

Johnson, G. A., H. Benveniste, R. D. Black, L. W. Hedlund, R. R. Maronpot, and B. R. Smith
1993. Histology by magnetic resonance microscopy. *Magnetic Resonance Quarterly*, 9(1):1–30. 3.1.1

Johnson, G. A., E. Calabrese, A. Badea, G. Paxinos, and C. Watson
2012. A multidimensional magnetic resonance histology atlas of the Wistar rat brain. *NeuroImage*, 62(3):1848–1856. 3.1, 3.1.1

Jones, B. F. and M. P. Witter
2007. Cingulate cortex projections to the parahippocampal region and hippocampal formation in the rat. *Hippocampus*, 17(10):957–976. 2.2.3.1

Jones, M. W. and M. A. Wilson
2005. Theta Rhythms Coordinate HippocampalPrefrontal Interactions in a Spatial Memory Task. *PLoS Biology*, 3(12):e402. 2.4.4

Jones, T. and E. A. Rabiner
2012. The development, past achievements, and future directions of brain PET. *Journal of Cerebral Blood Flow & Metabolism*, 32(7):1426–1454. 3.3.1.1

Jung, R. and A. E. Kornmller
1938. Eine methodik der ableitung iokalisierter potentialschwankungen aus subcorticalen hirngebieten. *European Archives of Psychiatry and Clinical Neuroscience*, 109(1):1–30. 2.3.1.2

Jung, T.-P., S. Makeig, C. Humphries, T.-W. Lee, M. J. Mckeown, V. Iragui, and T. J. Sejnowski
2000. Removing electroencephalographic artifacts by blind source separation. *Psychophysiology*, 37(02):163–178. 7.1, 7.1.3.3

Jutras, M. J., P. Fries, and E. A. Buffalo
2013. Oscillatory activity in the monkey hippocampus during visual exploration and memory formation. *Proceedings of the National Academy of Sciences*, 110(32):13144–13149. 2.3.1.2

Kajikawa, Y. and C. Schroeder
2011. How Local Is the Local Field Potential? *Neuron*, 72(5):847–858. 1.1.5.2

Kamondi, A., L. Acsdy, X. J. Wang, and G. Buzski
1998. Theta oscillations in somata and dendrites of hippocampal pyramidal cells in vivo: activity-dependent phase-precession of action potentials. *Hippocampus*, 8(3):244–261. 2.3.1.2, 2.7

Kandel, A. and G. Buzski
1993. Cerebellar neuronal activity correlates with spike and wave EEG patterns in the rat. *Epilepsy Research*, 16(1):1–9. 1.1.4.2

Kay, K., M. Sosa, J. E. Chung, M. P. Karlsson, M. C. Larkin, and L. M. Frank
2016. A hippocampal network for spatial coding during immobility and sleep. *Nature*, 531(7593):185–190. 2.2.2.1

Kenet, T., D. Bibitchkov, M. Tsodyks, A. Grinvald, and A. Arieli
2003. Spontaneously emerging cortical representations of visual attributes. *Nature*, 425(6961):954–956. 3.3.3.1

Kennedy, P. J. and M. L. Shapiro
2004. Retrieving Memories via Internal Context Requires the Hippocampus. *The Journal of Neuroscience*, 24(31):6979–6985. 2.2.2.2

Kepecs, A., N. Uchida, and Z. F. Mainen
2007. Rapid and Precise Control of Sniffing During Olfactory Discrimination in Rats. *Journal of Neurophysiology*, 98(1):205–213. 2.4.1

Kerkoerle, T. v., M. W. Self, B. Dagnino, M.-A. Gariel-Mathis, J. Poort, C. v. d. Togt, and P. R. Roelfsema
2014. Alpha and gamma oscillations characterize feedback and feedforward processing in monkey visual cortex. *Proceedings of the National Academy of Sciences*, 111(40):14332–14341. 1.4.2.2

Khan, B., F. Tian, K. Behbehani, M. I. Romero, M. R. Delgado, N. J. Clegg, L. Smith, D. Reid, H. Liu, and G. Alexandrakis
2010. Identification of abnormal motor cortex activation patterns in children with cerebral palsy by functional near-infrared spectroscopy. *Journal of biomedical optics*, 15(3):036008–036008. 3.3.2.3

Kjelstrup, K. B., T. Solstad, V. H. Brun, T. Hafting, S. Leutgeb, M. P. Witter, E. I. Moser, and M.-B. Moser
2008. Finite Scale of Spatial Representation in the Hippocampus. *Science*, 321(5885):140–143. 2.5, 2.2.3.3

Kjonigsen, L. J., S. Lillehaug, J. G. Bjaalie, M. P. Witter, and T. B. Leergaard
2015. Waxholm Space atlas of the rat brain hippocampal region: Three-dimensional delineations based on magnetic resonance and diffusion tensor imaging. *NeuroImage*, 108:441–449. 3.1, 3.1.1

Kleinfeld, D., P. Blinder, P. J. Drew, J. D. Driscoll, A. Muller, P. S. Tsai, and A. Y. Shih
2011. A Guide to Delineate the Logic of Neurovascular Signaling in the Brain. *Frontiers in Neuroenergetics*, 3. 3.2.3.2

Konopacki, J., M. B. MacIver, B. H. Bland, and S. H. Roth
1987. Carbachol-induced EEG thetaactivity in hippocampal brain slices. *Brain research*, 405(1):196–198. 2.3.1.2

Konorski, J.
1967. *Integrative activity of the brain: an interdisciplinary approach*. University of Chicago Press. 1.2.1

Kramis, R., C. H. Vanderwolf, and B. H. Bland
1975. Two types of hippocampal rhythmical slow activity in both the rabbit and the rat: relations to behavior and effects of atropine, diethyl ether, urethane, and pentobarbital. *Experimental Neurology*, 49(1 Pt 1):58–85. 2.6, 2.3.1.2

Kraus, B., R. Robinson, J. White, H. Eichenbaum, and M. Hasselmo
2013. Hippocampal Time Cells: Time versus Path Integration. *Neuron*, 78(6):1090–1101. 2.3.2

Kropff, E., J. E. Carmichael, M.-B. Moser, and E. I. Moser
2015. Speed cells in the medial entorhinal cortex. *Nature*, 523(7561):419–424. 2.3.2

Kubota, D.
2002. Endogenous Waves in Hippocampal Slices. *Journal of Neurophysiology*, 89(1):81–89. 2.3.1.3

Kunec, S., M. E. Hasselmo, and N. Kopell
2005. Encoding and Retrieval in the CA3 Region of the Hippocampus: A Model of Theta-Phase Separation. *Journal of Neurophysiology*, 94(1):70–82. 2.4.3

Knig, J. F. R. and R. A. Klippel
1974. *The rat brain: a stereotaxic atlas of the forebrain and lower parts of the brain stem*. R.E. Krieger. Google-Books-ID: bp3wAAAAMAAJ. 3.1.1

Lakatos, P.
2005. An Oscillatory Hierarchy Controlling Neuronal Excitability and Stimulus Processing in the Auditory Cortex. *Journal of Neurophysiology*, 94(3):1904–1911. 1.4.1

Lakatos, P., G. Karmos, A. D. Mehta, I. Ulbert, and C. E. Schroeder
2008. Entrainment of Neuronal Oscillations as a Mechanism of Attentional Selection. *Science*, 320(5872):110–113. 1.3.3.2

Landau, W. M., W. H. Freygang, L. P. Roland, L. Sokoloff, and S. S. Kety
1955. The local circulation of the living brain; values in the unanesthetized and anesthetized cat. *Transactions of the American Neurological Association*, 1(80th Meeting):125–129. 3.3.1.1

Landfield, P. W., J. L. McGaugh, and R. J. Tusa
1972. Theta Rhythm: A Temporal Correlate of Memory Storage Processes in the Rat. *Science*, 175(4017):87–89. 2.3.1.1, 2.4.3

Lassen, N. A., D. H. Ingvar, and E. Skinhj
1978. Brain function and blood flow. *Scientific American*, 239(4):62–71. 3.3.1.1

Lauritzen, M.
2005. Opinion: Reading vascular changes in brain imaging: is dendritic calcium the key? *Nature Reviews Neuroscience*, 6(1):77–85. 7.2.5

Lawrence, J. and C. J. McBain
2003. Interneuron Diversity series: Containing the detonation feedforward inhibition in the CA3 hippocampus. *Trends in Neurosciences*, 26(11):631–640. 7.2.2

Ledberg, A. and D. Robbe
2011. Locomotion-Related Oscillatory Body Movements at 612 Hz Modulate the Hippocampal Theta Rhythm. *PLoS ONE*, 6(11):e27575. 2.3.1.2, 2.4.1

Lee, A. K. and M. A. Wilson
2002. Memory of sequential experience in the hippocampus during slow wave sleep. *Neuron*, 36(6):1183–1194. 1.3.3.3, 2.3.1.3, 2.4.2

Lee, H., D. Dvorak, H.-Y. Kao, A. Duffy, H. Scharfman, and A. Fenton
2012. Early Cognitive Experience Prevents Adult Deficits in a Neurodevelopmental Schizophrenia Model. *Neuron*, 75(4):714–724. 2.4.4

Lein, E. S., M. J. Hawrylycz, N. Ao, M. Ayres, A. Bensinger, A. Bernard, A. F. Boe, M. S. Boguski, K. S. Brockway, E. J. Byrnes, L. Chen, L. Chen, T.-M. Chen, M. Chi Chin, J. Chong, B. E. Crook, A. Czaplinska, C. N. Dang, S. Datta, N. R. Dee, A. L. Desaki, T. Desta, E. Diep, T. A. Dolbeare, M. J. Donelan, H.-W. Dong, J. G. Dougherty, B. J. Duncan, A. J. Ebbert, G. Eichele, L. K. Estin, C. Faber, B. A. Facer, R. Fields, S. R. Fischer, T. P. Fliss, C. Frensley, S. N. Gates, K. J. Glattfelder, K. R. Halverson, M. R. Hart, J. G. Hohmann, M. P. Howell, D. P. Jeung, R. A. Johnson, P. T. Karr, R. Kawal, J. M. Kidney, R. H. Knapik, C. L. Kuan, J. H. Lake, A. R. Laramee, K. D. Larsen, C. Lau, T. A. Lemon, A. J. Liang, Y. Liu, L. T. Luong, J. Michaels, J. J. Morgan, R. J. Morgan, M. T. Mortrud, N. F. Mosqueda, L. L. Ng, R. Ng, G. J. Orta, C. C. Overly, T. H. Pak, S. E. Parry, S. D. Pathak, O. C. Pearson, R. B. Puchalski, Z. L. Riley, H. R. Rockett, S. A. Rowland, J. J. Royall, M. J. Ruiz, N. R. Sarno, K. Schaffnit, N. V. Shapovalova, T. Sivisay, C. R. Slaughterbeck, S. C. Smith, K. A. Smith, B. I. Smith, A. J. Sodt, N. N. Stewart, K.-R. Stumpf, S. M. Sunkin, M. Sutram, A. Tam, C. D. Teemer, C. Thaller, C. L. Thompson, L. R. Varnam, A. Visel, R. M. Whitlock, P. E. Wohnoutka, C. K. Wolkey, V. Y. Wong, M. Wood, M. B. Yaylaoglu, R. C. Young, B. L. Youngstrom, X. Feng Yuan, B. Zhang, T. A. Zwingman, and A. R. Jones
2007. Genome-wide atlas of gene expression in the adult mouse brain. *Nature*, 445(7124):168–176. 2.2.3.2, 3.1.1

Leker, R. R. and E. Shohami
2002. Cerebral ischemia and traumadifferent etiologies yet similar mechanisms: neuroprotective opportunities. *Brain Research Reviews*, 39(1):55–73. 3.2

Leski, S., H. Lindn, T. Tetzlaff, K. H. Pettersen, and G. T. Einevoll
2013. Frequency Dependence of Signal Power and Spatial Reach of the Local Field Potential. *PLoS Computational Biology*, 9(7):e1003137. 1.1.5.3, 1.4

Lettvin, J. Y., H. R. Maturana, W. S. McCulloch, and W. H. Pitts
1959. What the Frog's Eye Tells the Frog's Brain. *Proceedings of the IRE*, 47(11):1940–1951. 1.2.1

Lever, C., S. Burton, A. Jeewajee, J. O'Keefe, and N. Burgess
2009. Boundary Vector Cells in the Subiculum of the Hippocampal Formation. *The Journal of Neuroscience*, 29(31):9771–9777. 2.3.1.2, 2.3.2

Li, C.-y. T., M.-m. Poo, and Y. Dan
2009a. Burst Spiking of a Single Cortical Neuron Modifies Global Brain State. *Science*, 324(5927):643–646. 1.3.2.5

Li, J.-Y., T. B. J. Kuo, J.-C. Yen, S.-C. Tsai, and C. C. H. Yang
2014. Voluntary and involuntary running in the rat show different patterns of theta rhythm, physical activity, and heart rate. *Journal of Neurophysiology*, 111(10):2061–2070. 7.2.1

Li, L., Z. Ke, K. Y. Tong, and M. Ying
2010. Evaluation of Cerebral Blood Flow Changes in Focal Cerebral Ischemia Rats by Using Transcranial Doppler Ultrasonography. *Ultrasound in Medicine & Biology*, 36(4):595–603. **??**

Li, N., X. Jia, K. Murari, R. Parlapalli, A. Rege, and N. V. Thakor
2009b. High spatiotemporal resolution imaging of the neurovascular response to electrical stimulation of rat peripheral trigeminal nerve as revealed by in vivo temporal laser speckle contrast. *Journal of Neuroscience Methods*, 176(2):230–236. 3.3.2.2, 3.13

Lin, A.-L., P. T. Fox, J. Hardies, T. Q. Duong, and J.-H. Gao
2010. Nonlinear coupling between cerebral blood flow, oxygen consumption, and ATP production in human visual cortex. *Proceedings of the National Academy of Sciences*, 107(18):8446–8451. 3.2.4.3, 7.1.3.3

Lindauer, U., C. Leithner, H. Kaasch, B. Rohrer, M. Foddis, M. Fchtemeier, N. Offenhauser, J. Steinbrink, G. Royl, M. Kohl-Bareis, and U. Dirnagl
2010. Neurovascular coupling in rat brain operates independent of hemoglobin deoxygenation. *Journal of Cerebral Blood Flow & Metabolism*, 30(4):757–768. 3.2.2

Lindn, H., K. H. Pettersen, and G. T. Einevoll
2010. Intrinsic dendritic filtering gives low-pass power spectra of local field potentials. *Journal of Computational Neuroscience*, 29(3):423–444. 1.1.3.1

Lindn, H., T. Tetzlaff, T. Potjans, K. Pettersen, S. Grn, M. Diesmann, and G. Einevoll
2011. Modeling the Spatial Reach of the LFP. *Neuron*, 72(5):859–872. 1.1.4, 1.1.5.2

Lisman, J. and O. Jensen
2013. The Theta-Gamma Neural Code. *Neuron*, 77(6):1002–1016. 7.2.5

Lisman, J. E. and M. A. Idiart
1995. Storage of 7 +/- 2 short-term memories in oscillatory subcycles. *Science*, 267(5203):1512–1515. 2.4.2

Llins, R. R.
1988. The intrinsic electrophysiological properties of mammalian neurons: insights into central nervous system function. *Science (New York, N.Y.)*, 242(4886):1654–1664. 1.1.3.4, 1.3.2.2

Lo, E. H., T. Dalkara, and M. A. Moskowitz
2003. Mechanisms, challenges and opportunities in stroke. *Nature Reviews Neuroscience*, 4(5):399–414. 3.2.2

Logothetis, N. K.
2008. What we can do and what we cannot do with fMRI. *Nature*, 453(7197):869–878. 7.2.4

Logothetis, N. K.
2015. Neural-Event-Triggered fMRI of large-scale neural networks. *Current Opinion in Neurobiology*, 31:214–222. 3.3.1.1

Logothetis, N. K., O. Eschenko, Y. Murayama, M. Augath, T. Steudel, H. C. Evrard, M. Besserve, and A. Oeltermann
2012. Hippocampalcortical interaction during periods of subcortical silence. *Nature*, 491(7425):547–553. 1.8, 1.4.1, 7.3.3

Logothetis, N. K., J. Pauls, M. Augath, T. Trinath, and A. Oeltermann
2001. Neurophysiological investigation of the basis of the fMRI signal. *Nature*, 412(6843):150–157. 3.2.4.1, 7.2.4

Loomis, A. L., E. N. Harvey, and G. A. Hobart
1937. Cerebral states during sleep, as studied by human brain potentials. *Journal of Experimental Psychology*, 21(2):127–144. 1.3.3.1

Lorente De N, R.
1934. Studies on the structure of the cerebral cortex. II. Continuation of the study of the ammonic system. *Journal fr Psychologie und Neurologie*, 46:113–177. 2.2.2.1

Lovett-Barron, M., P. Kaifosh, M. A. Kheirbek, N. Danielson, J. D. Zaremba, T. R. Reardon, G. F. Turi, R. Hen, B. V. Zemelman, and A. Losonczy
2014. Dendritic Inhibition in the Hippocampus Supports Fear Learning. *Science*, 343(6173):857–863. 3.3.3.2

Lubenov, E. V. and A. G. Siapas
2009. Hippocampal theta oscillations are travelling waves. *Nature*, 459(7246):534–539. 1.1.2.3, 1.4.2.3, 2.3.1.2, 2.9, 7.2.2

Maccaferri, G. and C. J. McBain
1996. The hyperpolarization-activated current (Ih) and its contribution to pacemaker activity in rat CA1 hippocampal stratum oriens-alveus interneurones. *The Journal of Physiology*, 497(Pt 1):119. 2.3.1.2

Mace, E., G. Montaldo, B.-F. Osmanski, I. Cohen, M. Fink, and M. Tanter
2013. Functional ultrasound imaging of the brain: theory and basic principles. *IEEE*

Transactions on Ultrasonics, Ferroelectrics and Frequency Control, 60(3):492–506. 3.3.4, 4.2, 4.2, 4.1.3

Macrides, F., H. B. Eichenbaum, and W. B. Forbes
1982. Temporal relationship between sniffing and the limbic theta rhythm during odor discrimination reversal learning. *The Journal of Neuroscience: The Official Journal of the Society for Neuroscience*, 2(12):1705–1717. 2.3.1.2

Mac, E.
2012. *Dveloppement d'une nouvelle modalit d'imagerie fonctionnelle crbraleet tude de l'lasticit du cerveau par ultrasons.* PhD thesis, Paris 7. 4.1

Mac, E., G. Montaldo, I. Cohen, M. Baulac, M. Fink, and M. Tanter
2011. Functional ultrasound imaging of the brain. *Nature Methods*, 8(8):662–664. 3.3.4, 3.17, 4.3.3, 7.1.1

Malonek, D. and A. Grinvald
1996. Interactions Between Electrical Activity and Cortical Microcirculation Revealed by Imaging Spectroscopy: Implications for Functional Brain Mapping. *Science*, 272(5261):551–554. 3.3.1.2

Maquet, P., J. Pters, J. Aerts, G. Delfiore, C. Degueldre, A. Luxen, and G. Franck
1996. Functional neuroanatomy of human rapid-eye-movement sleep and dreaming. *Nature*, 383(6596):163–166. 2.4.5

Markov, N. T., J. Vezoli, P. Chameau, A. Falchier, R. Quilodran, C. Huissoud, C. Lamy, P. Misery, P. Giroud, S. Ullman, P. Barone, C. Dehay, K. Knoblauch, and H. Kennedy
2014. Anatomy of hierarchy: Feedforward and feedback pathways in macaque visual cortex: Cortical counterstreams. *Journal of Comparative Neurology*, 522(1):225–259. 1.4.2.3

Marr, D.
1971. Simple Memory: A Theory for Archicortex. *Philosophical Transactions of the Royal Society of London B: Biological Sciences*, 262(841):23–81. 2.1.4, 2.3.1.1

Mathiesen, C., K. Caesar, N. Akgren, and M. Lauritzen
1998. Modification of activity-dependent increases of cerebral blood flow by excitatory synaptic activity and spikes in rat cerebellar cortex. *The Journal of physiology*, 512(2):555–566. 3.2.4.1

McCaslin, A. F. H., B. R. Chen, A. J. Radosevich, B. Cauli, and E. M. C. Hillman
2011. in vivo 3d Morphology of AstrocyteVasculature Interactions in the Somatosensory Cortex: Implications for Neurovascular Coupling. *Journal of Cerebral Blood Flow & Metabolism*, 31(3):795–806. 3.2.3.2

McCormick, B. H., W. Koh, Y. Choe, L. C. Abbott, J. Keyser, D. Mayerich, Z. Melek, and P. Doddapaneni
2004. Construction of anatomically correct models of mouse brain networks. *Neurocomputing*, 58:379–386. 3.1.1

McNaughton, B. L.
1983. Activity-dependent modulation of hippocampal synaptic efficacy: some implications for memory processes. In *The Neurobiology of the Hippocampus*, Pp. 233–251. 2.3.1.1

Medvedev, A. V., J. M. Kainerstorfer, S. V. Borisov, A. H. Gandjbakhche, and J. VanMeter
2010. Seeing electroencephalogram through the skull: imaging prefrontal cortex with fast optical signal. *Journal of biomedical optics*, 15(6):061702–061702. 3.3.2.3

Mesquita, R. C., M. A. Franceschini, and D. A. Boas
2010. Resting state functional connectivity of the whole head with near-infrared spectroscopy. *Biomedical Optics Express*, 1(1):324–336. 3.3.2.3

Miao, P., H. Lu, Q. Liu, Y. Li, and S. Tong
2011. Laser speckle contrast imaging of cerebral blood flow in freely moving animals. *Journal of biomedical optics*, 16(9):090502–090502. 3.13, 3.3.2.2

Milner, B.
1962. Les troubles de la memoire accompagnant des lesions hippocampiques bilaterales. In *Physiologie de l'Hippocampe*, Pp. 257–272. Paris: ditions Recherche Scientifique. 2.1.1

Mohajerani, M. H., A. W. Chan, M. Mohsenvand, J. LeDue, R. Liu, D. A. McVea, J. D. Boyd, Y. T. Wang, M. Reimers, and T. H. Murphy
2013. Spontaneous cortical activity alternates between motifs defined by regional axonal projections. *Nature Neuroscience*, 16(10):1426–1435. 3.15, 3.3.3.1

Montaldo, G., M. Tanter, J. Bercoff, N. Benech, and M. Fink
2009. Coherent plane-wave compounding for very high frame rate ultrasonography and transient elastography. *IEEE Transactions on Ultrasonics, Ferroelectrics and Frequency Control*, 56(3):489–506. 4.1.1, 4.1.3

Montgomery, S. M., M. I. Betancur, and G. Buzsaki
2009. Behavior-Dependent Coordination of Multiple Theta Dipoles in the Hippocampus. *Journal of Neuroscience*, 29(5):1381–1394. 7.2.4

Montgomery, S. M., A. Sirota, and G. Buzsaki
2008. Theta and Gamma Coordination of Hippocampal Networks during Waking and Rapid Eye Movement Sleep. *Journal of Neuroscience*, 28(26):6731–6741. 2.4.5, 7.2.4

Moser, M.-B. and E. I. Moser
1998. Functional differentiation in the hippocampus. *Hippocampus*, 8(6):608–619. 2.2.3.3, 3.1.2

Mosso, A.
1880. *Sulla circolazione del sangue nel cervello dell'uomo : ricerche sfigmografiche*, royal college of surgeons of england edition. Roma : Coi tipi del Salviucci. 3.2.1

Murari, K., N. Li, A. Rege, X. Jia, A. All, and N. Thakor
2007. Contrast-enhanced imaging of cerebral vasculature with laser speckle. *Applied optics*, 46(22):5340–5346. 3.3.2.2

Murphy, T. H., J. D. Boyd, F. Bolaos, M. P. Vanni, G. Silasi, D. Haupt, and J. M. LeDue
2016. High-throughput automated home-cage mesoscopic functional imaging of mouse cortex. *Nature Communications*, 7:11611. 3.16, 3.3.3.2

Nadel, L.
1968. Dorsal and ventral hippocampal lesions and behavior. *Physiology & Behavior*, 3(6):891–900. 2.2.3

Nadel, L. and M. Moscovitch
1997. Memory consolidation, retrograde amnesia and the hippocampal complex. *Current Opinion in Neurobiology*, 7(2):217–227. 2.1.4

Nakai, J., M. Ohkura, and K. Imoto
2001. A high signal-to-noise Ca2+ probe composed of a single green fluorescent protein. *Nature Biotechnology*, 19(2):137–141. 3.3.3.2

Narayanan, N. S. and M. Laubach
2009. Methods for Studying Functional Interactions Among Neuronal Populations. In *Dynamic Brain Imaging*, F. Hyder and J. M. Walker, eds., volume 489, Pp. 135–165. Totowa, NJ: Humana Press. 4.4.4

Nerad, L. and D. K. Bilkey
2005. Ten- to 12-Hz EEG Oscillation in the Rat Hippocampus and Rhinal Cortex That Is Modulated by Environmental Familiarity. *Journal of Neurophysiology*, 93(3):1246–1254. 2.3.1.1

Newman, E. L., S. N. Gillet, J. R. Climer, and M. E. Hasselmo
2013. Cholinergic Blockade Reduces Theta-Gamma Phase Amplitude Coupling and Speed Modulation of Theta Frequency Consistent with Behavioral Effects on Encoding. *The Journal of Neuroscience*, 33(50):19635–19646. 2.3.1.4

Nguyen, J., N. Nishimura, R. N. Fetcho, C. Iadecola, and C. B. Schaffer
2011. Occlusion of cortical ascending venules causes blood flow decreases, reversals in flow direction, and vessel dilation in upstream capillaries. *Journal of Cerebral Blood Flow & Metabolism*, 31(11):2243–2254. **??**

Niedermeyer, E. and F. H. L. d. Silva
2005. *Electroencephalography: Basic Principles, Clinical Applications, and Related Fields*. Lippincott Williams & Wilkins. Google-Books-ID: tndqYGPHQdEC. 1.1.4.1

Niessing, J.
2005. Hemodynamic Signals Correlate Tightly with Synchronized Gamma Oscillations. *Science*, 309(5736):948–951. 7.2.4, 7.3

Nir, Y., M. Massimini, M. Boly, and G. Tononi
2013. Sleep and Consciousness. In *Neuroimaging of Consciousness*, A. E. Cavanna, A. Nani, H. Blumenfeld, and S. Laureys, eds., Pp. 133–182. Berlin, Heidelberg: Springer Berlin Heidelberg. 7.1.3.2

Nishimura, N., C. B. Schaffer, B. Friedman, P. D. Lyden, and D. Kleinfeld
2007. Penetrating arterioles are a bottleneck in the perfusion of neocortex. *Proceedings of the National Academy of Sciences*, 104(1):365–370. 3.1.2, ??

Nizar, K., H. Uhlirova, P. Tian, P. A. Saisan, Q. Cheng, L. Reznichenko, K. L. Weldy, T. C. Steed, V. B. Sridhar, C. L. MacDonald, J. Cui, S. L. Gratiy, S. Sakadi, D. A. Boas, T. I. Beka, G. T. Einevoll, J. Chen, E. Masliah, A. M. Dale, G. A. Silva, and A. Devor
2013. In vivo Stimulus-Induced Vasodilation Occurs without IP3 Receptor Activation and May Precede Astrocytic Calcium Increase. *The Journal of Neuroscience*, 33(19):8411–8422. 3.2.3.2

Nunez, P. L. and R. Srinivasan
2006. *Electric Fields of the Brain: The Neurophysics of EEG*. Oxford University Press. Google-Books-ID: fUv54as56_8C. 1.1.2.1, 1.1.2.3, 1.1.3.1, 1.3.2.1

Obrenovitch, T. P., S. Chen, and E. Farkas
2009. Simultaneous, live imaging of cortical spreading depression and associated cerebral blood flow changes, by combining voltage-sensitive dye and laser speckle contrast methods. *NeuroImage*, 45(1):68–74. 3.3.3.1

Ogawa, S., T.-M. Lee, A. R. Kay, and D. W. Tank
1990. Brain magnetic resonance imaging with contrast dependent on blood oxygenation. *Proceedings of the National Academy of Sciences*, 87(24):9868–9872. 3.3.1.1, 3.3.1.1, 3.9

O'Keefe, J. and J. Dostrovsky
1971. The hippocampus as a spatial map. Preliminary evidence from unit activity in the freely-moving rat. *Brain Research*, 34(1):171–175. 2.1.3, 2.2, 2.3.2

O'Keefe, J. and L. Nadel
1978. *The hippocampus as a cognitive map*. Clarendon Press. Google-Books-ID: A_VqAAAAMAAJ. 2.1.3, 2.1.4, 2.2.3.3, 2.3.1.1

O'Keefe, J. and M. L. Recce
1993. Phase relationship between hippocampal place units and the EEG theta rhythm. *Hippocampus*, 3(3):317–330. 2.3.2, 2.4.2

Ono, T., K. Nakamura, M. Fukuda, and R. Tamura
1991. Place recognition responses of neurons in monkey hippocampus. *Neuroscience Letters*, 121(12):194–198. 2.1.3

Osipova, D., D. Hermes, and O. Jensen
2008. Gamma Power Is Phase-Locked to Posterior Alpha Activity. *PLOS ONE*, 3(12):e3990. 1.4.1

Osmanski, B., C. Martin, G. Montaldo, P. Lanice, F. Pain, M. Tanter, and H. Gurden
2014a. Functional ultrasound imaging reveals different odor-evoked patterns of vascular activity in the main olfactory bulb and the anterior piriform cortex. *NeuroImage*, 95:176–184. 3.3.4, 7.1.1

Osmanski, B.-F., S. Pezet, A. Ricobaraza, Z. Lenkei, and M. Tanter
2014b. Functional ultrasound imaging of intrinsic connectivity in the living rat brain with high spatiotemporal resolution. *Nature Communications*, 5:5023. 3.17, 3.3.4

OHerron, P., P. Y. Chhatbar, M. Levy, Z. Shen, A. E. Schramm, Z. Lu, and P. Kara
2016. Neural correlates of single-vessel haemodynamic responses in vivo. *Nature*, 534(7607):378–382. 3.7, 3.2.4.1

Packer, A. M., L. E. Russell, H. W. P. Dalgleish, and M. Husser
2015. Simultaneous all-optical manipulation and recording of neural circuit activity with cellular resolution in vivo. *Nature Methods*, 12(2):140–146. 3.3.3.2

Papp, E. A., T. B. Leergaard, E. Calabrese, G. A. Johnson, and J. G. Bjaalie
2014. Waxholm Space atlas of the Sprague Dawley rat brain. *NeuroImage*, 97:374–386. 3.1.1, 4.9

Pastalkova, E., V. Itskov, A. Amarasingham, and G. Buzsaki
2008. Internally Generated Cell Assembly Sequences in the Rat Hippocampus. *Science*, 321(5894):1322–1327. 2.3.2

Patel, J., S. Fujisawa, A. Bernyi, S. Royer, and G. Buzski
2012. Traveling Theta Waves along the Entire Septotemporal Axis of the Hippocampus. *Neuron*, 75(3):410–417. 1.1.2.3, 1.4.2.3, 2.3.1.2, 7.2.2

Pauling, L. and C. D. Coryell
1936. The magnetic properties and structure of hemoglobin, oxyhemoglobin and carbonmonoxyhemoglobin. *Proceedings of the National Academy of Sciences*, 22(4):210–216. 3.3.1.1

Paxinos, G.
2004. *The Rat Nervous System*. Gulf Professional Publishing. Google-Books-ID: F5xkDtDL4AUC. 3.1

Paxinos, G., X.-F. Huang, M. Petrides, and A. W. Toga
2009a. *The rhesus monkey brain in stereotaxic coordinates, 2nd Edition*. San Diego: Elsevier Academic Press. 3.1.1

Paxinos, G. and C. Watson
1982. *The Rat Brain in Stereotaxic Coordinates*. Academic Press. Google-Books-ID: 0prYfdDbh58C. 3.1.1, 4.6

Paxinos, G., C. Watson, P. Carrive, M. Kirkcaldie, and K. Ashwell, eds.
2009b. *Chemoarchitectonic atlas of the rat brain, 2nd edition*, 2. ed edition. San Diego: Elsevier Academic Press. OCLC: 845417137. 3.1.1

Pellegrino, L. J.
1995. *Stereotaxic Atlas of the Rat Brain*, 2nd edition edition. New York: Springer. 3.1.1

Peppiatt, C. M., C. Howarth, P. Mobbs, and D. Attwell
2006. Bidirectional control of CNS capillary diameter by pericytes. *Nature*, 443(7112):700–704. 3.2.3.2

Perez-Orive, J., O. Mazor, G. C. Turner, S. Cassenaer, R. I. Wilson, and G. Laurent
2002. Oscillations and sparsening of odor representations in the mushroom body. *Science*, 297(5580):359–365. 1.3.3.4

Pernet, C. R., R. Wilcox, and G. A. Rousselet
2013. Robust Correlation Analyses: False Positive and Power Validation Using a New Open Source Matlab Toolbox. *Frontiers in Psychology*, 3. 7.1.3.3

Petzold, G. and V. Murthy
2011. Role of Astrocytes in Neurovascular Coupling. *Neuron*, 71(5):782–797. 3.2.2

Pfeiffer, B. E. and D. J. Foster
2013. Hippocampal place-cell sequences depict future paths to remembered goals. *Nature*, 497(7447):74–79. 2.3.1.3, 2.4.2

Phelps, M. E., E. J. Hoffman, N. A. Mullani, and M. M. Ter-Pogossian
1975. Application of annihilation coincidence detection to transaxial reconstruction tomography. *Journal of Nuclear Medicine: Official Publication, Society of Nuclear Medicine*, 16(3):210–224. 3.3.1.1

Pine, J.
1980. Recording action potentials from cultured neurons with extracellular microcircuit electrodes. *Journal of Neuroscience Methods*, 2(1):19–31. 1.1.2.3

Prewitt, R. L., D. C. Rice, and A. D. Dobrian
2002. Adaptation of Resistance Arteries to Increases in Pressure. *Microcirculation*, 9(4):295–304. 3.2.3.1

Quiroga, R. Q., L. Reddy, G. Kreiman, C. Koch, and I. Fried
2005. Invariant visual representation by single neurons in the human brain. *Nature*, 435(7045):1102–1107. 1.2.1

Raichle, M. E.
1998. Behind the scenes of functional brain imaging: A historical and physiological perspective. *Proceedings of the National Academy of Sciences*, 95(3):765–772. 3.2.1, 3.9

Raichle, M. E.
2009. A Paradigm Shift in Functional Brain Imaging. *Journal of Neuroscience*, 29(41):12729–12734. 7.1.3.2

Rajasethupathy, P., S. Sankaran, J. H. Marshel, C. K. Kim, E. Ferenczi, S. Y. Lee, A. Berndt, C. Ramakrishnan, A. Jaffe, M. Lo, C. Liston, and K. Deisseroth
2015. Projections from neocortex mediate top-down control of memory retrieval. *Nature*, 526(7575):653–659. 2.2.2.2

Ramn y Cajal, S. .-.
1911. *Histologie du systme nerveux de l'homme et des vertbrs. Cervelet, cerveau moyen, rtine, couche optique, corps stri, corce crbrale gnrale et rgionale, grand sympathique.* 2.2.2.1

Ranck, J.
1984. Head-direction cells in the deep cell layers of dorsal presubiculum in freely moving rats. *Society for Neuroscience Abstracts*, 10. 2.3.2

Ray, S. and J. H. Maunsell
2010. Differences in Gamma Frequencies across Visual Cortex Restrict Their Possible Use in Computation. *Neuron*, 67(5):885–896. 1.1.5.4

Redish, A. D. and D. S. Touretzky
1997. The Role of the Hippocampus in Solving the Morris Water Maze. *Computational Neuroscience*. 2.1.4, 2.3.1.4

Reivich, M., D. Kuhl, A. Wolf, J. Greenberg, M. a. Phelps, T. Ido, V. Casella, J. Fowler, E. Hoffman, A. Alavi, and others
1979. The [18f] fluorodeoxyglucose method for the measurement of local cerebral glucose utilization in man. *Circulation research*, 44(1):127–137. 3.3.1.1

Ren, X. and J. Malik
2003. Learning a classification model for segmentation. In *Computer Vision, 2003. Proceedings. Ninth IEEE International Conference on*, Pp. 10–17. IEEE. 7.1.3.3

Risold, P. Y. and L. W. Swanson
1996. Structural evidence for functional domains in the rat hippocampus. *Science (New York, N.Y.)*, 272(5267):1484–1486. 2.2.3.1

Rivas, J., J. M. Gaztelu, and E. Garcia-Austt
1996. Changes in hippocampal cell discharge patterns and theta rhythm spectral properties as a function of walking velocity in the guinea pig. *Experimental brain research*, 108(1):113–118. 2.3.1.2

Rosen, B. R., R. L. Buckner, and A. M. Dale
1998. Event-related functional MRI: Past, present, and future. *Proceedings of the National Academy of Sciences*, 95(3):773–780. 3.3.1.1

Rosenblatt, F.
1958. The perceptron: a probabilistic model for information storage and organization in the brain. *Psychological review*, 65(6):386. 1.2

Rousseau, F.
2003. *Mthodes d'analyse d'images et de calibration pour l'chographie 3D en mode main-libre*. PhD thesis, Universit Rennes 1. 4.1.1

Roy, C. S. and C. S. Sherrington
1890. On the Regulation of the Blood-supply of the Brain. *The Journal of Physiology*, 11(1-2):85–158.17. 3.2.1

Rvachev, M. M.
2010. On axoplasmic pressure waves and their possible role in nerve impulse propagation. *Biophysical Reviews and Letters*, 5(02):73–88. 7.2.2

Sainsbury, R. S.
1998. Hippocampal theta: a sensory-inhibition theory of function. *Neuroscience & Biobehavioral Reviews*, 22(2):237–241. 2.3.1.2

Salzberg, B. M., H. V. Davila, and L. B. Cohen
1973. Optical recording of impulses in individual neurones of an invertebrate central nervous system. *Nature*, 246(5434):508–509. 3.3.3.1

Schaffer, C. B., B. Friedman, N. Nishimura, L. F. Schroeder, P. S. Tsai, F. F. Ebner, P. D. Lyden, and D. Kleinfeld
2006. Two-Photon Imaging of Cortical Surface Microvessels Reveals a Robust Redistribution in Blood Flow after Vascular Occlusion. *PLOS Biol*, 4(2):e22. 3.1.2

Schnitzler, A. and J. Gross
2005. Normal and pathological oscillatory communication in the brain. *Nature Reviews Neuroscience*, 6(4):285–296. 1.3.2.2, 1.3.3.4, 2.4.4

Schoffelen, J.-M., J. Poort, R. Oostenveld, and P. Fries
2011. Selective Movement Preparation Is Subserved by Selective Increases in Corticomuscular Gamma-Band Coherence. *The Journal of Neuroscience*, 31(18):6750–6758. 1.4.2.3

Schomburg, E., A. Fernndez-Ruiz, K. Mizuseki, A. Bernyi, C. Anastassiou, C. Koch, and G. Buzski
2014. Theta Phase Segregation of Input-Specific Gamma Patterns in Entorhinal-Hippocampal Networks. *Neuron*, 84(2):470–485. 2.3.1.4, 2.10, 2.4.3, 7.2.4

Schridde, U., M. Khubchandani, J. E. Motelow, B. G. Sanganahalli, F. Hyder, and H. Blumenfeld
2008. Negative BOLD with Large Increases in Neuronal Activity. *Cerebral Cortex*, 18(8):1814–1827. 3.3.1.2

Schultz, W., P. Dayan, and P. R. Montague
1997. A neural substrate of prediction and reward. *Science (New York, N.Y.)*, 275(5306):1593–1599. 7.3.2.1

Schulz, D., S. Southekal, S. S. Junnarkar, J.-F. Pratte, M. L. Purschke, S. P. Stoll, B. Ravindranath, S. H. Maramraju, S. Krishnamoorthy, F. A. Henn, P. O'Connor, C. L. Woody, D. J. Schlyer, and P. Vaska
2011. Simultaneous assessment of rodent behavior and neurochemistry using a miniature positron emission tomograph. *Nature Methods*, 8(4):347–352. 3.3.1.3, 3.3.5

Schlvinck, M. L., A. Maier, F. Q. Ye, J. H. Duyn, and D. A. Leopold
2010. Neural basis of global resting-state fMRI activity. *Proceedings of the National Academy of Sciences*, 107(22):10238–10243. 7.2.4

Scoville, W. B. and B. Milner
1957. Loss of recent memory after bilateral hippocampal lesions. *Journal of Neurology, Neurosurgery & Psychiatry*, 20(1):11–21. 2.1.1, 2.1, 2.1.4

Scremin, O. U.
1995. Cerebral vascular system. In *The rat nervous system*, volume 2, Pp. 3–35. San Diego: Academic Press. 3.1.2, 3.2

Sei, H. and Y. Morita
1996. Acceleration of EEG theta wave precedes the phasic surge of arterial pressure during REM sleep in the rat. *Neuroreport*, 7(18):3059–3062. 2.4.5

Seidenbecher, T., T. R. Laxmi, O. Stork, and H.-C. Pape
2003. Amygdalar and hippocampal theta rhythm synchronization during fear memory retrieval. *Science (New York, N.Y.)*, 301(5634):846–850. 2.4.4

Senior, T. J., J. R. Huxter, K. Allen, J. O'Neill, and J. Csicsvari
2008. Gamma Oscillatory Firing Reveals Distinct Populations of Pyramidal Cells in the CA1 Region of the Hippocampus. *Journal of Neuroscience*, 28(9):2274–2286. 2.12

Sharp, P. S., K. Shaw, L. Boorman, S. Harris, A. J. Kennerley, M. Azzouz, and J. Berwick
2015. Comparison of stimulus-evoked cerebral hemodynamics in the awake mouse and under a novel anesthetic regime. *Scientific Reports*, 5:12621. 3.12, 3.3.2.1

Sheinberg, D. L. and N. K. Logothetis
1997. The role of temporal cortical areas in perceptual organization. *Proceedings of the National Academy of Sciences*, 94(7):3408–3413. 1.2.2

Shen, Q., S. Huang, and T. Q. Duong
2015. Ultra-high spatial resolution basal and evoked cerebral blood flow MRI of the rat brain. *Brain Research*, 1599:126–136. 3.2.4

Shih, A. Y., J. D. Driscoll, P. J. Drew, N. Nishimura, C. B. Schaffer, and D. Kleinfeld
2012. Two-photon microscopy as a tool to study blood flow and neurovascular coupling in the rodent brain. *Journal of Cerebral Blood Flow & Metabolism*, 32(7):1277–1309. 3.3.2.5, ??

Shih, A. Y., B. Friedman, P. J. Drew, P. S. Tsai, P. D. Lyden, and D. Kleinfeld
2009. Active dilation of penetrating arterioles restores red blood cell flux to penumbral neocortex after focal stroke. *Journal of Cerebral Blood Flow & Metabolism*, 29(4):738–751. ??

Shimomura, O., F. H. Johnson, and Y. Saiga
1962. Extraction, Purification and Properties of Aequorin, a Bioluminescent Protein from the Luminous Hydromedusan, Aequorea. *Journal of Cellular and Comparative Physiology*, 59(3):223–239. 3.3.3.2

Shipman, S. and R. Astur
2008. Factors affecting the hippocampal BOLD response during spatial memory. *Behavioural Brain Research*, 187(2):433–441. 7.2.1

Shmuel, A., E. Yacoub, J. Pfeuffer, P.-F. Van de Moortele, G. Adriany, X. Hu, and K. Ugurbil
2002. Sustained Negative BOLD, Blood Flow and Oxygen Consumption Response and Its Coupling to the Positive Response in the Human Brain. *Neuron*, 36(6):1195–1210. 3.3.1.2

Shung, K. K., G. Cloutier, and C. C. Lim
1992. The effects of hematocrit, shear rate, and turbulence on ultrasonic Doppler spectrum from blood. *IEEE transactions on biomedical engineering*, 39(5):462–469. 4.1.3

Siegel, M. S. and E. Y. Isacoff
1997. A genetically encoded optical probe of membrane voltage. *Neuron*, 19(4):735–741. 3.3.3.1

Siegle, J. H. and M. A. Wilson
2014. Enhancement of encoding and retrieval functions through theta phase-specific manipulation of hippocampus. *eLife*, 3:e03061. 2.4.3

Sigurdsson, T., K. L. Stark, M. Karayiorgou, J. A. Gogos, and J. A. Gordon
2010. Impaired hippocampalprefrontal synchrony in a genetic mouse model of schizophrenia. *Nature*, 464(7289):763–767. 2.4.4

Sirotin, Y. B. and A. Das
2009. Anticipatory haemodynamic signals in sensory cortex not predicted by local neuronal activity. *Nature*, 457(7228):475–479. 3.3.1.2, 3.11

Sirotin, Y. B., E. M. C. Hillman, C. Bordier, and A. Das
2009. Spatiotemporal precision and hemodynamic mechanism of optical point spreads in alert primates. *Proceedings of the National Academy of Sciences*, 106(43):18390–18395. 3.2.4.2

Skaggs, W. E., B. L. McNaughton, M. A. Wilson, and C. A. Barnes
1996. Theta phase precession in hippocampal neuronal populations and the compression of temporal sequences. *Hippocampus*, 6(2):149–172. 2.4.2

Smith, A. J., H. Blumenfeld, K. L. Behar, D. L. Rothman, R. G. Shulman, and F. Hyder
2002. Cerebral energetics and spiking frequency: The neurophysiological basis of fMRI. *Proceedings of the National Academy of Sciences*, 99(16):10765–10770. 3.2.4.1

Smith, M.-L., G. Bendek, N. Dahlgren, I. Rosn, T. Wieloch, and B. K. Siesj
1984. Models for studying long-term recovery following forebrain ischemia in the rat. 2. A 2-vessel occlusion model. *Acta Neurologica Scandinavica*, 69(6):385–401. 3.1.2

Sohal, V. S., F. Zhang, O. Yizhar, and K. Deisseroth
2009. Parvalbumin neurons and gamma rhythms enhance cortical circuit performance. *Nature*, 459(7247):698–702. 7.2.5

Sokoloff, L., M. Reivich, C. Kennedy, M. H. Des Rosiers, C. S. Patlak, K. D. Pettigrew, O. Sakurada, and M. Shinohara
1977. The [14c]deoxyglucose method for the measurement of local cerebral glucose utilization: theory, procedure, and normal values in the conscious and anesthetized albino rat. *Journal of Neurochemistry*, 28(5):897–916. 3.3.1.1

Somogyi, P., L. Katona, T. Klausberger, B. Lasztoczi, and T. J. Viney
2013. Temporal redistribution of inhibition over neuronal subcellular domains underlies state-dependent rhythmic change of excitability in the hippocampus. *Philosophical Transactions of the Royal Society B: Biological Sciences*, 369(1635):20120518–20120518. 2.3.1.2

Sotelo, C.
2003. Viewing the brain through the master hand of Ramon y Cajal. *Nature Reviews Neuroscience*, 4(1):71–77. 3.1.1

Spellman, T., M. Rigotti, S. E. Ahmari, S. Fusi, J. A. Gogos, and J. A. Gordon
2015. Hippocampalprefrontal input supports spatial encoding in working memory. *Nature*, 522(7556):309–314. 2.2.2.2, 7.4

Sperry, R. W.
1952. Neurology and the Mind-Brain Problem. *American Scientist*, 40(2):291–312. 7.3.2.1

Squire, L. R.
1986. Mechanisms of memory. *Science*, 232(4758):1612–1619. 2.1.2, 2.1.4

Squire, L. R.
1992. Declarative and Nondeclarative Memory: Multiple Brain Systems Supporting Learning and Memory. *Journal of Cognitive Neuroscience*, 4(3):232–243. 2.1, 2.1.2

Stefanovic, B., E. Hutchinson, V. Yakovleva, V. Schram, J. T. Russell, L. Belluscio, A. P. Koretsky, and A. C. Silva
2008. Functional reactivity of cerebral capillaries. *Journal of Cerebral Blood Flow & Metabolism*, 28(5):961–972. 3.2.4

Stensola, H., T. Stensola, T. Solstad, K. Frland, M.-B. Moser, and E. I. Moser
2012. The entorhinal grid map is discretized. *Nature*, 492(7427):72–78. 2.2.3.3

Stepan, J., J. Dine, and M. Eder
2015. Functional optical probing of the hippocampal trisynaptic circuit in vitro: network dynamics, filter properties, and polysynaptic induction of CA1 LTP. *Frontiers in Neuroscience*, 9. 7.2.2, 7.2

Steriade, M., D. A. McCormick, and T. J. Sejnowski
1993. Thalamocortical oscillations in the sleeping and aroused brain. *Science (New York, N.Y.)*, 262(5134):679–685. 1.3.2.3, 1.7, 1.3.2.5

Strange, B. A., M. P. Witter, E. S. Lein, and E. I. Moser
2014. Functional organization of the hippocampal longitudinal axis. *Nature Reviews Neuroscience*, 15(10):655–669. 2.3, 2.2.3.2, 2.2.3.3

Suddarth, S. A. and G. A. Johnson
1991. Three-dimensional MR microscopy with large arrays. *Magnetic Resonance in Medicine*, 18(1):132–141. 3.1.1

Sullivan, D., J. Csicsvari, K. Mizuseki, S. Montgomery, K. Diba, and G. Buzski
2011. Relationships between Hippocampal Sharp Waves, Ripples, and Fast Gamma Oscillation: Influence of Dentate and Entorhinal Cortical Activity. *The Journal of Neuroscience*, 31(23):8605–8616. 2.3.1.3

Sun, W., E. McConnell, J.-F. Pare, Q. Xu, M. Chen, W. Peng, D. Lovatt, X. Han, Y. Smith, and M. Nedergaard
2013. Glutamate-Dependent Neuroglial Calcium Signaling Differs Between Young and Adult Brain. *Science*, 339(6116):197–200. 3.2.3.2

Swanson, L. W., J. M. Wyss, and W. M. Cowan
1978. An autoradiographic study of the organization of intrahippocampal association pathways in the rat. *Journal of comparative neurology*, 181(4):681–715. 2.2.3

Takano, T., G.-F. Tian, W. Peng, N. Lou, W. Libionka, X. Han, and M. Nedergaard
2006. Astrocyte-mediated control of cerebral blood flow. *Nature Neuroscience*, 9(2):260–267. 3.2.3.2

Talbott, J., H. Wolff, and S. Cobb
1929. The cerebral circulation: Vii. changes in cerebral capillary bed following cervical sympathectomy. *Archives of Neurology & Psychiatry*, 21(5):1102–1106. 3.2.1

Tallini, Y. N., M. Ohkura, B.-R. Choi, G. Ji, K. Imoto, R. Doran, J. Lee, P. Plan, J. Wilson, H.-B. Xin, A. Sanbe, J. Gulick, J. Mathai, J. Robbins, G. Salama, J. Nakai, and M. I. Kotlikoff
2006. Imaging cellular signals in the heart in vivo: Cardiac expression of the high-signal Ca2+ indicator GCaMP2. *Proceedings of the National Academy of Sciences of the United States of America*, 103(12):4753–4758. 3.3.3.2

Tanter, M. and M. Fink
2014. Ultrafast imaging in biomedical ultrasound. *IEEE Transactions on Ultrasonics, Ferroelectrics, and Frequency Control*, 61(1):102–119. 3.3.4, 4.1.1

Tasaki, I., L. Carnay, and A. Watanabe
1969. Transient changes in extrinsic fluorescence of nerve produced by electric stimulation. *Proceedings of the National Academy of Sciences*, 64(4):1362–1368. 3.3.3.1

Taube, J. S., R. U. Muller, and J. B. Ranck
1990. Head-direction cells recorded from the postsubiculum in freely moving rats. I. Description and quantitative analysis. *The Journal of Neuroscience*, 10(2):420–435. 2.1.3, 2.3.2

Ter-Pogossian, M. M., M. E. Phelps, E. J. Hoffman, and N. A. Mullani
1975. A Positron-Emission Transaxial Tomograph for Nuclear Imaging (PETT). *Radiology*, 114(1):89–98. 3.3.1.1

Terrazas, A., M. Krause, P. Lipa, K. M. Gothard, C. A. Barnes, and B. L. McNaughton
2005. Self-Motion and the Hippocampal Spatial Metric. *The Journal of Neuroscience*, 25(35):8085–8096. 2.3.1.2

Theer, P., M. T. Hasan, and W. Denk
2003. Two-photon imaging to a depth of 1000 microm in living brains by use of a Ti:Al2o3 regenerative amplifier. *Optics Letters*, 28(12):1022–1024. 3.3.2.5

Thompson, C. L., S. D. Pathak, A. Jeromin, L. L. Ng, C. R. MacPherson, M. T. Mortrud, A. Cusick, Z. L. Riley, S. M. Sunkin, A. Bernard, R. B. Puchalski, F. H. Gage, A. R. Jones, V. B. Bajic, M. J. Hawrylycz, and E. S. Lein
2008. Genomic Anatomy of the Hippocampus. *Neuron*, 60(6):1010–1021. 2.2.3.2, 2.5

Tian, L., S. A. Hires, T. Mao, D. Huber, M. E. Chiappe, S. H. Chalasani, L. Petreanu, J. Akerboom, S. A. McKinney, E. R. Schreiter, C. I. Bargmann, V. Jayaraman, K. Svoboda, and L. L. Looger
2009. Imaging neural activity in worms, flies and mice with improved GCaMP calcium indicators. *Nature Methods*, 6(12):875–881. 3.3.3.2

Tian, P., I. C. Teng, L. D. May, R. Kurz, K. Lu, M. Scadeng, E. M. C. Hillman, A. J. D. Crespigny, H. E. DArceuil, J. B. Mandeville, J. J. A. Marota, B. R. Rosen, T. T. Liu, D. A. Boas, R. B. Buxton, A. M. Dale, and A. Devor
2010. Cortical depth-specific microvascular dilation underlies laminar differences in blood oxygenation level-dependent functional MRI signal. *Proceedings of the National Academy of Sciences*, 107(34):15246–15251. 3.2.3.2

Tort, A. B., M. A. Kramer, C. Thorn, D. J. Gibson, Y. Kubota, A. M. Graybiel, and N. J. Kopell
2008. Dynamic cross-frequency couplings of local field potential oscillations in rat striatum and hippocampus during performance of a T-maze task. *Proceedings of the National Academy of Sciences*, 105(51):20517–20522. 1.3.3.2, 1.4.1, 2.3.1.4

Tort, A. B., R. Scheffer-Teixeira, B. C. Souza, A. Draguhn, and J. Brankak
2013. Theta-associated high-frequency oscillations (110160hz) in the hippocampus and neocortex. *Progress in Neurobiology*, 100:1–14. 2.3.1.4

Tort, A. B. L., R. W. Komorowski, J. R. Manns, N. J. Kopell, and H. Eichenbaum
2009. Thetagamma coupling increases during the learning of itemcontext associations. *Proceedings of the National Academy of Sciences*, 106(49):20942–20947. 1.4.1, 7.4

Toth, K., T. F. Freund, and R. Miles
1997. Disinhibition of rat hippocampal pyramidal cells by GABAergic afferents from the septum. *The Journal of Physiology*, 500(2):463–474. 2.3.1.2

Traub, R. D.
2003. Fast Oscillations and Epilepsy. *Epilepsy Currents / American Epilepsy Society*, 3(3):77–79. 1.3.3.4

Traub, R. D., M. A. Whittington, I. M. Stanford, and J. G. Jefferys
1996. A mechanism for generation of long-range synchronous fast oscillations in the cortex. *Nature*, 383(6601):621–624. 7.2.5

Tsai, P. S., B. Friedman, A. I. Ifarraguerri, B. D. Thompson, V. Lev-Ram, C. B. Schaffer, Q. Xiong, R. Y. Tsien, J. A. Squier, and D. Kleinfeld
2003. All-optical histology using ultrashort laser pulses. *Neuron*, 39(1):27–41. 3.1.1

Uhlirova, H., K. Kl, P. Tian, M. Thunemann, M. Desjardins, P. A. Saisan, S. Sakadi, T. V. Ness, C. Mateo, Q. Cheng, K. L. Weldy, F. Razoux, M. Vandenberghe, J. A. Cremonesi, C. G. Ferri, K. Nizar, V. B. Sridhar, T. C. Steed, M. Abashin, Y. Fainman, E. Masliah, S. Djurovic, O. A. Andreassen, G. A. Silva, D. A. Boas, D. Kleinfeld, R. B. Buxton, G. T. Einevoll, A. M. Dale, and A. Devor
2016. Cell type specificity of neurovascular coupling in cerebral cortex. *eLife*, 5:e14315. 7.1.2

Ulanovsky, N. and C. F. Moss
2007. Hippocampal cellular and network activity in freely moving echolocating bats. *Nature Neuroscience*, 10(2):224–233. 2.3.1.2

Urban, A., E. Mace, C. Brunner, M. Heidmann, J. Rossier, and G. Montaldo
2014. Chronic assessment of cerebral hemodynamics during rat forepaw electrical stimulation using functional ultrasound imaging. *NeuroImage*, 101:138–149. 7.1.1

Valds-Hernndez, P. A.
2011. An in vivo MRI template set for morphometry, tissue segmentation, and fMRI localization in rats. *Frontiers in Neuroinformatics*, 5. 3.1.1

van Raaij, M. E., L. Lindvere, A. Dorr, J. He, B. Sahota, F. S. Foster, and B. Stefanovic
2011. Functional micro-ultrasound imaging of rodent cerebral hemodynamics. *NeuroImage*, 58(1):100–108. 3.3.4, 7.1.1

van Raaij, M. E., L. Lindvere, A. Dorr, J. He, B. Sahota, F. S. Foster, and B. Stefanovic
2012. Quantification of blood flow and volume in arterioles and venules of the rat cerebral cortex using functional micro-ultrasound. *NeuroImage*, 63(3):1030–1037. 3.1.2, 3.3.4

van Strien, N. M., N. L. M. Cappaert, and M. P. Witter
2009. The anatomy of memory: an interactive overview of the parahippocampalhippocampal network. *Nature Reviews Neuroscience*, 10(4):272–282. 2.4

Vanderwolf, C. and G. Baker
1986. Evidence that serotonin mediates non-cholinergic neocortical low voltage fast activity, non-cholinergic hippocampal rhythmical slow activity and contributes to intelligent behavior. *Brain Research*, 374(2):342–356. 2.3.1.2

Vanderwolf, C. H.
1969. Hippocampal electrical activity and voluntary movement in the rat. *Electroencephalography and Clinical Neurophysiology*, 26(4):407–418. 2.3.1.1, 2.3.1.2

Varga, V., B. Hangya, K. Krnitz, A. Ludnyi, R. Zemankovics, I. Katona, R. Shigemoto, T. F. Freund, and Z. Borhegyi
2008. The presence of pacemaker HCN channels identifies theta rhythmic GABAergic neurons in the medial septum: Characterization of medial septal HCN neurons. *The Journal of Physiology*, 586(16):3893–3915. 2.3.1.2

Vaucher, E. and E. Hamel
1995. Cholinergic basal forebrain neurons project to cortical microvessels in the rat: electron microscopic study with anterogradely transported Phaseolus vulgaris leucoagglutinin and choline acetyltransferase immunocytochemistry. *The Journal of neuroscience*, 15(11):7427–7441. 3.2.3.2

Vigneau-Roy, N., M. Bernier, M. Descoteaux, and K. Whittingstall
2014. Regional variations in vascular density correlate with resting-state and task-evoked blood oxygen level-dependent signal amplitude: Correlation Between Vascular Density and BOLD Amplitude. *Human Brain Mapping*, 35(5):1906–1920. 3.3.1.3

Vinogradova, O.
2001. Hippocampus as comparator: Role of the two input and two output systems of the hippocampus in selection and registration of information. *Hippocampus*, 11(5):578–598. 2.4.1

Volgushev, M., M. Chistiakova, and W. Singer
1998. Modification of discharge patterns of neocortical neurons by induced oscillations of the membrane potential. *Neuroscience*, 83(1):15–25. 1.3.2.5

von der Malsburg, C.
1973. Self-organization of orientation sensitive cells in the striate cortex. *Kybernetik*, 14(2):85–100. 1.2

Von Stein, A. and J. Sarnthein
2000. Different frequencies for different scales of cortical integration: from local gamma to long range alpha/theta synchronization. *International Journal of Psychophysiology*, 38(3):301–313. 1.4.1

Wang, X.-J.
2010. Neurophysiological and Computational Principles of Cortical Rhythms in Cognition. *Physiological Reviews*, 90(3):1195–1268. 1.3.2.2, 1.7

Wang, Y., S. Romani, B. Lustig, A. Leonardo, and E. Pastalkova
2014. Theta sequences are essential for internally generated hippocampal firing fields. *Nature Neuroscience*, 18(2):282–288. 2.4.2

Watrous, A. J., N. Tandon, C. R. Conner, T. Pieters, and A. D. Ekstrom
2013. Frequency-specific network connectivity increases underlie accurate spatiotemporal memory retrieval. *Nature Neuroscience*, 16(3):349–356. 7.2.1

Weber, B.
2015. Neurovascular Coupling. In *fMRI: From Nuclear Spins to Brain Functions*, K. Uludag, K. Ugurbil, and L. Berliner, eds., volume 30, Pp. 67–104. Boston, MA: Springer US. 3.12

Willis, T.
1664. *Cerebri anatome : cui accessit nervorum descriptio et usus.* Londini : typis Ja. Flesher, impensis Jo. Martyn & Ja. Allestry apud insigne Campanae in Coemeterio D. Pauli. 3.1.2

Wilson, M. A. and B. L. McNaughton
1994. Reactivation of hippocampal ensemble memories during sleep. *Science*, 265(5172):676–679. 2.3.1.3

Winkler, E. A., R. D. Bell, and B. V. Zlokovic
2011. Central nervous system pericytes in health and disease. *Nature Neuroscience*, 14(11):1398–1405. 3.2.2

Winson, J.
1978. Loss of hippocampal theta rhythm results in spatial memory deficit in the rat. *Science*, 201(4351):160–163. 2.3.1.1, 2.4.3

Wolansky, T., E. A. Clement, S. R. Peters, M. A. Palczak, and C. T. Dickson
2006. Hippocampal Slow Oscillation: A Novel EEG State and Its Coordination with Ongoing Neocortical Activity. *The Journal of Neuroscience*, 26(23):6213–6229. 2.3.1.1

Wolf, S., W. Supatto, G. Debrgeas, P. Mahou, S. G. Kruglik, J.-M. Sintes, E. Beaurepaire, and R. Candelier
2015. Whole-brain functional imaging with two-photon light-sheet microscopy. *Nature methods*, 12(5):379–380. 3.3.2.5

Wolf, T., U. Lindauer, A. Villringer, and U. Dirnagl
1997. Excessive oxygen or glucose supply does not alter the blood flow response to somatosensory stimulation or spreading depression in rats. *Brain Research*, 761(2):290–299. 3.2.2

Womelsdorf, T., J.-M. Schoffelen, R. Oostenveld, W. Singer, R. Desimone, A. K. Engel, and P. Fries
2007. Modulation of Neuronal Interactions Through Neuronal Synchronization. *Science*, 316(5831):1609–1612. 1.4.2.3

Wong, R. K., D. A. Prince, and A. I. Basbaum
1979. Intradendritic recordings from hippocampal neurons. *Proceedings of the National Academy of Sciences*, 76(2):986–990. 1.1.3.3, 7.2.5

Wood, E. R., P. A. Dudchenko, R. J. Robitsek, and H. Eichenbaum
2000. Hippocampal neurons encode information about different types of memory episodes occurring in the same location. *Neuron*, 27(3):623–633. 2.3.2

Wu, J., Y. He, Z. Yang, C. Guo, Q. Luo, W. Zhou, S. Chen, A. Li, B. Xiong, T. Jiang, and H. Gong
2014. 3d BrainCV: Simultaneous visualization and analysis of cells and capillaries in a whole mouse brain with one-micron voxel resolution. *NeuroImage*, 87:199–208. 3.1.1

Wulff, P., A. A. Ponomarenko, M. Bartos, T. M. Korotkova, E. C. Fuchs, F. Bhner, M. Both, A. B. L. Tort, N. J. Kopell, W. Wisden, and H. Monyer
2009. Hippocampal theta rhythm and its coupling with gamma oscillations require fast inhibition onto parvalbumin-positive interneurons. *Proceedings of the National Academy of Sciences*, 106(9):3561–3566. 1.4.2, 2.3.1.4, 7.2.5

Wlfle, S. E., D. J. Chaston, K. Goto, S. L. Sandow, F. R. Edwards, and C. E. Hill
2011. Non-linear relationship between hyperpolarisation and relaxation enables long distance propagation of vasodilatation: Mechanism enabling long distance propagation of dilatation. *The Journal of Physiology*, 589(10):2607–2623. 3.2.3.2

Xue, S., H. Gong, T. Jiang, W. Luo, Y. Meng, Q. Liu, S. Chen, and A. Li
2014. Indian-Ink Perfusion Based Method for Reconstructing Continuous Vascular Networks in Whole Mouse Brain. *PLOS ONE*, 9(1):e88067. 3.1.1

Yamamoto, J., J. Suh, D. Takeuchi, and S. Tonegawa
2014. Successful Execution of Working Memory Linked to Synchronized High-Frequency Gamma Oscillations. *Cell*, 157(4):845–857. 1.3.3.2, 2.3.1.4, 2.4.3

Yang, B., J. Treweek, R. Kulkarni, B. Deverman, C.-K. Chen, E. Lubeck, S. Shah, L. Cai, and V. Gradinaru
2014. Single-Cell Phenotyping within Transparent Intact Tissue through Whole-Body Clearing. *Cell*, 158(4):945–958. 3.1.1

Yao, J., L. Wang, J.-M. Yang, K. I. Maslov, T. T. W. Wong, L. Li, C.-H. Huang, J. Zou, and L. V. Wang
2015. High-speed label-free functional photoacoustic microscopy of mouse brain in action. *Nature Methods*, 12(5):407–410. 3.14, 3.3.2.4

Yemisci, M., Y. Gursoy-Ozdemir, A. Vural, A. Can, K. Topalkara, and T. Dalkara
2009. Pericyte contraction induced by oxidative-nitrative stress impairs capillary reflow despite successful opening of an occluded cerebral artery. *Nature Medicine*, 15(9):1031–1037. 3.2.3.2

Ylinen, A., I. Soltsz, A. Bragin, M. Penttonen, A. Sik, and G. Buzski
1995. Intracellular correlates of hippocampal theta rhythm in identified pyramidal cells, granule cells, and basket cells. *Hippocampus*, 5(1):78–90. 2.3.1.2, 2.3.1.2

Yu, X., C. Qian, D.-y. Chen, S. J. Dodd, and A. P. Koretsky
2014. Deciphering laminar-specific neural inputs with line-scanning fMRI. *Nature Methods*, 11(1):55–58. 3.3.1.3

Zhang, X., V. Y. Toronov, M. Fabiani, G. Gratton, and A. G. Webb
2005. The study of cerebral hemodynamic and neuronal response to visual stimulation using simultaneous NIR optical tomography and BOLD fMRI in humans. *Proceedings of SPIE Int Soc Opt Eng*, P. 566. 3.3.2.3

Zheng, C., K. Bieri, Y.-T. Hsiao, and L. Colgin
2016. Spatial Sequence Coding Differs during Slow and Fast Gamma Rhythms in the Hippocampus. *Neuron*, 89(2):398–408. 2.3.1.4

Ziv, Y., L. D. Burns, E. D. Cocker, E. O. Hamel, K. K. Ghosh, L. J. Kitch, A. E. Gamal, and M. J. Schnitzer
2013. Long-term dynamics of CA1 hippocampal place codes. *Nature Neuroscience*, 16(3):264–266. 3.16, 3.3.3.2

Zonta, M., M. C. Angulo, S. Gobbo, B. Rosengarten, K.-A. Hossmann, T. Pozzan, and G. Carmignoto
2003. Neuron-to-astrocyte signaling is central to the dynamic control of brain microcirculation. *Nature Neuroscience*, 6(1):43–50. 3.2.3.2

Appendix A

Article 3: Spatiotemporal clutter filtering of ultrafast ultrasound data highly increases Doppler and fUltrasound sensitivity.

Demené, C., T. Deffieux, M. Pernot, B.-F. Osmanski, V. Biran, J.-L. Gennisson, L.-A. Sieu, **A. Bergel**, S. Franqui, J.-M. Correas, I. Cohen, O. Baud, and M. Tanter 2015. Spatiotemporal clutter filtering of ultrafast ultrasound data highly increases Doppler and fUltrasound sensitivity. *IEEE Transactions on Medical Imaging*, 34(11):2271-2285

Spatiotemporal Clutter Filtering of Ultrafast Ultrasound Data Highly Increases Doppler and fUltrasound Sensitivity

Charlie Demené*, Thomas Deffieux, Mathieu Pernot, Bruno-Félix Osmanski, Valérie Biran, Jean-Luc Gennisson,
Lim-Anna Sieu, Antoine Bergel, Stéphanie Franqui, Jean-Michel Correas, Ivan Cohen,
Olivier Baud, and Mickael Tanter

***Abstract*—Ultrafast ultrasonic imaging is a rapidly developing field based on the unfocused transmission of plane or diverging ultrasound waves. This recent approach to ultrasound imaging leads to a large increase in raw ultrasound data available per acquisition. Bigger synchronous ultrasound imaging datasets can be exploited in order to strongly improve the discrimination between tissue and blood motion in the field of Doppler imaging. Here we propose a spatiotemporal singular value decomposition clutter rejection of ultrasonic data acquired at ultrafast frame rate. The singular value decomposition (SVD) takes benefits of the different features of tissue and blood motion in terms of spatiotemporal coherence and strongly outperforms conventional clutter rejection filters based on high pass temporal filtering. Whereas classical clutter filters operate on the temporal dimension only, SVD clutter filtering provides up to a four-dimensional approach (3D in space and 1D in time). We demonstrate the performance of SVD clutter filtering with a flow phantom study that showed an increased performance compared to other classical filters (better contrast to noise ratio with tissue motion between 1 and 10mm/s and axial blood flow as low as 2.6 mm/s). SVD clutter filtering revealed previously undetected blood flows such as microvascular networks or blood flows corrupted by significant tissue or probe motion artifacts. We report *in vivo* applications including small animal fUltrasound brain imaging (blood flow detection limit of 0.5 mm/s) and several clinical imaging cases, such as neonate brain imaging, liver or kidney Doppler imaging.**

***Index Terms*—Blood flow, Doppler imaging, singular value decomposition, ultrafast imaging, ultrasound.**

I. INTRODUCTION

EXTENSIVE work has been conducted over the past 30 years in order to suppress clutter signals originating from stationary and slowly moving tissue as they introduce major artifacts in ultrasonic blood flow imaging [1]. This operation remains a major challenge for the visualization of vascular paths and the measurement of blood flow velocities because tissue echoes and blood scatterers echoes tend to share common characteristics, especially in two widespread clinical cases e.g., when blood flow velocities become low (in particular in small vessels) or when tissue motion is important. These two configurations correspond both to major applications in general ultrasound imaging. On the one hand, imaging slow blood flows and therefore microvasculature is an issue in most organs as skin, muscles, placenta, as well as in tumors for cancer diagnosis. It is also of major importance in emerging fields such as fUltrasound imaging of brain activity where the neurovascular coupling occurs locally in very small vessels. On the other hand, imaging blood flow in fast moving tissue is a major issue in applications such as cardiac or abdominal (liver, kidney,…) imaging.

The reason why clutter filters fail to solve both situations mentioned above is due to the underlying assumption on which they are built. In the early history of Color Flow Imaging (CFI), clutter filtering has always been based on the fair assumption that tissue signal and blood flow signal have completely differing spectral characteristics: tissue motion is supposed very slow or non-existent whereas red blood cells are fast moving scatterers, meaning that demodulated tissue signal and blood

---

Manuscript received March 10, 2015; revised April 28, 2015; accepted April 28, 2015. Date of publication April 30, 2015; date of current version October 28, 2015. The research leading to these results has received funding from the European Research Council under the European Union's Seventh Framework Programme (FP7/2007-2013)/ERC grant agreement n° 339244-FUSIMAGINE. This work was also supported by LABEX WIFI (Laboratory of Excellence ANR-10-LABX-24) within the French Program 'Investments for the Future' under reference ANR-10-IDEX-0001-02PSL, by the Assistance Publique-Hôpitaux de Paris and by PremUP Foundation, Paris 75006 France. *Asterisk indicates corresponding author.*

*C. Demené is with the Institut Langevin, CNRS UMR 7587, INSERM U979, ESPCI ParisTech, 75005 Paris, France (e-mail: charlie.demene@espci.fr).

T. Deffieux, M. Pernot, B.-F. Osmanski, J.-L. Gennisson, S. Franqui, and M. Tanter are with the Institut Langevin, CNRS UMR 7587, INSERM U979, ESPCI ParisTech, 75005 Paris, France (e-mail: thomas.deffieux@espci.fr; mathieu.pernot@espci.fr; bruno-felix.osmanski@espci.fr; jl.gennisson@espci.fr; mickael.tanter@espci.fr).

V. Biran and O. Baud are with the INSERM U1141 and Neonatal Intensive Care Unit, Paris Diderot University, Children's hospital Robert Debré, APHP, 75019 Paris, France (e-mail: valerie.biran@rdb.aphp.fr; olivier.baud@rdb.aphp.fr).

L.-A. Sieu is with the Neuroscience Paris Seine, CNRS UMR8246, INSERM U1130, UPMC UMCR18, 75005 Paris, France and also with Institute of Translational Neurosciences (IHU-A-ICM), Pitié-Salpêtrière Hospital, 75013 Paris, France (e-mail: lim-anna_s@hotmail.fr).

A. Bergel and I. Cohen are with the Neuroscience Paris Seine, CNRS UMR8246, INSERM U1130, UPMC UMCR18, 75005 Paris, France (e-mail: antoine.bergel@cri-paris.org; ivan.cohen@upmc.fr).

S. Franqui is with the service de radiopédiatrie-Hôpital Bicêtre-Hôpitaux Universitaires Paris-Sud, Assistance Publique hôpitaux de Paris, 94270 Le Kremlin-Bicêtre, France (e-mail: stephanie.franchi@bct.aphp.fr).

J.-M. Correas is with the Institut Langevin, CNRS UMR 7587, INSERM U979, ESPCI ParisTech, 75005 Paris, France, and also with department of Adult Radiology, Necker University Hospital, 75015 Paris, France, and with Rene Descartes Medical University, 75006 Paris, France (e-mail: jean-michel.correas@nck.aphp.fr).

Color versions of one or more of the figures in this paper are available online at http://ieeexplore.ieee.org.

Digital Object Identifier 10.1109/TMI.2015.2428634

signal have non-overlapping spectra centered on the zero frequency and the Doppler frequency respectively. Based on this temporal dynamics assumption, the raw ultrasonic signal is filtered along the temporal dimension using finite impulse response (FIR) or infinite impulse response (IIR) filters [2], [3]. IIR filters present the advantage of having steeper roll-off than FIR for a given order, but they also exhibit a longer settling time because of the lack of correct outputs for the first temporal points. FIR filters present a short settling time (output is stable after only n points for an n-order FIR filter) but need a higher order to efficiently discriminate clutter from blood signal. In both cases a first limitation arises: due to real-time requirement and the use of focused ultrasonic beams to build the image, the number of temporal samples available in each spatial location is low (usually 8 to 16) and those filters are really difficult to optimize [4] for a general Doppler imaging application ranging from cardiac imaging (maximal tissue velocity) to microcirculation imaging (very low blood flow speeds). The problem of the settling time can be reduced by a proper initialization [5] in the case of IIR filters but the transient response cannot be completely canceled. On the other hand, another class of filters called standard linear regression (SLR) filters [6] do not exhibit any settling time and estimate the tissue signal by a linear regression on several temporal points of the ultrasound signal: based on the same assumption than mentioned above, it is assumed that the slow variations of the signal are exclusively due to tissue and the rapid fluctuations are exclusively due to blood flow. Finally, several techniques have been developed to adapt to each Doppler imaging situation by compensating background tissue motion: by estimating first tissue velocity and down-mixing the ultrasound temporal signal via a phase correction, the spectrum can be shifted so that the center frequency of the tissue signal match the zero frequency [7], [8]. The signal is then processed using a classical fixed cut-off filter to remove tissue echoes.

In all these methods, only the temporal information has been used because the hypothesis used to discriminate tissue signal and blood scatterers signal focused on their different spectral content. But it can also be noticed that spatial characteristics of tissue signal are different from those of blood scatterers. Along one M-mode line, tissue movement toward the transducer can be approximated by only a shift in the RF data (a phase shift for In Phase/Quadrature RF data) whereas moving red blood cells change the profile of the RF data itself. A brief explanation is that tissue is far less deformable than a red blood cell arrangement in plasma, and a small movement of tissue can be seen as a spatial shift of a speckle pattern whereas a movement of red blood cells implies a reorganization of the scatterers generating a different speckle pattern. In other words, tissue signal has a higher spatial coherence than blood signal in ultrasound imaging. Several authors suggested this hypothesis and introduced new clutter rejection methods based on this a priori: Ledoux *et al.* [9] proposed a clutter reduction simulation study based on the Singular Value Decomposition of the correlation matrix between successive temporal samples of a M-mode line. In this approach both 1D spatial and temporal information are used via the diagonalization of the spatiotemporal (time and depth) correlation matrix. Several strategies have emerged from this approach and an exhaustive review of these methods have been proposed by Yu and Lovstakken in 2010 [10]. Among those developments, important works such as the down-mixing approach using an eigen-based tissue motion estimation of Bjearum *et al.* [8] and the real time implementation of eigen-based clutter rejection proposed by Lovstakken *et al.* [11] have to be cited. Finally, Kruse and Ferrara [12] developed an original high frequency swept scan imaging setup whose datasets have been processed using principal component analysis to estimate blood velocity in presence of strong motion.

In all reported methods, discrimination between tissue and blood flow drastically suffer from a poor ensemble length, i.e., a poor number of ultrasound pulses per line of color. The use of focused beams imposes to adopt a line-per-line scan strategy (either electronically in the case of transducer arrays, or mechanically in the case of a single transducer) in order to cover an extensive field of view. As a consequence both the number of temporal samples (collected on a particular location before the system has to move to another location) and the number of spatial samples (acquired at different times and therefore having different characteristics) are limited. From a theoretical point of view, taking into account different spatial samples along the swept direction is even intrinsically difficult as these samples are not acquired simultaneously. Unfortunately, these characteristics of ultrasonic sequences in conventional ultrasound strongly limit the impact of singular value decomposition. SVD processing is a powerful signal processing tool but as for digital filters its full potential is obtained on large datasets.

Over the past decade, it was shown that ultrafast ultrasound imaging based on unfocused wave transmissions can acquire wide two-dimensional fields of view at very high frame rates (typically higher than 1000 frames per second). The fast growing number of emerging clinical applications of ultrafast imaging [13], [14] and exponential evolution of computation power of GPU based electronics permits to envision a soon change of paradigm in ultrasonic imaging. At the cost of a little loss in focusing capabilities, plane wave imaging enables the acquisition of a large amount of synchronous samples which, in the framework of clutter rejection filters, overcome severe limitations inherent to conventional focused transmissions.

Instead of collecting typically 16 temporal samples in a small spatial box before electronically moving to another location as in conventional Doppler imaging, ultrafast imaging uses plane waves to insonify the medium before beamforming the backscattered echoes into an image. This enables ultrafast imaging over a wide field of view at a framerate of several kHz. As ultrafast imaging relies on focusing in reception only, resolution is partially lost compared to classical ultrasound imaging schemes using focusing both in emission and reception. However, it has been demonstrated that resolution or motion estimation can be improved using a set of tilted plane or diverging waves combined after beamforming [15]–[17]. The ultrasonic modality based on coherent synthetic recombination of unfocused wave transmissions and used to visualize blood flows was called Ultrafast Doppler imaging.

In a former study, we reported that Ultrafast Doppler imaging improved Doppler sensitivity by a factor up to 30 compared to conventional Doppler imaging [18]. This is in large extent due to the temporal ensemble length of an Ultrafast Doppler dataset compared to a conventional Doppler dataset. As Ultrafast Doppler does not need electronic sweeping of the focused beam along the transducer array, temporal samples are acquired simultaneously in every pixel of the image. This means that for a 1 second acquisition at 1 kHz of frame rate, each pixel exhibits 1000 temporal points. The settling time of temporal filters is not an issue anymore and high order IIR with steep roll-of can be used as long as the first tens of temporal points are removed from the signal. The increased sensitivity of Ultrafast Doppler is in a quite large extent due to this highly efficient clutter filtering combined with a longer ensemble length and a “virtual” [19] dynamic focusing due to coherent recombination of different sonications.

However, to date, the only *a priori* used to filter out the clutter of Ultrafast Doppler Images was based on a temporal discrimination between tissue and blood flow motion [17], [18], [20]. Again, this assumption is not true in the case of slow blood flows or fast moving tissue where both spectra overlap. In these cases, spectral filters applied to Ultrafast Doppler encounter the same difficulties than mentioned previously to discriminate between tissue and blood flow.

In this paper, we present a way of rejecting clutter signals from Ultrafast Doppler datasets using Singular Value Decomposition (SVD) or Principal Component Analysis (PCA). Both 2D spatial and temporal coherence are used to separate tissue from blood flow, showing a considerable improvement in both the detection of slow blood flows and the removal of moving tissues. Thanks to ultrafast sequences, simultaneous raw data can be reshaped under large Casorati matrix form [21]. This article focuses on the straightforward use of singular value decomposition of this Casorati matrix for blood/tissue discrimination. However, the reader should note that very significant developments were achieved in the field of matrix regression in the last five years. Most of them are devoted towards low-rank matrix regression and signal separation, i.e., the so-called Robust PCA [22]. In addition to pure mathematical developments, these techniques have been widely used in other medical imaging modalities like magnetic resonance imaging (MRI) [23] and x-ray computed tomography [24].

II. THEORY

A theoretical framework is introduced in this section of the paper to explain the different steps of the clutter rejection algorithm and better understand its implications.

A. The Specificity of Ultrasound Signal

1) The Different Components of the Ultrasound Signal: An Ultrafast Doppler acquisition consists in a stack of beamformed ultrasound images (or a cineloop) and can be represented under the complex valued variable $s(x,z,t)$, where x stands for the lateral dimension (along the transducers array), z stands for depth in the medium in front of the ultrasonic probe, and t stands for time (sampled at a frequency noted Frame Rate from there on). It is assumed that this signal can be described as the summation of three contributions (1): c the clutter signal, b the blood signal, and n the electronical/thermal noise.

$$s(x,z,t) = c(x,z,t) + b(x,z,t) + n(x,z,t). \tag{1}$$

Those three contributions have different spatial and temporal characteristics. n can be considered as a zero-mean Gaussian white noise. The classical approach consists in assuming that blood signal is a high temporal frequency signal and that tissue signal is a low frequency signal. It must be also acknowledged that depending on the ultrasound frequency used for the acquisition, the backscattered energy of the blood signal can be 10 to 60 dB lower than energy of the tissue signal. Moreover, although spatial characteristics of blood and tissue signals are rarely investigated, they also convey different information.

2) Covariance Matrix of Neighboring Pixels: This section elucidates the spatiotemporal characteristics of blood signal and tissue signal, first qualitatively by introducing a simplified signal $\tilde{s}$ to illustrate the common statistical properties of neighboring pixels, and then quantitatively by constructing the covariance matrix of neighboring pixels.

Fig. 1 gives insight into the statistical properties of blood signal b and clutter signal c in the example of rat brain ultrasonic imaging. As stated before the temporal signal in one pixel exhibits low frequency fluctuations corresponding to tissue movement (in the imaginary part of the signal the three slow oscillations observed are due to tissue moving when the heart beats) and high frequency fluctuations due to actual blood cells motion. In order to compare spatially close temporal signals, a simplified signal $\tilde{s}(x,z,t) = s(x,z,t).\overline{s(x,z,t)}^{*}/|\overline{s(x,z,t)}|^{2}$ is calculated, where $\overline{s}$ is the time average value of s and * stands for complex conjugate. This simplified illustrative representation enables to get rid of any phase shift (via the product with the complex conjugate of the time averaged signal) and of amplitude difference (via the division with the squared modulus) between two pixel signals; and consequently to compare signals only on the basis of their shape. Fig. 1 shows that in neighboring pixels, simplified signals present very similar low frequency variations (tissue motion), whereas the rapid fluctuations (blood motion) do not present the same pattern from one pixel to another. This aspect is further investigated in Fig. 2, where the nine pixel signals of the second neighborhood of Fig. 1 are separated in blood (HF) and tissue (LF) signal with a temporal filter. It is clear that tissue signal is highly correlated and the covariance matrix of those nine signals exhibits a high degree of correlation, whereas the blood signal covariance matrix is almost diagonal, meaning that blood signal is poorly spatially coherent, even at a very local scale. Fig. 1 even shows that at large spatial scales, tissue signal is still quite coherent as the simplified signals are quite similar in shape between the two neighborhoods. Thus, tissue signal could be condensed in a few temporal signal accompanied by a set of spatially arranged complex coefficients required to recover the amplitude and phase shift proper to each pixel. In other words, tissue signal realization in all pixels forms a family of vectors whose cardinality is much higher than the dimension of the tissue vector subspace. This is an essential idea

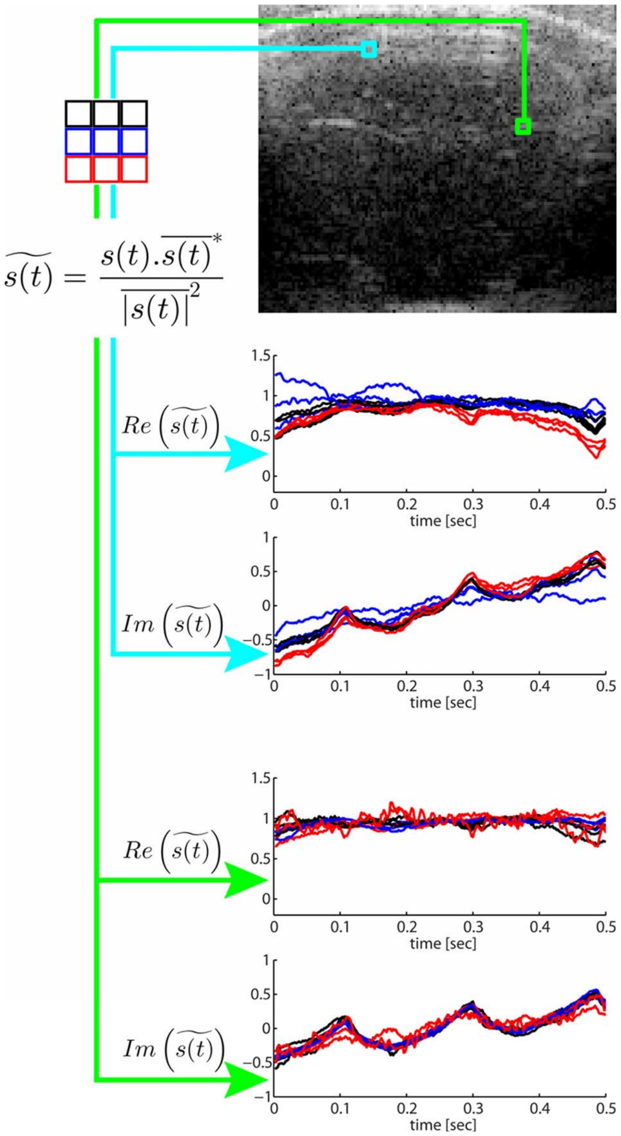

Fig. 1. Typical example of an Ultrafast Acquisition. The top image depicts $s(x, z, t = 0)$ of an Ultrafast acquisition acquired during 0.5 s at a Frame Rate of 500Hz, on the brain of a thinned skull rat (scale bar $= 1$ mm). To have an insight into the temporal dimension of this Ultrafast acquisition, two neighborhoods of nine pixels have been chosen in the image (green and cyan squares). Inside each pixel, the simplified signal $\tilde{s}(x, z, t)$ is calculated to get rid of phase difference and amplitude difference from one pixel to another. $\tilde{s}$ is then plotted with color respective to the position in the nine pixel neighborhood (black, blue or red). This illustrates that signal in close pixels is very similar in shape.

to understand the efficiency of the singular-based clutter filter presented in this paper.

Contrary to tissue signal, blood signal is not assumed to have high spatial coherence. In addition, tissue signal energy is much higher (10 to 50 dB) than blood signal energy, and a separation method based on covariance estimation certainly finds the highest covariance values for the tissue signal. This discrimination based on covariance estimation can be performed using the singular value decomposition of raw data.

B. Singular Value Decomposition of Ultrafast Ultrasonic Data

Let us consider the spatiotemporal matrix form of $s(x, z, t)$ corresponding to the raw data cineloop acquired during an ultrafast acquisition. $s(x, z, t)$ corresponds to set of $n_x \times n_z \times n_t$ samples where n_x, n_z and n_t are respectively the number of spatial samples along x-direction, the number of spatial samples[1] along z-direction and the number of time samples. The raw data matrix is reshaped under a Casorati matrix form by transforming time series data into a 2D space-time matrix form $\boldsymbol{S}$ with dimensions $(n_x \times n_z, n_t)$ as already proposed in other imaging modalities such as MRI and CT [22]–[26].

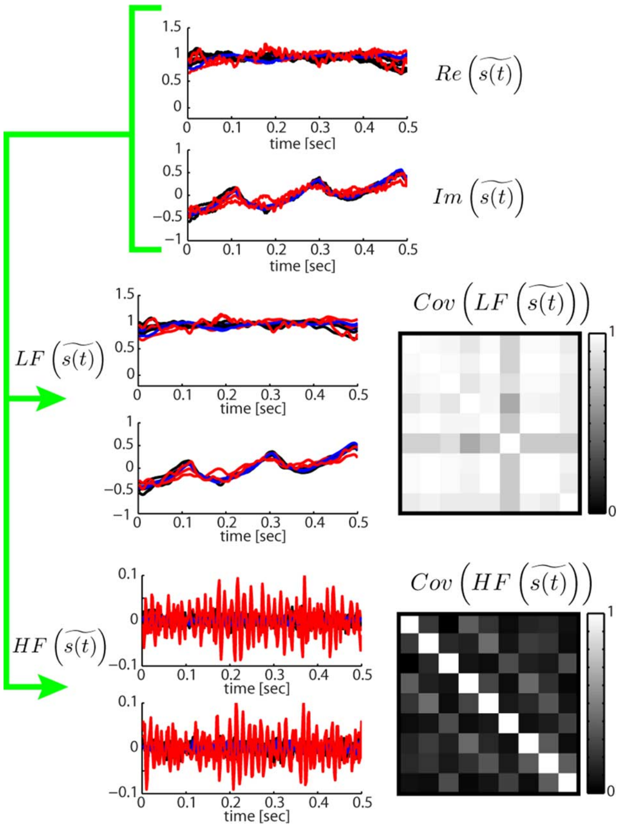

Fig. 2. The same data than in the green nine pixel neighborhood of Fig. 1 are filtered using a 50Hz cut off 4^{th} order Butterworth filter typically used to discriminate between tissue and blood flow signals, and on the graphs it can be observed that the low frequency (LF) part of the nine pixel temporal signal are really similar in shape and seem highly correlated, whereas the blood signal (HF) seem highly decorrelated. On the right are displayed the 9×9 covariance matrix (magnitude) of the normalized zero-mean complex signals, for the low frequency and high frequency part respectively. HF Blood signal is indeed highly decorrelated compared to LF tissue signal.

The singular value decomposition (SVD) of this Casorati matrix $\boldsymbol{S}$ consists in finding the three matrices such as:

$$\boldsymbol{S} = \boldsymbol{U}\boldsymbol{\Delta}\boldsymbol{V}^*. \tag{2}$$

Where $\boldsymbol{V}$ is a non-square $(n_x \times n_z, n_t)$ diagonal matrix, $\boldsymbol{U}$ and $\boldsymbol{V}$ are orthonormal matrices with respective dimensions $(n_x \times n_z, n_x \times n_z)$ and (n_t, n_t) and * stands for the conjugate transpose. Columns of $\boldsymbol{U}$ and $\boldsymbol{V}$ matrices correspond respectively to the spatial and temporal singular vectors of $\boldsymbol{S}$. One

---

[1] Note that all concepts described here are straightforwardly applicable for 4D data (3D space +1D time). For sake of simplicity, we restrict here the examples to a 3D case (2D space image + 1D time) which is the most routine case in biomedical ultrasound.

should also notice that $\boldsymbol{U}$ and $\boldsymbol{V}$ also correspond to the eigenvectors[2] of the respective covariance matrices $\boldsymbol{SS}^*$ and $\boldsymbol{S}^*\boldsymbol{S}$.

What is the physical meaning of the SVD of matrix $\boldsymbol{S}$? In fact, the singular value decomposition (SVD) or principal component analysis (PCA) can be thought of as decomposing a matrix $\boldsymbol{S}$ into a weighted, ordered sum of separable matrices $\boldsymbol{A}_i$. By separable, we mean that the matrix $\boldsymbol{S}$ can be written as an outer product of two vectors $A_i = U_i \otimes V_i$. Specifically, the matrix $\boldsymbol{S}$ can be decomposed as:

$$S = \sum_i \lambda_i \boldsymbol{A}_i = \sum_i \lambda_i U_i \otimes V_i. \tag{3}$$

Thus, the SVD can be used to find the decomposition of an ultrafast ultrasonic dataset into separable space and time filters. Here U_i and V_i are the i^{th} columns of the corresponding SVD matrices defined in (6), λ_i are the ordered singular values, and each $\boldsymbol{A}_{\text{i}}$ is a separable matrix. The number of non-zero λ_i is exactly the rank of the matrix. Importantly, one should keep in mind that each column V_i corresponds to a temporal signal with length n_t and each column U_i corresponds to a spatial signal with length n_t. Each vector U_i describes in fact a 2D spatial image I_i with dimensions (n_x, n_z).

As one can notice, the SVD of $\boldsymbol{S}$ decomposes the field into a sum of separable images I_i (characterized by a vector U_i) that are independently modulated by a temporal signal V_i. In other words, all pixels of the ultrasonic spatial images $I_i(x, z)$ characterized by the singular vector U_i behave with the same time signal $V_i(t)$.

Thus, thanks to the SVD processing, the spatiotemporal cineloop $s(x, z, t)$ corresponding to ultrasonic raw data can be rewritten as:

$$s(x, z, t) = \sum_{i=1}^{rank(\boldsymbol{S})} \lambda_i I_i(x, z) V_i(t). \tag{4}$$

In this decomposition, tissue displacements should be described mainly in the first singular values and singular vectors as their high spatiotemporal coherence insures that a large number of spatial pixels will exhibit the same time profile. On the contrary, blood signal should be found in lower singular values as they exhibit much lower spatiotemporal coherence. Thus, filtering the data using the SVD approach consists in calculating:

$$\boldsymbol{S}^f = \boldsymbol{SVI}^f\boldsymbol{V}^* = \boldsymbol{U\Delta}^f\boldsymbol{V}^*. \tag{5}$$

Where $\boldsymbol{S}^f$ is the filtered data set and $\boldsymbol{I}^f$ is a matrix filter, i.e., the diagonal identity matrix with zeros for the first diagonal elements, leading to a truncated $\boldsymbol{\Delta}^f$ diagonal matrix of singular values corresponding to the removal of tissue motion.

Interestingly, the classical clutter filter approach used in ultrasound imaging corresponding to a simple high pass filter can be written under a quite similar matrix formalism:

$$\boldsymbol{S}^f = \boldsymbol{SEI}^f\boldsymbol{E}^*. \tag{6}$$

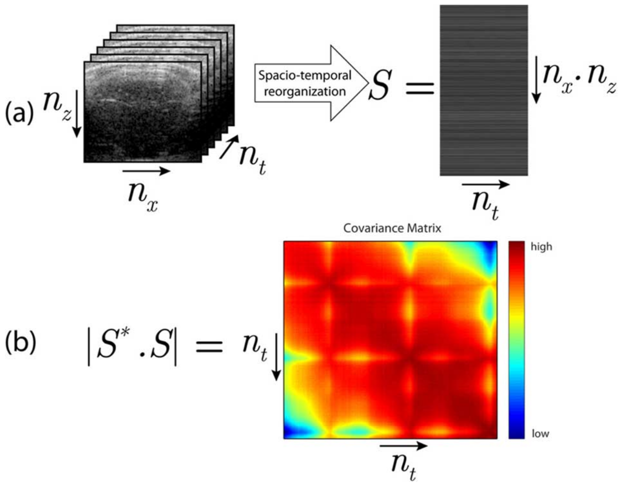

Fig. 3. (a) The ultrafast Doppler acquisition forms a 3D stack of images with 2 spatial dimensions and one temporal dimension (same data than Fig. 1). It is reshaped in one spatiotemporal representation (Casorati matrix) where all pixels at one time point are arranged in one column. As a consequence all time points for one pixel are arranged in one row. (b) The covariance matrix is presented here in magnitude and is of dimension $n_t \times n_t$.

Where $\boldsymbol{E}$ is the Fourier transform matrix and $\boldsymbol{I}^f$ is again the high pass filter, i.e., the diagonal identity matrix with zeros for the diagonal elements corresponding to low frequencies (the first and last ones with a classical FFT algorithm). In the light of this formulation both filters are temporal filters and rank-reducing for the tissue signal (the tissue is compressed on a subset of the spectrum that is then set to zero) but the SVD outperforms the Fourier decomposition according to the Eckart-Young theorem [27] as it provides a faster decrease of singular values and consequently a better tissue blood discrimination. In other words, the decomposition is better in the multidimensional SVD approach as the clutter basis vectors are calculated adaptively (through spatial averaging) and more optimally compared to the Fourier basis.

C. Implementation of the SVD Filter

Given the hypothesis of high spatiotemporal coherence for the tissue signal, the idea is to build a new spatiotemporal representation of the Ultrafast acquisition in the basis provided by the singular value decomposition. The first step is presented in Fig. 3(a) and consists in rearranging the Ultrafast Doppler acquisition into a 2D Casorati matrix $\boldsymbol{S}$ where one dimension is space and the other dimension is time. Singular value decomposition could be performed on this matrix $\boldsymbol{S}$ and directly give the new temporal singular vector basis $\boldsymbol{U}$ and the new spatial singular vector basis $\boldsymbol{V}$.

However, in most cases the Ultrafast Doppler acquisition presents many more spatial points (typically several 10 000) than temporal points (several hundreds or thousands), and it can be less demanding from a computing point of view to first form the $n_t \times n_t$ covariance matrix (Fig. 3(b)) and diagonalize it. This gives n_t temporal eigenvectors that are the right singular vector V_i of $\boldsymbol{S}$. Fig. 4(a) shows the spectral content of those eigenvectors sorted by decreasing eigenvalue. Interestingly, the largest eigenvalues are associated with the temporal singular vectors presenting the slowest variation. This is consistent with

---

[2] Singular Value Decomposition and Principal Component Analysis are two aspects of the same problem and one decomposition can lead to the other and vice versa as $S^*S = V\Delta^*U^*U\Delta V^* = V\Delta^2V^*$ and $SS^* = U\Delta^*V^*V\Delta U^* = U\Delta^2U^*$.

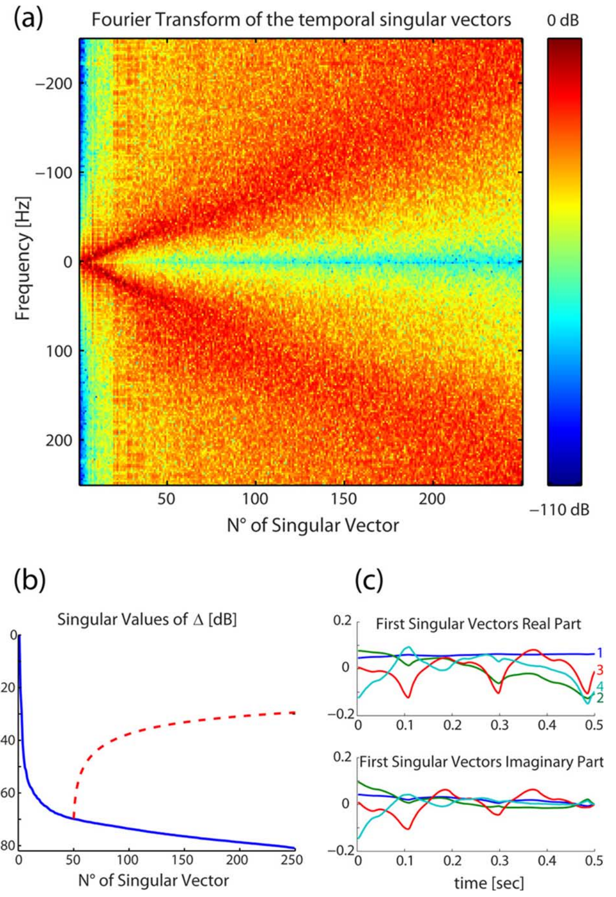

Fig. 4. (a) Spectral content estimation (via Periodogram with Tukey apodisation (0.2)) of all the right singular vectors, sorted with decreasing singular value. Low frequency temporal signal are associated with the highest singular values. As all singular vectors are normalized, energy in all spectra (all columns) is equal to one. (b) Singular values of the matrix Δ (solid blue) expressed in dB and cumulative sum of those singular values from n°50 (dashed red). (c) The first four singular vectors (associated to the largest singular values of the covariance matrix) of the covariance matrix are plotted versus time. It can be observed that they depict slow temporal variation (the first one is almost a constant value, the third one depicts clearly the pulsatility of tissue already observed in Fig. 1) and are devoid of the fast fluctuation of blood signal.

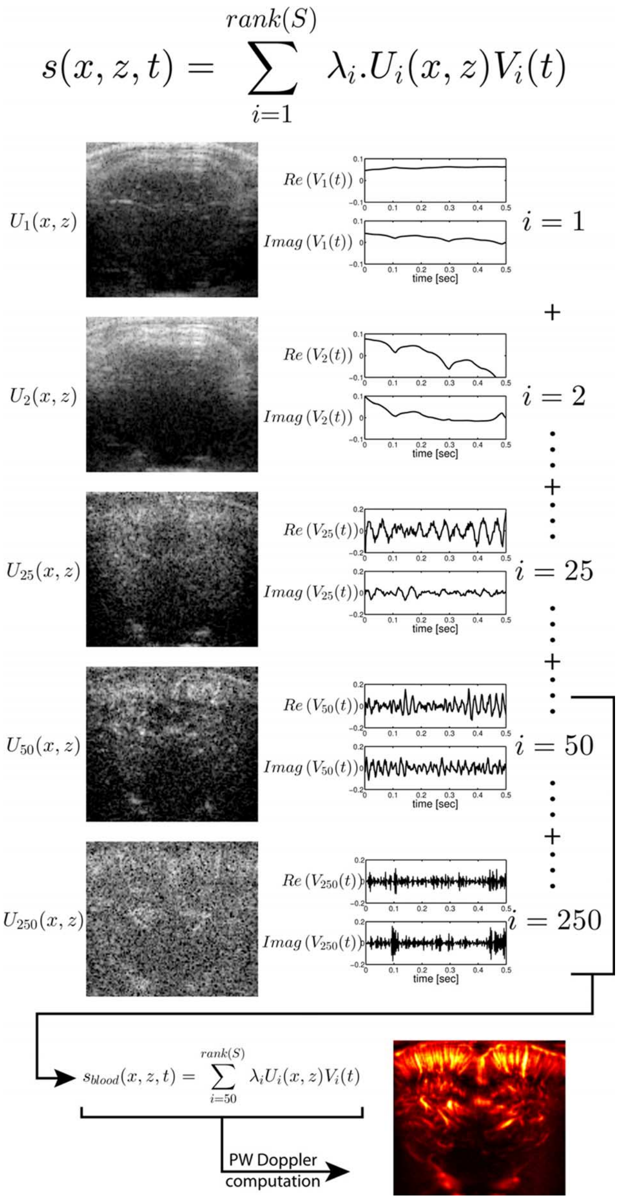

Fig. 5. The Ultrafast acquisition (same data than Fig. 1) is decomposed by the singular value decomposition into a set of spatiotemporal couples of vectors. The essential idea is that tissue signal is coherent enough to be quite similar over the entire image, and that it can be described by a set of vectors constituting a subspace of the temporal signal space, but much smaller. Indeed, by rejecting the first 49 couples of singular vectors, tissue signal is rejected and a very good PW Doppler image of the vascularisation in the rat brain is obtained.

spatially coherent tissue signal supposed to be quite similar in neighboring pixels in a way that enables to reduce the $n_x \times n_z$ realizations of tissue temporal signal on a much smaller subspace. As a consequence tissue signal is supposed to be condensed in the first singular vectors whereas blood and noise signals are described by the singular vectors associated with lower singular values. The eigenvalue itself is closely related to the energy associated the corresponding singular vector and Fig. 4(b) depicts the relative variation of those singular values: the dashed red line shows that with a threshold of 50 rejected singular values (see Fig. 5) the SVD clutter rejection will discriminate the supposedly tissue from a signal 30 dB below, which is really consistent with the expected relative difference between tissue energy and blood energy at that range of US frequencies (15 MHz). The weighted spatial vector $\lambda_i U_i$ are then computed by the projection $\boldsymbol{SV}$ as described in (5).

Finally using this decomposition, $s(x,z,t)$ can be decomposed on both a temporal basis and a spatial basis of singular vectors (Fig. 5). Based on the assumption that tissue signal is gathered in the first singular vectors, clutter rejection is performed using a threshold n (whose influence and choice will be discussed in the next part) on the number of singular vectors removed from the raw signal (7):

$$s_{blood}(x,z,t) = s(x,z,t) - \sum_{i=1}^{n} \lambda_i I_i(x,z)V_i(t). \qquad (7)$$

This filtered signal can then be processed using short time Fourier transform for blood flow speed measurement (as described in the methods section) or the energy per pixel can be computed (8) to produce the so called Power Doppler image.

$$PW(x,z) = \int |s_{blood}(x,z,t)|^2 dt. \qquad (8)$$

The efficiency of clutter rejection based on both space and time filtering of ultrafast data via SVD and its superiority to conventional temporal filtering will be demonstrated in the Results section with a phantom study and with several *in vivo* examples and in different imaging contexts.

III. Materials and Methods

In vivo Ultrafast acquisitions were performed using a programmable ultrasound scanner (Aixplorer, Supersonic Imagine, France) with dedicated Compound Plane Wave imaging ultrasound sequences [17], [16]. This technique uses plane wave emissions instead of the classical focused emissions, which enables to increase the framerate from a factor 10 to 100, and focusing is only achieved in reception via the beamforming process. To recover resolution, compounding is done by coherently adding several tilted plane wave emissions. With such a process, the framerate can reach the theoretical limit imposed by the time of flight of ultrasound, typically 10 000 Hz.

A. Phantom Study

In order to quantify the ability of SVD filtering to extract slow blood flows from moving tissue, a contrast to noise ratio (CNR) study has been conducted with ultrafast Doppler acquisitions on a Doppler phantom in presence of probe movement. The double benefit of using a phantom is to control precisely the acquisition conditions in terms of blood speed and tissue velocities, and to know exactly the geometry and position of the vessel for rigorous calculation of the CNR.

The ultrasonic probe was mounted on a linear motor (PI translation stage VT-80, one-directional repeatability 0.8 μm, bi-directional repeatability ± 10 μm) to enable periodic translation along image depth of amplitude 1 mm with a selected speed (1 to 10 mm/s with 1mm/s incremental steps). The field of view of the probe was adjusted on the longitudinal section of the 2 mm diameter tube of a Doppler phantom (Model 523A, ATS Laboratories, 404 Knowlton St, Bridgeport CT 06608 USA). The tube was approximately at a 35 mm depth, with a 75° angle to the probe axis, giving the possibility of reaching small axial velocities. A blood mimicking fluid (Doppler test fluid model 70, ATS Laboratories, 404 Knowlton St, Bridgeport CT 06608 USA) was injected in that tube with an adjustable pump (Ecoline VC-MS/CA8-6, ISMATEC) enabling mean fluid velocities measured at 1, 2, 4, 6 cm/s (thus 2.6, 5.1, 10.4 and 15.5 mm/s of axial velocities). Ultrafast acquisitions were performed using a 6 angles (ranging from $-5°$ to $5°$ with $2°$ incremental steps) compound plane wave ultrasound sequence and a 6 MHz ultrasonic probe (SL 10-2 Supersonic Imagine, France) (pitch 0.2 mm, elevation focus 35 mm, 96% Bandwidth @-6dB). The Pulse Repetition Frequency (PRF) was 6000 Hz, the frame rate of 1000 Hz and the number of frames 600. Twelve acquisitions were performed for each (tissue velocity, blood velocity) couple.

The imaged region of interest was 25.6 mm wide and ranged from 25 mm to 45 mm in depth. The known position of the tube was manually segmented on the BMode (avoiding bias of segmentation on the Doppler image) in order to give two areas (one for the vessel and one for the surrounding phantom (tissue), with a 0.5 mm dead zone in between), and the CNR was calculated as the classical:

$$CNR = \frac{\overline{PW}_{tube} - \overline{PW}_{tissue}}{std(PW_{tissue})}. \tag{9}$$

In this equation $\overline{PW}$ stand for the mean value of the power Doppler signal (in the tube or in the surrounding tissue), and std for the standard deviation. Three filtering methodologies were investigated: the 4^{th} order high-pass Butterworth filter, the varying phase increment down mixing approach described in [8] (consisting in a IQ demodulation using the lag one correlation phase averaged on a 5 pixel column neighborhood) followed by 4^{th} order high-pass Butterworth filter, and the SVD filtering approach. To avoid any bias induced by the choice of the cut off, every cut off has been tested for the three filters (meaning every cut off frequency for the first two methods, and every singular value threshold for the SVD filter), and the one giving the maximum CNR was kept for each (tissue velocity, blood velocity) couple.

B. Rat Brain Imaging

All experiments followed European Union and institutional guidelines for the care and use of laboratory animals. Adult (> 4-week-old) Sprague Dawley rats underwent a surgical thinning of the skull under anesthesia (Ketamine/Xylazine) to enable the propagation of ultrasound. They were then placed in a stereotaxic frame and maintained under 1.5% isoflurane during the time of the acquisition. Ultrafast Acquisition were performed using a 15 angles (ranging from -14° to 14° with 2° incremental steps) compound plane wave ultrasound sequence and a 15 MHz ultrasonic probe (Vermont, France) (pitch 0.08 mm, elevation focus 8 mm). Pulse Repetition Frequency (PRF) was 7500 Hz, enabling a frame rate of 500 Hz, enough to correctly sample axial blood flow speeds up to 2.6 cm/s. Ultrafast Doppler acquisitions lasted 0.5 s, enough to acquire 250 frames and to capture 3 cardiac cycles). Data are used for Fig. 1 to Fig. 5 and for Fig. 7.

C. Neonates Brain Imaging

Ultrafast Acquisition were performed using a 6 angles (ranging from $-5°$ to $5°$ with $2°$ incremental steps) compound plane wave ultrasound sequence and a 6 MHz ultrasonic probe (SL 10-2 Supersonic Imagine, France) (pitch 0.2 mm, elevation focus 35 mm, 96% Bandwidth @-6dB). Pulse Repetition Frequency (PRF) was 6000 Hz, enabling a frame rate of 1000 Hz, enough to correctly sample axial blood flow speeds up to 10.3 cm/s. Ultrafast Doppler acquisitions lasted 1 s, enough to acquire 1000 frames and to capture 2 to 3 cardiac cycles). This observational study was approved by the institutional review board (CCP: 'Comité de Protection des Personnes', i.e., Committee for the Protection of Persons, CCP agreement N°120601) and local ethical committee, and strictly complies with the ethical principles for medical research involving human subjects of the World Medical Association Declaration of Helsinki, and written consent was obtained from parents of participants. Data were obtained via a transfontanellar (anterior fontanel) Ultrafast Doppler acquisition of a brain parasagittal

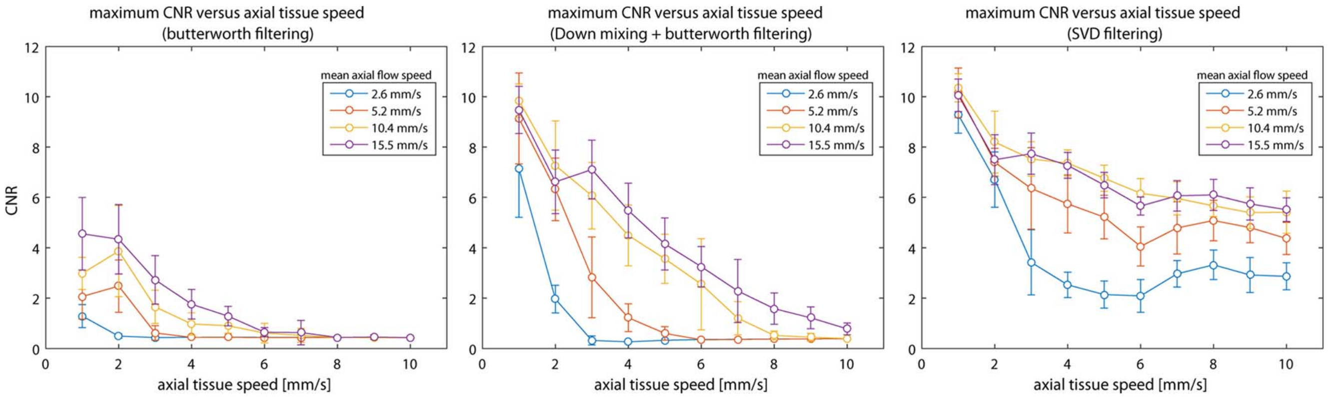

Fig. 6. Evolution of the CNR versus axial tissue velocity for various blood flow speed: phantom study. The same sets of data have been processed using 4^{th} order butterworth high pass filtering (left), down-mixxing prior to 4^{th} order butterworth high pass filtering (middle), and SVD filtering (right). For each measurement, the maximum CNR was found by testing all the possible cut off, and for each experimental condition twelve measurements were pooled to compute mean value (graph circles) and standard deviation (error bars).

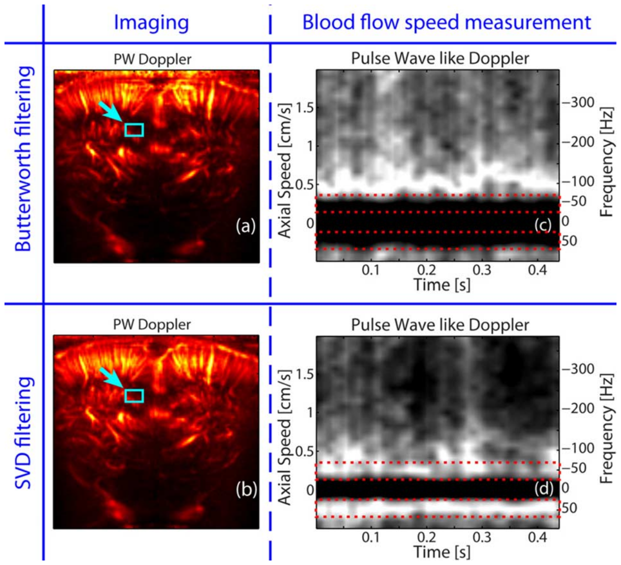

Fig. 7. Comparison of slow blood flow detection (critical for functional imaging) via temporal filtering and SVD filtering (same data than Fig. 1). In that case the rat is maintained in a stereotaxic frame and the probe is maintained in a probe support, the entire setup lying on an anti-vibration table. As a consequence the motion is minimum and consists only in the tissue pulsatility due to blood pressure changes during the cardiac cycle. The PW Doppler image obtained via temporal filtering (50Hz cut off frequency 4^{th} order Butterworth filter) (a) can be compared to the PW Doppler imaged obtained via SVD (b). The cyan arrow indicates the set of pixels where a pulse wave like Doppler profile has been calculated from the Ultrafast Doppler acquisition, in the case of Butterworth filtering (c) and SVD filtering (d). The key point here is the difference between the spectral bands cut by both filters. Blood signal energy is kept via SVD filtering in the two area surrounded by the dotted red rectangles.

section performed *in vivo* on a human neonate and Data are used for Fig. 8 to Fig. 11.

D. Kidney Imaging/ Liver Imaging

Probe and acquisition parameters were the same as for neonate imaging, except (angles: -3°3°; frame rate: 3000 Hz) for liver imaging, and (angles: -5° to 3°, step 2°; frame rate 1600 Hz) for kidney imaging.

Concerning pediatric liver imaging, the observational study was approved by the institutional review board (CCP: 'Comité de Protection des Personnes', i.e., Committee for the Protection of Persons, CCP agreement N° PP-14020) and local ethical committee, and strictly complied with the ethical principles for medical research involving human subjects of the World Medical Association Declaration of Helsinki, and written consent was obtained from parents of the participants. Data are used for Figs. 12 and 13.

Kidney transplant imaging was incorporated in the framework of a study conducted to assess whether Ultrafast Doppler could help providing a parametric map of the transplant vascularization and assessing normal and abnormal vascularization within the transplant to detect fibrosis and inflammation. This clinical study was approved by the French national authorities (clinical trial number 2012-A01070-43). After imaging the morphology of the kidney with Bmode, imaging of the renal transplant vascularization was performed by one radiologist (J.M.C) in the longitudinal axis with conventional Doppler Imaging. Once a good imaging plane was found the Ultrafast Doppler acquisition was launched. Data are used for Figs. 13 and 14.

E. Signal and Image Processing

Each Ultrafast Doppler acquisition was filtered using either a 4^{th} order butterworth filter with a 'symmetric' initialization (mirror reflecting of the 20 first points of the signal) and those first 20 points where then removed to cancel any settling time of the filter, or using the SVD filter described in this paper, or using the varying phase increment down mixing approach described in [8] (Figs. 6 and 11) prior to the same 4^{th} order Butterworth filtering. The PW Doppler image was then calculated as the square root of the mean value of the squared filtered signal (thus corresponding to the energy normalized by the number of samples). This raw data was used directly for the CNR computations of the phantom study. In order to improve visualization for the reader and for fair comparison without inducing perceptive bias, for the all clinical examples PW Doppler images (regardless of the filtering process) were normalized with the highest value at 1 and the minimum value at 0, and histogram equalization was performed with rigorously the same parameters to improve the reader visualization without inducing any perceptive bias.

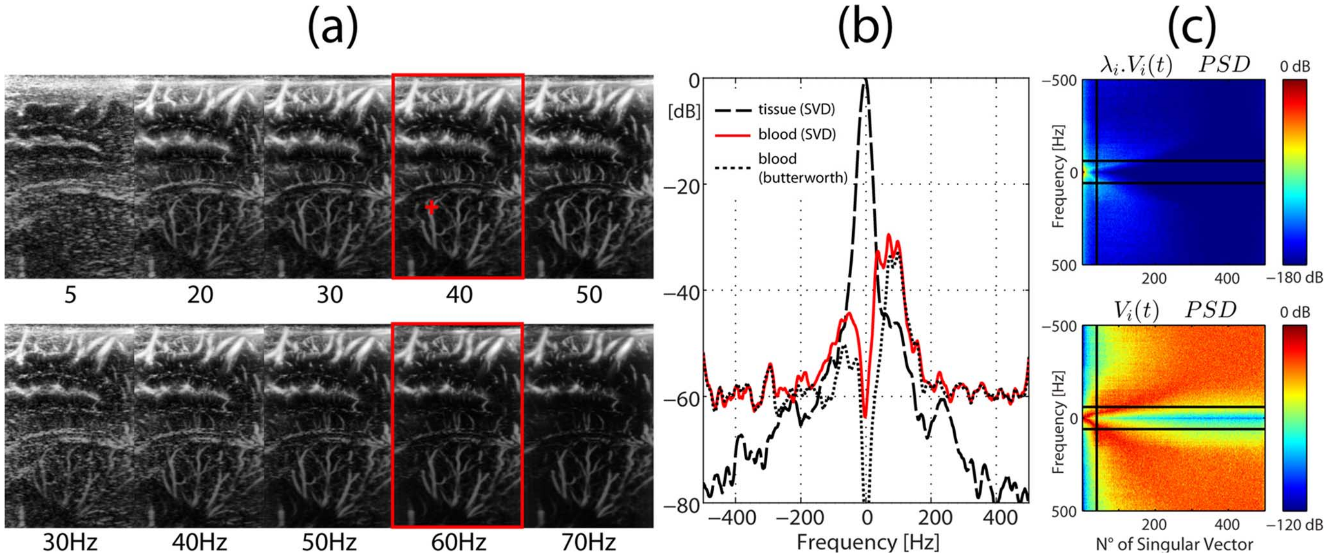

Fig. 8. Comparison between temporal filtering and SVD filtering, the ideal case: no motion and significant blood flow. (a) Effect of both increasing the number of rejected singular values (top) and increasing the temporal filter cut off frequency (bottom) on an Ultrafast Doppler acquisition (brain neonate imaging). For both methods the image that gave the best clutter rejection according to the clinicians has been framed in red. A region of interest has been chosen (red cross) in a vessel and power spectral estimation has been computed on the tissue signal (black dashed line) and blood signal (red solid line) *extracted via SVD filtering*, and blood signal (black dotted line) extracted via temporal Butterworth filtering (b). (c) Spectral diagrams (see Fig. 4(a)) (PSD stands for Power spectral Density): on top weighted with the singular value and on the bottom without weighting. Black lines represent temporal (horizontal) and singular-based (vertical) filtering of the signal.

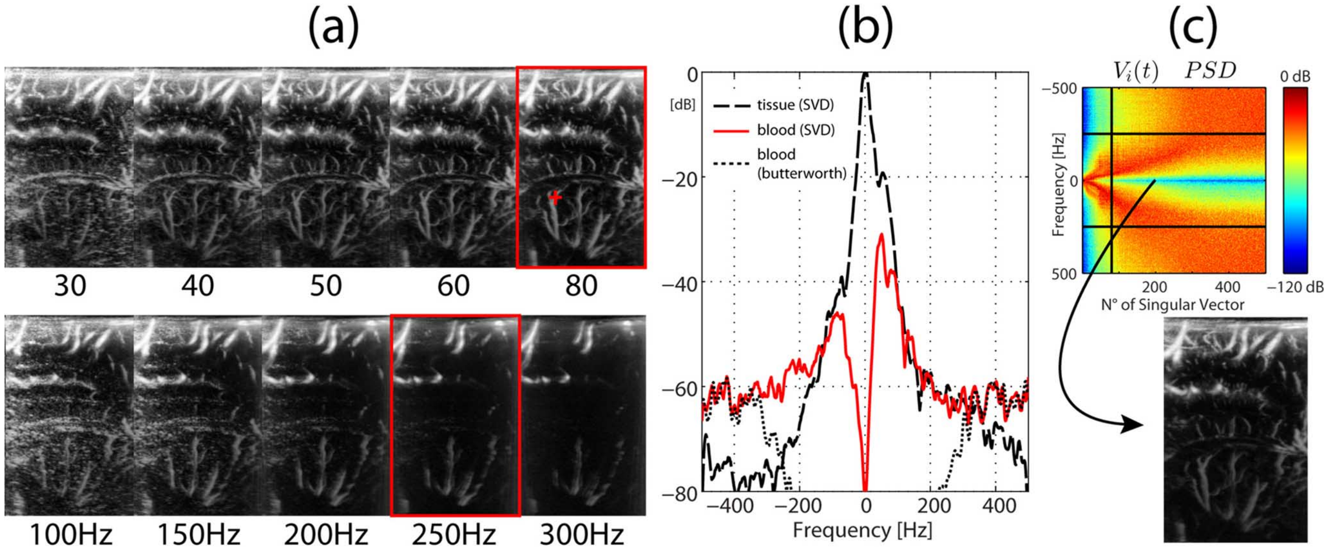

Fig. 9. Comparison between temporal filtering and SVD filtering, the strong motion case. Explanation of the different elements is the same than in Fig. 8, except for the image in (c) which depicts the image build from the energy lost in temporal filtering but kept in SVD filtering (i.e., the content of the energy in the rectangle drawn on spectral diagram top (c)).This acquisition was done 2 seconds after Fig. 8, the only difference is that strong motion was present in the moment of the acquisition.

The spectrograms of Figs. 7(c), 7(d) were generated via short time Fourier transform (32 samples sliding window, lag 2) on the temporal dimension of the pixels in the ROI. Each Fourier transform (meaning each column of the spectrogram) has its maximum set to 1 in order to improve readability. The spectrograms were then averaged in magnitude to be representative of the spectral content (linked to the axial velocity) in the ROI.

IV. RESULTS

A. Phantom Study

The phantom study enabled to quantify the improvement of Ultrafast Doppler detection ability by using SVD filtering versus other well-known methods (high-pass filtering, without or with down mixing) in various experimental conditions representative of the clinical setting for the detection of small vessels: low (1 mm/s) to important (10 mm/s) tissue motion and moderate (15.5 mm/s) to slow (2.6 mm/s) blood flow. Results of this study are presented in Fig. 6. It is striking to notice that even for very small tissue motion, the Butterworth filter alone gives very low values of CNR due to remaining clutter signal, compared to the two other approaches. If a reference value of 2 for the CNR is chosen for discrimination between tissue and flow, the Butterworth filter is unable to extract any blood signal of the explored blood speeds range as soon as

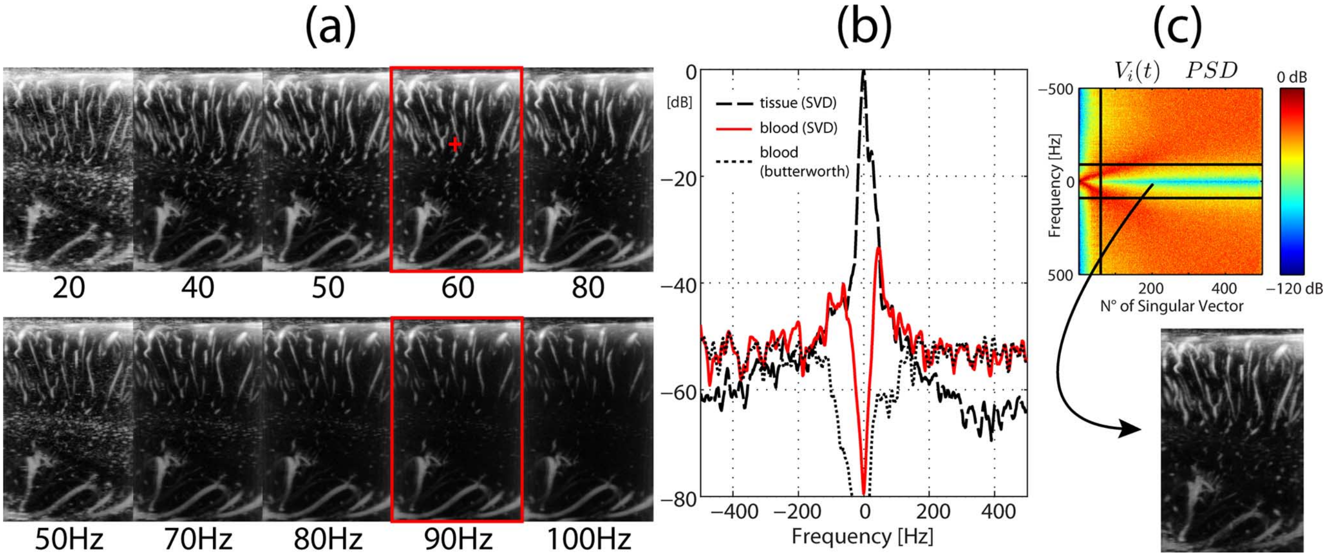

Fig. 10. Comparison between temporal filtering and SVD filtering, the very slow blood flow case. Explanation of the different elements is the same than in Fig. 9. This acquisition has been done in a parasagittal plane where blood vessels are smaller than in Figs. 8 and 9. The interest here is to show that without motion but in case of extremely slow blood flow, SVD filtering can still extract signal that could not be extracted via spectral discrimination.

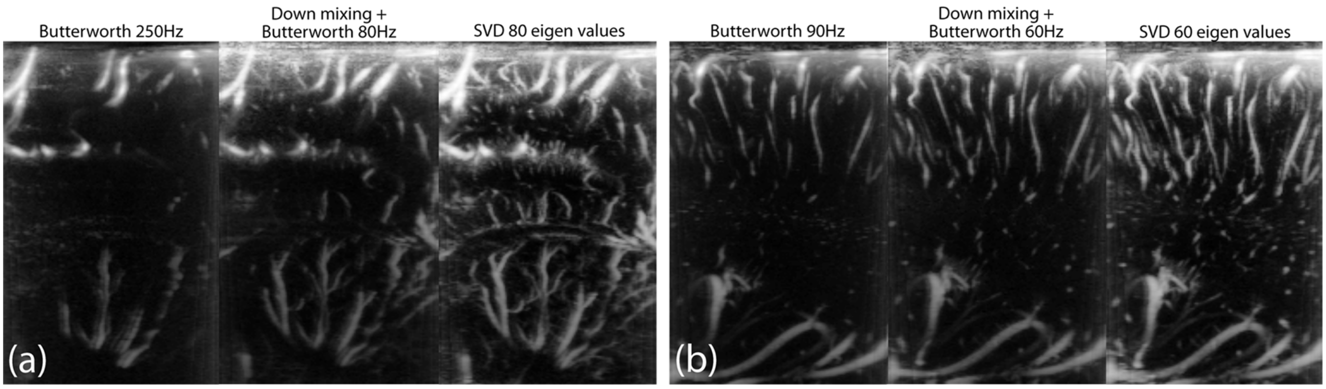

Fig. 11. Comparison of Butterworth filtering, down-mixing prior to Butterworth filtering and SVD filtering . (a) and (b) The data are the same than in Figs. 9 and 10 respectively and in each case the three images obtained with the best possible clutter rejection according to the clinician are presented side by side and in a larger format to enable proper comparison. Higher contrast and better small vessels delineation in the case of SVD filtering are unquestionable.

tissue motion exceeds 4mm/s. The lowest value of blood flow speed (2.6 mm/s) is not detected even for very low tissue speed (1 mm/s). This is not surprising as a spectral method cannot separate 2 signals with comparable speeds and an unfavorable 40 to 60 dB difference of energy. For very slow tissue velocity (1 mm/s) the down mixing approach and the SVD filtering give comparable results, except maybe at the slowest blood velocity that is better extracted via SVD filtering. But as soon as the tissue motion increases (tissue motion $>$ 4 mm/s), the CNR of the down mixing approach decreases rapidly whereas the SVD filtering seems more robust and tends to reach a plateau. This is due to fact that even if down mixing enables to bring back the spectrum of the tissue around the 0 Hz frequency, if the spectral content of tissue and blood flow are too overlapping because of comparable velocities they cannot be efficiently separated by a Fourier based filter, whereas the SVD filter can. SVD filtering appeared to be very robust in this configuration, since we measured a CNR above 2 for all the tested configurations, even when the mean axial blood flow velocity was lower than the tissue velocity (for a blood flow of 5.2 mm/s and a tissue motion of 10 mm/s, the CNR was 4.4 ± 0.6; for a blood flow of 2.6 mm/s and a tissue motion of 10 mm/s, the CNR was 2.9 ± 0.5).

B. The Functional Imaging Case

A first comparison of SVD clutter filtering and IIR Butterworth filtering is given (Fig. 7) in the framework of functional ultrasound imaging of brain activity (fUltrasound) [18], [20], [27], [28]. In fUltrasound, it is required to achieve high sensitivity Doppler imaging in order to track the hemodynamic changes due to neurovascular coupling occurring in very small vessels (i.e., mm/s blood flows). This figure is of capital importance to understand how SVD filtering improves both imaging and quantification enabled by Ultrafast Doppler. Figs. 7(a) and 7(b) show the comparison between the Power Doppler (PW) images obtained using SVD and temporal high pass filtering respectively on a thinned skull rat brain. The threshold for singular values and cut-off frequencies were chosen in order to provide the best image quality for both approaches respectively. The key point of this figure lies in the difference of detection of low flow speed depending on the filter.

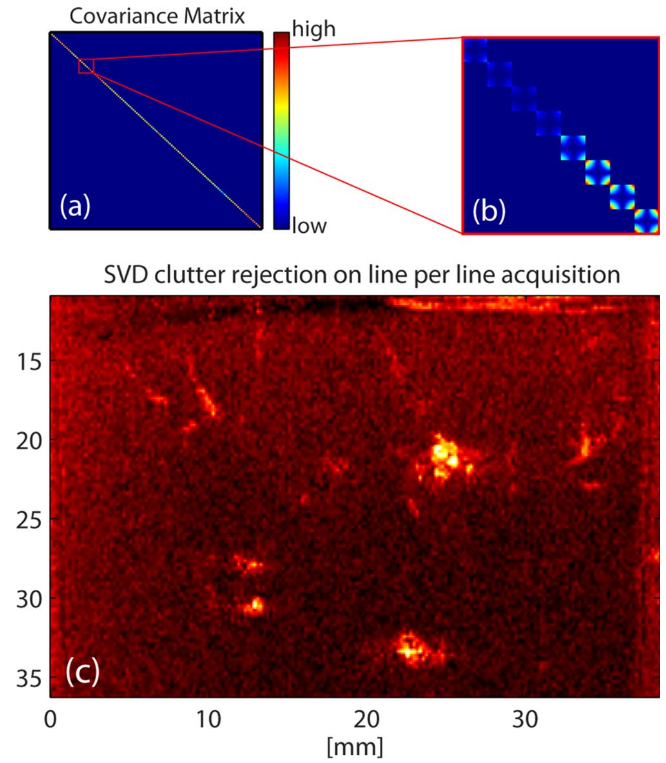

Fig. 12. Importance of the ensemble length for SVD Doppler filtering. An Ultrafast Doppler acquisition has been processed as if it were a line per line acquisition typical of focused ultrasound processed with the method described by Ledoux [9]. Instead of using all the data in the 3D matrix, only are kept the temporal points 1 to 16 for the first column of pixels, the temporal points 17 to 32 for the second column of pixels, and so on. This simulates a swept scan Doppler imaging strategy and the consequence is a lower ensemble length both for space and time. (a) Compared to the covariance matrix of Fig. 3, the covariance matrix for line per line acquisition is very sparse, with only 16×16 blocks on its diagonal. (b) a zoom on a small subregion on the covariance matrix reveals the small 16×16 blocks. (c) The Power Doppler image has been obtained using a SVD filter on each block of the covariance matrix, as would have been done in [9], with a removal of only the first singular vector. The image exhibits very poor sensitivity, and has to be compared to Fig. 13(a) which show the SVD filter result on the full matrix.

Pulse Wave Doppler is the classical ultrasound modality used to monitor the evolution of blood flow speed in one location of the image. The particularity of Ultrafast Doppler acquisition is that this kind of blood flow speed profile can be *a posteriori* computed in every location of the image, as described in [30]. A “Pulse Wave like” Doppler spectrogram can be computed in every pixel of the Ultrafast Doppler acquisition via short time Fourier transform of the In Phase/Quadrature signal, and has been calculated and averaged in magnitude over the region of interest (the set of pixel depicted by the cyan arrow) in both filtering cases (Figs. 7(c), 7(d)). What is of first importance on those spectrograms is the difference between the two filtered out bands of frequency depicted by the dashed red rectangles: the SVD filter is able to reject clutter without cutting entirely a the spectral band where tissue and flow are mixed, giving access to blood flow speed as low as 0.5 mm/s, whereas the 50 Hz cut off butterworth filter tends to cut everything below 2.5 mm/s. This explains why the smallest vessels are better detected via SVD filtering than via butterworth filtering, and in the case of fUltrasound, this difference is primordial since neurovascular coupling occurs at the capillary level, and the blood flow speed in the latter is known to be included in the 0.5-1.5 mm/s range [31].

C. Clinical Imaging

1) The Ideal Doppler Case: Beyond small animal imaging, the next comparisons are performed in clinical settings. A qualitative comparison of SVD clutter filtering and IIR Butterworth filtering is given by Fig. 8 to Fig. 10. The first example (Fig. 8) depicts the vasculature of cortical and thalamic areas. Motion is quite low during this acquisition and blood flow speeds are moderate (2 cm/s to 8 cm/s). Several values have been chosen for the number of rejected singular values and the cut off frequency of the butterworth filter and resulting Power Doppler images are presented. Out of the five examples presented, the best clutter rejection is obtained for 40 rejected singular values and 60 Hz of cut off frequency for SVD processing and conventional temporal filtering respectively. Even though this imaging situation is ideal (no motion artifacts) for the Butterworth high pass filtering, the number of visible blood vessels is bigger for SVD filtering than for Butterworth high pass filtering. It can be noticed that contrast is slightly higher with SVD filtering than with temporal filtering. Contrary to previous publications [4]–[6], [8]–[10] that only give a schematic or simulated representation of spectral distribution for tissue and blood signal, the large ensemble length available with Ultrafast Doppler enables to truly plot the spectral content of blood and tissue signal extracted via SVD filtering and to explain why in general SVD presents a better clutter rejection than temporal filtering. This has been done for each case (Fig. 8(b) to Fig. 10) where the spectral content of tissue signal (black dashed line) and of blood signal (red solid line) of the ROI defined on the image by a red cross mark and extracted via SVD are displayed. As a comparison the blood signal filtered via Butterworth filtering has also been plotted (black dotted line). In this imaging situation noise signal is roughly 60 dB below tissue signal, so the tails of the red solid spectra are mostly noise and not blood signal. In Fig. 8 it is clear that blood and tissue can be separated via temporal filtering because energy of blood signal is higher than energy of tissue in a certain spectral band (50 to 150 Hz), which is a required condition for the vessel to be detected in Power Doppler. This is the reason why temporal filtering gives quite good results in this first example. However it can be observed that the energy of blood signal extracted in the SVD processing is higher than in the temporal filtered extracted blood signal, which illustrates why SVD clutter rejection gives generally better contrast than temporal filters.

Fig. 8(c) represents the spectral content of $\lambda_i V_i(t)$ (upper image) and of $V_i(t)$ (lower image) versus the rank i of the singular value λ_i. On this representation in the singular vector space, the superimposed horizontal black lines represent the cutoff threshold of best Butterworth filtering and the vertical black line represent the cut-off threshold of best SVD filtering (vertical black line). The first image (top) enables to comprehend the relative differences in energy from the first singular vector to the last one, whereas the second one (bottom) enables to observe the differences between normalized spectral contents of individual temporal singular vector. For blood/tissue

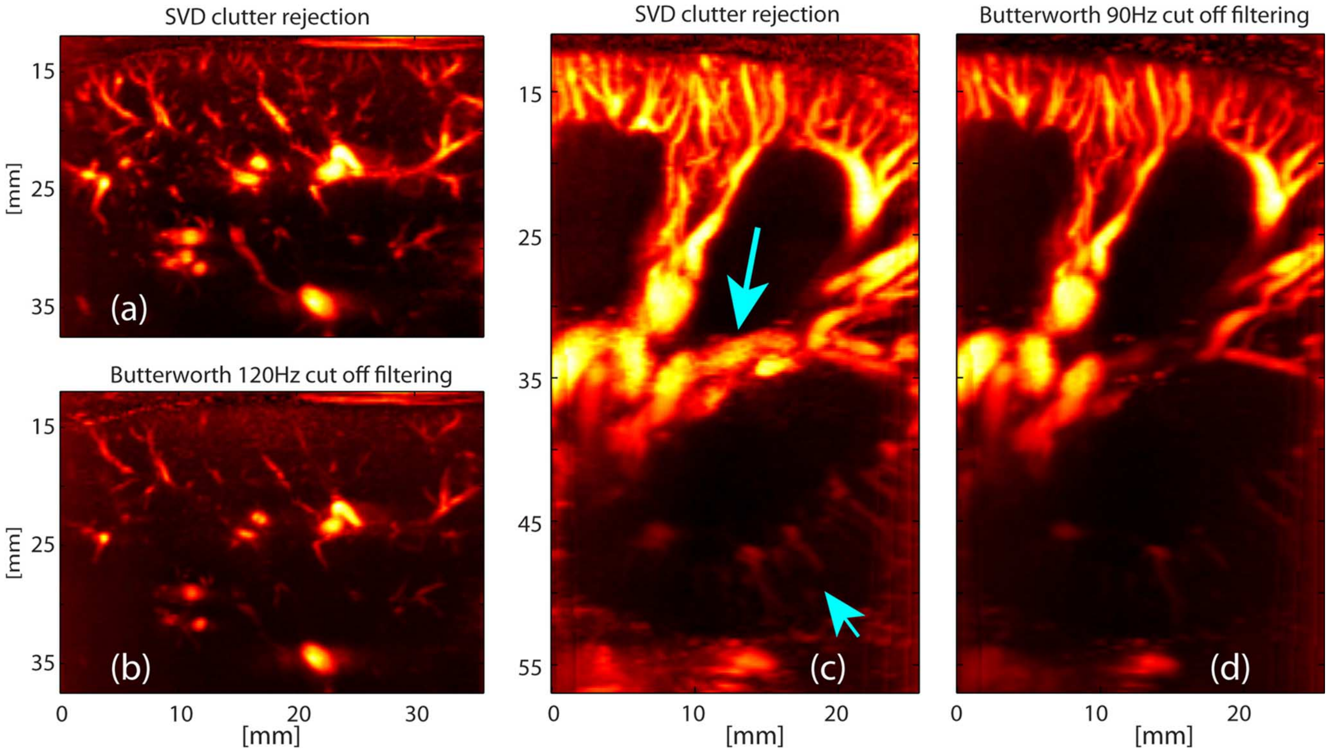

Fig. 13. Clinical examples of filtering improvement via SVD clutter rejection: (a) Ultrafast Doppler acquisition on a child (8 years old) liver processed via SVD, much more small vessels are detected than with butterworth filtering (b). (c) On a transplanted kidney, Ultrafast Doppler gives very good sensitivity with both processing but the few vessels with low flow speed (large vein, long arrow) (very small arteries, deep in the organ, small arrow) are almost completely filtered out by butterworth filtering (d).

discrimination, the first image may be the most important, because it represents the repartition of the total signal energy in a frequency-singular value space: trying to maximize the energy of blood signal over tissue signal in a Power Doppler image is related to the maximization of the integration of the energy in a portion of this frequency-singular value space. In the case of temporal filtering this subspace is chosen as the two rectangles above and below the two horizontal black lines, whereas in the case of SVD clutter rejection this subspace is chosen as the rectangle on the right of the vertical black line. With this representation the double advantage of SVD filtering over temporal filtering is obvious: whereas the latter leaves the "tails" of the tissue spectrum in the filtered signal and removes a great part of blood signal energy (low speeds), the vertical boundary of SVD filtering is much more optimal for the separation of tissue and blood. This explains the higher contrast for the SVD filtered Power Doppler image: although the main part of tissue signal is filtered by temporal Butterworth filtering, the huge difference of amplitude between tissue echoes and blood echoes makes the integration of the energy of tissue signal in the remaining spectral band not negligible compared to the integration of blood signal energy. Also a small part of blood signal is removed between the two horizontal lines.

2) The Strong Motion Case: In the presence of motion this difference becomes tremendous. Fig. 9 presents an acquisition done only two seconds after Fig. 8, but the neonate moved a little bit during this second acquisition, resulting in a strong motion artefact on the Power Doppler image. To recover a complete clutter rejection the cut off frequency of the temporal filtering as to be set to as high as 250 Hz (sampling frequency 1000 Hz) whereas a slight increase to 80 rejected singular values is enough in the case of SVD filtering. Even if a certain level of clutter is tolerated, any image processed with temporal filtering is far from depicting as much vessels as the SVD filtered image. The effect on the Power Doppler is obviously explained by the frequency-singular value diagram presented in (c): to filter pronounced high frequencies in the tissue signal, the temporal filter strategy is to increase the gap between the two horizontal lines, and almost completely filters out the blood signal. As depicted in the central spectrum (b), the vessel marked by the red cross mark would never be detected by temporal filtering because its energy is below tissue signal in every spectral domain. In Fig. 9(c) is displayed the Power Doppler image computed from the energy lying in the rectangle delimited by the singular-value threshold and the two cut off of the temporal filter. In other words it is the blood energy lost by the temporal filter compared to the SVD filter. It shows that a large amount of information is lost in the small vessels when using a temporal filter instead of the SVD filter.

3) The Very Slow Blood Flow Case: The last example in Fig. 10 shows that even with no motion artifacts, SVD filtering is much superior to detect really small vessels whose blood speed is not high enough to get out of the tail of the spectral content of tissue signal (red cross mark: a vessel appearing in SVD processed Power Doppler image and not in temporally processed Power Doppler image). Once again the contrast is higher with SVD processing. Finally, a zoomed view of the optimized Power Doppler images obtained respectively for temporal filtering, down mixing prior to temporal filtering, and SVD filtering is presented in Fig. 11 in order to emphasize the ability of multidimensional SVD filtering to provide better contrast and detect smaller vessels.

D. The Importance of the Plane Wave Imaging Ensemble Length

It was emphasized in the introduction that SVD filtering takes advantage of the large ensemble length provided by the Ultrafast Doppler technique compared to the classical focused emission technique. This is of primordial importance and is illustrated in Fig. 12. In this figure, Ultrafast Doppler data are processed as if they had been acquired with a swept scan strategy used in conventional Doppler: only the temporal points 1 to 16 are kept for the first column of the image, then only the temporal points 17 to 32 are kept for the second column and so on. This simulates a swept scan strategy used in CFI where only 16 temporal samples can be acquired per line because of the need to electronically quickly move to another location. Those data are then processed as proposed by Ledoux in [9]. The huge difference with Ultrafast Doppler SVD filtering lies both in the small number of temporal point acquired in each location and the lack of simultaneity of these temporal acquisitions, and that difference can be understood directly by looking at the covariance matrix: in each block of the covariance matrix the SVD filter has to find a subspace for tissue. As a consequence its ability to efficiently compress the tissue signal on a few singular vector before the subtraction operation is highly impaired.

V. DISCUSSION

SVD clutter rejection has been shown to improve significantly the sensitivity of Ultrafast Doppler in various imaging situations. It is especially efficient in two situations of major interest in Doppler imaging. It removes strong motion artifacts occurring during freehand exams usually downgrading the Doppler image quality. It also strongly improves detection of small vessels characterized by low flow speeds even if mild motion is present. For all studied configurations, SVD clutter rejection provided at least a higher contrast and generally superior detection capabilities. The outperformance of SVD clutter rejection is intrinsically linked with the ultrafast data acquisition. By providing multidimensional simultaneous ultrasonic data in 2D and soon in 3D at high frame rates, the ultrafast sequence can rely on much larger ensemble lengths in both time and space in order to discriminate tissue and probe motion from blood flow. Thus, the multidimensional SVD filter outperforms conventional temporal filters and leads to better discrimination because it takes into account large spatial ensemble lengths and the average statistics of the complete image is included. Finally, even in the most difficult situation where tissue motion is not completely stationary but rather low frequency and quite local, the SVD filtering works effectively to discriminate it from blood flow due fractal intrinsic properties of the vasculature. Indeed, the fractal nature of the vasculature implies that very low blood flows are present almost only in very small vessels much smaller than typical regions of tissues affected by the same range of motion. As their spatial statistics are different, the temporal variations of tissue and blood flow are nicely separated.

SVD filtering should have an important impact in the field of fUltrasound (functional ultrasound imaging of brain activity) since local hemodynamic changes linked to neurovascular coupling occur mainly in very small vessels where the blood flow speed is not measurable with conventional approaches. Moreover, the application of SVD filtering to ultrafast Doppler in the brain will be of particular interest for fUltrasound brain imaging of awake and freely moving animals where the optimal discrimination between tissue/probe motion artifacts and blood flow in small vessels becomes crucial.

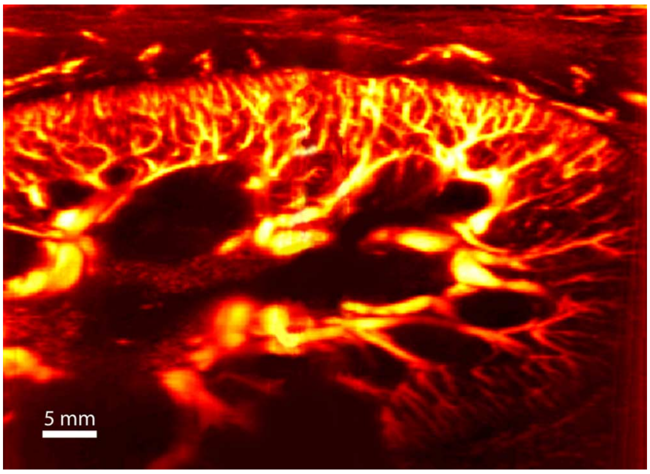

Fig. 14. Fusion (side to side concatenation with manual coregistration) of 2 Doppler images acquired in the same plane respectively on the left and right sides of the transplanted kidney of a human patient. The images are filtered via SVD filtering. The in vivo vascular network of the transplanted human kidney is delineated with a very high sensitivity without requiring the use of contrast agent.

The SVD clutter rejection also improves sensitivity and motion filtering in clinical applications such as kidney, liver, thyroid, heart imaging (data not shown). In this manuscript, results in neonate brain (Fig. 8 to Fig. 11), child liver and transplanted kidney (Fig. 13) were presented to illustrate the interest of this processing but many other unpresented data were acquired in thyroid and cardiac imaging and lead to the same conclusions. Neonate brain imaging is an interesting example of imaging application where it is difficult to ask patients to hold their breath. In such situations respiration motion combined to the ever-present pulsatility motion, are unavoidable. It is then difficult to filter out optimally slowly moving tissue from slow blood flow signal with a butterworth filter. In the liver example shown (Figs. 13(a) and 13(b)), tissue motion requires a 120Hz cut off frequency for the temporal filter and consequently vessels with blood speed below 1.5 $\mathrm{cm.s^{-1}}$ disappeared of the image, whereas SVD filtering is able to reject clutter without losing those small vessels. In the kidney example shown (Figs. 13(c) and 13(d)), tissue can be filtered out with a 90Hz cut off frequency for the temporal filter, and the blood flow speeds are consequent in most vessels ($> 1.2\ \mathrm{cm.s^{-1}}$), however SVD filtering still improves detection on venous structures in the central part of the image (long arrow) that present very low flow speeds ($\sim 0.8 \pm 0.2\ \mathrm{cm.s^{-1}}$) and completely disappear with temporal filtering. It is the same for deep small vessels whose signal is quite weak due to absorption (small arrow) and that can be quickly filtered out by a temporal filter. The sensitivity of Ultrafast Doppler combined with the discrimination capabilities of SVD filtering offers a level of detection never reached before with an ultrasound modality, even with the use of contrast agent (Fig. 14).

SVD clutter rejection is a powerful and versatile tool for Ultrafast Doppler imaging filtering, effective in many clinical applications. However this study presents some limitations, and a lot of areas for improvement have to be investigated. The first point is that no adaptive method for the choice of the threshold used for singular vector rejection has been proposed, but this is mainly due to the fact that the adjustment of this value is not as critical as for cut off frequency choice. It can be noticed that in all the examples presented in this paper a threshold of 80 rejected singular values would have given images with good quality, whereas temporal filter had to be precisely adjusted to reject clutter, with cut off frequencies ranging from 60 Hz to 250 Hz. However different strategies can be imagined for adaptive SVD clutter rejection: energy considerations on the level of the cumulative sum of the singular value can help, given an energy ratio in dB between blood signal and tissue signal depending on the acquisition parameters (ultrasound frequency, absorption coefficient . . .), to discriminate between the tissue subspace and the blood subspace of the singular vector space. A more sophisticated strategy is to calculate the central frequency of each individual temporal singular vector and to reject singular vector below a certain central frequency (a certain speed), strategy which do not overcome the problem of choosing a threshold because a certain speed has to be chosen, but which is adaptive to the amplitude of the motion present during the acquisition. Also, threshold can be dynamically chosen during the different phases of the cardiac cycle because the dimension of the tissue subspace increases for example during systole because of stronger tissue motion. These strategies will be presented with ongoing research in future work. Finally, the software beamforming capabilities provided by ultrasound scanners based on GPU boards [13] gives the physician the ability to adapt manually the singular value threshold to the desired image quality. This simplest strategy could turn out to be the most efficient compared to automatic approaches as the sonographers would rather manually optimize their image quality for different organs or patients.

Interestingly, robust and automatic approach for the choice of the filter threshold has been an extensive research topic in the applied mathematics community in the last decade. These approaches, i.e., the so-called Robust PCA [22], would permit to better choose the singular value thresholding. Our ultrasound problem fits to the context of robust PCA as the ultrasonic data acquired during ultrafast sequences can be seen as the superposition of a low-rank component (tissue motion) and a sparse component (blood motion).

First of all, the singular values of a random Gaussian matrix which corresponds to the noise component in (1) follows a Marchenko-Pastur distribution. This property can be taken benefit from to directly determine a rough statistical threshold by using Stein's Unbiased Risk Estimator (SURE method) as discussed by Candes *et al.* and Donoho *et al.* [21], [32]. In particular, Candes *et al.* applied the SURE method in order to determine an automatic threshold for the SVD decomposition in the context of dynamic MRI processing. In particular, they demonstrated the efficient use of the singular value thresholding (SVT) unbiased risk estimate for automated and optimized denoising of dynamic cardiac MRI series. The SURE method clearly demonstrated an improved assessment of myocardial perfusion. In this approach, the thresholding of singular values is not a hard-thresholding rule (*ie* replacing a subset of singular values by zeros), but rather introduce a soft-thresholding rule consisting in shrinking the singular values towards zero by a constant amount to determine during an iterative process. The outperformance of this more sophisticated approach will be evaluated in further works. Conversely to the other estimation approaches cited in Candes paper, we want to get rid of the main signal. Noise is present in addition to the blood signal in the low singular values subspace. However, as noted on Fig. 8(b), tissue signals (black curve) are 30 dB higher than blood flow signals (red curve) and blood flow signals are approximately 30 dB higher than the electronic noise level (tails of red curve). The accuracy and precision of local velocity estimation was studied both theoretically and experimentally in a previous paper using the same research platform [33].

Beyond the phantom study that provided quantitative Contrast to Noise Ratio data on the efficiency of SVD filtering compared to well-known other filtering algorithms, several points remain to clarify with quantitative data and controlled conditions, and will be addressed in future work. The range of tissue velocity explored in that phantom study has to be increased to cover high motion application, such as cardiac imaging, and the influence of the vessel size on the SVD filtering CNR has to be investigated and compared with other gold standard filters. Also, this study covered in plane tissue motion, but should also quantify the influence of out of plane motion.

The influence of the ensemble length has been underlined in this paper in terms of a comparison between really short ensembles (focused ultrasound) and very long ensembles (plane wave acquisitions). However the ensemble size used to build the Casorati matrix prior to SVD filtering has to be studied carefully, because it will be closely related to real-time capability of SVD filtering. In particular, temporal sliding windows or spatial-block processing will be investigated to find potential tradeoff between clutter rejection and computation time.

Computation is generally a bottleneck for real time imaging. With the current Matlab® implementation, and on an average quad core Xeon 2.66 GHz, the time to compute the SVD filtering is 0.5 s for a ($100 \times 128 \times 256$) Ultrafast acquisition, 1.7s for a ($100 \times 128 \times 512$) Ultrafast acquisition, 3.4 s for a ($200 \times 128 \times 512$) Ultrafast acquisition, and tend to be linear with the increase of the number of points in space and quadratic with the increase of the number of points in time (due to the choice of the covariance matrix presented in the method section). It is then indubitable that with the currently available processors, a reasonable choice for the processed temporal length of the Ultrafast Doppler acquisition and fastest C++ or GPU implementation, real time SVD filtering is reachable starting today.

Clinical data presented in this paper have been acquired with linear array and relatively high ultrasound frequency (6 MHz and 15 MHz). However this is not exclusive of other configuration and current work in our lab are conducted using Doppler SVD filtering with lower emission frequencies or phased array with diverging waves. Latest results on 3D ultrafast imaging rely on the use of SVD filtering with a 3 MHz probe and plane and diverging waves.

For some applications requiring very high performance levels for clutter filtering, the multidimensional SVD filter will become mandatory. It is the case for human brain ultrasound functional imaging, because freehand imaging of neurovascular coupling rest upon detection of really slow blood flow in arterioles and venules. Tremendous sensitivity of Ultrafast Doppler combined to optimal filtering abilities of SVD clutter rejection is a milestone toward that end. In cardiac imaging, the detection of myocardium vascularization without any contrast agents in the fast moving cardiac muscle would also strongly benefit from the use of such SVD approaches. Osmanski *et al.* proposed for Ultrafast Doppler imaging a demodulation approach for the discrimination of myocardium blood and tissue motion in 2012 [34]. The SVD clutter filtering can outperform this approach for the visualization of coronary arteries without contrast agents. Such high sensitivity vascular imaging without contrast agents could also be interesting for tumor vascularization characterization as blood flow in the tumor micro vascularization is today impossible to detect due to limited cut-off frequency thresholds of classical clutter filters necessary to cancel tissue motion artifacts.

Finally, it has been shown in this article that the SVD filter performance is increasing with the ensemble length both in space and time, this is the reason why SVD filtering applied on 2D spatial data provided by ultrafast imaging outperforms SVD filtering applied to 1D spatial data provided by conventional focused emissions. For this reason, the extension of SVD clutter filtering to 4D ultrasonic data (3D space + 1D time) provided by ultrafast matrix arrays [35] should lead to even better results and an additional improvement of filtered data in 3D Ultrafast Doppler imaging.

REFERENCES

[1] S. Bjaerum, H. Torp, and K. Kristoffersen, “Clutter filter design for ultrasound color flow imaging,” *IEEE Trans. Ultrason. Ferroelectr. Freq. Control*, vol. 49, no. 2, pp. 204–216, Jun. 2002.

[2] J. C. Willemetz, A. Nowicki, J. J. Meister, F. De Palma, and G. Pante, “Bias and variance in the estimate of the Doppler frequency induced by a wall motion filter,” *Ultrason. Imag.*, vol. 11, no. 3, pp. 215–225, Jul. 1989.

[3] C. Tysoe and D. H. Evans, “Bias in mean frequency estimation of Doppler signals due to wall clutter filters,” *Ultrasound Med. Biol.*, vol. 21, no. 5, pp. 671–677, 1995.

[4] Y. M. Yoo, R. Managuli, and Y. Kim, “Adaptive clutter filtering for ultrasound color flow imaging,” *Ultrasound Med. Biol.*, vol. 29, no. 9, pp. 1311–1320, Sep. 2003.

[5] A. P. Kadi and T. Loupas, “On the performance of regression and step-initialized IIR clutter filters for color Doppler systems in diagnostic medical ultrasound,” *IEEE Trans. Ultrason. Ferroelectr. Freq. Control*, vol. 42, no. 5, pp. 927–937, Sep. 1995.

[6] A. P. G. Hoeks, J. J. W. van de Vorst, A. Dabekaussen, P. J. Brands, and R. S. Reneman, “An efficient algorithm to remove low frequency Doppler signals in digital Doppler systems,” *Ultrason. Imag.*, vol. 13, no. 2, pp. 135–144, Apr. 1991.

[7] L. Thomas and A. Hall, “An improved wall filter for flow imaging of low velocity flow,” in *Proc. IEEE Ultrason. Symp.*, 1994, vol. 3, pp. 1701–1704.

[8] S. Bjaerum, H. Torp, and K. Kristoffersen, “Clutter filters adapted to tissue motion in ultrasound color flow imaging,” *IEEE Trans. Ultrason. Ferroelectr. Freq. Control*, vol. 49, no. 6, pp. 693–704, Jun. 2002.

[9] L. A. F. Ledoux, P. J. Brands, and A. P. G. Hoeks, “Reduction of the clutter component in Doppler ultrasound signals based on singular value decomposition: A simulation study,” *Ultrason. Imag.*, vol. 19, no. 1, pp. 1–18, Jan. 1997.

[10] A. C. H. Yu and L. Lovstakken, “Eigen-based clutter filter design for ultrasound color flow imaging: A review,” *IEEE Trans. Ultrason. Ferroelectr. Freq. Control*, vol. 57, no. 5, pp. 1096–1111, May 2010.

[11] L. Lovstakken, S. Bjaerum, K. Kristoffersen, R. Haaverstad, and H. Torp, “Real-time adaptive clutter rejection filtering in color flow imaging using power method iterations,” *IEEE Trans. Ultrason. Ferroelectr. Freq. Control*, vol. 53, no. 9, pp. 1597–1608, Sep. 2006.

[12] D. E. Kruse and K. W. Ferrara, “A new high resolution color flow system using an eigendecomposition-based adaptive filter for clutter rejection,” *IEEE Trans. Ultrason. Ferroelectr. Freq. Control*, vol. 49, no. 10, pp. 1384–1399, Oct. 2002.

[13] M. Tanter and M. Fink, “Ultrafast imaging in biomedical ultrasound,” *IEEE Trans. Ultrason. Ferroelectr. Freq. Control*, vol. 61, no. 1, pp. 102–119, Jan. 2014.

[14] J. Bercoff, M. Tanter, and M. Fink, “Supersonic shear imaging: A new technique for soft tissue elasticity mapping,” *IEEE Trans. Ultrason. Ferroelectr. Freq. Control*, vol. 51, no. 4, pp. 396–409, Apr. 2004.

[15] M. Tanter, J. Bercoff, L. Sandrin, and M. Fink, “Ultrafast compound imaging for 2-D motion vector estimation: Application to transient elastography,” *IEEE Trans. Ultrason. Ferroelectr. Freq. Control*, vol. 49, no. 10, pp. 1363–1374, Oct. 2002.

[16] G. Montaldo, M. Tanter, J. Bercoff, N. Benech, and M. Fink, “Coherent plane-wave compounding for very high frame rate ultrasonography and transient elastography,” *IEEE Trans. Ultrason. Ferroelectr. Freq. Control*, vol. 56, no. 3, pp. 489–506, Mar. 2009.

[17] J. Bercoff *et al.*, “Ultrafast compound Doppler imaging: Providing full blood flow characterization,” *IEEE Trans. Ultrason. Ferroelectr. Freq. Control*, vol. 58, no. 1, pp. 134–147, Jan. 2011.

[18] E. Mace *et al.*, “Functional ultrasound imaging of the brain: Theory and basic principles,” *IEEE Trans. Ultrason. Ferroelectr. Freq. Control*, vol. 60, no. 3, pp. 492–506, Mar. 2013.

[19] C. R. Cooley and B. S. Robinson, “Synthetic focus imaging using partial datasets,” in *Proc. IEEE Ultrasonics Symp.*, 1994, vol. 3, pp. 1539–1542.

[20] E. Macé *et al.*, “Functional ultrasound imaging of the brain,” *Nat. Methods*, vol. 8, no. 8, pp. 662–664, Jul. 2011.

[21] E. J. Candes, C. A. Sing-Long, and J. D. Trzasko, “Unbiased risk estimates for singular value thresholding and spectral estimators,” *IEEE Trans. Signal Process.*, vol. 61, no. 19, pp. 4643–4657, Oct. 2013.

[22] E. J. Candès, X. Li, Y. Ma, and J. Wright, “Robust principal component analysis?,” *J. ACM JACM*, vol. 58, no. 3, p. 11, 2005.

[23] R. Otazo, E. Candès, and D. K. Sodickson, “Low-rank plus sparse matrix decomposition for accelerated dynamic MRI with separation of background and dynamic components,” *Magn. Reson. Med.*, vol. 73, no. 3, pp. 1125–1136, Mar. 2015.

[24] H. Gao, H. Yu, S. Osher, and G. Wang, “Multi-energy CT based on a prior rank, intensity and sparsity model (PRISM),” *Inverse Probl.*, vol. 27, no. 11, p. 115012, Nov. 2011.

[25] Y. H. Sajan Goud Lingala, “Accelerated dynamic MRI exploiting sparsity and low-rank structure: k-t SLR,” *IEEE Trans. Med. Imag.*, vol. 30, no. 5, pp. 1042–54, 2011.

[26] Z.-P. Liang, “Spatiotemporal imaging with partially separable functions,” in *Proc. NFSI-ICFBI*, 2007, pp. 181–182.

[27] C. Eckart and G. Young, “The approximation of one matrix by another of lower rank,” *Psychometrika*, vol. 1, no. 3, pp. 211–218, Sep. 1936.

[28] B. F. Osmanski *et al.*, “Functional ultrasound imaging reveals different odor-evoked patterns of vascular activity in the main olfactory bulb and the anterior piriform cortex,” *NeuroImage*, vol. 95, pp. 176–184, Jul. 2014.

[29] B. F. Osmanski, S. Pezet, A. Ricobaraza, Z. Lenkei, and M. Tanter, “Functional ultrasound imaging of intrinsic connectivity in the living rat brain,” *Nature Commun.*, Oct. 2014.

[30] C. Demené *et al.*, “Ultrafast Doppler reveals the mapping of cerebral vascular resistivity in neonates,” *J. Cereb. Blood Flow Metab.*, Mar. 2014.

[31] K. P. Ivanov, M. K. Kalinina, and Y. I. Levkovich, “Blood flow velocity in capillaries of brain and muscles and its physiological significance,” *Microvasc. Res.*, vol. 22, no. 2, pp. 143–155, Sep. 1981.

[32] D. Donoho and M. Gavish, “Minimax risk of matrix denoising by singular value thresholding,” *Ann. Stat.*, vol. 42, no. 6, pp. 2413–2440, Dec. 2014.

[33] T. Deffieux, J.-L. Gennisson, B. Larrat, M. Fink, and M. Tanter, “The variance of quantitative estimates in shear wave imaging: Theory and experiments,” *IEEE Trans. Ultrason. Ferroelectr. Freq. Control*, vol. 59, no. 11, Nov. 2012.

[34] B.-F. Osmanski *et al.*, “Ultrafast Doppler imaging of blood flow dynamics in the myocardium,” *IEEE Trans. Med. Imag.*, vol. 31, no. 8, pp. 1661–1668, Aug. 2012.

[35] J. Provost *et al.*, “3D ultrafast ultrasound imaging in vivo,” *Phys. Med. Biol.*, vol. 59, no. 19, p. L1, Oct. 2014.

Appendix B

Article 4: Multi-plane wave imaging increases signal-to-noise ratio in ultrafast ultrasound imaging.

Tiran, E., T. Deffieux, M. Correia, D. Maresca, B.-F. Osmanski, L.-A. Sieu, **A. Bergel**, I. Cohen, M. Pernot, and M. Tanter 2015. multi-plane wave imaging increases signal-to-noise ratio in ultrafast ultrasound imaging. *Physics in Medicine and Biology*, 60(21):8549-8566.

OPEN ACCESS
IOP Publishing | Institute of Physics and Engineering in Medicine
Physics in Medicine & Biology
Phys. Med. Biol. 60 (2015) 8549–8566
doi:10.1088/0031-9155/60/21/8549

Multiplane wave imaging increases signal-to-noise ratio in ultrafast ultrasound imaging

Elodie Tiran[1], Thomas Deffieux[1], Mafalda Correia[1], David Maresca[1], Bruno-Felix Osmanski[1], Lim-Anna Sieu[2,3], Antoine Bergel[2,4], Ivan Cohen[2], Mathieu Pernot[1] and Mickael Tanter[1]

[1] ESPCI-ParisTech, PSL University, INSERM U979, CNRS UMR7587, Institut Langevin, 1 rue Jussieu, F-75005, Paris, France
[2] Neuroscience Paris Seine, University Pierre et Marie Curie UMCR18, INSERM U1130, CNRS UMR8246, 9 quai Saint Bernard, F-75005, Paris, France
[3] Institut des Neurosciences Translationnelles de Paris, Paris, France
[4] Ecole Doctorale Frontières du Vivant, Programme Bettencourt, Université Paris Diderot, Sorbonne Paris Cité, Paris, France

E-mail: mickael.tanter@espci.fr

Received 30 June 2015, revised 8 September 2015
Accepted for publication 11 September 2015
Published 21 October 2015

Abstract

Ultrafast imaging using plane or diverging waves has recently enabled new ultrasound imaging modes with improved sensitivity and very high frame rates. Some of these new imaging modalities include shear wave elastography, ultrafast Doppler, ultrafast contrast-enhanced imaging and functional ultrasound imaging. Even though ultrafast imaging already encounters clinical success, increasing even more its penetration depth and signal-to-noise ratio for dedicated applications would be valuable.

Ultrafast imaging relies on the coherent compounding of backscattered echoes resulting from successive tilted plane waves emissions; this produces high-resolution ultrasound images with a trade-off between final frame rate, contrast and resolution. In this work, we introduce multiplane wave imaging, a new method that strongly improves ultrafast images signal-to-noise ratio by virtually increasing the emission signal amplitude without compromising the frame rate. This method relies on the successive transmissions of multiple plane waves with differently coded amplitudes and emission angles in a single transmit event. Data from each single plane wave of increased amplitude can

0031-9155/15/218549+18$33.00

then be obtained, by recombining the received data of successive events with the proper coefficients.

The benefits of multiplane wave for B-mode, shear wave elastography and ultrafast Doppler imaging are experimentally demonstrated. Multiplane wave with 4 plane waves emissions yields a 5.8 ± 0.5 dB increase in signal-to-noise ratio and approximately 10 mm in penetration in a calibrated ultrasound phantom ($0.7\,\mathrm{d\,MHz^{-1}\,cm^{-1}}$). In shear wave elastography, the same multiplane wave configuration yields a 2.07 ± 0.05 fold reduction of the particle velocity standard deviation and a two-fold reduction of the shear wave velocity maps standard deviation. In functional ultrasound imaging, the mapping of cerebral blood volume results in a 3 to 6 dB increase of the contrast-to-noise ratio in deep structures of the rodent brain.

Keywords: Ultrasound imaging, ultrafast imaging, signal-to-noise ratio, frame rate, B-mode, shear wave elastography, Doppler imaging

(Some figures may appear in colour only in the online journal)

1. Introduction

Ultrafast plane wave imaging was introduced in the last decade as a way to maximize ultrasound imaging frame rate, with the initial goal of tracking shear wave propagation within the body (Tanter *et al* 2008). In order to reach the highest frame rate, a single plane wave is transmitted instead of line-per-line focused beams. This allows imaging frame rates up to 10 000 frames per second, depending only on the imaging depth. In this plane wave imaging approach there is no focalisation in transmission, but thanks to conventional beamforming in reception, the received data can be used to retrieve the localization of echoes. This lack of transmit focalization inevitably leads to poorer image quality, especially in terms of contrast, but ultrafast plane wave imaging still offered a new window on fast and transient phenomena.

Recently, our group developed a new way to improve the performance of ultrafast plane wave imaging by using coherent compounding of several tilted plane waves (Montaldo *et al* 2009, Bercoff *et al* 2011). By using appropriate time delays, the transmit focalization can be synthetically recreated in each pixel of the image thanks to the coherent summing of the backscattered echoes of a few plane waves transmitted with different angles. Such a coherent recombination was proposed in the framework of synthetic imaging for increased image quality (Karaman *et al* 1995, Lockwood *et al* 1998, Nikolov and Jensen 2003, Udesen *et al* 2008). Plane wave coherent compounding has been demonstrated to allow the realization of B-mode equivalent quality images as in the standard focused approach with only a third of the insonifications (Montaldo *et al* 2009), thus achieving both high quality and high frame rate, even in the case of very rapidly moving targets (Denarie *et al* 2013). A clear trade-off between high quality and high frame rate can be defined on the number of angles. This concept has then been applied to shear wave elastography and later to Doppler imaging (Bercoff *et al* 2011) and ultrafast diverging wave imaging (Papadacci *et al* 2014), and is now at the core of ultrafast imaging. The large number of current and potential future applications embraced by ultrafast ultrasound imaging (Tanter and Fink 2014) encourages the development of optimized sequences to improve the contrast, the signal-to-noise and the resolution of ultrafast images.

This paper investigates one of these improvements, as multiplane wave imaging is an ultrafast imaging technique based on coded coherent plane wave compounding that aims at

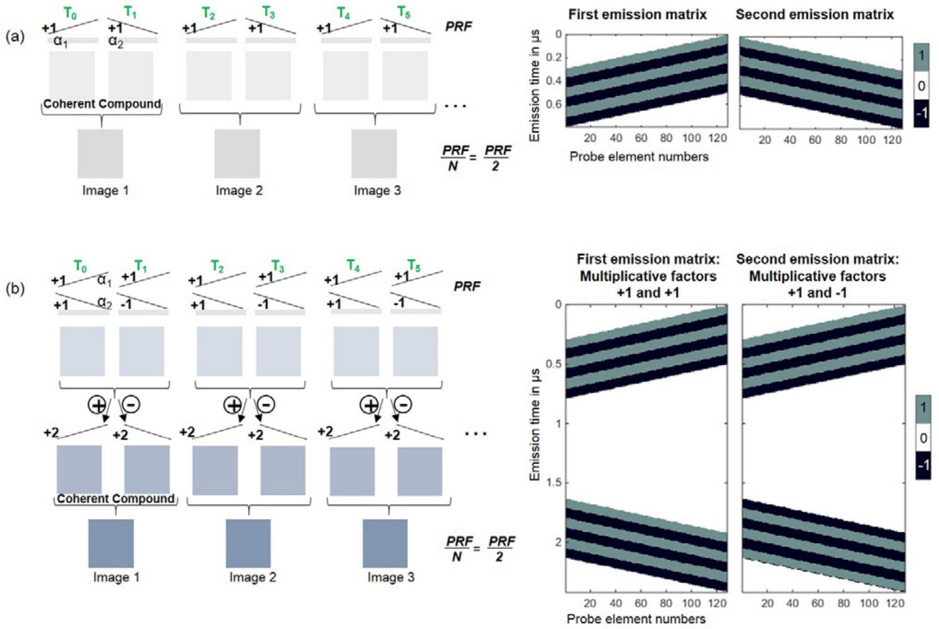

Figure 1. (a) Coherent plane wave compounding with $N = 2$ plane waves. (b) Multiplane wave compounding with $N = 2$ plane waves.

increasing the signal-to-noise ratio of ultrafast images without compromising neither frame rate nor resolution.

The multiplane wave method basic principles are detailed in section 2. Multiplane wave imaging performance is compared to the classical plane wave coherent compounding technique in section 3 in phantom B-mode acquisitions. Then multiplane wave imaging is also applied to shear wave elastography imaging and ultrafast Doppler imaging. We demonstrate how this novel imaging approach improves signal-to-noise ratio (SNR) and contrast of B-mode images, how it provides accurate elasticity maps with smaller variance for elastography applications, and how it detects deeper blood signals in Doppler mode. This technique could be of great interest for deep observations in the tissues where attenuation weakens the signal.

2. Multiplane wave imaging basic principles

A schematic representation of the classical coherent plane wave compounding method with $N = 2$ plane waves is represented in figure 1(a) (left part). At time T0 the medium is insonified with a first plane wave tilted with an angle α_1 and the backscattered echoes are recorded. Then, at time T1, the medium is insonified with a second plane wave tilted with an angle α_2 and the backscattered echoes are recorded. After delay-and-sum beamforming of the received data, two low quality radio frequency (RF) images are obtained. The coherent addition of these two images generates a higher quality image as described in Montaldo *et al* (2009). Each individual plane wave is transmitted with a fixed Pulse Repetition Frequency (PRF) which is limited by the propagation time, i.e. by the imaging depth. In the $N = 2$ plane waves example, two images from two different plane waves are required to create a single final image; as a result the final frame rate is half the PRF. More generally the final frame rate is equal to the PRF divided by the number of plane waves used in the coherent summation. Thus, the more plane waves are used for the final image, the better its quality but also the lower the frame rate. This highlights the conventional trade-off between image quality and frame rate of coherent plane wave compounding.

Multiplane wave imaging provides further improvement of the image signal-to-noise ratio for a given frame rate with an extremely simple mathematical and hardware implementation. The multiplane wave method improves the quality of final images by artificially increasing the amplitude of the transmit signal without compromising the frame rate. Indeed, the emitted waveform amplitude is often limited by ultrasound transducer electronic circuit characteristics, probe design or eventually by safety considerations such as Mechanical Index limits. Thus, as the amplitude is often already close to its maximum value, increasing the transmit amplitude is not directly possible.

The original solution proposed in this work is schematically represented in figure 1(b) (left part) in the case of $N = 2$ plane waves. At transmit time T0, two wavefronts tilted with two different angles α_1 and α_2 are quasi simultaneously transmitted into the medium with a very small interleaved delay dt. A multiplicative factor $+1$ is applied on both wavefronts. The backscattered echoes are received and stored in memories. At transmit time T1, the same wavefronts are transmitted again, but this time with multiplicative factors $+1$ for the first wavefront and -1 for the second one. Once again, the resulting echoes are received and stored in memories. At this step there are two RF images, one for each acquisition at times T0 and T1. Then the two images are coherently summed: in a first combination, the contributions of angle α_2 disappear in the linear regime of propagation thanks to the multiplicative factors applied on the angle α_2 $((+1) + (-1) = 0)$, whereas the contributions of angle α_1 are added $((+1) + (+1) = 2)$. Thus the summation enables to obtain the same image as if only a single transmit, tilted with an angle $\alpha_{1,}$ was sent with double amplitude. In a second combination, the subtraction of the two images makes the contributions of angle α_1 disappear $((+1) - (+1) = 0)$ while contributions for angle α_2 add up $((+1) - (-1) = 2)$. The subtraction enables to obtain the same image as if only a single transmit, this time tilted with an angle α_2, was also sent with double amplitude. Finally, the time delay dt between the two tilted plane waves is compensated for, and the two resulting images are coherently summed to obtain the final image, as done in the coherent plane wave compounding method.

The time between two consecutive images is only limited by the propagation time in the medium. As a consequence, if this set of multiplane waves is sent with the same plane wave coherent compounding technique PRF, the final frame rate will also be equal to PRF/N (in this example PRF/2). Thus, the multiplane approach leads to a virtual increase of the transmit signal amplitude without compromising the ultrafast frame rate.

In this multiplane wave example (figure 1(b)), since the emission matrix contains the two plane waves, its duration is at least twice longer (figures 1(a) and (b) right parts), resulting in a larger blind near field zone where the image cannot be reconstructed. Furthermore, a fixed pause approximately as long as the duration of the wavefront has been introduced between two plane waves to let transducers return to zero and avoid artefacts. Since the ultrasonic device cannot receive backscattered echoes until the emission is over, and as the emission matrix is longer in the multiplane wave case, the blind area on the surface of the image due to the emission duration is larger. The blind area is defined as $d_{\text{blind}} \sim c \times t_{\text{em}}/2$, with c the ultrasound celerity and t_{em} the emission duration. In this example (figures 1(a) and (b) right part) the classical coherent plane wave compounding method with $\alpha = \pm 1°$ gives $\text{d}_{\text{blind}} \sim 1540 \times 0.8 \times 10^{-6}/2 \sim 0.6\,\text{mm}$, whereas the $N = 2$ multiplane wave case with same inclination ($\alpha = \pm 1°$) gives a larger blind area: $d_{\text{blind}} \sim 1540 \times 2.4 \times 10^{-6}/2 \sim 1.8\,\text{mm}$. The blind area remains negligible for a small number of plane waves and for weak inclinations, but has to be taken into account in the case of a higher number of plane waves or higher inclinations. Fortunately, such a high number of plane waves will be mostly required for imaging deeper structures, relatively to the probe width.

The multiplane wave compounding method introduced with $N = 2$ plane waves can be generalized to any values of N. An appropriate combination of multiplicative factors $+1$ and -1 has to be applied to each set of plane waves, in order to reconstruct each plane wave of the set as if it had been sent separately from the others. In this work, an Hadamard matrix has been used because it creates independent vectors with $+1$ and -1 components (i.e. without losing the maximum amplitude level for each transmission). Hadamard matrices have many applications in signal processing, coding or cryptography (Horadam 2007) and have already been applied to synthetic aperture imaging in Ultrasound (Chiao *et al* 1997, Mosca *et al* 2008). An Hadamard matrix is a square matrix with $+1$ or -1 coefficients and whose rows are mutually orthogonal. One of the interesting properties of these matrices is that the multiplication of H_N (Hadamard matrix of order N) by its transpose is equal to N times the identity matrix:

$$H_N . H_N^t = N.I.$$

This property is used for the multiplane wave emission matrix, in order to reconstruct each single plane wave separately. The order of an Hadamard matrix must be 1, 2 or a multiple of 4. The smallest Hadamard matrix is $H_1 = [1]$. The following ones, of order 2^k (with $2 \leqslant k \in N$), can be computed using Sylvester's construction (Sylvester 1867):

$$H_2^k = \begin{bmatrix} H_2^{k-1} & H_2^{k-1} \\ H_2^{k-1} & -H_2^{k-1} \end{bmatrix},$$

with H_2 the Hadamard matrix of order 2, $H_2 = \begin{bmatrix} 1 & 1 \\ 1 & -1 \end{bmatrix}$. The column coefficients of H_N can been seen as the multiplicative factors used for the different emissions, whereas the row coefficients represent the combination of subtraction or addition operations needed to retrieve one plane wave individually with an amplitude N and cancel all the others (figure 2).

In this work, the Hadamard basis was used with N ranging from 2 to 32 plane waves.

The virtual increase of the emitted amplitude obtained by coherent summation is expected to result in an overall increase of the signal-to-noise ratio of the image. Assuming a white electronic noise in the acquisition boards, the time standard deviation of each pixel in the image should be divided by $\sqrt{N}$, ie a SNR gain of $10 \cdot \log 10(N)$ on the energy. When electronic noise is dominant over side lobes and clutter, such as in deep structures, a significant increase of the contrast can be expected compared to coherent plane wave compounding. Similarly, the improvement of the signal-to-noise ratio has a direct impact on other imaging modalities based on ultrafast imaging, such as shear wave elastography or ultrafast Doppler imaging.

3. Results

3.1. Performance quantification of B-mode imaging in phantom

The sequence was implemented on an Aixplorer$^{\text{TM}}$ ultrasound system (SuperSonic Imagine, Aix-en-Provence, France) running Matlab (MathWorks, Natick, Massachusetts, USA). The performance was assessed both in terms of signal-to-noise ratio and in terms of contrast using an imaging phantom (Small parts phantom, model 551, ATS laboratories, Bridgeport, USA) of 3 mm diameter anechoic inclusions embedded in a homogeneous speckle environment. The

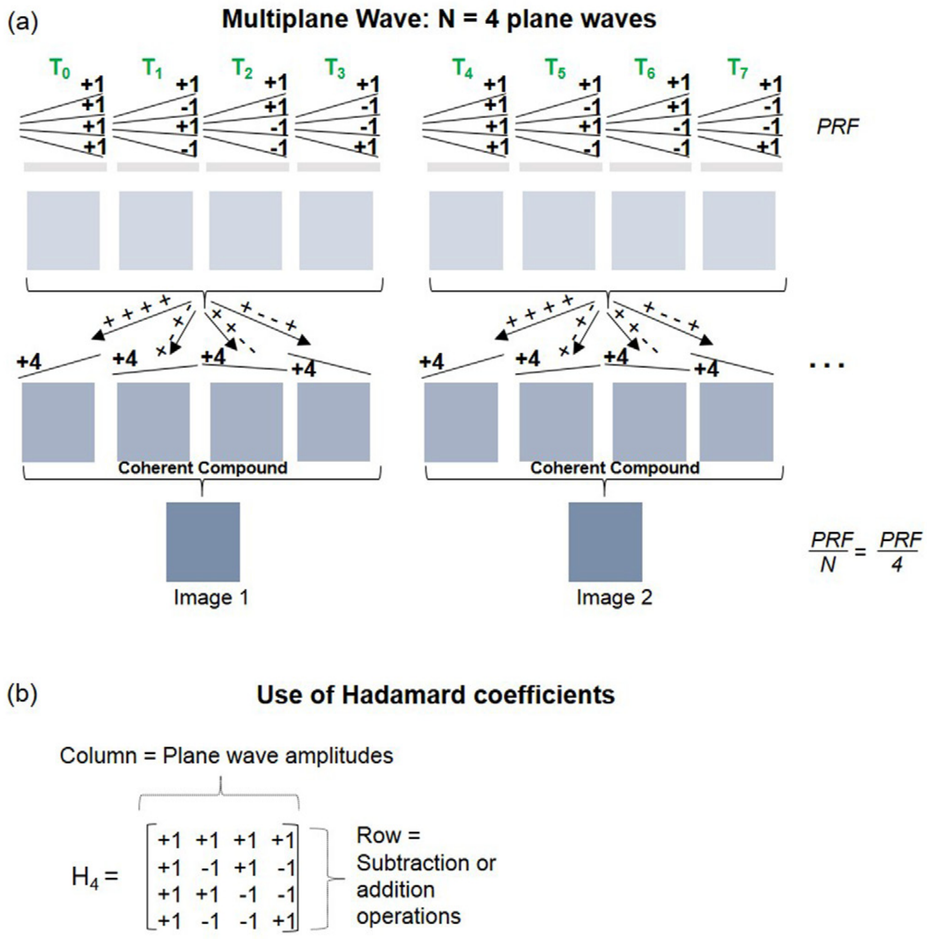

Figure 2. (a) Schematic representation of multiplane wave case with $N = 4$ plane waves. (b) Example of Hadamard matrix with $N = 4$.

128 first elements of a 160-element array working at 6 MHz central frequency with a 0.2 mm pitch (SuperSonic Imagine, Aix-en-Provence, France) were used and the receive bandwidth of the scanner was set at 90% using the on board finite impulse response (FIR) filter. One hundred frames were acquired both with coherent plane wave compounding and multiplane wave imaging.

In order to compare plane wave and multiplane wave image quality the SNR has been plotted as a function of depth. For each depth, the SNR has been averaged in the probe axis direction over a 10 pixels area containing inclusions. For each pixel, the ultrasonic signal has been computed as the mean over the 100 images and the noise as the standard deviation.

The performance was also assessed in terms of contrast. The contrast represents the ability of the imaging method to detect an anechoic object embedded in a homogeneous scattering medium. The contrast has been computed as follows:

$$\text{Contrast} = 10 \cdot \log_{10} \frac{\displaystyle\int_{x,z\,\in\,D_{\text{out}}} |h(x,z)|^2 \mathrm{d}x\mathrm{d}z}{\displaystyle\int_{x,z\,\in\,D_{\text{in}}} |h(x,z)|^2 \mathrm{d}x\mathrm{d}z}.$$

The numerator represents the background signal. It is computed as the mean of the 100 images in the chosen region of interest (ROI) close to the inclusion (D_{out}, 10×10 pixels $= 2\,\text{mm} \times 2.4\,\text{mm}$ rectangle). The denominator represents the anechoic inclusion signal and is computed as the mean of the 100 images in the chosen ROI in the inclusion area (D_{in}, same size as D_{out}).

SNR and contrast have been quantified for N ranging from 2 to 32 plane waves. In the case of a small number of plane waves, it is interesting to use a relatively high angular step $\Delta\theta$ between two successive plane waves (in this case $\Delta\theta = 2°$). Such a value ensures a good decorrelation of the received signals in the compounding step even with a low number of plane waves. A small number of plane waves further achieves a very high frame rate. Thus, this strategy is typically employed for ultrafast imaging based modalities. In case where a large number of plane waves is preferred, in order to perform higher quality imaging at lower frame rate, this configuration will quickly yield angular values higher than the directivity of the probe. In the case of a very high number of plane waves it is thus better to use an alternative strategy where a fixed maximal angular aperture $\theta_{\max}$ is chosen within the probe directivity, and with a variable angular step $\Delta\theta$ derived from the number of plane waves. In such a scenario, the frame rate is decreasing with the number of plane waves but quality is increasing.

3.1.1. High frame rate configuration with small number of plane waves.

SNR graphs as a function of depth were plotted in figure 3(a) for $N = 2$, 4 and 8 plane waves with a fixed $\Delta\theta = 2°$ between two successive plane waves. The blue thin curves represent the compound method and the red thick ones the multiplane method. Because of ultrasonic attenuation, the amplitude of the backscattered echoes decreases exponentially with depth, and as a result so does the recorded signal. On the contrary, noise mainly comes from electronics and can be assumed uniform in the image, whatever the depth. As a result the SNR, defined as the ratio between signal and noise, is decreasing exponentially with depth, as shown on all the SNR graphs in figure 3(a). The multiplane wave method always gives a better SNR than the compound method. Indeed, while the multiplane wave method emits $N = 2$, 4 or 8 plane waves at the same time, the compound method only emits 1 plane wave per emission. As the reconstructed signal is expected to be N times higher with multiplane and as the electronic noise is equivalent, the theoretical gain is $G_{\text{th}} = 10 \times \log_{10}(N_{\text{emissionMP}})$, $N_{\text{emissionMP}}$ being the number of plane waves sent at each emission with the multiplane wave method. Gains of $G_{\text{th}}(2) = 3$ dB, $G_{\text{th}}(4) = 6$ dB and $G_{\text{th}}(8) = 9$ dB can be assumed, which is consistent with the gains experimentally measured $G_{\text{exp}}(2) = 2.8 \pm 0.4$ dB, $G_{\text{exp}}(4) = 5.8 \pm 0.5$ dB, and $G_{\text{exp}}(8) = 8.3 \pm 0.6$ dB. The multiplane wave imaging SNR improvement gets more visible with depth. While the blue curves—plane wave compounding method—are almost totally flat and equal to zero in the area of the 5th inclusion (around depth 60 mm), the last two red curves ($N = 4$ and 8)—multiplane wave method—highlight the presence of the inclusion.

An improvement of image quality can clearly be seen in figure 3(b) where compound and multiplane wave images are compared side by side for the same number of plane waves. The multiplane wave method exhibits a visible improvement in deep areas. The deepest inclusion (around the depth 60 mm) emerges with the multiplane wave compound method using $N = 4$ plane waves, it is clearly visible with $N = 8$ plane waves, while it remains totally invisible with

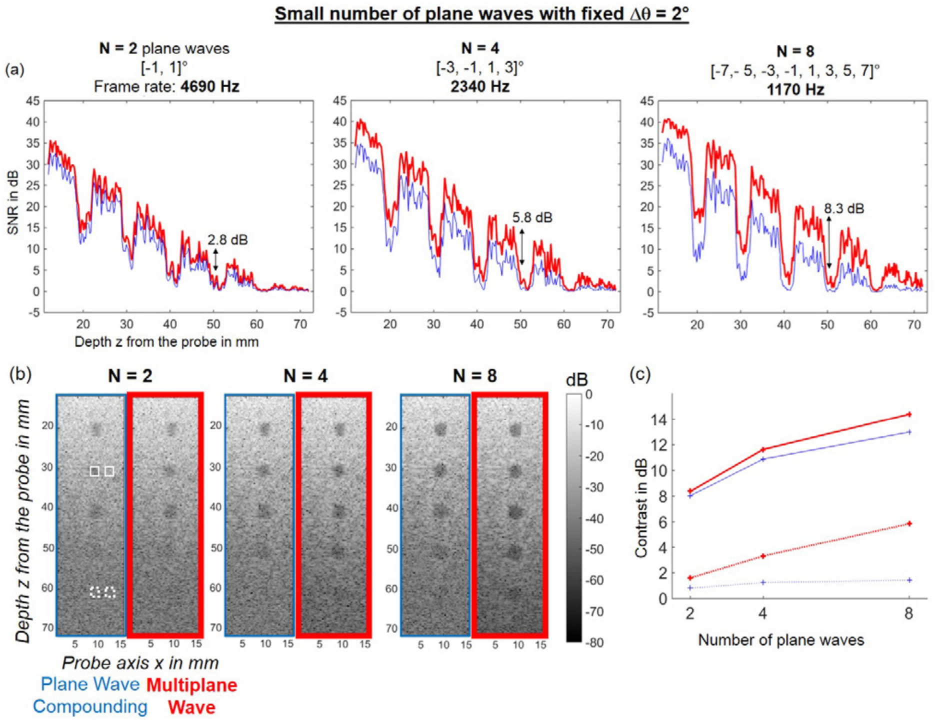

Figure 3. Quantification in terms of SNR and contrast using a small number of plane waves: comparison between coherent plane wave compounding (blue thin line) and multiplane wave (red thick line) using $N = 2$, 4 or 8 tilted plane waves with $\Delta\theta = 2°$. (a) Signal-to-noise ratio as a function of depth computed on an area containing inclusions. Note the SNR increase obtained with multiplane wave for the last inclusions. Gains experimentally measured ($G_{\text{exp}}(2) = 2.8 \pm 0.4$ dB, $G_{\text{exp}}(4) = 5.8 \pm 0.5$ dB, and $G_{\text{exp}}(8) = 8.3 \pm 0.6$ dB) are consistent with theoretical gains: $G_{\text{th}} = 10 \times \log_{10}(N)$, which corresponds respectively to 3 dB, 6 dB and 9 dB. (b) Corresponding B-mode images. (c) Contrast as a function of the number of plane waves used, for an inclusion close to the surface of the phantom (30 mm—solid line) and an inclusion deeper (60 mm—dotted line).

the coherent plane waves compound method, even with 8 plane waves. For both the methods, close to the surface the contrast improves when the number of plane waves increases. For the same number of plane waves - which also means the same frame rate—the contrast close to the surface increases slightly when using the multiplane wave method. These naked eye observations are confirmed with the graphs plotted in figure 3(c).

Two inclusions were investigated in figure 3(c): one close to the phantom surface (30 mm, framed with solid line) and another one deeper in the phantom (60 mm, framed with dotted line). The contrast of the inclusion closest to the surface is clearly improved by adding plane waves with both methods, yet the multiplane wave method only slightly improves contrast for the same amount of plane waves (figure 3(c) solid line). On the contrary, in deeper regions, the main factor improving contrast is the use of the multiplane wave method (figure 3(c) dotted line). With $N = 8$ plane waves, the gain of multiplane wave versus compound method is 4 dB, whereas the use of 8 plane waves instead of 4 with classical compound method leads to almost no gain.

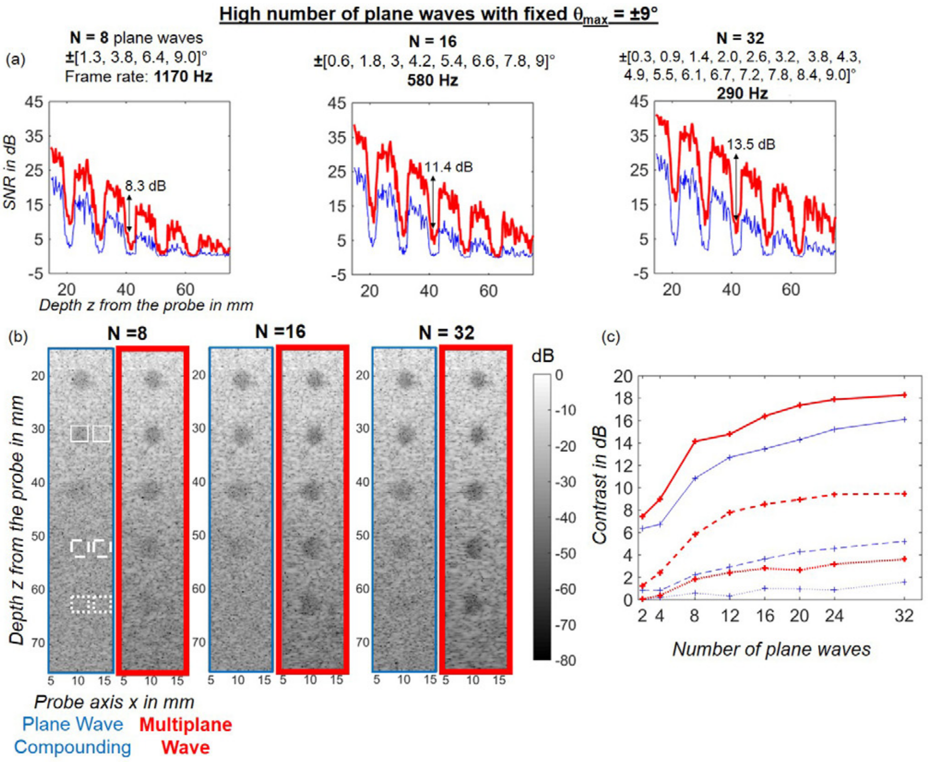

Figure 4. Quantification in terms of SNR and contrast for a high number of plane waves: comparison between coherent plane wave compounding (blue thin lines) and multiplane wave imaging (red thick lines). (a) SNR as a function of depth, computed on an area containing inclusions. (b) B-mode images using $N = 8$, 16 or 32 tilted plane waves with a fixed $\theta_{\max} = 9°$. The squares depict the localization of the inclusions used for contrast quantification in figure 4(c). (c) Contrast as a function of the number of plane waves used, for an inclusion close to the surface of the phantom (30 mm: solid line) and two inclusions deeper (~50 mm: dashed line and ~60 mm: dotted line).

3.1.2. High quality configuration with large number of plane waves. In figure 4, the performance of plane wave compounding and multiplane wave imaging are compared, using a high number of plane waves (up to $N = 32$ plane waves) with a fixed angular aperture. $\theta_{\max}$ is set at 9°, which ensures an angular step $\Delta\theta \geqslant 0.6°$ (the lowest useful value according to equation (12) of Montaldo *et al* (2009) for this probe) even for $N = 32$ plane waves. The blue thin curves represent the compound method and the red thick curves the multiplane method. Once again the SNR experimental gains $G_{\exp}(8) = 8.3 \pm 0.7$ dB, $G_{\exp}(16) = 11.4 \pm 0.7$ dB, and $G_{\exp}(32) = 13.5 \pm 0.6$ dB, are consistent with the theoretical gains $G_{\text{th}}(8) = 9$ dB, $G_{\text{th}}(16) = 12$ dB, and $G_{\text{th}}(32) = 15$ dB, computed using $G_{\text{th}} = 10 \times \log_{10}(N_{\text{emissionMP}})$, as seen in figure 4(a). The B-mode images also highlight the improvement of the image quality in depth thanks to multiplane wave imaging (figure 4(b)). The inclusion around the depth 60 mm remains invisible with plane wave compounding imaging, even with $N = 32$ plane waves, but is visible with multiplane wave imaging from $N = 8$ plane waves. For a high number of plane waves, the angular step $\Delta\theta$ becomes smaller, the plane waves are less decorrelated and the contrast starts to converge in figure 4(c).

Finally, for both small and large number of plane waves cases, the maximum achievable frame rate has been computed as $F_{\text{rate}} = \frac{1}{N \times t_{B/F}}$ with $t_{\text{B/F}}$ the back and forth time for the ultrasonic wave to reach the maximum imaging depth $d_{\max}$ ($d_{\max} = 80\,\text{mm}$ in these B-mode acquisitions) and N the number of plane waves. The values computed for $N = 2, 4, 8$ and $N = 8, 16, 32$ plane waves are respectively displayed in figures 3(a) and 4(a). Multiplane wave imaging has been previously introduced as a way to increase SNR without compromising frame rate but it can also be seen as a method to achieve a higher frame rate than plane wave compounding, with equivalent image quality.

As a conclusion, we experimentally confirmed here that the multiplane wave compound method performs better in terms of SNR and contrast, especially at depths where the electronic noise is the main factor of contrast loss. The use of the multiplane wave technique is of great help as it improves the image quality in terms of SNR but also in terms of contrast in deeper areas without decreasing the frame rate. In the following part, two modalities dedicated to applications that require a very high frame rate are presented: shear wave imaging (elastography) and ultrafast Doppler imaging. The benefits of the method will be investigated for both applications.

3.2. Shear wave imaging

In human soft tissues, low-frequency shear waves, typically 50 to 500 Hz, propagate at a very low speed (~1 to 10 m s^{-1}). Shear wave elastography imaging consists in imaging the tissue displacement induced by the shear waves by using compressional ultrasonic waves propagating at a high speed, around 1500 m s^{-1}. To observe the propagation of the shear wave, the frame rate must reach values typically higher than 1000 Hz. In this study, shear waves are generated by the acoustic radiation force of a 150 μs ultrasonic focused beam using the Supersonic Shear Imaging technique (Tanter *et al* 2008). The sequence was implemented on an Aixplorer$^{\text{TM}}$ ultrasound system (SuperSonic Imagine, Aix-en-Provence, France) running Matlab (MathWorks, Natick, Massachusetts, USA). The 128 first elements of a 160-element array working at 6 MHz central frequency with a 0.2 mm pitch (SuperSonic Imagine, Aix-en-Provence, France) were used and the receive bandwidth of the scanner was set at 90% using the on board FIR filter.

The shear wave propagation induced in a breast phantom (breast elastography phantom model 059, CIRS, Norfolk, USA) was imaged using 4 plane waves ($-3, -1, 1, 3°$) with coherent plane wave compounding (figure 5(a)) or with multiplane wave imaging (figure 5(b)). In both cases the PRF was set at 11.7 kHz. After compounding, the echographic images were thus obtained at a 2.9 kHz frame rate.

For both sequence, the time standard deviation of the particle velocity was quantified long after the shear wave propagation ($N = 10$ images) and spatially averaged in the square ROI depicted in figure 5. Standard deviations of $\sigma_{\text{PlaneWave}} = 0{,}329 \pm 0.004\,\text{mm s}^{-1}$, and $\sigma_{\text{MultiplaneWave}} = 0{,}159 \pm 0.002\,\text{mm s}^{-1}$ were measured (estimated over $N_{\text{acq}} = 10$ acquisitions). As expected, the multiplane wave sequence with $N = 4$ yields a two-fold reduction of the particle velocity time standard deviation ($\sigma_{\text{PlaneWave}}/\sigma_{\text{MultiplaneWave}} = 2.07 \pm 0.05$). This value is consistent with the theory in the case of 4 plane waves emission. This reduction in noise thanks to multiplane wave imaging can be seen in the tissue velocity images displayed in figure 5, especially in depth, as shown in the square ROI depicted for the two methods.

Tissue velocity estimates directly impact the computation of shear wave velocity maps as recently shown by Deffieux *et al* (2012). The benefits in terms of standard deviation were quantified on several acquisitions. The extent of reconstructed area in the shear wave velocity

(a) Plane wave compounding

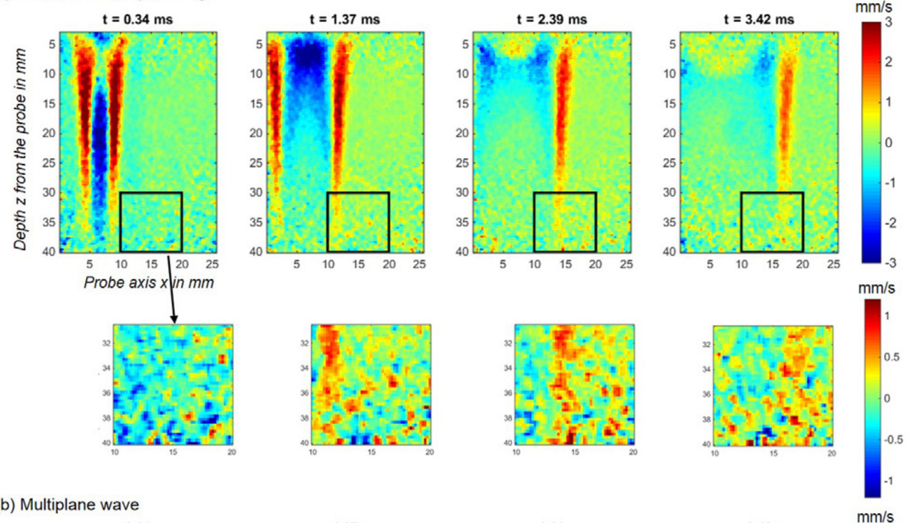

(b) Multiplane wave

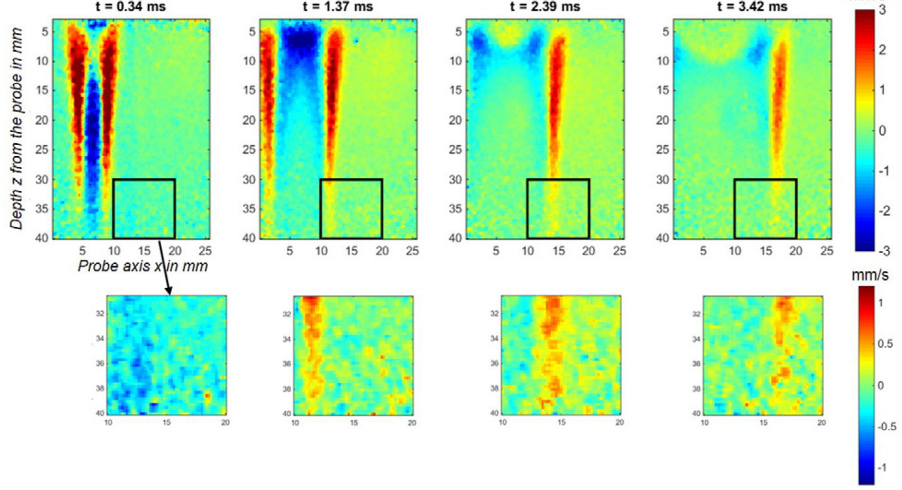

Figure 5. Shear wave imaging (elastography) on breast phantom using 4 angles (−3, −1, 1, 3°) using (a) coherent plane wave compounding or (b) multiplane wave imaging.

map was also investigated. The local estimation of the shear wave velocity is done by using a simple time of flight algorithm (Tanter *et al* 2008). The time of flight Δt is estimated by a cross-correlation between the displacement time profile at location x and at location $x + \Delta x$. In this experiment, Δx has been set at 1.2 mm and the same acquisition has been repeated 10 times, for the two imaging methods. The average shear velocity maps obtained on a breast phantom using this algorithm are represented in figure 6. For each pixel of the image, the standard deviation over the 10 acquisitions has been estimated. Then, the shear velocity pixel was only drawn when the corresponding standard deviation was less than 20% of the mean shear velocity, which corresponds to 0.4 m s^{-1} in this experiment. 'Reconstructed area' denotes the area containing the pixels that are below the threshold. The background image is

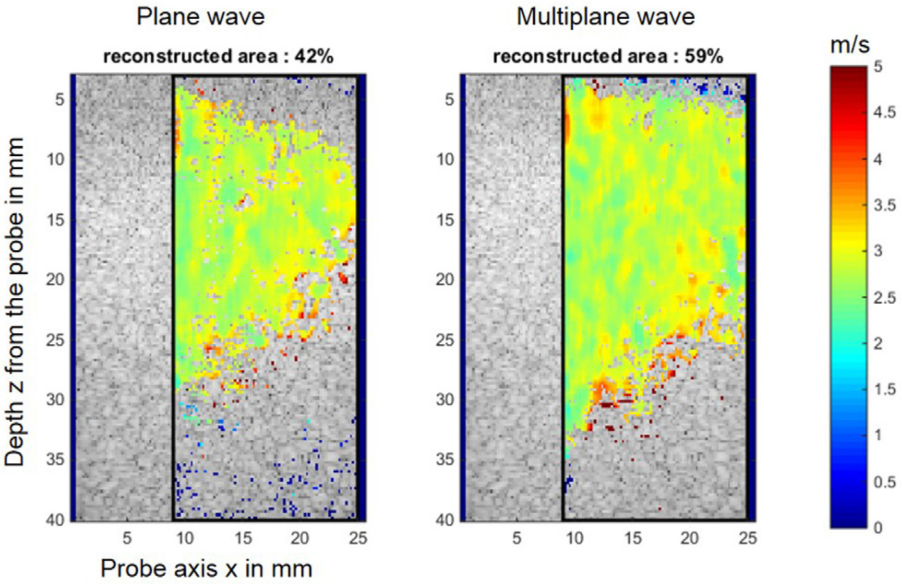

Figure 6. Shear wave imaging (elastography) on a breast phantom using 4 angles (−3 −1, 1, 3°). Comparison between coherent plane wave compound (left) and multiplane wave compound (right): average shear velocity map ($N = 10$ acquisitions) superimposed over B-mode image. A threshold was put on the standard deviation to select the shear velocity pixels to draw (0.4 m s^{-1}). Using coherent plane wave compound 42% of the image in the black rectangular box is reconstructed, with multiplane wave the surface of reconstruction rises 59%.

the B-mode image. By using coherent plane wave compound, 42% of the image in the black rectangular box is reconstructed, whereas with multiplane wave imaging the reconstructed area increases to 59%. Once again, the multiplane wave method enables deeper imaging than the coherent plane wave compounding method, thanks to the direct impact of the SNR on the estimation of shear wave velocity (Deffieux *et al* 2012).

The standard deviation of the shear wave velocity maps in the reconstructed area for the two sequences has been estimated using $N = 10$ acquisitions. Standard deviations $\sigma_{\mathrm{PlaneWave}} = 0.15 \pm 0.09$ m s^{-1}, and $\sigma_{\mathrm{MultiplaneWave}} = 0.07 \pm 0.05$ m s^{-1}. were measured. As expected, the multiplane wave sequence with $N = 4$ plane waves emission yields a halving of the shear wave velocity standard deviation in the reconstructed area. Once again, this value is consistent with the theory in the case of 4 plane waves emission since a decrease in the tissue velocity standard deviation also yields a decrease in shear wave velocity standard deviation (Deffieux *et al* 2012).

The multiplane wave approach leads to a strong improvement of the shear wave imaging accuracy: a noise reduction in the shear wave propagation movie induces a larger reconstruction of the shear velocity maps and a higher accuracy for the estimation of the local shear velocity.

3.3. In vivo ultrafast Doppler imaging

The multiplane wave imaging technique was applied to *in vivo* Ultrafast Doppler acquisitions of the living rat brain. Ultrafast Doppler imaging acquires samples simultaneously for all

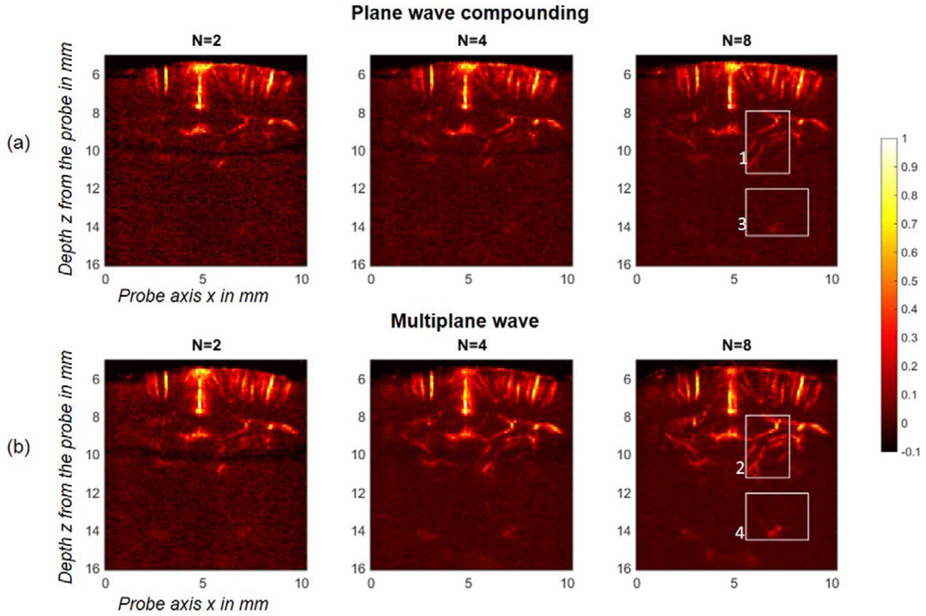

Figure 7. *In vivo* ultrafast Doppler imaging on a rat brain: comparison between (a) coherent plane wave compounding and (b) multiplane wave imaging using $N = 2$, 4 or 8 tilted plane waves: $[-1\ 1]°$, $[-3\ -1\ 1\ 3]°$, and $[-7\ -5\ -3\ -1\ 1\ 3\ 5\ 7]°$. Each image was normalized between its maximum value and its median background noise value ([0 1]), the dynamic range was then set between −0.1 and 1 in order to fully visualize the background noise dynamic. The four white rectangles are the areas zoomed and depicted in figure 8.

pixels in the image, whereas conventional Doppler successively focuses the beam along the transducer array to obtain the whole image (Bercoff *et al* 2011). Ultrafast Doppler acquisition relies on ultrafast frame rates, which means that typically for 1 s of acquisition, each pixel of the image contains 1000 temporal points. It has been shown that in the 16 plane waves coherent compounding case, this high frame rate enables a 30 times increase of the Doppler sensitivity compared to conventional Doppler (Mace *et al* 2013).

For this experiment the rat underwent a surgical thinning of the skull under anesthesia (Ketamine/Xylazine) to enable the propagation of ultrasound. It was then placed in a stereotaxic device and maintained under anesthesia (Ketamine/Medetomidine) during acquisition. The acquisitions were performed using a 15 MHz ultrasonic probe (128 elements, pitch 0.08 mm, Vermon, Tours, France) and an Aixplorer$^{\mathrm{TM}}$ ultrasound system (SuperSonic Imagine, Aix-en-Provence, France) running Matlab (MathWorks, Natick, Massachusetts, USA). The receive bandwidth of the scanner was again set at 90% using the on board FIR filter. The positioning was performed with a motor system controlled by Matlab. The two imaging methods were compared for $N = 2$, 4 and 8 plane waves tilted with angles separated by 2°, corresponding to the following sets $[-1\ 1]°$, $[-3\ -1\ 1\ 3]°$, and $[-7\ -5\ -3\ -1\ 1\ 3\ 5\ 7]°$. The Pulse Repetition Frequency was set at 1600 Hz, 3200 Hz and 6400 Hz respectively, in order to achieve 800 Hz frame rate for the final Doppler images after recombination. This frame rate is sufficient to correctly sample axial blood flow speed up to 4.1 cm s^{-1} without aliasing. Acquiring 200 frames in 0.4 s enables to capture 2 complete cardiac cycles. The Doppler images obtained by

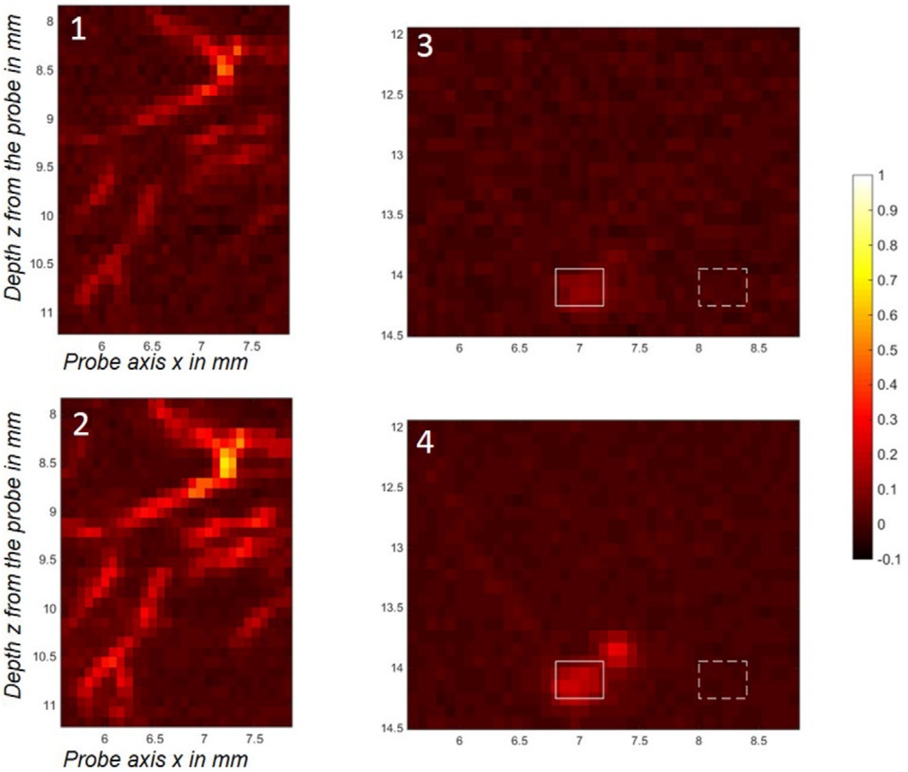

Figure 8. Zoom in on the 4 areas depicted in figures 7(a) and (b) for $N = 8$ planes waves case. Comparison between coherent plane wave compounding (up) and multiplane wave imaging (bottom) for vessels around 8.5 mm and 14 mm from the probe. The contrast to noise ratio has been calculated as $\text{CNR} = (\overline{\text{PW}}_{\text{vessel}} - \overline{\text{PW}}_{\text{tissue}}) / \text{std}(\text{PW}_{\text{tissue}})$, with $\overline{\text{PW}}_{\text{vessel/tissue}}$ the mean value of the power Doppler in an area containing vessel (solid line) or tissue (dotted line), and std the standard deviation. CNR was estimated at −1.8 dB, 5.5 dB and 8.2 dB for the plane wave Doppler image (respectively for 2, 4 and 8 plane waves) and 3.9 dB, 8.5 and 14.0 dB for the multiplane wave Doppler image (respectively for 2, 4 and 8 plane waves), showing a strong increase in detectability of the vessels in deep areas thanks to the multiplane sequence.

averaging over 200 frames are presented in figures 7(a) and (b) for the two ultrafast imaging techniques. For each set of plane waves, the multiplane wave method exhibits an improvement of the image compared to the coherent compound method: more vessels are visible, mostly in depth. The contrast-to-noise ratio (CNR) has been computed for vessels in a deep area (figure 8). The multiplane sequence leads to up to a 6 dB increase in detectability of the vessels in deep areas (around 14 mm from the probe) using $N = 8$ plane waves.

This improvement could be of great interest in the particular case of deep organs Doppler imaging such as the kidney. The use of multiplane wave imaging could also be of great interest for functional ultrasound imaging to assess deep structures or to increase SNR in transcranial functional imaging. For example, deep functional areas in the rat brain such as substancia nigra, amygdala or hypothalamus usually suffer from a lack of detectability caused by their depth. Since these areas lie at a similar depth as the ROI in which we found a 6 dB increase in CNR using 8 plane waves, we can expect a better signal-to-noise ratio for the functional activity of these areas thanks to multiplane wave imaging.

4. Discussion

In this work, a new ultrasonic sequence was introduced for ultrafast imaging with improved SNR and improved contrast compared to conventional coherent compounding imaging. The sequence is based on the emission of multiple plane waves with different inclinations and different coded amplitudes within the same transmit event. A Hadamard matrix $(-1, +1)$ was used to code the amplitude coefficients. By applying the appropriate coefficients on the received data, each data was reconstructed as if emitted by a single plane wave but with lower noise. The benefit of using an Hadamard matrix is twofold: first, it ensures the maximum amplitude level for each transmission. Second, the synthetic data recombination to retrieve the backscattered echoes for each plane wave is performed using extremely simple and robust operations (only additions and subtractions).

This sequence allows an increase of the SNR by a factor N and has successively been tested for $N = 2$, 4, 8, 16 and 32 plane waves. This SNR increase translates into a better image contrast, especially in deep areas of the image where the loss of contrast is mostly governed by electronic noise rather than clutter. This is particularly interesting for high noise applications such as deep organs, highly attenuating media or hypoechogeneous tissue.

This SNR increase is beneficial not only for the B-mode contrast but also for shear wave experiments as tissue velocity estimation quality is directly linked to the acquisition SNR (Deffieux *et al* 2012). For $N = 4$ emissions a halving of the tissue velocity standard deviation was observed.

A direct consequence of the SNR increase in the estimation of the tissue velocity field is a better estimation of shear wave velocity maps in shear wave elastography imaging. For $N = 4$ emissions, a two-fold reduction of the standard deviation of the shear wave velocity maps was observed as predicted by theory (Deffieux *et al* 2012). This is particularly relevant for deep organs imaging and staging, such as liver fibrosis staging or liver cancer imaging, where the estimation accuracy is critical and where SNR can be poor because of the depth of the region of interest. Increasing the acquisition SNR decreases both the shear wave velocity standard deviation and its bias.

In the case of ultrasensitive Doppler, a high number of images increases the overall sensitivity (Mace *et al* 2013). Increasing the SNR by using multiplane wave imaging directly brings an additional sensitivity of the Doppler image and so enables the detection of new vessels in the brain. Together with better spatiotemporal clutter rejection as demonstrated recently in (Demene *et al* 2015), the multiplane sequence can further increase the sensitivity of ultrasensitive Doppler sequence. This will enable a better detection of small blood flow variation for functional ultrasound imaging (Mace *et al* 2013) and reduce the decorrelation artefacts caused by noise in functional connectivity imaging (Osmanski *et al* 2014).

The multiplane wave sequence with N emissions is equivalent, SNR wise, to averaging received data N times—sometimes denoted N buffers accumulation. However, for the same SNR, the benefit of the multiplane sequence is to not lower the final frame rate, which can be critical for imaging highly moving organs such as the heart, for quantifying the fast flow with ultrafast Doppler, or for making measurements in stiff tissue where shear waves propagate very fast. For a given frame rate and a given SNR, the multiplane sequence requires less reception buffers and as a consequence reduces the amount of transferred and processed data. Both approaches can be implemented directly on the acquisition board, using very simple summations and subtractions prior to the data transfer to the main computer and beamforming.

The multiplane sequence is also equivalent in terms of SNR to a $\sqrt{N}$ fold increase of the emitted amplitude of individual plane waves. However, increasing the emitted amplitude is not always possible due to pulser limitation, probe voltage limitation and also mechanical index (MI) limitation in some cases. For this reason, the sequence is promising for many applications where a high frame rate is needed and signal-to-noise ratio is limited. One such application is shear wave elastography of the liver where SNR is critical to obtain high accuracy of the shear wave velocity measurement for fibrosis staging and where high frame rate is required to avoid breathing artefacts. The sequence must then be adapted to a curved array for abdominal imaging. Another application requiring both high frame rate and high SNR is cardiac shear wave elastography (Papadacci *et al* 2014). For this purpose, the multiplane sequence can be adapted to the use of diverging waves instead of plane waves.

For an equivalent MI, the multiplane wave sequence gives a higher spatial peak temporal average Intensity (ISPTA) than conventional coherent compounding sequence. However, this ISPTA increase is not a limiting factor when the ultrafast frame rate is required during limited periods and not continuously. This is the case for shear wave elastography where ultrafast imaging is performed only during tens of milliseconds to produce a quantitative elasticity map. For such applications, the Food and Drug Administration (FDA) requirements for ISPTA limits the number of ultrafast bursts performed in one second. When the ISPTA is the limiting factor, the only advantage of the multiplane sequence is its higher frame rate.

For a given SNR, the multiplane sequence allows the use of lower pressure; as a result, it could be beneficial for applications where the MI is limited and where high frame rate is required, such as in ultrafast contrast imaging techniques relying on time-dependent microbubbles echoes in the fundamental mode (Couture *et al* 2009). It could also be useful for cornea or retina Doppler imaging or shear wave elastography for which FDA requirements limits the mechanical index to 0.23.

Compared to coded emissions such as chirp or Golay codes (Chiao and Thomas 2000, Misaridis and Jensen 2005a, 2005b, 2005c), the multiplane sequence enables higher frame rate with lower complexity. The coding is here performed both in space and time and the decoding operation is only made of extremely simple operations. On the contrary, chirp excitations require a more complex deconvolution process whose efficiency can be altered by the medium attenuation.

Contrarily to chirp excitations, no *a priori* on the insonified medium is required with multiplane wave, even though linearity of the propagation must be enforced. Indeed, in this paper, we assume that the cancellation $(+1) + (-1) = 0$ is perfect, but non-linear propagation generates harmonic signals, that, if not filtered, will not cancel out in the combination step and will create range lobes, and ultimately reduce the image contrast. In our implementation, several steps have been made to filter out harmonic signals in the received data: emissions were made at the central frequency of the probes (6 and 15 MHz) and a 90% FIR bandwidth filter was applied at the reception. In such a configuration, the multiplane method is likely to work even in the presence of non-linearity.

Another possible limitation of the technique is fast motion, such as cardiac B-mode imaging where the cancellation of some waves might not be perfect due to phase coherence losses (Denarie *et al* 2013). In that case it might not be possible to use a large number of plane wave transmissions without additional motion correction steps. For a given number of plane waves and a given tissue velocity, the exact outcome of contrast decrease due to fast motion and of contrast enhancement due to lower noise is yet to be investigated.

The multiplane sequence relies on the amplitude encoding of plane waves instead of individual elements as in synthetic aperture. In this work, an Hadamard matrix was chosen and the different plane waves were encoded in amplitude (-1 or $+1$) with a small pause between them to avoid the superimposition of plane waves in the emission matrix. Superimposition of plane waves would allow shorter emission matrix and a reduction of the blind zone in the beginning of the image. However, the individual plane wave amplitudes would then have to be decreased to ensure that the superimposition amplitude remains below the maximum output amplitude of the scanner. Moreover, multiplane imaging will be mainly useful for deep imaging where a larger blind area caused by a long emission matrix is not a problem. However, it could be interesting to reduce the blind area by using more compact emissions matrix with appropriate plane waves superimposition in the particular case of high frequency imaging where attenuation can decrease the signal-to-noise ratio and where the probe driving voltage is generally much lower than the scanner maximum output.

5. Conclusion

In this work, a new ultrafast ultrasound imaging sequence based on multiple plane wave emission was proposed and validated. Multiplane wave imaging is a promising mode for ultrafast ultrasound imaging that allows the same high frame rates as coherent plane wave compounding, while significantly improving signal-to-noise ratio, without affecting spatial resolution. The improved signal-to-noise ratio directly impacts the contrast of B-mode images for deep structures where the electronic noise is predominant over clutter. It further significantly improves both the reconstruction and accuracy of shear wave velocity measurements and the overall quality of Power Doppler images. Multiplane wave imaging has the potential to further disrupt ultrafast based imaging modalities in many clinical applications especially for deep organs imaging.

Acknowledgments

The research leading to these results has received the funding from the European Research Council under the European Union’s Seventh Framework Programme (FP7/2007–2013) / ERC grant agreement no 339244-FUSIMAGINE. This work was also partly supported by the Agence Nationale de la Recherche under the program ‘Future Investments’ with the reference Laboratory of Excellence ANR-10-LABX-24 LABEX WIFI within the French Program ‘Investments for the Future’ under reference ANR-10- IDEX-0001-02 PSL.

References

Bercoff J, Montaldo G, Loupas T, Savery D, Meziere F, Fink M and Tanter M 2011 Ultrafast compound Doppler imaging: providing full blood flow characterization *IEEE Trans. Ultrason. Ferroelectr. Freq. Control* **58** 134–47

Chiao R Y and Thomas L J 2000 Synthetic transmit aperture imaging using orthogonal Golay coded excitation *2000 IEEE Ultrasonics Symp.* vol 2 pp 1677–80

Chiao R Y, Thomas L J and Silverstein S D 1997 Sparse array imaging with spatially-encoded transmits *1997 IEEE Ultrasonics Symp. 1997 Proc.* vol 2 pp 1679–82

Couture O, Bannouf S, Montaldo G, Aubry J-F, Fink M and Tanter M 2009 Ultrafast imaging of ultrasound contrast agents *Ultrasound Med. Biol.* **35** 1908–16

Deffieux T, Gennisson J-L, Larrat B, Fink M and Tanter M 2012 The variance of quantitative estimates in shear wave imaging: theory and experiments *IEEE Trans. Ultrason. Ferroelectr. Freq. Control* **59** 2390–410

Demene C *et al* 2015 Spatiotemporal clutter filtering of ultrafast ultrasound data highly increases Doppler and ultrasound sensitivity *IEEE Trans. Med. Imag.* pp 1–1

Denarie B, Tangen T A, Ekroll I K, Rolim N, Torp H, Bjastad T and Lovstakken L 2013 Coherent plane wave compounding for very high frame rate ultrasonography of rapidly moving targets *IEEE Trans. Med. Imag.* **32** 1265–76

Horadam K J 2007 *Hadamard Matrices and Their Applications* (Princeton, NJ: Princeton University Press)

Karaman M, Li P-C and O'Donnell M 1995 Synthetic aperture imaging for small scale systems *IEEE Trans. Ultrason. Ferroelectr. Freq. Control* **42** 429–42

Lockwood G R, Talman J R and Brunke S S 1998 Real-time 3D ultrasound imaging using sparse synthetic aperture beamforming *IEEE Trans. Ultrason. Ferroelectr. Freq. Control* **45** 980–8

Mace E, Montaldo G, Osmanski B, Cohen I, Fink M and Tanter M 2013 Functional ultrasound imaging of the brain: theory and basic principles *IEEE Trans. Ultrason. Ferroelectr. Freq. Control* **60** 492–506

Misaridis T and Jensen J A 2005a Use of modulated excitation signals in medical ultrasound: I. Basic concepts and expected benefits *IEEE Trans. Ultrason. Ferroelectr. Freq. Control* **52** 177–91

Misaridis T and Jensen J A 2005b Use of modulated excitation signals in medical ultrasound: II. Design and performance for medical imaging applications *IEEE Trans. Ultrason. Ferroelectr. Freq. Control* **52** 192–207

Misaridis T and Jensen J A 2005c Use of modulated excitation signals in medical ultrasound: III. High frame rate imaging *IEEE Trans. Ultrason. Ferroelectr. Freq. Control* **52** 208–19

Montaldo G, Tanter M, Bercoff J, Benech N and Fink M 2009 Coherent plane-wave compounding for very high frame rate ultrasonography and transient elastography *IEEE Trans. Ultrason. Ferroelectr. Freq. Control* **56** 489–506

Mosca F, Nicolas J-M, Kopp L and Couade M 2008 Temporal approach of the synthetic aperture imaging using Hadamard matrix *J. Acoust. Soc. Am.* **123** 3083

Nikolov S I and Jensen J A 2003 *In vivo* synthetic aperture flow imaging in medical ultrasound *IEEE Trans. Ultrason. Ferroelectr. Freq. Control* **50** 848–56

Osmanski B-F, Pezet S, Ricobaraza A, Lenkei Z and Tanter M 2014 Functional ultrasound imaging of intrinsic connectivity in the living rat brain with high spatiotemporal resolution *Nat. Commun.* **5** 5023

Papadacci C, Pernot M, Couade M, Fink M and Tanter M 2014 High-contrast ultrafast imaging of the heart *IEEE Trans. Ultrason. Ferroelectr. Freq. Control* **61** 288–301

Sylvester J J 1867 LX. Thoughts on inverse orthogonal matrices, simultaneous sign successions, and tessellated pavements in two or more colours, with applications to Newton's rule, ornamental tile-work, and the theory of numbers *Phil. Mag. Ser.* **4** 461–75

Tanter M, Bercoff J, Athanasiou A, Deffieux T, Gennisson J-L, Montaldo G, Muller M, Tardivon A and Fink M 2008 Quantitative assessment of breast lesion viscoelasticity: initial clinical results using supersonic shear imaging *Ultrasound Med. Biol.* **34** 1373–86

Tanter M and Fink M 2014 Ultrafast imaging in biomedical ultrasound *IEEE Trans. Ultrason. Ferroelectr. Freq. Control* **61** 102–19

Udesen J, Gran F, Hansen K L, Jensen J A, Thomsen C and Nielsen M B 2008 High frame-rate blood vector velocity imaging using plane waves: simulations and preliminary experiments *IEEE Trans. Ultrason. Ferroelectr. Freq. Control* **55** 1729–43

Appendix C

Article 5: 4D microvascular imaging based on ultrafast Doppler tomography.

Demené, C., E. Tiran, L.-A. Sieu, **A. Bergel**, J. L. Gennisson, M. Pernot, T. Deffieux, I. Cohen, and M. Tanter 2016. 4d microvascular imaging based on ultrafast Doppler tomography. *NeuroImage*, 127:472-483.

NeuroImage 127 (2016) 472–483

Contents lists available at ScienceDirect

NeuroImage

journal homepage: www.elsevier.com/locate/ynimg

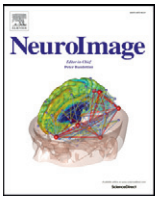

4D microvascular imaging based on ultrafast Doppler tomography

Charlie Demené [a,*], Elodie Tiran [a], Lim-Anna Sieu [b], Antoine Bergel [b], Jean Luc Gennisson [a], Mathieu Pernot [a], Thomas Deffieux [a], Ivan Cohen [b,1], Mickael Tanter [a,1]

[a] *Institut Langevin, ESPCI ParisTech, Paris Sorbonne Lettres Research University, CNRS UMR7587, INSERM U979, Paris, France*
[b] *Institut de Biologie Paris Seine, INSERM U1130, CNRS UMR8246, University Pierre & Marie Curie UMCR18, Paris, France*

ARTICLE INFO

Article history:
Received 8 July 2015
Accepted 4 November 2015
Available online 10 November 2015

Keywords:
Ultrasound imaging
Blood flow
Microvascular imaging
Ultrafast Doppler
3D rat brain
Tomography
Wiener filter

ABSTRACT

4D ultrasound microvascular imaging was demonstrated by applying ultrafast Doppler tomography (UFD-T) to the imaging of brain hemodynamics in rodents. In vivo real-time imaging of the rat brain was performed using ultrasonic plane wave transmissions at very high frame rates (18,000 frames per second). Such ultrafast frame rates allow for highly sensitive and wide-field-of-view 2D Doppler imaging of blood vessels far beyond conventional ultrasonography. Voxel anisotropy (100 μm × 100 μm × 500 μm) was corrected for by using a tomographic approach, which consisted of ultrafast acquisitions repeated for different imaging plane orientations over multiple cardiac cycles. UFT-D allows for 4D dynamic microvascular imaging of deep-seated vasculature (up to 20 mm) with a very high 4D resolution (respectively 100 μm × 100 μm × 100 μm and 10 ms) and high sensitivity to flow in small vessels (>1 mm/s) for a whole-brain imaging technique without requiring any contrast agent. 4D ultrasound microvascular imaging in vivo could become a valuable tool for the study of brain hemodynamics, such as cerebral flow autoregulation or vascular remodeling after ischemic stroke recovery, and, more generally, tumor vasculature response to therapeutic treatment.

Introduction

Brain microvascular imaging

Both preclinical and clinical research on cardiovascular pathologies would strongly benefit from images that provide both anatomic and hemodynamic information with high spatial and temporal resolution deep into tissues. However, current in vivo methods for assessing vasculature and hemodynamic changes in small vessels are known to be suboptimal. Although microscopic computed tomography (micro-CT) and magnetic resonance imaging (MRI) are capable of detecting vessels as small as ~50 μm with deep penetration, they remain limited by long scanning times and limited portability. In vivo acquisitions also suffer from supplementary limitations, mostly loss of resolution, control of the ionizing dose (CT) or the use of a contrast agent (Badea et al., 2008; Edelman, 1993). Moreover, their capability of assessing vascular hemodynamics remains very limited due to temporal resolutions that are much longer than a cardiac cycle. Without the use of a contrast agent, time-of-flight magnetic resonance angiography only enables the observation of the major vessels of small animal brains and requires several tens of minutes (Reese et al., 1999). Yet this technique allowed for the assessment of the effect of an MCA occlusion (Beckmann et al., 1999) and the vascular variability among different strains of mice (Beckmann, 2000). In order to visualize smaller vessels, state-of-the-art MRI angiographic techniques use contrast agents, and studies have shown impressive examples of in vivo cerebral microvascular imaging in cats (scan time 35 min) (Bolan et al., 2006) and rats (scan time 76 min) (Lin et al., 2009) with resolutions of approximately a hundred microns. However, none of these contrast-enhanced MRI techniques enable time-resolved angiography: the most recent advances (Hadizadeh et al., 2014) achieved a temporal resolution on the order of one second in humans (Willinek et al., 2008), which is not sufficient to resolve blood dynamics within a cardiac cycle and is associated with a degraded spatial resolution (millimetric). Micro-CT enables higher resolution, i.e., up to a few tens of μm (Chugh et al., 2009). With a long-lasting contrast agent and careful control of the radiation dose, such resolution can be achieved in vivo, with the potential for use in longitudinal studies (Starosolski et al., 2015). However, MR or CT equipment is heavy and incompatible with awake and freely moving animal imaging. Furthermore, intravascular contrast agents could penetrate the brain tissue due to an impaired blood–brain barrier, for example after prolonged ischemia, and could affect brain function.

Among the most advanced techniques for cerebrovascular imaging, is near-infrared II fluorescence imaging (NIR-II) (Hong et al., 2012, 2014). Indeed, NIR-II is capable of accomplishing what is typically done by several traditional techniques, including micro-CT, ultrasonography and MRI, and incorporates many desirable features, such as high spatial resolution (~30 μm) and fast acquisition (<200 ms), but

---

[*] Corresponding author at: Institut Langevin, 1 rue Jussieu, 75238 Paris Cedex 05, France.
E-mail address: charlie.demene@gmail.com (C. Demené).
[1] *IC and MT are co-last authors.*

http://dx.doi.org/10.1016/j.neuroimage.2015.11.014
1053-8119/

unfortunately lacks tissue penetration (<1–3 mm). Compared to conventional ultrasonography, NIR-II imaging is capable of resolving both arterial and venous vessels anatomically and hemodynamically. Most importantly, NIR-II imaging can be used to acquire hemodynamic data in conditions of reduced flow, such as in arterioles or venules, far below the detection limit of conventional Doppler ultrasonography. Another very promising technique for similar applications is photoacoustic microscopy, in its acoustic resolution (AR-PAM) (Yao and Wang, 2014) and optical resolution (OR-PAM) (Yao et al., 2015) declinations. Both offer high resolution and discrimination between oxy and deoxy-hemoglobin, but their limited penetration (<3 mm) prevents their application to whole-brain imaging in rodents or large animal models. Due to its scanning strategies, improved temporal resolution is achieved at the cost of a reduced field of view, and the use of a pulsed laser source in conjunction with the ultrasound system limits the dissemination and portability of the technique. Finally, laser speckle imaging TOVI (Kalchenko et al., 2014) enables very high resolution (5 μm), but limited penetration depth (1 mm), which restricts it to cortical structures.

A representative and non-exhaustive panel of vascular imaging techniques used for cerebral imaging is given in Table 1. The ultrafast Doppler tomography (UFD-T) technique described in this study has also been included for comparison. This table highlights that UFD-T can occupy a particularly interesting position among preclinical cerebrovascular imaging techniques. On the left side of the table, whole-brain imaging techniques that provide 10 to several hundreds μm resolutions and real 3D capabilities, but rely on heavy and costly equipment, are shown. Imaging techniques on the right side of the table exhibit finer resolutions and increased portability, but lack a penetration depth sufficient for whole-brain imaging and real 3D capabilities. UFD-T stands in between, with a penetration depth enabling in vivo whole-brain imaging, a good spatial resolution, a very high temporal resolution for dynamic imaging and equipment that is portable when compared to MRI, CT or an optical setup.

2D ultrafast ultrasound for vascular imaging

The recent advent of ultrafast ultrasound imaging (Tanter and Fink, 2014) led to the introduction of novel ultrasonic Doppler sequences based on plane wave transmissions (Bercoff et al., 2011) called ultrafast Doppler imaging. With the simultaneous acquisitions of echoes originating from a large field of view thousands of times per second, ultrafast Doppler imaging enables much higher sensitivity to small vessels than conventional Doppler, and allows for the measurement of flow velocities as low as 1 mm/s (compared to the typical 1–5 cm/s). Such an increase in sensitivity to slow flows, e.g. in small vessels, allowed for the imaging of the brain activity using *f*Ultrasound (by analogy to *f*MRI) in rodent models (Mace et al., 2013; Macé et al., 2011; Osmanski et al., 2014a, 2014b).

Although research into 3D acquisitions based on matrix probe technology is growing, ultrasound imaging remains today a 2D imaging technique with spatially anisotropic pixels, since the pixel dimension in the out-of-plane direction is typically 3 to 5 times larger than in the imaging plane: the in-plane resolution (the resolution linked to the transducer array aperture) is higher than in the transverse direction (the resolution linked to the acoustic lens focal width). For rodent brain imaging, it results in a typical 100 μm × 100 μm × 500 μm resolution when using a 15-MHz linear array.

Toward 3D: matrix arrays versus a mechanical scanning approach

3D ultrasound imaging can be based on two different acquisition modalities. Historically, the first one is based on a classical 1D array of

Table 1
Review of the in vivo microvascular imaging techniques used for small animal cerebral monitoring. Note that only the first four columns can be considered to be whole-brain modalities. The last three columns cannot be considered to be 3D imaging techniques. *UFD-T is invasive for the rat but could be performed through the skull for the mouse.

	Whole brain & *in vivo*							
In vivo imaging Modality	UFD-T	MRI (TOF)	MRI (contrast)	µCT (low dose)	Photoacoustic (AR-PAM)	Photoacoustic (OR-PAM)	NIR-II	Laser speckle TOVI
Depth	Whole brain	Whole brain	Whole brain	Whole brain	3 mm	<1mm	3 mm	<1mm
Resolution	~100 µm	~mm	~100 µm	~40 µm	~50-100 µm	lateral 3 µm axial 15 µm	10 µm	~5 µm
Acquisition time	20 min	~5-30 min	76 min	50 min	unknown	1 s	0.2 s	4 s
Need for contrast agents	No	No	Yes	Yes	No	No	Yes	Yes
In vivo	Yes	Yes	Yes	Yes	Yes	Yes	Yes	Yes
Cost	€	€€€	€€€	€€	€€	€€	€	€
Non-Invasiveness	Skull removed or thinned*	Yes	Contrast injection	Contrast injection	Scalp removed (mice)	Scalp removed (mice)	Yes	Scalp removed
Portability	++	---	--	-	+	+	++	+
Example	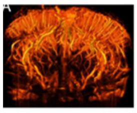	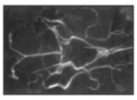	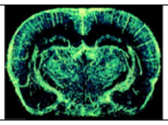	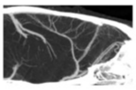	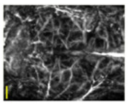		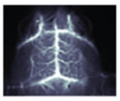	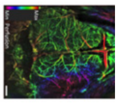
Reference	NA	(Beckmann et al., 1999)	(Lin et al., 2009)	(Starosolski et al., 2015)	(Yao and Wang, 2014)	(Yao et al., 2015)	(Hong et al., 2014)	(Kalchenko et al., 2014)

transducers capable of acquiring data in one 2D imaging plane and then translated along the transverse direction via a mechanical system to reconstruct a 3D volume (Downey and Fenster, 1995). It can be referred to as the mechanical scanning approach. The second modality is based on the technology of matrix arrays corresponding to 2D footprints of transducers: there is no need for a mechanical scan because addressing the 2D array of transducers with different electronic delays can mimic any position of the 1D array.

The focus dimensions constitute a fundamental difference between the two technologies. In the case of a 1D array, a good focus can be obtained in the imaging plane by applying delays to the recorded echoes. The size of the focal spot is typically of the order of the wavelength. However, in the elevation direction (out-of-plane direction), focusing is weak due to the small acoustical aperture in that direction, which results in anisotropic focalization properties in 3D. In the case of 2D matrix arrays, electronic delays can be applied along the two axes of the matrix and the focus spatial pitch becomes identical in all directions, hence resulting in isotropic voxels. On the other hand, 2D arrays are very expensive and require complex electronics, whereas 1D arrays are a widespread technology. As a first step toward 4D ultrafast Doppler imaging, the mechanical scanning approach was consequently more convenient to set up and for this reason was chosen for this study.

In this study, we propose an innovative imaging setup combining the high sensitivity of recently introduced ultrafast Doppler imaging and a novel tomographic strategy in order to perform 4D (three spatial dimensions and time) imaging of rodent whole-brain vasculature hemodynamics, with isotropic spatial voxels (50 μm × 50 μm × 50 μm) and an estimated 100 μm × 100 μm × 100 μm resolution. To recover an isotropic resolution, an original combination of rotations and translations was devised to ensure that spatial high-frequency information was available in every direction of the XY plane. All these acquisitions were then fused using a dedicated 3D Wiener deconvolution filter. We thus called this tomographic approach ultrafast Doppler tomography (UFD-T).

Material and methods

Ultrasonic acquisition sequence

Vascular images were obtained via the Ultrafast Compound Doppler Imaging technique (Bercoff et al., 2011). The electrocardiogram (ECG) of the rat was monitored and used to trigger the onset of each acquisition at the QRS segment of the ECG. Four hundred frames were acquired at a frame rate of 800 Hz for a total acquisition time of 0.5 s, thus ensuring the recording of several cardiac cycles (rodents generally have a 300 to 600 bpm cardiac frequency). Each frame was a Compound Plane Wave frame (Montaldo et al., 2009). In other words, it was built from the coherent summation of beamformed complex in-phase/quadrature images obtained from the successive insonification of the medium with plane waves tilted at specific angles. This compound plane wave imaging technique enables the re-creation, a posteriori, of a high-quality focus in the entire field of view with very few ultrasound emissions. Given the tradeoff between frame rate, resolution and imaging speed (images were beamformed and compounded on the fly to reduce the data size) of the whole volume, a frame consisted of eight compounded tilted plane waves separated by 2°. In order to discriminate blood signals from tissue clutter, the 400 Ultrafast Compound Doppler frame stacks were filtered using a dedicated spatiotemporal filter (Demene et al., 2015). This spatiotemporal filter used a singular value decomposition of the ultrasonic data to remove the tissue signal. Due to higher energy and higher spatial coherence, tissue signal was concentrated in the first pairs of temporal and spatial singular vectors. Therefore, by removing the first 60 singular values (a number based on experience) from the original signal, very efficient discrimination between tissue and blood signal was achieved and only the signal originating from the blood scatterers $c_\theta(x', y', z', t)$ was kept. The energy of this filtered in-phase/quadrature frame stack $c_\theta(x', y', z', t)$ was then computed in each pixel to build the Power Doppler Image $s_\theta(x', y', z')$.

$$s_\theta(x', y', z') = \int c_\theta(x', y', z', t)^2 .dt \qquad (1)$$

Experimental setup

A 15-MHz probe (128 elements) with a 0.1-mm pitch was used in this study and enabled a typical 100 × 100-μm resolution in the imaging plane. This probe was fitted with an acoustic lens with an elevation focal distance of 8 mm and an elevation focal width of 500 μm (Fig. 1A). This elevation focusing was achieved using an acoustic plastic curved lens located in front of the piezoelectric elements. It was mounted on a motorized setup enabling three degrees of translation (Physik Instrumente (PI) translation stage VT-80, 0.8-μm one-directional repeatability, ±10-μm bi-directional repeatability) and one degree of rotation (PI rotation stage DT-80, 0.01° one-directional repeatability, ±0.2° bi-directional repeatability). This setup enabled the acquisition of any vertical (i.e., containing the z-axis) (Figs. 1B and C) imaging planes. For a given orientation θ of the probe, a volume was acquired by translating the probe in steps of 200 μm. Then the probe was rotated along θ with 10° steps (see the Simulation of the 3D Point Spread Function section). For example, to acquire a volume of 12.8 × 12.8 × 20 mm, 18 orientations θ of the probe were used and for each orientation θ, 65 translation/imaging steps were performed.

Simulation of the 3D point spread function

In order to evaluate the efficiency of rotating the probe to reconstruct a volume with isotropic resolution, a simulation study was conducted using Field II (Jensen, 1996; Jensen and Svendsen, 1992) to estimate the 3D Point Spread Function (PSF) of the UFD-T imaging system. It is important for the understanding of the reader to precisely define the significance of "the UFD-T imaging system": it is the combination of plane wave ultrasound propagation, RF data beamforming, power Doppler calculations and mechanical translations. Consequently, to estimate the 3D PSF, we computed the backscattered ultrasound signal originating from a point source, beamformed the simulated RF data, and computed the magnitude of the resulting image (since the Power Doppler image is linked to the energy of the signal). This process was then repeated when moving the point source according to the mechanical translations, resulting in a 3D volume. This 3D volume was rotated along θ to build a final average volume, the latter being equal to the 3D PSF. Specifically, a 128-element focused linear array with the same technical characteristics as the ones detailed in the Experimental setup section was modeled in Field II. A point target was translated in the ultrasonic field from $y = -1.4$ mm to $y = 1.4$ mm with a y step of 0.2 mm (Fig. 1D), at $x = 0$ and $z = 12.8$ mm (corresponding aperture = 1), ($x = 0$, $y = 0$, $z = 0$) being the geometric center of the transducer array. This gave the 3D PSF of an imaging system that would use only the translation and not the rotation around θ (first 3D PSF of Fig. 1E), and, as expected, the −3 dB width and −6 dB width in the y dimension were 560 μm and 800 μm, respectively.

In order to evaluate the isotropy of the focal spot in the XY plane of the PSF when using the rotation along theta, the simulated volume was rotated around the z axis using different step sizes and averaged. As shown in Fig. 1E, two orthogonal orientations are not sufficient to recover the in-plane resolution, and even 45° rotation steps resulted in a PSF with preferred directions. The chosen volume reconstruction with 10° rotation steps is depicted in the bottom image: by averaging 18 volumes, an isotropic PSF was recovered and its −3 dB width (150 μm) (230-μm −6 dB-width) was improved when compared to what was obtained with only one scan in the elevation direction

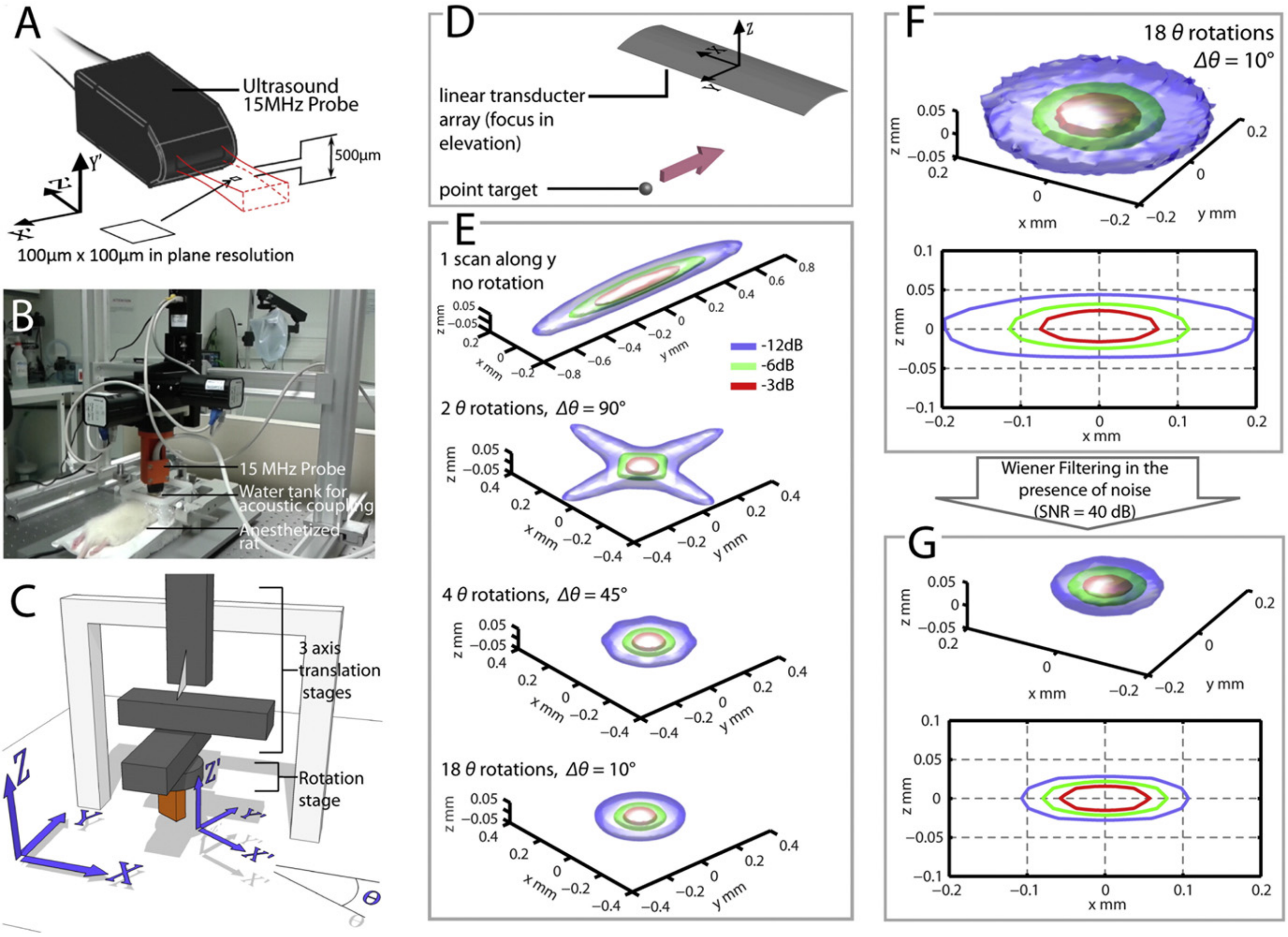

Fig. 1. A. 1D linear array used for ultrafast Doppler imaging. When using a 15-MHz transmit frequency, the in-plane resolution is 100 µm × 100 µm and the out-of-plane resolution is ~500 µm. B. Experimental 4D ultrasound angiography setup for rodent brain imaging. C. Schematic of the motorized axis: the 1D linear array was mounted on 3 translation axes and 1 rotation axis. The lab frame coordinates are (x,y,z) and the local frame coordinates of the imaging plane are (x′,y′,z′). D. Simulation of the 3D Point Spread Function (PSF) of the UFD-T system: using the software Field II, a linear transducer array mimicking our 15-MHz probe was designed and a point target was translated in the ultrasonic field along the y dimension. E. Evolution of the 3D PSF when rotating the probe along theta and averaging the translation PSFs: the 3 isosurfaces corresponding to −12 dB, −6 dB and −3 dB are depicted in 3D and perspective. The first one corresponds to one mechanical scan along y. The second one corresponds to the averaging of two scans along orthogonal directions, the third one to four directions of translation, and the last one to 18 directions of translation. F. 3D PSF for a reconstruction using 18 rotations 10° apart and corrupted by noise (SNR = 40 dB). The −3 dB width and −6 dB width of the isotropic PSF were 150 µm and 230 µm, respectively. G. Using the Wiener filter tuned with the known amplitude of the noise, this 3D PSF is reduced to a 90 µm −3 dB width (135 µm for the −6 dB width), which is comparable to the native in-plane resolution.

(560-µm −3 dB-width). However, this was still lower than the in-plane resolution (93-µm −3 dB width). A Wiener deconvolution filter in the Fourier domain was designed to recover this exact resolution in 3D and the result of this filter is presented in Figs. 1F and G.

Deconvolution filter

As presented in the previous section, the issue of recovering the resolution after averaging the volumes associated with different rotation angles is a problem of deconvolution. In other words, we have assessed with our simulation how a point source is transformed into a wide 3D volume by the UFD-T imaging system, and now we want to cancel this widening to obtain a 3D volume as close as possible to the real data (i.e., the real 3D spatial arrangement of blood in the imaged area). Deconvolution is a standard problem in image processing and is usually performed using a Wiener filter.

In this theoretical explanation, lowercase letters represent variables in the direct space (x,y,z), uppercase letters represent their Fourier transform in the k-space (k_x,k_y,kz), and bold uppercase letters represent their energy spectrum in the k-space. Our problem can be expressed as:

$$s(x,y,z) = psf(x,y,z) * e(x,y,z) + n(x,y,z) \tag{2}$$

where $s(x,y,z)$ is the 3D volume acquired by UFD-T (i.e., the observation), $psf(x,y,z)$ is the PSF described in the simulation section and displayed in Fig. 1E, $e(x,y,z)$ is the distribution of blood scatterers in the imaged volume, $n(x,y,z)$ is Gaussian white noise and * stands for convolution.

The optimal deconvolution in the presence of known noise was demonstrated by Wiener (1964) and consists of finding the filter $W(k_x,k_y,k_z)$ that minimizes the mean squared error in the Fourier domain between the estimator $\hat{E}(k_x, k_y, k_z) = W(k_x, k_y, k_z).\, S(k_x, k_y, k_z)$ and the input signal $E(k_x, k_y, k_z)$. The general form of the Wiener filter is given by:

$$W(k_x,k_y,\ k_z) = \frac{1}{PSF(k_x,\ k_y,\ k_z)} \cdot \frac{\boldsymbol{PSF}(k_x,k_y,\ k_z).\boldsymbol{E}(k_x,k_y,k_z)}{\boldsymbol{PSF}(k_x,k_y,\ k_z).\boldsymbol{E}(k_x,k_y,k_z) + \boldsymbol{N}(k_x,k_y,k_z)}. \tag{3}$$

The implementation of this filter required approximations, as certain quantities are not known a priori. $N(k_x,k_y,k_z)$ was assumed to be the spectrum of Gaussian white noise and was estimated by computing the variance σ^2 of the noise in the 3D observation volume, which was easily done in an area without blood. $\boldsymbol{PSF}(k_x, k_y, k_z)$. $\boldsymbol{E}(k_x, k_y, k_z)$ can then be approximated by $\mathbf{S}(k_x, k_y, k_z) - \sigma^2$. Therefore the implemented Wiener filter can be expressed as:

$$\hat{W}(k_x,k_y,\ k_z)=\frac{1}{PSF(k_x,\ k_y,\ k_z)}\cdot\frac{\mathbf{S}(k_x,k_y,\ k_z)-\sigma^2}{\mathbf{S}(k_x,k_y,\ k_z)}. \qquad (4)$$

The quantity $PSF(k_x, k_y, k_z)$ used in this implementation is equal to the Fourier transform of the simulated PSF. The filtered UFD-T volume was ultimately computed as follows:

$$\hat{e}(x,y,z)=\mathrm{TF}^{-1}\left[\hat{W}(k_x,k_y,\ k_z).S(k_x,k_y,\ k_z)\right]. \qquad (5)$$

Theoretical resolution

The improvement brought by the Wiener filtering process was quantified in order to determine the resolution of our technique. The key value for such a quantification is the SNR of UFD-T, which was evaluated to be 40 dB based on our experimental data. This very high value was due to the fact that noise averaging was present at several levels in the acquisition process: in the ultrafast power Doppler computation itself (averaging of 400 frames) and in the combination of the different angles (averaging of 18 angles). The result is a very low noise level, which in turn led to a very good performance of the Wiener filter. The Wiener filter offers a tradeoff between compression (in theory, in the absence of noise, the PSF could be shrunk to a spatial Dirac by the inverse filter) and distortion (in the presence of noise, the Wiener filter weighs the inverse filter based on the SNR). To compute the theoretical resolution, the simulated PSF was corrupted by Gaussian white noise in which the amplitude of the noise was 0.01 and the PSF amplitude was equal to 1 (Fig. 1F). Then the Wiener filter was applied. Fig. 1G shows a 90-μm −3 dB width and a 135-μm −6 dB width after Wiener filtering, which corresponds to the final resolution.

Animal preparation

All animals received humane care in compliance with the European Communities Council Directive of 2008 (2008/0211), and the study was approved by the institutional and regional committees for animal care. Adult Sprague Dawley rats aged 4–6 weeks underwent surgical craniotomy and implant of ultrasound-clear plastic prosthesis. Anesthesia was induced with 2% isoflurane and maintained by ketamine/xylazine (80/10 mg/kg), while body temperature was maintained at 36 °C with a heating blanket (Bioseb, France). A sagittal skin incision was performed across the posterior part of the head to expose the skull. Parietal bones were removed by drilling rectangular flaps and gently moving the bone away from the dura mater. Half of the frontal bone was similarly removed, thus exposing the cortex comprised between the olfactory bulb and the cerebellum, from Bregma +2 to Bregma −8 mm, with a maximal width of 14 mm. A plastic sheet of polymethylpentene was sealed in place with acrylic resin (GC Unifast TRAD) and residual space was filled with saline. We chose to open a large window in order to observe the whole neocortex and underlying structures. The choice to perform a large craniotomy rather than a thinned skull approach as performed in Osmanski et al. (2014b) was made to provide the best possible imaging conditions for 4D brain atlas acquisition. This type of surgery enabled cerebral imaging in the same rat for an extended experimental period of several months. Particular care was taken not to tear the dura in order to prevent cerebral damage. Animals recovered quickly, and after a conservative one-week rest period they were used for ultrasound data acquisition. In recording sessions, rats were anesthetized with isoflurane and ketamine/xylazine, with the head fixed in a stereotaxic frame and body temperature kept constant.

Data processing

Eighteen volumes with a rotation step size of 10° were acquired in vivo in a rat brain with the UFD-T system. Each volume was made of 65 Power Doppler (PW) images obtained as described in the Ultrasonic acquisition sequence subsection. Those volumes were interpolated to achieve an isotropic 50-μm-wide voxel $s_\theta(x', y', z')$. Each volume was rotated around the Oz axis to recast all the data in the lab frame coordinates (x, y, z):

$$s_\theta(x,y,z)=\mathrm{ROT}_{xOy}.s_\theta(x',y',z'). \qquad (6)$$

Due to the lack of information concerning the precision of assembly of the transducer array in the plastic body of the probe, we could not be sure that the geometric center of the array coincided with the geometric center of the plastic body, and therefore with the geometric center of the rotation. The consequence of such misalignment was an apparent circular shift of the imaged structures in the xOy plane for the different angles θ. This was taken into account by calculating the correlation in the xOy plane for each depth of a volume s_θ with the reference volume $s_{\theta\,=\,0°}$ and the median x lag x_θ^0 and y lag y_θ^0 for each angle theta.

The set of points (x_θ^0, y_θ^0) was then fitted on a circle using the Kasa method (Kasa, 1976) to take into account the a priori knowledge that the shift was circular and to smooth possible errors induced by the 2D correlation.

$$\left(x_\theta^0,y_\theta^0\right)\xrightarrow{\text{circle fit}}\left(\hat{x}_\theta^0,\hat{y}_\theta^0\right) \qquad (7)$$

In the end the eighteen volumes were registered and summed to give

$$s(x,y,z)=\sum_{i=\,-9}^{8}s_{\theta=i.10°}\left(x-\hat{x}_\theta^0,y-\hat{y}_\theta^0,z\right) \qquad (8)$$

$s(k_x,k_y,k_z)$ was then computed after a Tukey-window apodization of $s(x,y,z)$, onto which the deconvolution filter was applied to produce the final UFD-T volume $\hat{e}(x, y, z)$. Direct volume rendering of $\hat{e}$ was performed using Amira® (Visualization Sciences Group, FEI).

Spectral processing and blood speed profile calculation

If we consider the raw complex valued data $c_\theta(x', y', z', t)$ before the PW Doppler calculation, in each imaging plane a time/frequency description (spectrogram) of this signal can be calculated as:

$$S_\theta(x',y',z',f,t_0)=\left|\int_{t_0}^{t_0+t_w}c_\theta(x',y',z',t).e^{-j2\pi ft}.H\left(t-\left(t_0+\frac{t_w}{2}\right)\right).dt\right|^2. \qquad (9)$$

In this equation t_w is the temporal length of the Hann window H used to compute the Fourier transform. This calculation was used to compute the spectrograms in Fig. 8.

Speed selection before PW Doppler calculation

After SVD filtering of raw data acquisitions, we could optionally apply several band-pass frequency filters (6th order Butterworth band-pass filter), each giving access to maps of blood flow in different velocity ranges. Afterward, the filtering PW Doppler calculations were conducted. As each frequency bandwidth corresponded to a different range of blood-flow velocities (Bonnefous and Pesqué, 1986), it provided interesting insight into the spatial organization of different kinds of vessels (high flow in large arteries and low flow in arterioles and venules). This separation based on the blood speed is presented in Fig. 8E.

Power Doppler 4D imaging

The following concerns only Supplementary Video 2. After spatiotemporal filtering, a 6th order Butterworth temporal high-pass filter was used to select only the energy of red blood cells moving faster than 1 cm/s. In so doing, a marked change in PW Doppler level was obtained during systole and diastole. For each acquisition, the successive cardiac cycles were registered and averaged to obtain the PW Doppler temporal dynamics during one cardiac cycle. This created PW Doppler 3D volumes evolving over time. These 3D power Doppler volumes were individually filtered using the Wiener deconvolution filter, resulting in a 3D PW Doppler that evolved with time, with isotropic spatial resolution of 100 μm and a temporal resolution of 10 ms. This 4D volume is presented in Supplementary Video 2.

Result

Ultrafast Doppler imaging alone yields high but anisotropic spatial resolution

The concrete limitation of a simple 2D UFD acquisition in terms of the resolution in elevation is presented in Fig. 2, which depicts central images of two volumes that were acquired with two orthogonal translation directions and in which the vascular network of a rat brain in vivo is visible. In both cases the resolution in the imaging plane is high, but the resolution in the direction of the mechanical translation is deteriorated by the probe's low resolution in elevation (see Material and Methods section). In the case of acquisitions in the coronal XZ plane (Fig. 2A), small cortical arteries or deep ventral thalamic arteries could be observed in the coronal section (Fig. 2B), but resolution was highly deteriorated when the acquisition volume was observed in sagittal sections (Fig. 2C): the only vessels that were clearly discernible were the azygos pericallosal artery and the superior sagittal and straight sinuses. On the contrary, when the acquisition in the parasagittal YZ planes (Fig. 2D) were observed in sagittal sections of the volume (Fig. 2F), very small and deep vascular structures such as the median mesencephalic arteries or the dorsal periaqueductal arteries were observed, whereas almost nothing was distinguishable in coronal sections of the volume (Fig. 2E).

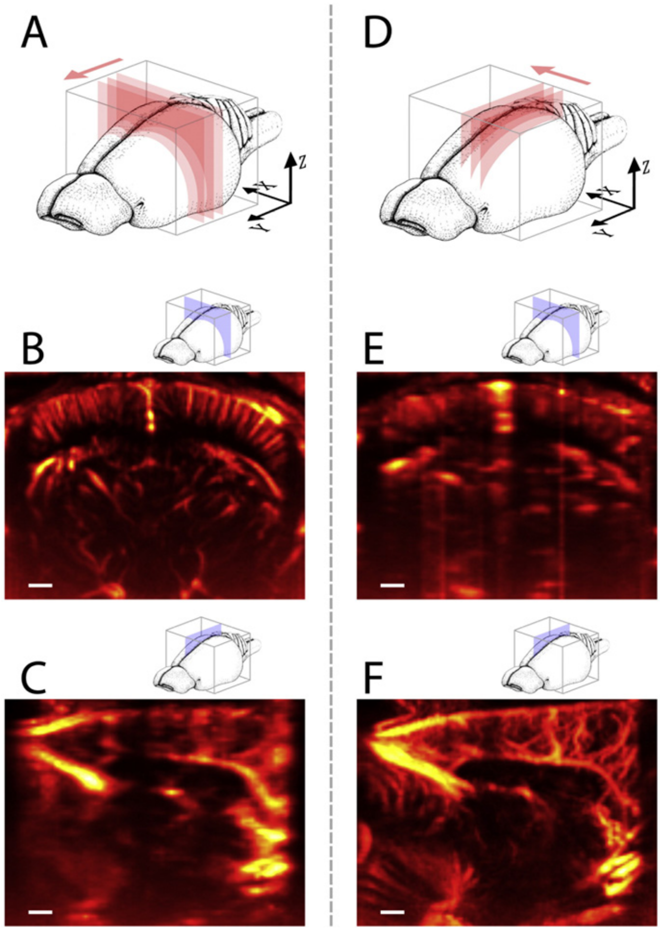

Fig. 2. Influence of the limited out-of-plane resolution. Scale bars: 1 mm. A. Acquisitions (pink rectangles) were performed as XZ coronal sections and the mechanical translation was conducted along the Y axis. B. 2D coronal image (blue rectangle) of the cerebral vasculature in the volume acquired in A: radial cortical vessels are precisely delineated, as well as deeper blood vessels in the hippocampus or thalamus. C. 2D sagittal image of the cerebral vasculature in the volume acquired in A: except for very large vessels, such as the venous sinuses or the pericallosal artery, the resolution of blood vessels is completely lost. D. Acquisitions (pink rectangles) were performed as YZ parasagittal sections and the mechanical translation was conducted along the X axis. E. 2D coronal image (blue rectangle) of the cerebral vasculature in the volume acquired in D: complete loss of resolution. F. 2D sagittal image of the cerebral vasculature in the volume acquired in D.

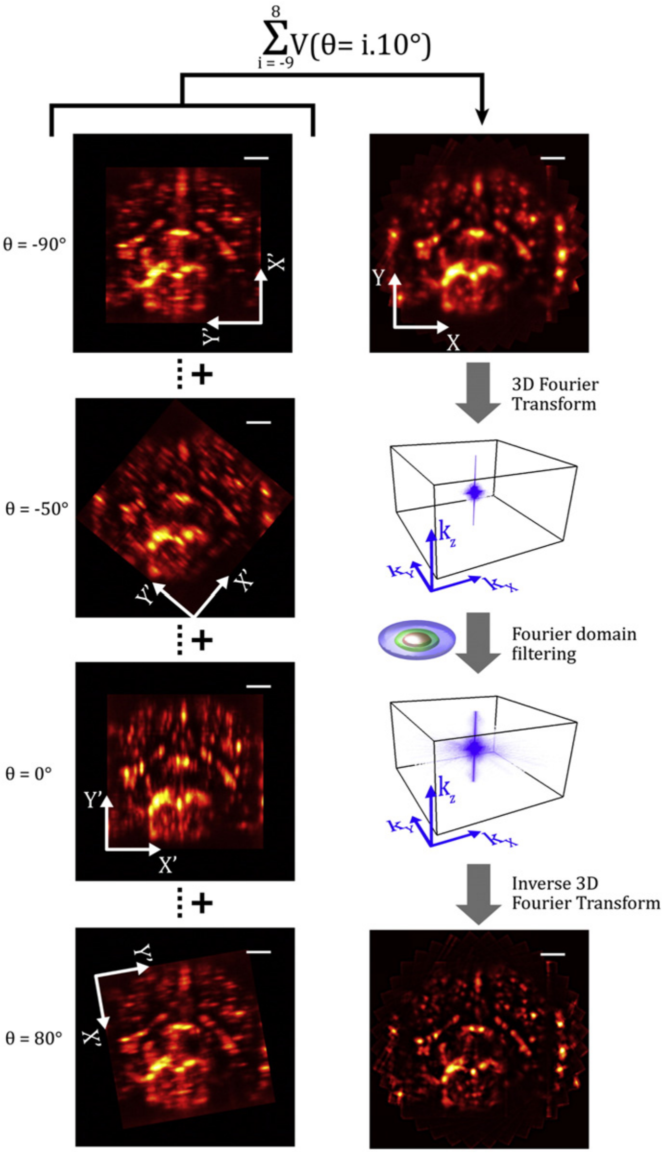

Fig. 3. *Schematic representation of the acquisition and filtering process. Images on the left represent an XY transverse section of each raw volume* $\mathbf{s}_\theta(\boldsymbol{x}, \boldsymbol{y}, \boldsymbol{z})$. *On the right, the summation of all the acquisitions performed at different angles (top), its 3D Fourier transform and the Fourier filtering process (middle) taking the 3D PSF into account, and the final result with improved resolution (bottom), are shown. Scale bar: 2 mm.*

High 3D isotropic spatial resolution using ultrafast Doppler tomography and the Wiener reconstruction

Raw data examples from one rat brain, displayed in transverse XY sections, are shown in Fig. 3: before summation, each volume $s_\theta(x,y,z)$ (see Material and methods section) was rotated back into the lab frame coordinates (x,y,z). Those transverse sections therefore represented the same vascular structures observed using different scanning orientations. It is interesting to note that the transverse sections of blood vessels appeared oblong in the Y′ direction, as predicted by our simulated PSF study. After summation, while vascular structures appeared to be more isotropic, the resolution was not recovered. It was only after Fourier domain filtering that the 100-μm resolution was recovered, in accordance with our simulation study (see Material and Methods section).

A precise qualitative comparison between raw summation and Wiener filtering is presented in Fig. 4: the raw summation resulted in blurry structures and it was difficult to distinguish two vessels, especially in situations in which one small vessel was close to a large one. The Wiener filter provided efficient deconvolution with a low level of noise. The Wiener filter approach was consequently validated for the reconstruction of in-vivo 3D UFD-T data. In Fig. 4B it can be noted that several vessels became discernible after filtering, whereas they were undetectable in Fig. 4A.

The limits of resolution were quantified both in the XY and in the XZ (equivalent to YZ) planes and results are shown in Fig. 5. The minimal distance required to distinguish two vessels appeared to be ~145 μm, while certain isolated vessels had a width at half maximum of ~80 μm in the XZ plane and of ~100 μm in the XY plane. Given the initial optimal resolution of the UFD-T technique without Wiener filtering (~100 μm at −3 dB), these results illustrate the benefits of applying a 3D Wiener filter to UFD-T.

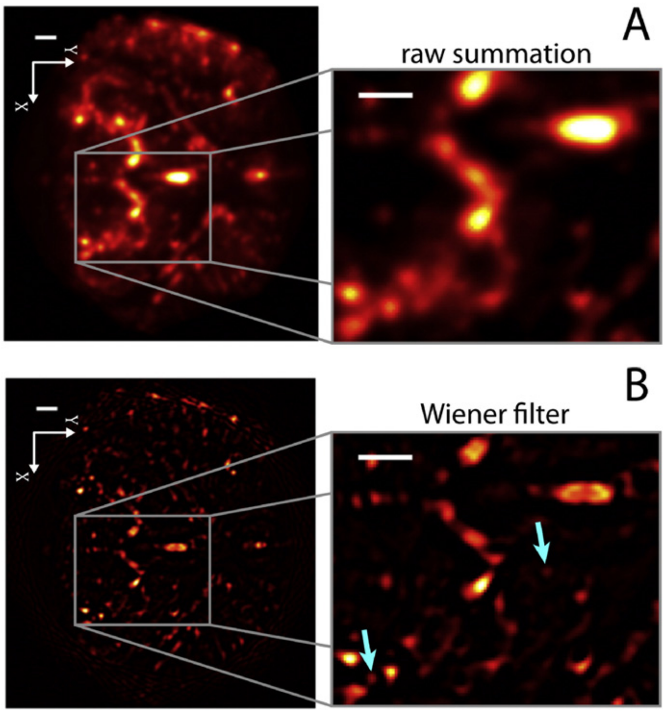

Fig. 4. Comparison between A. raw summation and B. Wiener filtering. In A, vascular structures have a large spatial extent and it is difficult to accurately assess the number of blood vessels, e.g., in the bottom-left corner of the image. Blood vessels that are indistinguishable in A become discernible using the Wiener filter (cyan arrows). Scale bar: 1 mm.

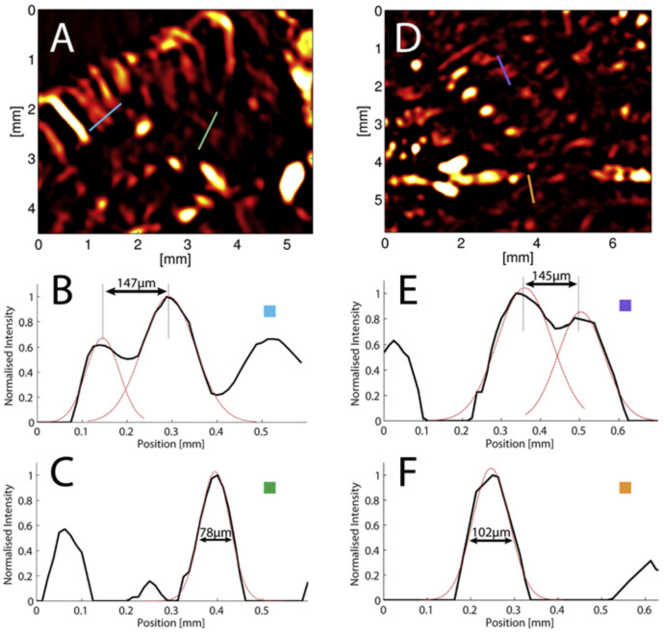

Fig. 5. Resolution evaluated in a 200-μm-thick slice of the 3D volume. A. Region of interest (ROI) in an XZ section. The resolution was quantified by selecting the two closest vessels within the ROI (blue line) and the thinnest vessel observable in the ROI (green line). B. Intensity profile along the blue line in A, in which the two-vessel section was fitted with Gaussian functions. C. Intensity profile along the green line in A, in which one vessel section was fitted with a Gaussian function. D. ROI in an XY section, in which the resolution was quantified by selecting the two closest vessels within the ROI (purple line) and the thinnest vessel observable within the ROI (orange line). E. Intensity profile along the purple line in D, in which the two-vessel section was fitted with Gaussian functions. F. Intensity profile along the orange line in D, in which one vessel section was fitted with a Gaussian function.

In vivo rat whole-brain anatomical description

Fig. 6 summarizes the capabilities of UFD-T in terms of in vivo angiographic detection. Projections of 1-mm-thick slices were extracted from a UFD-T volume and compared against a reference in terms of rat blood vessel description, i.e., the Scremin chapter in *The Rat Nervous System* (Paxinos, 1995), which was obtained using a casting technique based on the injection of tainted neoprene into the arterial and venous system. The main sinuses, i.e., the superior sagittal sinus, the inferior sagittal sinus and the straight sinus were easily observable in a medial sagittal section (Fig. 6a). The corpus callosum occupied an area without blood vessels, and one can follow the path of the anterior cerebral artery to the azygos anterior cerebral artery and the azygos pericallosal artery. While the latter are big vessels, many smaller vessels could also be observed, such as the dorsal periaqueductal arteries, the median mesencephalic arteries and the thalamo-perforating arteries, irrigating respectively the superior colliculus, mesencephalon and medial thalamic nuclei. In a more lateral section (Fig. 6e), subcortical and cortical penetrating arteries were observable, as well as the big longitudinal hippocampal artery providing the main blood supply to the hippocampus. The anterior and posterior striate arteries, which irrigate the caudate putamen, were also well depicted.

The eight coronal sections presented in Fig. 6i–p are approximately the same as the eight sections presented in (Scremin, 1995) and depict the same arteries. In the rostral part (Fig. 6i–k), the anterior, medial and posterior striate arteries were observable. In the medial part (Fig. 6l–n), the vascular network of the hippocampus was clear, as were the dorsal and ventral thalamic arteries. The two anterior choroidal arteries, branching from the internal carotids, were clearly depicted. In the most caudal regions (Fig. 6o–p), the lateral and dorsal periaqueductal arteries, which irrigate the superior colliculus, and the posterior lateral choroidal arteries and longitudinal hippocampal arteries, which stem from the posterior cerebral artery, were clearly visible.

The eight transverse sections presented in Fig. 6q–x are of striking importance because they are the first transverse sections of the rat vascular network ever obtained with an ultrasound modality. Indeed the resolution in XY transverse sections is conditional upon the tomographic approach. In the first layers, one can observe the cross section of numerous cortical blood vessels (Fig. 6q). Fig. 6r shows, with an unprecedented resolution for an in vivo imaging modality, the parallel organization of the transverse hippocampal arteries stemming perpendicularly from the longitudinal hippocampal artery as described in (Coyle, 1978). Deeper in the volume, the vessels surrounding the superior colliculus and their branches penetrating inside can be observed (Fig. 6t–u). Another important result is the depth of penetration of ultrafast Doppler Imaging, which enabled the observation of an almost complete arterial circle (Circle of Willis) (Fig. 6x), including the superior cerebellar arteries, the posterior cerebellar arteries, the posterior communicating arteries, the internal carotid, and the partial observation in that section of the anterior cerebral arteries.

All of these cross sections showed that UFD-T is a whole-brain-capable 3D vascular imaging modality with high resolution (100 μm) and even higher detection abilities: some of the vessels depicted here were much smaller than 100 μm (for example cortical penetrating arteries are generally between 50 and 100 μm, and transverse hippocampal arteries between 30 and 70 μm). Finally, UFD-T allowed for a combination of penetration depth and resolution unprecedented for an in vivo angiographic method, and provided results comparable to ex vivo casting techniques with a detection ability roughly limited to vessels larger than 50 μm in diameter.

High-quality 3D reconstruction of the rat whole-brain vasculature

UFD-T offers angiographic and complete 3D rendering abilities that can compete with state-of-the-art 3D vascular imaging techniques. Casting techniques often require complex perfusion protocols and samples that are cut in slices, which can result in damages and also dramatically complicate the vascular 3D reconstruction. UFD-T implemented in conjunction with the Wiener filter allowed for the direct acquisition and rendering of an entire 3D volume. This 3D rendering offered several advantages: an arbitrary cutting plane, segmentation of anatomical structures to isolate only the supplying vascular network and better architectural understanding of the vascular structures. This is illustrated in Fig. 7 and Video 1, which show views of a 3D rendering of the vascular network of a rat brain. In Figs. 7A and B, which represent views of the whole volume from the back and the front, respectively, one can appreciate the profusion of blood vessels depicted by the UFD-T technique: cortical blood vessels are the most numerous since they are in the first layers of the tissue where absorption of the ultrasound is very low, but deep vessels are also well depicted, e.g., around and inside the thalamus. The 3D vascular network supplying the hippocampus is depicted in blue in Fig. 7C: the longitudinal hippocampal artery and its perpendicular ramifications (transverse hippocampal arteries) are visible, as well as the hippocampal venous system that lies on the opposite side. The structure of the vascular supplying network of the hippocampus can be assessed, showing how the blood vessels wrap around the curved shape of this particular structure. The deep structures were also isolated (orange) to improve readability and render the Circle of Willis, and to highlight how the hippocampal network is connected to the deep vessels. In Fig. 7D, a small portion of the caudal part of the vascular network was depicted to improve readability: the straight sinus is clearly visible, as well as cortical and supra-collicular vessels.

4D hemodynamics assessment of the rat whole-brain vasculature

In addition to high 3D resolution, UFD-T also offers an intrinsically high temporal resolution. Fig. 8 illustrates how several quantities can be extracted from a single ultrafast Doppler acquisition, in addition to the Power Doppler image. For instance, Fig. 8B shows how the cardiac pulsations (red arrows) can be extracted from the tissue pulsatility obtained by analyzing the tissue motion in the entire imaging plane. Additionally, blood-flow speed profiles can be retrieved in each voxel of the 3D volume (Figs. 8C and D). This is particularly interesting for conducting a comparison between the blood-flow speed profiles extracted from various locations. For instance, in Fig. 8D, the blood flow accelerations due to cardiac impulses (red arrows) are detected, identifying this vessel as an artery, whereas in Fig. 8C, the blood flow is not pulsatile, indicating that the depicted vessel can be identified as a vein. This information was available throughout the entire UFD-T volume, thus enabling the computation of blood-flow speeds in different vessels and allowing for the discrimination between arterial and venous flow.

Video 2 shows the evolution of the power Doppler signal, obtained after filtering for blood flows above a given speed (1 cm/s), when sampled every 10 ms during one cardiac cycle in the entire 3D volume. In this movie, one can observe both the increase in PW Doppler during the cardiac systolic pulse and the small motion of the vessels due to changes in blood pressure during the cardiac cycle. Some veins can also be identified by their apparent non-pulsatile dynamics.

Discrimination based on the blood-flow speed could also be conducted, as presented in Fig. 8E. By applying a bank of band-pass filters onto the signal after SVD spatiotemporal filtering, a range of blood-flow speeds could be isolated, and, as a result, vessels could be selected according to their size. Insights into the spatial organization of different kinds of vessels (fast flow in large arteries and slow flows in arterioles and venules) could be inferred, as each frequency bandwidth corresponded to a different range of blood-flow velocities. Interestingly, one can see that vessels could be easily depicted with 1- to 2-mm/s flow velocities and even with velocities lower than 1 mm/s. Moreover, a clear differentiation could be achieved between regions corresponding to high speed (larger vessels) and low speed (small vessels). The 2-mm/s to 4-mm/s region was strongly apparent in the overall cortical and hippocampal areas, whereas larger vessels (16–18 mm/s) were clustered near the surface of the cortex before dividing into smaller vessels in deeper regions.

Discussion

In this study, UFD-T was introduced as a novel in vivo technique for 4D microvascular imaging and was demonstrated in small animal brains. Based on ultrafast Doppler ultrasound imaging, UFD-T is capable of providing high-sensitivity images at low speed flows (~1 mm/s), corresponding to small arterioles and venules of the brain. In order to achieve an isotropic resolution using a linear probe, a tomographic scanning approach requiring successive translation/rotation scans, in conjunction with a dedicated 3D Wiener deconvolution filter, was proposed. 3D rendering showed angiographic capabilities competitive with state-of-the-art vascular imaging techniques and also presented several additional advantages. It enabled the depiction of rodent brain vasculature with high sensitivity (~1 mm/s), high resolution (~100 μm3) and high penetration (>15 mm) without the use of a contrast agent. The technique also allowed for the creation of animal-specific vascular atlases. Since UFD-T is based on ultrafast Doppler imaging, a large quantity of information is available when compared to conventional focused ultrasound. Using techniques described in Bercoff et al. (2011) and Demené et al. (2014), the temporal evolution of blood volume and blood-flow speed during a cardiac cycle can be retrieved in each pixel of an ultrafast Doppler acquisition. This enables both the capture of hemodynamics during one cardiac cycle and the calculation of parametric maps that describe the hemodynamic state of the vascular network. It gives access to time-resolved information on whole-brain

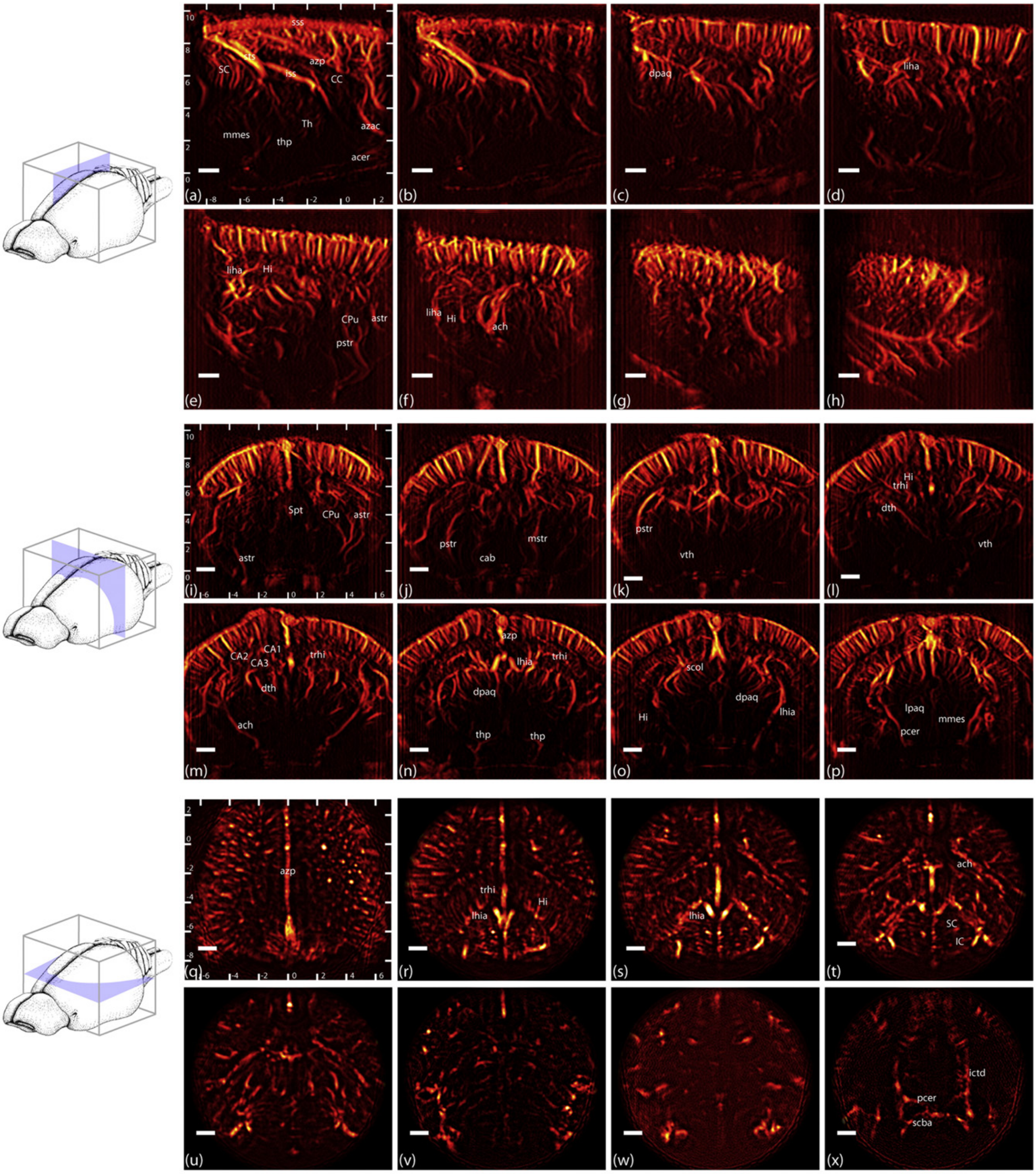

Arteries and Sinuses

acer	anterior cerebral artery
ach	anterior choroidal artery
astr	anterior striate arteries
azac	azygos anterior cerebral artery
azp	azygos pericallosal artery
cab	caudal ascending basal forebrain arteries
dpaq	dorsal periaqueductal arteries
dth	dorsal thalamic arteries
ictd	internal carotid artery
iss	inferior sagittal sinus
lapq	lateral periaqueductal arteries
lhia	longitudinal hippocampal artery
mmes	median mesencephalic arteries
mstr	medial striate arteries
pcer	posterior cerebral artery
pstr	posterior striate arteries
scba	superior cerebellar arteries
scol	supracollicular arterial network
sss	superior sagittal sinus
sts	straight sinus
thp	thalamo-perforating arteries
trhi	transverse hippocampal arteries
vth	ventral thalamic arteries

Structures

CA1,2,3	fields CA1, CA2, CA3 of the hippocampus
CC	Corpus callosum
CPu	Caudate putamen
Hi	Hippocampus
IC	Inferior colliculus
Spt	Septum
SC	Superior colliculus
Th	Thalamus

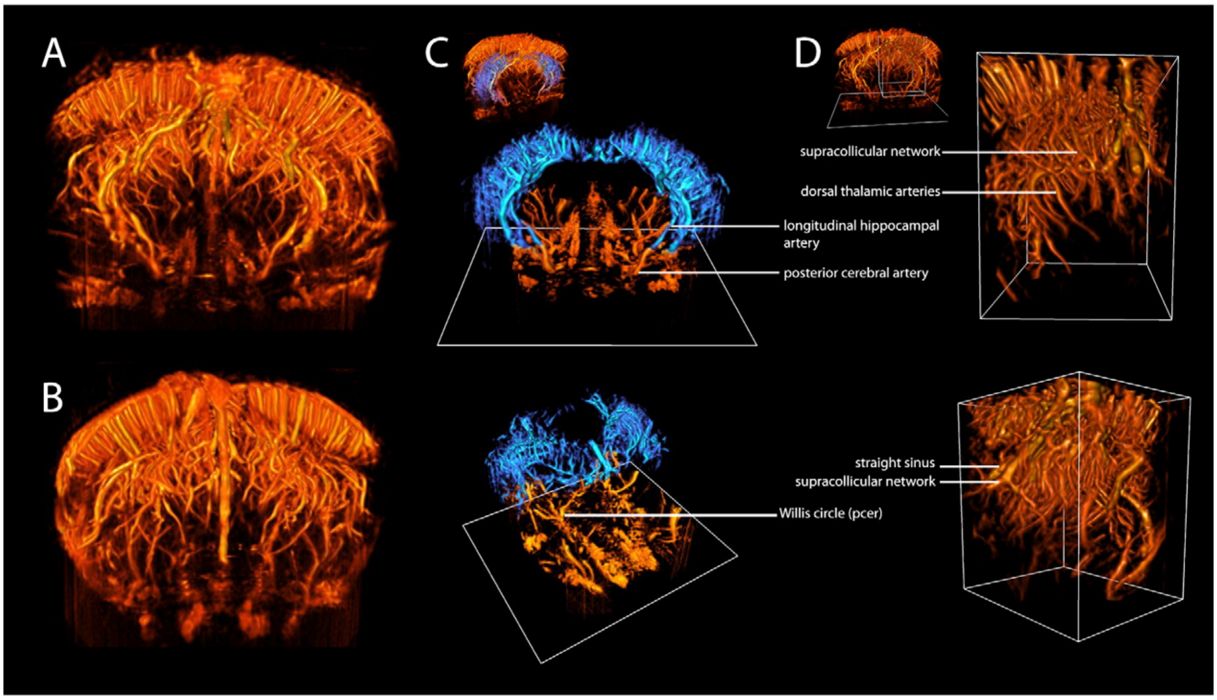

Fig. 7. Several views of 3D rendering of a UFD-T volume. A. Back view and B. front view of the complete vascular network acquired with the UFD-T technique. C. Segmentation of the hippocampus enabled the isolation of its vascular supplying network (in blue), and its connection to the deep vascular structures (in orange). Top is the back view, bottom is the three-quarters front view, inset is the location of the hippocampus structures within the whole vascular volume. D. Details of the supra collicular network and cortical arteries in the caudal part of the acquisition. Top is the front view, bottom is the three-quarters back view, inset is the location of the volume within the whole vascular system.

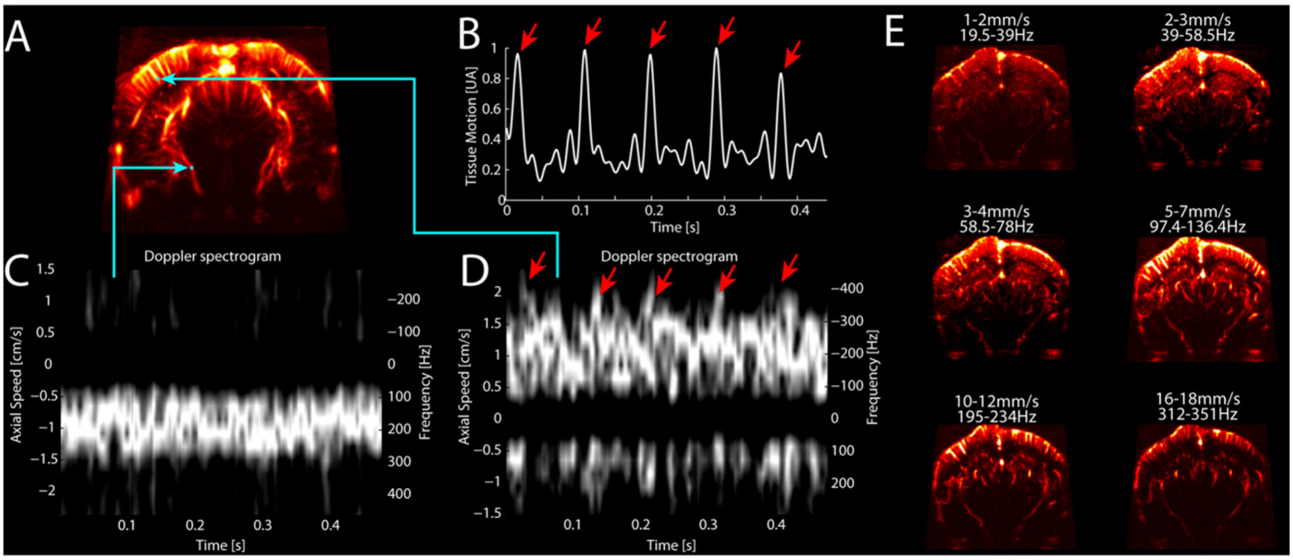

Fig. 8. 4D capabilities of UFD-T: in each imaging plane, the Doppler signal has a high temporal resolution. A. Image of slice 14 acquired at the angle $\theta = 0°$, showing the locations where blood-flow speeds have been computed. B. In each slice, the global tissue motion (see Material and methods) can be retrieved and corresponds to the cardiac pulsations. Using a spectrogram description of the Doppler signal, the blood speed profile can be retrieved in each pixel: C. in the large vein indicated by a cyan arrow, the blood flow profile is quite regular, with a non-pulsatile flow; D. in the cortical artery indicated by a cyan arrow, the blood flow is pulsatile (velocity peaks are indicated by red arrows). E. By using a bank of band-pass filters, several ranges of speed can be selected and PW Doppler images constructed for each of these speed ranges. The image gain is the same for all six images.

hemodynamics with unprecedented temporal resolution (~1 ms). This temporal resolution is of particular interest for small-animal imaging. Indeed, although magnetic resonance imaging made tremendous progress in the last decade with the emergence of high temporal and spatial resolution MR angiography (4D-MRA) in clinics (Hadizadeh et al., 2014; Willinek et al., 2008), the temporal

---

Fig. 6. Representative 1-mm-thick slices of the UFD-T volume acquired in one rat. All coordinates are defined according to the Paxinos Atlas (Paxinos, 1995). From (a) to (h), parasagittal sections centered respectively on lateral +0.25, +0.75, +1.75, +2.75, +3.75, +5.25, +5.65, +6.65. From (i) to (p), coronal sections centered on bregma +0.6, −0.4, −1.4, −2.4, −3.4, −4.4, −5.4, −6.4. From (q) to (x), transverse sections centered on interaural +7.75, +6.75, +6.25, +5.75, +5.25, +3.75, +2.25, +0.75. For each series, the first image includes a millimetric grid giving the coordinates as described in the Paxinos Atlas and with regard to the bregma and the interaural points. The main blood vessels are annotated, as are a few structures to help the orientation of the reader. Scale bar: 1 mm.

resolution achieved in 4D-MRA imaging remains longer than one cardiac cycle.

The method proposed in this study will lead to several applications. The high temporal and spatial resolutions will provide a way to better understand and potentially revisit fundamental phenomenon, including cerebral autoregulation (Willie et al., 2014), for example after an insult, such as a cardiac arrest or a stroke. In numerous studies, autoregulation assessment is based on measurements of cerebral blood flow in one location only (Kainerstorfer et al., 2015; Lee et al., 2011; Petersen et al., 2015), whereas with our technique we envision the possibility of assessing autoregulation in different specific areas of the brain. Additionally, the possibility of keeping the animal alive during imaging with this kind of resolution opens a whole new field of applications in the monitoring of angiogenesis in various experimental conditions, such as longitudinal developmental studies, tumor injection or recovery and vascular remodeling (Liu et al., 2014) after stroke, or reperfusion following a drug injection such as rTPA. It will also be an interesting tool for stroke studies, as it will provide vascular information on blood flow dynamics, hyperperfusion and hypoperfusion, and resistivity index during stroke. Beyond brain applications, 4D ultrasound angiography could be of particular interest for tumor vasculature studies in small-animal models.

With the portability of ultrasound systems and the small size of ultrasonic probes, the use of UFD-T could extend to high resolution 3D imaging in awake animals. The extent of fUltrasound capabilities to portable imaging on awake and freely moving animals has already been done very recently with ultrafast Doppler imaging (Sieu et al., 2015; Urban et al., 2015), establishing the relevance of fUltrasound to neuroscience. While the paper from Urban et al. focuses on reproduction in awake animals of 2D fUS imaging results previously described in anesthetized animals such as resting state functional connectivity assessment (Osmanski et al., 2014b) and blood volume response in the barrel cortex during whisker stimulation (Macé et al., 2011), the study of Sieu et al. takes a step forward by presenting combined 3D portable fUltrasound imaging and EEG recording in awake and freely moving animals during absence seizures and behavioural tasks. Sieu et al. provided several imaging planes by using a very light micromotor moving the ultrasound probe, which was mounted directly onto the skull of a rat, and was the first attempt at achieving 3D fUltrasound imaging in freely moving animals, although without achieving the resolutions presented herein with the tomographic approach. This setup (EEG + light motorized probes + fUltrasound) allowed, for example, for the correlation of hemodynamics and electrical activity during epileptic seizures in a selected strain of rat (GAERS) modeling absence seizure, showing adverse effect according to the spatial location in 3D. It also allowed for the correlation of fUltrasound whole-brain imaging with theta oscillations during behavioral tasks in rats in a maze, showing during locomotion a hyperperfusion in the somato-sensory cortex and the hippocampus, and a hypoperfusion in the ventral thalamus. This approach is a first step toward 4D fUltrasound in freely moving rats.

It is also a required tool for the creation of animal-specific rodent neurovascular atlases. While standard vascular atlases and templates already exist, the most advanced approach for the construction of whole-brain vascular atlases in small animals requires the combination of 14 h of high-field MRI imaging and 2 h of μCT scans, both of which are conducted in ex vivo brains (Dorr et al., 2007) with a 30-μm resolution. However, we think that in some particular cases it could be helpful to acquire an animal-specific vascular reference on the fly. This could be particularly relevant when studying models for developmental disorders, such as retarded growth, because growth cannot be approximated by a simple scaling of the structures. The availability of high-quality, on-the-fly whole-brain atlases will be vital in the emerging field of fUltrasound, as it will strongly ease the matching and registration between functional activity maps assessed by fUltrasound and the structural atlases of the brain. Even if in-vivo MRI and CT can provide 3D vascular imaging (Lin et al., 2009; Starosolski et al., 2015), the portability and versatility of an Ultrafast Ultrasound scanner will be an advantage in functional studies.

4D ultrasound UFD-T angiography also has limitations. For instance, attenuation tends to limit sensitivity at large depths (beyond ~15 mm at 15 MHz) and thus may lower the precision at which structures such as the Circle of Willis can be delineated. Strategies aiming to increase ultrasonic energy without reducing the imaging frame rate are currently being studied in our lab. Also, the necessity to trepan or at least to thin the skull bone to facilitate transcranial propagation is a clear limitation in the case of rat brain imaging. However, a large number of imaging techniques presented as minimally invasive (such as the last four columns of Table 1) are used for mouse brain imaging. Recent studies from our group, which have not yet been published, demonstrate that it is possible to perform very good transcranial acquisitions in mice and young rats, as their skull bone is thinner. In that case, our technique would be minimally invasive. Moreover, translation to clinical imaging could be possible for some niche but particularly interesting applications, such as human newborn imaging in pediatric radiology, since transfontanellar imaging of brain vasculature was recently acquired with unprecedented quality via ultrafast Doppler imaging (Demené et al., 2014).

A second limitation of our tomographic approach is the long acquisition time (typically 20 min of ultrasonic acquisition for the whole rat brain, completed with ~2 h of signal processing). This limitation is due in part to the acquisition of several cardiac cycles (~500 ms) for each 2D image. Nevertheless, even if this acquisition time is long, it remains competitive when compared to MRI/μCT approaches, and can be decreased by reducing the number of probe orientations, at the cost of a lower, yet still high, reconstruction quality. Specifically, using 30° steps instead of 10° steps resulted in an acquisition time reduced to 6 min. Further optimization of fast scanning sequences is the object of ongoing work. Moreover, this acquisition time limitation is not a physical bottleneck. Indeed, the future replacement of the tomographic approach using motorized 1D linear probes by ultrafast imaging using 2D matrix probes will lead to 4D acquisitions at ultrafast frame rates in real time, as recently demonstrated by our group in cardiac imaging (Provost et al., 2014). Using 2D matrix probes, the acquisition time for one-cardiac-cycle, 4D angiography could drop from 20 min down to real time, i.e.,~300 ms in rats. In the long term, the development of miniature ultrasonic matrix arrays equipped with miniaturized cables in conjunction with the UFD-T reconstruction approach should allow for the high-quality acquisition of the complete brain vascularization in awake and mobile rats in less than one second, enabling the observation of naturally occurring or induced vascular events in real time.

Supplementary data to this article can be found online at http://dx.doi.org/10.1016/j.neuroimage.2015.11.014.

Acknowledgments

The research leading to these results has received funding from the European Research Council under the European Union's Seventh Framework Programme (FP7/2007–2013)/ERC *grant agreement* no 339244-FUSIMAGINE. This work was also partly supported by the Agence Nationale de la Recherche under the program “Future Investments” with the reference Laboratory of Excellence ANR-10-LABX-24 LABEX WIFI within the French Program “Investments for the Future” under reference ANR-10-IDEX-0001-02 PSL and the program “Investissements d'avenir” ANR-10-IAIHU-06.

References

Badea, C.T., Drangova, M., Holdsworth, D.W., Johnson, G.A., 2008. In vivo small-animal imaging using micro-CT and digital subtraction angiography. Phys. Med. Biol. 53, R319. http://dx.doi.org/10.1088/0031-9155/53/19/R01.

Beckmann, N., 2000. High resolution magnetic resonance angiography non-invasively reveals mouse strain differences in the cerebrovascular anatomy in vivo. Magn.

Reson. Med. 44, 252–258. http://dx.doi.org/10.1002/1522-2594(200008)44:2<252::AID-MRM12>3.0.CO;2-G.

Beckmann, N., Stirnimann, R., Bochelen, D., 1999. High-resolution magnetic resonance angiography of the mouse brain: application to murine focal cerebral ischemia models. J. Magn. Reson. 140, 442–450. http://dx.doi.org/10.1006/jmre.1999.1864.

Bercoff, J., Montaldo, G., Loupas, T., Savery, D., Mézière, F., Fink, M., Tanter, M., 2011. Ultrafast compound Doppler imaging: providing full blood flow characterization. IEEE Trans. Ultrason. Ferroelectr. Freq. Control 58, 134–147. http://dx.doi.org/10.1109/TUFFC.2011.1780.

Bolan, P.J., Yacoub, E., Garwood, M., Ugurbil, K., Harel, N., 2006. In vivo micro-MRI of intracortical neurovasculature. NeuroImage 32, 62–69. http://dx.doi.org/10.1016/j.neuroimage.2006.03.027.

Bonnefous, O., Pesqué, P., 1986. Time domain formulation of pulse-Doppler ultrasound and blood velocity estimation by cross correlation. Ultrason. Imaging 8, 73–85.

Chugh, B.P., Lerch, J.P., Yu, L.X., Pienkowski, M., Harrison, R.V., Henkelman, R.M., Sled, J.G., 2009. Measurement of cerebral blood volume in mouse brain regions using micro-computed tomography. NeuroImage 47, 1312–1318. http://dx.doi.org/10.1016/j.neuroimage.2009.03.083.

Coyle, P., 1978. Spatial features of the rat hippocampal vascular system. Exp. Neurol. 58, 549–561. http://dx.doi.org/10.1016/0014-4886(78)90108-5.

Demene, C., Deffieux, T., Pernot, M., Osmanski, B.F., Biran, V., Gennisson, J.-C., Sieu, L.-A., Bergel, A., Franqui, S., Correas, J.M., Cohen, I., Baud, O., Tanter, M., 2015. Spatiotemporal clutter filtering of ultrafast ultrasound data highly increases Doppler and fUltrasound sensitivity. IEEE Trans. Med. Imaging 1–1. http://dx.doi.org/10.1109/TMI.2015.2428634.

Demené, C., Pernot, M., Biran, V., Alison, M., Fink, M., Baud, O., Tanter, M., 2014. Ultrafast Doppler reveals the mapping of cerebral vascular resistivity in neonates. J. Cereb. Blood Flow Metab. http://dx.doi.org/10.1038/jcbfm.2014.49.

Dorr, A., Sled, J.G., Kabani, N., 2007. Three-dimensional cerebral vasculature of the CBA mouse brain: a magnetic resonance imaging and micro computed tomography study. NeuroImage 35, 1409–1423. http://dx.doi.org/10.1016/j.neuroimage.2006.12.040.

Downey, D.B., Fenster, A., 1995. Vascular imaging with a three-dimensional power Doppler system. AJ. Am. J. Roentgenol. 165, 665–668.

Edelman, R.R., 1993. MR angiography: present and future. Am. J. Roentgenol. 161, 1–11. http://dx.doi.org/10.2214/ajr.161.1.8517285.

Hadizadeh, D., Marx, C., Gieseke, J., Schild, H., Willinek, W., 2014. High temporal and high spatial resolution MR angiography (4D-MRA). RöFo—Fortschritte Auf Dem Geb. Röntgenstrahlen Bildgeb. Verfahr. 186, 847–859. http://dx.doi.org/10.1055/s-0034-1366661.

Hong, G., Diao, S., Chang, J., Antaris, A.L., Chen, C., Zhang, B., Zhao, S., Atochin, D.N., Huang, P.L., Andreasson, K.I., Kuo, C.J., Dai, H., 2014. Through-skull fluorescence imaging of the brain in a new near-infrared window. Nat. Photonics 8, 723–730. http://dx.doi.org/10.1038/nphoton.2014.166.

Hong, G., Lee, J.C., Robinson, J.T., Raaz, U., Xie, L., Huang, N.F., Cooke, J.P., Dai, H., 2012. Multifunctional in vivo vascular imaging using near-infrared II fluorescence. Nat. Med. 18, 1841–1846. http://dx.doi.org/10.1038/nm.2995.

Jensen, J.A., 1996. FIELD: A Program for Simulating Ultrasound Systems. 10th Nordicbaltic Conference on Biomedical Imaging vol. 4, Suppl. 1, pp. 351–353 (PART 1:351–353).

Jensen, J.A., Svendsen, N.B., 1992. Calculation of pressure fields from arbitrarily shaped, apodized, and excited ultrasound transducers. IEEE Trans. Ultrason. Ferroelectr. Freq. Control 39, 262–267. http://dx.doi.org/10.1109/58.139123.

Kainerstorfer, J.M., Sassaroli, A., Tgavalekos, K.T., Fantini, S., 2015. Cerebral autoregulation in the microvasculature measured with near-infrared spectroscopy. J. Cereb. Blood Flow Metab. 35, 959–966. http://dx.doi.org/10.1038/jcbfm.2015.5.

Kalchenko, V., Israeli, D., Kuznetsov, Y., Harmelin, A., 2014. Transcranial optical vascular imaging (TOVI) of cortical hemodynamics in mouse brain. Sci. Rep. 4. http://dx.doi.org/10.1038/srep05839.

Kasa, I., 1976. A circle fitting procedure and its error analysis. IEEE Trans. Instrum. Meas. IM-25, 8–14. http://dx.doi.org/10.1109/TIM.1976.6312298.

Lee, J.K., Brady, K.M., Mytar, J.O., Kibler, K.K., Carter, E.L., Hirsch, K.G., Hogue, C.W., Easley, R.B., Jordan, L.C., Smielewski, P., Czosnyka, M., Shaffner, D.H., Koehler, R.C., 2011. Cerebral blood flow and cerebrovascular autoregulation in a swine model of pediatric cardiac arrest and hypothermia*. Crit. Care Med. 39, 2337–2345. http://dx.doi.org/10.1097/CCM.0b013e318223b910.

Lin, C.-Y., Lin, M.-H., Cheung, W.-M., Lin, T.-N., Chen, J.-H., Chang, C., 2009. In vivo cerebromicrovasculatural visualization using 3D ΔR2-based microscopy of magnetic resonance angiography (3DΔR2-mMRA). NeuroImage 45, 824–831. http://dx.doi.org/10.1016/j.neuroimage.2008.12.030.

Liu, J., Wang, Y., Akamatsu, Y., Lee, C.C., Stetler, R.A., Lawton, M.T., Yang, G.-Y., 2014. Vascular remodeling after ischemic stroke: mechanisms and therapeutic potentials. Prog. Neurobiol., 2013 Pangu Meeting on Neurobiology of Stroke and CNS Injury: Progresses and Perspectives of Future 115, pp. 138–156. http://dx.doi.org/10.1016/j.pneurobio.2013.11.004.

Macé, E., Montaldo, G., Cohen, I., Baulac, M., Fink, M., Tanter, M., 2011. Functional ultrasound imaging of the brain. Nat. Methods 8, 662–664. http://dx.doi.org/10.1038/nmeth.1641.

Mace, E., Montaldo, G., Osmanski, B., Cohen, I., Fink, M., Tanter, M., 2013. Functional ultrasound imaging of the brain: theory and basic principles. IEEE Trans. Ultrason. Ferroelectr. Freq. Control 60, 492–506. http://dx.doi.org/10.1109/TUFFC.2013.2592.

Montaldo, G., Tanter, M., Bercoff, J., Benech, N., Fink, M., 2009. Coherent plane-wave compounding for very high frame rate ultrasonography and transient elastography. IEEE Trans. Ultrason. Ferroelectr. Freq. Control 56, 489–506. http://dx.doi.org/10.1109/TUFFC.2009.1067.

Osmanski, B.F., Martin, C., Montaldo, G., Lanièce, P., Pain, F., Tanter, M., Gurden, H., 2014a. Functional ultrasound imaging reveals different odor-evoked patterns of vascular activity in the main olfactory bulb and the anterior piriform cortex. NeuroImage 95, 176–184. http://dx.doi.org/10.1016/j.neuroimage.2014.03.054.

Osmanski, B.-F., Pezet, S., Ricobaraza, A., Lenkei, Z., Tanter, M., 2014b. Functional ultrasound imaging of intrinsic connectivity in the living rat brain with high spatiotemporal resolution. Nat. Commun. 5, 5023. http://dx.doi.org/10.1038/ncomms6023.

Paxinos, G., 1995. The Rat Nervous System. Gulf Professional Publishing.

Petersen, N.H., Ortega-Gutierrez, S., Reccius, A., Masurkar, A., Huang, A., Marshall, R.S., 2015. Dynamic cerebral autoregulation is transiently impaired for one week after large-vessel acute ischemic stroke. Cerebrovasc. Dis. Basel Switz. 39, 144–150. http://dx.doi.org/10.1159/000368595.

Provost, J., Papadacci, C., Arango, J.E., Imbault, M., Fink, M., Gennisson, J.-L., Tanter, M., Pernot, M., 2014. 3D ultrafast ultrasound imaging in vivo. Phys. Med. Biol. 59, L1. http://dx.doi.org/10.1088/0031-9155/59/19/L1.

Reese, T., Bochelen, D., Sauter, A., Beckmann, N., Rudin, M., 1999. Magnetic resonance angiography of the rat cerebrovascular system without the use of contrast agents. NMR Biomed. 12, 189–196. http://dx.doi.org/10.1002/(SICI)1099-1492(199906)12:4<189::AID-NBM557>3.0.CO;2-O.

Scremin, O.U., 1995. Cerebral vascular system. The Rat Nervous System. Academic Press, San Diego, pp. 3–35.

Sieu, L.-A., Bergel, A., Tiran, E., Deffieux, T., Pernot, M., Gennisson, J.-L., Tanter, M., Cohen, I., 2015. EEG and functional ultrasound imaging in mobile rats. Nat. Methods http://dx.doi.org/10.1038/nmeth.3506 (advance online publication).

Starosolski, Z., Villamizar, C.A., Rendon, D., Paldino, M.J., Milewicz, D.M., Ghaghada, K.B., Annapragada, A.V., 2015. Ultra high-resolution in vivo computed tomography imaging of mouse cerebrovasculature using a long circulating blood pool contrast agent. Sci. Rep. 5, 10178. http://dx.doi.org/10.1038/srep10178.

Tanter, M., Fink, M., 2014. Ultrafast imaging in biomedical ultrasound. IEEE Trans. Ultrason. Ferroelectr. Freq. Control 61, 102–119. http://dx.doi.org/10.1109/TUFFC.2014.6689779.

Urban, A., Dussaux, C., Martel, G., Brunner, C., Mace, E., Montaldo, G., 2015. Real-time imaging of brain activity in freely moving rats using functional ultrasound. Nat. Methods 12, 873–878. http://dx.doi.org/10.1038/nmeth.3482.

Wiener, N., 1964. Extrapolation, Interpolation & Smoothing of Stationary Time Series—With Engineering Applications. MIT Press, Cambridge, Mass.

Willie, C.K., Tzeng, Y.-C., Fisher, J.A., Ainslie, P.N., 2014. Integrative regulation of human brain blood flow. J. Physiol. 592, 841–859. http://dx.doi.org/10.1113/jphysiol.2013.268953.

Willinek, W.A., Hadizadeh, D.R., von Falkenhausen, M., Urbach, H., Hoogeveen, R., Schild, H.H., Gieseke, J., 2008. 4D time-resolved MR angiography with keyhole (4D-TRAK): more than 60 times accelerated MRA using a combination of CENTRA, keyhole, and SENSE at 3.0 T. J. Magn. Reson. Imaging 27, 1455–1460. http://dx.doi.org/10.1002/jmri.21354.

Yao, J., Wang, L.V., 2014. Photoacoustic brain imaging: from microscopic to macroscopic scales. Neurophotonics 1, 011003. http://dx.doi.org/10.1117/1.NPh.1.1.011003.

Yao, J., Wang, L., Yang, J.-M., Maslov, K.I., Wong, T.T.W., Li, L., Huang, C.-H., Zou, J., Wang, L.V., 2015. High-speed label-free functional photoacoustic microscopy of mouse brain in action. Nat. Methods 12, 407–410. http://dx.doi.org/10.1038/nmeth.3336.

Appendix D

Article 6: Mesure simultanée des dynamiques neuronale et vasculaire chez l'animal mobile. (In French)

Sieu, L.-A., **A. Bergel**, E. Tiran, T. Deffieux, M. Pernot, J.-L. Gennisson, M. Tanter, and I. Cohen 2016. Mesure simultanée des dynamiques neuronale et vasculaire chez l'animal mobile. *Médecine/Sciences*, 32(5):444-447.

11. Cimino I, Casoni F, Liu X, *et al.* Novel role for anti-Müllerian hormone in the regulation of GnRH neuron excitability and hormone secretion. *Nat Commun* 2016 ; 7 : 10055.

RÉFÉRENCES

12. Giacobini P, Parkash J, Campagne C, *et al.* Brain endothelial cells control fertility through ovarian-steroid-dependent release of semaphorin 3A. *PLoS Biol* 2014 ; 12 : e1001808.

13. Parkash J, Messina A, Langlet F, *et al.* Semaphorin7A regulates neuroglial plasticity in the adult hypothalamic median eminence. *Nat Commun* 2015 ; 6 : 6385.

14. Moore AM, Prescott M, Marshall CJ, *et al.* Enhancement of a robust arcuate GABAergic input to gonadotropin-releasing hormone neurons in a model of polycystic ovarian syndrome. *Proc Natl Acad Sci USA* 2015 ; 112 : 596-601.

15. Catteau-Jonard S, Pigny P, Reyss AC, *et al.* Changes in serum anti-mullerian hormone level during low-dose recombinant follicular-stimulating hormone therapy for anovulation in polycystic ovary syndrome. *J Clin Endocrinol Metab* 2007 ; 92 : 4138-43.

16. Solorzano C, Beller J, Abshire M, *et al.* Neuroendocrine dysfunction in polycystic ovary syndrome. *Steroids* 2012 ; 77 : 332-7.

17. Naulé L, Mhaouty-Kodja S. Le récepteur neural des œstrogènes bêta : un nouvel acteur dans la maturation pubertaire femelle. *Med Sci (Paris)* 2016 ; 32 : 452-5.

NOUVELLE

Mesure simultanée des dynamiques neuronale et vasculaire chez l'animal mobile

Lim-Anna Sieu[1,2], Antoine Bergel[1,3], Elodie Tiran[2], Thomas Deffieux[2], Mathieu Pernot[2], Jean-Luc Gennisson[2], Mickaël Tanter[2], Ivan Cohen[1]

[1] Inserm U1130, CNRS UMR8246, université Pierre et Marie Curie UMCR18, 9, quai Saint-Bernard, 75005 Paris, France ;
[2] Institut Langevin, ESPCI ParisTech, PSL Research university, CNRS UMR7587, Inserm U979, Paris, France ;
[3] Université Paris Diderot, Sorbonne Paris Cité, école doctorale Frontières du Vivant (FdV), Programme Bettencourt, Paris, France.
ivan.cohen@upmc.fr

> La communauté scientifique prend progressivement conscience de l'importance d'aborder les questions de neurophysiologie par le biais d'approches globales qui puissent capturer de façon concomitante le traitement neuronal de l'information et les activités métaboliques du tissu nerveux. Les mécanismes fondamentaux impliqués dans le fonctionnement dynamique des réseaux neuronaux et leurs dysfonctionnements pathologiques ne peuvent être déchiffrés que par leur intégration dans un contexte plus global : celui du codage de l'information par les neurones et de la bioénergétique des tissus reposant sur l'irrigation vasculaire [1]. En fait, les multiples rétroactions entre les activités électriques et métaboliques représentent la règle plutôt que l'exception. Jusqu'à récemment, ces deux facettes du fonctionnement cérébral n'ont été abordées séparément que par manque de méthode appropriée pour accéder à une vision globale. Ceci a donc motivé le développement de stratégies expérimentales mesurant simultanément ces différents paramètres dans des conditions naturelles.

Équilibre et déséquilibres neuro-métaboliques

Afin d'explorer le cerveau sain, il est possible d'utiliser des techniques d'imagerie cérébrale mesurant le métabolisme et identifiant ainsi, de façon non invasive, les aires cérébrales activées par la réalisation d'une tâche cognitive. Ces mesures indirectes de l'activité neuronale reposent sur le fait que la genèse de potentiels d'action dissipe les gradients ioniques de part et d'autre de la membrane cellulaire du neurone, et que les pompes transmembranaires qui rétablissent ces gradients consomment de l'ATP. Lorsqu'une aire cérébrale est activée, une telle consommation énergétique provoque, avec un délai de l'ordre de la seconde, une vasodilatation des artères afin de fournir un surplus de glucose et d'oxygène. Ce mécanisme neuro-vasculaire, nommé « hyperémie[1] fonctionnelle » ou couplage neuro-vasculaire, constitue ainsi une mesure dynamique des activités cérébrales à travers l'ensemble du cerveau.

Réciproquement, un déséquilibre entre l'activité des neurones et le métabolisme tissulaire est associé à un nombre croissant de pathologies. Des défauts de perfusion cérébrale brusques et localisés provoquent des pertes de capacités cognitives spécifiques (une perte de production de la parole, ou aphasie, lors d'un défaut de perfusion de l'aire de Broca par exemple), tandis qu'un défaut chronique et diffus est associé aux démences. Plus récemment, il est apparu que la maladie d'Alzheimer débute par un défaut de couplage neuro-vasculaire, altérant la barrière hémato-encéphalique et diminuant la capacité à éliminer le peptide bêta-amyloïde [2, 3] (**➔**).

(➔) Voir la Synthèse de F. Gosselet *et al.*, *m/s* n° 11, novembre 2011, page 987

Un autre exemple de déséquilibre entre activité vasculaire et activité neuronale est l'épilepsie. Toutes les épilepsies sont liées à une hyperactivité neuronale. Or on sait également qu'un bas débit sanguin cérébral provoque des convulsions. Plus récemment, dans un modèle de crise convulsive, il a été montré que l'inhibition de l'enzyme lactate déhydrogénase, pivot de la régulation métabolique, bloque les crises [4]. Pour les épilepsies avec

---

[1] Augmentation du flux sanguin dans une zone de l'organisme.

DOI : 10.1051/medsci/20163205006

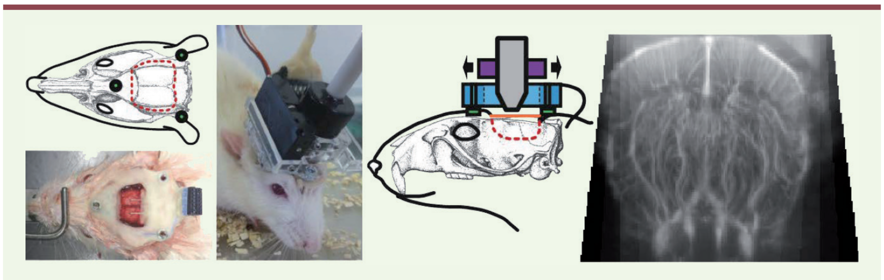

Figure 1. Préparation chirurgicale d'un rat pour EEG-fUS. La calotte osseuse est réséquée, suivant la ligne pointillée rouge en vue de dessus, et remplacée par une prothèse plastique perméable aux ultrasons. Après quelques jours de récupération, trois écrous sont disposés autour de la fenêtre pour fixer la sonde ultrasonore. Le support de la sonde est motorisé, mais le poids total n'empêche pas le mouvement de l'animal. L'échographe relié à la sonde produit un plan image du réseau vasculaire, dont on estime en chaque point les variations de flux sanguin par rapport au niveau moyen. EEG : électroencéphalographie ; fUS : imagerie ultrasonore fonctionnelle (adapté de [10]).

absence[2], il a été découvert que les crises sont régulées par le neuropeptide Y qui est à la fois vasoconstricteur et angiogénique [5].

Concilier EEG avec IRM ou mesures optiques

Afin d'aborder des questions au niveau global neuro-métabolique, un développement technique complexe a consisté à adapter l'électroencéphalographie (EEG), permettant d'enregistrer l'activité électrique à la surface du crâne, pour la rendre compatible avec l'IRM (imagerie par résonance magnétique) [6]. L'IRM fonctionnelle (mesurant le signal BOLD, *blood-oxygen-level dependent*) estime la distribution sanguine en se basant sur l'aimantation de l'hémoglobine [7]. Sa sensibilité et sa résolution augmentent avec l'intensité du champ magnétique utilisé. Cependant, les mesures obtenues sont difficiles à corréler directement avec un enregistrement électrique neuronal, car les champs magnétiques intenses utilisés par l'IRM génèrent des courants électriques induits qui brouillent la détection des activités électriques physiologiques de faible amplitude. Des appareils EEG spécifiques ont donc été développés pour limiter au maximum les artéfacts causés par le champ magnétique. Appliquée au singe, cette technique a permis, par exemple, de montrer que les événements EEG *sharp wave-ripple*[3], supposés aider la coordination entre aires cérébrales, correspondent à une large activation du néocortex et du cortex limbique, et à une inhibition du diencéphale et du mésencéphale [8]. Cette approche a cependant ses limites. Outre la difficulté technique, sa sensibilité est limitée, imposant de moyenner de nombreux événements sans discerner leur variabilité. De plus, l'IRM est un appareil massif, nécessitant un approvisionnement permanent en hélium, dont la disponibilité reste limitée. Enfin, si l'immobilité du sujet dans l'IRM est une nécessité à laquelle il est possible de répondre par sédation chez le rongeur et par contention chez le primate (tout en maintenant la mobilité des membres supérieurs), elle limite cependant considérablement l'éventail des expériences possibles.

Une approche alternative consiste à utiliser l'imagerie optique pour observer les activités vasculaires cérébrales. En effet, l'oxy-hémoglobine est rouge, alors que la déoxy-hémoglobine est plus proche du bleu. En mesurant le spectre d'un faisceau lumineux qui diffuse à travers un volume de tissu, on peut donc estimer son irrigation et le niveau d'oxygénation du sang. Cependant, cette approche est limitée par la forte diffraction de la lumière dans le tissu nerveux, liée aux forts écarts d'indice optique entre le milieu extracellulaire, essentiellement aqueux, et les multiples compartiments contenant des tissus gras, comme la myéline. Des variations métaboliques sont observables à la surface du cortex, en enlevant un volet osseux dans le crâne. Cette approche a permis par exemple d'observer, chez le rat, comment un foyer épileptique provoque un afflux sanguin au détriment des régions voisines [9]. Cette approche est facile à combiner avec des enregistrements EEG, relativement accessible, et permet éventuellement l'étude d'animaux mobiles. Le volume exploré par ce type d'imagerie se limite toutefois à la surface du cortex.

EEG et imagerie ultrasonore fonctionnelle (fUS)

L'imagerie vasculaire cérébrale par Doppler ultrasonore ultrarapide possède des atouts permettant d'étudier l'animal éveillé mobile. Elle présente une excellente sensibilité grâce à un échographe ultrarapide permettant de réaliser plus de 10 000 images par seconde. Elle permet de détecter des fluctuations du débit sanguin 50 fois plus faibles que sur les échographes conventionnels. Avec cet échographe ultrarapide, un plan de 200 microns d'épaisseur peut être observé avec une résolution de 100-120 microns, jusqu'à une profondeur de 15 mm depuis la surface du cerveau, ce qui est suffisant pour étudier l'étendue dorso-ventrale du cerveau du rat adulte. En combinant 200 images consécutives, on peut estimer en chaque point de l'image la

---

[2] Décharge épileptique associée à une altération de la conscience d'environ 10 secondes, une « absence » durant laquelle le regard devient fixe et aucune réaction n'est observée.

[3] Les *sharp-wave ripples* (SPW-R) sont des événements électrophysiologiques, spécifiques de l'hippocampe, composés d'ondes de grande amplitude associées à des oscillations rapides.

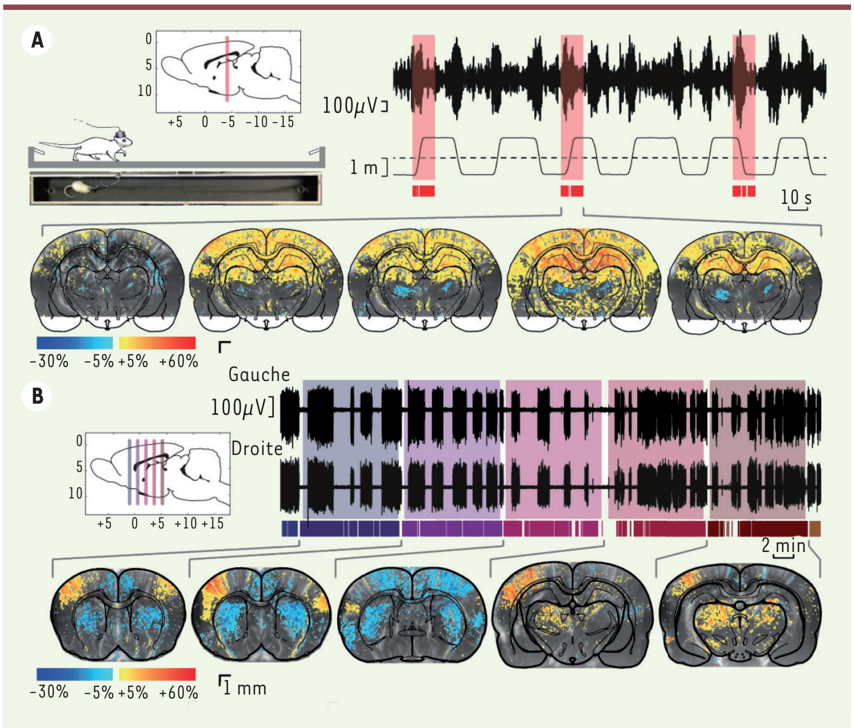

Figure 2. Navigation spatiale et crises épileptiques. Les plans d'imagerie, coronaux, sont indiqués sur les vues de côté du cerveau dans les encadrés. ***A.*** L'animal court d'un bout à l'autre d'un couloir de 2 mètres pour trouver de l'eau. On enregistre l'EEG de l'hippocampe au rythme thêta (6-9Hz, associé au traitement de l'information spatiale) et la position de l'animal. Par fUS, on image un plan fixe incluant l'hippocampe, pendant les périodes de mobilité (boîtes rouges). Les séquences d'images sont alignées par rapport au moment où l'animal passe au milieu de la piste, au maximum du thêta. La série d'images montre la variation de volume sanguin pour des intervalles de temps de allant de -1s à +3s. Hippocampe, cortex somatosensoriel (codant pour les informations provenant de la surface du corps) et thalamus dorsal sont activés, alors que le thalamus ventral est hypoperfusé. ***B.*** Crises d'absence spontanées chez le rat GAERS (*genetic absence epilepsy in rats from Strasbourg*) éveillé, un modèle d'épilepsie absence [11]. La sonde enregistre chaque plan pendant une dizaine de minutes, tandis que des électrodes corticales à droite et à gauche détectent les crises généralisées. La comparaison des images prises pendant ou entre des crises révèle que les crises sont associées à une hyperactivité du cortex somatosensoriel et des aires thalamiques, tandis que des aires corticales voisines et le striatum présentent une vasoconstriction. EEG : électroencéphalographie ; fUS : imagerie ultrasonore fonctionnelle (adapté de [10]).

quantité de particules échogènes en mouvement, autrement dit les cellules sanguines, et particulièrement les globules rouges. Leur concentration étant homogène, la mesure indique le volume local du réseau sanguin, qui est normalisé par rapport à un niveau moyen sur une période de référence. Mis à part les effets liés au battement cardiaque, les variations se produisent sur une échelle de temps de l'ordre de la seconde. La distorsion des ultrasons par la voûte crânienne impose de s'affranchir de la barrière osseuse. Pour la mise au point, nous avons réalisé des expériences aiguës sur le rat, au moyen d'une trépanation. Pour conserver largeur et profondeur du champ d'observation, augmenter la durée d'expérimentation ainsi que l'éventail des protocoles expérimentaux, la calotte crânienne est maintenant remplacée par un film de polymère [10]. Un système mécanique permet d'attacher une sonde miniaturisée sur la tête et de la déplacer à distance à l'aide d'un moteur *(Figure 1)*. Le volume ainsi accessible comprend le système nerveux central situé entre les bulbes olfactifs et le cervelet, qui inclut cortex, thalamus et hippocampe.

Les avantages de la méthode ultrasonore sont significatifs par rapport aux autres techniques d'exploration fonctionnelle. La sensibilité est fortement accrue puisqu'on peut suivre en direct l'hémodynamique fonctionnelle, dans toute sa variabilité. La sonde étant d'une taille de l'ordre du centimètre, avec un câble souple pouvant atteindre 2 mètres, l'animal peut bouger la tête et se mouvoir dans un environnement de test comportemental. Les ultrasons ne perturbent pas le champ électromagnétique généré par l'activité cérébrale, permettant des enregistrements simultanés de l'EEG sans artefact et avec du matériel standard. Enfin le coût et la maintenance de l'équipement sont largement inférieurs à ceux de l'IRM et comparables aux approches optiques.

L'approche globale neuro-métabolique au moyen de l'EEG couplé au fUS permet notamment d'étudier l'activation des aires cérébrales dans des tâches de navigation spatiale, en relation avec les activités rythmiques détectées par l'EEG et associées à la mémoire spatiale *(Figure 2A)*. L'absence de sédation permet de s'intéresser à des pathologies qui y seraient sensibles, comme les épilepsies *(Figure 2B)*. Les prochains développements techniques, tels que l'imagerie simultanée de plusieurs plans ou le couplage aux techniques optiques grâce à la fenêtre transparente, devraient aider à aborder avec une efficacité accrue les questions de codage neuronal de l'information et des pathologies neuro-vasculaires. ◊

Simultaneous recording of neuronal and vascular dynamics in mobile animals

LIENS D'INTÉRÊT

Les auteurs déclarent n'avoir aucun lien d'intérêt concernant les données publiées dans cet article.

RÉFÉRENCES

1. Logothetis N. What we can do and what we cannot do with fMRI. *Nature* 2008 ; 453 : 869-78.
2. Shih AY, Blinder P, Tsai PS, *et al*. The smallest stroke: occlusion of one penetrating vessel leads to infarction and a cognitive deficit. *Nat Neurosci* 2013 ; 16 : 55-63.
3. Gosselet F, Candela P, Cecchelli R, Fenart L. La barrière hémato-encéphalique : une nouvelle cible thérapeutique dans la maladie d'Alzheimer ? *Med Sci (Paris)* 2011 ; 27 : 987-92.
4. Sada N, Lee S, Katsu T, *et al*. Targeting LDH enzymes with a stiripentol analog to treat epilepsy. *Science* 2015 ; 347 : 1362-7.
5. van Raay L, Jovanovska V, Morris MJ, O'Brien TJ. Focal administration of neuropeptide Y into the S2 somatosensory cortex maximally suppresses absence seizures in a genetic rat model. *Epilepsia* 2012 ; 53 : 477-84.
6. Logothetis NK. Intracortical recordings and fMRI: an attempt to study operational modules and networks simultaneously. *Neuroimage* 2012 ; 62 : 962-9.
7. Ogawa S, Lee TM, Kay AR, Tank DW. Brain magnetic resonance imaging with contrast dependent on blood oxygenation. *Proc Natl Acad Sci USA* 1990 ; 87 : 9868-72.
8. Logothetis NK. Neural-event-triggered fMRI of large-scale neural networks. *Curr Opin Neurobiol* 2015 ; 31 : 214-22.
9. Ma H, Zhao M, Schwartz TH. Dynamic neurovascular coupling and uncoupling during ictal onset, propagation, and termination revealed by simultaneous *in vivo* optical imaging of neural activity and local blood volume. *Cereb Cortex* 2013 ; 23 : 885-99.
10. Sieu LA, Bergel A, Tiran E, *et al*. EEG and functional ultrasound imaging in mobile rats. *Nat Methods* 2015 ; 12 : 831-4.
11. Depaulis A, David O, Charpier S. The genetic absence epilepsy rat from Strasbourg as a model to decipher the neuronal and network mechanisms of generalized idiopathic epilepsies. *J Neurosci Methods* 2016 ; 260 : 159-74.

NOUVELLE

De nouveaux types cellulaires identifiés par séquençage haut débit sur cellule unique

Stanislas Quesada[1-3], Philippe Jay[1-3]

[1]CNRS, UMR-5203, Institut de Génomique Fonctionnelle, 141, rue de la Cardonille, Montpellier, F-34094, France ;
[2]Inserm, U1191, Montpellier, F-34094, France ;
[3]Université de Montpellier, Montpellier, F-34000, France.
philippe.jay@igf.cnrs.fr

> Une récente étude [1] a permis de mettre à jour de nouveaux types cellulaires au sein de l'épithélium intestinal. Au-delà de son intérêt en physiologie digestive, ce travail princeps ouvre une voie nouvelle dans la caractérisation de l'identité cellulaire qui pourrait se révéler féconde tant en recherche fondamentale que pour la meilleure compréhension des processus pathologiques.

L'épithélium intestinal : tissu complexe et outil de recherche

L'épithélium intestinal constitue la principale interface de l'organisme avec son environnement extérieur. Sa surface totale atteint les 200 m^2. Il s'agit du tissu disposant du plus haut taux de renouvellement de l'organisme, avec un cycle de renouvellement de 3 à 5 jours [2].

Au niveau de l'intestin grêle, l'épithélium présente une structure en cryptes et villosités *(Figure 1)*. Les cryptes qui sont des invaginations dans le stroma sous-jacent, constituent le compartiment de prolifération. Les villosités, qui sont des protrusions dans la lumière intestinale, ne portent, quant à elles, que les cellules différenciées exerçant des fonctions particulières. Le renouvellement de l'épithélium s'effectue selon un schéma en tapis roulant, du fond des cryptes, où se concentrent les cellules souches, jusqu'à l'apex des villosités où les cellules différenciées se détachent par exfoliation. Les cellules souches donnent naissance à des cellules progénitrices. Ces cellules prolifèrent de manière très active au niveau du compartiment d'amplification transitoire, dans les parois des cryptes. Les cellules produites cessent de proliférer et

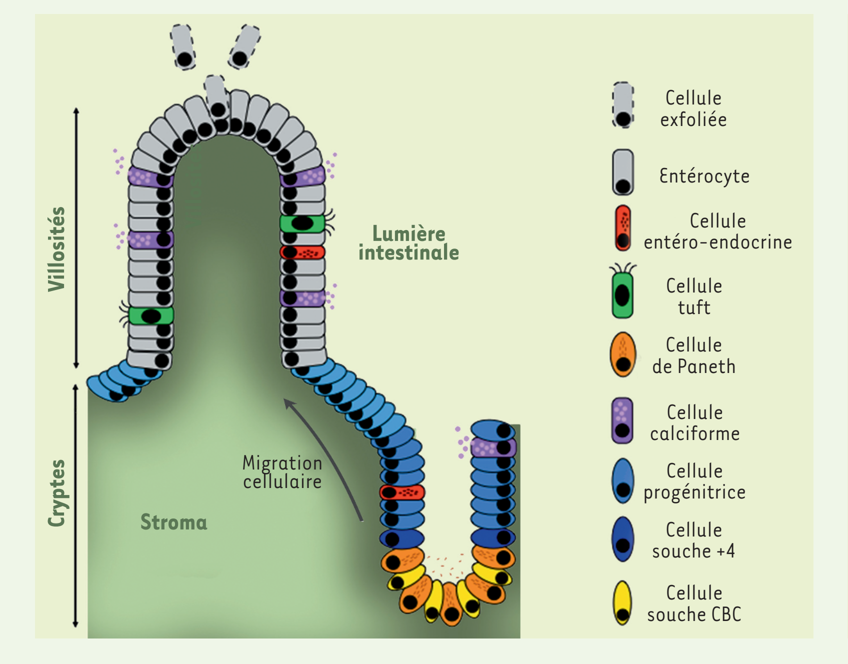

Figure 1. ***Structure de l'épithélium de l'intestin grêle et différents types cellulaires.***

DOI : 10.1051/medsci/20163205007

Appendix E

Supplementary Tables

.

Tissue	Density (kg/m^3)	Speed ($m.s^{-1}$)	Acoustic Impedence $kg/m^2/s$
Grease	0.92×10^3	1446	1.33×10^6
Muscle	1.07×10^3	1542 - 1626	$1.65\text{-}1.74 \times 10^6$
Blood	1.06×10^3	1566	1.66×10^6
Bone	$1.38\text{-}1.81 \times 10^3$	2070 - 5350	$3.75\text{-}7.38 \times 10^6$
Brain	1.03×10^3	1505 - 1612	$1.55\text{-}1.66 \times 10^6$
Liver	1.06×10^3	1566	1.66×10^6
Kidney	1.04×10^3	1567	1.62×10^6
Lung	0.40×10^3	650	0.26×10^6
Air	1.2×10^3	333	0.4×10^6
Distilled Water	1.00×10^3	1480	1.48×10^6

Table E.1 – Acoustic Parameters in different human organs in comparison with air and reference media Adapted from [Berson, 2000].

Frequency (MHz)	Axial Resolution (mm)	Penetration (mm)
2	3	0.77
3.5	170	0.44
5	120	0.31
7.5	80	0.20
10	60	0.15

Table E.2 – Indicative Values of Axial Resolution and Maximal Depth Penetration for various Ultrasound Emission Frequencies. Adapted from [Rohling, 1998].

Theta rhythm is a prominent oscillatory pattern of EEG strongly associated with active locomotion and REM sleep. While it has been shown to play a crucial role in communication between brain areas and memory processes, there is a lack of extensive data due to the difficulty to image global brain activity during locomotion behavior. In this thesis, I developed an approach that combines local field potential recordings (LFP) and functional ultrasound imaging (fUS) to unrestrained rats. For the first time, I could image the hemodynamic responses associated with theta rhythm in most central nervous system (CNS) structures, with high spatial (100 x 100 x 400 μm) and temporal (200 ms) resolutions. During running and REM sleep, hemodynamic variations in the hippocampus, dorsal thalamus and cortices (S1BF, retrosplenial) correlated strongly with instantaneous theta power, with a delay ranging from 0.7 to 2.0 s after theta peak. Interestingly, mid (55-95 Hz) and high gamma (100-150 Hz) instantaneous power better explained hemodynamic variations than mere theta activity, while low-gamma (30-50 Hz) did not. Hippocampal hyperaemia followed sequentially the trisynaptic circuit (dentate gyrus - CA3 region - CA1 region) and was considerably strengthened as the task progressed. REM sleep revealed brain-wide tonic hyperaemia, together with phasic high-amplitude vascular activation starting in the dorsal thalamus and fading in cortical areas, which we referred to as “vascular surges”. Strong bursts of hippocampal high gamma (100-150 Hz) robustly preceded these surges, while the opposite was not true. Taken together, these results reveals the spatio-temporal dynamics of hemodynamics associated with locomotion and REM sleep and suggest a strong link between theta, high-gamma rhythms and brain-wide vascular activity.

Le rythme thêta est un rythme cérébral associé à l’activité locomotrice et au sommeil paradoxal. Bien que son implication dans la communication entre régions du cerveau et processus mnésiques ait largement été démontrée, il persiste un manque de données extensives dû à la difficulté d’imager l’ensemble de l’activité cérébrale dans des conditions naturelles de locomotion et d’exploration. Dans cette thèse, j’ai développé une approche qui combine l’enregistrement des potentiels de champs locaux à l’imagerie ultrasonore fonctionnelle (fUS) sur l’animal en mouvement libre. Pour la première fois, j’ai pu révéler les réponses hémodynamiques associées au rythme thêta dans la plupart des structures du système nerveux central avec de bonnes résolutions spatiale (100 x 100 x 400 μm) et temporelle (200 ms). Pendant la locomotion et le sommeil, les variations hémodynamiques de l’hippocampe, du thalamus dorsal et du cortex (retrosplenial, somatosensoriel) corrèlent fortement avec la puissance instantanée du signal thêta hippocampique, avec un décalage temporel variant de 0.7 s à 2.0 s selon les structures. De manière intéressante, les rythmes gamma hippocampiques moyen (55-95 Hz) et rapide (100-150 Hz) expliquent la variance des signaux hémodynamiques mieux que le seul rythme thêta, alors que le rythme gamma lent (30-50 Hz) est non pertinent. L’hyperémie fonctionnelle de l’hippocampe suit séquentiellement la boucle tri-synaptique (gyrus denté - région CA3 - région CA1) et se renforce considérablement à mesure que la tâche progresse. Lors du sommeil paradoxal, j’ai observé une hyperémie tonique globale ainsi que des activations phasiques de grande amplitude initiées dans le thalamus et terminant dans les aires corticales, que nous avons appelées “poussées vasculaires”. De fortes bouffées d’activité gamma rapide (100-150 Hz) précèdent de manière robuste ces poussées vasculaires, l’inverse n’étant pas vrai. Dans l’ensemble, ces résultats révèlent la dynamique spatio-temporelle des signaux hémodynamiques associés à la locomotion et au sommeil paradoxal et suggèrent un lien fort entre rythmes thêta, gamma rapide et activité vasculaire globale.